

https://dspace.org/

Hot deformation and corrosion behaviour of low-cost + titanium alloys with aluminium, vanadium and iron addictions

Bodunrin, Michael Oluwatosin

2018

https://hdl.handle.net/10539/26579

Bodunrin, Michael Oluwatosin (2018) Hot deformation and corrosion behaviour of low-cost (a+ß) titanium alloys with aluminium,vanadium and iron additions, University of the Witwatersrand, Johannesburg, <http://hdl.handle.net/10539/26579>

Downloaded from a DSpace repository. https://dspace.org/

Hot deformation and corrosion behaviour of low-cost α+β titanium alloys with aluminium, vanadium and iron additions

Michael Oluwatosin Bodunrin

977667

School of Chemical and Metallurgical Engineering

University of the Witwatersrand, Johannesburg



A thesis submitted to the Faculty of Engineering and the Built Environment in fulfilment of the requirements for the degree of *Doctor of Philosophy* in Metallurgical Engineering

October, 2018

Declaration

I, Michael Oluwatosin Bodunrin, hereby declare that this doctoral thesis is my own original work. The thesis is submitted for the award of Doctor of Philosophy in Metallurgical Engineering in the School of Chemical and Metallurgical Engineering, University of the Witwatersrand, Johannesburg, South Africa. This work has not been submitted for any other degree in any other University.

……

Michael Oluwatosin **Bodunrin**

October, 2018

Abstract

This thesis presents information on the development and processing of potentially low-cost α+β Ti-Al-V-Fe alloys. The major problem addressed in this research is the high cost of titanium and its alloys which have limited their widespread use since commercial production began in the 1950s. Two cost reducing research approaches: substitution of low-cost for expensive alloying elements, and the optimisation of hot working parameters were adopted in the development and processing of the low-cost Ti-Al-V-Fe alloys.

In the first approach, two sets of low-cost alloys were developed based on the composition of commercial grade Ti-6Al-4V, the most utilised titanium alloy. The first set of alloys were designed by partial and full substitution of expensive vanadium with iron, a low-cost beta stabiliser, producing Ti-6Al-3V-1Fe, Ti-6Al-2V-2Fe, Ti-6Al-1V-3Fe and Ti-6Al-4Fe alloys. The second set of alloys was designed by both partial replacement of vanadium with iron and the reduction of aluminium content from 6 to 4.5 wt%, producing: Ti-4.5Al-3V-1Fe, Ti-4.5Al-2V-2Fe and Ti-4.5Al-1V-3Fe alloys. The influence of varying composition on the microstructure, hardness and corrosion behaviour was evaluated.

Thermo-Calc software with the TTTi3 database was used to determine the phases present, their relative amounts and transformation temperatures under equilibrium conditions. The alloys were then produced by vacuum arc melting. The microstructure and hardness of as-cast samples and annealed samples of each alloy were evaluated. The results from the Thermo-Calc modelling showed that the beta transus temperature of the alloys reduced with increasing iron content while the volume fraction of the beta phase increased with increasing iron content. When compared to wrought Ti-6Al-4V alloy, the iron-containing alloys had a lower transus temperature but a higher volume fraction of beta phase. The annealed alloy showed a reduction in the volume fraction of beta phase since there was sufficient time for the beta-alpha transformation to take place during annealing.

The hardness of iron-containing alloys increased with increasing iron content in both as-cast and annealed conditions. The hardness of the wrought Ti-6Al-4V alloy was lower than all the iron-containing low-cost alloys except Ti-4.5Al-3V-1Fe. The annealed samples were harder than the as-cast alloys. The increase in hardness was attributed to the Fe content, reduction in lath thickness and oxygen contamination during casting and heat treatment.

The corrosion behaviour of the annealed iron-containing alloys were compared with the wrought Ti-6Al-4V alloy in solutions of sulphuric acid, sodium chloride and mixed sulphuric acid /sodium chloride. Open circuit potential and linear polarisation measurements were carried out. Ti-6Al-

1V-3Fe and Ti-4.5Al-1V-3Fe alloys had superior corrosion resistance to commercial Ti-6Al-4V in both sulphuric acid and sodium chloride solutions.

Cost analysis on the low-cost alloys showed that about 7% ($175.6/100 kg) lower cost savings can be achieved by replacing 3 wt% V with Fe in Ti-6Al-4V. The advantage of cost with the improved hardness and corrosion resistance was used as a basis for selecting Ti-6Al-1V-3Fe and Ti-4.5Al-1V-3Fe for further work, *i.e.* optimisation of hot working parameters as the second cost reducing approach.

In the second approach, the two selected experimental alloys were machined to rectangular samples and subjected to isothermal compression testing at varied temperatures (750 - 950°C) and strain rates (0.001 - 10 s^{-1}) on a Gleeble 3500 thermomechanical simulator. The analysis of stress-strain curve and processing maps were used to determine the optimum processing condition during hot working. The activation energy for hot working of the alloys was determined using the hyperbolic-sine constitutive equation. The commercial grade Ti-6Al-4V alloy with a complex initial microstructure was also investigated. The flow curves exhibited distinct features under different deformation conditions. This indicated that flow behaviour is dependent on process variables such as strain rate, deformation temperatures, total strain and initial microstructures.

Processing maps showed that the optimum processing conditions for the Ti-6Al-4V, Ti-4.5Al-1V-3Fe and Ti-6Al-1V-3Fe alloys were ~940°C/1 s^{-1}, ~900°C/0.1 s^{-1} and ~900°C/0.01 s^{-1} respectively. Microstructural analysis revealed that the dominant softening mechanisms at the identified optimum processing conditions in both Ti-6Al-1V-3Fe and Ti-4.5Al-1V-3Fe alloys were dynamic recrystallisation of the prior beta grains and dynamic globularisation of the alpha phase respectively. Dynamic globularisation occurred much faster and easier in the lower aluminium alloy Ti-4.5Al-1V-3Fe (0.1 s^{-1}) than in the Ti-6Al-1V-3Fe alloy (0.01 s^{-1}). The activation energy for hot working of the alloys was higher in Ti-6Al-4V and Ti-6Al-1V-3Fe than in Ti-4.5Al-1V-3Fe. Some of the regions of instability were identified as ≥ 935°C/0.05 - 0.1 s^{-1} for Ti-6Al-4V, 750 - 780°C/1.2 - 10 s^{-1} for Ti-4.5Al-1V-3Fe and 750 - 870°C/0.9 - 10 s^{-1}, Ti-6Al-1V-3Fe. The microstructures of the samples deformed in these regions revealed non-uniform deformation, voids and cracking as the unsafe softening mechanisms. These regions should be avoided when processing the alloys to save cost and prevent waste of materials.

Dedication

This work is dedicated to the South Africa titanium industry and to everyone who has contributed knowledge to the advancement of light alloys. It is my wish that one day the industry will produce local grade alloys that will be available for the use of mankind.

Acknowledgements

“Agbajo owo la fin soya, ajeji owo kan ko gbe eru de ori” meaning ‘we beat the chest with our five fingers combined and a single hand at times cannot lift up a heavy luggage to the head or its destination - An old Yoruba adage.

I give glory to God Almighty. I do not have enough words to describe my Creator, foundation, my source of wisdom, strength, good health and sustenance. I will ceaselessly thank Jehovah for His mercies endure forever.

It will be totally unacceptable if I do not express my profound gratitude to my supervisors and career advisers, Prof. Lesley H. Chown, Prof. Josias W. van der Merwe and Prof. Kenneth K. Alaneme.

Prof. Chown, a woman that is more than a supervisor to me, I cannot thank you enough for your patience, support, love, understanding, empathy, corrections and constructive criticism that have seen me this far. I thank you for all the sacrifices you have made to ensure that I complete this doctoral programme.

Prof. van der Merwe, my amiable co-supervisor for treating me with respect at all times. Your contributions to the entire success of this programme cannot be overemphasized. Thanks for always helping out in the lab when necessary and your immense contributions to the corrosion aspect of my work. I will never forget the 8hours’ drive we had in Cape Town when I arrived in 2014 and the swimming classes you offered me in Ghana in May, 2017. To me these experiences are beyond what one gets from a supervisor-student relationship. Thank you!

Prof. Alaneme, my supervisor from another AMSEN node, thanks for encouraging me to follow this path. You picked me amongst many others and you laid the foundation that my career thrives on today. Thanks for your advice and contributions to my work.

There is actually no alternative way of describing an unforgivable sin should I fail to express my appreciation to Prof. Cornish and the entire staff of the DST-NRF Centre of Excellence in Strong Materials (CoE-SM) and the African Materials Science and Engineering Network (AMSEN). Prof. Lesley A. Cornish, Director of the DST-NRF CoE-SM and AMSEN, thank you for bringing me to Wits University for my doctoral studies and for providing the mentorship that has led to the success of many postgraduate students including me. I appreciate all your timely comments, corrections and contributions each time my work has to pass through your desk. Thanks for the

outstanding role model that you are. I will always cherish the friendly hours I had with your family in the United Kingdom.

Ms Casey Sparkes, the manager DST-NRF CoE-SM and AMSEN, your love and support towards me is indescribable. You believed in me right from the very start and during the most difficult times, your faith in me was sufficient to keep me going. Thank you so much.

Ms Jacqueline Jacobs and Mrs Marina Labuschagne, words are not enough to express sincere gratitude for the support I enjoy from you, especially when I needed to attend several conferences to present my research work.

Mrs Moira Messenger, your faith in me was established *ab initio*. You said I should let you know once I finish the programme. You never thought I would fail or drop out. Thanks so much. Those words mean a lot to me.

My sincere gratitude goes to all the members of staff in the School of Chemical and Metallurgical Engineering, University of the Witwatersrand for providing me with a good environment to carry out my research work.

I would like to extend my appreciation to the entire staff of the Department of Metallurgical and Materials Engineering, Federal University of Technology Akure, Ondo State, Nigeria. Thanks so much for providing me with the platform to pursue my doctoral degree.

Prof. J.O. Borode, Prof. J. A. Omotoyinbo and Prof. B.O. Adewuyi, I appreciate you for your fatherly support and encouragement all through my doctoral programme.

I will not forget to mention the assistance of Mintek, especially Mr Edson Muhuma for assisting me with casting of my alloys. Thank you so much.

It will be extremely difficult to mention all my friends and mentees that have contributed to my successful stay at the University of the Witwatersrand. It is very true to say that without you, there is no me. Adefunke, Ayo, Abejide, Mac-Gregor, Uzochuckwu, Xiluva, Sarah, Sarah Rich, Biola, Ash, Nnana, Bukola, Fortunate, Liberty, Desmond, Dawid, Steva, Ezinne, Moshood, Adaraja, Chipozya, Mats'olo, Ranti and the entire AMSEN family. I say a very big thank you.

Special thanks to my mentors and career adviser, Prof. and Mrs Daramola, Prof and Mrs Okosun, Prof. Olubambi, Dr and Prof. Mrs Akinlabi, Dr Nthabiseng, Pastor Gbenga and Titi Ojo. Your support and prayers got me this far.

To my parents Mr and Mrs Bodunrin; my siblings Ayotunde and Damilola Bodunrin; my in-laws Mr Dayo Adeniji, Mrs Ohikhueme and Mrs Theresa Jigide, my guardians Mr and Mrs Babalola, I say thank you. I would not have come this far without you all.

Lastly to my beloved wife Rachael and daughter Lesley, I cannot find any words to adequately describe my feelings. You two are the best things that have ever happened to me.

Contributions from this study

Journal Articles

- Bodunrin, M.O., Chown, L.H., van der Merwe, J.W., Alaneme, K.K. (2018). Corrosion behaviour of Ti-Al-xV-yFe experimental alloys in 3.5 wt% NaCl and 3.5M H_2SO_4. *Mater. Corros*, 1-11.https://doi.org/10.1002/maco.201709709
- Bodunrin, M.O., Chown, L.H., van der Merwe, J.W., Alaneme, K.K. Hot deformation behaviour of Ti-6Al-4V. *International Journal of Materials Forming (IJFO)*.[in press]

Conference Proceedings

- Prozesky, D.J., Bodunrin, M.O., Chown, L.H., 2017. Hot-deformation behaviour of α+β Ti-Al-V-Fe experimental alloys. *AIP Conf. Proc*. 1896, 160019. https://doi.org/10.1063/1.5008194

Science Communication Article

- Bodunrin, M.O., 2016. Titanium: metal of the future – *Science Today*. https://sciencetoday.co.za/2016/11/14/titanium-metal-of-the-future/

Details of these publications, oral and poster presentations given, and awards stemming from this PhD work are detailed in Appendix J.

Table of Contents

Chapter 1: Introduction 1

1.1 Background and Problem Statement 1

1.2 Justification of the Research 4

1.3 Research Questions 5

1.4 Research Hypothesis 5

1.5 Aim and Objectives 6

1.6 Thesis Structure 6

Chapter 2: Literature Review 8

2.1 Overview of titanium alloys 8

2.1.1 History of titanium metal 8

2.1.2 Applications of titanium alloys 9

2.1.3 Classification of titanium alloys 9

2.1.4 Alpha alloys 11

2.1.5 Beta alloys 12

2.1.6 α+β alloys 14

2.1.7 Correlation between microstructure and properties of α+β alloys 19

2.2 Production of titanium alloys – an overview 23

2.2.1 Ingot production processes 23

2.2.2 Primary conversion process 26

2.2.3 Secondary processing of titanium alloys 27

2.3 Research on low-cost titanium alloys 29

2.3.1 Substitution of alloying elements 30

2.3.2 Optimisation of Hot Working and Machining Processes 34

2.3.3 Classification of constitutive models 44

2.3.4 Construction and interpretation of processing maps 46

2.3.5 Hot deformation mechanisms- processing maps and microstructural validation 50

2.4 Microstructural evolution during hot working 56

2.5 Corrosion behaviour of titanium alloys 60

2.5.1 Overview 60

2.5.2 Corrosion behaviour in acidic solution 62

2.5.3 Corrosion behaviour in sodium chloride and physiological solutions 67

2.5.4 Summary 68

2.6 Summary of the literature review and identifying the research gap 72

2.7 Design Consideration 73

Chapter 3: Experimental Procedure 75

3.1 Materials 75

3.2 Development of Ti-Al-V-Fe experimental alloys 75

3.2.1 Selection of composition for Ti-Al-V-Fe experimental alloys....75
3.2.2 Thermo-Calc Modelling....76
3.2.3 Powder compaction....76
3.2.4 Casting....76
3.2.5 Cutting....76
3.2.6 Heat Treatment....76
3.2.7 Cost of starting materials....77
3.3 Metallography....78
3.3.1 Mounting....78
3.3.2 Grinding and Polishing....78
3.3.3 Etching....78
3.4 Characterisation of the alloys....79
3.4.1 Microstructural analysis....79
3.4.2 X-ray diffraction....80
3.5 Screening of the alloys....80
3.5.1 Hardness testing....80
3.5.2 Corrosion Testing....80
3.6 Hot compression testing....81
3.7 Analysis of stress-strain data....83
3.7.1 Processing Maps....83
Chapter 4: Development of experimental Ti-Al-V-Fe alloys.... 85
4.1 Thermo-Calc Modelling....85
4.2 Compositional Analysis....85
4.3 Phase Analysis....86
4.4 Optical micrographs and SEM images....90
4.5 Hardness....99
4.6 Discussion: Influence of composition and heat treatment....99
4.6.1 Alloying elements – iron and vanadium....99
4.6.2 Alloying element - aluminium....104
4.6.3 Annealing....107
4.6.4 Oxygen as an impurity element....108
4.7 Summary of results....108
Chapter 5: Corrosion behaviour of Ti-Al-V-Fe experimental alloys.... 110
5.1 H_2SO_4 Environment....110
5.2 NaCl Environment....119
5.3 Sulphuric Acid + Sodium Chloride Environment....123
5.4 Discussion....125
5.5 Summary of Results....130

Chapter 6: Influence of a complex initial micro-structure on the hot deformation behaviour of commercial Ti-6Al-4V 131

6.1 Scope 131

6.2 Flow stress 131

6.2.1 Strain rate of $0.01s^{-1}$ 131

6.2.2 Strain rate of $0.1\ s^{-1}$ 132

6.2.3 Strain rates of $1\ s^{-1}$ and $10\ s^{-1}$ 132

6.3 Adiabatic Heating 134

6.4 Processing maps and microstructural validation 137

6.4.1 Stable deformation region 140

6.4.2 Unstable deformation region 142

6.5 Microstructural Evolution 143

6.5.1 Dynamic globularisation of alpha grains 144

6.5.2 Deformation Heating 149

6.5.3 Phase Transformation 151

6.6 Summary 153

Chapter 7: Hot working of experimental Ti-6Al-1V-3Fe and Ti-4.5Al-1V-3Fe alloys 155

7.1 Scope 155

7.2 Analysis of flow stress for experimental Ti-Al-V-Fe alloys 155

7.2.1 Adiabatic corrections 161

7.3 Processing maps and validation 162

7.3.1 Power dissipation maps 162

7.3.2 Prediction of instability domain at a strain of 0.6 166

7.3.3 Microstructural validation of the processing maps 167

7.4 Microstructural Evolution 170

7.4.1 Influence of deformation temperatures 170

7.4.2 Influence of strain rate 177

7.5 Summary 180

7.5.1 Stress-strain behaviour 180

7.5.2 Processing maps 180

7.5.3 Microstructural evolution 181

Chapter 8: Activation energy for hot working of Ti-6Al-4V, Ti-6Al-1V-3Fe and Ti-4.5Al-1V-3Fe alloys 182

8.1 Hyperbolic-sine equation for derivation of activation energy - an overview 182

8.2 Determination of activation energy (Q_{HW}) and constitutive constants 185

8.3 Summary 190

8.4 Implication of the research findings 192

Chapter 9: Conclusions and Recommendations 194

9.1 Conclusions 194
9.2 Suggestions for further research 198

Chapter 10: References 199

Appendix A: Thermo-Calc command macro file(.tcm) for alloying simulation 220

Appendix B: Cost analysis on the compositions of theexperimental alloys 221

Appendix C: Gleeble script language for isothermal compression testing 222

Appendix D: Flow stresses of rectangular and cylindrical samples 227

Appendix E: Thermo-Calc simulations 228

Appendix F: Temperature increase of Ti-6Al-4V during deformation 232

Appendix G: Supplementary results for hot compression testing of Ti-6Al-4Valloy 233

Appendix H: Hot deformation behaviour of Ti-6Al-*x*V-*y*Fe alloys (Prozesky *et al.* 2017) and calculations from experimental data for Ti-6Al-1V-3Fe and Ti-4.5Al-1V-3Fe alloys 235

Appendix I: Supplementary results from corrosion testing 246

Appendix J: Awards, presentations and publications 250

List of Figures

Figure 2.1: Components made from titanium alloys (Salem *et al.*2014; Liszewski, 2015). 10

Figure 2.2: Structure of titanium: (a) hexagonal closed packed of alpha phase, (b) body centred cubic of beta phase (Leyens and Peters, 2003). 10

Figure 2.3: Classification of beta stabilising elements (Yang, 2015). 13

Figure 2.4: Common microstructures developed in α+β titanium alloys: (a) fully lamellar (b) fully equiaxed and (c) bimodal (Salem *et al.*,2014). 15

Figure 2.5: Processing steps for obtaining fully lamellar microstructures of α+β titanium alloys (Lütjering and Williams, 2007). 15

Figure 2.6: Processing steps for beta processed fully lamellar microstructures of α+β titanium alloys (Lütjering and Williams, 2007). 16

Figure 2.7: Processing steps for developing a bimodal structure (Lütjering, 1999). 16

Figure 2.8: Processing steps for developing an equiaxed structure of α+β titanium alloys slowly cooled in the bimodal phase region (Lütjering and Williams, 2007). 17

Figure 2.9: Processing steps for developing an equiaxed structure of α+β titanium alloys recrystallised at low temperatures (Lütjering and Williams, 2007). 17

Figure 2.10: Processing steps for obtaining mill-annealed structures (Lütjering and Williams, 2007). 18

Figure 2.11: Mill-annealed structure in Ti-6Al-4V alloy (Gil *et al.*, 2001) 19

Figure 2.12: Relationship between cooling rate and elongation of Ti-6Al-4V. 20

Figure 2.13: Flow stress showing different stages during hot deformation.(Sajadifar and Yapici, 2014). 45

Figure 2.14: Schematic diagram of a Raj map (Kutumarao and Rajagopalachary, 1996). 47

Figure 2.15: Schematic representation of (a) a non-linear power dissipater and (b) an ideal power dissipator (Omar and Prado, 2012). 49

Figure 2.16: Processing map for AZ31 magnesium alloy showing a region of instability (Rao *et al.*, 2012) 50

Figure 2.17: (a) Schematic diagram of dynamic globularisation of alpha laths in Ti-6Al-4V (Seshacharyulu *et al.*, 2002). (b) TEM image showing an early stage of globularisation of alpha laths. The arrows show cusping of the alpha phase at the alpha and beta subgrains (Balachandran *et al.*, 2017). 52

Figure 2.18: Microstructural manifestation during hot deformation of aTi-6Al-4V alloy (Seshacharyulu *et al.*, 1999; Motyka *et al.*, 2012). 54

Figure 3.1: Procedure for alloy development. 75

Figure 3.2: Hot compression samples: (a) cylindrical, and (b) rectangular. 82

Figure 3.3: Hot compression testing of titanium alloy in the Gleeble 3500®. 82

Figure 3.4: Schematic diagram of the isothermal compression testing schedule. 82

Figure 4.1: XRD patterns of as-cast Ti-6Al-*x*V-*y*Fe and wrought Ti-6Al-4V alloys. 87

Figure 4.2: XRD patterns of annealed Ti-6Al-*x*V-*y*Fe and wrought Ti-6Al-4V alloys. 87

Figure 4.3: XRD patterns of as-cast Ti-4.5Al-*x*V-*y*Fe and wrought Ti-6Al-4V alloys. 88

Figure 4.4: XRD patterns of annealed Ti-4.5Al-*x*V-*y*Fe and wrought Ti-6Al-4V alloys. 88

Figure 4.5: EDX spectrum of α phase in Ti-6Al-3V-1Fe alloy. 90

Figure 4.6: EDX spectrum of β phase in Ti-6Al-3V-1Fe alloy. 90

Figure 4.7: Optical micrographs of as-cast and annealed alloys showing Widmanstätten α-laths embedded within prior beta grains. Blue arrows are pointing to prior beta grain boundaries. 92

Figure 4.8: Relationships between Fe content and prior beta grain size in a) Ti-6Al-*x*V-*y*Fe and b) Ti-4.5Al-*x*V-*y*Fe alloys..... 93

Figure 4.9: SEM-BSE images of as-cast alloys with contrast and brightness adjustment (left) and the same images processed using imageJ software (right), showing alpha laths (dark) in a retained beta (light) matrix. 95

Figure 4.10: SEM-BSE images of annealed samples (left) and the same images processed using imageJ software (right), showing α laths (dark) and retained interplatelet β (light). 97

Figure 4.11: Relationship between Fe content and β phase fraction in as-cast and annealed alloys: a) Ti-6Al-*x*V-*y*Fe and b) Ti-4.5Al-*x*V-*y*Fe. 98

Figure 4.12: Relationship between Fe content and α lath thickness in a) Ti-6Al-*x*V-*y*Fe and b) Ti-4.5Al-*x*V-*y*Fe alloys. 98

Figure 4.13: Relationship between Fe content and hardness in a) Ti-6Al-*x*V-*y*Fe and b) Ti-4.5Al-*x*V-*y*Fe alloys..... 99

Figure 4.14: Beta transus temperatures obtained from Equation 4.1 and Thermo-Calc, without O and N..... 101

Figure 4.15: As-cast experimental alloys - influence of Al content on the beta phase fraction..... 105

Figure 4.16: Annealed experimental alloys - influence of Al content on the beta phase fraction. 105

Figure 4.17: Influence of Al content on prior beta grain size of as-cast experimental alloys..... 106

Figure 4.18: Comparison between the hardness of Ti-6Al-*x*V-*y*Fe and Ti-4.5Al-*x*V-*y*Fe alloys.. 106

Figure 5.1: Variation of open circuit potential measurement in 3.5 M H_2SO_4 with time for a) Ti-6Al-*x*V-*y*Fe and b) Ti-4.5Al-*x*V-*y*Fe alloys..... 110

Figure 5.2: SEM-SE images showing the surface of samples after immersion in 3.5 M H_2SO_4 at OCP for 3600 s, before cleaning: a) Ti-6Al-4V, b)Ti-6Al-3V-1Fe, c)Ti-6Al-2V-2Fe, d) Ti-6Al-1V-3Fe, e) Ti-6Al-4Fe,f) Ti-4.5Al-3V-1Fe, g) Ti-4.5Al-2V-2Fe and h) Ti-4.5Al-1V-3Fe..... 112

Figure 5.3: EDX spectra of selected experimental alloys after immersion in 3.5 M H_2SO_4 at OCP for 3600 s, before cleaning: a) Ti-6Al-3V-1Fe, b) Ti-6Al-1V-3Fe, c) Ti-6Al-4Fe and d) Ti-4.5Al-2V-2Fe. 113

Figure 5.4: SEM-SE images showing the surface of selected samples after immersion in 3.5 M H_2SO_4 at OCP for 3600s, after cleaning: a) Ti-6Al-4V, b) Ti-6Al-3V-1Fe, c) Ti-6Al-4Fe, d) Ti-4.5Al-2V-2Fe and e) Ti-4.5Al-1V-3Fe. 114

Figure 5.5: EDX spectra of selected experimental alloys after immersion in 3.5 M H_2SO_4 at OCP for 3600 s: a) Ti-6Al-3V-1Fe, b) Ti-6Al-4Fe, c) Ti-4.5Al-2V-2Fe and d) Ti-4.5Al-1V-3Fe (after cleaning). 115

Figure 5.6: EDX spot analysis on the uncorroded α-Ti phase (*i.e.* with no Fe) in Ti-6Al-4Fe experimental alloy. 116

Figure 5.7: EDX spot analysis on the corroded β-Ti phase (*i.e.* with Fe) in Ti-6Al-4Fe experimental alloy. 116

Figure 5.8: Potentiodynamic polarisation for 6 wt% Al alloys immersed in 3.5 M H_2SO_4 solution at 25°C.The arrows point to transient currents. 117

Figure 5.9: Polarisation curves for 4.5 wt% Al alloys immersed in 3.5 M H_2SO_4 solution at 25°C. Arrow points to transient current..... 119

Figure 5.10: Variation of OCP measurements for a) Ti-6Al-*x*V-*y*Fe and b) Ti-4.5Al-*x*V-*y*Fe alloys in 3.5 wt% NaCl solution at room temperature..... 120

Figure 5.11: Polarisation curves for Ti-6Al-xV-yFe alloys immersed in 3.5 wt% NaCl solution at 25°C. Arrow points to transient current. 121

Figure 5.12: Polarisation curves for Ti-4.5Al-*x*V-*y*Fe alloys immersed in 3.5 wt% NaCl solution at 25°C. The red arrow points to distinct transpassive behaviour, while the black arrow points to suppressed transpassive behaviour..... 122

Figure 5.13: Variation of OCP for Ti-6Al-4V and selected experimental alloys in 3.5M H_2SO_4+1.75wt% NaCl at 25°C. 124

Figure 5.14: Polarisation curves for Ti-4.5Al-*x*V-*y*Fe alloys immersed in 3.5 M H_2SO_4 + 1.75 wt% NaCl solution at 25°C. 124

Figure 5.15: Corrosion rates against nominal Fe for experimental alloys immersed in 3.5 M H_2SO_4 solution at 25°C..... 129

Figure 5.16: Corrosion rates against nominal Fe for experimental alloys immersed in 3.5 wt% NaCl solution at 25°C..... 129

Figure 6.1: True stress-strain curves obtained by uniaxial compression testing of Ti-6Al-4V alloy in the temperature range of 750 - 950°C and at strain rates of: (a) 0.01 s^{-1}, (b) 0.1 s^{-1} , (c) 1 s^{-1} and (d) 10 s^{-1}. 133

Figure 6.2: Strain versus time profile showing that strain rates changed at low strain (~0.02) when the Ti-6Al-4V sample was deformed at 750°C/0.01 s^{-1}. 134

Figure 6.3: Effect of testing temperature and strain rate on the peak stress of Ti-6Al-4V. 135

Figure 6.4: Programmed (expected) temperatures *vs.* the actual (measured) temperatures as a function of strain for deformation of Ti-6Al-4V at: a) 750°C/10 s^{-1} and b) 800°C/1 s^{-1} for the alloy Ti-6Al-4V. 136

Figure 6.5: Measured temperature increase against programmed deformation temperatures at strain rates of: a) 1 $s^{-1}$and b) 10 s^{-1} for the alloy Ti-6Al-4V. 136

Figure 6.6: Stress-strain curves for corrected and uncorrected flow stress at a) 750°C/10 s^{-1} and b) 800°C/1 s^{-1} for the alloy Ti-6Al-4V. 137

Figure 6.7: Power efficiency map at a strain of 0.2. 139

Figure 6.8: Microstructure of the as-received Ti-6Al-4V bar in the mill-annealed condition a) optical micrograph and b) SEM-BSE image showing alpha grains and a network of intergranular beta. 139

Figure 6.9: Optical micrographs of Ti-6Al-4V deformed to a total strain of 0.2: a) region A:780°C/1 s^{-1} and b) region B:920°C/1 s^{-1}, showing lath bending and serrated alpha in a) and globular alpha in b). 139

Figure 6.10: Processing maps of Ti-6Al-4V alloys at total strains of: a) 0.5 and b) 0.6, showing the safe (hatched) and unsafe (red) deformation areas. 141

Figure 6.11: Optical micrographs (a & b) and SEM-BSE images (c & d) of Ti-6Al-4V microstructures deformed in the stable region: a & c) 900°C/0.01 s^{-1}, b& d) 950°C/1 s^{-1}. The red arrows show globular alpha grains, while the blue arrows show transformed beta. 142

Figure 6.12: Microstructure of Ti-6Al-4V deformed in the unstable region, showing non-equiaxed grains as an indication of heterogeneous deformation: a) optical micrograph and b) SEM-BSE image. 143

Figure 6.13: Optical micrographs of Ti-6Al-4V samples deformed at a strain rate of 0.01 s^{-1} and temperatures of: a) 800°C b) 850°C c) 900°C and d) 950°C showing serrated α, large and fine globular α at temperature <950°C (light phase- red arrow) and transformed β at 950°C (dark phase- blue arrow). 145

Figure 6.14: Optical micrographs of Ti-6Al-4V samples deformed at 1 s^{-1} strain rate: a) 800°C b) 850°C c) 900°C and d) 950°C. The red arrows show globular α, while the blue arrows show transformed β 146

Figure 6.15: Optical micrographs of deformed Ti-6Al-4V samples at 10s^{-1} a)800°C, b)850°C, c)900°C and d) 950°C. The green arrows point to serrated α grains, red to globular α and blue to transformed β. 149

Figure 6.16: SEM-BSE images of Ti-6Al-4V samples deformed at 950°C at strain rates of a) 0.01 s^{-1} b) 1 $s^{-1}$and c) 10 s^{-1} showing primary α (globular - red arrow) and transformed β - blue arrow. 152

Figure 7.1: True stress-strain curves obtained by rectangular axial compression testing of Ti-6Al-1V-3Fe in the temperature range of 750 - 950°C and at strain rates of: a) 10 s^{-1}, b) 1 s^{-1}, c) 0.1 s^{-1}, d) 0.01 s^{-1} and e) 0.001 s^{-1}. 157

Figure 7.2: True stress-strain curves obtained by rectangular axial compression testing of Ti-4.5Al-1V-3Fe in the temperature range of 750 - 950°C and at strain rates of: a) 10 s^{-1}, b) 1 s^{-1}, c) 0.1 s^{-1}, d) 0.01 s^{-1} and e) 0.001 s^{-1}. 158

Figure 7.3: The effect of testing temperature and strain rate on the peak stress of: a) Ti-6Al-1V-3Fe and b) Ti-4.5Al-1V-3Fe alloys. 159

Figure 7.4: Measured and programmed temperature against strain for (a) Ti-6Al-1V-3Fe at 750°C/10 s^{-1} and (b) Ti-4.5Al-1V-3Fe at 800°C/1 s^{-1}. 161

Figure 7.5: Corrected and measured flow stress as a function of strain for: a) Ti-6Al-1V-3Fe at 750°C/10 s^{-1} and b) Ti-4.5Al-1V-3Fe at 800°C/1 s^{-1}. 162

Figure 7.6: Power dissipation efficiency maps for Ti-6Al-1V-3Fe alloys at a strain of: a) 0.1, b) 0.2, c) 0.3, d) 0.4, e) 0.5 and f) 0.6. 164

Figure 7.7: Power dissipation efficiency maps for Ti-4.5Al-1V-3Fe alloys at a strain of: a) 0.1, b) 0.2, c) 0.3, d) 0.4, e) 0.5 and f) 0.6. 165

Figure 7.8: Processing maps at a strain of 0.6 for: a) Ti-6Al-1V-3Fe and b) Ti-4.5Al-1V-3Fe alloys. The red regions are regions of unsafe deformation, A and B are safe regions with the highest dissipation efficiency. 167

Figure 7.9: Initial microstructures for showing a basket-weave Widmanstätten structure in large prior beta grains. Ti-6Al-1V-3Fe: a) Optical, b) SEM-BSE; and Ti-4.5Al-1V-3Fe: c) optical and d) SEM-BSE. 168

Figure 7.10: Final microstructure of Ti-6Al-1V-3Fe deformed samples. 900°C/0.1 s^{-1}: a) optical c) SEM-BSE , 750°C/10 s^{-1}: b) optical and d) SEM-BSE. 169

Figure 7.11: Final microstructure of deformed samples for Ti-4.5Al-1V-3Fe. 900°C/0.01 s^{-1}: a and e) optical c) SEM-BSE , 750°C/10 s^{-1}: b) optical - and d) SEM-BSE. 171

Figure 7.12: SEM-BSE images of Ti-6Al-1V-3Fe alloy deformed at a strain rate of 10 s^{-1} and deformation temperatures of: a) 750°C, b) 800°C, c) 850°C, d) 900°C, e) 950°C and f) 950°C. 173

Figure 7.13: SEM-BSE images of Ti-6Al-1V-3Fe alloy deformed at a strain rate of 0.1s^{-1} and deformation temperatures of:a) 750°C b) 800°C c) 850°C d) 900°C e) 950°C and f) 950°C (higher magnification). Black arrows show the bending of lath and red arrows show globular α. 174

Figure 7.14: SEM-BSE images of Ti-4.5Al-1V-3Fe alloy deformed at a strain rate of 10 s^{-1} and deformation temperatures of:a) 750°C b) 800°C c) 850°C d)900°C and e) 950°C. Arrow points to bending and rotation of laths. 175

Figure 7.15: SEM-BSE images ofthe Ti-4.5Al-1V-3Fe alloy deformed at a strain rate of 0.01 s^{-1} and deformation temperatures of: a) 750°C, b) 800°C, c) 850°C, d) 900°C and e) 950°C. The red arrows are pointing to globular α. 176

Figure 7.16: SEM-BSE images of Ti-6Al-1V-3Fe alloy deformed at a temperature of 900°C and strain rates of: a) 10 s^{-1}, b) 1 s^{-1}, c) 0.1 s^{-1}, d) 0.01 s^{-1} and e) 0.001 s^{-1}. The arrows point to globular α. 178

Figure 7.17: SEM-BSE images of Ti-4.5Al-1V-3Fe alloy deformed at 900°C and strain rates of: a) 10s^{-1},b) 1s^{-1},c) 0.1 s^{-1}, (d) 0.1s^{-1},(higher mag.),e) 0.01 s^{-1},f) 0.01 s^{-1}(higher mag.) and g) 0.001 s^{-1}. The arrows point to globular α. 179

Figure 8.1: Determination of material constants for Ti-6Al-4V: a) ń, b) β, c) n, d) Q = Rn S and (e) A. 188

Figure 8.2: Determination of material constants for Ti-6Al-1V-3Fe: a) ń, b) β, c) n, d) Q = Rn S and e) A. 189

Figure 8.3: Determination of materials constants for Ti-4.5Al-1V-3Fe: a) ń, b) β, c) n, d) Q = Rn S and e) A. 190

List of Tables

Table 2.1: ASTM grades of alpha titanium alloys (Lütjering and Williams, 2007). 12

Table 2.2: Common beta titanium alloys (Weiss and Semiatin, 1998; and Lütjering and Williams, 2007). 14

Table 2.3: Important processing parameters for developing fully lamellar microstructures. 15

Table 2.4: Important processing parameters for a fully equiaxed structure (Lütjering and Williams, 2007). 18

Table 2.5: Melt related defects and their possible causes (Lütjering and Williams, 2007). 25

Table 2.6: Previous studies on the constitutive modelling of hot working of titanium alloys..... 37

Table 2.7: Previous studies on processing maps of titanium alloys..... 40

Table 2.8: Models for constructing a Raj map (Kutumarao and Rajagopalachary, 1996)..... 48

Table 2.9: Previous studies on microstructural evolution during hot working of titanium alloys..... 57

Table 2.10: Previous studies on corrosion behaviour of titanium alloys immersed in sodium chloride and physiological solutions. 70

Table 3.1: Targeted compositions of the experimental alloys, in wt%. 75

Table 3.2: Price list for Ti, Al, V and Fe powders. 77

Table 3.3: Estimated cost of making 100 kg of the Ti-Al-V-Fe alloys. 78

Table 3.4: Grinding and polishing procedure for Ti-Al-V-Fe alloys..... 79

Table 3.5: Hot compression testing parameters for the commercial and experimental alloys. 83

Table 4.1: Thermo-Calc results for the Ti-Al-V-Fe alloys using the TTTi3 titanium database.... 85

Table 4.2: EDX compositions of as-cast experimental alloys. 86

Table 4.3: EDX compositions of annealed experimental alloys. 86

Table 4.4: Crystallographic data of phases present in the as-cast and annealed alloys. 89

Table 4.5: Composition of α and β phases by EDX, in wt%. 89

Table 4.6: Beta phase fraction estimated from the SEM images. 98

Table 4.7: Beta transus temperatures, using Equation 4.1 and Thermo-Calc. 101

Table 4.8: Lattice parameters of bcc beta phase in the experimental alloys. 103

Table 5.1: Electrochemical parameters obtained for 6Al alloys immersed in 3.5 M H_2SO_4 solution at 25°C. 118

Table 5.2: Electrochemical parameters obtained for 4.5 wt% Al alloys immersed in 3.5 M H_2SO_4 solution at 25°C. 119

Table 5.3: Electrochemical parameters for 6 wt%Al alloys immersed in 3.5 wt% NaCl at 25°C. 122

Table 5.4: Electrochemical parameters for 4.5 wt% Al alloys immersed in 3.5 wt% NaCl at 25°C. 123

Table 5.5: Electrochemical parameters for alloys immersed in 3.5 M H_2SO_4+1.75 wt% NaCl at 25°C. 125

Table 6.1: Average grain size of alpha phase at a strain rate of 1 s^{-1}. 146

Table 6.2: Volume fraction of beta phase at different temperatures and strain rates. 151

Table 7.1: Interpretation of the power efficiency map and optimum working conditions for the Ti-6Al-1V-3Fe alloy. 166

Table 7.2: Interpretation of the power efficiency map and optimum working conditions for the Ti-4.5Al-1V-3Fe alloy. 166

Table 8.1: Equations for determining constitutive constants. 186

Table 8.2: Material constants and activation energy for hot working of titanium alloys. 186

Table 8.3: Activation energy for hot working of some commercial and experimental titanium alloys. 191

Table 8.4: Typical hot working parameters of some industrial processes (Jaspers and Dautzenberg, 2002; Odenberger *et al.*, 2011; Alabort *et al.*, 2016). 193

List of abbreviations

(α+β)	the two-phase alpha plus beta phase field
α+β	the alpha plus beta titanium alloy type
ASBs	Adiabatic shear bands
bcc	Body centred cubic
BE	Blended elemental
BSE	Back-scattered electron
CP-Ti	Commercially pure titanium
CSIR	Council for Scientific and Industrial Research
DRV	Dynamic recrystallisation
DRX	Dynamic recovery
EIS	Electrochemical impeadance spetroscopy
EDX	Electron dispersive X-ray spectroscopy
FEG-SEM	Field-Emission Gun Scanning Electron Microscope
hcp	Hexagonal closed packed
HDH	Hydrogenation-dehydrogenation or hydride–dehydride process
LCB	Low-cost beta
OCP	Open circuit potential
PM	Powder metallurgy
Q_{HW}	Activation energy for hot working
Q_{SD}	Activation energy for self-diffusion
SEM	Scanning electron microscopy
SEI	Secondary electron imaging
XRD	X-ray diffraction

Chapter 1: Introduction

This chapter provides a brief introduction to the entire thesis. The background and problem statement, research justification, research questions and objectives and the thesis structure are all presented in this chapter.

1.1 Background and Problem Statement

Titanium and its alloys are generally recognised as very important metallic materials due to their high specific strength, good hardenability, excellent fatigue and crack propagation resistance, low thermal expansion coefficient, biocompatibility and excellent corrosion resistance (Welsch *et al.*, 1993; Leyens and Peters, 2003; Boyer, 2010; Polmear *et al.*, 2017). Similar to aluminium and magnesium, titanium is classified as a light metal due to a low density of 4.54 g/cm^3 (Welsch *et al.*, 1993; Donachie, 2000; Leyens and Peters, 2003). Despite being the ninth most abundant element, titanium does not exist in pure form, but occurs mostly in oxide form as rutile and ilmenite in the earth's crust because of the highly negative enthalpy formation of its oxides (Charlu *et al.*, 1974; Lütjering and Williams, 2007)

Titanium is the fourth most abundant structural metal after iron, aluminium and magnesium (Leyens and Peters, 2003). More than one hundred alloys of titanium have been developed as either alpha (α), alpha+beta (α+β) or beta (β) alloys to meet the requirements of one or more applications (Joshi, 2006). However, only about 20 of these alloys have been produced on a commercial scale with Ti-6Al-4V - known as the "titanium workhorse" - accounting for about 50-70% of the titanium market (Polmear *et al.*, 2017). Ti-6Al-4V is the most versatile α+β titanium alloy and is mostly used in the aerospace and chemical industries. Over 70% of this alloy was utilised in the production of aircraft parts (Donachie, 2000; Leyens and Peters, 2003). The versatility of the titanium workhorse is attributed to the balanced mechanical properties and the possibility of manipulating the microstructure via heat treatment. Ti-6Al-4V remains the most investigated α+β alloy compared to other candidate titanium alloys (Sen and Ramamurty, 2010; Long *et al.*, 2014).

Titanium alloys have the potential of replacing conventional metallic systems such as steel, aluminium and cast iron in many land-based applications in the biomedical, sports, jewellery, automobile and power generation sectors. However, due to high cost of manufacturing, titanium alloys are limited to special purpose applications in mainly automotive, chemical and aerospace applications (Wang, 1996; Nochovnaya et al., 2008; Wang *et al.*, 2012b). The high cost of

titanium is attributed mainly to the difficulty of extracting the metal from its oxide ore due to its high affinity for interstitial contaminants (carbon, oxygen and nitrogen), poor machinability, multi-stage hot-working, the high energy required for double or triple remelting, ingot homogenisation and heat treatment (Carman *et al.*, 2011). Furthermore, titanium alloys usually undergo a series of hot working processes before they are made into finished or semi-finished products. The complexity in hot working of titanium alloys increases the cost of the alloys, arising from sensitivity to: compositional and microstructural changes, strain rates, strain and deformation temperatures (Duan *et al.*, 2007; Wang *et al.*, 2012a). Froes *et al.* (2007) analysed the cost of titanium alloys and reported that the cost of a titanium ingot was approximately fifty times that of steel and ten times that of aluminium, with costs further escalated by complex processing steps. In another cost analysis of titanium alloys made by Samaterials (2014), it was reported that producing ingots accounted for 30% of the total manufacturing cost. The primary conversion of the ingot to mill products, such as plates, bars and billets, accounts for 30% of the entire cost of titanium alloys with about 20% loss of materials experienced during the process. The secondary fabrication or machining of titanium mill products to final shapes accounted for 40% of the total processing cost with ~90% of materials wasted during this process (Samaterials, 2014).

Research efforts to reduce the cost of titanium alloys and to extend their application have been on-going since the Kroll process (Kroll, 1940) was invented. The major routes that have been considered to achieve this include:

- Total replacement of expensive alloying elements with low-cost elements that fulfil similar functions,
- Improving material utilisation during processing, such as by the powder metallurgy (PM) route to produce near-net shapes,
- Optimisation of hot-working and machining processes,
- The adoption of novel processing techniques such as the electrochemical deoxidation metalysis using the Fray, Farthing and Chen Process (Benson *et al.*, 2016; Chen *et al.*, 2000), the Cristal Metals Armstrong process (Xu *et al.*, 2017) and the FAST-forge process (Weston and Jackson, 2017) for producing low-cost titanium alloys.

Fujii *et al.*(2002) replaced expensive vanadium with iron to produce low-cost Ti-Fe-O-N and Ti-Fe-Al alloys. Wang *et al.*(2012b) developed Ti-Al-Cr-Fe alloys using a Cr-Fe master alloy. While the idea of replacing expensive with lower cost alloying elements remains very promising, one challenge is the formation of intermetallic compounds or unwanted phases in the alloys. For example, most of the lower cost alloying elements (iron, chromium and nickel) that stabilise the

beta phase are eutectoid formers, whereas the expensive elements (vanadium, molybdenum and niobium) are isomorphous beta stabilisers in titanium alloys. The elements that undergo an eutectoid reaction with titanium form intermetallic phases under equilibrium conditions (Fujii *et al.*, 2002). These intermetallic phases are undesirable because they have detrimental effects on the mechanical properties and corrosion performance of titanium alloys (Fujii *et al.*, 2002; Fujii and Takahashi, 2002).

Optimisation of deformation processes has been done using constitutive equations and processing maps (Duan *et al.*, 2007; Sen *et al.*, 2007), which assisted in determining optimum processing parameters for manufacturing defect-free titanium profiles, hence reducing energy costs and decreasing production time. The constitutive equation relates the flow stress to other deformation parameters such as deformation temperature, strain rates, stress and strain. Developing this model would make it easier to: determine the optimum processing parameters for hot working of the alloys, determine the activation energy required to deform the alloys and predict the flow stress more easily for die filling (in closed die forging) and press load capacity. The equations could serve as input data for finite element modelling, computer based simulation and optimisation. The processing map aids in predicting defect-free regions and regions dominated by defects while subjecting the material to deformation under various processing conditions.

In this research study, the development of low-cost Ti-Al-V-Fe alloys for land-based applications is presented. The low-cost alloys, sometimes referred to as experimental alloys in this thesis, contain less than 10 wt% of Al, V, and Fe combined, and were compared to wrought Ti-6Al-4V as a reference alloy. The addition of Fe was due to its low-cost, strong beta stabilising effect and a stronger solid solution strengthening effect than vanadium (Chen *et al*., 2011). Iron, the major element in steel, is known to be highly susceptible to corrosion. The addition of iron to titanium raised some concern about the corrosion resistance of the Ti-Al-V-Fe alloys. The influence of iron additions on the corrosion performance of the alloys was evaluated in various corrosive media and the results are presented in the subsequent chapters.

The low-cost alloys were produced by casting and two basic design steps were followed:

- Partial substitution of vanadium with iron in commercial Ti-6Al-4V and a reduction in Al content from 6 wt% to 4.5 wt%.
- Optimisation of the deformation behaviour of the as-cast experimental alloys.

These two steps address the problems of expensive alloying elements and multi-stage forging of titanium alloys which escalate the cost. The option of partial and not full substitution of vanadium was chosen to retain some of this isomorphous alloying element to help suppress the formation

of intermetallic compounds which has been reported in previously developed low-cost titanium alloys (Fujii *et al*., 2002; Fujii and Takahashi, 2002). Furthermore, optimisation of the hot working process would help simplify the complex hot working of the alloys during primary conversion from ingots to semi-finished and finished products.

1.2 Justification of the Research

South Africa has substantial reserves of titanium beach sands that can be beneficiated, developed into alloys and used for the manufacture of various titanium components (Campbell, 2013). However, there is no substantial downstream beneficiation or alloy development of titanium in Africa (Clark, 2012; Wild, 2013). Moreover, South Africa, the second largest producer of titanium ore (ilmenite) after Australia, exports the ore at a cost of 0.29 USD/kg and then imports the processed metal at 30 USD/kg (Wild, 2013). This is uneconomical and limits the potential of the South African titanium industry. There is a drive by government to utilise this abundant resource by developing a titanium metal beneficiation industry by 2020. This new industry, with the assistance of the Advanced Metals Initiative of the Department of Science and Technology (AMI-DST) and the Titanium Centre of Competence of the Department of Trade and Industry (TiCoC-dti), is expected to expand the titanium alloy manufacturing industry in South Africa, make the country a global player in the titanium industry and improve the economy (Clark, 2012; Wild, 2013).

The CSIR has developed and patented a metallothermic reduction process producing powder directly from $TiCl_2$ (Van Vuuren, 2009; Wild, 2013). A multi-million dollar pilot plant was commissioned in 2012, with the aim of making the process continuous. The titanium powder, about the same price as titanium sponge, would be produced at a rate of 2 kg/hour. Due to design problems, this pilot plant is still not operational and the titanium powder is not available for testing, hence the performance of the powder as a raw material for the development of alloys is yet to be evaluated (CSIR, 2018).

This research work entailed the development of low-cost Ti-Al-V-Fe alloys for land-based applications using elemental powders as starting materials. The initial intention was to use the CSIR-produced titanium powder in this research. However, commercial titanium powder had to be used since the pilot plant is still not operational.

It is believed that the findings from this work will still be relevant for assessing the suitability of the CSIR titanium powder for alloy development in the future. There may be iron pick-up during the CSIR powder making process. Most titanium finished and semi-finished products are rolled, forged or extruded during processing. Determining the optimum processing parameters for the

deformation of Ti-Al-V-Fe alloys by laboratory experimentation, simulation and modelling would serve as a foundation for further research on other alloys. The utilisation of the optimum processing parameters for forming processes on an industrial scale would save time, energy and cost. The low-cost Ti-Al-V-Fe alloys with varied compositions could be used for other general applications, such as in automobiles, military equipment, sports equipment, chemical processing, and structures where the extensive testing and qualification processes for the rigorous quality requirements in the aerospace industry are not required.

Besides titanium, two of the three added elements (vanadium and iron) required for this research work are readily available in South Africa, especially as South Africa remains the second largest producer of vanadium after China (USGS, 2014).

1.3 Research Questions

(i) What are the effects of partial substitution of vanadium with iron and the reduction in aluminium content on the microstructure and hardness of Ti-Al-V-Fe experimental alloys?

(ii) What influence do the partial substitution of vanadium with iron and the reduction in aluminium content have on the corrosion behaviour of Ti-Al-V-Fe alloys?

(iii) What is the influence of a complex initial microstructure[1] on the hot deformation behaviour of a Ti-6Al-4V commercial alloy? Can information derived from the hot deformation behaviour of Ti-6Al-4V serve as the basis for determining the optimum working conditions of the experimental alloys?

(iv) What influence does the alloy composition have on the hot deformation behaviour of the experimental alloys? What are the optimum hot working conditions and dominant softening mechanisms during deformation of the experimental Ti-Al-V-Fe alloys?

1.4 Research Hypothesis

It is envisaged that low-cost α+β Ti-Al-V-Fe alloys with a composition based on the commercial Ti-6Al-4V alloy can be developed for a wide range of applications, if the factors that contribute to the high cost of titanium alloys such as: starting materials, production routes, compositional

[1] Complex initial microstructure refers to the typical microstructure obtained in wrought titanium products when complete globularisation of elongated alpha plates does not occur during ingot breakdown and post deformation heat treatment.

variations and hot working parameters (working temperature, stress, strain, microstructural evolution, strain rate) can be optimised. This was the focus of this research work.

1.5 Aim and Objectives

The aim of this research work was to develop low-cost α+β Ti-Al-V-Fe alloys for land-based applications by using elemental powders as the starting material. This was achieved by the following specific objectives:

(i) Producing as-cast Ti-Al-V-Fe alloys using varied Al, V, Fe additions via vacuum arc melting.

(ii) Assessing the influence of alloy compositions - partial substitution of vanadium with iron and reduction in aluminium content - on the microstructural evolution and hardness of the as-cast alloys.

(iii) Evaluating the influence of alloy composition - partial substitution of vanadium with iron and reduction in aluminium content - on the corrosion behaviour of the produced alloy in sulphuric acid, sodium chloride and mixed sulphuric acid and sodium chloride solutions.

(iv) Establishing the dominant softening mechanisms and optimum processing conditions during deformation of a commercial Ti-6Al-4V alloy with complex initial microstructure.

(v) Assessing the influence of alloy composition on the hot deformation behaviour of experimental Ti-Al-V-Fe alloys. Determining the dominant softening mechanisms and optimum working conditions during deformation of the alloys.

1.6 Thesis Structure

This thesis is divided into four parts. Part I contains the first three chapters of the thesis. Chapter 1 is the introductory section of the thesis, where the research problem is stated and the motivation for the research is detailed. The research hypothesis, questions, aim and specific objectives are presented in this chapter. The second chapter contains the systematic review of literature based on the findings of previous authors. The factors contributing to the high cost of titanium alloys are discussed and the several research approaches adopted to reduce the cost of titanium alloys are summarised. The scientific principles which provide the fundamental understanding of some of the methods adopted in the experimental procedure are also presented in Chapter 2. Generally the research gaps in the development of low-cost titanium alloys are also summarised. The third chapter which is the last chapter in Part I of the thesis, presents the experimental methods that

were used to provide answers to the research questions presented in Chapter 1. The main contributions of this work are presented in parts II and III.

Part II of this thesis contains two chapters (Chapters 4 and 5) that address the first and second research questions. Chapter 4 presents the results and discussion on the influence of partial substitution of vanadium with iron and reduction of aluminium content on the microstructural evolution and hardness of the low-cost experimental alloys. Chapter 5 contains the results and discussion on the influence of partial substitution of vanadium with iron and the reduction of aluminium content on the corrosion performance of the low-cost experimental alloys. The alloys with the most desirable performance from a cost, microstructure and corrosion point of view were selected for further studies and presented in Part III.

Part III contains four chapters (Chapters 6 - 9) which focus on the hot deformation behaviour of the commercial Ti-6Al-4V and experimental alloys. The chapters address the third and fourth research questions. This part also includes the overall conclusions drawn from the research. Chapter 6 presents the results and discussion on the hot deformation behaviour of the commercial Ti-6Al-4V alloy with a complex initial microstructure. Chapter 7 presents the results and discussion on the hot deformation behaviour of the experimental alloys. The optimum conditions for hot working of the commercial and experimental alloys are established in this section. Chapter 8 presents the influence of alloying element on the activation energy for hot working of the alloys. Chapter 9 provides the research conclusions and recommendations for future work.

Part IV of this thesis covers the list of references cited in the work and the supplementary information which is presented in the appendices.

Chapter 2: Literature Review

This chapter comprises a systematic review of the findings that have been reported by authors in books, journal articles, conference proceedings and technical reports. A general overview of the metallurgy of titanium is given and the factors contributing to the cost of titanium alloys were established from the literature. Previous research efforts on cost reduction of titanium alloys were examined and the research gap that is yet to be filled was established.

2.1 Overview of titanium alloys

2.1.1 History of titanium metal

In 1791, Gregor, an amateur mineralogist, clergyman and chemist discovered ilmenite, magnetic iron sand, in Cornwall, United Kingdom. Four years later, Klaproth analysed an unknown oxide of an element in Hungary and named the oxide rutile and the element, titanium (Lütjering and Williams, 2007).

Titanium is present in the earth's crust as the fourth most abundant structural element after aluminium, iron and magnesium, and is difficult to isolate from its ore. Several efforts to isolate titanium from its ore using sodium, magnesium and calcium with titanium tetrachloride in an intermediate step proved abortive. This was ascribed to the high affinity of titanium for oxygen, nitrogen and other interstitial elements (Polmear *et al.*, 2017). Conversely, between 1937 and 1940, Kroll successfully reduced titanium from titanium tetrachloride using magnesium in an inert gas environment (Kroll, 1940). This process has remained the dominant process for producing titanium metal on a commercial scale. The product obtained from the process is called titanium sponge due to its spongy and porous appearance (Lütjering and Williams, 2007).

It took over 100 years since titanium was discovered to develop the first set of commercial alloys. The target application for these alloys was the aerospace industry in the 1940s after the Second World War (Sinigaglia *et al.*, 1978). This industry still remains the largest consumer of titanium alloys to date (Lütjering and Williams, 2007).

Despite the dominance of the Kroll process, there have been many research efforts to produce titanium metal in powder form to reduce fabrication costs and promote the advancement of the downstream sector. However, a fully commercialised continuous process for the production of titanium metal from its ore is not readily available (Lütjering and Williams, 2007; CSIRO, 2016). The reaction temperature of the Kroll process is high, usually about 800 - 850°C and the entire process is done in vacuum or inert gas. These process requirements make titanium metal

expensive. Additionally, the variable chemical purity from the Kroll batch process means that a large stockpile of different matching compositions needs to be maintained, which adds to the cost of this process (van Tonder, 2010).

Australia's CSIRO (Australian Titanium, 2012; CSIRO, 2016) and South Africa's CSIR (van Vuuren, 2009; Campbell, 2013; CSIR, 2018) have independently attempted to develop continuous processes for producing titanium metal powder. However, there is a lot more to be improved to make these processes viable, internationally acceptable and competitive.

2.1.2 Applications of titanium alloys

The applications of titanium alloys are divided into traditional and niche applications. The traditional applications include the aerospace and the chemical industries (Lütjering and Williams, 2007; Polmear *et al*., 2017). Since the early 1950s, titanium alloys were used predominantly for the production of aircraft frames and engines in the aerospace sector due to titanium's specific strength and ability to maintain properties at elevated temperatures when compared to aluminium alloys, titanium's strongest competitor in this sector. However, there were cases of titanium combustion in turbine engines which limited their use in the aerospace sector (Zhao *et al.*, 1999; Rugg *et al.*, 2016). The improvement in titanium technology led to development of titanium aluminides and other burn resistant titanium alloys that are capable of withstanding operating temperatures of 650°C (Wang *et al.*, 2004; Zhao *et al.*, 2006). The excellent corrosion resistance of titanium alloys makes them well-suited for use in the chemical industries as fittings and pressure vessels (Lütjering and Williams, 2007).

Niche applications of titanium include biomedical implants, racing cars for Formula One, consumer products such as jewelleries, watches, cameras, kitchen utensils and various kinds of sporting goods (Leyens and Peters, 2003; Polmear, 2005). Typical components made from titanium alloys are shown in Figure 2.1. The choice of applications is determined by a number of factors such as the alloy class, properties and cost of alloys.

2.1.3 Classification of titanium alloys

Commercially pure titanium exhibits two allotropic phase transformations. At ambient temperature to 882 ± 2°C, pure titanium has a hexagonal close packed *(hcp)* structure but transforms to a body centred cubic *(bcc)* structure above this temperature (Welsch *et al.*, 1993; Polmear *et al.*, 2017). The temperature at which this transition takes place is known as the beta transus temperature (Leyens and Peters, 2003). The different lattice structures for alpha and beta titanium are shown in Figure 2.2. Alloying elements play a crucial role in classifying titanium alloys. These elements can be added to retain the alpha, beta or both phases at room temperature.

The elements which raise the beta transus temperature are referred to as alpha stabilisers while elements which lower the beta transus temperature are referred to as beta stabilising elements (Leyens and Peters, 2003). To produce titanium alloys with a specific phase, it is important to control the amount of the elements as these could lead to other variants such as the near-α, near-β and intermetallic compounds. A typical intermetallic compound includes bulk titanium aluminides that are now developed for high temperature applications due to their good creep resistance (Leyens and Peters, 2003). The processing, composition, structure and properties of alpha titanium alloys and beta titanium alloys are presented in the following sections. Since the targeted alloy type in this study is α+β, detailed information is provided on the composition, processing, structure and properties of the α+β titanium alloys.



Figure 2.1: Components made from titanium alloys (Salem *et al.*2014; Liszewski, 2015).

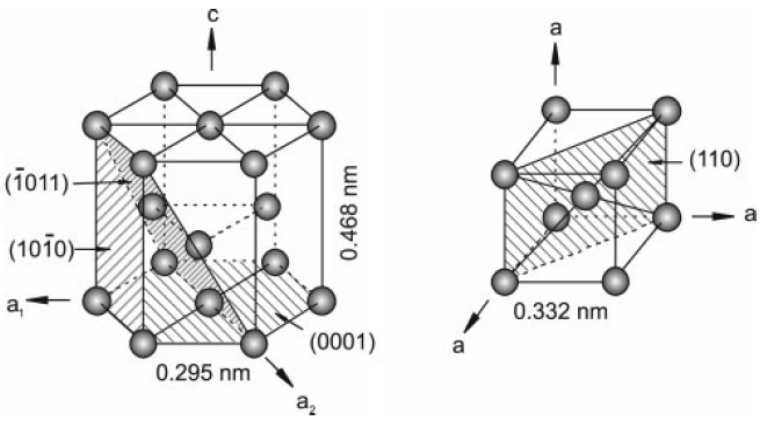

Figure 2.2: Structure of titanium: (a) hexagonal closed packed of alpha phase, (b) body centred cubic of beta phase (Leyens and Peters, 2003).

2.1.4 Alpha alloys

The alpha titanium alloys include commercially pure titanium (CP-Ti) and the near alpha alloys. These alloys have a hexagonal closed packed structure at ambient temperature (Welsch *et al.*, 1993; Polmear, 2005). Interstitial elements such as oxygen, nitrogen and carbon and substitutional elements such as aluminium and tin are the common alpha stabilisers which raise the beta transus temperature. Among the interstitial elements that stabilise the alpha phase, oxygen and nitrogen are added intentionally for strengthening, while other elements are impurities (Boyer, 1996; Lütjering and Williams, 2007). The commercially pure titanium alloys are classified as different grades (ASTM Grades 1, 2, 3 and 4) with varying contents of oxygen and iron. The alpha and the near-alpha alloys contain aluminium and tin, with aluminium remaining the most important alpha stabilising alloying element (Lütjering and Williams, 2007). These alloying elements are added within specific limits to prevent loss in ductility (Leyens and Peters, 2003). An empirical formula used in the design of alpha alloys is the aluminium equivalent weight (Leyens and Peters, 2003):

$$Al\ eq.(wt\%) = Al + 1/3\,Sn + 1/6\,Zr + 10\,O \qquad \textbf{Equation 2.1}$$

To prevent embrittlement of alpha alloys, it has been recommended that the aluminium equivalent should not exceed 9 wt% (Leyens and Peters, 2003). However, in alpha alloys containing aluminium as the major alpha stabiliser, the maximum concentration of aluminium has been set at 6 wt%, as concentrations higher than 6 wt% promote the formation of the Ti_3Al phase. Ti_3Al has been reported to cause embrittlement in the alpha alloys (Fujii and Takahashi, 2002; Leyens and Peters, 2003).

The properties of the alpha alloys are directly influenced by the composition, and are primarily considered for applications where corrosion resistance is required, such as in the chemical and petrochemical industries. Alpha alloys with small additions of platinum group metals, such as Ti-Ru and Ti-Pd, were developed specifically for improved corrosion resistance (Leyens and Peters, 2003; Jackson and Boyer, 2010). Generally, alpha alloys exhibit moderate strength, have excellent formability and weldability but they hardly respond to heat treatment. Table 2.1 summarises the different grades of alpha alloys. The near-alpha alloys contain up to 2 wt% of the beta stabilising elements such as iron, molybdenum and vanadium, to improve the solid solution strengthening of the alloys (Boyer, 1995). The typical microstructure of these alloys is dispersed beta within the alpha grains. The dispersed beta helps in controlling grain growth during process annealing by pinning the grain boundaries. Thermomechanical processing of the alloys is targeted towards controlling grain size and crystallographic texture (Flower, 1990; Lütjering and Williams, 2007; Prasad *et al.*, 2015).

The major disadvantage of the alpha alloys are that microstructural control for improved strength is difficult to achieve when compared to α+β and beta alloys. As a result, strength levels in alpha alloys are insufficient for structural applications (Lütjering and Williams, 2007).

Table 2.1: ASTM grades of alpha titanium alloys (Lütjering and Williams, 2007).

ASTM Grade	O wt% (max.)	Fe wt% (max.)	Yield strength (MPa)
Grade 1	0.18	0.20	170
Grade 2	0.25	0.30	275
Grade 3	0.35	0.30	380
Grade 4	0.40	0.50	480
Ti-0.2Pd (Grade 7)	0.25	0.30	275
Ti-0.2Pd (Grade 11)	0.18	0.20	170
Ti-0.2Pd (Grade 16)	0.25	0.30	275
Ti-0.2Pd (Grade 17)	0.18	0.20	170
Ti-0.1Ru (Grade 26)	0.25	0.30	275
Ti-0.1Ru (Grade 27)	0.18	0.20	170
Ti-0.3Mo-0.9Ni (Grade 12)	0.25	0.30	345
Ti-3Al-2.5V (Grade 9)	0.15	0.25	485
Ti-3Al-2.5V-0.05Pd (Grade 18)	0.15	0.25	485
Ti-3Al-2.5V-0.1Ru (Grade 28)	0.15	0.25	485
Ti-3Al-2.5Sn (Grade 6)	0.20	0.50	795
Ti-3Al-2.5Sn ELI	0.15	0.25	725

2.1.5 Beta alloys

Beta titanium alloys have the body centred cubic structure at room temperature (Duerig *et al.*, 1980). These alloys can either be beta-rich or metastable-beta depending on the concentration of the alloying elements. The alloying elements that stabilise the beta phase in titanium include molybdenum, vanadium, iron, chromium, nickel and niobium (Weiss *et al*., 1986). Molybdenum, vanadium and niobium are isomorphous beta stabilisers, while chromium, iron and nickel are typical eutectoid formers as shown in Figure 2.3.

The beta alloys are different from the α+β alloys because the beta alloys contain a sufficiently high concentration of beta stabilisers which causes 100% beta phase to be retained at room temperature. Usually, a martensitic transformation occurs when α+β alloys are quenched from the beta phase during heat treatment. This martensitic transformation does not occur in beta alloys due to the high concentration of beta stabilising elements (Lütjering and Williams, 2007). The elemental beta stabilising effect is described by the molybdenum equivalent expressed in Equation 2.2 (Weiss and Semiatin, 1998). This equation is used for designing both beta and α+β

titanium alloys. To fully stabilise the beta phase, the equivalent molybdenum content must at least be 10%. Some important beta titanium alloys that have been developed on a commercial scale are presented in Table 2.2. A more comprehensive list of the different beta alloys is presented by Weiss and Semiatin (1998). These alloys are attractive for structural applications because high strength levels can be achieved compared with other classes of titanium alloys due to their excellent response to heat treatment. The low elastic modulus, high specific strength and comparable corrosion resistance to the α+β alloys are major advantages of beta alloys, and have made the alloys suitable for use in the biomedical sector (Weiss and Semiatin, 1998).

$$Mo\ eq.(wt\%) = Mo + 0.67V + 0.44W + 0.28\,Nb + 0.22Ta + 1.6Cr + 1.25Ni + 1.7Co + 2.9Fe - 1.0Al \qquad \textbf{Equation 2.2}$$

High formability can be achieved in beta alloys due to more slip systems being available in the *bcc* structure in comparison to the *hcp* structure in alpha alloys (Polmear *et al.*, 2017). As a result, some beta alloys are easily cold worked without defects. The metastable beta titanium alloys can be aged using different temperatures, holding time and heating rate to achieve a wide range of microstructural changes and mechanical properties. Appropriate processing parameters are essential to ensure the satisfactory performance of beta alloys in service. This is because variations in processing parameters, such as strain rate, cooling rate, solution treating temperatures, ageing temperature, influence the microstructural features of beta grain size, grain boundary alpha, primary and secondary alpha and volume fraction of alpha precipitates. Detailed information on the effect of processing parameters on the microstructure and properties of beta titanium alloys have been reported (Lütjering and Williams, 2007).

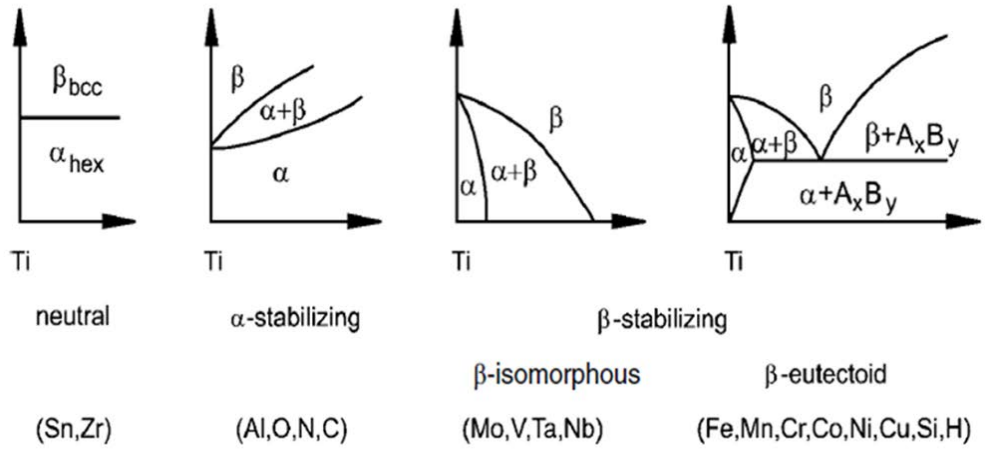

Figure 2.3: Classification of beta stabilising elements (Yang, 2015).

The major disadvantage of these alloys includes the high cost of producing the alloys due to the high concentration of expensive alloying elements such as Mo and V. In addition, the use of

euctectoid stabilisers such as Fe and Cr pose segregation problems in many beta titanium alloys (Weiss and Semiatin, 1998).

Table 2.2: Common beta titanium alloys (Weiss and Semiatin, 1998; and Lütjering and Williams, 2007).

Alloy	Composition	Category	Mo Equivalent
Ti-17	Ti-6Al-2Sn-4Zr-6Mo-4Cr	Beta-rich	5.4
SP-700	Ti-4.5Al-3V-2Mo-2Fe	Beta-rich	5.3
Beta-CEZ	Ti-5Al-2Sn-2Cr-2Mo-4Z**r**	Beta-rich	5.1
Ti-10-2-3	Ti-10V-2Fe-3Al	Metastable	9.5
Beta 21S	Ti-15Mo-2.7Nb-3Al-0.2Si	Metastable	18
Ti-LCB	Ti-4.5Fe-6.8Mo	Metastable	13
Ti-15-3	Ti-15V-3Cr-3Al-3Sn	Metastable	12
Beta C	Ti3Al-8V-6Cr-4Mo	Metastable	16
B120VCA	Ti-13V-11Cr-3Al	Metastable	23

2.1.6 α+β alloys

The α+β grades of titanium alloys have both *hcp* and *bcc* structures at room temperature. The volume fraction of the bcc beta phase is usually 5 - 40 vol.% (Leyens and Peters, 2003; Polmear, 2005). The α+β alloys are the most utilised group of titanium alloys due to the balanced mechanical properties offered by these alloys. Among the α+β grades, Ti-6Al-4V (Grade 5) has accounted for more than 50% of the total titanium alloys used to date (Boyer, 1996; Bauristhene *et al.*, 2013). It is also the most researched and developed alloy (Leyens and Peters, 2003). A wide range of microstructural features can be obtained in α+β titanium alloys by carefully selecting the processing conditions (Brun *et al.*, 1998). For example, the different types of microstructures obtained in Ti-6Al-4V have a significant influence on the mechanical properties and overall performance in service (Lütjering, 1998; Weiss and Semiatin, 1998, 1999). Three common microstructures can be developed in α+β titanium alloys: fully lamellar, fully equiaxed and bimodal microstructures (Figure 2.4). The different processing techniques used in obtaining these microstructures are briefly discussed in this section.

Fully lamellar structure

To produce a fully lamellar structure in α+β alloys, two processing methods can be adopted. The first method involves four processing steps shown in Figure 2.5. These steps include homogenisation in the beta phase field, deformation in the beta or (α+β) phase region, recrystallisation and annealing. The critical processing parameter when developing this microstructure is the cooling rate during recrystallisation. Lamellar thickness increases with

decrease in cooling rates. The most important processing parameters when adopting this processing route are summarised in Table 2.3.

The second method is commonly referred to as beta processed lamellar structure. In this process, the recrystallisation step in the first method is completely omitted. The steps involved are presented in Figure 2.6, parameters such as strain rate, cooling rate, time and temperature are well controlled during deformation to achieve the fully lamellar structure. The advantage of unrecrystallised lamellae is that grain boundary alpha is broken up. In this process, the cooling rate after deformation has the most significant influence on the width and volume fraction of the lamellae. The influence of thickness and volume fraction of lamellae on the mechanical properties of titanium alloys is presented in Section 2.1.7.

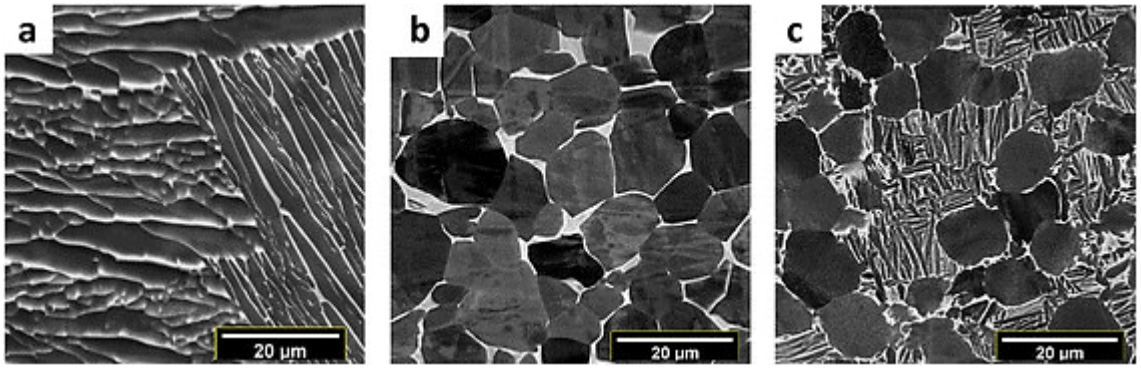

Figure 2.4: Common microstructures developed in α+β titanium alloys: (a) fully lamellar (b) fully equiaxed and (c) bimodal (Salem *et al.*,2014).

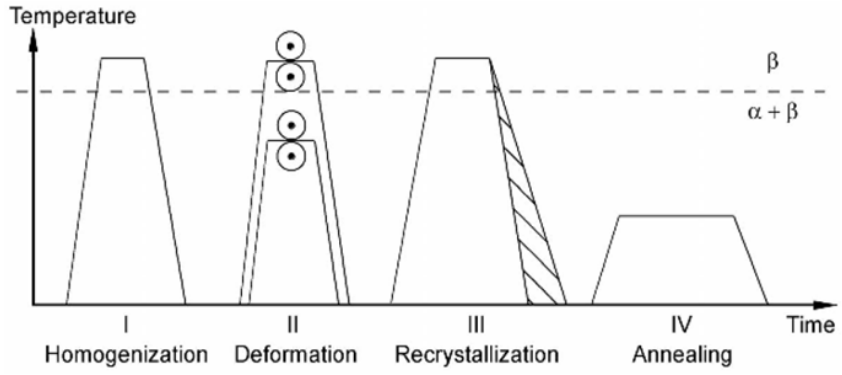

Figure 2.5: Processing steps for obtaining fully lamellar microstructures of α+β titanium alloys (Lütjering and Williams, 2007).

Table 2.3: Important processing parameters for developing fully lamellar microstructures.

Processing step	Important parameters	Microstructural Features
III	Cooling rate	Size of alpha colonies; width of alpha lamellae; grain boundary alpha layer
IV	Annealing temperature	Ti_3Al in alpha; secondary alpha in beta

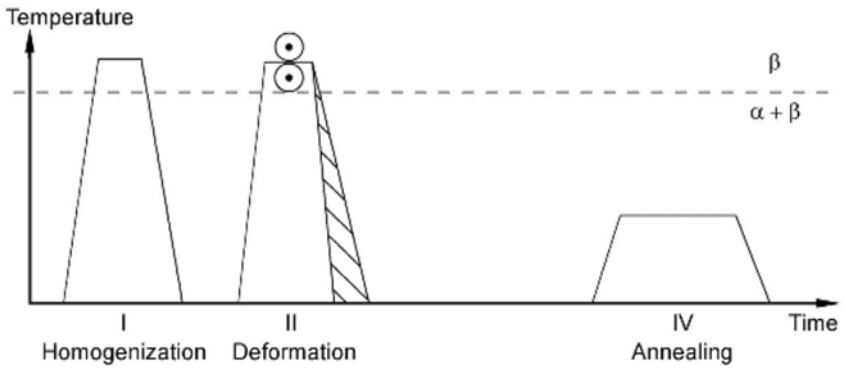

Figure 2.6: Processing steps for beta processed fully lamellar microstructures of α+β titanium alloys (Lütjering and Williams, 2007).

Bimodal structure

Similar to the first method used in developing fully lamellar structures, bimodal structures can be obtained in four processing steps: homogenisation in the beta phase field, deformation in the (α+β) phase region, recrystallisation and finally ageing or stress relief annealing. One unique feature of these processing steps is that deformation is carried out in the (α+β) phase region. The critical parameters that control the resultant microstructural features when developing a bimodal structure are: the cooling rate after homogenisation in step I, recrystallisation in step III, as well as the annealing temperature in the final step. This is illustrated schematically in Figure 2.7. The cooling rate controls the width of the alpha lamellae and primary alpha, while the annealing temperature controls the volume fraction of the primary alpha that is present in the microstructure. A lower cooling rate favours thicker alpha lamellae and a higher volume fraction of primary alpha since there will be more time for migration of grain boundaries of the different phases. The mechanism of forming bimodal structures has been explained by the penetration of beta phase at the alpha/alpha boundaries which splits the lamellar alpha into globules (Lütjering,1999).

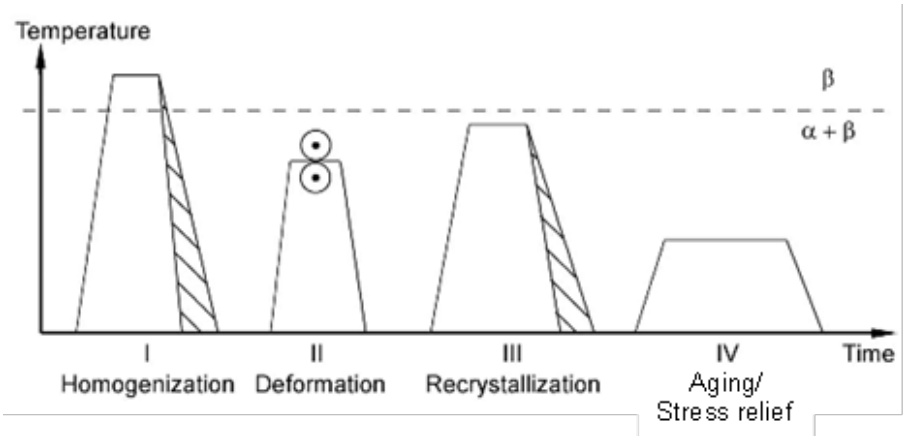

Figure 2.7: Processing steps for developing a bimodal structure (Lütjering, 1999).

Fully equiaxed microstructure

Fully equiaxed microstructures can be achieved in titanium alloys by two processing methods shown in Figure 2.8 and Figure 2.9. The first method is similar to the process used for obtaining a bimodal structure but the major difference is that the recrystallisation step is followed by a sufficiently slow cooling rate. In this case, the resultant microstructure has larger equiaxed grains than the primary alpha of the bimodal structure (Lütjering and Williams, 2007).

The second method involves carrying out a recrystallisation treatment at a temperature low enough for the volume fraction of primary alpha to be at equilibrium. At the same time, the recrystallisation temperature is sufficiently high for equiaxed alpha to recrystallise from the lamellar structure. The mechanism of forming the fully equiaxed structure is similar to that of the bimodal structure, but in this case, the phenomenon is reversed so that the alpha grains penetrate into the beta/beta boundaries and break the beta into globules (Ivasishin and Lütjering, 1993; Lütjering, 1998). The important processing parameters for obtaining a fully equiaxed structure is shown in Table 2.4**.**

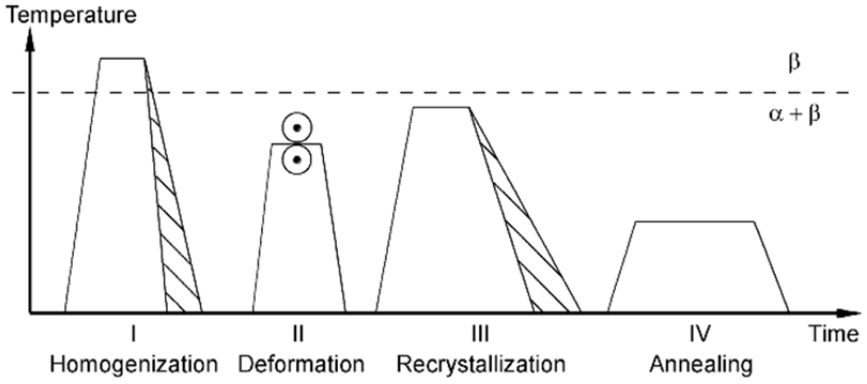

Figure 2.8: Processing steps for developing an equiaxed structure of α+β titanium alloys slowly cooled in the bimodal phase region (Lütjering and Williams, 2007).

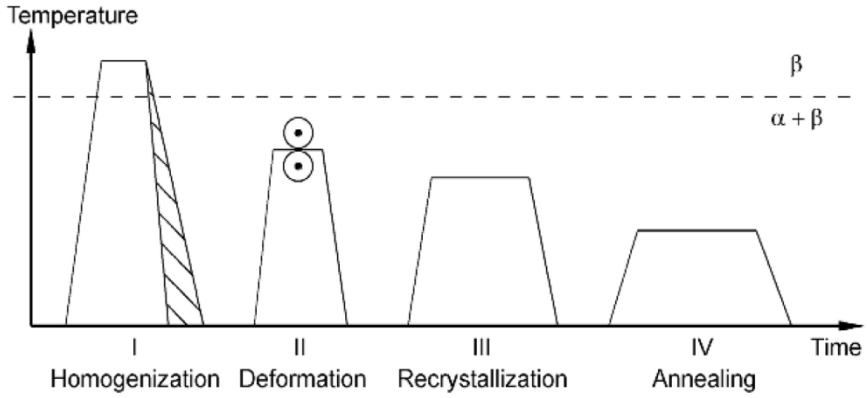

Figure 2.9: Processing steps for developing an equiaxed structure of α+β titanium alloys recrystallised at low temperatures (Lütjering and Williams, 2007).

Table 2.4: Important processing parameters for a fully equiaxed structure (Lütjering and Williams, 2007).

Processing step	Important parameters	Microstructural features
I	Cooling rate	Width of alpha lamellae (alpha grain size)
II	Deformation temperature; deformation degree; deformation mode	Texture density; dislocation density.
III	Slow cooling, low annealing temperature	Fully equiaxed structure
IV	Annealing temperature	Ti_3Al in alpha phase; secondary alpha in beta

The different processing steps for obtaining the three basic microstructures in α+β alloys have been briefly described. These steps involve deformation in either the beta or the (α+β) phase region. This indicates that thermomechanical processing remains a very crucial step for microstructural control in the development of titanium alloys. The effects of these microstructures on mechanical properties and overall performance in service are presented in Section 2.1.7.

In addition to the different processing steps for obtaining the fully lamellar, bimodal and fully equiaxed microstructures in α+β titanium alloys, as outlined in this section, another important processing method is the mill-annealing method. Most titanium wrought products such as billets and slabs are supplied in the mill-annealed condition which provides a wide range of microstructures. The processing steps are shown in Figure 2.10 where the recrystallisation step used for obtaining a fully equiaxed structure (Figure 2.8 - 2.9) is omitted. The resultant microstructure is complex as it is usually undefined. Typical mill-annealed structures in Ti-6Al-4V are shown in Figure 2.11. The microstructures show partially recrystallised alpha and beta grains, and deformed alpha lamellae.

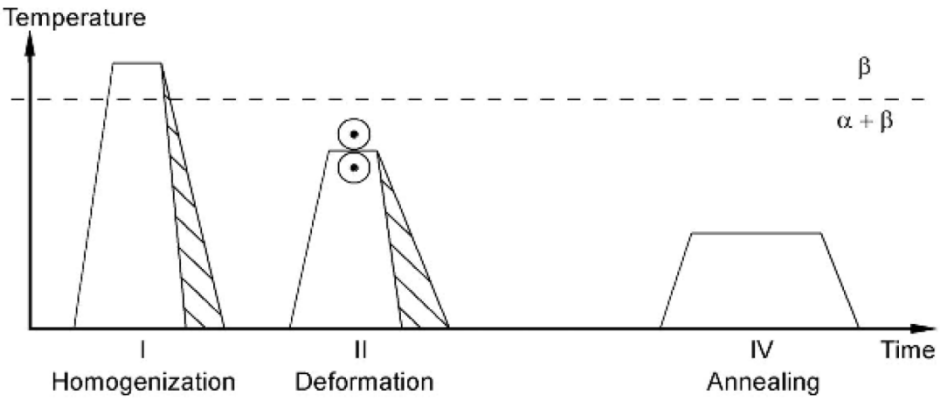

Figure 2.10: Processing steps for obtaining mill-annealed structures (Lütjering and Williams, 2007).

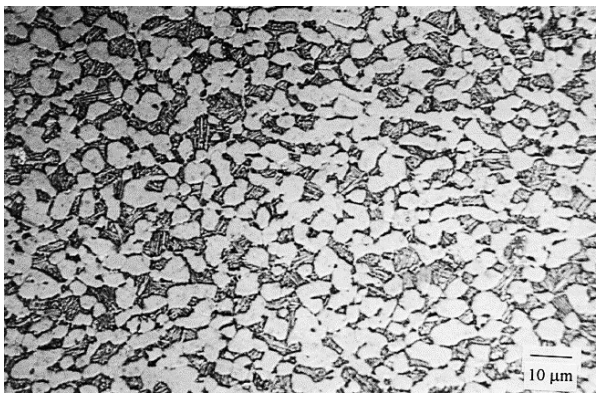

Figure 2.11: Mill-annealed structure in Ti-6Al-4V alloy (Gil *et al.*, 2001)

While finished titanium alloy components rarely contain this type of complex microstructure, it can be seen in semi-finished products such as billets, which are then processed into finished components. Therefore, it is quite important to understand how this complex microstructure influences the deformation process during conversion of the semi-finished products to final components. The influence of a complex microstructure on hot deformation behaviour of Ti-6Al-4V is discussed in detail in Chapter 6.

2.1.7 Correlation between microstructure and properties of α+β alloys

A summary of the correlation between the different microstructural features of the α+β alloys and the mechanical properties, such as yield strength, tensile ductility, fatigue strength, crack nucleation resistance, crack propagation resistance and fracture toughness, is presented in this section.

For a fully lamellar structure, the most important microstructural feature is the size of the alpha colonies which determines the slip length. The alpha colony size is influenced by controlling the cooling rate after heat treatment in the beta phase field. At a low cooling rate, coarse lamellae are formed, while at a very high cooling rate ($8000°Cs^{-1}$), colonies having a typical martensitic structure are formed (Donachie, 2000).

Sieniawski *et al.* (2013) reported that the yield strength of α+β titanium alloys increased with increasing cooling rate. In other words, decreasing the alpha colony size favours an increase in yield strength. This trend is also consistent with the fatigue strength of the alloys which increased with a decrease in alpha colony size. Decreasing slip length increases resistance to crack nucleation and crack propagation in α+β alloys with fully lamellar microstructures. This is because small alpha colonies are effective obstacles to dislocation motion and crack propagation when compared with alpha lamellae. With smaller alpha colonies, cracks and dislocation

branching occurs quite easily and thus increase the yield strength and crack propagation resistance of the alloys (Hall, 1997; Lütjering and Williams, 2007; Ping *et al.*, 2015).

The relationship between cooling rate (which determines the slip length of the alpha lamellae) and the tensile ductility of different α+β alloys is shown in Figure 2.12 (Sieniawski *et al.*, 2013). It is seen that increasing cooling rate increased the tensile ductility of the alloys to a maximum after which there was a drastic drop in ductility with a further increase in cooling rate.

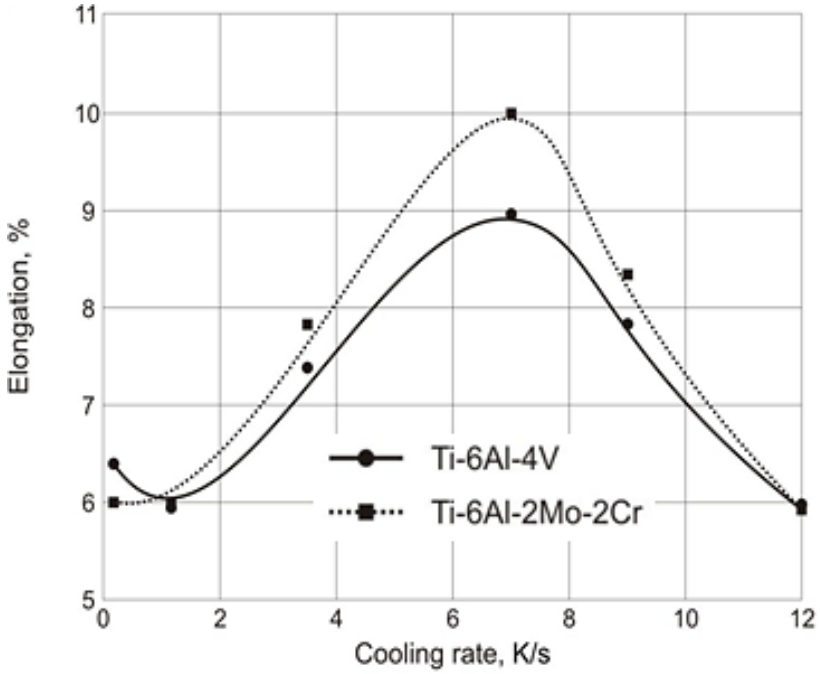

Figure 2.12: Relationship between cooling rate and elongation of Ti-6Al-4V.

The transition from the region of increased ductility to rapid loss of ductility indicates that there is an effective alpha colony size for obtaining the optimum ductility in α+β alloys with a fully lamellar structure (Lütjering and Williams, 2007). The loss of ductility with increasing cooling rate has been explained by the change in fracture mode as the size of the alpha colony decreases. The fracture surface of the alloys with alpha lamellae shows a ductile, trans-crystalline type of fracture with dimples. However, a ductile inter-crystalline simple type of fracture is observed in alloys with alpha colonies. These fracture modes are dominant at the continuous alpha layers around the beta boundaries (grain boundary alpha). This same region serves as the preferential site for crack nucleation.

The amount of ductility loss after peak ductility is reached, is determined by two factors. The first factor, which had a significant influence on ductility of α+β alloys with a fully lamellar structure, is the prior beta grain size. The ductility loss in these alloys can be decreased by reducing the size of the prior beta grains through thermomechanical processing (Brun *et al.*, 1998). This decreased the slip length and enhanced the ductility of the alloys. The second factor is the difference in strength between the alpha matrix and the continuous alpha layer on the beta

grain boundaries. This does not seem to have a significant influence on the ductility of α+β alloys when compared to high strength beta alloys (Lütjering and Williams, 2007; Sieniawski *et al.*, 2013). Unlike the high strength beta alloys where there is a large variation between the strength of the continuous alpha layer and the beta matrix, there is little difference between the alpha matrix and the alpha layers at the beta grain boundaries (Sieniawski *et al.*, 2013). The influence of the continuous alpha layer on the properties of high strength beta alloys is not discussed in this review as this study is centred on the development of α+β titanium alloys.

An increasing α colony size increases the fracture toughness of α+β alloys with fully lamellar structures. Detailed explanations of the mechanisms are fully described by Lütjering and Williams (2007).

For α+β alloys with bimodal microstructures, two microstructural features have been considered important:

- The size of the beta grains which is directly proportional to the distance between the primary alpha grains
- Alloying element partitioning effects.

To obtain the desired beta grain size, the cooling rate from the beta phase field (shown in step I of Figure 2.7) must be carefully selected. The size of the alpha colonies in the beta grains of the bimodal structure is usually smaller than that of the fully lamellar structure. Consequently, the slip length of α+β alloys with a bimodal structure is smaller than those with fully lamellar structures (Lütjering, 1998).

When comparing the mechanical properties of the bimodal structure with the fully lamellar structure on the basis of slip length, it is expected that the alloys with bimodal microstructures would exhibit better yield strength, tensile ductility, crack nucleation resistance and crack propagation resistance. However, it has been reported that resistance to crack propagation is much lower in α+β alloys with bimodal microstructures (Lütjering and Williams, 2007). This is explained in terms of the alloying element partitioning effects which cause elements that are less soluble in a phase to diffuse preferentially to another phase where they are more soluble. The partitioning effect of alloying elements has been shown to increase with increasing volume fraction of primary alpha, and has an effect on both yield strength and crack nucleation resistance (Lütjering, 1998; Rafi *et al.*, 2013; Jadhav *et al.*, 2017). However, its effects on fracture toughness, ductility and crack propagation are negligible as those are mainly controlled by slip length and the alpha colony size (Lütjering and Williams, 2007).

The yield strength of α+β alloys with a bimodal structure is dependent on the contributions of both alpha colony size and the alloying element partitioning effect. The maximum yield strength in these alloys is usually attained when the volume fraction of the primary alpha phase is 10 - 20% (Jadhav *et al.*, 2017). Hence, a higher volume fraction of primary alpha would indicate that the partitioning effect would contribute most to increasing strength, while a lower volume fraction would result in the dominance of slip length contributions to the yield strength of the alloys. The crack nucleation resistance in these alloys decreases with an increase in the amount of primary alpha. The alloying element partitioning effect increases with increasing amounts of primary alpha, therefore, alpha stabilisers would diffuse from the lamellar alpha in the beta grains into the primary alpha grains. The alpha lamellae then become less strengthened and more prone to crack nucleation (Lütjering, 1998).

For a fully equiaxed structure in α+β alloys, the most important microstructural feature is the alpha grain size, which again determines the effective slip length. Hence, smaller grain sizes favour a high yield strength, tensile ductility, and resistance to crack initiation compared to large alpha grains. However, larger grains have a superior fracture toughness compared to small grains (Lütjering, 1998).

On a commercial scale, it is much easier to develop alloys with a fully equiaxed structure than a fully lamellar structure for applications where high cycle fatigue strength is required. This is because a grain size of ~6 μm in a fully equiaxed structure has been reported to yield the best combination of properties (Lütjering and Williams, 2007). To achieve a grain size of ~6 μm in alloys with a fully lamellar structure, a cooling rate of about 1000°C/min is required, which can only be achieved in very thin sections and not in heavy section profiles. The challenge is similar in alloys with bimodal structures, because it is quite difficult to achieve primary alpha with an average grain size smaller than 10 μm due to the high recrystallisation temperature (Donachie, 2000).

The resistance of a fully equiaxed structure to crack initiation is higher than that of a fully lamellar structure when the thickness of the alpha plates in the fully lamellar structure is the same as the primary grain size in the fully equiaxed structure. In contrast, Wu *et al.* (2013) showed that a bimodal structure displayed a higher resistance to crack initiation than a fully equiaxed structure. They reported that the fully equiaxed structure had a faster crack propagation rate than both the fully lamellar and the bimodal structures (Leyens and Peters, 2003). This was due to the easy propagation of cracks through the interconnected primary alpha grains without any obstacles in the fully equiaxed structure. However, cracks in bimodal and lamellar structures propagate through the lamellar grains at a much slower rate due to shorter slip lengths. The shorter slip

lengths serve as obstacles to crack propagation that cause branching of cracks and thus lower the rate at which the cracks propagate (Broichhausen and van Kann, 1973; Lütjering, 1998; Ankem and Greene, 1999; Banerjee and Williams, 2013).

In summary, the commercial production of titanium alloys for optimum performance in service involves selection of appropriate alloying elements as well as a good combination of processing parameters. This is a complex and expensive task because processing of titanium alloys is time and energy consuming. The different routes for commercial production of titanium alloys are presented in the following sections.

2.2 Production of titanium alloys – an overview

To develop lower-cost titanium alloys, it is important to understand the most commonly used commercial process for production of titanium alloys, which can be divided into three major sections: the ingot production, primary conversion and secondary conversion processes. Ingots are produced from melted sponge titanium and other alloying elements. Primary conversion is the deformation stage where shaping of ingots to mill products is achieved, while the secondary conversion process is the machining of the mill products.

2.2.1 Ingot production processes

This is the primary method of producing titanium and its alloys. The primary raw materials for formulating titanium alloys include titanium sponge and other alloying elements (Donachie, 2000). Melting remains the most crucial part of this process because producing a sound ingot requires adequate control to avoid the introduction of defects. Defects introduced into titanium alloys during melting can hardly be removed by remelting or subsequent processing methods such as forging or extrusion. As a result, the production of titanium via the liquid route is much more expensive (Donachie, 2000; Lütjering and Williams, 2007).

To date, there are two commercial melting methods that are adopted in developing titanium and its alloys: vacuum arc remelting and cold hearth melting (Donachie, 2000; Lütjering and Williams, 2007). The vacuum arc remelting method is the most developed and utilised method for commercial production of a wide range of titanium alloys. For example, a titanium ingot of up to 20 000 kg with a diameter of 100 cm can be produced using this method. The larger ingots are more economic because melting time and reloading of the furnace becomes shorter. In addition, losses experienced during conversion of ingots to final components are lower with larger ingots. The ingots are usually cylindrical in shape and are often inverted and melted twice to improve homogeneity of the alloys (Donachie, 2000; Lütjering and Williams, 2007).

The cold hearth melting is a more recent melting method which was specifically designed to produce rotor grade titanium alloys (Mitchell, 1998; Akhonin *et al.*, 2003; Zhang *et al.*, 2008). Either plasma arc melting or electron beam melting is used (Blackburn and Malley, 1993). In both cases, there is a copper hearth which contains the molten titanium. In the cold hearth melting, the rate of heat input for melting is balanced against the rate of heat extraction during solidification; which creates and maintains a thin wall of solid titanium commonly referred to as the skull. The skull is always in contact with the hearth and prevents the molten alloy from having contact with the hearth (Lütjering and Williams, 2007).

The cold hearth melting techniques offer some advantages over the vacuum arc remelting technique (Mitchell, 1998; Zhang *et al*., 2008). It allows for a refining process which helps in the dissolution of oxygen- or nitrogen-rich defects. The reuse of titanium scrap and machine turnings can easily be melted without defects. It introduces gravity separation of high density inclusions such as tungsten carbide tool bits or tungsten carbide electrode tips when reclaimed scrap is used as raw materials. These inclusions are trapped in the mushy zone of the skull and are not transmitted into the ingot. Additionally, non-axisymmetric castings such as slabs and bars of ~12 000 kg can be produced directly. Most importantly, the melting process is amenable to sensors for real-time process control and detection of process variations during melting (Lütjering and Williams, 2007).

Despite the advantages of the cold hearth melting technique, rotor grade titanium alloys still require vacuum arc remelting as a final step, as cold hearth melting could introduce some process defects into the ingot. For example, aluminium evaporates and condenses on the roof of the melting chamber during cold hearth melting of titanium alloys (Akhonin *et al*., 2003; Zhang *et al.*, 2008). The aluminium can fall back into the melt and form aluminium-rich zones in the ingots. Vacuum arc remelting helps to homogenise the ingots containing the aluminium rich spots. In addition, cold hearth melting does not have sufficiently high superheat prior to solidification, causing the ingot to have a rough surface. Vacuum arc remelting gives a smooth surface finish that is required in rotor grade alloys (Lütjering and Williams, 2007).

Since vacuum arc remelting remains indispensable to the development of titanium alloys, it is important to discuss the carefully controlled melting conditions to avoid defects (Donachie, 2000; Lütjering and Williams, 2007). The various defects that can be introduced during melting of titanium alloys are classified into five different types as shown in Table 2.5 (Lütjering and Williams, 2007)**.**

Table 2.5: Melt related defects and their possible causes (Lütjering and Williams, 2007).

Defect Type	Possible Causes
Type I – Hard alpha or high interstitial defects	Melting and remelting – small water leak, air leak, aggressive grinding during ingot conditioning. Sponge production – fires during handling or shearing. First melt electrode production – fires during compaction, improperly conditioned scrap, contaminated master alloy, and contamination during welding.
Type II – Alpha stabilised	
Type III – High density inclusions	Scrap additions: tungsten welding electrodes, tool bits mixed into turnings
Type IV – Beta flecks	Melting segregation, conversion too close to transus, adiabatic heating effects
Type V – Voids	Incorporation of shrinkage pipe

These defects are avoided by ensuring that the following important parameters are frequently monitored:

- The melting environment - to prevent Type I and II defects. Air or water leaks in pipes and vacuum chamber may allow the introduction of nitrogen or oxygen contamination into the melt. Water leaks may also lead to hydrogen explosion. Molten titanium is very reactive and nitrogen contamination can lead to the formation of nitrogen-rich TiN. This compound is very hard and brittle and is commonly referred to as hard alpha, which can fracture under low stress and can cause incipient cracks in the material (Avyle *et al.*, 1998; Lütjering and Williams, 2007).

- The size of the molten pool on top of the ingot - has to be controlled by continuously adjusting the melt rate. This is achieved by using lower power settings (such as 200 - 275 instead of 400 - 500 kVA) and reducing the ingot diameter from 100 to 75 cm. Controlling the melt rate prevents freezing segregation which occurs in some alloys such as Ti-17, Ti-10V-2Fe-3Al and other alloys containing substantial amount of eutectoid forming elements (Fe, Ni, Cu, Cr). The segregation of these elements causes beta flecks in titanium alloys and makes the alloys more susceptible to fatigue failures (Avyle *et al.*, 1998; Patel and Fiore, 2016).

- The vacuum arc furnaces are equipped with an electrical coil at the top of the ingot mould to create an electromagnetic field which stirs the molten metal. The coils also help to prevent the arc from jumping sideways. This improves homogeneity of the alloys (Avyle *et al.*, 1998; Lütjering and Williams, 2007; Patel and Fiore, 2016). The coil also centralises the arc to prevent hydrogen explosion which is caused by side-wall-melt-through of the water cooled copper crucible. A titanium melting furnace needs to be built in an explosion proof enclosure and need to be operated remotely (Poulsen, 2000).

- As the final section of the ingot is approached, the melt rate is decreased by decreasing the power in multiple steps. This procedure minimises the extent of shrinkage and type II defects at the top of the ingot (Avyle *et al.*, 1998; Lütjering and Williams, 2007; Patel and Fiore, 2016).

2.2.2 Primary conversion process

The end products of the primary production process are billets, bars, sheets, plates and casting electrodes. Grinding of slabs and turning of round ingot on the lathe are common conditioning practices that are carried out to ensure a smooth surface finish and adequate removal of stress concentrators. Additionally, these processes also remove the oxygen-rich layer. These stress concentrators may initiate cracks during subsequent thermomechanical processing (Sibum, 2003; Lütjering and Williams, 2007)

Among the different primary products, billet and sheet account for about 84%, while bar and casting electrodes account for 14% and 2% respectively (Lütjering and Williams, 2007). Billets are classified as semi-finished products, while sheets and plates (usually with a thickness > 25 mm) are finished products. These products are subjected to either forging or rolling for initial shaping and proper microstructural control. However, casting electrodes are only conditioned and remelted in the furnace to produce castings of titanium alloys (Donachie, 2000; Lütjering and Williams, 2007).

In general, the thermomechanical treatment in this stage includes the initial step of working the alloys in the beta phase field to break down the cast structure. This is done at ~150°C above the beta transus temperature, depending on the type of alloy. This is followed by controlled cooling and working in the (α+β) phase field at temperatures of ~30-50°C below the beta transus temperature, which recrystallises the initial lath microstructure. The recrystallised microstructure is then annealed or stress-relieved, depending on the alloy type and the intended application. For billets, a recrystallised microstructure makes the alloys amenable to subsequent thermomechanical processing during shaping of the alloys (Weiss *et al.*, 1986; Dieter *et al.*, 2003; Wanjara *et al.*, 2005). The different processing steps for achieving the desired microstructures at this stage have been described in Section 2.1.6. Careful selection of thermomechanical processing parameters is very important during the primary conversion process to avoid defects in the products. The main parameters that require adequate control include deformation temperature, amount of deformation and the rate of deformation (Semiatin *et al.*, 1997; Weiss and Semiatin, 1998). Titanium alloys have poor thermal conductivity which makes them prone to adiabatic heating during thermomechanical processing. Adiabatic heating is prevalent at high deformation rates and low deformation temperatures. Defects such as localised deformation within the

adiabatic shear bands, as well as strain induced porosity are easily introduced into the workpiece. These defects are nucleation sites for fatigue failures of titanium alloys (Donachie, 2000; Leyens and Peters, 2003; Lütjering and Williams, 2007), and are not easily repaired by subsequent deformation during shaping of the alloys. More information on the defects associated with thermomechanical processing is provided in Section 2.3.5.

2.2.3 Secondary processing of titanium alloys

This stage involves shaping of primary products, mostly billets, into components for use in targeted applications. This makes the sales of titanium billets higher than the other products obtained from the primary processing stage. To shape titanium billets into finished components, the three different operations that are commonly used are forging, ring rolling and machining (Lütjering and Williams, 2007).

Forging has remained the principal shaping process and has continued to develop since titanium production began in the 1950s (Leyens and Peters, 2003). During forging, components can be formed into desired shapes and the microstructures can be controlled for improved in-service performance (Donachie, 2000). Titanium alloys are forged with hammers or large presses. The forging hammer is either drop or steam driven, while the forging press is driven by mechanical screws or hydraulic actuators. The large press is designed for tighter control of important forging parameters such as strain, strain rate and temperature. It is used for producing components for high performance applications (Lütjering and Williams, 2007).

Forging of titanium alloys is usually done in a closed or open die (Kuhlman, 2005). Closed die forging requires the workspace to be laterally constrained, which is not the case in open die forging (Donachie, 2000). To improve the outputs of these forging methods, different models are being developed. These constitutive models (which will be discussed in later sections) are now available in different software packages such as DEFORM (Scientific Forming Technologies Corporation, 2018) and ABAQUS for optimal control of the deformation process during forging. The selection of the best forging method is largely dictated by the level of microstructural control for a particular application (Lütjering and Williams, 2007).

Despite the advances in the forging of titanium alloys, the cost implication of forged components has remained a subject of concern (Kuhlman, 2005). For example, there are a limited number of large forge presses available globally. Forging of titanium components for high performance applications requires very large presses that are capable of providing the pressure matching the higher flow stresses of titanium alloys. Additionally, components made from titanium alloys are subjected to multi-stage forging (Jackson and Boyer, 2010) which means several forging dies are required. Therefore, the forged components from these presses are expensive (Lütjering and

Williams, 2007). Forged aerospace structures need to be machined to satisfy the light weight requirement of aerospace components. It is difficult to produce the required microstructure when forging near-net shaped components. As a result, large components are forged and then machined into small components that will still retain the desired microstructure. The additional step of machining the forged titanium components makes it more expensive (Lütjering and Williams, 2007), especially as titanium alloys are difficult to machine.

Ring rolling is used for making products such as cylinders and rings. The difference between cylinders and rings is the ratio of diameter to axial height, with rings having a higher ratio (Lütjering and Williams, 2007). The profiles are formed by piercing a hole in the centre of the billet to create a thick walled cylinder. Unlike forging, ring rolling hardly requires machining. Ring rolled products are seamless and have good mechanical properties in the circumferential direction (Welsch *et al.*, 1993; H. Yang *et al.*, 2011)

Machining is an essential processing step in the manufacture of components from titanium alloys. Starting from ingot conditioning to shaping of finished titanium products, metal removal operations are always critical (Donachie, 2000). In general, machining of titanium alloys are considered to be a very difficult and expensive operation when compared with aluminium and steel (Kahles *et al.*, 1985; Narutaki *et al.*, 1983). Titanium alloys have low thermal conductivity and as a result, heat is generally not dissipated easily between the tool and the work-piece interface, which causes tool wear. This problem becomes more aggravated when machining is done at a very high speed (Narutaki *et al.*, 1983; Davim, 2014; Pramanik, 2014). To reduce tool wear, titanium alloys are generally rough machined at slow speed compensated with large depths of cut, then finish machined at higher speeds but much lower depths of cut, usually 0.5 mm. (Jackson and Boyer, 2010).

There has been a lot of improvement in the development of cutting tools for titanium alloys from carbides and ceramic materials but these tools are very expensive. Hence, the cost of removing a unit volume of titanium does not necessarily reduce the total cost of the operation if tool life extension is incorporated into the calculation (Donachie, 2000; Veiga *et al.*, 2013; Pramanik and Littlefair, 2015).

During machining operations such as milling and turning, improved coolants provide effective heat removal. As it is difficult to deliver the required volume of coolant into the bottom of the deep hole during drilling, special drill bits known as coolant-fed bits are used. This escalates the cost of drilling titanium alloys (Lütjering and Williams, 2007).

When machining titanium alloys for applications where high resistance to fatigue is required, three machining steps are used: drilling, reaming and honing. These steps help to avoid any surface damage during machining, but are very expensive. To effectively determine the cutting speed and feed rate during machining of titanium alloys, the type of alloy and the specific machining operation must be carefully considered. For example, it is generally easier and faster to machine CP titanium than higher strength alloys such as Ti-6Al-4V (Donachie, 2000; Lütjering and Williams, 2007). Hence, machinability is an important property to consider when developing new titanium alloys.

Another factor that contributes to the difficulty in machining titanium alloys is the potential of introducing defects into the machined components, especially when dull or damaged tools are used (Donachie, 2000). Surface damage is difficult to detect in titanium alloys when compared with aluminium and steel. This surface damage could have serious consequence when the components are subjected to loading conditions in service (Lütjering and Williams, 2007).

In summary, titanium alloys are very sensitive to slight changes in composition and processing parameters during casting, shaping and machining. This makes it extremely important to select the appropriate parameters during processing if defects and waste of materials have to be minimised. The complexity of selecting the most appropriate processing parameters makes titanium alloys very expensive.

2.3 Research on low-cost titanium alloys

As mentioned in the previous sections, the widespread application of titanium alloys is limited by high cost. There have been several research efforts that are targeted towards cost reduction of titanium alloys. Froes *et al*. (2004) reported that the driving force for titanium research is not necessarily improvement in properties, but cost reduction. The search for alternative beneficiation techniques to the Kroll process such as the Armstrong process (Gerdemann, 2001) could be very effective in reducing the cost of titanium. The implication of this is that beneficiation techniques that are low-cost and continuous would reduce the cost of manufacturing titanium-based components.

The search for low-cost and continuous beneficiation processes for titanium is still on-going. Meanwhile, other approaches currently used in the development of cost-effective titanium components include: the replacement of expensive with less expensive alloying elements, optimisation of hot working processes for shaping and microstructural control, and determination of optimum parameters for machining of titanium alloys (Fujii, 1998; Fujii *et al.*, 2003).

2.3.1 Substitution of alloying elements

Fujii *et al*. (2002) reported that the first step to consider while reducing the cost of titanium alloys is to replace expensive alloying elements with low-cost elements that fulfil similar functions. The different alloying elements that stabilise either the alpha or beta phase are discussed in Sections 2.1.3 - 2.1.6. Among the alpha stabilisers, aluminium remains the most important element (Leyens and Peters, 2003). In developing low-cost titanium alloys, the aluminium content has been decreased or replaced by other cheap alpha stabilisers such as oxygen, nitrogen and carbon (Fujii *et al*., 2002). Although aluminium is affordable when compared to titanium, it has been reported to decrease hot workability of titanium alloys during deformation and consequently increases manufacturing costs (Fujii *et al*., 2002) .

Most beta stabilising elements used in titanium alloys, such as vanadium, molybdenum and niobium, are isomorphous with the beta phase, but are very expensive. To reduce costs, researchers have replaced isomorphous elements with eutectoid beta stabilisers such as iron, chromium, and nickel (Fujii and Takahashi, 2002; Bolzoni *et al*., 2012; Chen and Hwang, 2012; Bolzoni *et al*., 2016).

The exact choice and amount of the less expensive alloying elements is determined by the intended applications for the alloys. Fujii and Takahashi (2002) developed low-cost ternary Ti-Al-Fe alloys by replacing vanadium with iron. They investigated a wide range of compositions and proposed that Ti-3.5Al-1Fe and Ti-5.5Al-1Fe alloys could be used as low-cost alternatives to Ti-3.5Al-2.5V and Ti-6Al-4V respectively. The authors concluded that Ti-5.5Al-1Fe exhibited unique properties such as a high fatigue strength to ductility relationship, with strength levels up to 1000 MPa after solution treating and annealing. The major disadvantage of these alloys is the possibility of forming FeTi when the alloys are used at temperatures above 450°C.

Fujii *et al*. (2002) developed Ti-Fe-O-N alloys by replacing aluminium with oxygen and nitrogen and vanadium with iron. The alloys had high tensile strength (up to 1000 MPa), and excellent workability, corrosion resistance and weldability. The authors concluded that the alloys were suitable for use in applications where temperatures did not exceed room temperature.

Koike *et al*. (2005) built on the work of Fujii *et al*. (2002) by investigating cast Ti-Fe-O-N alloys for dental applications. The authors evaluated the tensile properties, mould filling capacity, corrosion characteristics and grindability of the alloys. The results were compared with commercially pure titanium and Ti-6Al-4V designed for dental applications. They found that the strength of the alloys was 20% higher than that of commercially pure titanium, but were 30% lower than Ti-6Al-4V. The Ti-Fe-O-N exhibited superior grindability and wear resistance when compared to both commercially pure titanium and Ti-6Al-4V.

Nonchovnaya *et al*. (2008) improved the work of Fujii *et al*. (2002) and Koike *et al*. (2005) to determine the optimum compositions of Ti-Fe-O-N alloys. They reported that the Ti-1.5Fe-0.49O - 0.05 N alloy was the optimum for cold and hot deformation, corrosion resistance and biocompatibility. This alloy also attracted the interest of Bettles *et al*.(2011), who investigated the role of microstructure on the mechanical behaviour of Ti-1.64wt% Fe containing varying amounts of oxygen and nitrogen as alpha stabilisers. The different microstructures were obtained by varying the annealing temperature and the oxygen and nitrogen contents. They found that the room temperature mechanical properties of the alloys were sensitive to slight changes in annealing temperature and composition of the alloys. The authors concluded that a higher nitrogen content changed the recrystallised texture of the alloys from basal to prismatic planes. This change in microstructural feature had good influence on the strength and ductility of the alloys.

Despite the interesting findings reported on low-cost alloys proposed by Fujii *et al*. (2002), these alloys were rarely commercialised. The reasons for this could not be obtained from the literature. However, it could be that challenges such as segregation of iron during melting, insufficient cost reduction for titanium industry to invest and limited capacity to produce low-cost alloys for non-aerospace sectors were the reasons why the alloys were never commercialised.

Kuroda *et al*. (2005) developed Ti-Fe-Ta beta alloys as low-cost beta alloys which have superior properties to the Ti-6Al-4V and Ti-6Al-7Nb alloys mostly used for manufacturing of biomedical components. The authors added up to 10 wt% Fe to the alloys, which were cold rolled and solution treated at ~745°C for 3600 s. The alloys were also corrosion tested in Hank's solution. Their results showed that Ti-8Fe-8Ta, Ti-8Fe-8Ta-4Zr and Ti-10Fe-10Ta-4Zr had ultimate tensile strengths of 1066 MPa, 1051 MPa and 1092 MPa and ductility values of 10%, 10% and 6% respectively. The alloys had superior strength and corrosion resistance to conventional biomedical alloys such as Ti-6Al-4V ELI, Ti-6Al-7Nb and Ti-13Nb-13Zr, and they exhibited equivalent elongation to fracture after annealing.

Wang *et al*. (2012b) reported that a Cr-Fe master alloy could be used as an alternative to vanadium in the successful development of low-cost titanium alloys for automobile springs. The authors produced α+β Ti-3Al-2.1Cr-1.3Fe and Ti-2.1Cr-1.3Fe alloys via vacuum arc remelting and investigated the effect of cooling rate on microstructure and tensile properties. These results showed that the cooling rate had a significant effect on the microstructure and tensile properties of the alloys. In both alloys, a martensitic phase was formed after solution treating above the beta transus and water quenching. The presence of the martensitic phase increased the tensile strength, but decreased the ductility in the alloys. Samples subjected to furnace cooling did not contain any

martensitic phase. The alloys consisted of alpha lamellae embedded within the prior beta grains. The tensile strength increased with cooling rate, while the ductility decreased. Ti-3Al-2.1Cr-1.3Fe exhibited superior tensile strength than Ti-2.1Cr-1.3Fe, but had a lower ductility. The fracture surface of the alloys showed dimples irrespective of the cooling rate and composition.

Zhu *et al*. (2014) developed a low-cost α+β Ti-4.5Al-6.9Cr-2.3Mn alloy using Cr and Mn as inexpensive beta stabilising elements. The microstructure and the mechanical properties were investigated at room temperature. The alloy had a fracture strength of ≤1191 MPa, yield strength of ≤928 MPa and a ductility of ≤10.7%. The alloys, produced using a split copper crucible, did not show any segregation of chromium and manganese in the as-cast form. However, segregation of chromium and manganese was seen at the prior β boundaries after thermomechanical treatment.

Although most of the studies discussed are on low-cost α+β alloys, several other low-cost alloys have been developed by researchers. These alloys were developed by using a combination of two or more inexpensive elements, or mixing both expensive and inexpensive alloying elements to stabilise the beta phase. Bhattacharjee *et al*. (2007), Seagle (1996) and Gunawarman *et al.* (2005) developed low-cost titanium alloys by using iron or iron-molybdenum master alloys as beta stabilisers or strengtheners in titanium alloys.

One important low-cost titanium alloy that became popular in the 2000s was the TIMETAL LCB (low-cost beta) consisting of inexpensive alloying elements with 4.5 wt% Fe (Ti-4.5Fe-6.8Mo-1.5Al). This alloy was produced using Fe-Mo master alloy and mostly used as suspension springs in the 2000 model Volkswagen Lupo FSI, Ford Focus and Ferrari Challenge Stradale due to its superior strength and sufficient ductility in comparison with other beta alloys. The cold formability and mechanical properties of the alloy were comparable with that of high strength steel. The increased use of the Fe-Mo master alloy caused an increase in the cost of Fe-Mo master alloy; this led to an increase in the production cost of TIMETAL LCB. Consequently, production of automotive spring using the alloy has reduced (Kosaka et al., 2005; Redmore, 2011).

The low-cost alloys discussed in this section were developed via the conventional casting route. In the last 15 years, there have been several other low-cost alloys developed using other processing routes. The motivation is to produce near net-shaped components which will allow manufacturers to reduce the cost of machining after casting and working. Some of these processing routes include direct metal deposition and blended elemental powder metallurgy (Froes, 1998; Leyens and Peters, 2003). Some processing routes have successfully been used to fabricate commercial Ti-6Al-4V alloys (Dinda *et al*., 2008; Bolzoni *et al*., 2012; Safdar *et al*.,

2012). Other researchers have explored these routes to produce low-cost titanium alloys and composites (Liu *et al.*, 2006; Lou *et al.*, 2016; Sharma *et al.*, 2016).

The advancement in the technology of producing titanium metal powders has led to an increase in the development of powder metallurgy components (Froes, 1998). Commonly used titanium powders include sponge titanium fines and hydrogenation/dehydrogenation (HDH) powder. Fujita *et al*. (1996) investigated the microstructure and properties of the Ti-4.5Al-3V-2Fe-2Mo (SP 700) alloy produced by blended elemental powder metallurgy for jewellery applications. The authors compared the microstructure and properties of the alloy made from either titanium sponge fines or HDH powder as starting materials. Compared to Ti-6Al-4V, the sintered alloy showed superior sinterability, a more homogenous microstructure, better mechanical properties and better workability. The enhancement in the microstructural features and properties was attributed to the addition of iron and molybdenum in the alloy. The HDH titanium powders produced better mechanical properties than the sponge fines. This was attributed to the lower chlorine content in the HDH titanium powder.

Chen *et al*. (2011) developed low-cost Ti-Fe alloys for biomedical applications by replacing expensive vanadium with iron. The effects of cooling method and iron addition on the alpha phase formation and mechanical properties of the sintered alloy were evaluated. They found that using sufficiently high holding temperatures such as 740°C, a large amount of beta phase could be formed with alpha precipitates within the prior beta grains. This microstructural feature resulted in a good combination of strength, hardness and elongation.

Carman *et al*. (2011) investigated the influence of alloying elements on the microstructural evolution of a near-beta Ti-5Al-5Mo-5V-2Cr-1Fe alloy produced via blended elemental powder metallurgy. The authors concluded that the addition of fast diffusing elements in titanium improved homogenisation and the combination of mechanical properties in the alloys. Molybdenum and vanadium were reported to diffuse slowly, increasing the homogenisation time during sintering, whereas aluminium and iron promoted rapid homogenisation.

Joshi *et al*. (2013) developed Ti-6Al-4V and Ti-1Al-8V-5Fe alloys using TiH feedstock. Production of Ti-1Al-8V-5Fe via the ingot metallurgy route was discontinued because of the formation of beta flecks caused by segregation of iron at more than 2 wt% in the alloy. The researchers explored the powder metallurgy approach to develop the alloys and subjected the alloys to thermomechanical processing. It was concluded that after thermomechanical processing the alloys showed mechanical properties that matched those of the alloys when produced via the ingot metallurgy route. The thermomechanical processing helped to reduce the porosity in the sintered alloys and hence improved the mechanical properties.

Bolzoni *et al*. (2012) developed low-cost titanium alloys using blended elemental (BE) powder metallurgy (PM) and inexpensive alloying elements. In their studies, they substituted vanadium with spherical powders of 430 stainless steel (Bolzoni *et al*., 2012) and 85Fe/15Ni (Bolzoni *et al*., 2016). The researchers found that the properties of the sintered alloy were comparable to wrought Ti-6Al-4V commercial alloys. Also, using the PM production route, the formation of an intermetallic phases in the sintered alloys was suppressed. The authors proposed that the sintered α+β Ti - 430 stainless steel and Ti-85Fe/Ni alloys were low-cost alternatives to Ti-6Al-4V.

From these studies, it can be inferred that iron remains an important element in the development of low-cost titanium alloys (Polmear *et al*., 2017), for the following reasons:

- Iron has a capacity to strongly stabilise the beta phase.
- Iron is the lowest cost beta stabilising element.
- Iron has a high strengthening effect in titanium alloys.
- The fast diffusivity in titanium helps to improve sinterability of titanium alloys.

The major disadvantage of using iron in titanium alloys is segregation which could lead to the formation of intermetallic compounds, such as TiFe, or beta flecks in the alloys (Fujii and Takahashi, 2002; Bolzoni *et al*., 2012; Chen and Hwang, 2012; Bolzoni *et al*., 2016). Although the emergence of blended elemental powder metallurgy can address this to a large extent, large and complex-shaped components cannot be made using existing powder metallurgy techniques (W. Peng *et al.*, 2013a; Souza *et al.*, 2015b).

Therefore, it becomes imperative to use low-cost alloying elements in alloys that can be produced via conventional casting without the formation of intermetallic compounds.

Apart from the use of low-cost alloying elements, the recent advances in the additive manufacturing or 3D printing of titanium powders have shown that it will be possible to develop low-cost and efficient near-net shaped titanium alloy components in the future (Edwards *et al.*, 2013; Dutta and Froes, 2017). Additive manufacturing of titanium alloys has been reported to either minimise or eliminate the need for the expensive hot working and machining processes (Dutta and Froes, 2017).

2.3.2 Optimisation of Hot Working and Machining Processes

To reduce the manufacturing cost of titanium alloys, the second approach is to optimise the shaping or forming process (Fujii and Takahashi, 2002), which is mostly done by thermomechanical working, machining or a combination of both. As discussed in Section 2.2.2, in general titanium alloys are very sensitive to changes in parameters controlling the thermomechanical and machining processes, so it is essential to optimise these parameters. This

is quite important as cost-effective shaping of the alloys is not the only benefit realised, but adequate microstructural control in the final component can also be obtained. Shaping technologies such as high speed machining is carried out at strain rates that are in the order of 10^6 s^{-1} (Zhang *et al*., 2016). Some level of deformation and microstructural changes could occur during this process (Yan *et al*., 2013; Pramanik and Littlefair, 2015; Sharma *et al*., 2017). Hence, controlling microstructural evolution and achieving cost-effective shaping of titanium components with minimal waste have drawn the attention of researchers.

The research efforts focussing on the optimisation of hot working and machining of metallic alloys have evolved over time. It commenced with the description of the shape of the stress-strain curves obtained during simulated deformation tests, such as isothermal compression testing under plane strain or uniaxial conditions and hot tensile testing (Prasad, 2003). However, the uncertainties in this method led researchers to develop constitutive equations to describe the stress-strain curves, make basic predictions, and obtain information about rate controlling mechanisms during processing. The major disadvantage of this method is that the optimum processing conditions during shaping cannot be established. Consequently, advances in research efforts led to the introduction of processing maps (Prasad *et al*., 2015). Processing maps not only determine the optimum combination of processing parameters for shaping and microstructural control, but could also delineate the 'safe' and 'unsafe' combinations of processing parameters. In recent times, the combination of constitutive equations and processing maps has been used to optimise the shaping of metallic workpieces, particularly titanium and its alloys (Chen *et al.*, 2008; Balasundar *et al.*, 2013a; Fan *et al.*, 2013a; Nayan *et al.*, 2014).

Optimisation based on constitutive modelling

The studies presented in Table 2.6 mostly focused on deformation at elevated temperatures and a limited range of strain rates (10^{-3} - 100 s^{-1}). This does not truly represent shaping by rolling and extrusion, and metal removal operations (cutting, milling and drilling). Therefore, the models developed by these researchers only addressed manufacturing operations such as forging. To fill this gap, Chen *et al*. (2015) developed constitutive models describing the flow behaviour of Ti-6Al-4V over a wide range of temperatures (20 - 900°C) and strain rates (10^{-4} - 10^4 s^{-1}) respectively. Their study involved isothermal compression of Ti-6Al-4V samples under quasi-static and dynamic strains rates using DNS-100 test machines with a load capacity of 100 kN and an enhanced Split Hopkinson bar. Testing on the DNS was done at strain rates of 0.0001 - 0.01 s^{-1} while the Split Hopkinson was used at 2500 - 10000 s^{-1}. The authors found that the flow behaviour was temperature dependent. The workability and ductility of the alloy changed at deformation temperatures above 500°C. Based on their observation, four models: Johnson-Cook

(Johnson and Cook, 1983), Khan-Huang-Liang (Khan *et al.*, 2000), modified Johnson-Cook and modified Khan-Huang-Liang (G. Chen *et al.*, 2015), were used to describe the flow behaviour of the alloy under the different deformation conditions. The variables of the four models were calculated using a genetic algorithm optimisation method. It was concluded that the four models could accurately predict the flow stress of Ti-6Al-4V alloy over the entire test range since standard deviation was within 4 - 13%.

However, the modified Johnson-Cook and modified Khan-Huang-Liang models provided more accuracy when predicting the flow behaviour of the material under dynamic conditions such as higher strain rates of 2500 – 10000 s^{-1}.

The literature summarised in Table 2.6 showed that different types of constitutive models are used to describe the flow behaviour of titanium alloys depending on the analyses of the stress-strain curves. The accurate prediction of flow stress from the models is very important. However, obtaining an accurate prediction is rather a daunting task, as combining two or more models is sometimes required (W. Peng *et al.*, 2013a; Souza *et al.*, 2015b).

There are other cases where an additional optimisation step was included to improve the accuracy and reliability of the predictions from the constitutive models. A succinct description of the different types of constitutive models is presented in Section 2.3.3 based on the work of Chen *et al.* (2015). The different deformation mechanisms such as dynamic recovery and dynamic recrystallisation suggested by the constitutive analyses are described in Sections 2.3.4 and 2.3.5. Constitutive models are used as finite element codes in finite element analysis of the manufacturing processes of titanium alloys. Therefore, these models should not only predict the flow stress accurately, but be very simple as well. Abakri *et al.* (2015) developed simplified constitutive models for describing the hot working behaviour of steels, but the suitability of the models for describing the hot deformation behaviour of titanium alloys is yet to be reported.

Table 2.6: Previous studies on the constitutive modelling of hot working of titanium alloys.

Authors	Alloy type	Alloy	Model	Test parameters			Main findings
				Temperature (°C)	Strain rate (s^{-1})	Strain (%)	
Khan *et al.* (2004)	α+β	Ti-6Al-4V	*cf.* Johnson-Cook and Khan-Huang-Liang	-40 - 482	10^{-5} - 3378	30&70	Khan-Huang-Liang model - better agreement with experimental data than Johnson-Cook
Vo *et al.* (2007)	Near-α	IMI-834	Self-consistent	975 - 1100	0.1 & 1.0	80	> 1025C: DRV and DRX caused softening. At lower temperatures, lamellar kinking was observed.
Zong *et al.*(2009)	α+β	TC11	Arrhenius Equation	750 - 900	0.1 - 10	40 & 60	DRX occurred at 950°C and 10^{-3} s^{-1}
Zeng *et al.* (2009)	α	CP-Ti	Arrhenius Equation	400 - 700	10^{-3} - 1	90	Work-hardening: dominant at lower temperatures and higher strain rates. Flow softening: higher temperatures and lower strain rates. Materials constants were functions of strain.
Gao *et al.* (2011)	α+β	Ti-6Al-4V	*cf.* Gao-Zhang-Yang for hcp metals, Johnson-Cook Zerilli-Armstrong	77 - 798	10^{-3} - 6000	60	Gao-Zhang-Yang for hcp metals gave a better prediction of the flow stress than Johnson-Cook and Zerilli-Armstrong models. Material constants optimised using multivariable non-linear regression.
Wang *et al.* (2010)	Metastable β	Ti2448	Arrhenius and Avrami equations	750 - 850	10^{-3} - 63	70	Softening caused by DRV at high strain rates (> 1 s^{-1}), DRXn caused flow softening at lower strain rates (< 1 s^{-1}). Levenberg-Marquardt algorithm used to optimise materials constants.
Peng *et al.* (2013b)	Near- α	Ti-60	*cf.* Arrhenius eqn & Artificial Neural Network	970 - 1120	10^{-2} - 10	80	Softening mechanism changed from DRX at low strain rates (≤0.1 s^{-1}) to flow localisation and cracking at higher strain rates (≥ 1 s^{-1}). Artificial neural network provided a better prediction of the flow stress.

Pondatawit *et al*. (2014)	α+β	Ti-6Al-4V	*cf*. Cingara, Ebrahimi and Shafiei equations	900 - 1050	0.1, 1 & 10	80	The combination of Cingara, Ebrahimi and Shafiei equations predicted the flow stress to a high degree of accuracy when compared with Cingara or hyperbolic-sine equations alone, as the combination allowed for the incorporation both work-hardening and dynamic recrystallisation.
Souza *et al*. (2015b)	α+β	Ti-6Al-4V	Avrami, and Estrim & Mecking	750 - 920	10^{-2} - 10	80	Softening occurred due to adiabatic heating at higher strain rates, while at lower strain rates microstructural changes such as coarsening of equiaxed alpha grains and an increase in beta phase fraction led to flow softening. The combination of Avrami's and Estrim and Mecking's models gave better prediction than Estrim and Mecking's model alone.
Chen *et al*. (2015)	α+β	Ti-6Al-4V	*cf*. Johnson-Cook, Khan-Huang-Liang, mod. Johnson-Cook, & mod. Khan-Huang-Liang genetic algorithm	20 - 900	10^{-2} - 10^{4}	25	The four models were able to predict flow stress under quasi-static and dynamic strains rates. The modified Johnson-Cook and modified Khan-Huang-Liang provided more accuracy when predicting the flow behaviour of the material under dynamic conditions such as higher strain rates of 2500 - 10000 s^{-1}.

Optimisation based on processing maps

The advances in finite element methods have led to the development of rigid viscoplastic FEM techniques which paved way for the successful prediction of deformation behaviour of metallic materials. FEM can be used to establish the constitutive relationships between strain rate, strain and temperature as an empirical or algebraic equation. This equation helps to identify the rate controlling mechanism for a given plasticity problem.

However, the difficulty in arriving at a unique or optimum solution to a general plasticity problem during deformation led to the development of processing maps (Prasad and Seshacharyulu, 1998a). Processing maps help to describe dynamic material behaviour during hot working. The difficulty in deriving the constitutive relationship for different dynamic restoration processes dominating deformation is largely overcome by dynamic material models (Prasad, 2003). The information derived from processing maps could be incorporated into the finite element method in an explicit manner. This made it possible to obtain a unique solution for any plasticity problem during deformation (Prasad and Seshacharyulu, 1998a).

Processing maps help to delineate the “safe” and “unsafe” processing regimes during deformation under different strain rate and temperature conditions. The concept of dynamic materials modelling and the procedures for developing processing maps from experimental data are described by Prasad *et al*. (2015). However, a general overview of the concept is presented in Section 2.3.4.

Processing maps have been used to optimise processing of a wide range of metallic alloys, including titanium. Some of the studies are presented in Table 2.7. Most of these studies focussed on as-cast and wrought titanium alloys. However, a few studies involving titanium alloys developed via powder metallurgical routes are also presented.

Table 2.7: Previous studies on processing maps of titanium alloys.

Author	Alloy type	Alloy	Test parameters			Main findings
			Temperature (°C)	Strain rate (s^{-1})	Strain (%)	
Prasad *et al*. (1984)	α+β	Ti-6242	890 - 1010	10^{-3} - 10	4&60	The optimum condition for forging the alloy was 927°C and 10^{-3} s^{-1}. In the temperature range of 899°C to 982°C, dynamic recrystallisation and phase transformation were the dominant mechanisms influencing the efficiency of power dissipation, while at 1010°C and low strain rates, wedge cracking controlled the power dissipation efficiencies.
Prasad and Secharchayulu (1998b)	α , Near-α and α+β	CP-Ti, IMI-834 and α+β Ti-6Al-4V	750 - 1050	10^{-3} - 100	40&60	The domain of dynamic recrystallisation occurred at 725°C and 0.001 s^{-1}. This domain shifted to higher strain rates and temperatures when the oxygen content in the pure titanium was lowered. The alloys with a transformed beta initial microstructure exhibited spheroidisation of lamellae at lower temperatures and beta superplasticity at high temperatures when deformed at slow strain rates. In titanium alloys with fully equiaxed structures, the domain of superplasticity was observed in the (α+β) range, while dynamic recrystallisation occurred in the beta phase field with about 55% power dissipation efficiency. A wide domain of instability was caused by adiabatic shear band formation at high strain rates.
Poletti *et al*. (2010)	α+β	Ti-6Al-4V +0.1 wt% B +0.1 wt%C	850 - 1000	10^{-3} - 10	10, 20&30	At low strain rates (≤0.1 s^{-1}), large values of power dissipation efficiency were obtained, while at higher strain rates, the power dissipation values were very low. The high power dissipation was ascribed to superplasticity, especially when deformation was carried out at 950°C. However, lower dissipation efficiency was ascribed to cracking and debonding of TiB at low temperatures and porosity evolving at triple grain boundaries at temperatures above 1000°C.
Balaamsubranayam and Prasad (2002)	β	Ti-10V-4.5Fe-1.5Al	650 - 950	10^{-3} - 10^{2}	60	The domain of dynamic recrystallization was between 750 and 850°C. The highest efficiency of dissipation was at 850°C and 0.01 s^{-1}. Regions of unsafe forging were seen at a strain rate of 10 s^{-1} and a wide range of temperatures due to manifestation of flow localisation.

Author	Alloy type	Alloy	Test parameters			Main findings
			Temperature (°C)	Strain rate (s^{-1})	Strain (%)	
Jia *et al*. (2011b)	Near- α	Ti60	960 - 1100	10^{-3} - 10	60	Dynamic globularisation was the dominant softening mechanism in the (α+β) phase field, while dynamic recovery and dynamic recrystallisation were dominant in the beta phase field. The unsafe regions to be avoided during processing of the alloy were 960 - 980°C and 0.3 - 10 s^{-1} and 990 - 1110 °C and 0.58 - 10 s^{-1} strain rates.
Zhu *et al*. (2012)	Metastable β	TC-21	1000 - 1050	10^{-3} - 63	30, 45, 60 & 75	Softening was caused by adiabatic heating at strain rates (> 1 s^{-1}) while dynamic recrystallisation caused flow softening at lower strain rates (< 1 s^{-1}) for samples deformed to total strains of strain of 30 %, 45 % and 60 %. For samples deformed to a strain of 75%, flow localisation occurred even at slow strain rate of 0.001 s^{-1} and temperature of 1000°C.
Wang *et al*. (2012a)	α+β	Ti-3.0Al-3.7Cr-2.0Fe-0.1B	850 - 950	10^{-1} - 10	70	Dynamic recrystallisation dominated the deformation process at strain rate >1 s^{-1} and the degree of recrystallisation increased with increasing strain rate. No region of instability was obtained in the processing map, since the tested variables were not as broad.
Qu *et al*. (2012)	α+β	As-cast ATI	950 - 1150	0.1, 1 & 10	50	Deformation in the (α+β) phase field was dominated by the globularisation of the alpha platelets, while softening in the (α+β) phase field was dominated by dynamic recovery in the beta phase. The optimal conditions for ingot breakdown of the as-cast alloy included temperatures >1000°C and strain rates > 0.1 s^{-1}. They recommended that a strain > 50 % should be used to obtain a more recrystallised microstructure in the alloy.
Fan *et al*. (2013a)	α+β	Ti-6Al-4V	750 - 920	10^{-2} - 10	80	The optimal deformation condition was obtained at ~855°C and 0.01 s^{-1} with a peak efficiency of 65%. This region was dominated by dynamic globularisation. The instability domain to be avoided during processing of the metal was indicated as deformation occurring at low temperatures and moderate strain rates or high strain rates (≥1 s^{-1}), at all temperatures.

Author	Alloy type	Alloy	Test parameters			Main findings
			Temperature (°C)	Strain rate (s^{-1})	Strain (%)	
Bai *et al*. (2014)	α+β	Ti-6Al-4V	750 - 850	10^{-3} - 1	50	No region of instability was shown on the processing map and the optimal processing condition for hot working was 850°C and 0.01 s^{-1} strain rate. The entire deformation process under the tested condition was dominated by dynamic recovery and dynamic recrystallization.
Balasundar *et al*. (2013b)	Near-α	TITAN 29	850 - 1100	$3x10^{-4}$ - 10	50	The optimum conditions for breaking the as-cast structure were: 1000 - 1070°C and $3x10^{-4}$ - 10^{-3} s^{-1} with a power dissipation efficiency of 40 - 46% for dynamic globularisation of alpha phase. 1070 - 1100°C and 1 - 10 s^{-1} with a power dissipation efficiency of 40 - 50 % for dynamic recrystallisation of the beta phase. During ingot breakdown of TITAN 29, working at deformation temperatures of 800 - 980°C and strain rates of $3x10^{-4}$ - 10 s^{-1} should be avoided. These regions were dominated by flow instabilities such as wedge cracking and voids.
Balsundar *et al*. (2017)	α+β	BT3-1	850 - 1060	$3x10^{-4}$ - 1	60	Deformation was controlled by superplasticity when the alloys were deformed at temperatures within the (α+β) phase field, while dynamic recrystallisation of the beta phase dominated the deformation in the beta phase field. Partial dynamic recrystallisation occurred when the alloy was deformed near the beta transus temperature with fine globular primary alpha pinning the migrating beta grain boundaries.
Rao and Pasad (2010)	γ-TiAl	γ-TiAl with *in situ* carbide and silicide	800 - 1050	10^{-4} - 1	80	Safe processing window was 850 - 1025°C and 0.0001 - 0.001 s^{-1} with a peak power dissipation efficiency of 52%. The power dissipation efficiency indicated dynamic recrystallisation as the dominant softening mechanism. The unsafe region to be avoided when deforming the alloys was 0.0003 s^{-1}/ 800°C and 0.03 s^{-1}/1050°C, as this region is dominated by cracking.

Author	Alloy type	Alloy	Test parameters			Main findings
			Temperature (°C)	Strain rate (s^{-1})	Strain (%)	
Rao *et al*. (2011)	γ-TiAl	Ti-46Al-4Nb-2Cr-2Mn	925 - 1050	10^{-4} - 10	80	The safe processing window for the alloy was 923 - 1025°C at 0.0001 - 0.001 s^{-1} and 1023 - 1050°C at 0.01 s^{-1}. The peak dissipation efficiency obtained in this region was 50% which corresponded to dynamic recrystallisation of the α-TiAl phase. The alloys should not be subjected to hot working at strain rates > 1 s^{-1} because of the manifestation of instability such as cracking.
Gupta *et al*. (2012)	γ +α2-TiAl	Ti-48Al-2Cr-2Nb, Ti-48Al-2Cr-2Nb-0.1B and Ti-48Al-2Cr-2Nb-0.1B alloys	750 - 1250	10^{-3}, 10^{-2} & 10^{-1}	50	The safe processing conditions for all the alloys lay within the temperature range of 950 - 1150°C and strain rates of 0.01 s^{-1} with dynamic recrystallisation dominating the region.
Kim *et al*. (2016)	α+β	Ti-6Al-4V	800 - 1100	10^{-3} - 10	100	Deformation at higher temperatures in the beta phase field and higher strain rates was associated with dynamic recrystallisation of the beta grains. The optimal processing condition for the sintered Ti-6Al-4V was 945°C and 0.001 s^{-1} which had the highest power dissipation efficiency of 46%.

From the surveyed literature (Tables 2.6 and 2.7), it can be seen that the hot working process can easily be optimised using a combination of experimental stress-strain curves, constitutive modelling and processing maps obtained by dynamic materials modelling. However, the selection of an appropriate constitutive model to accurately describe the stress-strain behaviour and the dominant mechanisms requires a detailed understanding of the various constitutive models that are available, as well as the interpretation of the processing maps. As can be seen in this section, different alloys may require a single or a combination of constitutive models to accurately determine the kinetics of the hot working process. In addition, it can be seen that a combination of safe and unsafe mechanisms controlling the deformation process changes as the processing parameters change. Sections 2.3.3 - 2.3.5 provide more information on the types of constitutive models that are generally used in optimising the hot working process. The construction of processing maps and the basic interpretation of terminologies such as power dissipation efficiency are also presented.

2.3.3 Classification of constitutive models

During forming processes such as rolling, extrusion and forging, the response of materials to imposed variables is described in four different stages of the flow stress as shown in Figure 2.13 (Sajadifar and Yapici, 2014). Stage I is characterised by a rapid increase in flow stress due to work hardening and dynamic recovery at lower strains. In this stage, the rate of dynamic recovery is much lower than the rate of work hardening. Stage II (the transition stage) is characterised by an increase in the rate of dynamic recovery and the onset of dynamic recrystallisation. The flow stress still increases but not as steeply as in stage I. The third stage is characterised by a drop in flow stress, usually attributed to dynamic recrystallisation causing flow softening of the material. At this stage, flow softening is more dominant than work hardening. The last stage (IV) is referred to as the steady-state stage where the steady flow stress shows that the degree of flow softening caused by dynamic recrystallisation or dynamic recovery is in equilibrium with work hardening.

An ideal constitutive equation should accurately predict the flow stress at every stage of the deformation process. The models should describe the dependence of flow stress on strain, strain rate and deformation temperature, strain rate history, anisotropic and isotropic strain hardening behaviour. The series of constitutive models developed by previous authors (Section 2.3.2) have shown that a good prediction of the flow stress can be obtained from the different types of models, which can be classified into three groups: phenomenological, physical and artificial neural networks (Lin and Chen, 2011). Regardless of the constitutive model used, the complex nature of the hot working process has necessitated continuous modification of the models to improve the accuracy of predictions and kinetic analysis.

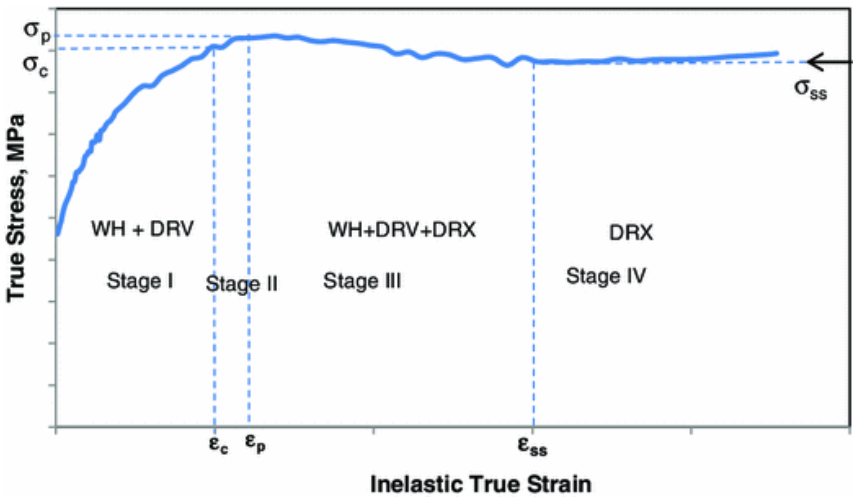

Figure 2.13: Flow stress showing different stages during hot deformation.(Sajadifar and Yapici, 2014).

Among the various types constitutive models used in the past, Lin and Chen (2011) found that the phenomenological models remain the simplest and most utilised. The models, developed using observation and fitting of experimental data, are simple as they require only a few material constants, can easily be calibrated and used as finite element codes. Conversely, phenomenological models cannot produce an accurate description of the physical process such as thermal activation of dislocation movements and thermodynamics. The most common phenomenological model is the Johnson-Cook model (Johnson and Cook, 1983) while the Arrhenius model (Sellars and Tegart, 1966) is the simplest form of phenomenological model. Other models in this category include the Khan-Huang-Liang model (Khan *et al.*, 2004), Voce-Kock model (Kocks, 1976; Kocks and Mecking, 2003), Khan-Liang-Farrohk (Farrokh and Khan, 2009), and the Fields-Backofen (Jia *et al.*, 2016) model. All these models have been modified and improved by researchers since they were first developed (Lin *et al.*, 2008; G. Chen *et al.*, 2015; Lin and Chen, 2011). One common characteristic of phenomenological models is the relationship between flow stress and other parameters expressed in Equation 2.3 (Johnson and Cook, 1983; Khan *et al*., 2004; Farrokh and Khan, 2009; Lin and Liu, 2010; Lin and Chen, 2011; Lin *et al*., 2016):

$$\sigma = (\varepsilon, \dot{\varepsilon}, T) \qquad \textbf{Equation 2.3}$$

where σ is the stress, ε is the strain, $\dot{\varepsilon}$ is the strain rate and T is the temperature.

Based on the consulted literature, a hyperbolic sine form of the Arrhenius constitutive model with the incorporation of the Zener-Hollomon parameter (Zener and Hollomon, 1944) remains the most utilised phenomenological model for describing hot working of metallic alloys, especially titanium alloys (Lin and Chen, 2011). This equation has been further modified to compensate for

strain effects during deformation, thus making it suitable to describe the behaviour of materials over a wide range of testing temperatures, strain and strain rates (Lin *et al., 2008)*. Although this modification was initially made for 42CrMo steel, other researchers have used it to describe the flow response of titanium alloys (Peng *et al.*, 2013b; Porntadawit *et al.*, 2014).

The different physical models to describe or predict plastic flow during hot working are the: Zerilli-Armstrong (Zerilli and Armstrong, 1987), Preston-Tonks-Wallace (Preston *et al.*, 2003), Rusinek-Klepaczko (Rusinek and Klepaczko, 2001) and Estrim-Mecking models (Estrin and Mecking, 1984). These models use physical quantities such as thermodynamics and thermal activation of dislocation movement. This has become necessary since phenomenological predictions cannot accurately describe flow behaviour when there are large changes in internal microstructure of the material accompanying the deformation process (Lin and Chen, 2011). The major weakness of these physically-based models is that large material constants need to be derived and some of the constants need to be measured accurately using high precision facilities. Consequently, the models become very complex before generated data can be fed as a code into commercial finite element software (Lin and Chen, 2011).

The artificial neural networks are robust models for solving non-linear problems such as the constitutive relationship of process variables during hot working. Artificial neural networks have been used successfully to describe the flow behaviour of titanium alloys during hot working (Lin and Chen, 2011). However, the major shortcoming of the approach is that the artificial neural network is dependent on preliminary information from either phenomenological or physically based models.

2.3.4 Construction and interpretation of processing maps

Prior to the development of processing maps from dynamic materials modelling, the constitutive relationship between process variables and response of materials during hot working was described by atomistic and kinetic models (Prasad and Seshacharyulu, 1998a). The limitation of these models is the inability to describe the mechanism controlling the hot working process in multiphase metallic alloys and the deformation behaviour of the alloy at high strain rates.

Froes and Ashby (1982) were the first researchers to develop processing maps which involved plotting stress against homologous temperature of 0.2 - 0.8 T_m (where T_m is the melting temperature of the metal). It was later reported that this map could only describe deformation processes carried out at quasi-static strain rates such as creep (Prasad *et al.*, 2015), whereas industrial processing of metals is carried out at high deformation speeds and higher temperatures. The high temperature helps to deform the metals to very large strains in a single step without the

onset of fracture. Consequently, Raj (Prasad *et al*. 2015) developed a new set of processing maps based on the work of Froes and Ashby (1982). The map, named after Raj, could show the different mechanisms dominating a particular region of temperature and strain rate on the map. Therefore, these maps were able to provide basic information about the 'safe' (defect free) and 'unsafe' (defect prone) regions during processing (Prasad and Seshacharyulu, 1998a; Prasad *et al*., 2015). A typical example of a Raj micro-mechanistic map is shown in Figure 2.14, while the different models for constructing the map are presented in Table 2.8.

In Figure 2.14, the safe region is marked by dynamic recrystallization (DRX), while the unsafe regions are marked by cavity, and wedge-cracking. The Raj map is very useful in describing and optimising the deformation behaviour of pure metals and dilute alloys. However, too much atomistic data are required for commercial alloys , hence making it difficult and impractical to develop the Raj maps for commercial alloys (Kutumarao and Rajagopalachary, 1996).

Prasad *et al.* (1984) built on the work of previous authors and particularly expanded on modelling the intrinsic workability of metallic materials initiated by Gegel (1980). They sought to answer the fundamental question of how a material responds to imposed variables during hot working.

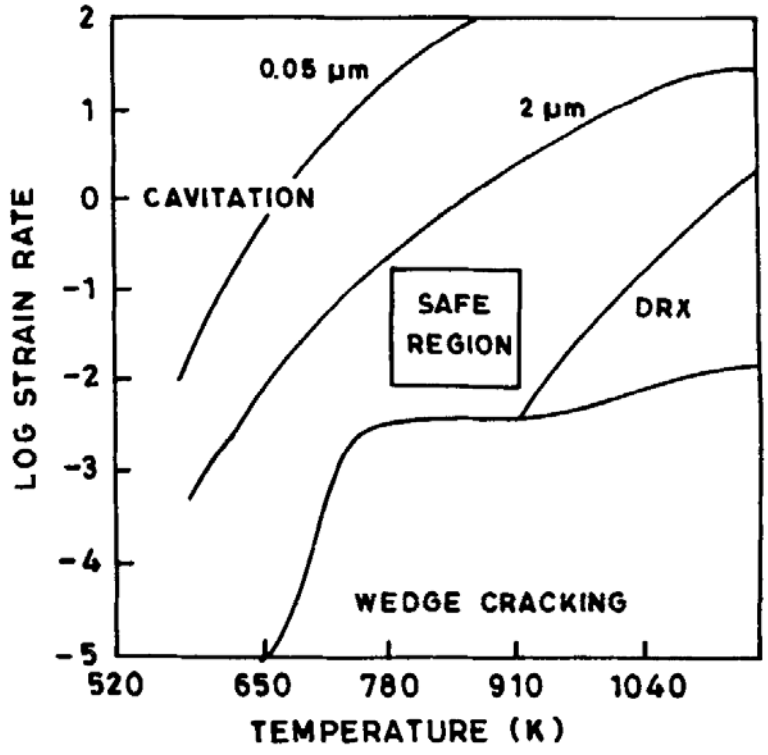

Figure 2.14: Schematic diagram of a Raj map (Kutumarao and Rajagopalachary, 1996).

Table 2.8: Models for constructing a Raj map (Kutumarao and Rajagopalachary, 1996).

Mechanism	Constitutive equation	Condition
Cavity formation	$\dot{\varepsilon}_d = \frac{118(1-\nu)\left(1-2\nu+\frac{2}{\pi}\right)}{\left(\frac{5}{6}-\nu\right)^2}\frac{\Omega G}{kT}\frac{\delta D_b f_v}{p^3}$	Ductile fracture if $\dot{\varepsilon} > \dot{\varepsilon}_d$
Wedge cracking	$\dot{\varepsilon}_w = \frac{8\sigma_v \Omega \delta D_b}{dkTf_b p^2}$	Wedge cracking if $\dot{\varepsilon} < \dot{\varepsilon}_w$
Dynamic recrystallization	$\dot{\varepsilon}_r = Z(\varepsilon_{cr})\exp\left(-\frac{Q}{RT}\right)$	Not a detrimental mechanism
Adiabatic heating induced localization	$\dot{\varepsilon}_h = A'\exp\left(-\frac{Q}{RT}\right)\left[\frac{nRT^2\rho C_p}{QG}\right]^n$	Adiabatic shear banding if $\dot{\varepsilon} > \dot{\varepsilon}_h$

Hot working equipment such as forging, rolling and extrusion dies were considered to be systems which transfer power obtained from the source as energy to the material (Prasad *et al*., 1984). The material in this case is the workpiece undergoing deformation. The material is considered as another system which responds to the induced power transferred to it. A simple mathematical expression for describing the instantaneous response of the material to the imposed strain rate at constant temperature (T) and strain rate history (M) is given in Equation 2.4 (Prasad *et al*., 1984):

$$\bar{\sigma} = K\dot{\bar{\varepsilon}}^m|_{TM} \qquad \textbf{Equation 2.4}$$

where $\bar{\sigma}$ is the instantaneous response of the work piece or effective flow stress; K and m are the material constants; $\dot{\bar{\varepsilon}}$ is the applied strain rate.

The workpiece is seen as a non-linear dissipater of power while it undergoes plastic strain to assume the shape of the dies in the deformation zone. The power dissipated by the workpiece is divided into two different components: thermal and microstructural changes. The thermal content of the dissipated power is usually larger than the power dissipated due to microstructural changes. A schematic representation of a typical non-linear dissipater is shown in Figure 2.15. The total power dissipated in relation to the instantaneous response of the material is expressed in Equation 2.5 (Prasad *et al*., 1984):

$$P \equiv G + J = \bar{\sigma}.\dot{\bar{\varepsilon}} \qquad \textbf{Equation 2.5}$$

where P is total power dissipated; G is a thermal constant; J is microstructural content. Note that $\bar{\sigma}.\dot{\bar{\varepsilon}}$ is the area of the rectangle in Figure 2.15.

The partitioning power between the thermal content and the microstructural content is referred to as the strain rate sensitivity parameter (m) which changes with changes in temperature and strain rate. In the dynamic materials model, the microstructural content (J) reaches a maximum when m is equal to 1. Therefore, the J content of a material undergoing deformation is usually compared with J_{max} to obtain the power dissipation efficiency (η) expressed in Equation 2.6. The

power dissipation is expressed in terms of the strain rate sensitivity parameter *m* in Equation 3.3 (Chapter 3).

$$\eta = \frac{J}{J_{max}} \qquad \textbf{Equation 2.6}$$

Power dissipation efficiency values obtained under varying conditions of strain rate and temperatures can be represented on a contour plot known as a power dissipation map. The power dissipation values represent the rate of entropy production due to microstructural changes under the imposed strain rate and temperature at a given strain.

The different microscopic phenomena occurring during hot working dissipate different iso-efficiency values. Some of the microscopic phenomena are beneficial to hot working, while others are detrimental. Dynamic recovery, dynamic recrystallisation and superplasticity dissipate power with unique efficiencies when compared with microscopic phenomena such as flow localisation, cracking, kink bands, adiabatic shear bands and other detrimental microscopic phenomena (Prasad *et al*., 2015). To differentiate between beneficial and detrimental microscopic phenomena during material forming operations, an instability criterion was developed by Prasad (2015) based on the extremum principle of irreversible thermodynamics. The mathematical expression for Prasad's instability criterion is presented in Equation 3.4.

Any microstructural change which occurs in a material when the instability criterion is negative will cause instability. The instability values can be represented on a contour plot under varied temperatures and strain rates to obtain the instability maps. The superimposition of a power dissipation efficiency map and an instability map is known as a processing map. An example of a processing map is shown in Figure 2.16 (Rao *et al*., 2011).

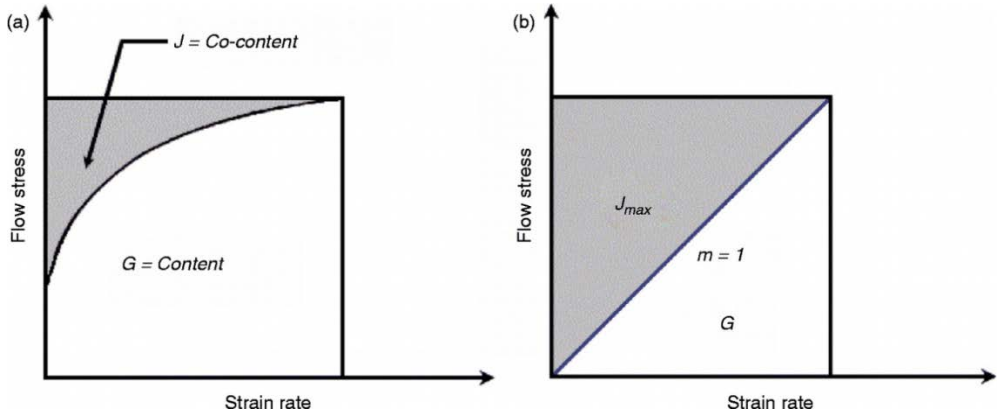

Figure 2.15: Schematic representation of (a) a non-linear power dissipater and (b) an ideal power dissipator (Omar and Prado, 2012).

Although Prasad's instability criterion has been used to develop processing maps for a wide range of titanium alloys and other metals, other researchers have found that Prasad's instability criterion failed to identify unsafe deformation regions in some metals. Consequently other instability

criteria have been developed by some researchers and have been reviewed by Murty and co-workers (2002).

Poletti *et al.* (2010) used Murty's criterion that was derived based on Zeigler's continuum principles to delineate the safe and unsafe regions during deformation of titanium alloys. Murty's criterion (Murty *et al.*, 2002) has also attracted the interest of other researchers (Gupta *et al.*, 2012).

2.3.5 Hot deformation mechanisms- processing maps and microstructural validation

To obtain reliable information from processing maps, deformed samples are subjected to microstructural investigations to ascertain the mechanisms controlling the deformation process (Prasad *et al.*, 2015). The power dissipation efficiency values obtained on the processing map is validated against the microstructural features of the deformed samples. Based on the work of previous authors, a number of hot deformation mechanisms have been reported.

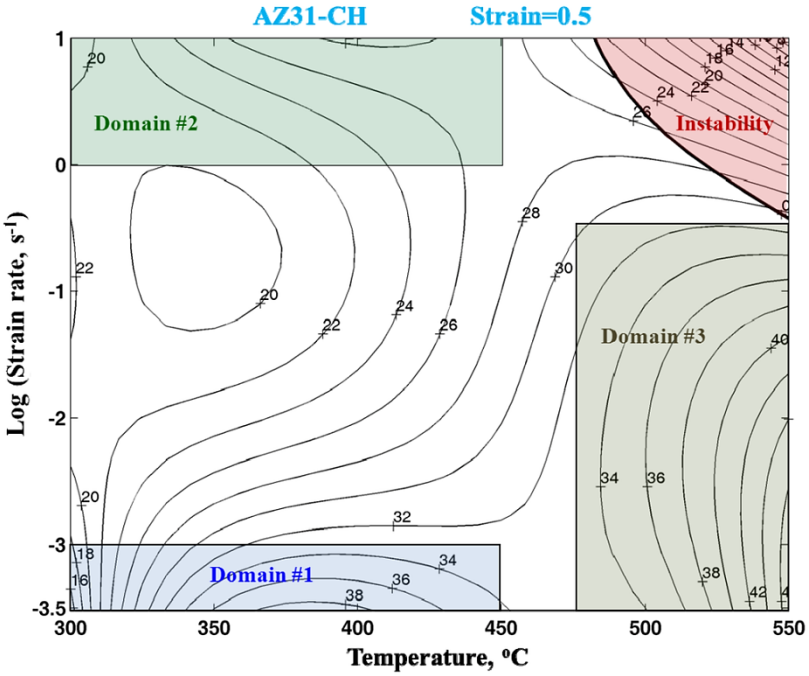

Figure 2.16: Processing map for AZ31 magnesium alloy showing a region of instability (Rao *et al.*, 2012)

These mechanisms are either termed 'safe' or 'unsafe' for material processing (Kutumarao and Rajagopalachary, 1996; Murty *et al.*, 2000; Poletti *et al.*, 2010; Rao and Prasad, 2010; Prasad *et al.*, 2015). This section presents the mechanisms influencing softening during deformation and corresponding power dissipation efficiency values as described by Prasad and co-workers (Prasad and Seshacharyulu, 1998b; Prasad, 2003; Prasad *et al.*, 2015). The first sets of mechanisms discussed are the safe mechanisms which include: dynamic recrystallisation, dynamic recovery and superplasticity. These domains have been largely identified by several authors during testing of titanium alloys as presented in Section 2.3.2.

Dynamic recrystallisation

Dynamic recrystallisation (DRX) is a safe and desirable mechanism, occurring during deformation as recrystallisation by simultaneous nucleation and growth. DRX does not only improve the intrinsic workability of materials but also changes the microstructure of the materials (Poliak and Jonas, 2003). For example, as-cast titanium alloys have a lamellar structure, which is converted into a globular or equiaxed microstructure that makes subsequent processing of the material much easier. This conversion of lamellar or acicular structures into globules during deformation is sometimes called dynamic globularisation or geometric dynamic recrystallisation (Song *et al.*, 2009; Wu *et al.*, 2011; Song *et al.*, 2014; Li *et al.*, 2015b). Semiatin *et al.* (1999) found that local deformation causes rotation of the α-laths, leading to a change in orientation of up to ~20°. The β phase can then readily penetrate the α/α boundaries created by the lath rotation. Another explanation was that shearing of the α laths generate low- and high- angle boundaries at ~30°. The existing boundaries created by shear can be readily penetrated by the growing β-phase. It was emphasised that complete globularisation can occur if the width of the α lath is less than two times the penetration of the β cusps. Secharchayulu *et al.* (2002) also explained that dynamic globularisation occurs in steps (Figure 2.17a) which include:

- shearing of alpha laths due to the applied shear strain;
- generation of dislocations of opposite signs along the line of shear;
- nucleation of a dislocation interface along the line of shear due to cancellation of dislocations with opposite signs at the intersecting slip planes, and
- migration of the interface by diffusion to minimise the surface energy by forming the globules.

These explanations emphasise that the creation of an α/α interface by shearing, bending and rotation of the α-laths and the penetration of β-phase grains into the α/α boundaries are the critical steps for dynamic globularisation to take place. Figure 2.17b (Balachandran *et al.*, 2017) shows a bright field image of the initial process of dynamic globularisation of alpha phase grains in a titanium alloy.

Dynamic recrystallisation usually occurs around the homologous temperature of 0.7 - 0.8 T_m (where T_m is the absolute melting temperatures of the metal) and a strain rate of about 0.1 - 1 s^{-1} for materials with a low stacking fault energy, whereas the strain rates can be 0.0001 - 1 s^{-1} for materials with a high stacking fault energy (Prasad *et al.*, 2015).

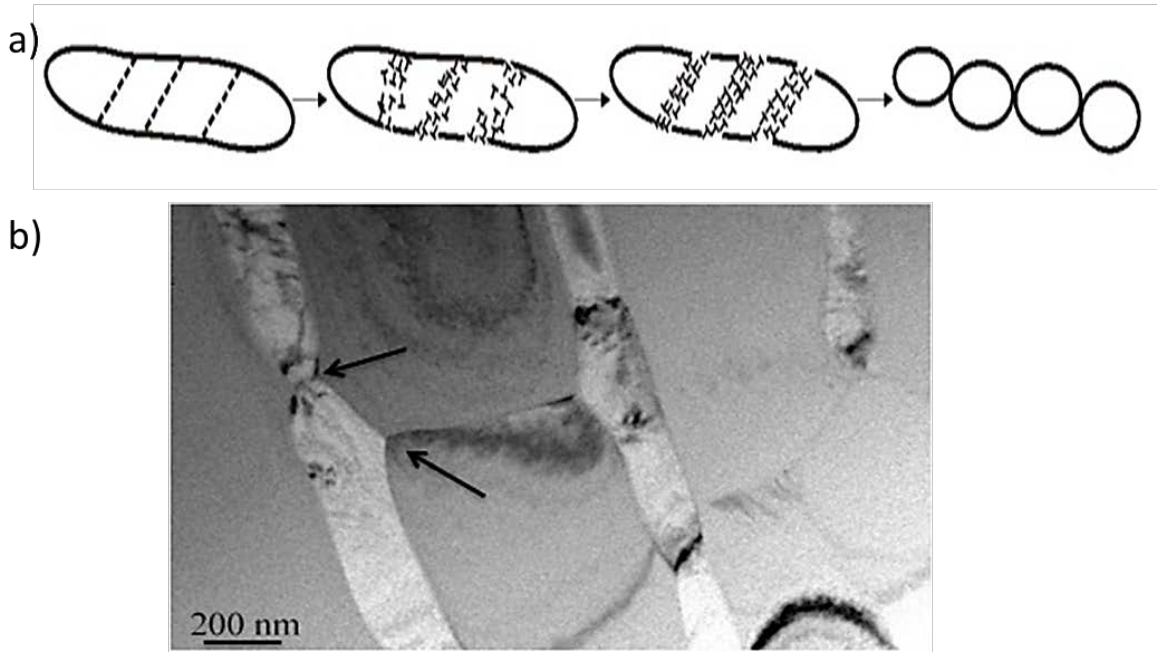

Figure 2.17: (a) Schematic diagram of dynamic globularisation of alpha laths in Ti-6Al-4V (Seshacharyulu *et al.*, 2002). (b) TEM image showing an early stage of globularisation of alpha laths. The arrows show cusping of the alpha phase at the alpha and beta subgrains (Balachandran *et al.*, 2017).

On the stress-strain curve, dynamic recrystallisation is often indicated by broad peaks and/or oscillations prior to the steady-state flow stress. However, as unsafe deformation mechanisms such as cracking also produce flow stress oscillations, DRX must be verified using other techniques such as processing maps and microstructural examination (Prasad *et al.*, 2015). On the processing map, the typical power dissipation efficiency values for dynamic recrystallisation are usually between 30 and 35% for low stacking fault energy metals, such as copper and nickel, while up to 40 and 50 - 55% can be obtained in medium and high stacking fault energy metals, respectively. The grain boundaries in dynamically recrystallised structures are usually finer than the pre-deformed microstructure and the average grain diameter increases sigmoidally with temperature at the strain rate favouring dynamic recrystallisation. In addition, grain size decreases with increasing strain rates at dynamic recrystallisation temperatures (Prasad *et al.*, 2015).

Dynamic recovery

This is another safe deformation mechanism caused by climbing and gliding of thermally activated dislocations. Quan *et al.*(2012) and Chen *et al* .(2014) found that dynamic recovery on the stress-strain curve occurred when there was steady-state stress without a prior broad stress peak. This claim has been reported to be inconsistent since Prasad *et al.*(1984) and Prasad and Seshacharyulu (1998b) showed that dynamic recrystallisation could also occur even when the flow stress was in a steady-state. Dynamic recovery occurs at warm working temperatures,

usually around the homologous temperatures of 0.4 - 0.6 T_m. The process is dominated by diffusion of rate-controlling atoms during deformation. The microstructure in a deformed sample contains well-defined subgrains which are free of dislocations. Weiss and Semiantin (1998), Chen *et al.* (2008) and Fan *et al.* (2013b) found serrated grains in lamellar initial structures. These microstructural features are signatures of dynamic recovery. On processing maps, the power dissipation efficiency values for dynamic recovery are usually in the range of 10 - 30 % (Prasad and Seshacharyulu, 1998b).

Superplasticity

Superplasticity can be considered a 'safe' deformation mechanism if it is adequately controlled, otherwise it may cause defects such as wedge cracking or void formation (Prasad and Seshacharyulu, 1998b; Alabort *et al.*, 2015). Superplasticity occurs by grain boundary sliding and dislocation accommodated flow at the grain boundary triple junctions (Alabort *et al*., 2016). The superplasticity domain on processing maps is shown by higher power dissipation efficiency values, usually in the order of 60% and a closer iso-efficiency contour line as the strain rate decreases. Unlike dynamic recrystallisation, superplasticity does not lead to reconstitution of the microstructure. Superplasticity can be verified by hot tensile testing, where very high tensile elongations of over 100% occur. This makes the mechanism useful for sheet metal forming or deep drawing processes. Superplasticity occurs at a homologous temperature of 0.7 - 0.8T_m and mostly at strain rates lower than 0.01 s^{-1} (Prasad *et al.*, 1984; Prasad and Seshacharyulu, 1998a; Seshacharyulu *et al.*, 1999). However, Langdon *et al.*(1998) and Mabuchi and Higashi (1998) have found superplasticity at strain rates up to 0.1 s^{-1}. Superplasticity has been reported to be very sensitive to initial microstructures (Alabort et al., 2015). For example, beta transformed structures in titanium alloys restrict superplasticity since the interfaces cannot slide easily, due to their characteristic crystallographic orientations, whereas superplasticity occurs easily in equiaxed structures. Detailed information on superplasticity is reported by Alabort *et al*. (2016).

The second sets of mechanisms that will be discussed are the 'unsafe' mechanisms occurring during deformation, which include: wedge cracking, void formation, intercrystalline cracking, prior particle cracking and flow instability processes (Prasad *et al.*, 1984; Prasad and Seshacharyulu, 1998a). Figure 2.18 (Seshacharyulu *et al*., 1999; Motyka *et al*., 2012) shows typical microstructural manifestations occurring in various titanium alloys during hot deformation.

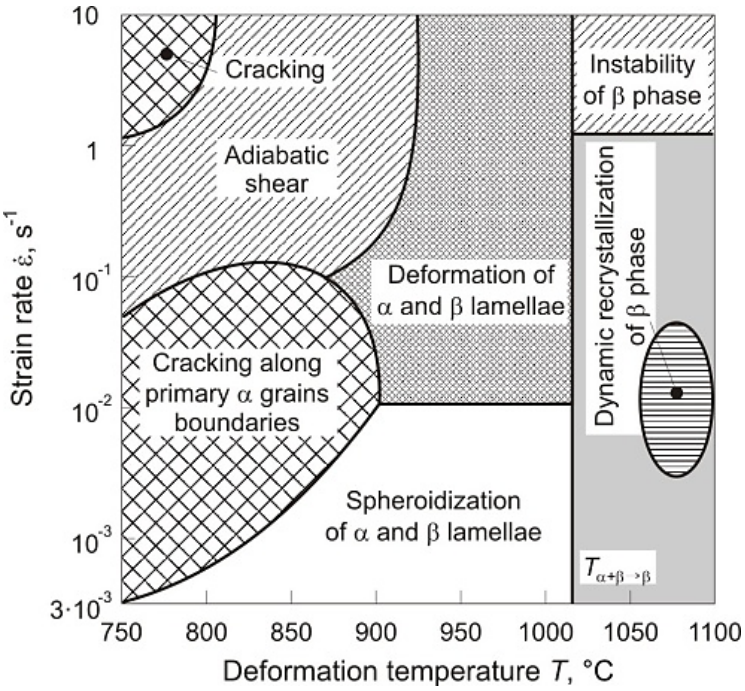

Figure 2.18: Microstructural manifestation during hot deformation of aTi-6Al-4V alloy (Seshacharyulu *et al*., 1999; Motyka *et al*., 2012).

Wedge cracking

Wedge cracking occurs when materials are deformed at very low strain rates and higher temperatures (Prasad and Seshacharyulu, 1998a). Under the conditions of low strain rates and higher deformation temperatures, grain boundary sliding occurs under shear stress and diffusion rates are not as fast as required, this leads to the formation of wedge cracking at the grain boundary triple point junctions. On the processing map, the power dissipation efficiency values and features of wedge cracking are similar to that of superplasticity, therefore detailed microstructural examination and tensile ductility testing are used to distinguish between wedge cracking and superplasticity. Wedge cracking can be avoided by increasing strain rates or decreasing the deformation temperature (Prasad and Seshacharyulu, 1998a).

Void formation

Voids form at low temperatures and high strain rates, especially when hard particles are present within the soft metal matrix, as in metal matrix composites or hard inclusions such as tungsten in titanium and aluminium alloys (Hinode *et al.*, 1989; Rao *et al.*, 1989). The deformation causes the particle-matrix interface to crack since the soft matrix would flow plastically and the particles do not deform. At this interface, stress rises to a point where either the particle cracks or the interface separates, leading to microstructural damage in the material. The void formation domain should always be avoided during processing.

Intercrystalline cracking

Intercrystalline cracking usually occurs under the conditions of either high strain rates or high deformation temperatures. At high strain rates, adiabatic temperature rise may occur, possibly causing incipient melting which aggravates cracking along the grain boundaries (Whitehouse and Clyne, 1993). Also, at high temperatures, the diffusion of elements increases and sometimes causing segregation of alloying elements or formation of low melting point compounds at the grain boundaries (Prasad and Seshacharyulu, 1998a). This promotes intercrystalline cracking.

Prior particle boundary cracking

Prior particle boundary cracking is common in alloys made via the powder metallurgy route. This mechanism occurs when starting powders which have picked up impurities or formed surface oxides or nitrides which serve as crack initiation sites during deformation. When samples produced via powder metallurgy are deformed at low strain rates and low deformation temperatures, crack initiation and propagation may likely occur (Rajamuthamilselvan, 2013). One effective way of preventing prior particle boundary cracking is by deforming at elevated temperatures where dynamic recrystallisation easily occurs and the prior particles located on the grain boundaries can be redistributed (Prasad and Seshacharyulu, 1998a).

Flow instability process

The two most common flow instabilities that manifest during deformation are adiabatic shear band formation and flow localisation. Adiabatic shear band formation occurs at high strain rates when there is not enough time for heat generated from the plastic work to be conducted away to the surroundings (Hines and Vecchio, 1997; Xu *et al*., 2001; Landau *et al*., 2016). The flow stress in the deformation band will be decreased and further plastic flow will become localised. Adiabatic shear bands (ASBs) are nucleation sites for crack initiation and propagation, and could also cause recrystallisation or phase transformation along the shear planes. ASBs occur at an angle of 45° to the principal axis. Detailed information on the formation of adiabatic shear bands and prediction of their occurrence has been reported (Odeshi *et al*., 2006; Longère and Dragon, 2007; Castellanos *et al*., 2009; Soltani, 2013). These works considered that adiabatic shear bands are formed in a material when the decrease in strength due to heating is more than the strength increase due to the combined effect of strain and strain rate hardening.

Flow localisation is the second most common form of flow instability (Prasad *et al.*, 2015). It is generally manifested in the form of curved or wavy macroscopic bands which are oriented at ~30 - 40° to the principal axis. Flow localisation mostly occurs when materials are deformed at high strain rates.

Other unsafe deformation mechanisms not covered in this review include Lüders bands (Dewey, 1965) and kink bands (Hill, 1952). Lüders bands occur as a result of dynamic strain ageing when deformation is done at low strain rates while kink bands occur in textured materials when deformation is carried out at high strain rates (Prasad and Seshacharyulu, 1998a).

Based on the literature surveyed in this section, dynamic recrystallisation has been largely reported as the dominant safe softening mechanism over a wide range of titanium alloys that were considered. Although superplasticity is desirable for sheet metal components used in automobile and aerospace applications, it requires adequate control to avoid the formation of wedge cracks. Warm working may be desirable, especially for reducing the cost of energy for bulk processing of titanium alloys. However, it must be ensured that dynamic recovery dominates the process since it is the safe mechanism during warm working. All unsafe deformation mechanisms must be carefully avoided, especially adiabatic shear bands and flow localisation which are the major unsafe deformation mechanisms.

2.4 Microstructural evolution during hot working

In previous sections, more attention has been paid to the influence of process variables such as strain rate, strain and temperature on the intrinsic workability of titanium alloys. However, there are other factors which have a significant influence on the workability of titanium alloys. These factors include alloy composition and initial microstructures. The influence of alloy composition, measured in terms of aluminium equivalent, molybdenum equivalent and oxygen content, on the workability and properties of titanium alloys was briefly mentioned in previous sections. This section provides a review of literature (Table 2.9) on the influence of pre-deformation microstructures on the workability of titanium alloys. Emphasis is placed on the microstructural evolution that occurs during deformation.

The variety of microstructures in titanium alloys has ignited the interest of researchers. Consequently, researchers investigated the influence of important microstructural features such as: prior beta grain size, alpha colony size, alpha and beta lamellar thickness, and lamellar spacing on the general deformation behaviour of titanium alloys.

Table 2.9: Previous studies on microstructural evolution during hot working of titanium alloys.

Author	Alloy type	Alloy	Microstructural feature/ Initial microstructure	Test parameters			Main findings
				Temperature (°C)	Strain rate (s^{-1})	Strain (%)	
Prasad *et al*. (2000)	α+β	Ti-6Al-4V	Prior beta grain size: (0.5-1 mm) and (2-3 mm)	750 - 1100	10^{-4} - 10^{2}	60	Domain of dynamic globularisation of α lamellae in prior beta grains and superplasticity of beta grains - insensitive to prior β grain size. Refinement of prior β grains before hot working restricted workability - widened domains where imposed process variables could cause potential microstructural damage in the alloy.
Semiantin and Beiler (2001)	α+β	Ti-6Al-4V	α platelet thickness (0.4-10 μm). Fully Lamellar	815, 900 & 955	0.1 - 10	65	Plastic flow was controlled by dislocation glide and climb.
Haung *et al*. (2009)	α+β	TC11	Equiaxed	900 - 1060	0.01 - 10	85	Dynamic recrystallisation of alpha phase occurred at 900 - 960°C. Increasing the total strain beyond 40% at the strain rate of 1 s^{-1} increased instability in the form of adiabatic shear bands.
Guan *et al*. (2012)	α+β	Ti-6Al-4V	Lamellar spacing /Fully lamellar	400 - 700	10^{-3} - 1	90	Finer lamellar spacing produced a higher flow stress for a given temperature and strain rate.
Chen and Cao (2012)	α+β	TC11	Equiaxed	800 - 980	0.01 - 0.1	75	Discontinuous dynamic recrystallisation of the beta phase dominated at 980°C. At the lowest deformation temperature (850°C), the microstructure showed that dynamically recrystallised alpha grains were dominant at all strain rates.
Li *et al*. (2013)	Near- β	Ti-5Al-5Mo-5V-1Cr-1Fe	Thick and thin α-lamellae/Fully lamellar	750 - 800	0.001 - 0.1	20, 40 &70	Deformation resistance of the alloy with thick lamellae was higher due to greater resistance of the thick lamellae to plastic flow, while the alloy with thin lamellae had lower resistance to plastic flow. Thin lamellae fragmented easily into fine alpha grains.

Author	Alloy type	Alloy	Microstructural feature/ Initial microstructure	Test parameters			Main findings
				Temperature (°C)	Strain rate (s^{-1})	Strain (%)	
Balasundar *et al*. (2014)	Near-α		acicular	923 - 1030	0.0003 - 0.001	65	Globular alpha increased with increasing temperature and decreasing strain rate.
Xu *et al*. (2014)	α+β	Ti-6Al-4V	Transitional microstructure: partially equiaxed αgrains, elongated αgrains, network of intergranular β	800 - 950	0.01 - 10	60	Transitional microstructure transformed to fine equiaxed α grains through dynamic globularisation. Recommended hot working parameters: 820 - 910°C and 0.001 - 0.1 s^{-1}, while the instability region at 800 - 880°C and 0.3 -10 s^{-1} should be avoided.
Luo *et al*. (2015)	α+β	Ti-6Al-4V	Alpha phase volume fraction & alpha grain size	860 - 960	0.01-10	80	An increase in the alpha volume fraction would increase the flow stress, while increasing the alpha grain size resulted in a decrease in flow stress.
Li *et al*. (2015b)	α+β	Ti-5Al-2Sn-4Mo-4Cr	elongated + equiaxed primary alpha grains and Widmanstätten alpha platelets	770 - 870	0.01, 0.1, 1 & 5	10 - 70	Dynamic recrystallisation of the elongated alpha phase was responsible for flow softening at a strain rate of 0.01 s^{-1}, while the alloy with the platelet structure showed kinking as the dominant softening mechanism. For both microstructures, deformation heating was dominant at strain rates > 0.0 1 s^{-1}.

Several authors have found that phase transformation contributes to flow softening of titanium alloys during deformation (Ding *et al.*, 2002; Souza *et al.*, 2015). Roberts *et al*. (1970) are of the earliest researchers to report strain induced phase transformation in Ti-6Al-4V. Yang *et al*. (1991) studied the mechanical behaviour and microstructural evolution during superplastic deformation of Ti-6Al-4V. They showed that during tensile testing at temperatures of ~850°C, there was an increase in the beta phase fraction with increase in strain. The conclusion drawn from the study was consistent with the work of Roberts *et al*. (1970), who explained that an increase in vacancy concentration imposed by deformation, decreased the distance travelled by alloying element atoms and, as a result, the rate of diffusion of these elements is increased. Since phase transformation is influenced by the rate of atomic diffusion, the reduction in the distance travelled by atoms during deformation influenced the deformation-induced phase transformation in Ti-6Al-4V.

Koike *et al*. (2000) investigated the microstructural changes occurring in α+β Ti-5.5Al-1Fe alloys during superplastic deformation. They found that the beta transus temperature of the alloy decreased from 997°C to 927°C during superplastic deformation due to:

- The agglomeration of beta phase to grain boundaries perpendicular to the tensile axis
- The increase in volume fraction of the beta phase.

Koike *et al*. (2000) also found that increasing the stress at the alpha grain boundaries by up to 100 MPa decreased the beta to alpha phase transformation from 997°C to 927°C in the Ti-Al-Fe alloy. The authors concluded that deformation-induced phase transformation during superplastic forming could reduce the beta transus temperature by up to 90°C.

He *et al*. (2012) studied the evolution of microstructure of Ti-6Al-4V alloy during concurrent hot deformation and phase transformation. The researchers had two sets of samples prepared for heat treatment and for thermomechanical treatment. The heat treated samples were not deformed but were heated to 1025°C, held for 180 s and quenched to achieve a single beta phase. Thereafter, the samples were heated to 800°C, 600°C and 400°C. For comparison, the single phase samples were subjected to deformation on a Gleeble 3500 thermomechanical simulator at 800°C, 600°C and 400°C. Concurrent hot deformation and phase transformation reduced the alpha grain size and increased the kinetics of the beta-to-alpha phase transformation (attributed to strain enhanced phase transformation since the volume fraction of the alpha phase was higher in the deformed samples when compared with the heat treated sample).

Degham-Mashandi and Dippenaar (2012) followed a similar procedure to assess the occurrence of strain induced phase transformation during thermomechanical processing of a Ti-6Al-2Sn-

4Zr-6Mo alloy. It was found that strain induced transformation occurred in the alloy and could be used to refine the microstructure.

2.5 Corrosion behaviour of titanium alloys

2.5.1 Overview

Corrosion is the degradation of materials which occurs as a result of electrochemical reactions between the material and the environment. There are different forms of corrosion which include uniform corrosion, pitting corrosion, crevice corrosion, hydrogen induced cracking, stress corrosion cracking and microbial induced corrosion (Fontana, 1986; Balasubramaniam, 2009). Titanium and its alloys are generally known as corrosion-resistant alloys, which is why the material is used in chemical and biomedical industries (Shoesmith and Noël, 2010). When compared to steel, aluminium and magnesium, titanium is more corrosion-resistant in most corrosive solutions due to the chemically inert and tenacious oxide film that is formed on the surface of the metal (Fontana, 1956; Virtanen, 2012). Titanium reacts aggressively with oxygen when exposed to air or aqueous solutions, forming either a crystalline or non-crystalline oxide film. The oxide film exists as either anatase or rutile and the durability of the film has a strong influence on the corrosion resistance of the alloy (Tomashov *et al*., 1974). Commercially pure titanium and near alpha titanium alloys are more corrosion resistant than the other forms of titanium alloy, *i.e.* the α+β and the β alloys. This has been attributed to the fact that alloying elements modify the oxide film, either improving or destroying the protectiveness of the oxide film (Tomashov *et al*., 1974; Shoesmith and Noël, 2010). The addition of manganese, vanadium and aluminium has been found to reduce the protectiveness of the oxide film, while corrosion resistance of titanium alloys containing noble metals such as palladium and ruthenium has been increased significantly (Tomashov *et al*., 1974; Virtanen, 2012).

Apart from the effect of alloying elements on the durability of the oxide film, the type of environment to which titanium is exposed has an influence on the corrosion resistance (Shoesmith and Noël, 2010; Virtanen, 2012). Although titanium alloys are resistant to corrosion in oxidising environments, in strong reducing acids such as hydrochloric and sulphuric acid, the oxide film of titanium dissolves readily and the alloy is activated and prone to attack (Shoesmith and Noël, 2010). If the concentration of the acid is strong enough, a titanium hydride film is formed on the surface of titanium once the oxide film has been dissolved. The titanium hydride film is equally protective, but it does not form spontaneously like anatase and rutile (Shoesmith and Noël, 2010). When compared to other conventional metals, the potential at which the oxide film on the surface of titanium and its alloys dissolves is far from the potential at which natural corrosion occurs. Therefore, titanium alloys still maintain their corrosion resistance superiority

over other conventional alloys. The only environment where titanium and its alloys are extremely susceptible to corrosion is in fluoride-containing environments. This is why titanium dental components are thoroughly investigated for corrosion resistance in fluoride-containing environments (Myers *et al*., 1984; Shoesmith and Noël, 2010).

Passivation occurs in titanium alloys and this makes the alloys prone to localised corrosion such as pitting, crevice and stress corrosion cracking (Fontana, 1956; Neville and McDougall, 2001; Schenk, 2001; Shoesmith and Noël, 2010). Investigations have shown that titanium alloys are resistant to pitting and microbial-induced corrosion, even in strong reducing acids, because of the spontaneous repassivation of dissolved oxide. However, titanium alloys are highly susceptible to crevice corrosion and environmentally assisted cracking which promotes corrosion (Fontana, 1956; Shoesmith and Noël, 2010; Virtanen, 2012). The two most common forms of environmentally assisted cracking in titanium are hydrogen induced cracking and stress corrosion cracking. Shoesmith and Noël (2010) and Virtanen (2012) found that the spontaneous repassivation of titanium makes stress corrosion cracking somewhat difficult, but titanium suffers stress corrosion cracking in halide-containing aqueous environments under the conditions of low pH, high temperature and high concentration of halides. Near-alpha alloys containing significant amounts of aluminium and tin are most susceptible to stress corrosion cracking, but addition of interstitial elements such as C, N and O can be used to control stress corrosion cracking in the alloys. Detailed information about the stress corrosion cracking of titanium was reported by Shoesmith and Noël (2010). For hydrogen induced cracking to occur, a substantial amount of hydrogen has to be absorbed. Since the solubility of hydrogen is very low in the alpha phase, and the solubility and diffusion of hydrogen in the beta phase is very high, α+β and β alloys are the most susceptible to hydrogen induced cracking (Schenk, 2001; Shoesmith and Noël, 2010). This is because in α+β alloys, hydrogen induced cracking is sensitive to the volume fraction and morphology of the microstructure (Shoesmith and Noël, 2010).

Although titanium alloys are generally considered to be corrosion-resistant, the alloying elements, microstructure and environmental conditions could make the materials susceptible to corrosion of the materials in service. Therefore, newly developed titanium alloys which have been treated to obtain desired microstructures are corrosion tested in environments similar to the intended applications. A review of the literature on newly-developed and commercial alloys in different environments is presented in Sections 2.5.2 - 2.5.3 where each section focuses on the different tested environments. The most common environments considered are the acidic, marine and physiological solutions.

2.5.2 Corrosion behaviour in acidic solution

As far back as the 1970s, several researchers were interested in studying the behaviour of the passive film formed on the surface of titanium alloys when immersed in acidic solutions. The first set of studies focused on understanding the mechanisms controlling the passivation and dissolution of titanium alloys.

Brieter (1970) carried out a galvanostatic study of passivity and breaking down of passivity of titanium in hydrochloric solutions. The electrode potential and impedance were measured as a function of time when a current of 10 mA was passed through the electrolyte. The alloys were polished in different reagents prior to immersion. It was found that the anodic current was used mainly for oxide formation until a maximum was reached. However, the oxide thickness did not increase with exposure time in the hydrochloric environment. This observation was consistent even at varied HCl concentrations of between 0.1 and 10 M. Breakdown of passivity occurred at potentials within the range of 11.5 - 14.5 V. This caused dissolution of the titanium electrode. The increased dissolution area decreased the electrode potential.

Owen *et al*. (1972) investigated the dissolution of Ti-6Al-4V in the cathodic potential range in 5 N hydrochloric acid. An annealed Ti-6Al-4V sample was polished before exposure to hydrochloric acid under open circuit potential and a controlled potential of -742 mV (*vs.* SCE). Localised corrosion (pitting) occurred preferentially on the uncoated alpha phase because a thin hydride layer which dissolves readily in hydrochloric acid, was formed on the alpha phase, while a thick hydride layer was formed on the beta phase. The hydride layer was formed after dissolution of the protective oxide (TiO_2) film in a strong reducing acid environment. The dissolution of the oxide layer and the activation of the titanium alloy occurred at the potential of -650±50 mV.

Tomashov *et al.* (1974) carried out a more comprehensive study on the anodic passivation and corrosion behaviour of titanium and titanium alloys in non-oxidising acid at elevated temperature. About 37 alloys containing a wide range of binary and ternary systems were investigated. The major alloying elements that were added to titanium in different weight ratios included niobium, tin, manganese, aluminium, zirconium, vanadium, molybdenum, tantalum and palladium. The different microstructural phases developed in the alloys were: alpha, beta, (α+β), (ω+β), (ɤ+β), with ω and ɤ representing martensite and an intermetallic compound respectively. The researchers adopted a number of methods in their study including electrochemical, gravimetric, analytical, metallography, X-ray and electron diffraction techniques. They found that for pure titanium that was polarised anodically to 1 V in 40% sulphuric acid at 80°C, there was an electrochemical transition of TiO_2^+ as the preferred anodic process. The region of passivity on

the polarisation curve decreased as the temperature increased from 25°C to 90°C. The thickness of the passive film formed at the more positive potential was less than the thickness of the passive film formed at the less positive potential. The protective strength of the oxide film was dependent more on the structure of the passive film than the thickness of the film. It was explained that the passive film had two layers: the barrier layer which has the anatase structure, and the porous layer which has the rutile structure. The anatase layer was found to be dominant when polarisation occurs at more positive potentials, while the rutile layer, which is porous, was dominant at the less positive potential (+0.7 V). Therefore, the researchers proposed that the protection offered by the titanium oxide layer is more effective when the amount of defects in the oxide layer and its ionic conductivity is reduced. In other words, the anatase layer which is usually in contact with the metal has less defects and ionic conductivity than the outer rutile layer. Thickening of the anatase layer on the surface of titanium alloys offers more protection when exposed to corrosive solutions.

Secondly, the influence of alloying elements in binary and ternary alloys on the dissolution of the anodic oxide film was evaluated. It was reported that the addition of elements such as aluminium, vanadium and zirconium increased the rate of anodic dissolution of the oxide layer, while the addition of manganese and zinc decreased the dissolution rate. The addition of tin to titanium was found to have no effect on the rate of dissolution of the oxide layer. When the alloying elements were added in small quantities, the dissolution rate of the oxide layer was similar to that of the pure titanium, except in Ti-Al and Ti-Zr binary alloys. The rate of dissolution is largely dependent on the amount of defects and the ionic conductivity induced into the oxide layer when the alloying element atoms diffuse into the lattice of the oxide (Tomashov *et al*., 1974).

The influence of microstructure on the passivation and electrochemical behaviour of high alloyed titanium was evaluated in 40% sulphuric acid. It was established that a single phase beta Ti-Mo alloy had a more stable passive region than when the same alloy contained the beta phase with either the alpha or omega phase. The alpha and omega phases dissolved preferentially to the beta phase in sulphuric acid when the alloy was in the active potential range. A higher amount of the Mo-enriched beta phase was observed on the surface of the alloy. In contrast, in 40% sulphuric acid at the polarisation potential of about +0.74 V corresponding to the transpassive region of the alloy, the beta phase dissolved preferentially to the alpha and transformed beta (omega) phases (Tomashov *et al*., 1974).

The corrosion behaviour of binary Ti-5Cr and ternary Ti-5Cr-15Ta alloy systems were studied in 5% hydrochloric acid (Tomashov *et al*., 1974). It was observed that chromium increased the

dissolution rate of the oxide layer, while the introduction of tantalum decreased the dissolution rate. Similar to the other binary alloys that were investigated, the alloys containing two phases had inferior corrosion properties to the single phase alloys in both systems. The formation of intermetallic compounds such as $TiCr_2$ and $(TiTa)Cr_2$ both increased the dissolution rate of the oxide layer. Finally, the evaluation of corrosion behaviour in an α+β Ti-20Nb-0.2Pd ternary alloy in hydrochloric and sulphuric acid showed that the alloy was stable in both environments due to the high niobium content (Tomashov *et al*., 1974).

Caprani and Fraynet (1979) developed a reaction model to describe the mechanism of dissolution and passivation of titanium in concentrated hydrofluoric, fluorinated sulphuric and hydrochloric acid. They found that titanium dissolved in concentrated hydrochloric acid as Ti (III) and Ti (IV), and that the dissolution of titanium was similar in the three acid media. When the current - voltage graph was analysed, the reaction model, similar to that proposed for fluorinated sulphuric acid, was consistent with that of concentrated sulphuric acid. However, the model which described the oxide formation with respect to changes in potential for hydrochloric acid differed from that of fluorinated sulphuric acid.

Poillieu *et al*. (1997) investigated the thickness, structure and composition of titanium oxide films using surface analysis techniques such as X-ray photoelectron spectroscopy, Rutherford backscattering, X-ray diffraction and atomic force spectroscopy. Although previous authors had established that films formed on titanium and its alloys were composed of titanium dioxide (rutile), Poillieu *et al*. (1997) stated that there had been prior disagreement on the structure and exact composition of the film. They observed that the passive film was composed of an amorphous TiO_2 outer layer of about 10 - 20 nm thick and an intermediate TiO_x layer in contact with the metallic substrate. The composition of the TiO_x layer was not easily determined, but they established that the TiO_2 layer was sensitive to the environment, and its thickness decreased with longer exposure time. The authors recommended a stabilisation procedure which increased the thickness of the TiO_2 outside layer. They concluded that the ability of the TiO_2 layer to withstand corrosion depended on the thickness of the layer, and not modification of the surface compound's composition, as reported by previous authors.

Marino *et al*. (2001) investigated the stability of potentially grown anodic oxide films on titanium alloys in buffered aqueous phosphoric acid solution. This work added to the existing knowledge on the oxide formation and dissolution of titanium and its alloys in sulphuric and hydrochloric acid solutions as described by previous authors (Tomashov *et al*., 1974; Blackwood *et al*., 1988; Blackwood and Peter, 1989). The pH of the solution was 1 - 5 and the samples were exposed to the solution at room temperature and low voltages. The anodisation rate for the oxide film was

evaluated using electrochemical methods and the oxide film was characterised using X-ray diffraction and scanning electron microscopy. The authors found that the oxide film was stable in the phosphoric acid; and the growth rate of the film was 2.5 nm/V, irrespective of the pH of the solution. The oxide film was free of pores and was very compact. Ageing the oxide film enhanced its stability and homogeneity. The authors confirmed that traces of monoclinic Ti_3O_5 were present in the thicker films when the potential was greater than 3 V. Generally, the oxide film mainly comprised orthorhombic TiO_2.

Güleryüz and Çimenoğlu (2004) proposed that thermal oxidation could improve the corrosion and corrosion-wear resistance of Ti-6Al-4V. They reported that thermal oxidation treatment at 650 - 650°C produced a corrosion- and wear-resistant surface layer. They confirmed that oxide thickness and oxygen diffusion depth increased with increasing oxidation depth and time. The oxide layer mainly comprised anatase and rutile. The optimum oxidation temperature and time for producing a corrosion resistant surface for Ti-6Al-4V alloy in 5 M hydrochloric acid was 600°C and 60 hours.

From the above studies, it can be seen that several factors influence the formation, structure, stability and dissolution of the surface oxide film in titanium alloys: temperature, composition of the alloy, concentration and pH of the acidic solution. Once the role of these factors on the oxide formation and dissolution behaviour of titanium alloys exposed to acidic media were understood, researchers then began to examine the corrosion behaviour of titanium alloys produced by different routes. The influence of production processes was reported and the corrosion behaviour of the different alloys was compared. The determination of corrosion rates for different titanium alloys is very important in forecasting the life span of titanium components in service.

Krysa *et al*. (1997) investigated the corrosion rate of titanium in 1 - 4 M sulphuric acid at temperatures of 25 - 60°C, and found that corrosion rates increased linearly with increasing H_2SO_4 molar concentration. Prior etching with 5% hydrofluoric acid significantly shortened the time for self-activation of titanium in sulphuric acid. They recommended that during industrial pre-treatment of titanium alloys with hydrochloric acid or sulphuric acid, an initial step of etching in 5% HF could help decrease the corrosion rate.

Adijani *et al*. (2000) investigated the effect of adding a beta-ethyiphenylketocyclohexyl amino hydrochloride inhibitor to sulphuric acid on the corrosion behaviour of commercially pure titanium used as heat exchanger tubes. The tubes had a build-up of calcium carbonate and magnesium hydroxide scales and were usually cleaned by uninhibited sulphuric acid. The investigation was done under different conditions by immersion, potentiodynamic and Tafel plot techniques. It was concluded from immersion and polarisation measurements that the corrosion

rate was negligible when the inhibitor was used, as there was no hydrogen pick-up under the various testing conditions.

Van der Lingen and Sandenbergh (2001) investigated the influence of ruthenium additions on the cathodic modification and corrosion performance of titanium in hydrochloric acid. Ruthenium was chosen because it is the cheapest amongst the platinum group of metals and its suitability for replacing expensive palladium was evaluated. The tests were carried out in 25% hydrochloric acid at room temperature. Different titanium alloys containing different additions of ruthenium, palladium and ASTM Grade 2 titanium were tested. It was observed that a secondary phase containing 10 wt% Ru and 5 wt% Fe was formed in the Ti-Ru alloys. An additional alloy with 10 wt% Ru and 5 wt% Fe was then developed as a cathodic material to identify the mechanism controlling the cathodic modification in the Ti-Ru alloy. It was found that ruthenium was a suitable cathodic modifier in titanium, similar to palladium. The presence of ruthenium in titanium pushed the corrosion potential to a more positive potential and promoted passivation. However, it was established that ruthenium acted differently to palladium as the Ti-Ru-Fe secondary phase acted as the cathodic modifier rather than elemental ruthenium. The authors concluded that the fine nature of the Ti-Ru-Fe secondary phase caused faster enrichment of the phase on the surface of the titanium alloy, thereby decreasing the corrosion rate in the alloy.

Magoda *et al*. (2004) studied the corrosion behaviour of Ti-6Al-4V in concentrated hydrochloric and sulphuric acid media using open circuit potential (OCP), potentiodynamic polarisation and electrochemical impedance spectroscopy (EIS) techniques. The concentrations of the electrolytes were varied from 0.5 - 4 M and 1 - 9 M for sulphuric acid and hydrochloric acid respectively. It was found that SO_4^{2-} accelerated the active dissolution of Ti-6Al-4V more than Cl^-. Consequently, the oxide film on the surface of the alloy dissolved faster in sulphuric acid than in hydrochloric acid. The dissolution of the oxide film increased with increasing concentration of the electrolytes. Compared with pure titanium, Ti-6Al-4V exhibited slightly higher corrosion resistance than pure titanium. This contradicted the general experience that corrosion resistance of pure titanium was higher than in two-phase alloys containing aluminium, vanadium, zirconium and molybdenum (Tomashov *et al*., 1974; Shoesmith and Noël, 2010).

Bautisha *et al*. (2005) developed a lower cost Ti-6Al-4V alloy by powder metallurgy (PM). The influence of sintering on the corrosion behaviour of the alloy was investigated using electrochemical impedance spectroscopy in 2 N and 6 N hydrochloric acid solutions. The oxidation resistance of the PM alloy was studied at temperatures of 900°C, 1000°C and 1100°C using scanning electron microscopy and X-ray diffraction techniques. In a low hydrochloric acid concentration, the corrosion resistance of the PM alloy was comparable to that of wrought Ti-

6Al-4V, but in solutions with higher hydrochloric acid concentrations the PM Ti-6Al-4V alloy had lower corrosion resistance than CP titanium alloys produced via PM. The oxidation resistance of the PM alloys was superior to that of the wrought alloys.

Devilliers *et al*. (2006) investigated the behaviour of titanium in sulphuric acid. Their findings were similar to previous work (Blackwood and Peter, 1989; Tomashov *et al*., 1974). The authors stated that electrochemical methods were not reliable enough to study the dissolution of the TiO_2 film on the titanium-electrolyte interface, due to instant passivation of the alloys as dissolution progressed. They emphasised that it was only when the rate of dissolution was greater than the rate of passivation that the surface of titanium subjected to active corrosion could be observed through electrochemical techniques. Building on their claim, it was proposed that an electro-analytical determination of Ti (IV) species in the acid electrolytic solution was a convenient tool for detecting *in situ* dissolution of TiO_2 and the corrosion of titanium.

A comparative study on the influence of chloride and sulphate ions on the corrosion behaviour of CP titanium and Ti-6Al-4V in oxalic acid was carried out by Fekyy (2009). The substrates were subjected to OCP measurements, polarisation and EIS techniques. The concentration of oxalic acid, sulphates, chloride ions and temperatures were varied. It was found that corrosion current density increased with increasing temperature and concentration of the electrolyte for both alloys. CP titanium had superior corrosion resistance than Ti-6Al-4V under all testing conditions. This is in agreement with the findings of previous authors (Tomashov *et al*., 1974; Virtanen, 2012), except Magoda *et al*. (2004). The influence of chloride and sulphate ions on the oxide film resistance (the resistance of the TiO_2 formed on the surface of the alloy to anionic attack in the solution) of pure titanium and Ti-6Al-4V was studied. The oxide film resistance decreased with increasing chloride ion concentration up to 1 mM but higher Cl^-concentrations led to an increase in the oxide film resistance. In contrast, increasing the concentration of sulphate ions caused a continuous decrease in the oxide film resistance. This further affirms the claim of Magoda *et al*. (2004) that sulphate ions cause a more severe attack on pure titanium and titanium alloys.

2.5.3 Corrosion behaviour in sodium chloride and physiological solutions

Titanium alloys are used extensively in marine and biomedical applications. Consequently, titanium alloys are tested in varied concentrations of sodium chloride solutions to evaluate the performance of the alloys against corrosion when exposed to simulated marine environments. Apart from the evaluation of corrosion resistance of titanium alloys in both acidic and sodium chloride solutions, there has been considerable research on the corrosion performance of titanium alloys in physiological solutions. These solutions are usually simulated body fluids, such as 0.9%

NaCl solution, Hank's solution and phosphate buffered solution. The increasing use of titanium alloys in the manufacture of biomedical components has motivated several studies on corrosion performance in biomedical environments. Some of the articles published on the corrosion behaviour of titanium alloys are summarised in Table 2.10.

2.5.4 Summary

From the above-reviewed articles, it can be observed that electrochemical techniques such as open circuit potential, potentiodynamic polarisation and electrochemical impedance spectroscopy are the major techniques used in studying the corrosion behaviour of titanium and its alloys. The corrosion behaviour of titanium alloys depends on the structure and thickness of the oxide film formed on the surface of the alloy when immersed in corrosive solutions. However, it is still not clear if it is the thickness or the structure of the oxide film that offered the desired protection to the substrates. Reports on the formation and dissolution of the oxide film, especially in reducing acid media, are quite contradictory. From the literature used for this review, it can be seen that formation and dissolution of oxide films is mostly studied in reducing acid media since the oxide film is spontaneously formed in oxidising media and thus increase in thickness with exposure time.

Studies in this literature survey showed that increased concentration of electrolytes and temperature promotes dissolution of the passive film and also reduces the general corrosion resistance of titanium alloys. Sulphate ions (SO_4^{2-}) have been found to be the most potent ions in reducing acid causing dissolution of an oxide film on the surface of titanium alloys.

The role of alloying elements on the formation and dissolution of the oxide film was surveyed. According to some studies, the addition of aluminium and vanadium can promote dissolution of the film in acidic media, while other elements like ruthenium and palladium slow down the rate of film dissolution. The high cost of ruthenium and palladium has led researchers to also study the effect of low-cost alloying elements, *e.g.* molybdenum, chromium and niobium, on the corrosion resistance of titanium alloys. The results obtained from these studies were positive, as molybdenum and niobium in particular improved the corrosion performance of titanium alloys. Interestingly, iron, one of the lowest cost alloying elements in titanium, has been reported to offer improved corrosion resistance when it is used as a substitute for vanadium in commercial Ti-6Al-4V alloys. When used as a co-beta stabiliser in β titanium alloys, reports have shown that iron had no detrimental effect on the corrosion behaviour.

The different processing techniques used in developing titanium alloys results in a wide range of microstructures. These microstructures respond differently when exposed to corrosive media. Previous studies have shown that it is beneficial to have a single and homogenous phase rather

than combination of phases when developing titanium alloys. Preferential dissolution of the alpha and martensitic phases in acidic media was found in alloys containing more than one phase. It is thus important to control the microstructure of newly-developed titanium alloys.

The complexity of corrosive media has an influence on the dissolution of oxide film and the overall corrosion resistance of titanium alloys. Although physiological fluids are usually complex solutions containing more than one anion, titanium alloys are generally reported to perform well in these solutions especially when compared to stainless steel. Other complex solutions such as mixed HCl and NaCl have an adverse effect on the corrosion performance of titanium alloys (Sinigaglia *et al.*, 1978). There is a limited number of studies on the corrosion behaviour of titanium alloys in these complex solutions when compared to the different solutions considered in this review. Therefore, it becomes imperative to investigate existing and newly-developed alloys in complex solutions.

Table 2.10: Previous studies on corrosion behaviour of titanium alloys immersed in sodium chloride and physiological solutions.

Author	Alloy type	Alloy	Treatment	Test parameters			Main findings
				Temperature (°C)	Solution	Technique	
Aragon and Hulbert (1972)	α+β	Ti-6Al-4V & 316L stainless steel	-	25	Simulated body fluid and bovine plasma	OCP & Potentiodynamic Polarisation	Activation of Ti-6Al-4V occurred after 10 - 15 hours, after which the corrosion rate began to increase. The dissolution time for Ti-6Al-4V was 176 times slower than for 316L stainless steel.
Kobayashi *et al*. (1998)	α+β	Ti-6Al-7Nb	Alloying (Nb)	37	0.9% NaCl + 1.0 lactic acid	OCP, Potentiodynamic Polarisation & EIS	The formation of Nb^{5+} cations decreased the concentration of defects in the passive film of the Ti-6Al-7Nb alloy.
Ramires and Gaustalsi (2001)	α & α+β	Ti-Pd and Ti-6Al-4V	Alloying (Pd)	25	0.9% NaCl	Triangular potential sweep, Potentio-dynamic polarisation, Electrochemical Impedance Spectroscopy	The addition of palladium improved the corrosion resistance of CP-Ti, while the presence of aluminium and vanadium in Ti-6Al-4V showed inferior corrosion resistance than the Ti-Pd alloy.
Choubey *et al*. (2004)	α+β	Ti-6Al-4V, Ti-6Al-4Nb, Ti-6Al-4Fe & Ti-5Al-2.5Fe	Alloying (Fe and Nb)	37	Hank's solution	Potentiodynamic Polarisation	The estimated corrosion rates of the alloys were comparable. The corrosion behaviour of Ti-6Al-4V was not affected significantly on substituting vanadium with niobium and iron.
Nishimira *et al*. (2010)	β	Ti-8Mo-5Fe	Alloying (Mo-Fe master alloy)	25	10 mass% NaCl	Electrochemical impedance spectroscopy	The addition of iron did not affect the corrosion resistance of both alpha and beta phases in Ti-8Mo-5Fe.
Oleivera *et al*. (2014)	α+β	Ti-6Al-4V	Plasma-assisted physical vapour deposited TiN, TiAlN/TiAlCrN coatings	25, 60 and 80	3.5 wt% NaCl	OCP, Potentiodynamic Polarisation & EIS	The coated alloy had improved corrosion resistance over the uncoated Ti-6Al-4V alloy. The increase in temperature decreased the corrosion resistance of both coated and uncoated alloy.

Author	Alloy type	Alloy	Treatment	Test parameters			Main findings
				Temperature (°C)	Solution	Technique	
Pimenova and Starr (2006)	α+β	Ti-*x*Al-*y*Fe	Direct metal deposition + Alloying (Al and Fe)	25	Hank's solution	OCP, Potentiodynamic Polarisation & EIS	The addition of aluminium and iron in high amounts (>15 wt%) caused heterogeneous distribution of alloying elements in the microstructure of the alloy. This promoted the dissolution of titanium alloys.
Cisak *et al*(2016)	α+β	Ti-6Al-4V	-	25	NaCl	Salt Spray	NaCl had a detrimental effect on Ti-6Al-4V when deposited at high temperature in the presence of moist air.
Dai *et al*. (2016)	α+β	Ti-6Al-4V	Selective laser melting	25	3.5 wt% NaCl	OCP, Potentiodynamic Polarisation & EIS	SLM Ti-6Al-4V alloy had worse corrosion resistance compared to its commercial counterpart.
Lu *et al.*(2016)	α+β	Ti-6Al-*x*Fe	Alloying (Fe)	25	Simulated body fluid	OCP, Potentiodynamic Polarisation & EIS	The superior corrosion resistance observed in the alloys was explained by the oxides of aluminium and iron formed on the surface of the passive TiO_2 passive film.
Bai *et al.*(2016)	α , α+β and β	CP-Ti, Ti-6Al-4V and Ti-24Nb-4Zr-8Sn	Alloying (Nb)	37	Phosphate buffered solution	OCP, Potentiodynamic Polarisation & EIS	The corrosion behaviour of Ti-24Nb-4Zr-8Sn was comparable to that of CP-Ti, but Ti-6Al-4V had inferior corrosion resistance to both CP-Ti and Ti-24Nb-4Zr-8Sn. The superior corrosion resistance of the biomedical alloy over the Ti-6Al-4V alloy can be attributed to the single oxide film formed on the surface of the alloy just like that of CP-Ti. The formation of Nb^{5+} cations decreased the concentration of defects in the passive film of the biomedical Ti-25Nb-4Zr-8Sn alloy and thus decreased corrosion rate.

2.6 Summary of the literature review and identifying the research gap

The major factors contributing to the high cost of titanium alloys have been presented in this literature review. The difficulty in extracting titanium from either ilmenite or rutile, the use of expensive alloying elements and complex processing techniques during forming and machining operations were all mentioned as contributing factors to highly priced titanium components. The research efforts seeking to address these factors that were considered in this review are:

- Seeking to establish a cost effective, efficient and continuous beneficiation process to obtain pure titanium powder from $TiCl_4$
- The use of inexpensive alloying elements in the design of lower cost titanium alloys, and
- Optimising the forming process parameters to reduce manufacturing costs.

Based on the surveyed literature on α+β titanium alloys, it was observed that in developing low-cost titanium alloys, most researchers have considered total replacement of expensive isomorphous beta stabilisers *e.g.* vanadium, molybdenum and niobium, with iron, chromium, and manganese that undergo a eutectoid reaction. Although this initiative has shown that the cost of titanium alloys can be reduced while maintaining good mechanical properties, the major disadvantage is the formation of intermetallic phases which are generally detrimental to the mechanical and corrosion properties of α+β titanium alloys.

One way of preventing the formation of these intermetallic phases is to retain some isomorphous beta stabilisers when introducing low-cost euctectoid beta stabilisers. For example, partial substitution of vanadium in Ti-6Al-4V with iron could help suppress the formation of intermetallic compounds. Prior published work on both experimental and commercial α+β alloys which considered partial substitution of expensive isomorphous beta stabilisers with eutectoid beta stabilisers is sparse. It is only recently that Yu *et al.* (2017) investigated the sinterability of α+β Ti-Al-V-Fe alloys using fine hydrogenated-dehydrogenated titanium powder, Al-V master alloy and iron powders. From their results, they concluded that the fast diffusion of iron atoms in titanium: enhanced the sinterability, homogenised the microstructure of the alloy and reduced microporosity in the alloy. However, the mechanical properties of the alloys were poor due to oxygen contamination of the as-received powders. No prior work was found on Ti-Al-V-Fe alloys produced via the ingot metallurgy route.

This research therefore considers the partial substitution of vanadium in Ti-6Al-4V with iron, a eutectoid former, strong beta stabiliser, and the lowest cost beta stabilising element. The design

considerations for the set of low-cost Ti-Al-V-Fe alloys developed in this study are presented in Section 2.7. The newly-developed alloys were produced via the ingot metallurgy technique. Thereafter, they were subjected to corrosion and hot deformation testing to provide new information on the role of the partial substitution of vanadium with iron on the corrosion resistance and high temperature forming behaviour of the alloys.

It was established from the literature review that the two major methods for optimising the forming and machining operations of titanium alloys include constitutive modelling and dynamic materials modelling by processing maps. Since there is no literature available on the Ti-Al-V-Fe alloys studied in this work, processing maps were used to determine the optimum processing conditions and the underlying mechanisms during hot working. The information obtained from this study will be very useful in converting the new Ti-Al-V-Fe alloys from as-cast material to semi-finished and finished components.

The research approach considered in this study would help to address the challenge of high cost contributed by expensive alloying elements and complex hot working of titanium alloys.

2.7 Design Consideration

The selection of compositions for the experimental low-cost alloys is based on literature published on low-cost α+β titanium alloys. Fujii *et al*. (2002) found that the addition of aluminium increased hot deformation resistance and decreased hot workability which leads to several disadvantages including: resistance to rolling mill power, increased labour for removal of surface defects and reduced yield. Consequently, this adds up to higher manufacturing costs.

Leyens and Peters (2003) found that when the aluminium equivalent is greater than 9 wt% or the aluminium content exceeded 6 wt%, formation of a brittle Ti_3Al intermetallic phase was highly favoured. Ti_3Al is detrimental to the properties of titanium alloys, especially when the aluminium content exceeds 6 wt% (Zhu *et al*., 2014).

Several articles are available on the total replacement of high-cost vanadium with lower-cost iron (Esteban *et al.*, 2008; Bolzoni *et al.*, 2012; Wang *et al.*, 2012b). However, no literature on partial replacement of vanadium with iron in cast α+β titanium alloys has been found. The addition of iron as an alloying element in the development of lower-cost α+β titanium alloys must not exceed 2% due to segregation effects and compromised homogeneity of the alloy after casting (Nochovnaya *et al*., 2008).

Therefore, this research work focused on developing experimental alloys within the composition ranges:

- Titanium ≥ 90 wt%
- Aluminium = 4 - 6 wt%
- Vanadium = 1 - 4 wt%
- Iron = 1 - 4 wt%

where the sum of vanadium + iron = 4.

These considerations were adopted in developing the low-cost Ti-Al-V-Fe alloys. The facilities, techniques and procedures used in achieving this work are presented in Chapter 3.

Chapter 3: Experimental Procedure

This chapter provides information on the starting materials, consumables, facilities and experimental methods used in this study. A detailed description is given on the production of the experimental alloys, characterisation techniques, hot compression testing and corrosion testing. The modelling techniques used in analysing the stress-strain data obtained from the hot compression tests are also described.

3.1 Materials

The starting powders utilised in this research work were: aluminium (149 μm diameter), titanium (149 μm), vanadium (44 μm) and iron (44 μm).

3.2 Development of Ti-Al-V-Fe experimental alloys

The steps followed while developing the experimental alloys are presented in Figure 3.1.

3.2.1 Selection of composition for Ti-Al-V-Fe experimental alloys

The design consideration for selection of composition for the new alloys is detailed in Section 2.7. The targeted compositions of the experimental alloys and the corresponding molybdenum equivalent values obtained from Equation 2.2 are listed in Table 3.1.The experimental alloys have higher molybdenum equivalent values than the commercial Ti-6Al-4V alloy.

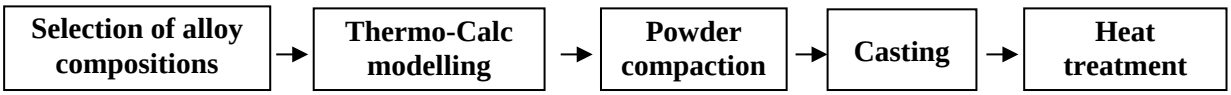

Figure 3.1: Procedure for alloy development.

Table 3.1: Targeted compositions of the experimental alloys, in wt%.

Alloy #	Ti	Al	V	Fe	Mo_{eq}
1	90	6	3	1	-1.09
2	90	6	2	2	1.14
3	90	6	1	3	3.37
4	90	6	-	4	5.60
5	91.5	4.5	3	1	0.41
6	91.5	4.5	2	2	2.64
7	91.5	4.5	1	3	4.87
Ti-6Al-4V	**90**	**6**	**4**	**-**	**-3.32**

3.2.2 Thermo-Calc Modelling

Thermo-Calc modelling was carried out to predict the possible equilibrium phases in the alloys, determine the amounts of the phases (in atomic percent), transformation temperatures and other critical temperatures under equilibrium conditions.

The targeted alloy compositions were then entered into the model using the titanium database (TTTI3) to obtain the desired information. The Thermo-Calc file (.tcm) that was used in the modelling is presented in Appendix A.

3.2.3 Powder compaction

The Ti, Al, V and Fe starting powders were weighed using an electronic balance in the proportions given in Table 3.1 to provide a total mass of 10 g for each sample. The powders were then mixed and cold compacted in a 20 mm diameter die under a pressure 220 kPa using a hydraulic press. The compacts were then taken for melting.

3.2.4 Casting

The alloy compacts were melted in a water-cooled, copper-crucible electric arc furnace to produce as-cast button samples and 50 x 50 mm square ingots. The button samples were used to study the microstructure, hardness and corrosion behaviour of the alloys, while the square ingots were used for hot compression testing. Prior to melting, a 5×10^{-3} bar vacuum environment was created in the melting chamber and purged with argon gas to remove oxygen. The process was repeated three times. A pure titanium sample which served as an oxygen getter was first melted to further minimise oxygen contamination before melting the alloy compacts. The as-cast button samples were turned and melted twice to homogenise the ingots, while the square samples were turned and melted three times since they were larger than the buttons.

3.2.5 Cutting

The as-cast, annealed and deformed samples were sectioned into two (at the centre) to expose the cross-sectional area of the alloys. A diamond coated blade fitted on the Struers Secotom-10 precision cutting machine was used to cut the samples, at a rotating speed of 2000 rpm and a feed rate of 0.025 mm/s. Water was used as the coolant throughout the cutting of the samples to prevent the samples heating up during the process.

3.2.6 Heat Treatment

Each of the as-cast button samples was sectioned into two. One of the halves was sealed in a silica glass tube filled with argon gas for heat treatment, while the other half of the as-cast sample was mounted and prepared for microstructural examination and microhardness testing. The

sealed samples were solution-treated at 790°C in a muffle furnace for four hours followed by air cooling. The heat treatment was carried out to homogenise the as-cast samples and to investigate the effect of annealing on the microstructure and hardness of the alloys. The annealed samples were also subjected to corrosion testing described in Section 3.5.2. The annealing parameters were selected based on the recommended annealing treatment for α+β titanium alloys (Gilbert and Shannon, 1991).

3.2.7 Cost of starting materials

The targeted compositions were used to estimate the cost of stabilising the beta phase by vanadium and iron in the α+β titanium alloys. Vanadium is about 150 times more expensive than iron. Table 3.2 shows the price of the elements in the alloys as reported by Sigma-Aldrich in June, 2017 (note that these prices are based on high purity powders in small quantities for analytical purposes, so do not accurately reflect bulk commercial alloying costs).

Table 3.2: Price list for Ti, Al, V and Fe powders.

Sigma-Aldrich Price List 03/07/2017			
Element	**Mass (g)**	**Price (ZAR)**	**Price (ZAR/g)**
Ti 99.99%*	50	1330	27
Al 99.5% *	200	3950	20
V 99.9% *	50	7320	146
Fe ≥99.9% *	500	546	1

* trace metals basis

To estimate the potential cost savings from partial substitution of vanadium with iron, a cost analysis (see Appendix B) was done based on the commercial price of bulk alloying materials such as ASTM Grade 2 Ti, 60% aluminium - 40% vanadium master alloy and commercially pure elemental aluminium, vanadium and iron. Table 3.3 presents a summary of the costs of the experimental alloys in comparison with Ti-6Al-4V alloy and the cost savings in percent. Up to 7% can be saved by partial substitution of 3 wt % vanadium with iron in Ti-6Al-*x*V-*y*Fe and 6% can be saved in Ti-4.5Al-xV-yFe alloys**.**

Table 3.3: Estimated cost of making 100 kg of the Ti-Al-V-Fe alloys.

Alloys	Cost per 100 kg ($)	Cost savings per 100 kg ($)	Cost savings per 100 kg (%)
Ti-6Al-4V	**2500.00**	-	-
Ti-6Al-3V-1Fe	2441.47	58.53	2.30
Ti-6Al-2V-2Fe	2382.93	117.07	4.70
Ti-6Al-1V-3Fe	**2324.40**	**175.61**	**7.00**
Ti-6Al-4Fe	2263.86	234.14	9.40
Ti-4.5Al-3V-1Fe	2475.50	24.50	1.00
Ti-4.5Al-2V-2Fe	2416.97	83.03	3.30
Ti-4.5Al-1V-3Fe	**2358.43**	**141.57**	**5.70**

3.3 Metallography

The preparation of the samples for microstructural analysis by cutting, mounting, grinding, polishing and etching is described.

3.3.1 Mounting

The sectioned samples were too small to handle and needed support for polishing, hardness testing and microscopy. Therefore the samples were mounted in Struers Polyfast resin using an Opal 410 hot mounting press. This was done at a temperature of 180°C and a pressure of 6 bar for a period of 6 minutes, with water as the coolant during the entire process.

3.3.2 Grinding and Polishing

Grinding and polishing were done to produce a mirror-like surface finish on the samples for microscopy and hardness testing. Grinding was done manually on an Imptech grinding machine using an abrasive silicon carbide paper of different grit sizes, while the samples were polished on a Struers Tegramin-20® automatic polishing machine using MD-Chem polishing cloths. Detailed steps that were employed for grinding and polishing of the samples are presented in Table 3.4. The grinding and polishing procedure was obtained by adapting the recommendations presented in the application notes on metallographic preparation of titanium alloys (Vander Voort, 1999, 2014; Struers, 2016).

3.3.3 Etching

The polished samples were etched by swabbing with standard Kroll's reagent for 20 seconds. The etchant consisted of 92 ml of deionised water, 6 ml of nitric acid and 2 ml of hydrofluoric acid. After etching, the samples were cleaned with ethanol in an ultrasonic bath and dried with

compressed air in readiness for microscopy. Since Kroll's reagent contains hydrofluoric acid, standard safety precautions described by Koontz (2013) were followed to prevent exposure. The material's safety data sheet was read prior to the use of the reagent. The etching was done in a fume hood with extraction and adequate personal protective equipment such as goggles, face shield, closed shoes, long trousers, nitrile (22 ml) gloves, and acid resistant aprons were used. The Kroll's reagent waste was poured into a chemically compatible container, sealed with a lid, properly labelled and kept in the space dedicated for waste chemicals in the laboratory. When etching was completed, a pickup request for the HF waste was placed with the service provider.

Table 3.4: Grinding and polishing procedure for Ti-Al-V-Fe alloys.

Parameters	Steps				
	1	2	3	4	5
Abrasive (Silicon Carbide- P Grade)/ Polishing cloth	P400	P1600	P2400	P4000	MD Chem
Coolant	Water	Water	Water	Water	Non-crystallising colloidal silica suspension + 30% hydrogen peroxide
Platen speed/direction	320 rpm	320 rpm	320 rpm	320 rpm	150 rpm/contra
Specimen speed	-	-	-	-	
Force	Hand	Hand	Hand	Hand	15 N
Time	1 min	1 min	1 min	1 min	20 minutes

3.4 Characterisation of the alloys

The microstructural features of the alloys were analysed using optical and scanning electron microscopy (SEM), compositions were determined using energy dispersive spectroscopy (EDX) on the SEM, while the identification of phases was done using X-ray diffraction (XRD).

3.4.1 Microstructural analysis

The microstructures of the as-cast and heat treated alloys were examined using a Leica DM 6000® optical microscope. The deformed samples obtained from isothermal hot compression testing (discussed in Section 3.6) were also examined. A high resolution Zeiss Sigma Field Emission Scanning Electron Microscope (FEG-SEM) equipped with both back-scattered and Oxford energy dispersive X-ray (EDX) detectors was used to analyse all the samples. The FEG-SEM was operated in back-scattered electron imaging (BSE) mode at 15 kV to distinguish the phases present in the alloys. EDX spot and area analyses were performed to determine the compositional variations in the alloys. The amount of phases present, thickness of laths and average grain diameters were determined using ImageJ v3.25 freeware (ImageJ, 2018). The microstructures of

the corroded samples immersed in different corrosive media discussed in Section 3.5.2 were examined by SEM in secondary electron imaging (SEI) mode.

3.4.2 X-ray diffraction

X-ray diffraction (XRD) patterns of both as-cast and annealed samples were obtained by taking measurements within the range of $2\theta = 10 - 110°$ using a Bruker D2 Phaser® diffractometer, with a cobalt K_α radiation source. The machine was operated at generator settings of 30 kV and 20 mA at a temperature of 25°C. The patterns obtained were analysed using PANalytical (v3.0e) X'pert Highscore software.

3.5 Screening of the alloys

After assessing the cost and performing microstructural analyses, the experimental alloys were screened by assessing the influence of substituting vanadium with iron on the hardness and corrosion behaviour of the alloys. The results obtained from the tests were compared with wrought Ti-6Al-4V results and are presented in the subsequent chapters. Based on the results, only two alloys were selected for hot-compression testing.

3.5.1 Hardness testing

The Vickers hardness of the as-cast and the heat treated experimental alloys was measured using a FutureTech FM700® microhardness tester fitted with a diamond indenter. The measurements were taken under a load of 300 g and a dwell time of 10 s according to ASTM standard E92-17(ASTM E 92-17, 2017). Five readings were taken at different positions on each alloy and the average $HV_{0.3}$ and standard deviation were calculated.

3.5.2 Corrosion Testing

Electrochemical corrosion testing was performed only on the heat treated experimental alloys. The samples were cut, cold mounted in Crystal Clear® resin and allowed to cure for 24 hours. The exposed surface of the alloys was ground to P2400 grit; the samples were rinsed in distilled water and dried in air. The surface area of the samples exposed to the corrosive solutions was 0.25 cm^2. A wrought Ti-6Al-4V alloy was also prepared and tested for comparison. A conventional three-electrode, electrochemical cell connected to an AutoLab® potentiostat/galvanostat was used for the electrochemical testing. A graphite rod was used as the counter electrode while Ag/AgCl saturated in 3 M KCl served as the reference electrode under all test conditions. Open circuit potential (OCP) and potentiodynamic polarisation tests were performed on the samples at ambient temperature in 3.5 M H_2SO_4, 3.5 wt% NaCl, and 3.5M H_2SO_4 + 1.75 wt% NaCl solutions. All the solutions were prepared using analytical grade

chemicals. The OCP measurements were taken for 3600 s in both H_2SO_4 and NaCl environments, while the scan only lasted for 1200 s in the more aggressive H_2SO_4+NaCl mixed solution. In the H_2SO_4 and H_2SO_4+NaCl solutions, linear potentiodynamic scans were performed on the samples from -0.5 V to 2.5 V at a scan rate of 0.2 mV/s. A cyclic potentiodynamic scan was carried out in NaCl from -0.5 V to 2.5 V at a scan rate of 2 mV/s, to evaluate the susceptibility of the alloys to pitting corrosion in chloride solutions.

The corrosion current density (i_{corr}) with associated corrosion voltage (E_{corr}), and the corrosion rate was determined by the polarisation technique according to ASTM standard G59-97 (Badea *et al*., 2010; ASTM G59-97, 2014).

3.6 Hot compression testing

The commercial Ti-6Al-4V alloy and two experimental alloys: Ti-6Al-1V-3Fe and Ti-4.5Al-1V-3Fe, were subjected to isothermal compression testing using a Gleeble 3500® thermo-mechanical simulator. The two experimental alloys were selected for the test based on cost, hardness and corrosion performance.

Cylindrical samples having dimensions of Ø8 x 12 mm were machined from the commercial Ti-6Al-4V alloy, while the experimental alloys in the as-cast + heat treated condition were machined to 8 x 8 x 12 mm rectangular samples since it was much easier to machine rectangular samples from the 50 x 50 mm square ingots (Figure 3.2). A few rectangular samples were also machined from the commercial alloy and were compressed under similar conditions to the cylindrical samples. All the samples were machined using electrical discharged machining. The dimensions of the samples were carefully selected to ensure that the aspect ratio of the samples was less than 1.1 as recommended by Roebuck *et al*.(2006). The stress-strain curves obtained from the tests carried out on the rectangular and cylindrical samples of the commercial alloy were comparable (Appendix D).

Prior to hot compression testing, a chromel-alumel thermocouple was welded to the mid span of the test samples using a spot welder. The samples were then placed on the Hydrawedge autoloader. Graphite foil and nickel paste were placed between the Iso-T tungsten carbide anvils and the specimen to reduce the effect of friction during deformation. The test parameters listed in Table 3.5 were then entered into the Quicksim software using the (.hds) program. The program was then converted to Gleeble Script Language (.gsl) before running each experiment. A typical gsl program for the hot compression test is shown in Appendix C. For each test, the samples were heated directly to the deformation temperature at a rate of 5°C/s, and held at this temperature for 360 s for homogenisation (Figures 3.3 and 3.4). Thereafter, the samples were deformed at the

specified strain rate followed by compressed air cooling. The isothermal compression schedule for the test is shown in Figure 3.4.

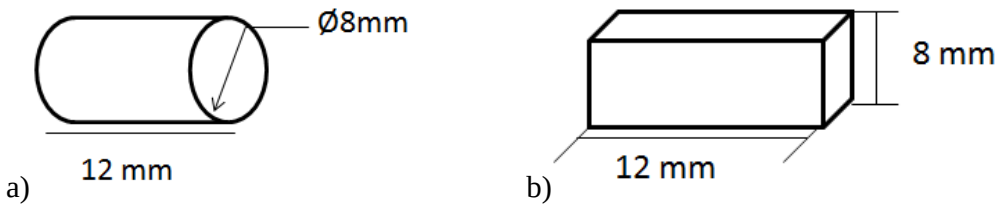

Figure 3.2: Hot compression samples: (a) cylindrical, and (b) rectangular.

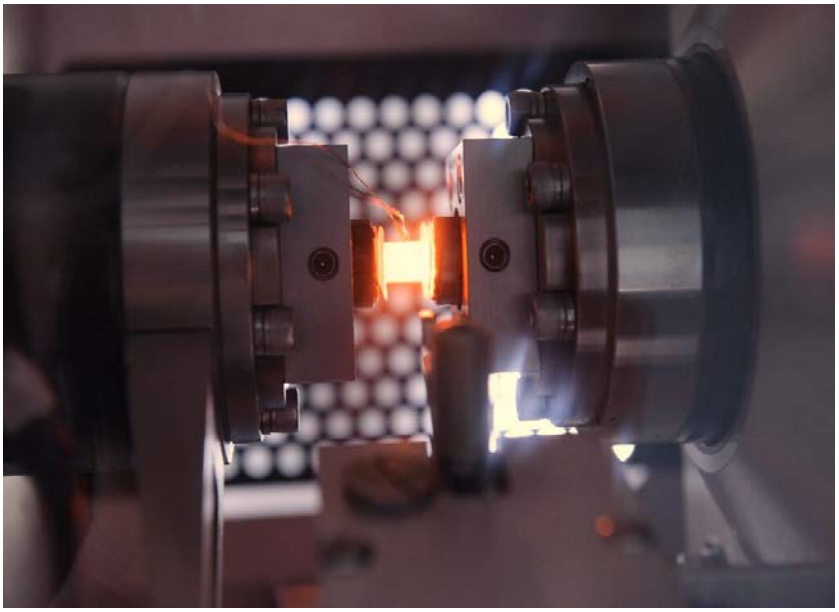

Figure 3.3: Hot compression testing of titanium alloy in the Gleeble 3500®.

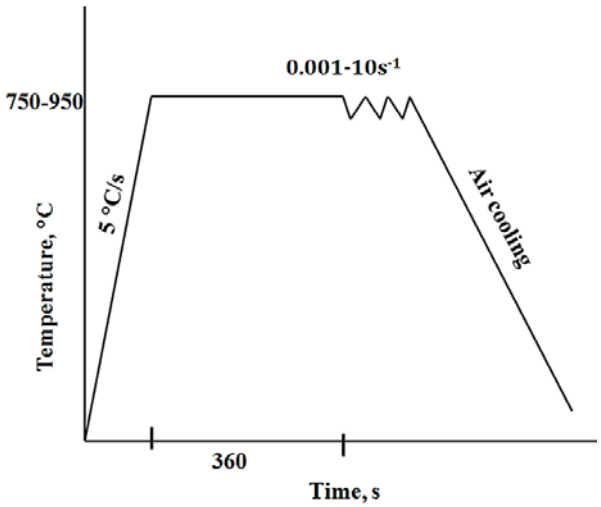

Figure 3.4: Schematic diagram of the isothermal compression testing schedule.

To validate the experiment, the barrelling coefficient of the compressed samples was determined from Equation 3.1 as defined by Roebuck *et al.* (2006) and Li *et al.*(2010). Only the samples with barrelling coefficients less than1.1 were accepted:

$$B = 4 \times \frac{\Delta r}{r} \times \frac{\Delta h}{h}$$ **Equation 3.1**

where B is barrelling coefficient; r is initial radius of the sample; h is final height of the sample; Δh is= reduction in height of the sample after compression; and Δr is the difference between the maximum radius and the radius of the top of the sample.

In the rectangular sample, Δr, was obtained by dividing the difference between the maximum width of the compressed sample and the width of the top of the sample by 2.

Table 3.5: Hot compression testing parameters for the commercial and experimental alloys.

Deformation parameters		**Temperature (°C)**				
Strain	**Strain rate (s^{-1})**	**750**	**800**	**850**	**900**	**950**
0.6	0.001	▲▼	▲▼	▲▼	▲▼	▲▼
0.6	0.01	●▲▼	●▲▼	●▲▼	●▲▼	●▲▼
0.6	0.1	●▲▼	●▲▼	●▲▼	●▲▼	●▲▼
0.6	1	●▲▼	●▲▼	●▲▼	●▲▼	●▲▼
0.6	10	●▲▼	●▲▼	●▲▼	●▲▼	●▲▼

● = Ti-6Al-4V; ▲= Ti-6Al-1V-3Fe; and ▼ = Ti-4.5Al-1V-3Fe

3.7 Analysis of stress-strain data

The three common methods used to assess the hot deformation behaviour of metallic alloys include analysing the shape of the stress strain curves, constitutive modelling and processing maps. The stress-strain data obtained from the hot compression tests were plotted to analyse the shape of the stress-strain curves and processing maps were developed using the stress-strain data to obtain the dominant softening mechanisms and optimum hot working conditions for the alloys. Additionally, the activation energy for hot working of the alloys was determined using the hyperbolic sine Arrhenius equation (Sellars and Tegart, 1966).

3.7.1 Processing Maps

Processing maps were developed by superimposing power dissipation maps and an instability maps as described in Section 2.3.5 (Prasad, 2003). The strain rate sensitivity parameter m is defined as the inverse of the stress exponent n or the increase in stress needed to cause a specific increase in plastic strain rate at a given temperature. The slope of the $ln\,\sigma$ vs. $ln\,\dot{\varepsilon}$ plot was used to determine m by Equation 3.2. A cubic spline fit was used to determine the intermediate data

points for *m* as a function of strain rate in the temperature range of 750 - 950°C. The efficiency of power dissipation (η) was obtained from the strain rate sensitivity parameter using Equation 3.3 (Prasad, 2003).

$$m = \frac{\partial \ln \sigma}{\partial \ln \dot{\varepsilon}} \qquad \textbf{Equation 3.2}$$

$$\eta = \frac{2m}{m+1} \qquad \textbf{Equation 3.3}$$

Using these values, power efficiency maps were plotted to represent the pattern in which power is dissipated via microstructural changes occurring in the material during deformation, such as dynamic recrystallisation, dynamic recovery and superplasticity. The instability criterion $\xi\dot{\varepsilon}$ proposed by Prasad *et al.* (2015) in Equation 3.4 and Murty *et al.* (2002) in Equation 3.5 were both used to identify the domain of instability during deformation.

$$\xi\dot{\varepsilon} = \frac{\partial \ln(m/m+1)}{\partial \ln \dot{\varepsilon}} + m < 0 \qquad \textbf{Equation 3.4}$$

$$\xi(\dot{\varepsilon}) = \frac{2m}{\eta} - 1 < 0 \qquad \textbf{Equation 3.5}$$

Chapter 4: Development of experimental Ti-Al-V-Fe alloys

This chapter presents the experimental results addressing the first and second research objectives. The influence of partial substitution of vanadium with iron, reduction in aluminium concentration and annealing on the microstructure and hardness of the experimental alloys are discussed. A summary of the experimental findings is also given.

4.1 Thermo-Calc Modelling

Table 4.1 lists the results obtained from Thermo-Calc simulation using the TTTi3 titanium database. The estimated beta-transus temperature and the predicted volume fraction of the beta phase at 800°C under equilibrium conditions are presented. The results show that the volume fraction of the beta phase increased with increasing iron content in the alloys. An inverse relationship exists between the beta-transus temperature and increasing iron content in the alloys. The transformation curves for the simulations are shown in Appendix E.

Table 4.1: Thermo-Calc results for the Ti-Al-V-Fe alloys using the TTTi3 titanium database.

Samples	Composition (wt %)				β-transus temp (°C)	Phases present at 800 °C (mol%)	
	Ti	Al	V	Fe		α-Ti (*hcp*)	β-Ti (*bcc*)
Ti-6Al-4V	90	6.0	4	0	944	86	14
Ti-6Al-3V-1Fe	90	6.0	3	1	937	75	25
Ti-6Al-2V-2Fe	90	6.0	2	2	932	68	32
Ti-6Al-1V-3Fe	90	6.0	1	3	925	61	39
Ti-4.5Al-3V-1Fe	91.5	4.5	3	1	909	68	32
Ti-4.5Al-2V-2Fe	91.5	4.5	2	2	905	61	39
Ti-4.5Al-1V-3Fe	91.5	4.5	1	3	899	54	46
Ti-6Al-4Fe	90	6	-	4	921	55	45

4.2 Compositional Analysis

The average compositions of both the as-cast and annealed experimental alloys are presented in Table 4.2 and Table 4.3 respectively. The average compositions were obtained by EDX analysis on four different locations on the alloys and were compared against the targeted nominal compositions. It can be seen that the actual compositions of both the as-cast and annealed experimental alloys were comparable to the targeted nominal compositions.

Table 4.2: EDX compositions of as-cast experimental alloys.

Sample	Nominal (wt %)				Actual (wt %)			
	Ti	Al	V	Fe	Ti	Al	V	Fe
Ti-6Al-4V w	**90**	**6**	**4**	**-**	**89.9**	**6.0**	**4.1**	**-**
Ti-6Al-3V-1Fe	90	6	3	1	90.2 ±0.3	5.7 ±0.1	3.0 ±0.3	1.1 ±0.2
Ti-6Al-2V-2Fe	90	6	2	2	89.8 ±0.1	5.7 ±0.2	2.3 ±0.2	2.2 ±0.2
Ti-6Al-1V-3Fe	90	6	1	3	89.9 ±0.2	5.8 ±0.1	1.2 ±0.2	3.1 ±0.1
Ti-4.5Al-3V-1Fe	91.5	4.5	3	1	91.2 ±0.2	4.3 ±0.1	3.3±0.2	1.2 ±0.1
Ti-4.5Al-2V-2Fe	91.5	4.5	2	2	90.8 ±0.1	4.6 ±0.2	2.2 ±0.2	2.4 ±0.1
Ti-4.5Al-1V-3Fe	91.5	4.5	1	3	91.2 ±0.2	4.3 ±0.2	1.2 ±0.1	3.3 ±0.1
Ti-6Al-4Fe	90	6		4	89.8 ±0.2	6.0 ±0.1	-	4.2 ±0.2

*w = wrought alloy, composition of the Ti-6Al-4V alloy was obtained from the supplier.

Table 4.3: EDX compositions of annealed experimental alloys.

Sample	Nominal (wt %)				Actual (wt %)			
	Ti	Al	V	Fe	Ti	Al	V	Fe
Ti6Al4V w	**90**	**6**	**4**	**-**	**89.9**	**6**	**4.1**	**-**
1	90	6	3	1	89.8 ±0.1	5.7 ±0.1	3.7 ±0.1	0.8 ±0.1
2	90	6	2	2	89.4 ±0.3	5.6 ±0.1	2.7 ±0.1	2.3 ±0.3
3	90	6	1	3	89.1 ±0.2	5.7 ±0.2	1.9 ±0.1	3.3 ±0.1
4	91.5	4.5	3	1	90.8 ±0.1	4.2 ±0.1	3.7 ±0.1	1.3 ±0.1
5	91.5	4.5	2	2	90.4 ±0.3	4.4 ±0.1	2.7 ±0.2	2.5 ±0.2
6	91.5	4.5	1	3	90.6 ±0.1	4.5 ±0.1	1.3 ±0.1	3.6 ±0.2
7	90	6		4	89.4 ±0.3	5.9 ±0.1	-	4.7 ±0.2

4.3 Phase Analysis

The phases present in the as-cast and annealed experimental alloys were identified by X-ray diffraction analyses presented in Figures 4.1 to 4.4 and SEM images presented in section 4.4. From the XRD results, the dominant phases in all the alloys were α-hcp, β-bcc and TiO_2 in both as-cast and annealed conditions. Other phases that were identified in the experimental alloys and the commercial alloy were iron titanium oxide and vanadium oxide respectively. An unidentified peak was present in the annealed Ti-6Al-1V-3Fe alloy. The crystallographic data of the detected phases are presented in Table 4.4. In Figures 4.1 and 4.2, the as-cast and annealed Ti-6Al-3V-1Fe alloy did not show any peak corresponding to the β-bcc phase. The reason for this is not known, but Oh *et al*. (2011) found a similar result for a Ti-6Al-4V alloy.

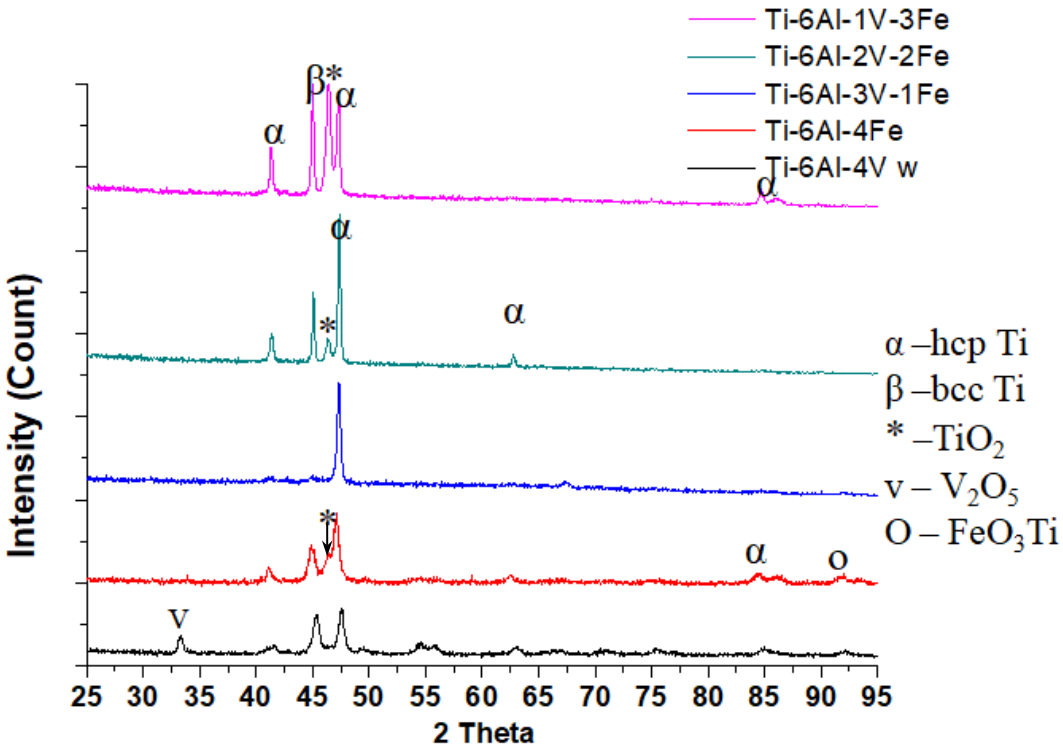

Figure 4.1: XRD patterns of as-cast Ti-6Al-*x*V-*y*Fe and wrought Ti-6Al-4V alloys.

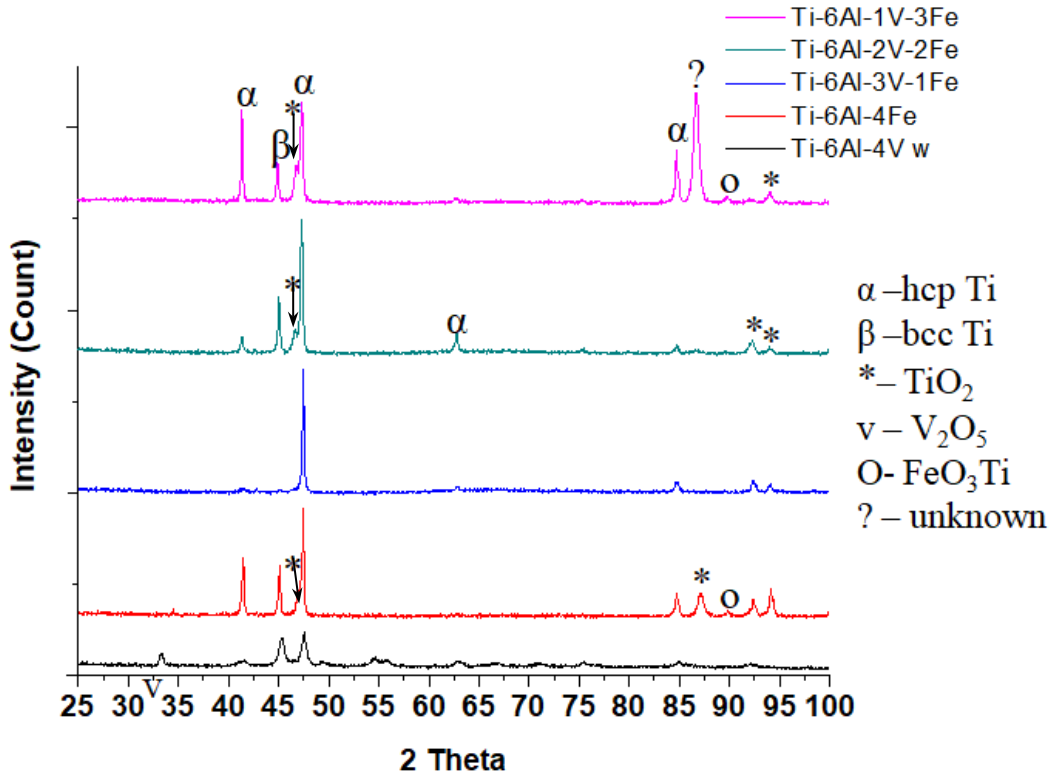

Figure 4.2: XRD patterns of annealed Ti-6Al-*x*V-*y*Fe and wrought Ti-6Al-4V alloys.

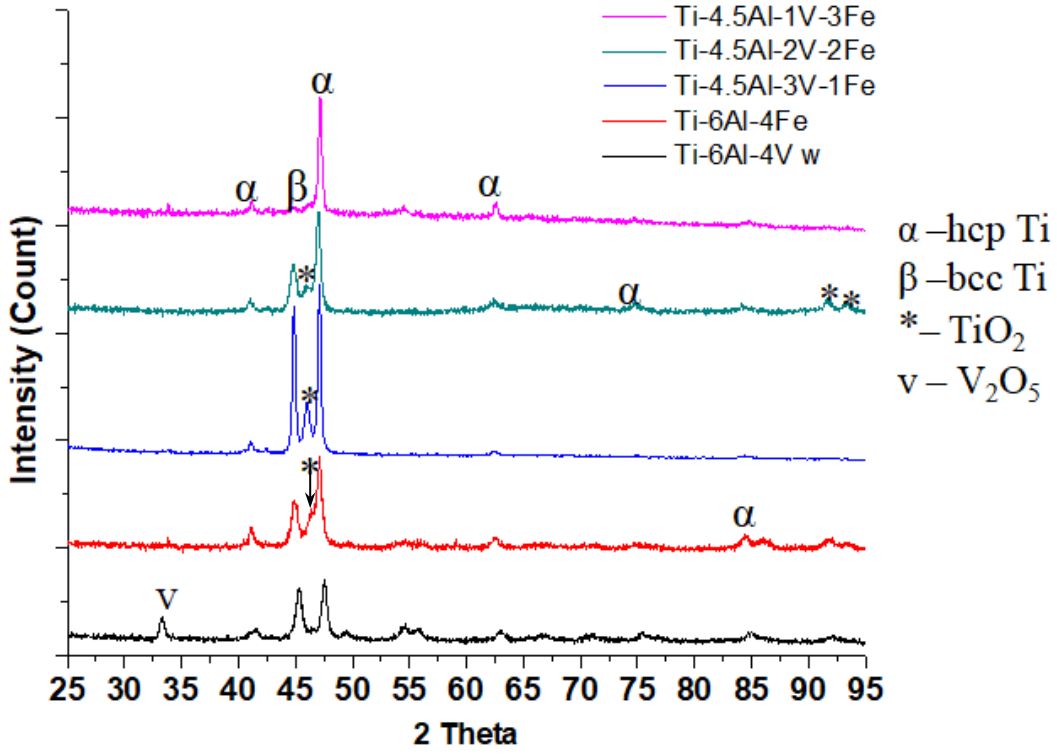

Figure 4.3: XRD patterns of as-cast Ti-4.5Al-*x*V-*y*Fe and wrought Ti-6Al-4V alloys.

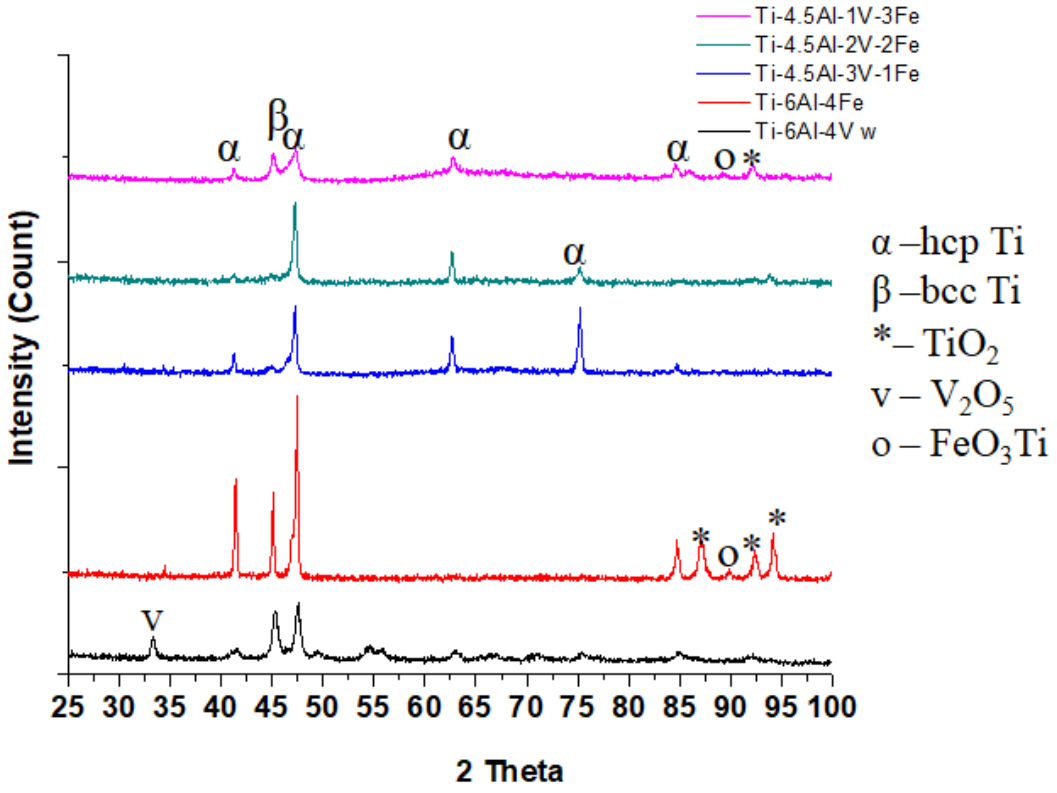

Figure 4.4: XRD patterns of annealed Ti-4.5Al-*x*V-*y*Fe and wrought Ti-6Al-4V alloys.

The phases present in the alloys were identified by carrying out EDX spot analyses on four different spots of the light and dark regions of the SEM images. The average composition of the phases obtained for Ti-6Al-1V-3Fe from EDX is presented in Table 4.5, with the representative EDX spectra presented in Figures 4.5 and 4.6. The dark phase was α-Ti which contained Ti, Al and V, while the light phase marked as 'interplatelet β' was β-Ti containing Ti, Al, V and Fe. The presence of Fe in the light region (Figure 4.6) confirmed that it was the β-Ti phase, because Fe has a low solubility in the α-Ti phase and thus is rejected from the α-Ti phase to preferentially settle and stabilise the β-Ti phase where it has a higher solubility (Gil *et al.*, 2001). Safdar *et al.* (2012) used a similar procedure to identify the alpha and beta phases in a selective laser melted titanium alloy. They reported that there was no Fe in the alpha phase, but only in the beta phase of the alloy.

Table 4.4: Crystallographic data of phases present in the as-cast and annealed alloys.

Phase	Space group (no.)	*a* (Å)	*b*(Å)	*c* (Å)	Cell vol. (10^6 pm^3)	Reference
α-Ti (hcp)	*P63/mmc* (194)	2.9505	2.9505	4.6826	35.30	044-1294
β-Ti (bcc)	*Im-3m* (229)	3.3065	3.3065	3.3065	36.15	044-1288
TiO_2 (orthorhombic)	*Pbnm* (62)	4.9010	9.4530	2.9580	137.04	049-1433
FeO_3Ti (Rhombohedral)	*R-3(148)*	5.0884	5.0884	14.093	316.01	029-0733
V_2O_5 (Tetragonal)	*P E*	14.2590	14.2590	12.5760	2556.94	045-1074

Table 4.5: Composition of α and β phases by EDX, in wt%.

	α		β	
Elements	**As-cast**	**Annealed**	**As-cast**	**Annealed**
Al	7.3 ±2.5	6.0 ±0.1	5.8 ±0.1	4.0 ±0.4
Ti	89.7 ±2.3	91.6 ±0.1	90.2 ±0.1	81.4 ±0.8
V	3.0 ±0.2	2.4 ±0.2	3.3 ±0.1	8.9 ±0.5
Fe	-	-	0.7 ±0.1	5.7 ±0.5

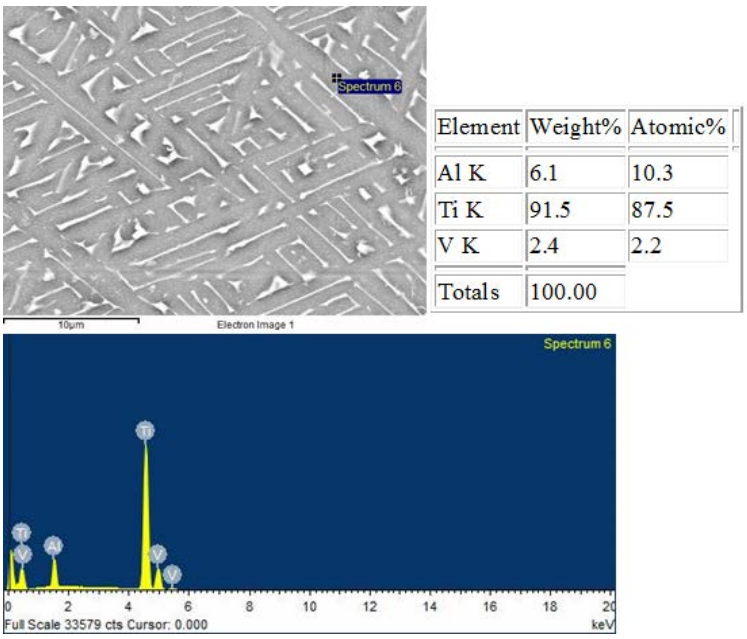

Figure 4.5: EDX spectrum of α phase in Ti-6Al-3V-1Fe alloy.

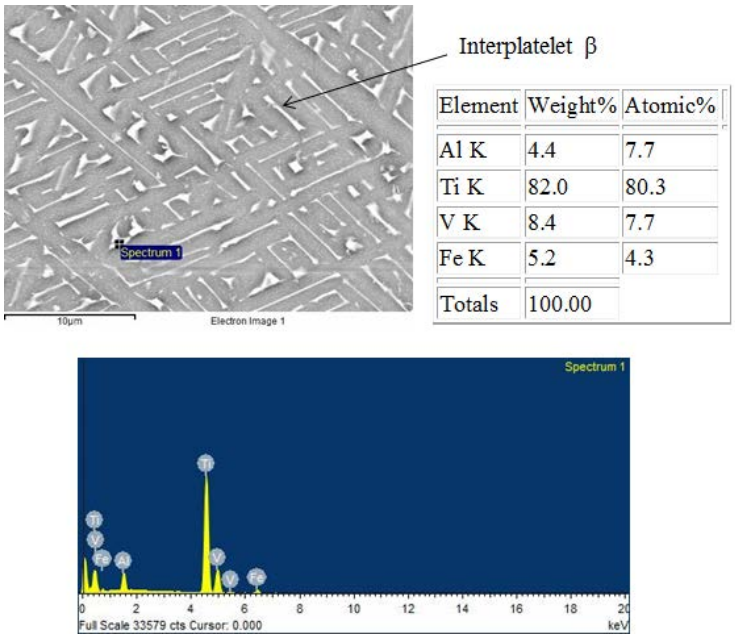

Figure 4.6: EDX spectrum of β phase in Ti-6Al-3V-1Fe alloy.

4.4 Optical micrographs and SEM images

The microstructures of the as-cast and annealed samples are presented in Figure 4.7. The Widmanstätten α-laths were embedded within the large prior β grains. The average sizes of the prior β grains for the as-cast and annealed alloys were within the range of 300 - 500 µm, which is consistent with the prior β grain size in α+β Ti-alloys reported by Lütjering and Williams (2007). Figure 4.8 shows the relationship between the Fe content in the alloys and the average size of the prior β grains. The relationship does not fit well on a curve, except in annealed Ti-4.5Al-*x*V-*y*Fe alloys. The large error bars indicated that the grain sizes varied over wide ranges, making it difficult to deduce the effect of iron addition on the prior beta grain size.

As cast

Annealed

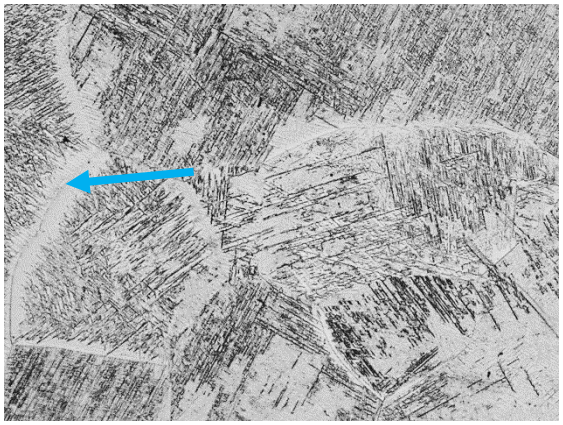

a)



b)

Ti-6Al-3V-1Fe



c)

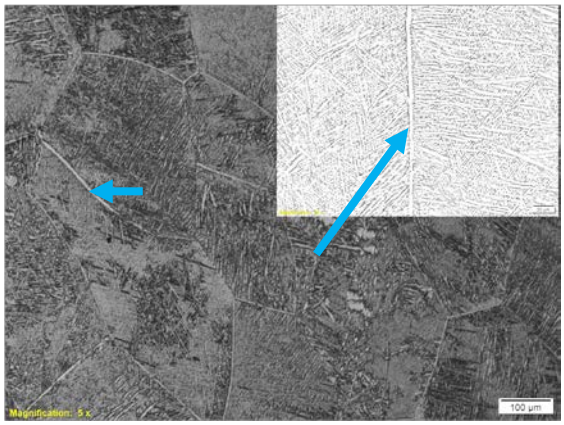

d)

Ti-6Al-2V-2Fe

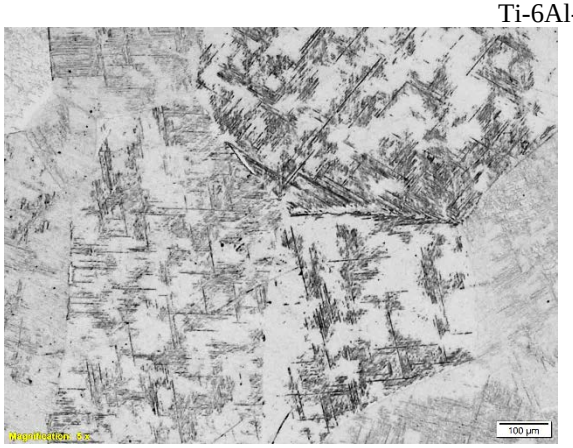

e)

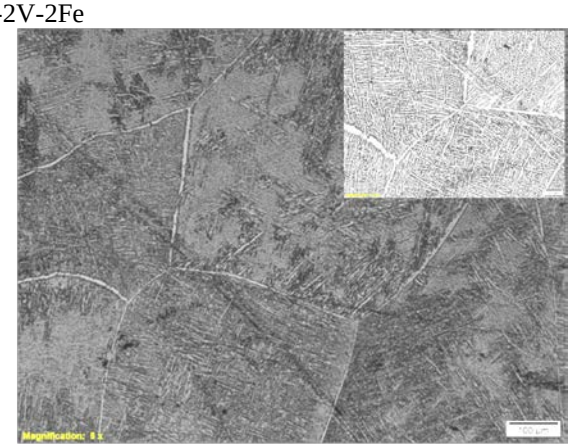

f)

Ti-6Al-1V-3Fe

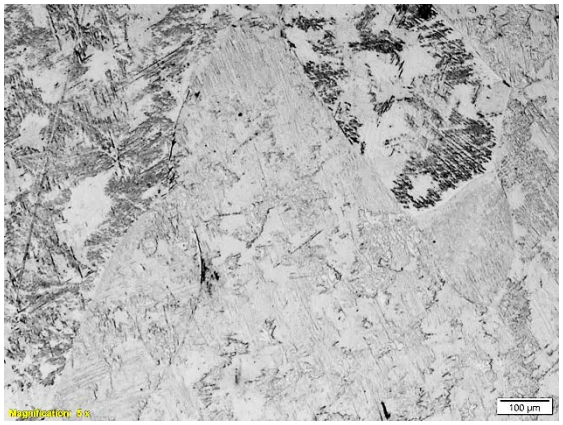

g)

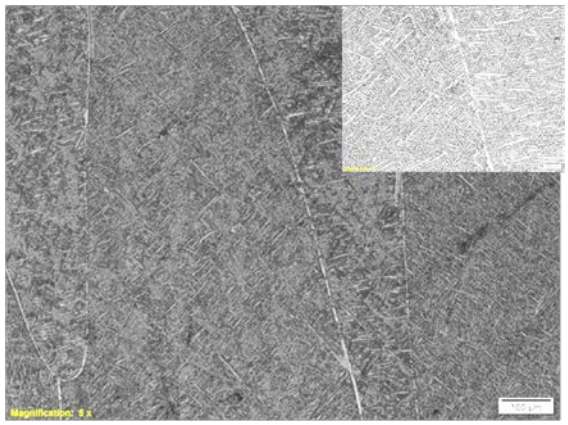

h)

Ti-6Al-4Fe

As cast | Annealed

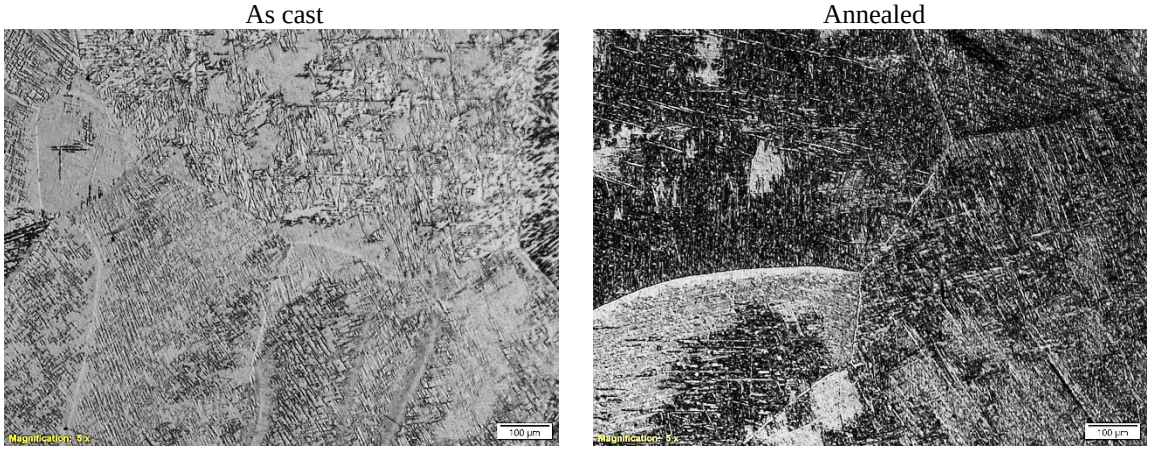

i) j)

Ti-4.5Al-3V-1Fe

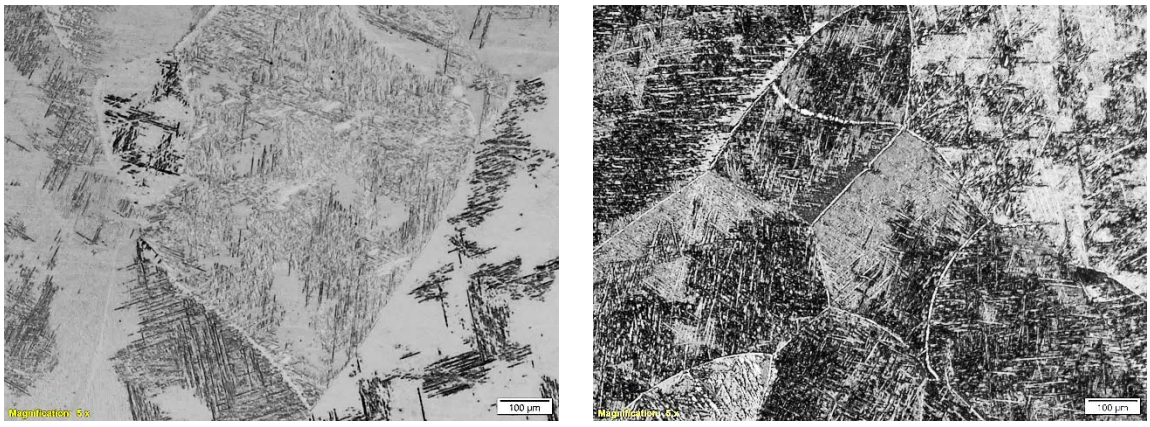

k) l)

Ti-4.5Al-2V-2Fe

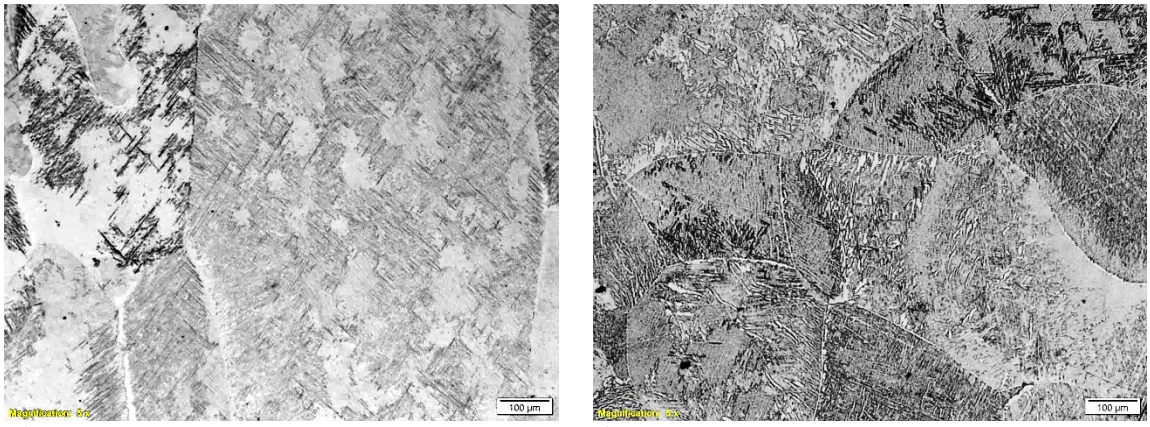

m) n)

Ti-4.5Al-1V-3Fe

Figure 4.7: Optical micrographs of as-cast and annealed alloys showing Widmanstätten α-laths embedded within prior beta grains. Blue arrows are pointing to prior beta grain boundaries.

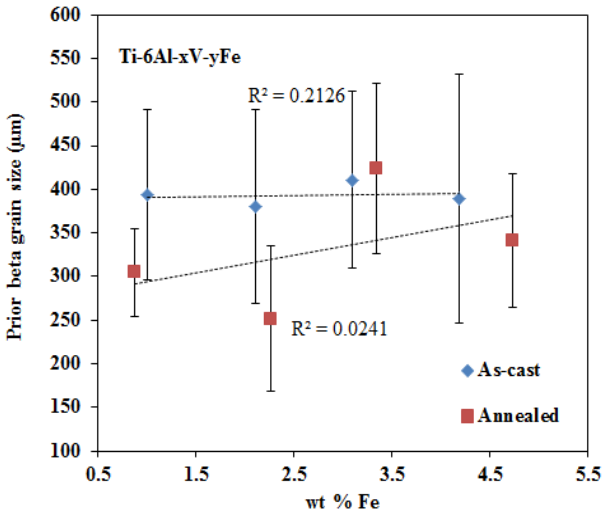

a)

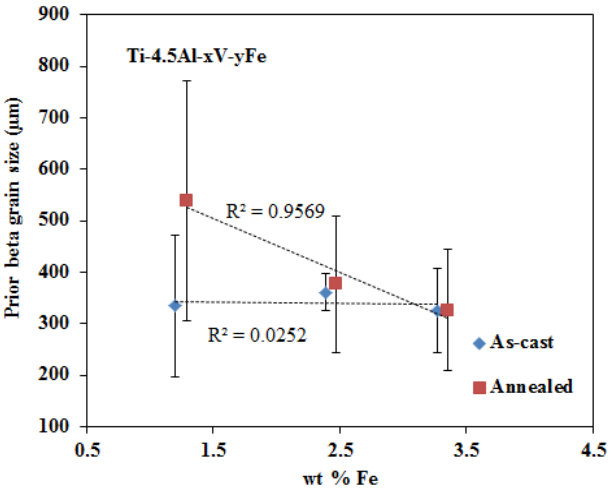

b)

Figure 4.8: Relationships between Fe content and prior beta grain size in a) Ti-6Al-*x*V-*y*Fe and b) Ti-4.5Al-*x*V-*y*Fe alloys.

The BSE SEM images (Figures 4.9 - 4.10) confirmed the presence of α-laths and retained interplatelet β in the alloys. Both contrast and brightness adjustment were used on the SEM BSE images (left) in an attempt to provide sufficient contrast between the αThe SEM images were processed using imageJ freeware as there was no distinct contrast between the α and β phases in the original SEM images. The volume fraction of the β-phase and the thickness of the α-laths were then estimated from several SEM images taken at different locations on the same sample. The relationship between the Fe content and volume fraction of β-phase in both as-cast and annealed alloys is presented in Figure 4.11 and Table 4.6. The volume fraction of β-phase in the annealed alloys was less than in the as-cast alloys. However, in both conditions, the volume fraction of the beta phase increased with increase in Fe content.

Actual **Processed on ImageJ**

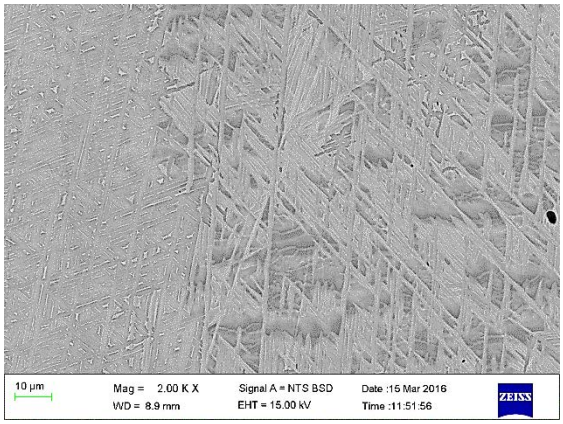

a)

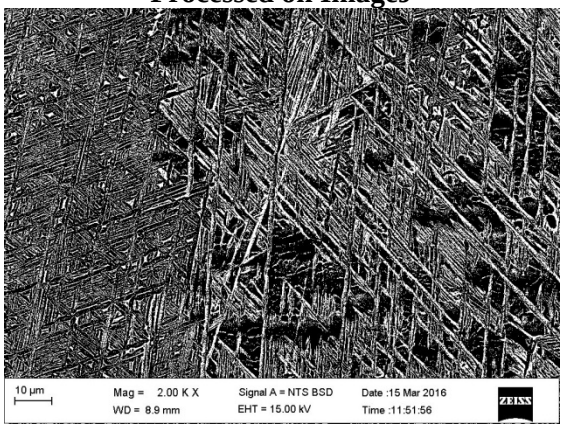

b)

Ti-6Al-3V-1Fe

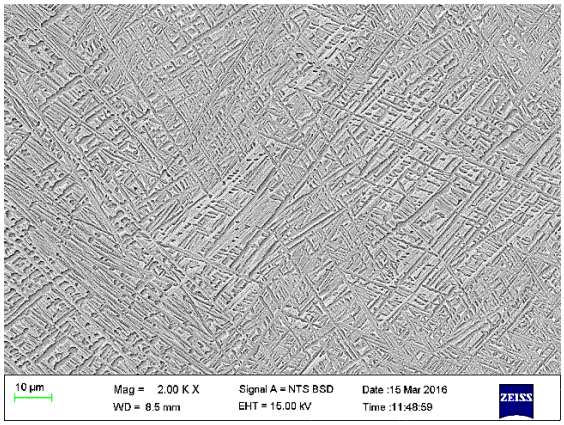

c)

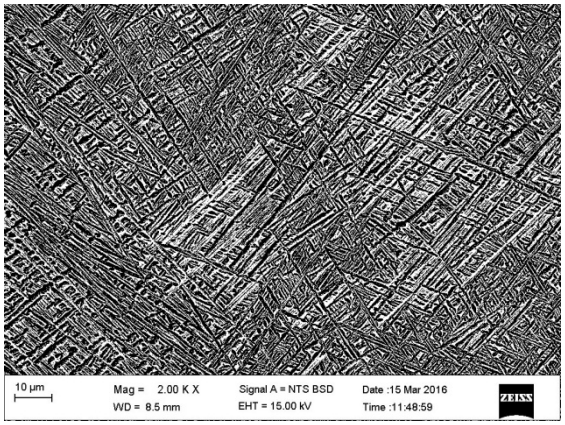

d)

Ti-6Al-2V-2Fe

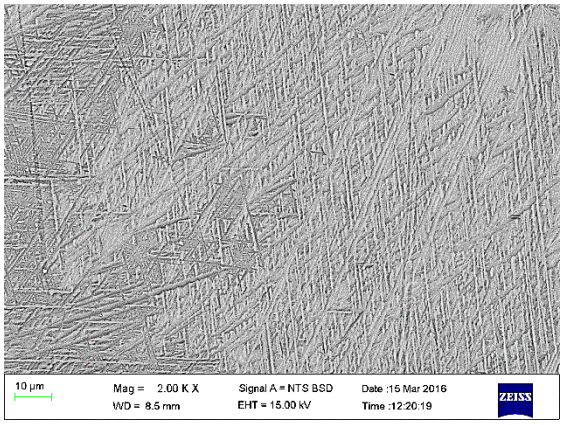

e)

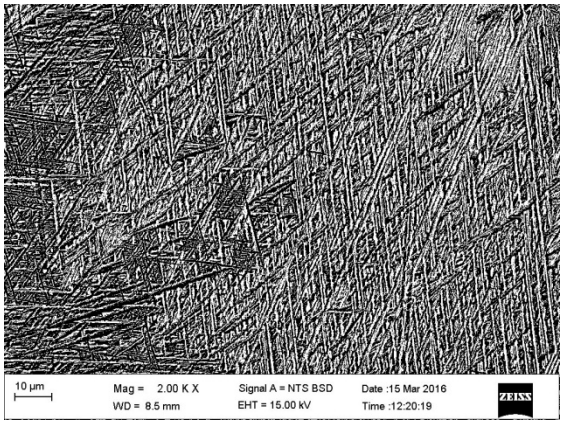

f)

Ti-6Al-1V-3Fe

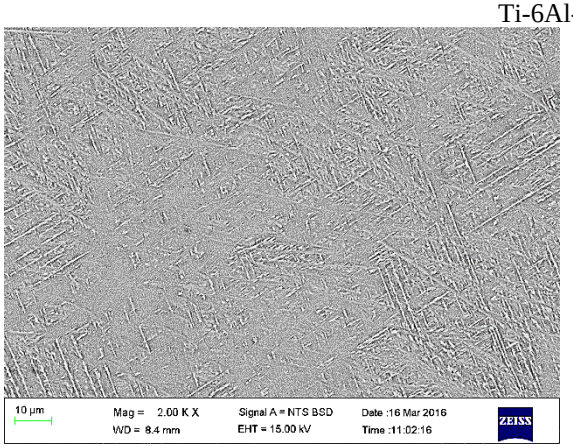

g)

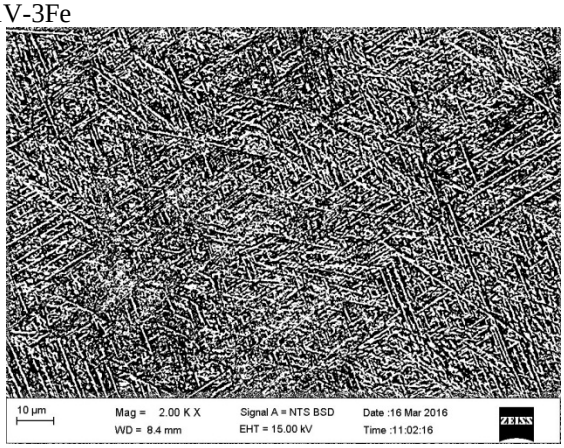

Ti-6Al-4Fe h)

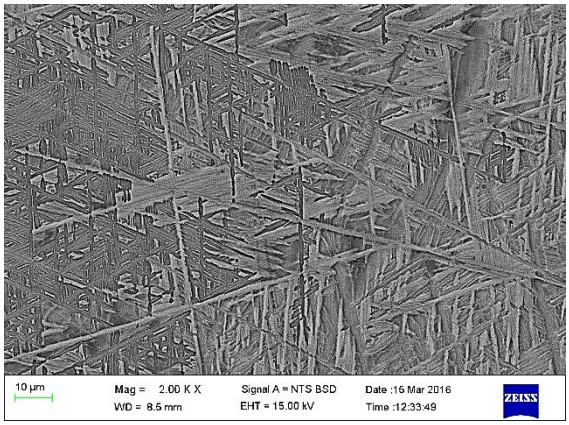

i)

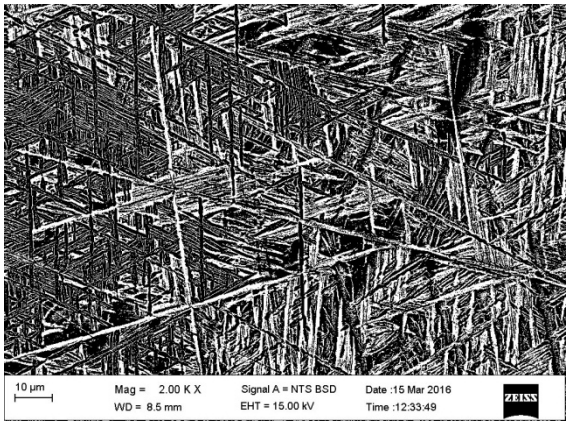

j)

Ti-4.5Al-3V-1Fe

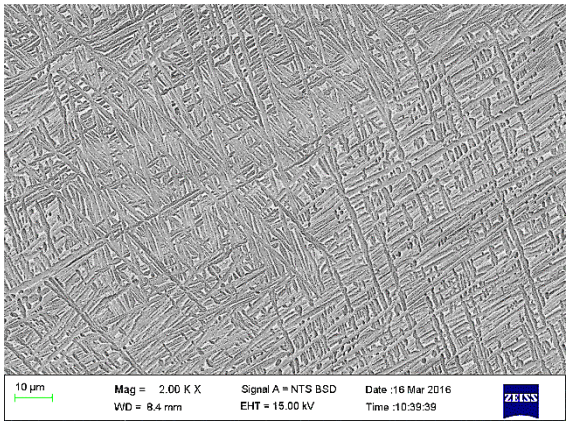

k)

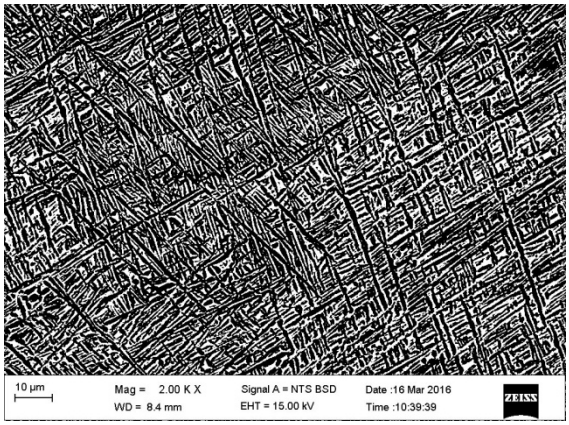

l)

Ti-4.5Al-2V-2Fe

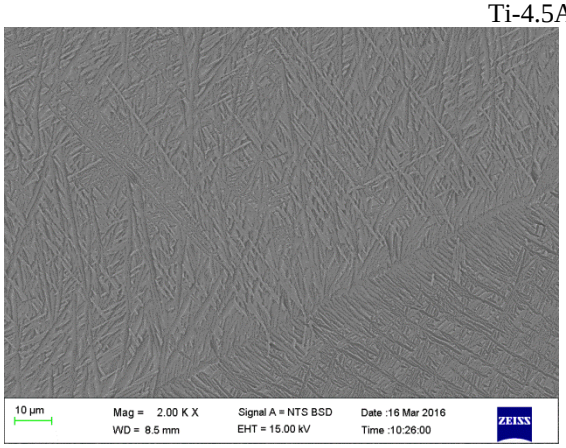

m)

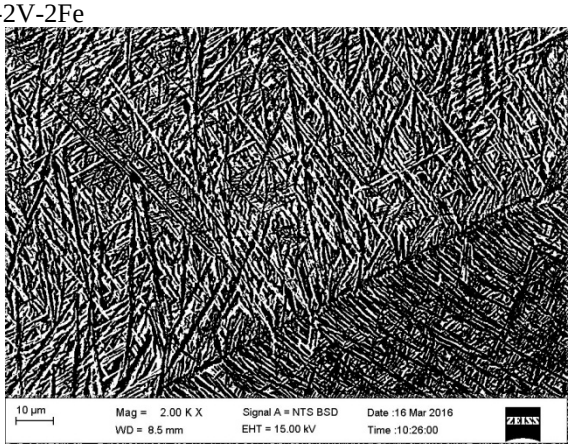

n)

Ti-4.5Al-1V-3Fe

Figure 4.9: SEM-BSE images of as-cast alloys with contrast and brightness adjustment (left) and the same images processed using imageJ software (right), showing alpha laths (dark) in a retained beta (light) matrix.

Actual

Processed

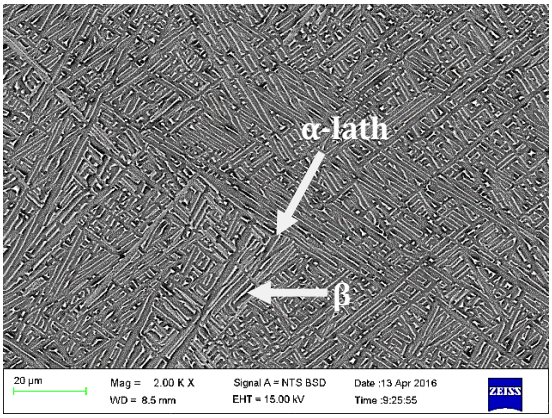

a)

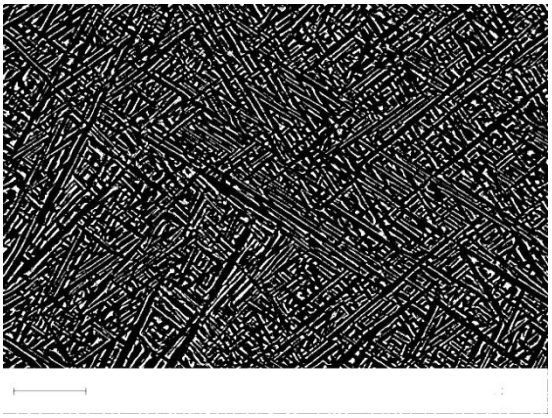

b)

Ti-6Al-3V-1Fe

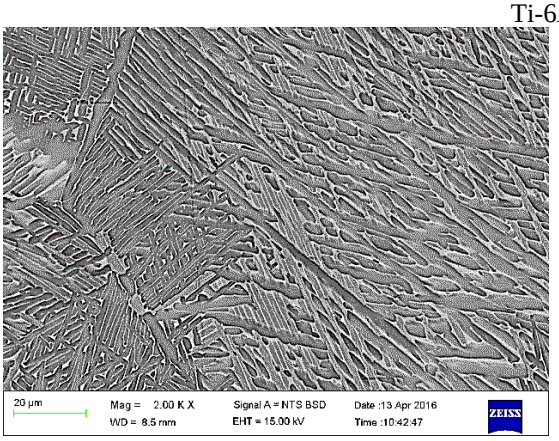

c)



d)

Ti-6Al-2V-2Fe

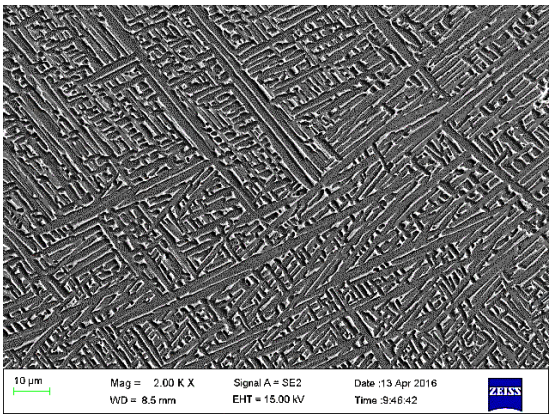

e)



f)

Ti-6Al-1V-3Fe

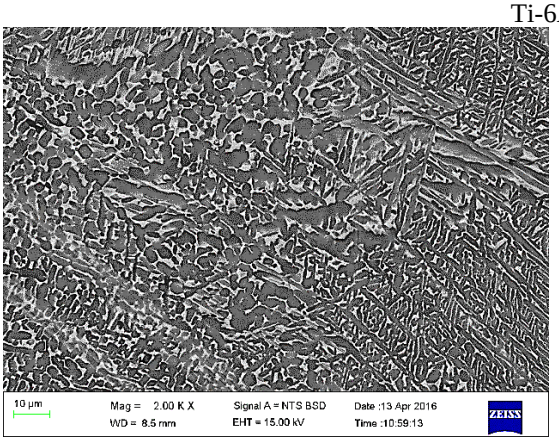

g)

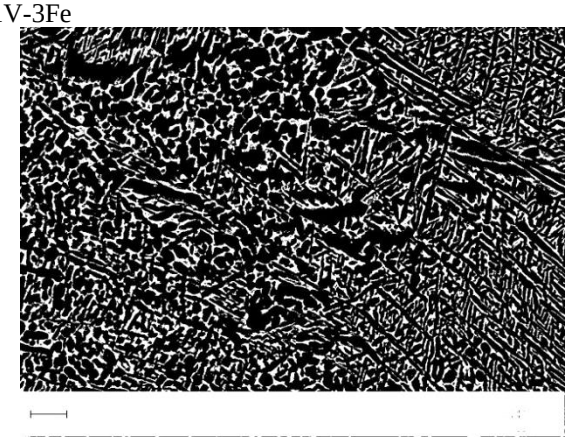

h)

Ti-6Al-4Fe

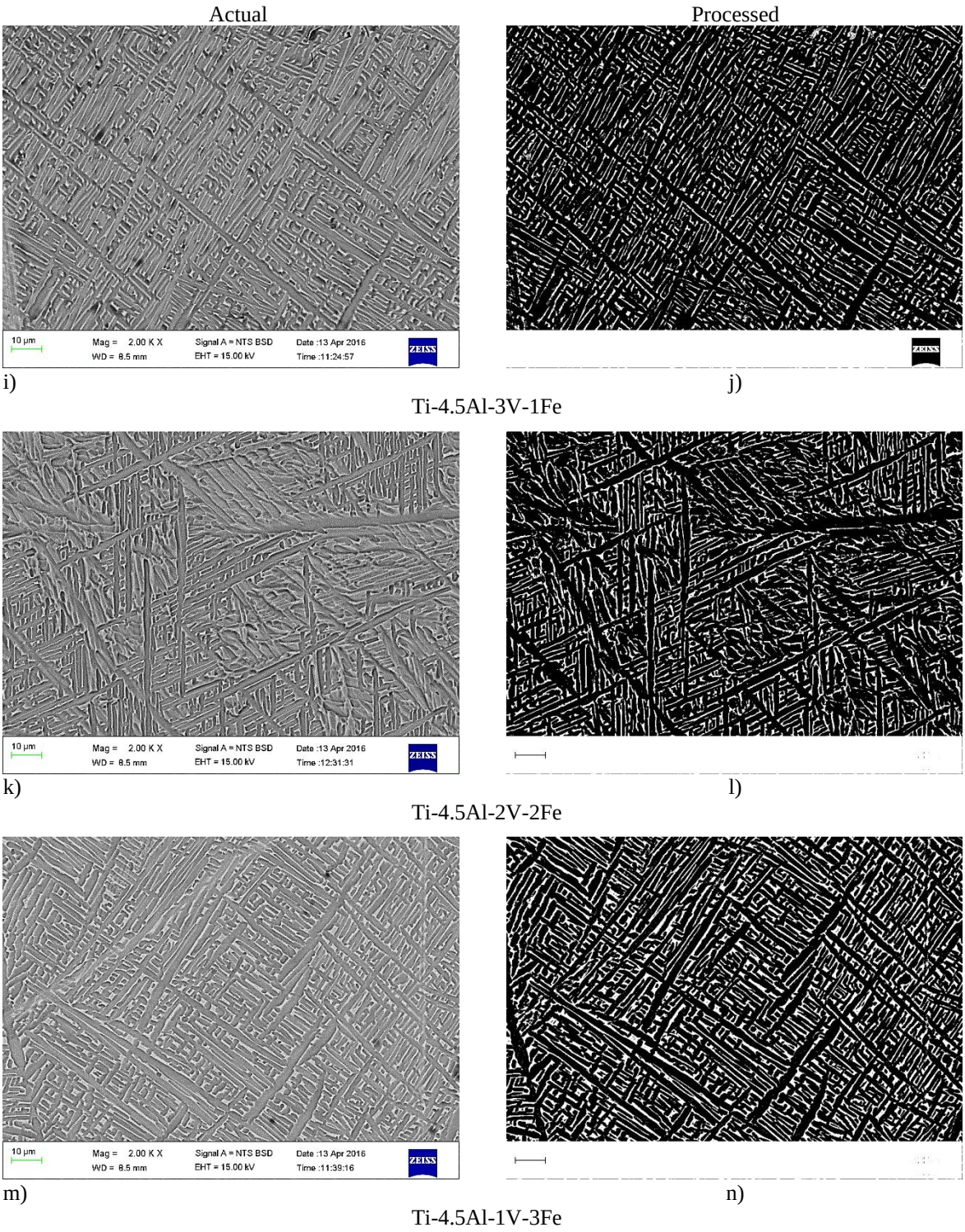

Figure 4.10: SEM-BSE images of annealed samples (left) and the same images processed using imageJ software (right), showing α laths (dark) and retained interplatelet β (light).

Figure 4.12 shows the influence of Fe content on the thickness of α-laths in both as-cast and annealed alloys. Again, the large error bars made it difficult to deduce an accurate relationship between Fe content and the lath thickness of the alloys. However, considering the general trend,

the lath thickness decreased with increasing Fe content in the as-cast alloys. There was an increase in lath thickness with increasing Fe content in the annealed samples, except in Ti-5.9Al-4.7Fe (nominal Ti-6Al-4Fe) where there was a slight decrease in thickness (Figure 4.12a).

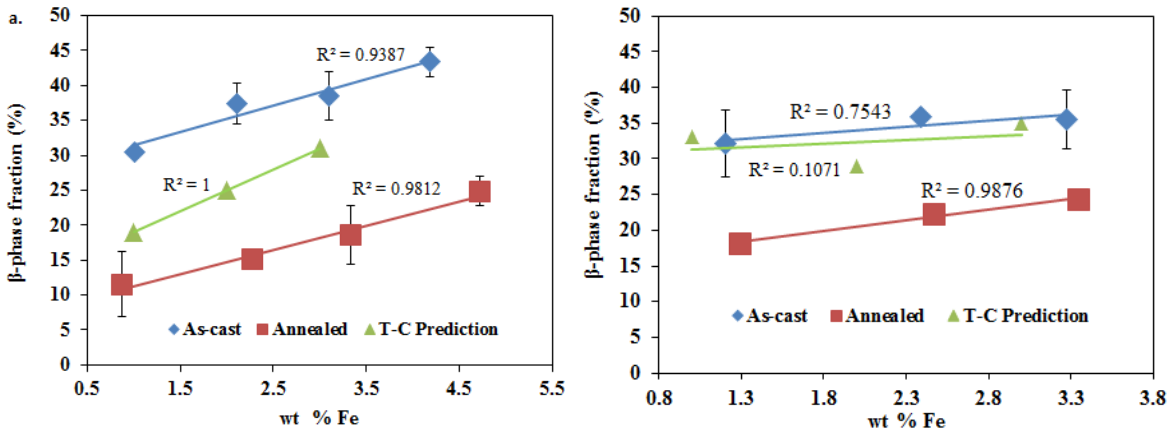

Figure 4.11: Relationship between Fe content and β phase fraction in as-cast and annealed alloys: a) Ti-6Al-*x*V-*y*Fe and b) Ti-4.5Al-*x*V-*y*Fe.

Table 4.6: Beta phase fraction estimated from the SEM images.

Alloy	Beta phase fraction (%)	
	As-cast	Annealed
Ti-6Al-3V-1Fe	31	12
Ti-6Al-2V-2Fe	38	15
Ti-6Al-1V-3Fe	39	19
Ti-4.5Al-3V-1Fe	32	18
Ti-4.5l-2V-2Fe	36	22
Ti-4.5Al-1V-3Fe	43	23
Ti-6Al-4Fe	48	24

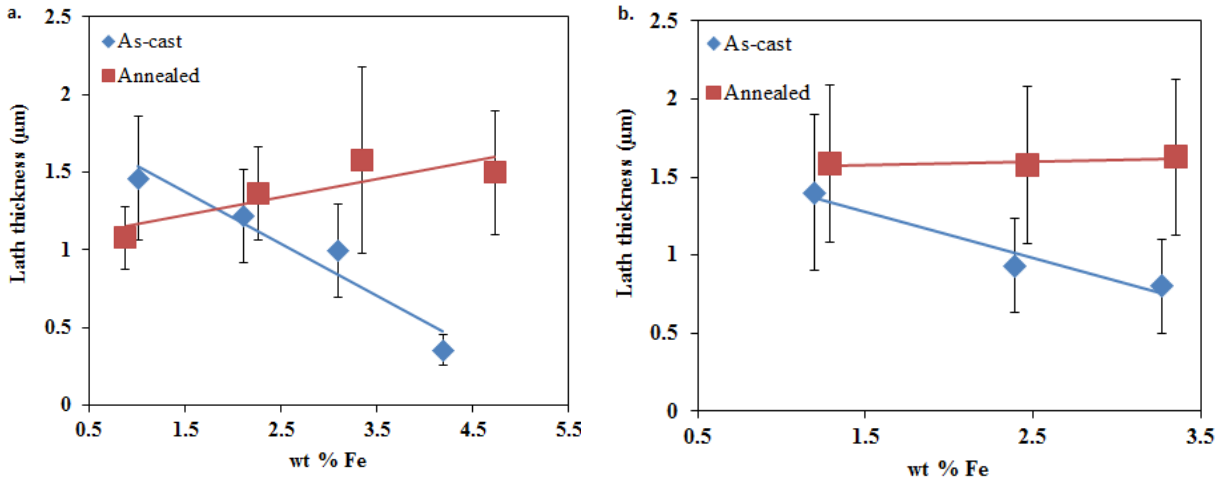

Figure 4.12: Relationship between Fe content and α lath thickness in a) Ti-6Al-*x*V-*y*Fe and b) Ti-4.5Al-*x*V-*y*Fe alloys.

4.5 Hardness

The hardness of the experimental Ti-6Al-*x*V-*y*Fe and Ti-4.5Al-*x*V-*y*Fe alloys in both as-cast and annealed conditions is shown in Figure 4.13. The hardness values of the experimental alloys were higher than those of the wrought commercial Ti-6Al-4V alloy, except for Ti-6Al-3V-1Fe (same HV) and Ti-4.5Al-3.3V-1.2Fe (lower HV). The annealed samples had higher hardness values than wrought Ti-6Al-4V and the as-cast samples. For most of the experimental alloys in both as-cast and annealed conditions, the hardness increased with increasing Fe content except in Ti-6Al-1V-3Fe where there was a slight drop in hardness. The increase in hardness with increasing Fe is not conclusive as the oxygen, nitrogen and carbon levels in the alloys were not measured. Dissolved oxygen, nitrogen and carbon in titanium alloys contribute significantly to their hardness (Gil *et al.*, 2001; Simbi and Scully, 1996; Gil and Planell, 2000).

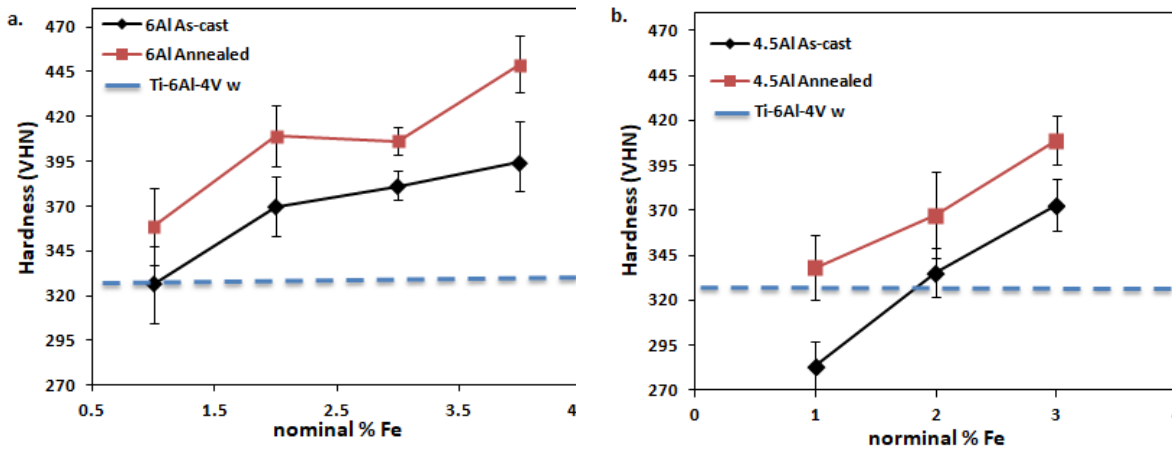

Figure 4.13: Relationship between Fe content and hardness in a) Ti-6Al-*x*V-*y*Fe and b) Ti-4.5Al-*x*V-*y*Fe alloys.

4.6 Discussion: Influence of composition and heat treatment

The influence of composition (alloying elements) and heat treatment on the microstructure and hardness of the experimental alloys is discussed.

4.6.1 Alloying elements – iron and vanadium

From the results in Sections 4.1 - 4.4, for most cases, an increase in iron content and corresponding decrease in vanadium content increased the volume fraction of the beta phase in the experimental alloys. The trend in the volume fraction of beta phase predicted by the Thermo-Calc simulation was comparable to the volume fraction obtained from image analysis of the

micrographs. The general increase in the beta phase fraction with increasing Fe was due to the strong beta stabilising effect of Fe (Chen *et al*., 2011; Pereloma *et al*., 2012). Based on the molybdenum equivalent (Equation 2.2), the beta stabilising factor of Fe is about three times stronger than molybdenum and four times stronger than vanadium (Polmear *et al*., 2017). Thermo-Calc modelling (Table 4.1) showed that increasing of the Fe content lowered the beta transus temperature.

Guo *et al*.(2005) found that for Ti systems containing more than two alloying elements, the beta transus temperature (β_T) obtained by the Thermo-Calc simulation may be underestimated. As a result, they developed an empirical model (Equation 4.1) using artificial neural network for more accurate predictions of the beta transus temperature in titanium alloys with more than two alloying elements:

$$\beta_T = 882 + 21.1 * Al - 11.8 * V - 15.4 * Fe \qquad \textbf{Equation 4.1}$$

The model was used to calculate the beta transus temperature of the experimental alloys and the results are listed in Table 4.7. An increase in Fe still decreased the beta transus temperature but the values were slightly higher than those predicted by Thermo-Calc (T-C), as shown in Figure 4.14. These results show that Fe is a strong beta stabilising element which increased the beta phase fraction in the experimental alloys.

The beta transus temperatures of Ti-6Al-4V predicted by both Thermo-Calc and Equation 4.1 were lower than the actual beta transus temperature reported in literature. The actual beta transus temperature of Ti-6Al-4V is usually between 970°C and 1015°C, depending on the composition (Lütjering *et al.*, 2000; Seshacharyulu *et al.*, 2002; Porntadawit *et al.*, 2014). The presence of other elements such as oxygen and nitrogen was initially not considered when computing the beta transus temperature of the commercial Ti-6Al-4V and experimental Ti-6Al-*x*V-*y*Fe alloys. Therefore, it is expected that the actual beta transus temperatures of the experimental alloys may be higher than the temperatures calculated in this study.

The oxygen and nitrogen contents in the experimental alloys were not measured as the facility needed for the measurement could not be accessed. However, the maximum permissible oxygen (0.2 wt% O) and nitrogen levels (0.05 wt% N) for the commercial ASTM Grade 5 (ASTM B348 - 13, 2013) Ti-6Al-4V alloy were added to the alloy compositions in Thermo-Calc to assess the effect of oxygen and nitrogen addition on the beta transus temperatures of the alloys. The results are presented in Table 4.7 and detailed in Appendix E. As expected, the beta transus temperatures increased with the addition of oxygen and nitrogen. However, the Thermo-Calc prediction that the beta transus temperature would increase with increasing iron content in the experimental alloys was anomalous.

Table 4.7: Beta transus temperatures, using Equation 4.1 and Thermo-Calc.

Alloys	Beta transus: Eqn 4.1 (°C)			Beta transus T-C (°C)	
	Nominal	As-cast	Annealed	No O & N	O, N added
Ti-6Al-4V	961	-	-	944	1032
Ti-6Al-3V-1Fe	958	952	945	937	1040
Ti-6Al-2V-2Fe	954	943	939	932	1049
Ti-6Al-1V-3Fe	951	941	928	925	1065
Ti-6Al-4Fe	947	944	935	921	1080
Ti-4.5Al-3V-1Fe	926	917	906	909	1008
Ti-4.5l-2V-2Fe	923	916	905	905	1021
Ti-4.5Al-1V-3Fe	919	907	909	899	1035

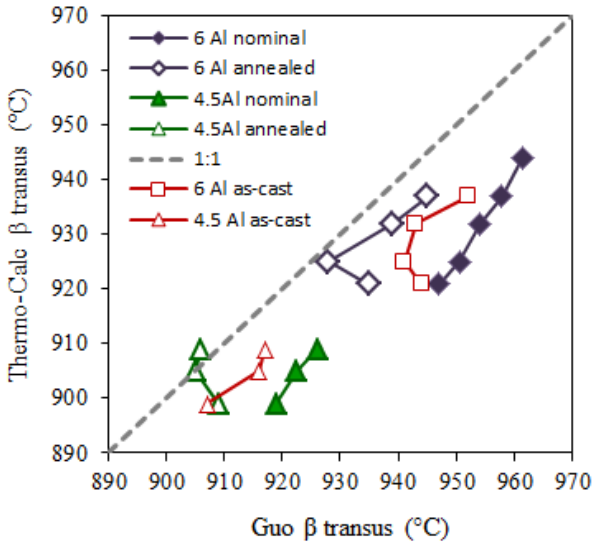

Figure 4.14: Beta transus temperatures obtained from Equation 4.1 and Thermo-Calc, without O and N.

The relationship between iron content and the prior beta grain size showed a poor linear fit except in the annealed Ti-4.5Al-*x*V-*y*Fe alloy (Figure 4.8). There were also large variations in the prior beta grain sizes as indicated by the large error bars. These observations indicated that Fe addition did not directly translate to either refining or coarsening of the prior beta grains. The effect of solute elements on the prior beta grain size of titanium alloys has been studied by Dobromyslov and Elkin (2001); Baloyi (2011); Pereloma *et al.* (2012) and Kopova *et al.* (2016), but studies on the influence of iron addition have been inconsistent. Liu *et al.* (2006) and Pereloma *et al.* (2012) found that in powder metallurgy titanium alloys, iron addition caused grain coarsening of the prior beta grains due to fast diffusion of Fe in Ti. The diffusion of iron in Ti is faster than the self-diffusion of Ti (Nakajima *et al.*, 1996a, 1996b). Since iron is more stable in the beta than the alpha phase, with a maximum solubility of 22 at.% Fe (Matyka *et al.*, 1979; Kopova *et al.*, 2016), its fast diffusion promoted grain coarsening of the beta phase. Dobromyslov and Elkin (2001) and Baloyi (2011) found that Fe refined the grains of the beta phase due to iron's smaller atomic

radius of 0.124 nm in comparison with titanium (0.145 nm). The substitution of Ti with Fe atoms would therefore cause a reduction in the beta lattice parameter and consequently refine the grains. Similar observations were reported for alloying elements such as vanadium, chromium and manganese (Baloyi, 2011; Dobromyslov and Elkin, 2001). Based on these reports, it appears that two competing phenomena - the rate of diffusion and the change in lattice parameter - control the prior beta grain size of iron-added titanium alloys.

The disparities between the conclusions drawn from other studies may be due to the difference in production routes *i.e.* casting and powder metallurgy. However, in the work of Bermingham *et al*. (2008), theoretical solute-based analysis was used to study the effect of aluminium and vanadium on the grain refinement mechanism in cast titanium alloys. The theory is described in Equation 4.2 and 4.3, where the relationship between the solute concentration and the grain restriction factor is given in Equation 4.2 and the dependence of grain size on the grain restriction factor is given in Equation 4.3. Solute atoms with a higher grain restriction factor would cause more grain refinement in titanium alloys. Bermingham *et al*. (2008) found that vanadium and aluminium had insignificant effects on the grain restriction factor in titanium alloys, while boron, oxygen and iron had significant grain restriction factors, so addition of these elements would refine the prior beta grains.

$$Q = m_1 c_o (k - 1) \qquad \textbf{Equation 4.2}$$

$$\mathrm{d} = \frac{1}{\sqrt[3]{\rho . f}} + \frac{b_1 \Delta T_n}{Q} \qquad \textbf{Equation 4.3}$$

where Q is the grain restriction factor, m_1 is the slope of the liquidus, c_o is solute concentration in binary alloys, k is the partition coefficient, d is the grain size, ρ is density of nuclei, f is the fraction of particles activated, b_1 is a constant and $\Delta T_n$is is undercooling necessary to activate nucleation.

In this study, the titanium alloys contained both vanadium and iron as beta-stabilising elements. These elements both have smaller atomic radii than titanium, so refinement of the prior beta grains was expected. Increasing iron should cause more grain refinement since it has a smaller atomic radius than vanadium (0.132 nm) and Fe has a significant effect on the grain restriction factor in titanium. To verify if vanadium and iron caused refinement of the prior beta grains, the lattice parameter of the bcc phase was calculated from the XRD results using Bragg's law (Bragg and Bragg, 1913):

$$n\lambda = 2d_{hkl} \sin\theta \qquad \textbf{Equation 4.4}$$

$$d_{hkl} = \frac{a}{\sqrt{h^2 + k^2 + l^2}} \qquad \textbf{Equation 4.5}$$

where n equals 1, 2, 3…, λ is the wavelength, d_{hkl}, is the d-spacing, a is the lattice parameter and θ is the diffraction angle.

The peak of the beta phase on the XRD spectra (Figures 4.3 – 4.4) was observed at the position where the intensity was 100%, which corresponded to the (101) plane. The calculated lattice parameters of the bcc phase in the alloys are listed in Table 4.8. The lattice parameters for most of the alloys were marginally larger than the standard lattice parameter for beta-Ti (a = 3.3065 Å). This suggests that iron and vanadium additions did not refine the prior beta grains. Kopova *et al.* (2016) found that Fe additions did not cause a noticeable difference in the grain size of a Ti-Nb-Zr-Ta-Sr-Fe biomedical beta alloy. The marginal increase in the lattice parameter of most of the alloys in the current study indicated that a possible increase in the prior beta grain size may have occurred due to the fast diffusion of iron in titanium.

However, it is thought that the presence of vanadium in the alloys impedes the excessive coarsening of the beta grains since the diffusion of vanadium in titanium is slower than iron (Pereloma *et al*., 2012).

The increasing hardness with increasing Fe content observed in the experimental alloys (Figure 4.13) could be attributed to the increase in the amount of beta phase in the alloys. An increase in beta phase decreased the lath thickness of the alpha phase as seen in Figure 4.12. Filip *et al*. (2003) and Carman *et al*. (2011) found that α lath refinement occurred with increasing beta phase fraction. The movement of dislocations through thin laths is much more difficult than in coarse laths (Gil *et al.*, 2001). The branching of dislocations in thin laths demands more energy for dislocations to move, thereby increasing the strength and hardness of the alloys. In addition, iron has been reported to induce solid solution strengthening effects in titanium alloys due to the large difference in the atomic radii of iron and titanium (Leyens and Peters, 2003; Lütjering and Williams, 2007; Polmear *et al.*, 2017). This solid solution strengthening effect of Fe could have also contributed to the increased hardness of the experimental alloys with increasing Fe content. Baloyi (2011) reported that the hardness of binary Ti-Fe and Ti-Mn alloys increased with increase in iron and manganese additions respectively.

Table 4.8: Lattice parameters of bcc beta phase in the experimental alloys.

Alloys	Lattice parameter a (Å)	
	As-cast	Annealed
Ti-6Al-4V wrought	3.283 Å	
Ti-6Al-3V-1Fe	3.326	3.294
Ti-6Al-2V-2Fe	3.306	3.306
Ti-6Al-1V-3Fe	3.308	3.315
Ti-4.5Al-3V-1Fe	3.318	3.299
Ti-4.5Al-2V-2Fe	3.320	3.318
Ti-4.5Al-1V-3Fe	3.325	3.318
Ti-6Al-4Fe	3.315	3.301

4.6.2 Alloying element - aluminium

Aluminium stabilises the alpha phase and raises the beta transus temperature (Polmear *et al*., 2017). A reduction in aluminium should reduce the beta transus temperature and consequently increase the proportion of the beta phase. This is confirmed by the Thermo-Calc modelling results (Table 4.1) as well as the empirical model developed by Guo *et al*. (2005), in Table 4.7.

However, experimental results (Figure 4.15) did not show a significant difference between the beta volume fractions in the as-cast alloys containing 6 wt% Al and 4.5 wt% Al. After annealing (Figure 4.16), the alloys with lower Al content showed an increase in the beta phase fraction due to alloying element partitioning. This will be discussed further in Section 4.6.3. Some of the error bars in Figures 4.15 and 4.16 are not visible, as the errors are small and are covered by the symbol.

As mentioned in Section 4.6.1, the influence of aluminium on the prior beta grain size was investigated by Bermingham *et al*. (2008). The authors explained that despite the marginal decrease in the beta grain size with increasing aluminium additions, an undetected element present in the as-cast alloys caused the decrease in grain size. They made their conclusion from theoretical solute-based analysis which revealed that the grain refining power of aluminium in titanium is negligible when compared with other elements such as boron and oxygen. It was emphasised that the grain refinement of prior beta grains in Ti-6Al-4V alloyed with boron was based on the assumption that aluminium and vanadium have no significant grain refinement power on titanium alloys. Otherwise, the Ti-6Al-4V alloy which contains a total of 10 wt% solute elements would not have been refined with boron if aluminium and vanadium had significant grain refinement power on titanium.

Figure 4.17 shows the influence of aluminium content on the prior beta grain size of the as-cast experimental alloys. The large error bars made it difficult to establish any accurate relationship between aluminium content and prior beta grain size. However, by considering the general trend, the average grain size of the alloys containing 6 wt% aluminium was slightly larger than alloys containing 4.5 wt% Al. If aluminium had refined the prior beta grains, it was expected that alloys containing more aluminium should have had smaller beta grains, but the opposite was observed. This supports the conclusion that the grain refining power of aluminium on the prior beta grains of these titanium alloys was insignificant.

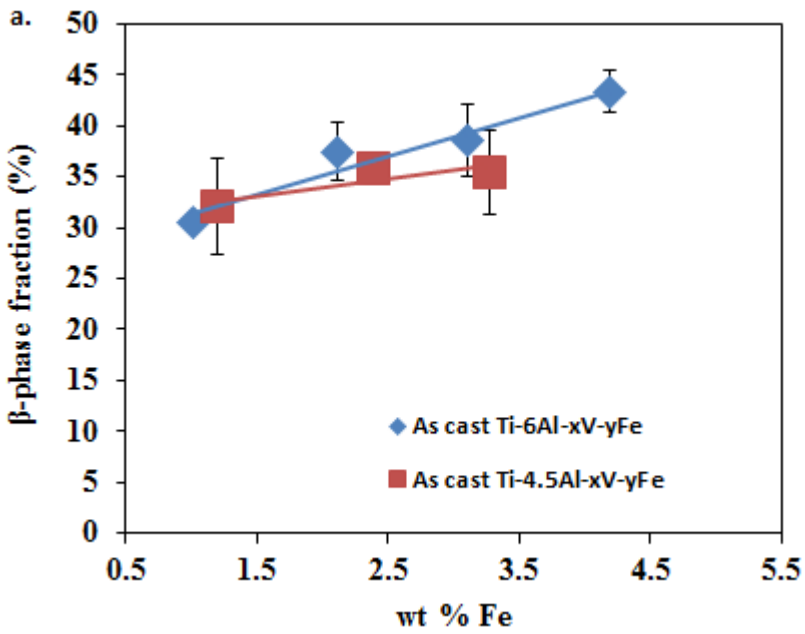

Figure 4.15: As-cast experimental alloys - influence of Al content on the beta phase fraction.

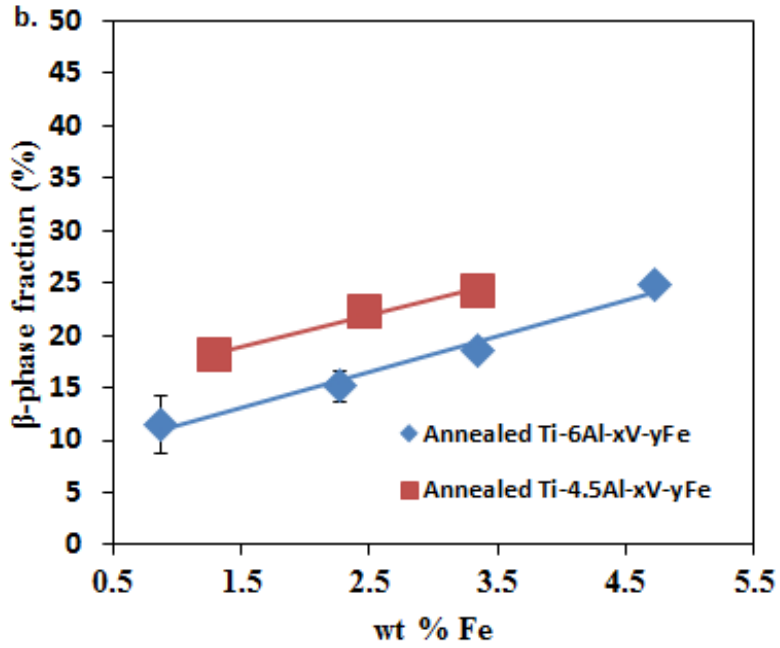

Figure 4.16: Annealed experimental alloys - influence of Al content on the beta phase fraction.

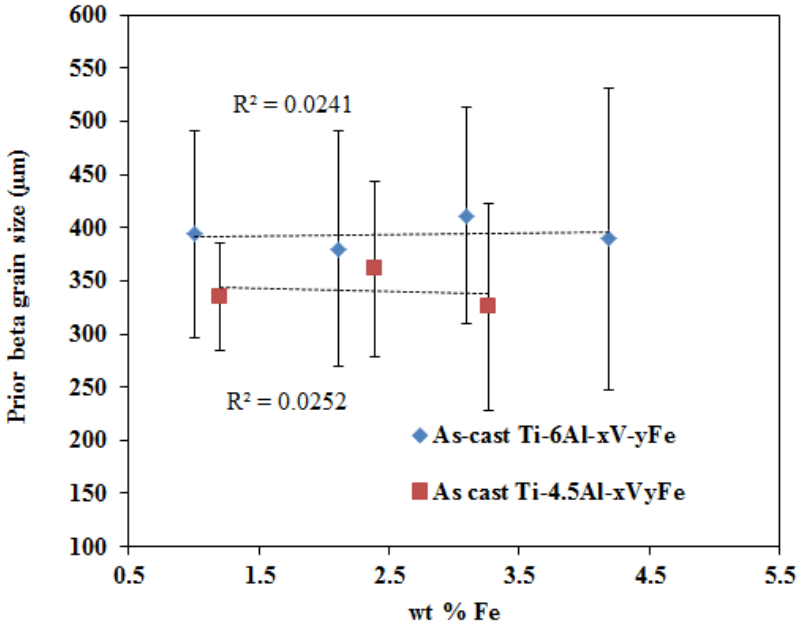

Figure 4.17: Influence of Al content on prior beta grain size of as-cast experimental alloys.

The amount of aluminium influenced the hardness of the experimental alloys. As shown in Figure 4.18, an increase in aluminium content from 4.5 to 6.0 wt% Al increased the hardness of the experimental alloys. This was expected, as it has been reported that the hardness of α+β titanium alloys is the sum of the hardness of the individual phases (Liu and Welsch, 1988). The increase in hardness with higher aluminium content can be attributed to the solid solution strengthening effect of aluminium which is predominant in the alpha phase of the alloys (Leyens and Peters, 2003). This effect is caused by the large difference in the atomic radii of titanium and aluminium (Leyens and Peters, 2003).

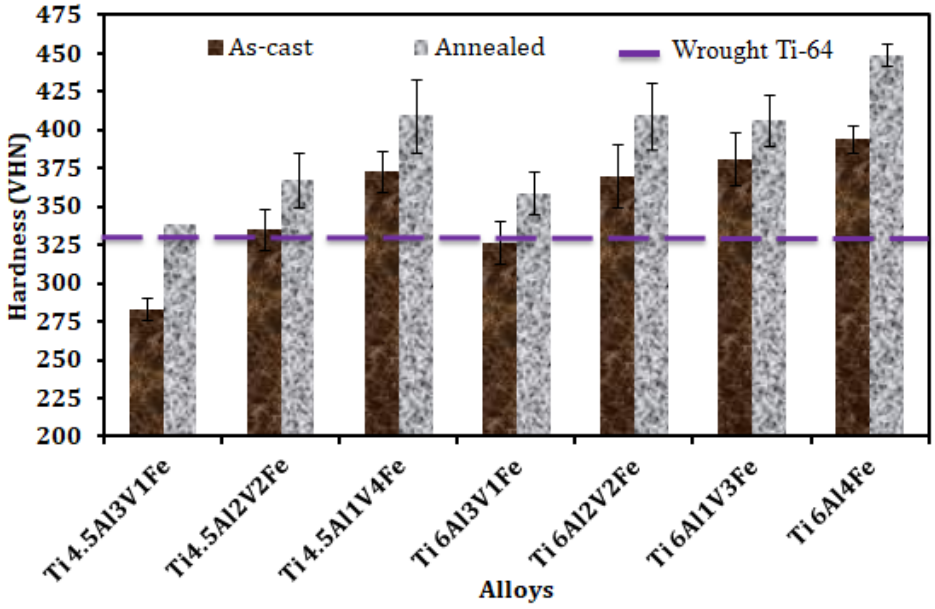

Figure 4.18: Comparison between the hardness of Ti-6Al-*x*V-*y*Fe and Ti-4.5Al-*x*V-*y*Fe alloys.

4.6.3 Annealing

Annealing the experimental alloys decreased the beta phase fraction, but increased the α lath thickness and the hardness of the alloys due to alloying element partitioning (Liu and Welsch, 1988) and possible oxygen and nitrogen uptake. The experimental alloys were cast on a water-cooled copper hearth which led to rapid solidification and a short cooling time. The fast cooling rate would not give enough time for transformation of bcc-β to hcp-α phase. Hence, more beta phase was retained at room temperature, since the weight fraction of the beta stabilisers in the alloys was high enough to retain the phase. This is clear in the SEM images of the as-cast samples (Figure 4.9), where more bcc-β (light) phase was seen than in the annealed alloys (Figure 4.10).

Annealing increased the diffusion time, promoting the diffusion-controlled bcc-β to hcp-α transformation. This decreased the amount of bcc-β retained in the alloys at room temperature, and also promoted the growth of the α-laths. Annealing and a slow cooling rate increase the phase fraction and thickness of α-laths in α+β titanium alloys (Ahmed and Rack, 1998; Gil *et al.*, 2001; Jovanović *et al.*, 2006). The aluminium atoms trapped in the beta phase during casting would diffuse to the alpha phase during annealing, while iron and vanadium would be rejected from the alpha phase to preferentially stabilise the beta phase (Lütjering and Williams, 2007).

Figure 4.15 shows that, in the as-cast condition, no significant difference was observed in the beta phase fraction between the experimental alloys containing 4.5 wt% and 6 wt% aluminium. This is probably due to the rapid solidification and high cooling rate on the water-cooled copper hearth, which trapped atoms of Al, V and Fe in the phases where they have low solubility.

In the annealed experimental alloys containing 4.5 wt% Al, the rejection of Al, V and Fe from the phase where they have low solubility and the diffusion to the phase where they have higher solubility, led to a higher beta phase fraction compared to experimental alloys containing 6 wt% Al (Figure 4.16). This was expected, as aluminium is an alpha phase stabiliser. The higher beta phase fraction in the 4.5 wt% Al experimental alloys concurs with the trend in beta transus temperature (Table 4.7). The alloys containing 4.5 wt% Al had lower beta transus temperatures, which indicates that the alloys were expected to have higher beta phase fractions than those with 6 wt% Al.

The reason for the increase in hardness of the experimental alloys due to annealing is not clear, as an increase in thickness of the alpha laths and a decrease in hardness were expected. However, the hardness increase could have been due to an increase in volume fraction of the alpha phase in the annealed samples. The alpha phase is known to be harder than the beta phase in titanium alloys except under aging conditions (Liu and Welsch, 1988; Lin, 2015). Additionally, the

hardness increase after annealing could have been due to an increase in dissolved oxygen during annealing, which is discussed in Section 4.6.4.

4.6.4 Oxygen as an impurity element

Oxygen is a very important alloying element in titanium, as it stabilises the alpha phase and increases the strength and hardness of titanium alloys (Liu and Welsch, 1988; Leyens and Peters, 2003; Lütjering and Williams, 2007). The amount of oxygen in titanium alloys must be controlled because of its detrimental effect on ductility (Liu and Welsch, 1988; Leyens and Peters, 2003; Lütjering and Williams, 2007).

In this study, the experimental alloys were produced and heat treated under an inert (argon) atmosphere to prevent oxygen contamination. However, XRD patterns (Figure 4.1 - 4.4) showed oxide peaks (TiO_2 and FeO_3Ti) in both as-cast and annealed experimental alloys. Oxygen contamination could have been introduced as surface oxide layers on the starting Ti, Fe, V and Al powders or during casting and heat treatment. The influence of oxygen on the microstructural features could not be evaluated from the optical and SEM images, but the XRD spectra show that the oxide peak intensity increased with increasing amount of iron in both the as-cast and annealed Ti-6Al-*x*V-*y*Fe alloys. The oxide XRD peaks were more distinct in the Ti-6Al-*x*V-*y*Fe alloys (Figures 4.1 - 4.2) than in the Ti-4.5Al-*x*V-*y*Fe samples (Figures 4.3 - 4.4).

It is likely that the presence of oxygen in the alloys contributed to the hardness, as the hardness increase correlated with an increase in relative intensity of the oxide peaks. The hardness of the annealed Ti-6Al-*x*V-*y*Fe alloys increased despite these samples containing coarse laths. The as-cast Ti-6Al-3V-1Fe, with no observable oxide peak, had the lowest hardness while the other alloys containing 2 and 4wt % Fe had higher hardness values.

Dissolved oxygen in the annealed samples seems to have contributed substantially to the increased hardness. The oxide peaks in the diffraction patterns (Figure 4.2 and 4.4) confirmed that oxygen contamination had occurred. Kahveci and Welsch (1986) and Liu and Welsch (1988) investigated the influence of oxygen on the hardenability of titanium alloys. They concluded that oxygen caused hardening effects in both alpha and beta titanium alloys. Liu and Welsh (1988) found that the hardening effect of oxygen in alpha and beta phases was the same, and that the hardness increase of the alpha and beta phases was additive in α+β titanium alloys.

4.7 Summary of results

The influence of alloy composition by partial substitution of vanadium with iron, and reduction of the aluminium content and annealing on the microstructure and hardness of experimental Ti-6Al-*x*V-*y*Fe and Ti-4.5Al-*x*V-*y*Fe alloys was investigated.

The as-cast and annealed experimental alloys contained mostly α and β phases, with minor amounts of TiO_2, FeO_3Ti and V_2O_5 oxides at room temperature. The β-phase fraction increased with increasing iron concentration in the as-cast alloys, but decreased after annealing.

In the as-cast condition, changing the aluminium content from 6 to 4.5 % Al had an insignificant effect on the beta phase fraction. After annealing, decreasing the aluminium concentration increased the beta phase fraction, since there was less Al to stabilise the alpha phase.

It is likely that annealing caused partitioning of alloying elements by allowing enough time for diffusion-controlled bcc-β to hcp-α transformation to take place. The volume fraction of the alpha phase in the annealed samples was higher than in the as-cast samples.

The as-cast and annealed microstructures contained Widmanstätten α-laths within the prior β-grains. There was no obvious relationship between the concentration of iron and the prior β grain size due to the large error bars. There was also no evidence of grain refinement with increase in aluminium, iron or vanadium.

Hardness increased with increasing iron content in all 6 wt% Al and 4.5 wt% Al samples. The sample with the highest hardness was Ti-6Al-4Fe. Decreasing the aluminium content from 6 wt% to 4.5 wt% decreased the hardness. The relationship between iron content and lath thickness was difficult to deduce because of the large error bars. However, the general trend indicated the possibility of lath refinement with increasing iron content in the experimental alloys. Lath refinement, and solid solution strengthening by iron, aluminium and dissolved oxygen may have increased the hardness of the alloys in both as-cast and annealed conditions.

Chapter 5: Corrosion behaviour of Ti-Al-V-Fe experimental alloys

This chapter addresses the third research objective. The results obtained from open circuit potential (OCP) and linear polarisation scans of the Ti-6Al-*x*V-*y*Fe and Ti-4.5Al-*x*V-*y*Fe experimental alloys in three solutions: 3.5M H_2SO_4, 3.5 wt% NaCl and a mixed solution of 3.5M H_2SO_4+1.75wt% NaCl are presented in Sections 5.1 to 5.3. The behaviour of the alloys was compared with commercial grade Ti-6Al-4V alloy supplied in wrought form. A detailed discussion of the results is presented in Section 5.4 and the influence of alloying elements on the corrosion behaviour of the alloys is discussed and summarised.

5.1 H_2SO_4 Environment

The open circuit potentials of Ti-6Al-4V and the annealed experimental Ti-6Al-*x*V-*y*Fe and Ti-4.5Al-*x*V-*y*Fe alloys traced for 3600 s in 3.5 M sulphuric acid solution at ambient temperature are presented in Figure 5.1. The OCP of Ti-6Al-4V increased towards anodic values throughout the exposure time, while the Ti-6Al-*x*V-*y*Fe and Ti-4.5Al-*x*V-*y*Fe experimental alloys decreased towards the cathodic region. In the Ti-6Al-*x*V-*y*Fe series (Figure 5.1a), the OCP of Ti-6Al-3V-1Fe was the highest of the experimental alloys, and decreased gradually toward the cathodic region for the entire period of immersion. The OCP values of Ti-6Al-2V-2Fe, Ti-6Al-1V-3Fe and Ti-6Al-4Fe (with > 1wt% Fe) decreased rapidly to -600 mV in less than 200 s of immersion and remained stable for the rest of the exposure time.

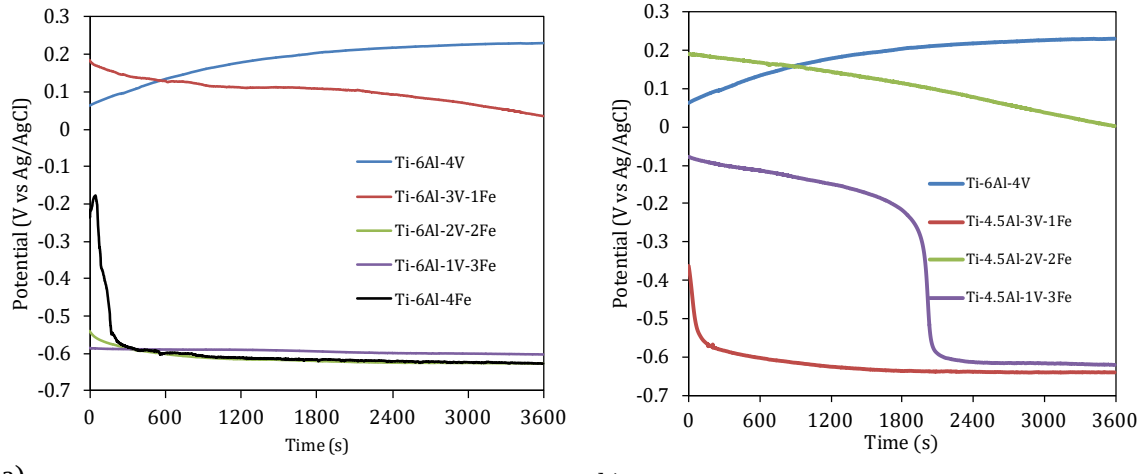

a) b)

Figure 5.1: Variation of open circuit potential measurement in 3.5 M H_2SO_4 with time for a) Ti-6Al-*x*V-*y*Fe and b) Ti-4.5Al-*x*V-*y*Fe alloys.

In the Ti-4.5Al-*x*V-*y*Fe series alloys (Figure 5.1b), the Ti-4.5Al-2V-2Fe alloy had the highest OCP value throughout the immersion period and showed a gradual decrease in OCP. The Ti-4.5Al-1V-3Fe and Ti-4.5Al-3V-1Fe alloys showed a sharp decrease in OCP to about -600 mV after 200 s and 2100 s respectively.

The SEM images obtained from the immersed alloys at OCP are presented in Figure 5.2. The SEM images taken at lower magnification are presented in Appendix I. These images were obtained prior to the cleaning of the samples. The representative EDX spectra obtained from the area analyses of the immersed samples before cleaning are presented in Figure 5.3. The presence of oxygen in the EDX spectra of various samples confirmed the formation of an oxide film on the surface of the immersed alloys. However, the oxygen peak was masked by the presence of other elements and it was difficult to adequately quantify the oxygen presence. It can be seen in Figure 5.2 that the inherent oxide films formed on the surface of the iron-added experimental alloys with both 6 wt% Al and 4.5wt% Al were not as protective as that on the Ti-6Al-4V. The severity of corrosion attack, as indicated by the amount of corrosion product formed on the alloys, increased with increasing Fe content in both Ti-6Al-*x*V-*y*Fe and Ti-4.5Al-*x*V-*y*Fe. This is most apparent in the Ti-6Al-4Fe alloy where Fe was the only beta stabilising element. More corrosion product was seen on the surface of Ti-6Al-4Fe than on the other experimental alloys.

Figure 5.4 shows the SEM images of selected samples of the experimental alloys that were cleaned in distilled water and dried in air after the OCP scan in 3.5 M H_2SO_4. It can be seen that the Ti-6Al-4Fe (Figure 5.4c) and Ti-4.5Al-1V-3Fe (Figure 5.4e) alloys with a higher amount of Fe suffered severe corrosion attack. However, there was no severe attack on Ti-6Al-3V-1Fe and Ti-4.5Al-2V-2Fe samples. Figures 5.6 and 5.7 show that selective corrosion attack on the Ti-6Al-4Fe occurred in the beta phase where the solubility of Fe is high. Also, there are visible pits on the Ti-4.5Al-1V-3Fe alloy due to corrosion attack. This observation is corroborated by the EDX spectra obtained for the selected experimental alloys (Figure 5.5). The EDX spectra of Ti-6Al-4Fe and Ti-4.5Al-1V-3Fe (Figures 5.5b and d) show the presence of oxygen peaks together with what appears to be grain boundary cracks. This suggests that the rather thick oxides or corrosion products were not easily removed after cleaning the samples as a result of the severe attack. The Ti-6Al-3V-1Fe and Ti-4.5Al-2V-2Fe samples with less corrosion attack did not show any oxygen peaks, indicating easy removal of corrosion products.

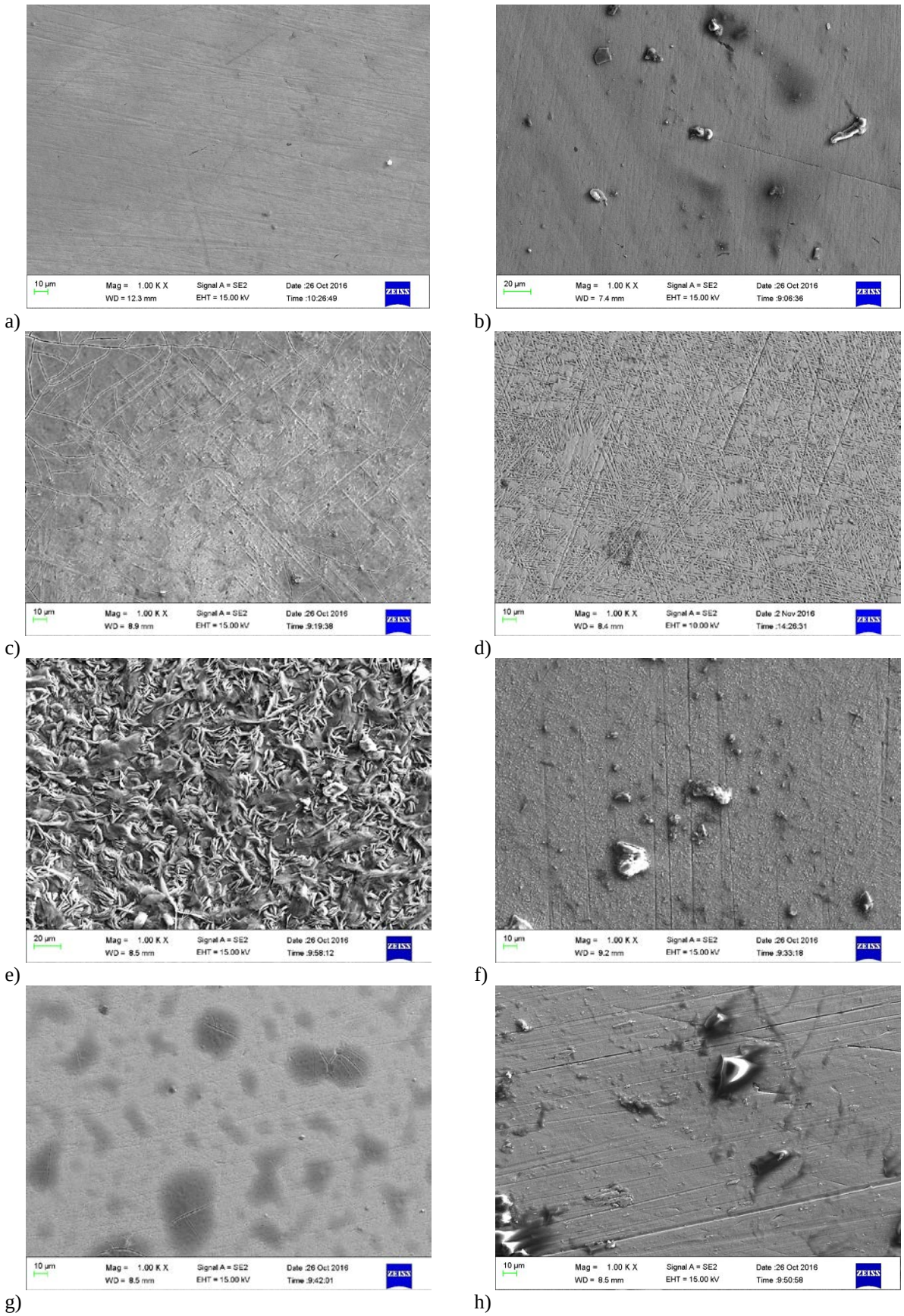

Figure 5.2: SEM-SE images showing the surface of samples after immersion in 3.5 M H_2SO_4 at OCP for 3600 s, before cleaning: a) Ti-6Al-4V, b)Ti-6Al-3V-1Fe, c)Ti-6Al-2V-2Fe, d) Ti-6Al-1V-3Fe, e) Ti-6Al-4Fe,f) Ti-4.5Al-3V-1Fe, g) Ti-4.5Al-2V-2Fe and h) Ti-4.5Al-1V-3Fe.

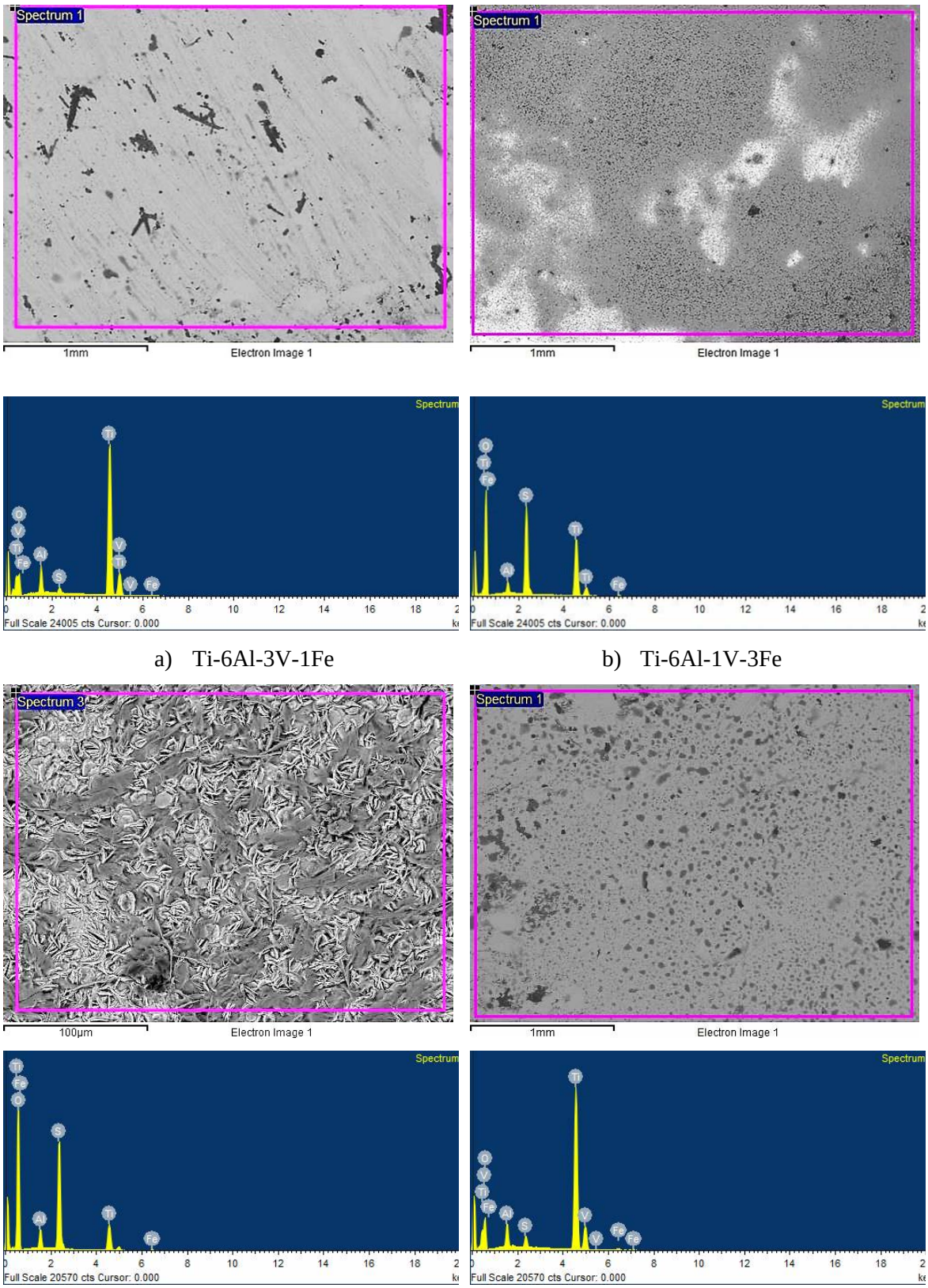

a) Ti-6Al-3V-1Fe

b) Ti-6Al-1V-3Fe

c) Ti-6Al-4Fe

d) Ti-4.5Al-2V-2Fe

Figure 5.3: EDX spectra of selected experimental alloys after immersion in 3.5 M H_2SO_4 at OCP for 3600 s, before cleaning: a) Ti-6Al-3V-1Fe, b) Ti-6Al-1V-3Fe, c) Ti-6Al-4Fe and d) Ti-4.5Al-2V-2Fe.

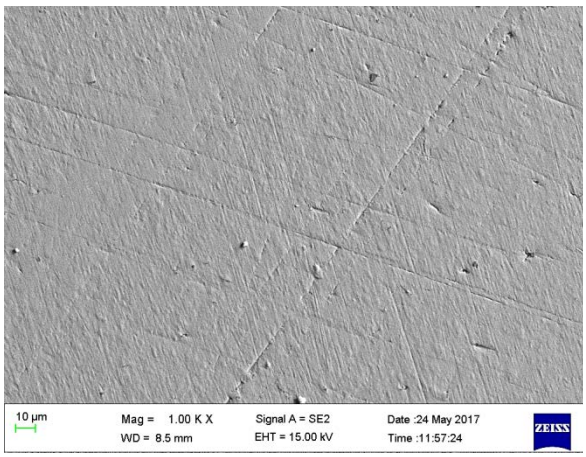

a)

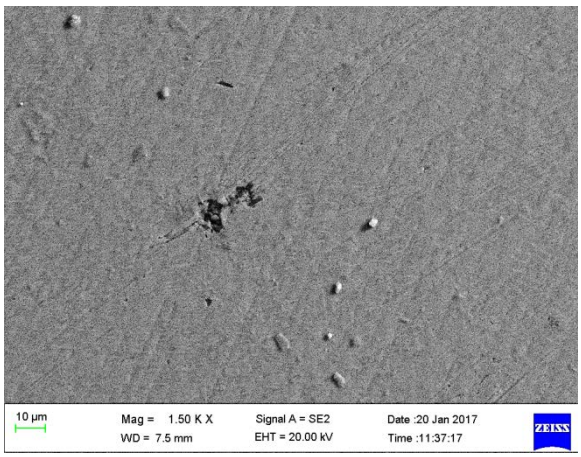

b)

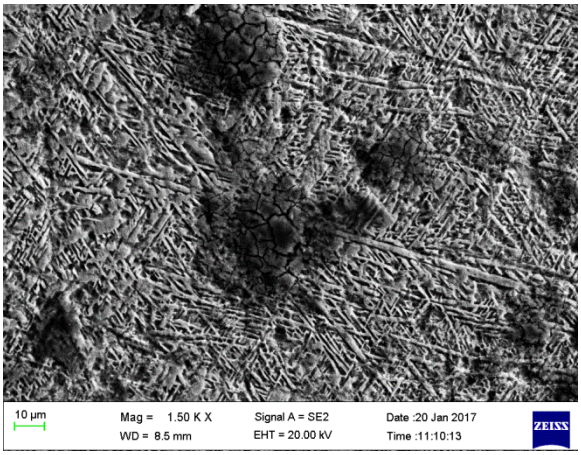

c)

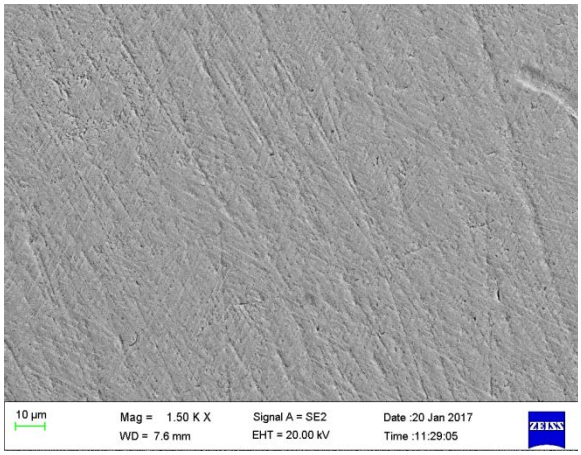

d)

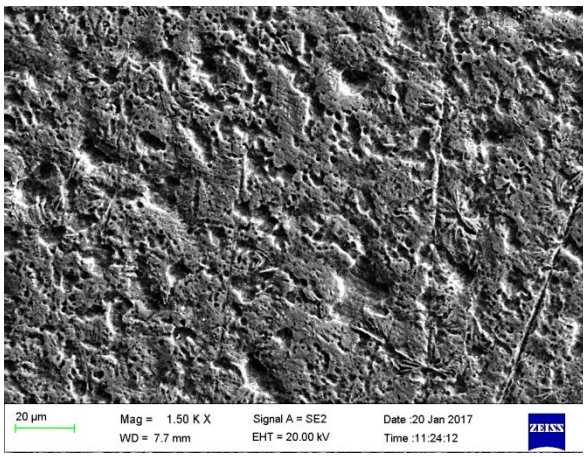

e)

Figure 5.4: SEM-SE images showing the surface of selected samples after immersion in 3.5 M H_2SO_4 at OCP for 3600s, after cleaning: a) Ti-6Al-4V, b) Ti-6Al-3V-1Fe, c) Ti-6Al-4Fe, d) Ti-4.5Al-2V-2Fe and e) Ti-4.5Al-1V-3Fe.

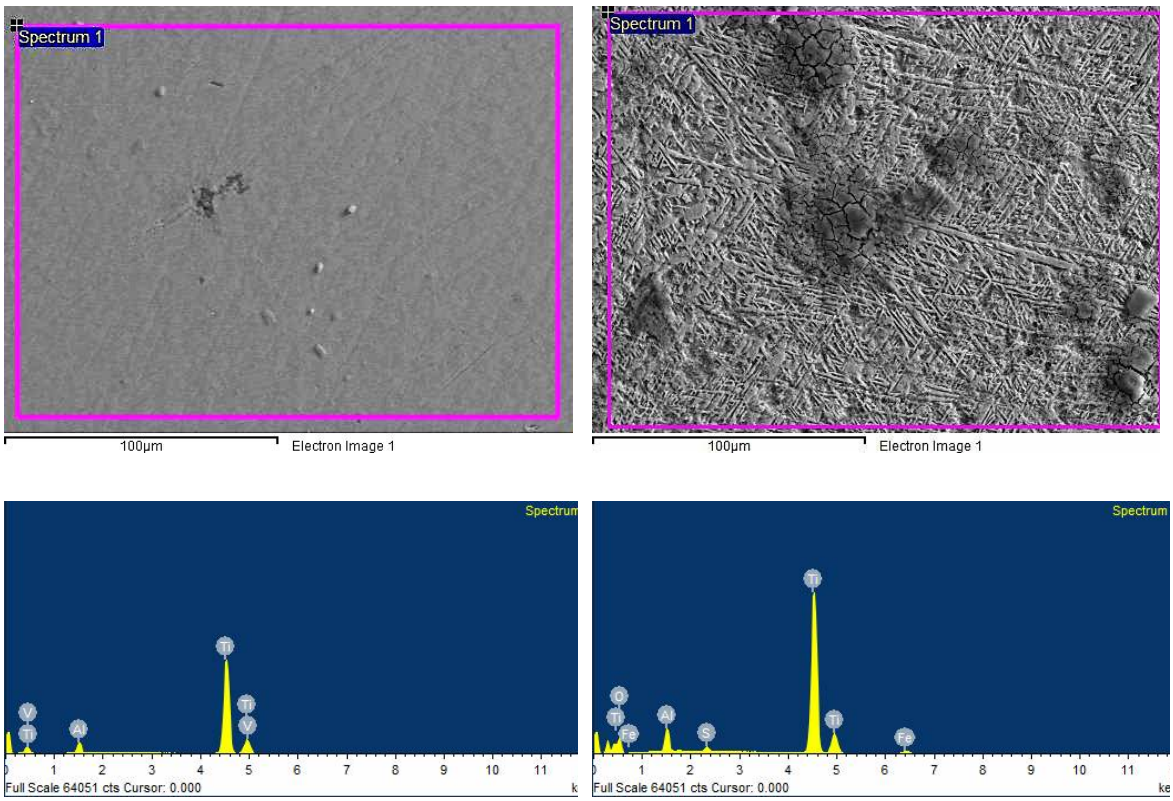

a) Ti-6Al-3V-1Fe b) Ti-6Al-4Fe

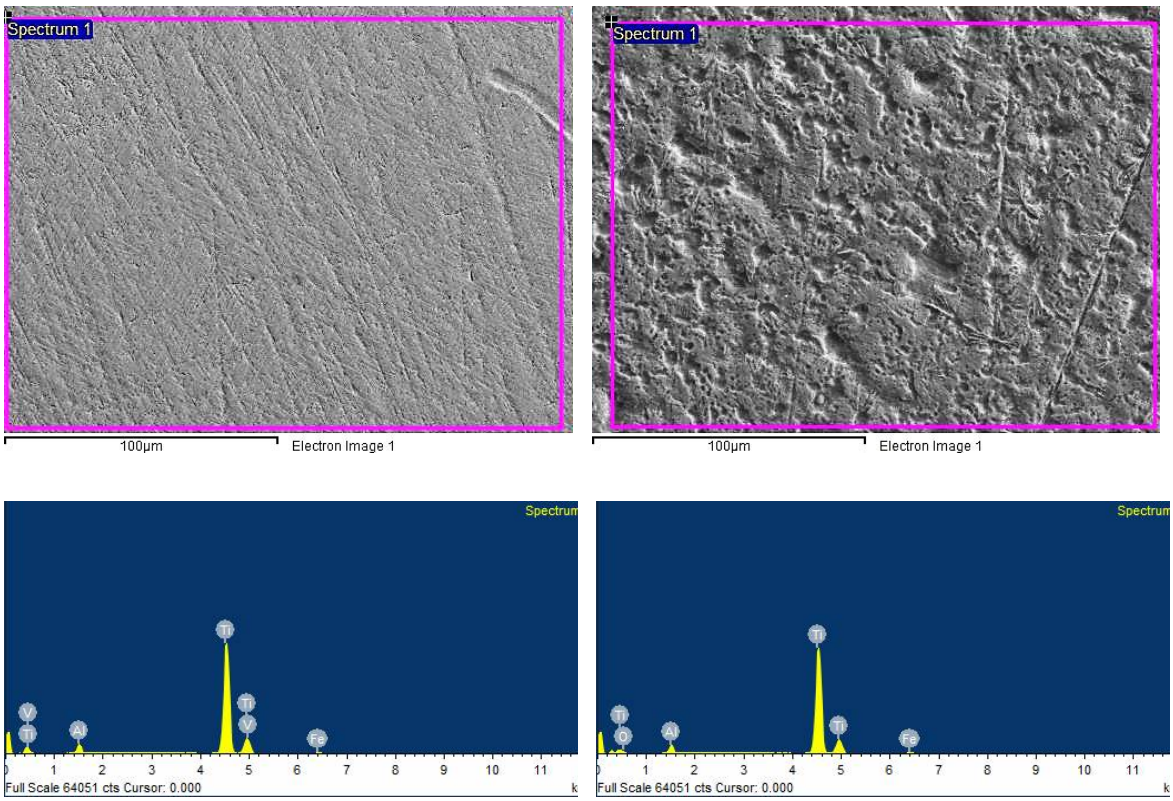

c) Ti-4.5Al-2V-2Fe d) Ti-4.5Al-1V-3Fe

Figure 5.5: EDX spectra of selected experimental alloys after immersion in 3.5 M H_2SO_4 at OCP for 3600 s: a) Ti-6Al-3V-1Fe, b) Ti-6Al-4Fe, c) Ti-4.5Al-2V-2Fe and d) Ti-4.5Al-1V-3Fe (after cleaning).

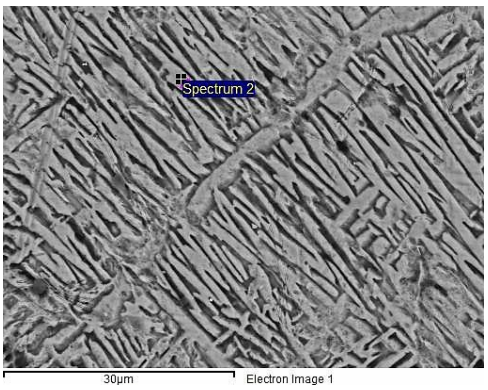

Element	Weight%	Atomic%
Al K	5.8	9.9
Ti K	94.2	90.1
Totals	100.00	

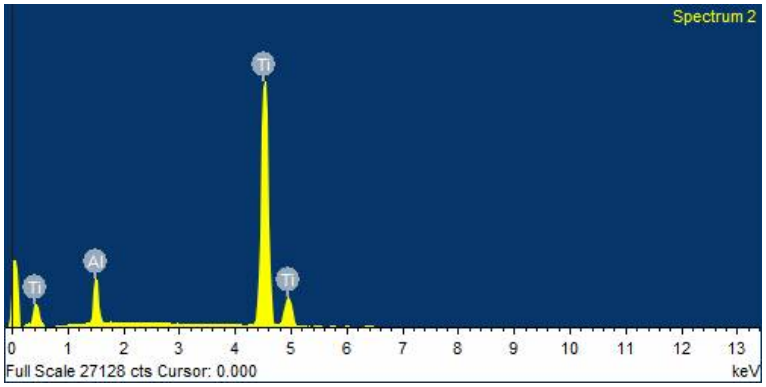

Figure 5.6: EDX spot analysis on the uncorroded α-Ti phase (*i.e.* with no Fe) in Ti-6Al-4Fe experimental alloy.

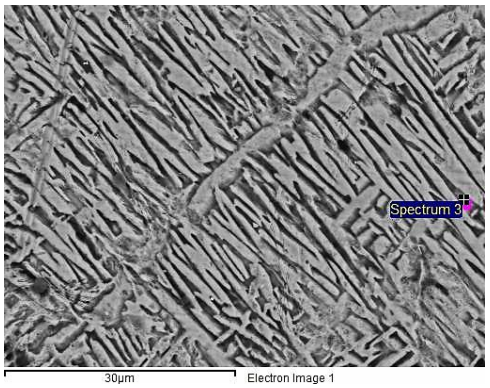

Element	Weight%	Atomic%
O K	12.4	29.2
Al K	3.9	5.5
S K	0.6	0.7
Ti K	79.2	62.1
Fe K	3.9	2.6
Totals	100.00	

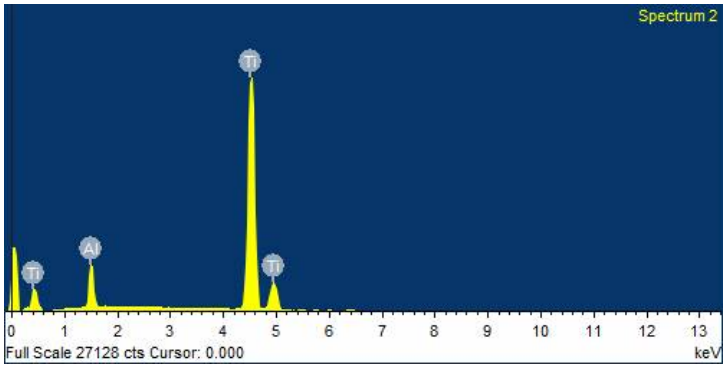

Figure 5.7: EDX spot analysis on the corroded β-Ti phase (*i.e.* with Fe) in Ti-6Al-4Fe experimental alloy.

Figure 5.8 shows the linear potentiodynamic polarisation curves of the Ti-6Al-4V and the experimental 6 wt% Al alloys obtained after OCP scanning in 3.5 M H_2SO_4 for 1200 s. The response of the alloys during polarisation showed that the corrosion behaviour of the alloy was sensitive to the presence of the beta stabilising elements in the alloys. The corrosion behaviour of the two alloys which both contain one beta stabilising element, *i.e.* commercial Ti-6Al-4V and experimental Ti-6Al-4Fe, were comparable, while the experimental alloys containing V + Fe as beta stabilisers followed a different trend. All the alloys displayed active-to-passive transition behaviour and Ti-6Al-1V-3Fe had the lowest critical current density. The i_{corr} values of the experimental alloys containing both Fe and V as beta stabilising elements were much lower than the alloys with either Fe or V. The lowest i_{corr} was observed in Ti-6Al-1V-3Fe.

The passivation current density (i_p) and breakdown potential (E_b) of the experimental alloys containing both Fe and V were ~10^{-5} Acm^{-2} and 1.8 V, respectively. Conversely, Ti-6Al-4V and Ti-6Al-4Fe with one beta stabilising element did not show a breakdown potential at 1.8 V. This suggests that these two alloys would grow a more stable passive film in the anodic region than the other experimental alloys. Unlike Ti-6Al-4V, the anodic passive film of Ti-6Al-4Fe showed transient currents immediately after the active nose, indicating the breaking and rebuilding of the passive film. Also, the passivation current of Ti-6Al-4Fe was lower than Ti-6Al-4V at potentials above 0.4 V.

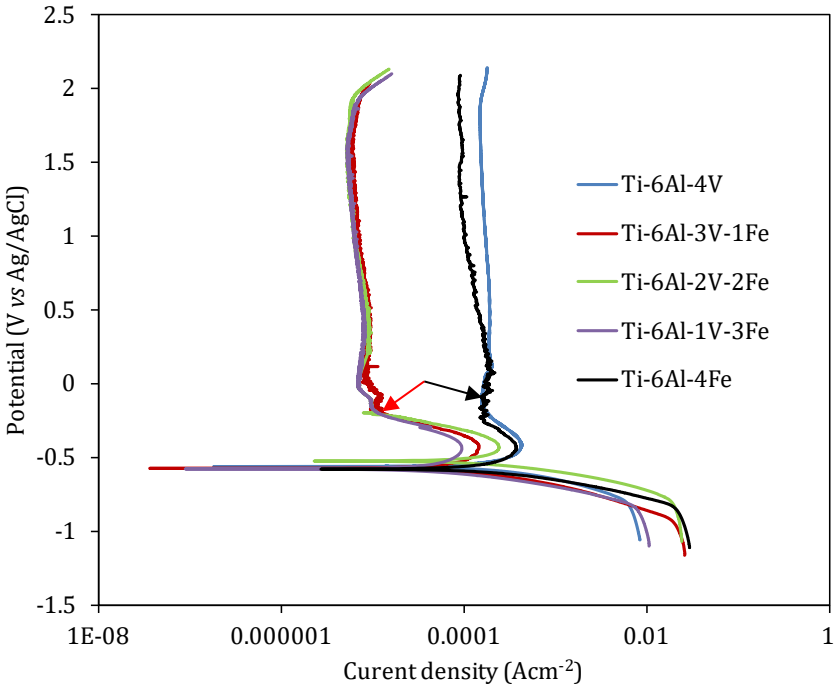

Figure 5.8: Potentiodynamic polarisation for 6 wt% Al alloys immersed in 3.5 M H_2SO_4 solution at 25°C.The arrows point to transient currents.

Table 5.1 presents the corrosion parameters determined from the potentiodynamic curves. The corrosion potentials (E_{corr}) of all the alloys were in a narrow range of -0.581 V to -0.527 V, but the corrosion current densities (i_{corr}), polarisation resistance (Rp) and corrosion rates showed substantial differences.

Ti-6Al-4V exhibited the highest corrosion current density and corrosion rate, slightly higher than the experimental alloys Ti-6Al-2V-2Fe and Ti-6Al-4Fe, while the alloys Ti-6Al-3V-1Fe and Ti-6Al-1V-3Fe had the lowest corrosion rate.

The corrosion rate of 1.59 mm/y obtained for the wrought Ti-6Al-4V sample was lower than the corrosion rate of 140 mpy (≈3.6 mm/y) reported by Magoda *et al*. (2004) in 3.5 M H_2SO_4. The difference in corrosion rates may be due to the different alloy compositions and to differing microstructures *(*Mogoda *et al.*, 2004).

Table 5.1: Electrochemical parameters obtained for 6Al alloys immersed in 3.5 M H_2SO_4 solution at 25°C.

Alloys	Equivalent Weight	E_{corr} (V *vs.* Ag/AgCl)	OCP_{1200s} (V *vs.* Ag/AgCl)	i_{corr} (µA/cm^2)	Rp	Corr. rate (mm/y)
Ti-6Al-4V	11.82	-0.562	-0.578	182	142	1.59
Ti-6Al-3V-1Fe	11.81	-0.570	-0.658	76	338	0.67
Ti-6Al-2V-2Fe	11.83	-0.528	-0.603	168	154	1.47
Ti-6Al-1V-3Fe	11.83	-0.581	-0.571	72	195	0.63
Ti-6Al-4Fe	11.80	-0.579	-0.546	167	155	1.46

The polarisation curves of the 4.5 wt% Al alloy series immersed in 3.5 M H_2SO_4 is shown in Figure 5.9. The corrosion behaviour of the alloys followed a similar trend to the 6 wt% Al alloys, also showing sensitivity to the number of beta stabilising elements. Alloys containing both Fe and V displayed lower passivation currents and critical current densities than Ti-6Al-4V. Ti-4.5Al-2V-2Fe and Ti-4.5Al-1V-3Fe had similar E_{corr} values to Ti-6Al-4V and displayed active to passive transitions similar to the commercial alloy. However, in Ti-4.5Al-3V-1Fe, transient currents can be seen at anodic potentials (-0.35 to -0.1 V) just above the corrosion potential of the alloy. Ti-4.5Al-3V-1Fe showed a higher E_{corr} and lower i_{corr} than Ti-6Al-4V and the other experimental alloys. The electrochemical parameters obtained from the polarisation curves for the 4.5 wt% Al alloy series are listed in Table 5.2. The corrosion current densities and the corrosion rates of the experimental alloys were all lower than for Ti-6Al-4V. The E_{corr} of Ti-4.5Al-3V-1Fe (-0.348 V) was much higher than that of Ti-6Al-4V, the 6 wt% Al alloys and the other 4.5 wt% Al experimental alloys, and had the lowest corrosion rate of 0.08 mm/y.

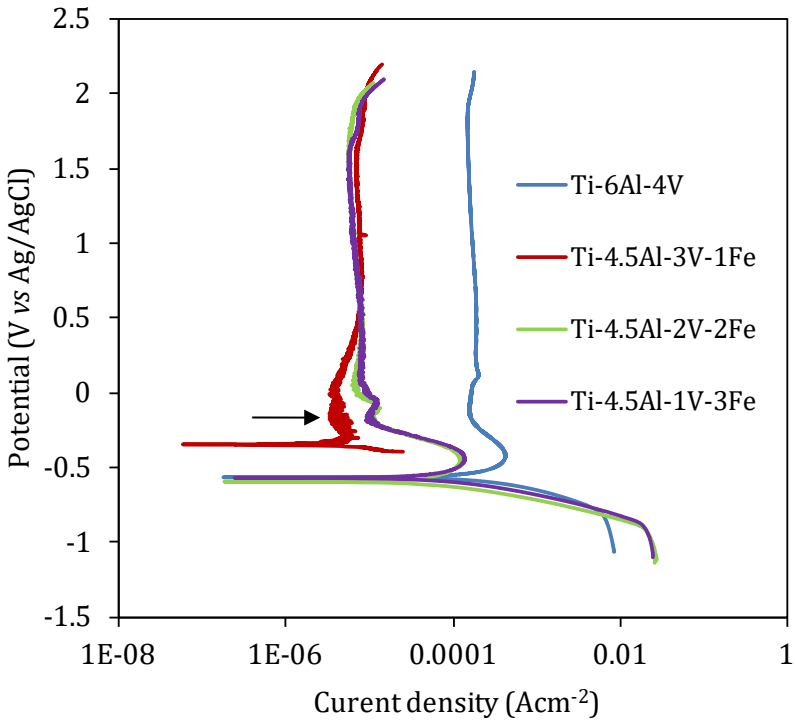

Figure 5.9: Polarisation curves for 4.5 wt% Al alloys immersed in 3.5 M H_2SO_4 solution at 25°C. Arrow points to transient current.

Table 5.2: Electrochemical parameters obtained for 4.5 wt% Al alloys immersed in 3.5 M H_2SO_4 solution at 25°C.

Alloys	Equivalent Weight	E_{corr} (V vs Ag/AgCl)	i_{corr} (μA/cm^2)	Rp	Corr. rate (mm/yr)
Ti-6Al-4V	11.82	-0.562	182	142	1.59
Ti-4.5Al-3V-1Fe	11.93	-0.348	9	2867	0.08
Ti-4.5Al-2V-2Fe	11.92	-0.591	56	462	0.49
Ti-4.5Al-1V-3Fe	11.93	-0.566	71	365	0.63

5.2 NaCl Environment

The variation of OCP with exposure time for commercial Ti-6Al-4V and experimental Ti-6Al-*x*V-*y*Fe and Ti-4.5Al-*x*V-*y*Fe alloys immersed in 3.5 wt% NaCl are shown in Figure 5.10. The OCP of Ti-6Al-4V increased and became more noble with increasing exposure time. In the Ti-6Al-*x*V-*y*Fe series, except for Ti-6Al-3V-1Fe, the iron-containing experimental alloys showed a slight increase in OCP with increasing exposure time. When 1 wt% Fe substituted 1 wt% V (Ti-6Al-3V-1Fe), the lowest OCP value was recorded and the curve fluctuated throughout. These fluctuations have been reported to indicate the dissolution and repassivation of the protective

TiO_2 layer (Parkhutik, 2006). The OCP values of the experimental alloys containing 2 - 4 wt% Fe were similar at 3600 s.

The OCP values of the experimental Ti-4.5Al-*x*V-*y*Fe alloys were lower than Ti-6Al-4V. Similar to Ti-6Al-4V, the OCP of the Ti-4.5Al-3V-1Fe showed a steady increase with increasing exposure time. The higher OCP value of the commercial alloy indicates that the oxide layer was more stable than those formed on the experimental alloys. Both Ti-4.5Al-2V-2Fe and Ti-4.5Al-1V-3Fe displayed a slight increase in OCP with exposure time. Ti-4.5Al-2V-2Fe had the lowest OCP, with breakdown and forming of the oxide layer after ~3300 s immersion in 3.5 wt% NaCl.

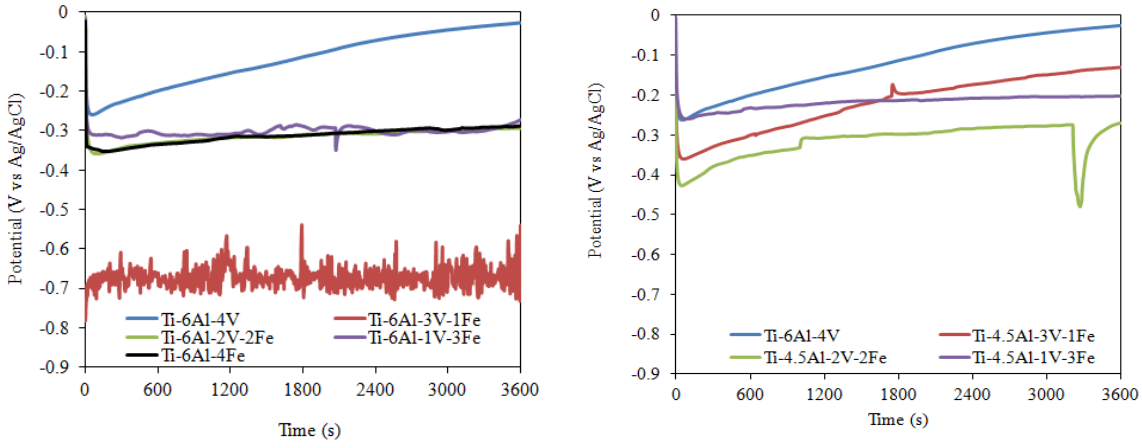

a) b)

Figure 5.10: Variation of OCP measurements for a) Ti-6Al-*x*V-*y*Fe and b) Ti-4.5Al-*x*V-*y*Fe alloys in 3.5 wt% NaCl solution at room temperature.

The cyclic polarisation curves for Ti-6Al-4V and the experimental 6Al alloys in 3.5 wt% NaCl are presented in Figure 5.11. The active nose seen in the alloys when polarised in sulphuric acid solution was not seen in the 3.5 wt% NaCl tests. This indicates that the passive film was formed spontaneously during anodic polarisation in 3.5 wt% NaCl solution. A clearly defined Tafel slope in the anodic region was not seen in all the alloys, similar to the behaviour of Ti-6Al-4V in 3.5 wt% NaCl reported by Dai *et al*. (2016). The reverse scan of all the alloys moved in an anticlockwise direction, indicating resistance to pitting corrosion. Yu and Scully (1997) found that titanium alloys were resistant to pitting corrosion in aerated chloride environments. Ti-6Al-4V exhibited stable pitting at anodic potentials of 5.9 V_{SCE} (~5.5 $V_{Ag/AgCl}$) in 5 M HCl at 37°C. Seah *et al*. (1998) also found that a sintered Ti-6Al-4V alloy exhibited high pitting resistance when polarised in a dilute NaCl solution. However, the concentration of the NaCl solution was not reported.

The passivation currents for the experimental alloys containing iron were comparable, but higher than that of the commercial Ti-6Al-4V alloy. The breakdown potential of Ti-6Al-3V-1Fe was the lowest among the tested alloys. In the alloys containing more than 1wt% Fe, the current density in the transpassive region was lower than that of Ti-6Al-4V and Ti-6Al-3V-1Fe.

The corrosion parameters determined from the polarisation curves are listed in Table 5.3. The E_{corr} values of the alloys were similar and the i_{corr} values were in the same decade as Ti-6Al-4V, except for Ti-6Al-3V-1Fe, where the high i_{corr} gave the highest corrosion rate of 0.0039 mm/y. Ti-6Al-3V-1Fe also had the largest transpassive region, indicating its inferior corrosion resistance to the other alloys in NaCl. There were traces of transient currents in the passive region of this alloy which indicate instability of the formed anodic passive film. The polarisation results were in agreement with the OCP results from Figure 5.10.

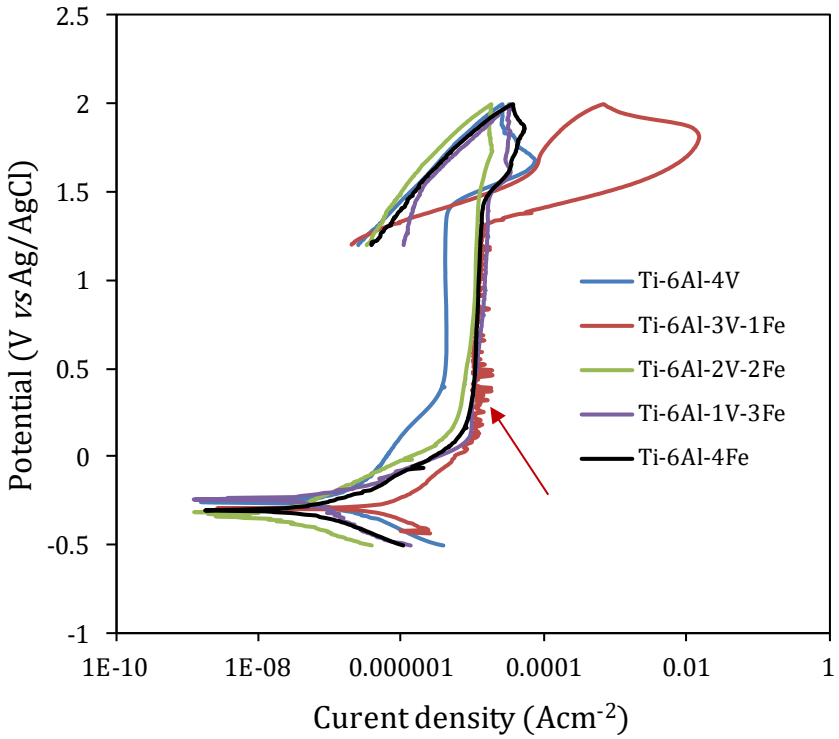

Figure 5.11: Polarisation curves for Ti-6Al-xV-yFe alloys immersed in 3.5 wt% NaCl solution at 25°C. Arrow points to transient current.

The polarisation curves for the Ti-4.5Al-*x*V-*y*Fe alloy series immersed in 3.5 wt% NaCl are presented in Figure 5.12**.** The alloys showed some similarities in corrosion behaviour to the Ti-6Al-*x*V-*y*Fe alloys, displaying spontaneous passivation in NaCl solution with the reverse scans of the polarisation curves moving in an anticlockwise direction. This indicated that the Ti-4.5Al-*x*V-*y*Fe alloys were also resistant to pitting corrosion in NaCl environment. Additionally, distinct transpassive behaviour was seen in the alloy Ti-4.5Al-3V-1Fe, but was suppressed in the other experimental alloys.

Table 5.3: Electrochemical parameters for 6 wt%Al alloys immersed in 3.5 wt% NaCl at 25°C.

Alloys	Equivalent weight	E_{corr} (V *vs*. Ag/AgCl)	i_{corr} (µA/cm^2)	Rp	Corr. rate (mm/yr)
Ti-6Al-4V	11.82	-0.246	0.087	299029	0.0008
Ti-6Al-3V-1Fe	11.81	-0.297	0.450	58455	0.0039
Ti-6Al-2V-2Fe	11.83	-0.324	0.026	1000000	0.0002
Ti-6Al-1V-3Fe	11.83	-0.293	0.067	388993	0.0006
Ti-6Al-4Fe	11.80	-0.300	0.050	505245	0.0005

The difference in the corrosion behaviour of the 6Al and 4.5Al alloys can be seen when comparing the passivation current of the experimental alloys. In the 4.5Al alloys, the passivation current decreased with increasing Fe content, whereas the passivation currents were similar in the 6Al alloys. Unlike the 6 wt% Al alloys, which all showed higher passivation currents than Ti-6Al-4V, only the Ti-4.5Al-3V-1Fe and Ti-4.5Al-2V-2Fe alloys had a higher passivation current than Ti-6Al-4V. The passivation current for Ti-4.5Al-1V-3Fe was lower than that of Ti-6Al-4V. Table 5.4 shows the electrochemical parameters obtained from the polarisation curves in Figure 5.12. The E_{corr} values are quite different, unlike in the Ti-6Al-*x*V-*y*Fe alloys. The highest corrosion current density and highest corrosion rate was observed in Ti-4.5Al-3V-1Fe. The alloy also had the least polarisation resistance. Similar corrosion current densities and corrosion rates (0.0002 mm/y) were obtained in Ti-4.5Al-2V-2Fe and Ti-4.5Al-1V-3Fe alloys, which were lower than that of commercial Ti-6Al-4V (0.0008 mm/y).

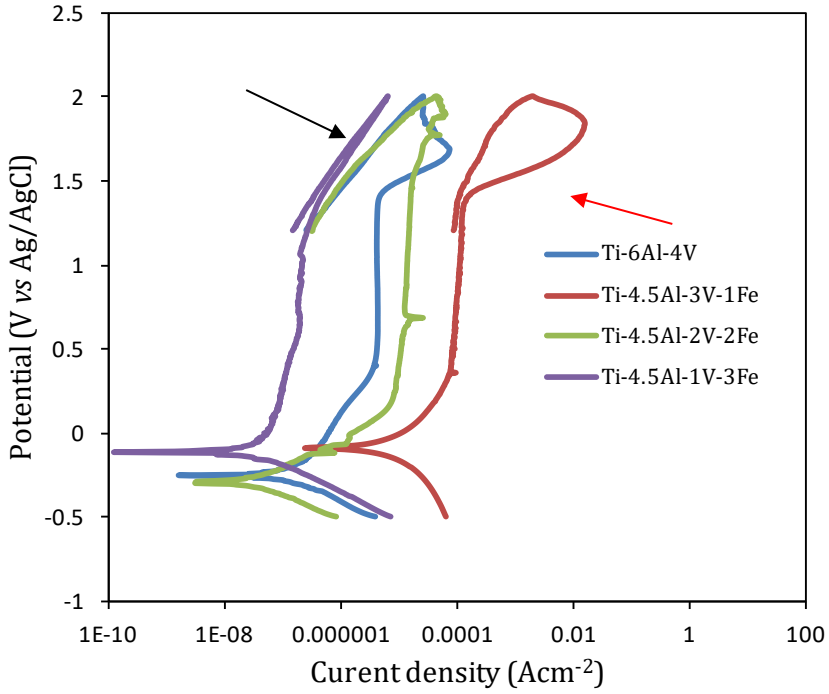

Figure 5.12: Polarisation curves for Ti-4.5Al-*x*V-*y*Fe alloys immersed in 3.5 wt% NaCl solution at 25°C. The red arrow points to distinct transpassive behaviour, while the black arrow points to suppressed transpassive behaviour.

Table 5.4: Electrochemical parameters for 4.5 wt% Al alloys immersed in 3.5 wt% NaCl at 25°C.

Alloys	Equivalent Weight	E_{corr} (V vs Ag/AgCl)	i_{corr} (μA/cm^2)	Rp	Corr. rate (mm/y)
Ti-6Al-4V	11.82	-0.246	0.087	299029	0.0008
Ti-4.5Al-3V-1Fe	11.93	-0.090	3.150	8238	0.0300
Ti-4.5Al-2V-2Fe	11.92	-0.294	0.027	959899	0.0002
Ti-4.5Al-1V-3Fe	11.93	-0.112	0.026	1000000	0.0002

5.3 Sulphuric Acid + Sodium Chloride Environment

Ti-6Al-1V-3Fe and Ti-4.5Al-1V-3Fe were selected for testing in the mixed solution of 3.5 M H_2SO_4+ 0.75 wt% NaCl. This selection was based on the advantage of cost over the other experimental alloys, as well as the corrosion performance of these alloys in the individual 3.5 M H_2SO_4 and 3.5 wt% NaCl solutions. The corrosion performance of the alloys was compared against Ti-6Al-4V and the experimental Ti-6Al-4Fe alloy. The OCP curves for the alloys in the mixed H_2SO_4+NaCl solution are presented in Figure 5.13. The OCP of both Ti-6Al-4V and Ti-4.5Al-1V-3Fe alloys decreased towards the cathodic region, indicating the dissolution of the inherent oxide film formed on the alloy surfaces. Although the OCP of Ti-6Al-1V-3Fe and Ti-6Al-4Fe were comparable, the OCP of Ti-6Al-4Fe fluctuated throughout the period of immersion. This fluctuation indicated the dissolution and repassivation of the oxide layer on the surface. The OCP values at 1200 s for the commercial and experimental alloys were similar.

The polarisation curves of the selected alloys in the H_2SO_4 + NaCl solution are shown in Figure 5.14. The potentiodynamic curves of Ti-6Al-4V, Ti-6Al-1V-3Fe and Ti-4.5Al-1V-3Fe followed similar trends in the mixed solution, showing similar E_{corr}, active to passive transitions and a range of passivity prior to dissolution of the passive film in the transpassive region. The breakdown potential of Ti-6Al-4V (E_b= 2.1 V) was slightly higher than that of Ti-6Al-1V-3Fe and Ti-4.5Al-1V-3Fe (E_b= 1.8 V). Unlike these alloys, the potentiodynamic polarisation curves of the Ti-6Al-4Fe alloy showed erratic behaviour, and the results were not easily reproducible.

The E_{corr} of Ti-6Al-4Fe was higher than of the other alloys. Ti-6Al-4Fe did not show a distinct active to passive transition but the passivation current was higher than that of Ti-6Al-4V, Ti-6Al-1V-3Fe and Ti-4.5Al-1V-3Fe. There were small transient currents in Ti-6Al-1V-3Fe and Ti-4.5Al-1V-3Fe, while transient currents dominated the Ti-6Al-4Fe curve in the anodic region. This shows that Ti-6Al-4Fe suffered considerable breakdown and formation of the protective oxide film. This observation is in agreement with the OCP curves presented in Figure 5.13.

The corrosion parameters listed in Table 5.5 show that the E_{corr} values obtained for the Ti-6Al-4V and Ti-6Al-1V-3Fe alloys were comparable, and the corrosion current density and corrosion rate of the experimental alloy were ~2.5 times higher. For Ti-4.5Al-1V-3Fe, the E_{corr} was slightly higher than that of Ti-6Al-4V and the corrosion current density and corrosion rates were ~1.8 times higher. Only the electrochemical parameters of Ti-6Al-4Fe alloy have error bars because the polarisation curves were not reproducible after multiple measurements. The polarisation curves of other alloys were reproducible.

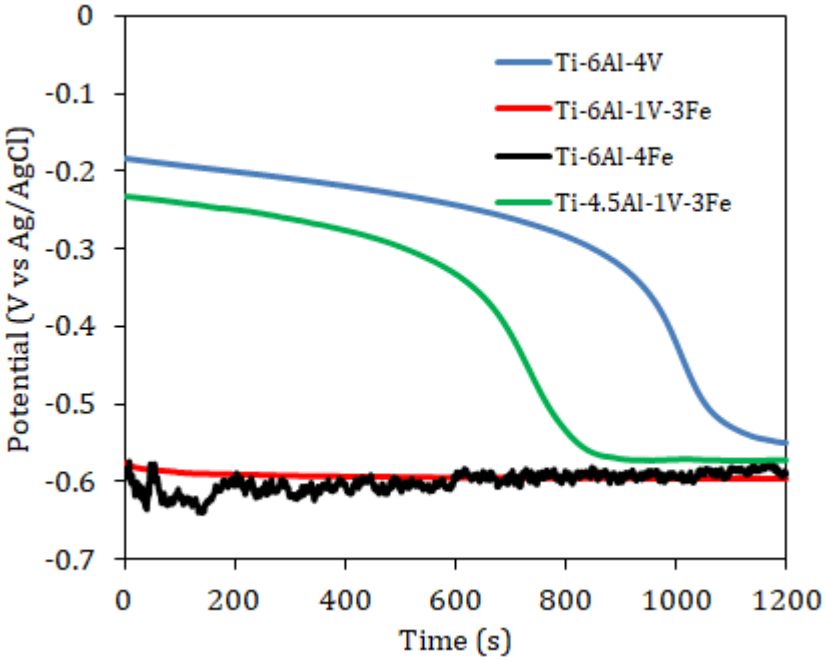

Figure 5.13: Variation of OCP for Ti-6Al-4V and selected experimental alloys in 3.5M H_2SO_4+1.75wt% NaCl at 25°C.

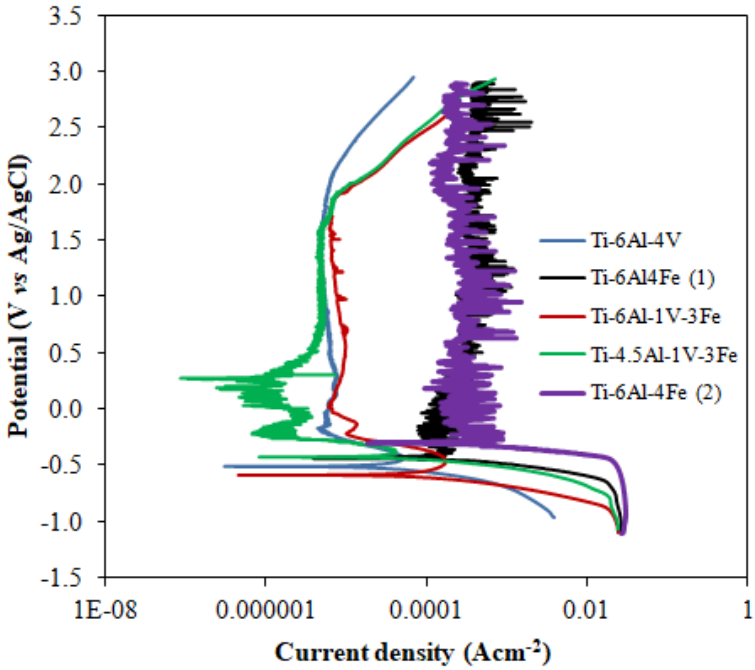

Figure 5.14: Polarisation curves for Ti-4.5Al-*x*V-*y*Fe alloys immersed in 3.5 M H_2SO_4 + 1.75 wt% NaCl solution at 25°C.

Table 5.5: Electrochemical parameters for alloys immersed in 3.5 M H_2SO_4+1.75 wt% NaCl at 25°C.

Alloy	Equivalent Weight	E_{corr} (V)	i_{corr} (µA/cm^2)	Rp	Corr. rate (mm/y)
Ti-6Al-4V	11.82	-0.512	39	669.1	0.34
Ti-6Al-1V-3Fe	11.83	-0.586	96	270.2	0.84
Ti-6Al-4Fe	11.80	-0.376 ±0.1	1786.5 ±276.5	14.7 ±2.3	15.6 ±2.4
Ti-4.5Al-1V-3Fe	11.93	-0.431	68	384.0	0.60

5.4 Discussion

The good corrosion resistance of titanium and its alloys in many corrosive environments has been attributed to the spontaneous formation of a stable and adherent passive film on the surface of the metal (Atapour *et al*., 2010, 2011). The oxide film has two layers, the inner anatase (TiO) layer close to the metal, and the outer rutile (TiO_2) layer of the exposed samples (Ciszak *et al*., 2016; Pouilleau *et al*., 1997). When titanium is alloyed with other metallic elements, the oxides of these elements are also found in small quantities in the main titanium oxide layers (Atapour *et al*., 2011; Ciszak *et al*., 2016). Hence, the stability of the oxide film can be influenced by alloy composition in addition to factors such as the concentration of corrosive solution, temperature, immersion time and complexity of the anions in the solutions (Atapour *et al*., 2010).

The OCP measurement was used to evaluate the passivity of the oxide film formed on the surface of Ti-6Al-4V and the experimental alloys in different solutions. Ti-6Al-4V showed an increase in OCP towards nobler values in both 3.5 M H_2SO_4 (Figure 5.1) and 3.5 wt% NaCl (Figure 5.10) solutions. This increase in OCP has been attributed to the growth of the oxide layer on the alloy (Atapour *et al*., 2010b). However, the experimental alloys showed different behaviour in 3.5 wt% NaCl and 3.5 M H_2SO_4 solutions. Dissolution of the oxide film, known as self-activation (Caprani and Frayret, 1979; Devilliers *et al*., 2006), was seen in 3.5 M H_2SO_4, while a gradual increase in the OCP was seen in 3.5 wt% NaCl solution. Ti-6Al-4V, which displayed increased OCP values in both solutions, showed a decrease in OCP towards more active values in the mixed 3.5 M H_2SO_4 + 1.75 wt% NaCl solution. The variations in the OCP behaviour of the alloys confirmed that the alloys are sensitive to composition and corrosive solutions. Tomashov *et al*. (1974) reported that alloying elements like Al, V, Mo, Zr and Nb promoted the anodic dissolution of a passive film in sulphuric acid by increasing the defects and ionic conductivity of the film when the alloying elements enter the lattice of the film. Addition of aluminium to titanium promotes the dissolution of TiO_2 oxides (Aragon and Hulbert, 1972; Choubey *et al*., 2004). The anodic reaction governing the dissolution of titanium is well reported (Caprani and Frayret, 1979; Mogoda *et al.*, 2004; Atapour *et al.*, 2010a):

$$Ti \longrightarrow Ti^{3+} + 3e \qquad \textbf{Equation 5.1}$$

The dissolution of the TiO_2 film formed on the experimental alloys in solutions containing sulphuric acid was in agreement with the previous research (Mogoda *et al.*, 2004; Devilliers *et al.*, 2006). The protective film formed on titanium alloys rapidly dissolves in concentrated reducing acids such as sulphuric, oxalic and hydrochloric acid (Owen *et al*., 1972; Sinigaglia *et al*., 1978; Fekry, 2009).

There was no evidence of dissolution of the Ti-6Al-4V alloy after 3600 s immersion in sulphuric acid at OCP, while the experimental alloys containing Fe showed dissolution. The experimental alloys with 2 - 4 wt% Fe attained a stable OCP of -600 $mV_{Ag/AgCl}$ after exposing for 3600 s, close to the stable potential of about -660 mV_{SCE} (-621 $mV_{Ag/AgCl}$) of pure titanium after self-activation in strong acids (Devilliers *et al*., 2006). The dissolution of the iron-containing alloys was confirmed in Figure 5.2. The dissolution of the alloys was evidently increasing with increasing Fe content in the alloys. When 3 wt% Fe was added, substituting 3 wt% V in the experimental alloy, the SE image (Figure 5.2d) showed that the alloy was already in the active state. Evidence of corrosion attack was seen in the alloy containing 4 wt% Fe as the sole beta stabilising agent. In a mixed solution of H_2SO_4 + NaCl, the OCP recorded at 1200 s for both commercial and selected experimental alloys were similar. The dissolution of the passive film on the alloys can be attributed to the complexity of the SO_4^{2-} and Cl^- ions in the solution (Atapour *et al*., 2011).

Based on the OCP results, it can be concluded that the experimental alloys were more stable in NaCl than in H_2SO_4 and H_2SO_4 + NaCl solutions. The potentiodynamic polarisation results presented in Figure 5.12 and 5.14 and Table 5.2 - 5.5 showed the superior corrosion resistance of all the alloys in NaCl solution than in the other test solutions. The behaviour of the experimental alloys in the different solutions is consistent with the work of Magoda *et al*.(2004) and Atapour *et al.*(2011), which indicated that titanium and its alloys are susceptible to corrosion in sulphide containing solutions, but are more corrosion resistant in sodium chloride solutions. In addition, increasing the iron content increases corrosion rates when corrosion rates exceed 130 μm/y (Donachie, 2000).

When comparing the corrosion performance of the commercial Ti-6Al-4V alloy and the experimental Ti-6Al-*x*V-*y*Fe and Ti-4.5Al-*x*V-*y*Fe alloys, it was insufficient to draw conclusions from the OCP measurements. This is because the behaviour of the oxide film formed on the alloy surface when exposed to corrosive solutions at OCP differs from the oxide film grown during anodic polarisation (Blackwood *et al*., 1988). Blackwood and Peter (1989) reported that an oxide film can be grown on titanium through anodic polarisation in 3 M H_2SO_4 and the dissolution of the resultant film is uniform and very slow compared to the oxide film that is formed at OCP.

Therefore, the electrochemical parameters obtained from anodic polarisation of both commercial and experimental alloys were compared to describe the corrosion behaviour of the alloys.

In an H_2SO_4 solution, the experimental alloys containing both Fe and V as beta stabilising elements had better corrosion resistance than the alloys containing only one beta stabilising element, *i.e.* either Fe or V, including commercial Ti-6Al-4V. With comparable E_{corr} values, the passivation current of the experimental Ti-6Al-*x*V-*y*Fe and Ti-4.5Al-*x*V-*y*Fe alloys containing Fe and V was ~10 times lower than that of the commercial alloy. Additionally, the corrosion rates and the critical current densities for passivation were lower in the experimental alloys containing Fe and V than in the commercial alloy.

In 3.5 wt% NaCl, all the experimental alloys except Ti-6Al-3V-1Fe had lower corrosion rates than commercial Ti-6Al-4V (Table 5.3 and Table 5.4). The lowest corrosion rate was observed in the experimental alloys containing equal amounts of the two beta stabilising elements (Ti-6Al-2V-2Fe and Ti-4.5Al-2V-2Fe). From these results, it would appear that the partial substitution of vanadium with iron is beneficial for corrosion resistance. It is still unclear how iron contributes to the low corrosion rates observed in the experimental alloys, but previous work on iron-containing titanium alloys have shown improved corrosion performance over commercial Ti-6Al-4V (Kuphasuk *et al.*, 2001; Choubey *et al.*, 2005; Pimenova and Starr, 2006).

Lu *et al.*(2016) reported that Ti-6Al-4Fe showed a lower corrosion rate in simulated body fluid (pH = 7.4) due to a compact layer of aluminium and iron oxide which protected the TiO_2 film from dissolving. Fujii *et al.* (2002) also reported that Ti-1%Fe-0.3%O-0.04%N had higher corrosion resistance than Ti-6Al-4V in a boiling NaCl+HCl solution. They proposed that the presence of dissolved nitrogen in the alloy could have improved the corrosion resistance. Kuphashuk *et al.* (2001) reported that commercially pure Ti and iron-containing alloys such as Ti-5Al-2.5Fe and Ti-4.5Al-3V-2Mo-2Fe (SP 700) had lower corrosion rates than Ti-6Al-4V and NiTi alloys in a 37°C Ringer's solution. A detailed experimental study on the kinetics and stability of the passive film that grows during anodic polarisation of the experimental alloys is needed to fully understand mechanisms influencing the passivation behaviour.

In mixed 3.5 M H_2SO_4+1.75 wt% NaCl solution, the experimental alloys containing two beta stabilisers (Fe and V) showed higher corrosion rates and lower breakdown potentials than the commercial Ti-6Al-4V alloy, despite having comparable E_{corr} values. This suggests that the alloys were sensitive to the multiple anion types present in the solution. Ti-6Al-4V was also sensitive in this combined solution, as it showed a large active to passive transition nose (Figure 5.14) compared to the active nose displayed in the 3.5 M H_2SO_4 solution (Figures 5.8 and 5.9).

The active to passive transition behaviour in titanium alloys has been reported to be a sign of incomplete passivation (Atapour *et al.*, 2011) , which would result in vacancies in the oxide film. Anions such as Cl^- and SO_4^{2-} can fill these vacancies and cause corrosion attack on the metal. The experimental alloy containing only Fe as the beta stabiliser had a very high corrosion rate and transient current in the passive region when polarised in the mixed H_2SO_4 + NaCl solution. This makes Ti-6Al-1V-3Fe a preferred choice over Ti-6Al-4Fe if any of the low-cost options was to be applied in this environment.

To assess the influence of Al reduction on the corrosion performance of the experimental alloys in the sodium chloride and sulphuric acid solutions, the corrosion rates of the experimental alloys for each solution were plotted against nominal %Fe (Figures 5.15 and 5.16). In a sulphuric acid solution (Figure5.15), the corrosion rates of the experimental alloys containing 4.5 wt% Al were lower than those of the alloys with 6 wt% Al for most cases. However, the corrosion rates of experimental Ti-6Al-1V-3Fe, Ti-6Al-3V-1Fe and Ti-4.5Al-1V-3Fe were very similar.

The experimental alloys containing 4.5 wt% Al had lower corrosion rates than the 6 wt% Al alloys in sulphuric acid. This observation concurs with the reports of Choubey *et al.* (2004) who have found that an increase in Al content in titanium alloys is detrimental to corrosion performance (Choubey *et al.*, 2004). The corrosion rates of alloys immersed in the sodium chloride solution are shown in Figure 5.16. The reduction in Al content had little influence on the corrosion performance of experimental alloys containing ≥2% Fe. However, Ti-4.5-Al-3V-1Fe had the highest corrosion rates of the experimental alloys, followed by Ti-6Al-3V-1Fe.

Ti-4.5Al-1V-3Fe had a lower corrosion rate than Ti-6Al-1V-3Fe (Table 5.6) in the mixed sodium chloride and sulphuric acid solution. The lower corrosion rate of the experimental alloys containing less Al indicates that higher aluminium is detrimental to the corrosion performance of the alloys.

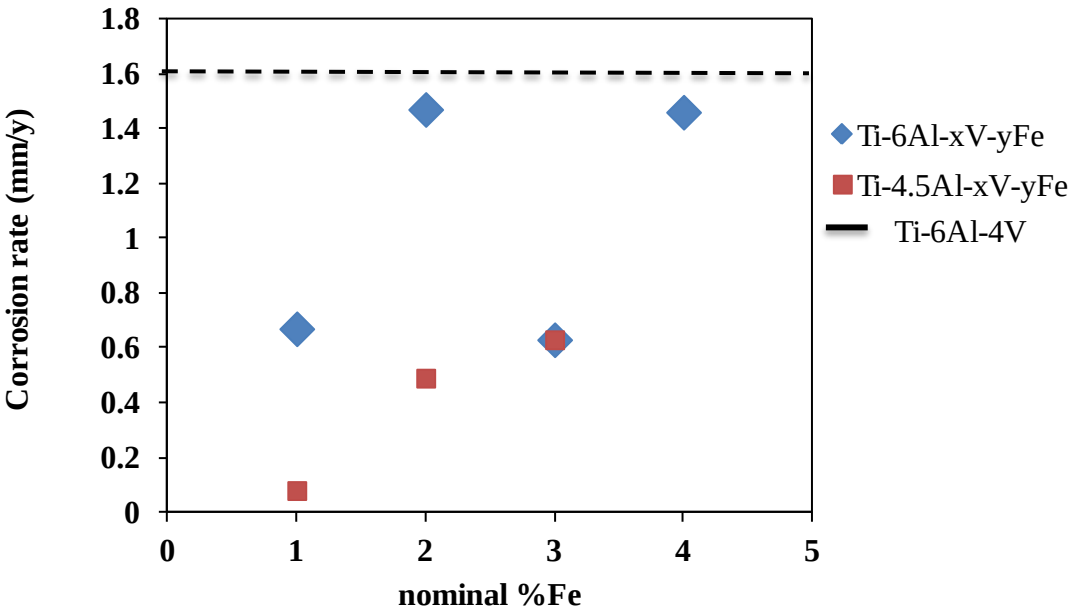

Figure 5.15: Corrosion rates against nominal Fe for experimental alloys immersed in 3.5 M H_2SO_4 solution at 25°C.

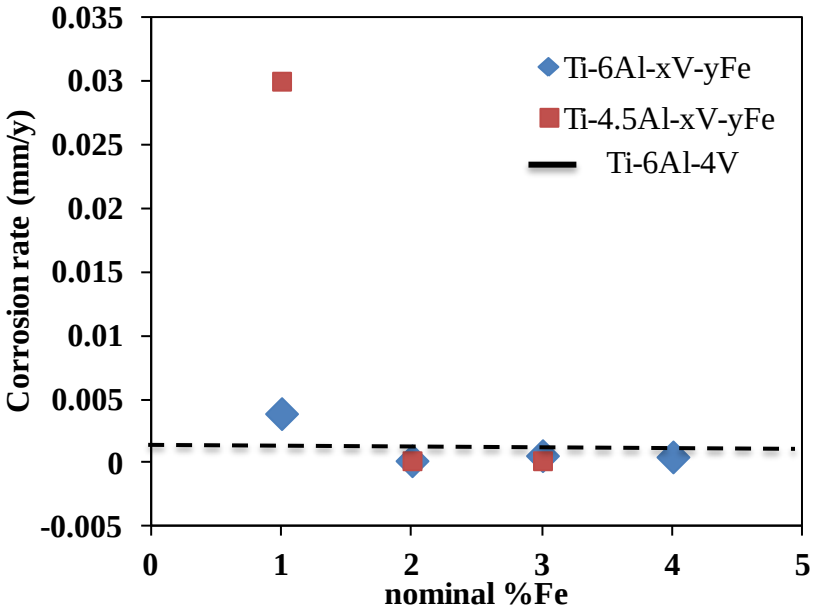

Figure 5.16: Corrosion rates against nominal Fe for experimental alloys immersed in 3.5 wt% NaCl solution at 25°C.

5.5 Summary of Results

The experimental alloys showed good corrosion resistance, similar to commercial Ti-6Al-4V in 3.5 wt% NaCl solutions. The partial substitution of V with more than 1 wt% Fe (Ti-6Al-2V-2Fe, Ti-6Al-1V-3Fe, Ti-4.5Al-2V-2Fe and Ti-4.5Al-1V-3Fe alloys) yielded lower corrosion rates than that of Ti-6Al-4V.Based on their corrosion performance, these alloys could be studied further for potential use as low-cost replacements for the Ti-6Al-4V alloy in marine industries, *i.e.* in NaCl environments.

In 3.5M H_2SO_4, the experimental alloys containing both Fe and V as β stabilisers (Ti-6Al-3V-1Fe; Ti-6Al-2V-2Fe and Ti-6Al-1V-3Fe) showed better corrosion resistance than Ti-6Al-4V, with lower corrosion rates, critical current densities and passivation currents.

In a mixed solution of 3.5 M H_2SO_4 + 1.75 wt% NaCl, commercial Ti-6Al-4V displayed superior corrosion resistance to the experimental Ti-6Al-1V-3Fe, Ti-4.5Al-1V-3Fe and Ti-6Al-4Fe alloys. However, when considering a lower cost alloy than Ti-6Al-4V in the mixed solution, Ti-6Al-1V-3Fe and Ti-4.5Al-1V-3Fe would be preferred over Ti-6Al-4Fe.

A slight decrease in aluminium content (*e.g.* from 6 to 4.5 wt% Al), with the addition of Fe and V as beta stabilisers (*e.g.* totalling 4% in a combination of 3 - 1, 2 - 2 or 1 - 3 wt%) could slightly reduce the corrosion rate of the experimental alloys in all of the tested environments.

Chapter 6: Influence of a complex initial microstructure on the hot deformation behaviour of commercial Ti-6Al-4V

In this chapter, the results obtained from isothermal compression testing of commercial Ti-6Al-4V alloy bar with a complex initial microstructure are presented. This study became necessary since it was ascertained from the literature survey that previous studies on the hot deformation of Ti-6Al-4V alloy have focused on either fully lamellar, fully equiaxed or bimodal initial microstructures. In addition, it was important to carry out preliminary hot forming on a readily-available commercial titanium alloy before testing the experimental alloys. Results from testing of Ti-6Al-4V served as the basis upon which the compression testing parameters for the experimental alloys were selected. The deformation behaviour of Ti-6Al-4V was evaluated using stress-strain curves and processing maps. The microstructural evolution as a function of deformation temperature and strain rates is also presented.

6.1 Scope

This chapter is divided into two parts: Sections 6.2 - 6.4 cover the analysis of flow stress and correction of adiabatic heating and the development of processing maps. Section 6.5 covers the microstructural evolution that occurred during deformation and the summary of the results is presented in Section 6.6.

6.2 Flow stress

The stress-strain curves obtained from uniaxial compression testing of the Ti-6Al-4V alloy under different deformation temperatures and strain rates are presented in Figure 6.1. The trends of the stress-strain curves are discussed below.

6.2.1 Strain rate of $0.01s^{-1}$

The flow stress (Figure 6.1a) increased to an initial sharp peak, followed by a sudden drop at a strain of ~0.02. A second peak was seen at all testing temperatures at a strain of ~0.05, but was barely noticeable at 950°C. At deformation temperatures of 800, 850 and 900°C, the second peak was lower than the first, and was higher when tested at 750°C. Continuous flow softening was observed at deformation temperatures below 900°C, while at 950°C a steady-state flow stress was observed. No previous reports of the initial peak phenomenon in Ti-6Al-4V were found by

the author, but it has been reported in other titanium alloys (Duan *et al.*, 2007; Jia et al., 2011a). The initial peak observed at this strain rate is more than likely misleading, as it was caused by a change in strain rate at very low strain (~0.02), as opposed to a phenomenon driven by microstructural changes. The strain *vs.* time profiles for the sample deformed at 750°C/0.01 s^{-1} are shown in Figures 6.2 a – d. A change in strain rate was evident at very low strain ~0.02 (Figures 6.2a and b). The strain rate obtained at strain values higher than 0.02 (Figure 6.2c) was the intended strain rate of 0.01 s^{-1}, whereas a higher strain rate of 0.07 s^{-1} was obtained at strains below 0.02 (Figure 6.2d).

In comparison, the strain *vs.* time profile of the sample deformed at 950°C/0.01 s^{-1} (Figures 6.2e – f) shows that there was no change in strain rate, and no associated initial peak on the stress-strain curve.

The strain versus time profiles of samples deformed at strain rates higher than >0.01 s^{-1} did not show any change in strain rate.

6.2.2 Strain rate of 0.1 s^{-1}

The initial peak phenomenon accompanied by a drastic drop in flow stress, as observed at a strain rate of 0.01 s^{-1} (Section 6.2.1), only occurred at 900 and 950°C at this strain rate (Figure 6.1b). This was due to a change in strain rate at low strain (~0.02). A slight increase in flow stress at strain values of ~0.25 - 0.50, followed by quasi-steady flow stress in the range of 0.05 - 0.20 strain is discernible on the flow stress curves. Steady-state stress was attained at strains higher than 0.50 for testing temperatures from 750 - 900°C, while continuous flow softening was observed at 950°C.

6.2.3 Strain rates of 1 s^{-1} and 10 s^{-1}

The flow curves for tests carried out at higher strain rates (1 and 10 s^{-1}) are shown in Figure 6.1 c and d respectively. There was a distinct dip in the stress-strain curves at 800 - 950°C at a strain rate of 1 s^{-1}, but it was much less pronounced at 10 s^{-1}. The flow stress at both strain rates reached a peak, followed by an oscillating flow stress for all test temperatures at the strain rate of 0.1 s^{-1}, and test temperatures >750°C at the strain rate of 10 s^{-1}.

The oscillatory behaviour was more pronounced at 1 s^{-1}. Also at 1 s^{-1}, the oscillation at 900°C and 950°C appeared to be steady, while continuous flow softening accompanied the oscillating flow stress at temperatures lower than 900°C. At the strain rate of 10 s^{-1} and strain of ~0.4, a similar trend was observed for temperatures lower than 950°C, while steady-state stress was observed at 950°C.

Generally, the flow softening trends observed in the stress-strain curves in Figure 6.1 were:

- Continuous flow softening at temperatures below 950°C,
- The appearance of oscillating flow stresses at 0.1 - 1 s^{-1}, and
- Steady-state flow stress at 950°C.

The oscillatory flow stress behaviour and broad peaks suggest dynamic recrystallisation (Luton and Sellars, 1969; Huang and Logé, 2016).

The steady-state stress suggests either dynamic recovery or dynamic recrystallisation (McQueen and Bourell, 1987; McQueen and Jonas, 1975). Continuous flow softening suggests adiabatic heating or dynamic globularisation of alpha plates (Seshacharyulu *et al.*, 2002; Fan *et al.*, 2013b), flow localisation, and wedge cracking as the likely softening mechanisms dominating the hot working process (Prasad and Seshacharyulu, 1998b). As already noted, flow stress is dependent on strain rate and deformation temperature. This is further emphasised in Figure 6.3, where the peak stress increased with increasing strain rate and with decreasing deformation temperature. Further microstructural analysis was necessary to determine the dominant softening mechanism, and is discussed in Sections 6.4 and 6.5**.**

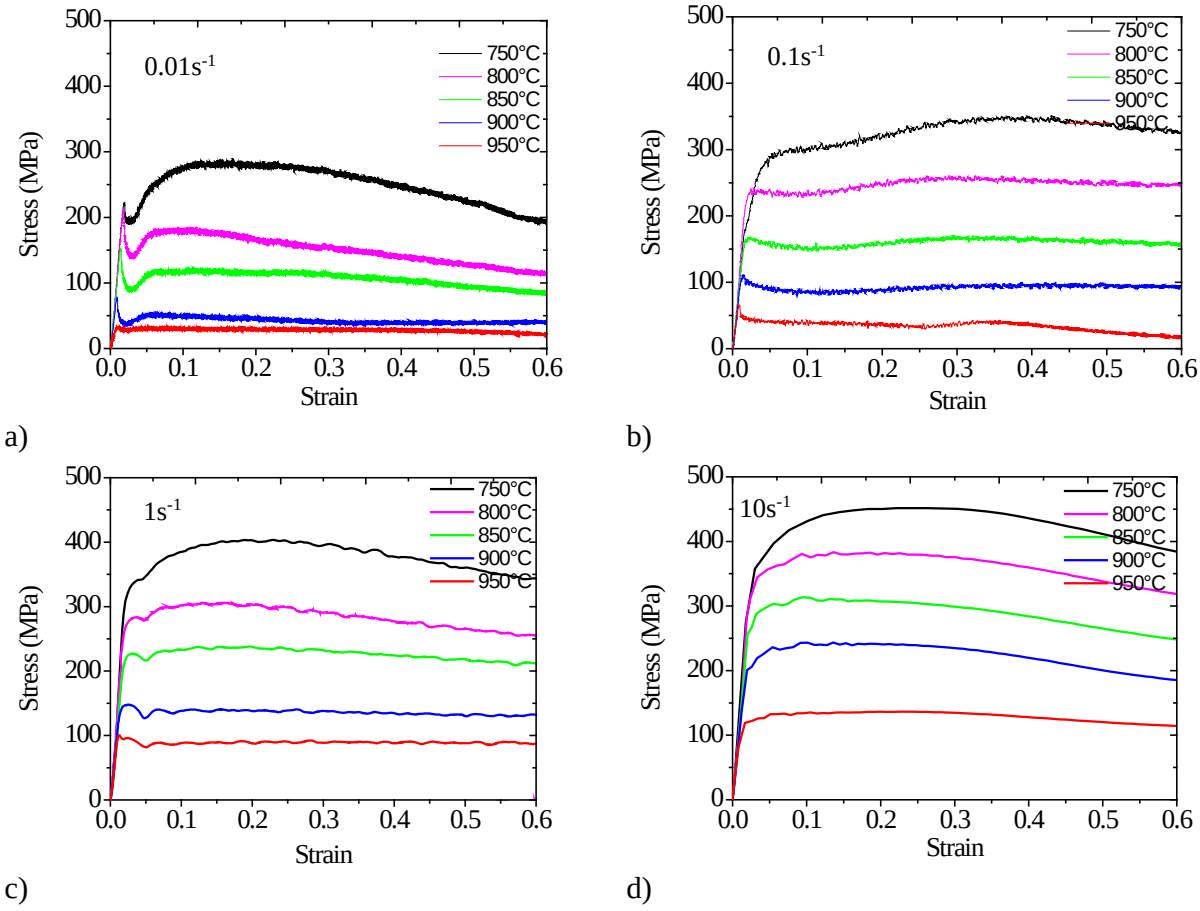

Figure 6.1: True stress-strain curves obtained by uniaxial compression testing of Ti-6Al-4V alloy in the temperature range of 750 - 950°C and at strain rates of: (a) 0.01 s^{-1}, (b) 0.1 s^{-1}, (c) 1 s^{-1} and (d) 10 s^{-1}.

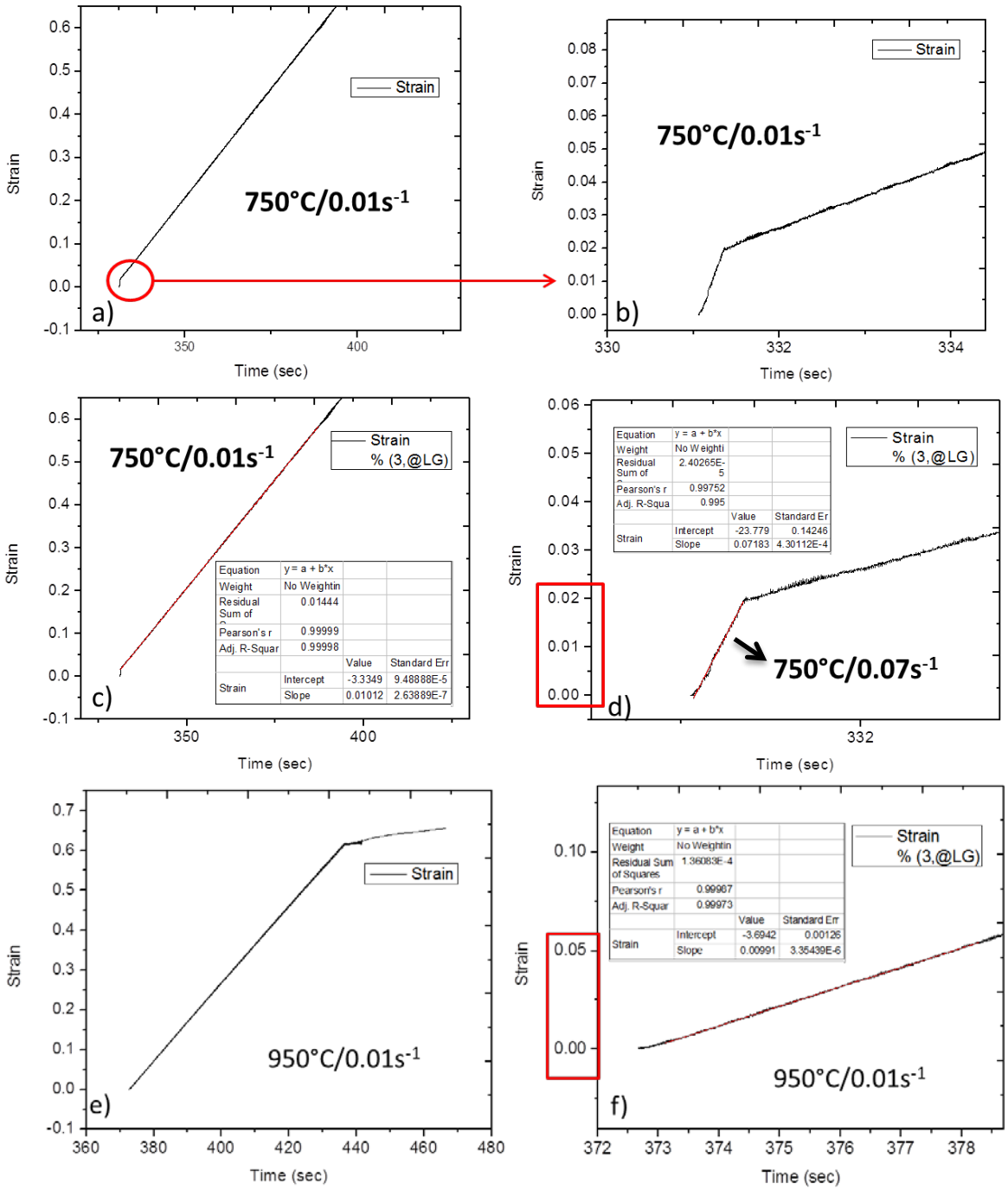

Figure 6.2: Strain versus time profile showing that strain rates changed at low strain (~0.02) when the Ti-6Al-4V sample was deformed at 750°C/0.01 s^{-1}.
The arrow in Figure 6.2d indicates a strain rate of 0.07 s^{-1}, which is much higher than the required strain rate, which was attained in Figure 6.2c.

6.3 Adiabatic Heating

During hot working at lower temperatures (<850°C) and strain rates above quasi-static strain rates of 10^{-3} s^{-1} (Kara *et al.*, 2013), Ti-6Al-4V experiences a temperature increase due to plastic working like many other metallic alloys (Goetz and Semiatin, 2001; Jia *et al.*, 2011b). The heat generated due to plastic work is not all transferred from the workpiece to the anvils and then

dissipated to the environment. As a result, the measured temperature is higher than the programmed temperature, and the flow stress is lower than expected for the programmed temperature. As the reliability of processing maps depends largely on the validity of the flow stress values, the flow stresses obtained under adiabatic conditions need to be corrected for the increase in temperature. The temperature increase during this adiabatic heating can be estimated by Equation 6.1 (Goetz and Semiatin, 2001):

$$\Delta T = \frac{0.95 \times \acute{\eta}}{\rho\, C_p} \int \sigma \delta \varepsilon \qquad \textbf{Equation 6.1}$$

where ΔT is change in temperature, $\acute{\eta}$ is adiabatic correction factor (otherwise known as the Taylor Quinney factor), ρ is density, C_p is specific heat capacity, and $\int \sigma \delta \varepsilon$ is area under the stress-strain curve. The values of $\acute{\eta}$ are: 0.25 (strain rate of 0.01 s^{-1}), 0.50 (strain rate of 0.1 s^{-1}), 0.75 (strain rate of 1 s^{-1}) and 1.0 (strain rate of 10 s^{-1}) (Goetz and Semiatin, 2001).

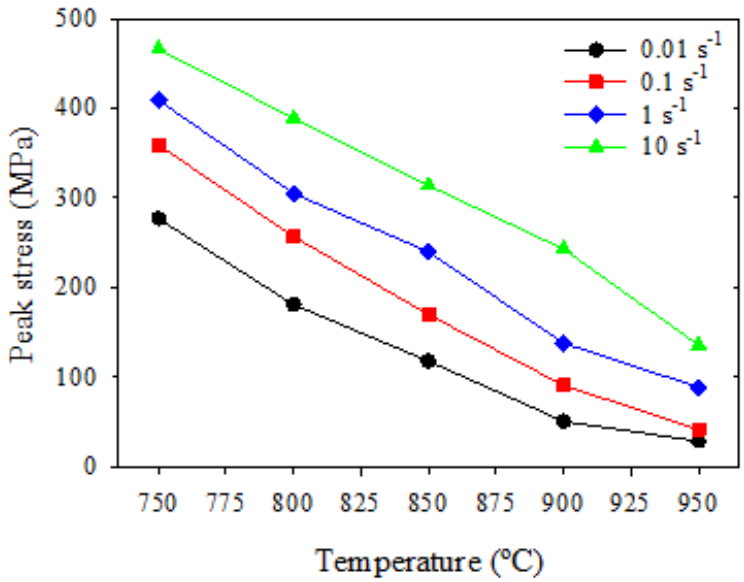

Figure 6.3: Effect of testing temperature and strain rate on the peak stress of Ti-6Al-4V.

Adiabatic heating occurred during deformation of Ti-6Al-4V for tests at: 750°C (0.1 - 10 s^{-1}), 800°C (0.1 - 10 s^{-1}) and 850°C (0.1 - 10 s^{-1}), and 900°C (1 - 10 s^{-1}). The stress-strain curves for these tests (Figure 6.1) showed continuous flow softening which could be due to adiabatic heating. The microstructural manifestation of deformation heating is discussed in Section 6.5.2.

Figure 6.4 shows the differences between the programmed (expected) temperatures and the actual (measured) temperatures against strain for the 750°C/10 s^{-1} and 800°C/1 s^{-1} tests. Other graphs showing the differences between the programmed and actual temperatures are presented in Appendix F. The actual temperature, measured by a chromel-alumel thermocouple, steadily increased over the duration of the compression test segment to higher than the programmed

temperatures.

Comparison between the calculated temperature increase using Equation 6.1 and the measured temperature increase obtained from the chromel-alumel thermocouple (highest and average) is presented in Figure 6.5. Equation 6.1 cannot be used to predict the temperature increase for these Gleeble tests, as it overestimated the adiabatic heating under all conditions except at 800°C/1 s^{-1} where it was lower. Castellanos *et al.*(2009), Longère and Dragon (2007), Soltani (2013) and Zaera *et al.* (2013) found that the adiabatic correction factor either consistently underestimated or overestimated the adiabatic heating. Longére and Drango (2007) and Soltani (2013) noted that Equation 6.1 assumes absolute adiabatic conditions, whereas in reality, some heat is still transferred to the thermocouple and jaws or anvils. Hence, the temperature increase due to adiabatic heating is always specific to the equipment being used.

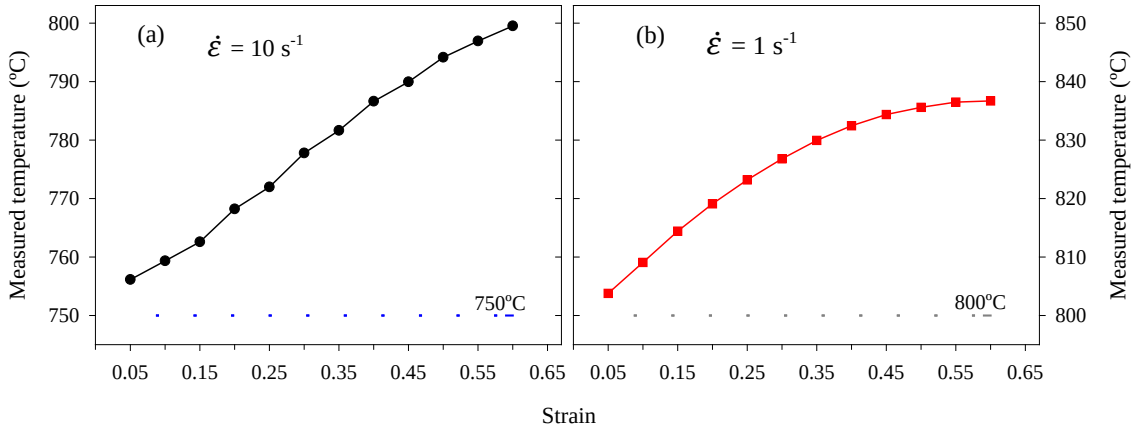

Figure 6.4: Programmed (expected) temperatures *vs.* the actual (measured) temperatures as a function of strain for deformation of Ti-6Al-4V at: a) 750°C/10 s^{-1} and b) 800°C/1 s^{-1} for the alloy Ti-6Al-4V.

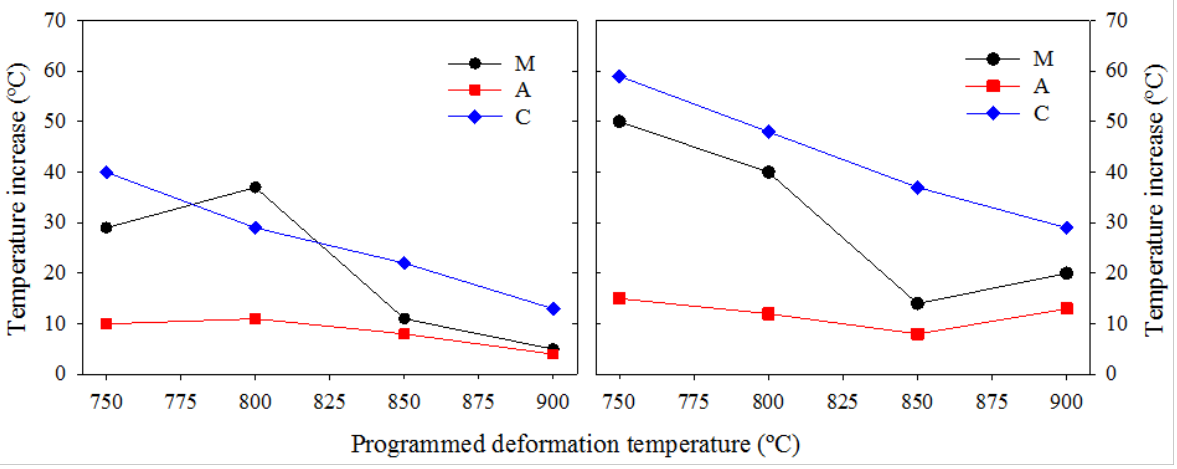

**M: highest temperature increase measured by the thermocouple; A: average temperature increase obtained from thermocouple measurement; C: temperature increase obtained from Equation 6.1*

Figure 6.5: Measured temperature increase against programmed deformation temperatures at strain rates of: a) 1 $s^{-1}$and b) 10 s^{-1} for the alloy Ti-6Al-4V.

As the differences between the temperatures predicted using Equation 6.1 and the actual/measured temperatures from the thermocouple were significant, the flow stress was corrected using linear interpolation between $\ln \sigma$ and 1000/T (in K) based on the actual temperature increase measured directly by the thermocouple. This was done to ensure that the stress values obtained at the programmed temperatures and strain rates could be compared. The differences between the corrected and uncorrected stresses are shown for 750°C/10 s^{-1} and 800°C/1 s^{-1} in Figure 6.6.

Continuous flow softening was still noticeable after correction and therefore cannot be solely attributed to adiabatic heating. This suggested that the probable mechanisms responsible for flow softening were dynamic recrystallisation; dynamic recovery or flow localisation. The corrected flow stress values as a function of deformation temperature and strain rate are presented in Appendix G-1. These corrected stress values were used to develop the processing maps in Section 6.4, and also to determine the activation energy for hot working in Chapter 8.

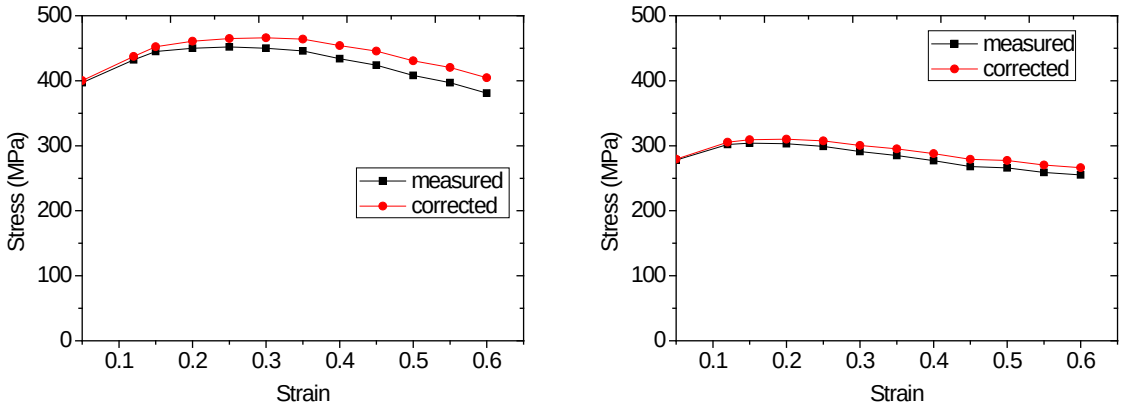

Figure 6.6: Stress-strain curves for corrected and uncorrected flow stress at a) 750°C/10 s^{-1} and b) 800°C/1 s^{-1} for the alloy Ti-6Al-4V.

6.4 Processing maps and microstructural validation

The major benefit of processing maps is their usefulness in identifying the most advantageous region for hot working of metallic alloys. The stable and unstable regions for a Ti-6Al-4V alloy with a complex initial microstructure were determined and are discussed in this section. Processing maps provide an explicit description of a material's response to applied deformation parameters. This response is expressed in terms of microstructural evolution obtained during hot working (Prasad *et al.*, 2015).

Power dissipation values represent the rate of entropy production due to microstructural changes under the imposed strain rate and temperature at a given strain (Prasad and Seshacharyulu,

1998a). Figure 6.7 shows the power dissipation map generated for Ti-6Al-4V at a selected strain of 0.2. The major domains of dynamic recrystallisation (DRX) were observed on the map, corresponding to regions where the power dissipation efficiencies (η) were between 0.35 - 0.50 (35 - 50%) which is typical of DRX for low stacking fault energy metals (Prasad and Seshacharyulu, 1998a). The peak power dissipation efficiency was obtained at a deformation temperature and strain rate of ~940°C/1.7 s^{-1} (η = 49%). The criteria for instability described in Equation 3.4 and 3.5 were not met at this strain, therefore no region of instability was observed. Similar behaviour was observed in processing maps constructed for strains of 0.1, 0.3 and 0.4, which are given in Appendix G-2.

To validate the processing map constructed for a strain of 0.2 (Figure 6.7), Ti-6Al-4V alloy samples were compression tested to a maximum strain of 0.2 at deformation temperatures of 780°C and 920°C, which were initially not tested. These regions on the map are marked as A (780°C/1 s^{-1}) and B (920°C/1 s^{-1}) where ln (1 s^{-1}) = 0 in Figure 6.7.

The microstructures of the as-received Ti-6Al-4V alloy (Figure 6.8) and samples deformed in regions A and B (Figure 6.9) were compared. The observed features were consistent with the power dissipation efficiency values. The as-received alloy consisted of a mixture of elongated alpha, partially equiaxed alpha and a network of intergranular beta. The microstructures of the sample deformed in regions A and B (Figure 6.9) differed from the as-received microstructure.

The sample tested under region A conditions (780°C/1 s^{-1}) contained long serrated α grains, well-defined α subgrains and intergranular β (Figure 6.9a). This suggests that flow softening in region A occurred mainly by dislocation glide and climb (Chen *et al.*, 2008).

The sample tested under region B conditions (920°C/1 s^{-1}) showed fully globular α grains and an increased amount of beta phase (Figure 6.9b). Balasundar *et al*., (2013b) reported that globular α grains formed by a type of dynamic recrystallisation, which provided the flow softening mechanism in region B.

It was expected that restoration due to dislocation climb (Chen *et al.*, 2008) would be the dominant softening mechanism in region A, with a corresponding power dissipation efficiency of ~18%. It was also anticipated that dynamic recrystallisation corresponding to the power dissipation efficiency of ~43% would be the main softening mechanism in region B. Prasad *et al*. (2015) stated that significant reconstitution of microstructure was evidence of dynamic recrystallisation. As expected from Figures 6.7 and 6.9, dynamic recovery was the softening mechanism in region A, while dynamic recrystallisation was the softening mechanism in regions B.

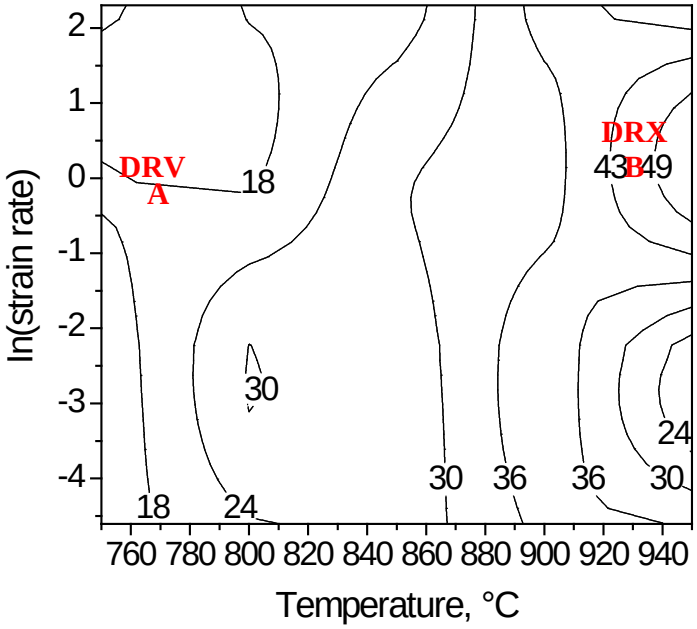

Figure 6.7: Power efficiency map at a strain of 0.2.

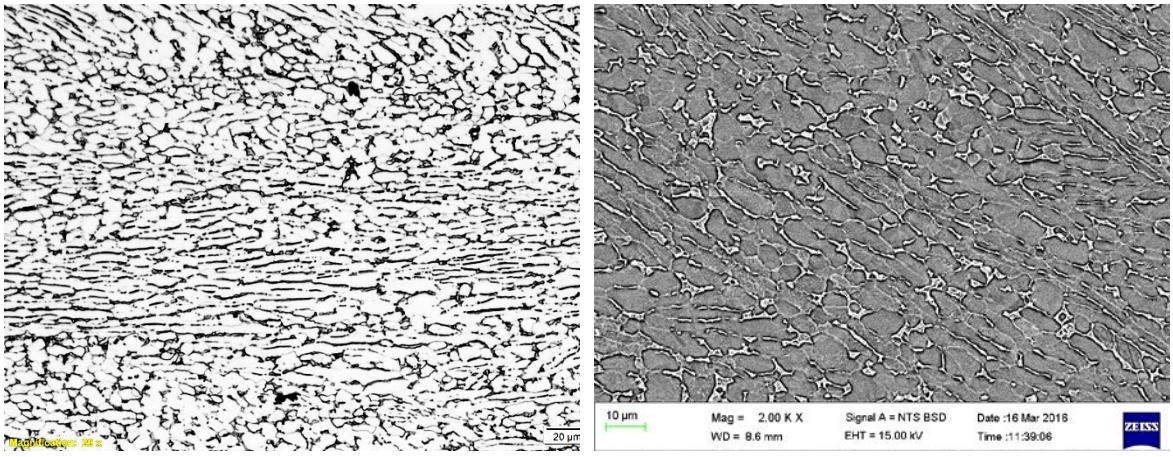

a) b)

Figure 6.8: Microstructure of the as-received Ti-6Al-4V bar in the mill-annealed condition a) optical micrograph and b) SEM-BSE image showing alpha grains and a network of intergranular beta.

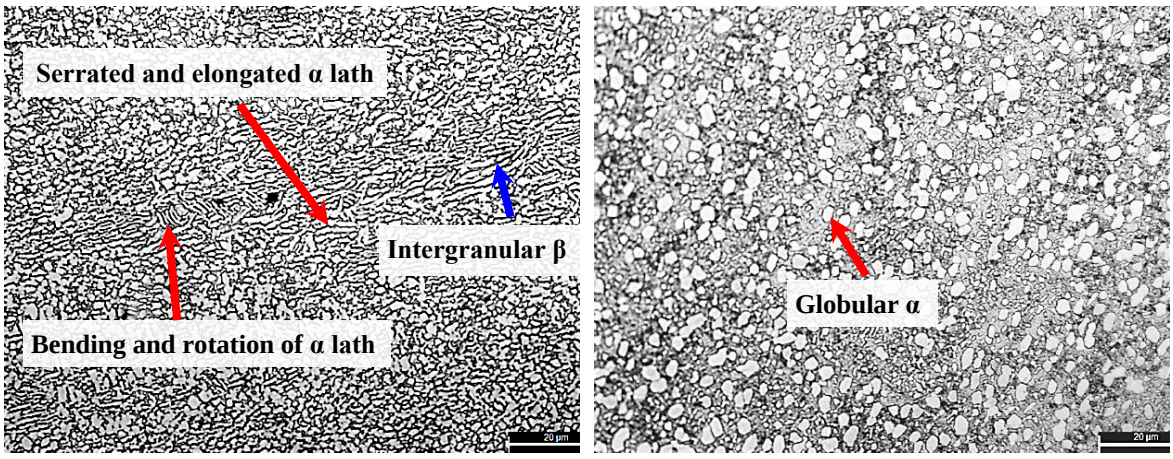

a) b)

Figure 6.9: Optical micrographs of Ti-6Al-4V deformed to a total strain of 0.2: a) region A:780°C/1 s^{-1} and b) region B:920°C/1 s^{-1}, showing lath bending and serrated alpha in a) and globular alpha in b).

Figure 6.10 shows the processing maps for Ti-6Al-4V at total strains of 0.5 and 0.6 respectively. The regimes on these maps differ from those at a strain of 0.2 (Figure 6.7), as both stable and unstable deformation regions occurred at 0.5 and 0.6 strains due to non-steady state conditions with increasing strain. The stable and unstable regions are discussed in Sections 6.4.1and 6.4.2**.**

The variations in the processing maps at different strains can be attributed to the transient flow stresses observed under different deformation conditions in Figure 6.1. Seshacharyulu *et al.* (2000) reported that the processing maps obtained at different strains for Ti-6Al-4V with either fully lamellar or equiaxed initial structures were similar at all strains during deformation. Similar results were found by Fan *et al.* (2013b) in a Ti-7333 near-beta alloy and Huang *et al.* (2009) in α+β Ti-6.5Al-3.5Mo-1.5Zr-0.3Si alloy with an equiaxed microstructure. So, it is concluded that the complex initial microstructure of the Ti-6Al-4V alloy considered in this study contributed to the transient flow stresses and the different processing maps obtained at different strains.

6.4.1 Stable deformation region

There is a wide processing window for safe deformation ($\xi > 0$) as shown in the processing maps at strains of 0.5 and 0.6 (Figure 6.10) under different deformation conditions. At a total strain of 0.5, a region with peak efficiency of 67% was identified at 945ºC/0.4-1.5 s^{-1} and is hatched in Figure 6.10a. This hatched region represents a domain of either dynamic recrystallisation or superplasticity.

At a strain of 0.6 (Figure 6.10b), an area representing the domain of dynamic recrystallisation or superplasticity was seen with a peak efficiency of 76% at 940°C/0.4-1.7 s^{-1}. As the power dissipation efficiency at ~940°C/0.4-1.7s^{-1} was higher than 60%, this could be a domain of superplasticity (Seshacharyulu *et al*., 2000). However, the conditions for superplasticity in alloys must satisfy the following: strain rates lower than 0.01 s^{-1} (Prasad *et al*., 2015) to allow grain boundary sliding (Alabort *et al*., 2016), power dissipation efficiencies higher than 60% and closer contour lines with decreasing strain rate. Unlike dynamic recrystallisation, where large scale reconstitution of microstructure occurs, microstructural reconstitution does not occur during superplastic deformation (Prasad *et al*., 2015). The strain rates at which these high power dissipation efficiency domains were observed are too high to accommodate grain boundary sliding. Also, as the iso-efficiency contour lines in Figure 6.10 are widely spaced and do not get closer with decreasing strain rate, it is proposed that dynamic recrystallisation or globularisation was the main flow softening mechanism during deformation.

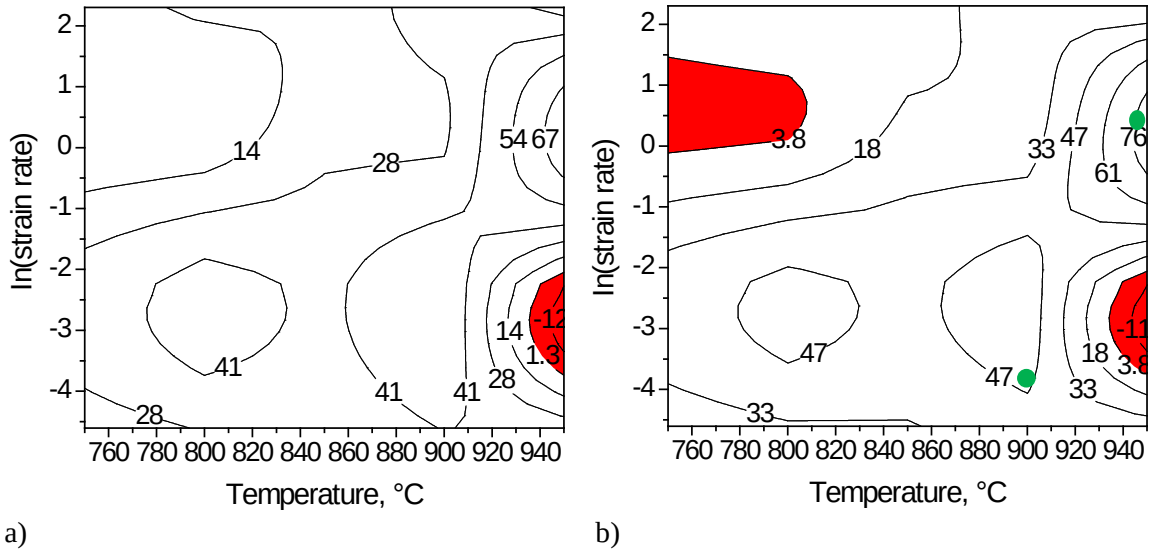

Figure 6.10: Processing maps of Ti-6Al-4V alloys at total strains of: a) 0.5 and b) 0.6, showing the safe (hatched) and unsafe (red) deformation areas.

Figure 6.11 shows the optical micrographs and corresponding secondary electron SEM images of samples deformed in the stable region (900°C/0.01 s^{-1} and 950°C/1 s^{-1}), the green spots in Figure 6.10b. The microstructure was different to the initial microstructure and contains globular alpha grains. The mechanism of dynamic recrystallisation which formed globular α grains from the elongated α grains has been attributed to localised, high energy shear bands generated within the alpha lamellae which allow the penetration of beta phase at the α/α interfaces (Seshacharyulu *et al.*, 2002; Sen *et al.*, 2010; Guan *et al.*, 2012). This eventually separates the lamellar alpha grains into smaller segments (Semiatin *et al.*, 1997). Globular alpha grains are seen in Figure 6.11.

The volume fraction of beta phase in the samples deformed at 900°C was 37% and at 950°C was 64%. This indicated that the α to β phase transformation also contributed to flow softening at high temperatures. An increase in the amount of beta phase makes deformation easier, since the beta phase is softer than the alpha phase at higher temperatures (Weiss and Semiatin, 1998). The beta phase has a bcc structure which has more slip planes available for deformation than the hcp alpha phase (Lütjering and Williams, 2007). The steady-state flow stress observed at higher temperatures (Figures 6.1a, c and d) indicated easier deformation due to an increase in the beta phase fraction. The influence of different strain rates and deformation temperatures on the two flow softening mechanisms identified here, dynamic globularisation and phase transformation, are discussed further in Section 6.5.

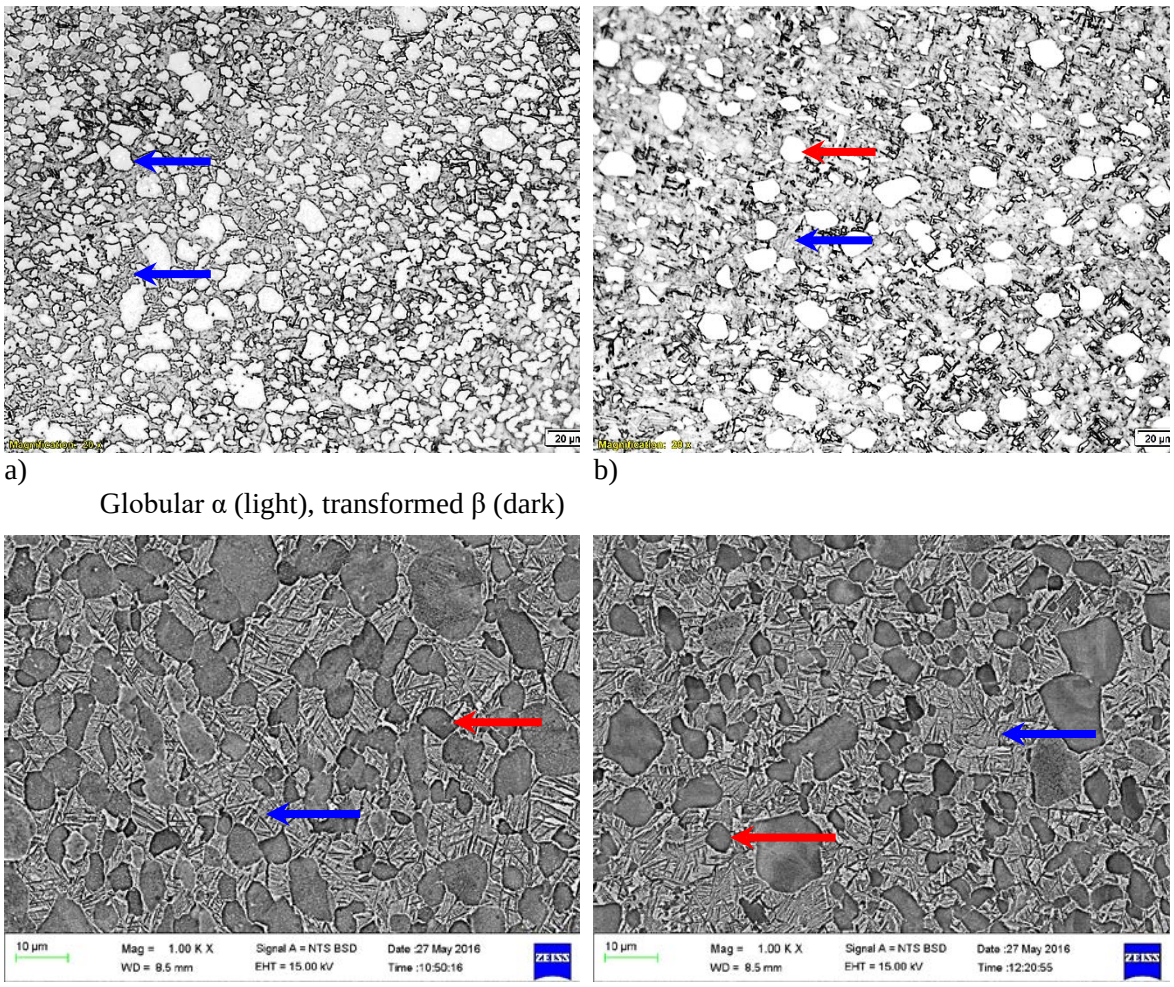

a) b)

Globular α (light), transformed β (dark)

c) d)

Globular α (dark), transformed β (light)

Figure 6.11: Optical micrographs (a & b) and SEM-BSE images (c & d) of Ti-6Al-4V microstructures deformed in the stable region: a & c) 900°C/0.01 s^{-1}, b& d) 950°C/1 s^{-1}. The red arrows show globular alpha grains, while the blue arrows show transformed beta.

6.4.2 Unstable deformation region

The regions of instability ($\xi < 0$) were observed at tempertures above 935°C/0.05-0.1 s^{-1} at 0.5 and 0.6 strains, as well as 750-810°C/1-2.7 s^{-1} at a strain of 0.6 (regions shaded in red in Figure 6.10). The microstructure of the sample deformed at 950°C/0.1 s^{-1} and to a strain of 0.6 is presented in Figure 6.12. The exact flow instability in this region cannot be clearly defined from the optical and SEM micrographs in Figure 6.12 due to transformation during cooling from the deformation temperature (Luo *et al.*, 2009). However, features such as non-equiaxed grains and suppressed recrystallisation within islands of recrystallised grains indicate that heterogeneous deformation occurred in this region. These unstable regions should be avoided during processing of Ti-6Al-4V with a complex initial microstructure.

The processing maps obtained in this study were compared to those of Ti-6Al-4V with either lamellar (Seshacharyulu *et al.*, 2002) or equiaxed (Seshacharyulu *et al.*, 2000) starting

microstructures. The safe and unsafe domains on the maps in this study (Figure 6.5) are different from those with a fully equiaxed starting microstructure. Also, regimes identified as unstable by Seshacharyulu *et al.* (2000) and Seshacharyulu *et al.* (2002), fall within the stable deformation region in this study. The regime of instability observed in this study was absent in their work on Ti-6Al-4V with fully lamellar or fully equiaxed structures. The variations in the region of instability exhibited by the Ti-6Al-4V alloy has been attributed to different strains and initial microstructures of the alloy (Luo *et al.*, 2009).

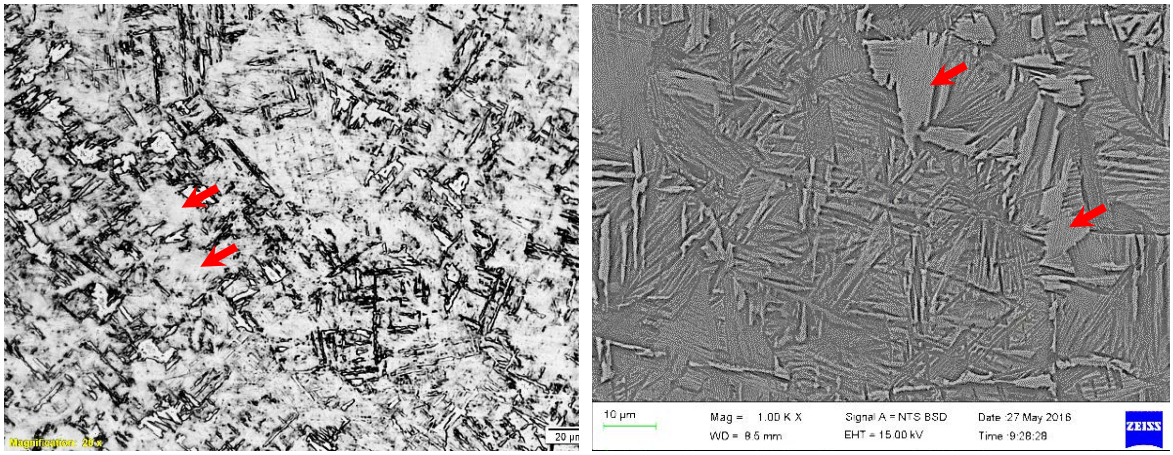

a) b)

Arrows point to non-equiaxed grains

Figure 6.12: Microstructure of Ti-6Al-4V deformed in the unstable region, showing non-equiaxed grains as an indication of heterogeneous deformation: a) optical micrograph and b) SEM-BSE image.

6.5 Microstructural Evolution

The dominant softening mechanisms during deformation in both stable and unstable regions were established from the processing maps in Section 6.4. The role of other softening mechanisms such as phase transformation and deformation heating has also been mentioned. In this section, selected post-deformation microstructures are critically examined to assess the influence of deformation temperatures and strain rates on the flow softening mechanisms.

During thermomechanical processing of titanium alloys, the occurrence of flow softening is largely attributed to one or more of the following mechanisms: deformation heating, dynamic recovery, dynamic globularisation and phase transformation (Prasad and Seshacharyulu, 1998b; Huang *et al.*, 2009; Li *et al.*, 2015b). These mechanisms can be readily identified from the microstructure of the deformed samples. The optical micrographs of samples deformed at different strain rates and deformation temperatures are shown in Figure 6.13.

The different features in the micrographs show that the deformation parameters influenced the microstructure of the samples, as discussed under the following sub-headings: dynamic globularisation, deformation heating and phase transformation.

6.5.1 Dynamic globularisation of alpha grains

Strain rate of 0.01 s^{-1}

Figure 6.13 presents the micrographs of samples deformed over the range 800 - 950°C and at a constant strain rate of 0.01 s^{-1}. Dynamic recovery and dynamic globularisation both influenced the deformation process at this strain rate. The elongated alpha grains were either rotated or serrated at deformation temperatures below 900°C. This is in agreement with previous studies on titanium alloys where serrated and rotated alpha grains were found (Semiatin *et al*., 1997; Jia *et al*., 2011b; Li *et al*., 2015a; Kim *et al*., 2016).

The rotation of α grains, formation of sub-grains with low angle boundaries, dislocation climb and glide are all indicative of dynamic recovery occurring during hot deformation (Wanjara *et al*., 2005; Jia *et al*., 2011a; Lin and Liu, 2010). Zhu *et al.* (2012) and Fan *et al.* (2013a) found that when TC 21 and Ti-7333 alloys were deformed, respectively, serrated grains (irregular grain boundaries) gave microstructural evidence of dynamic recovery. The serrated grains occurred due to interaction of dislocations with the boundaries of the alpha lamellae and the elongation of the lamellae with increasing strain. At a certain critical strain, which is high enough to cause dynamic globularisation, the serrated alpha grains fragmented into small globules (Semiatin *et al.*, 1997).

Traces of fine dynamically globularised alpha grains at 800°C and 850°C were found (Figures 6.13 a and b). This indicates that incomplete dynamic globularisation seemed to have started at 800°C and progressed when deformation was carried out at 850°C. The average grain sizes of the globularised alpha grains were 5.7±1.7 µm at 800°C and 8.3±2.3 µm at 850°C. Also, the aspect ratio of the elongated α lamellae increased from 4.3±2.3 µm to 6.8±3.6 µm. This shows that a low deformation speed and increasing deformation temperature led to grain growth of the alpha phase.

When the deformation temperature was increased to 900°C, there was near-complete globularisation of alpha grains (Figure 6.13 c). Large globular grains were visible in the microstructure, indicating grain growth of the equiaxed alpha phase due to a long deformation time at a low strain rate. Transformed β in the form of α′ martensite can be seen within the prior beta grains at 950°C (Figure 6.13 d). The transformed β is more visible in the Figure 6.16a SEM image.

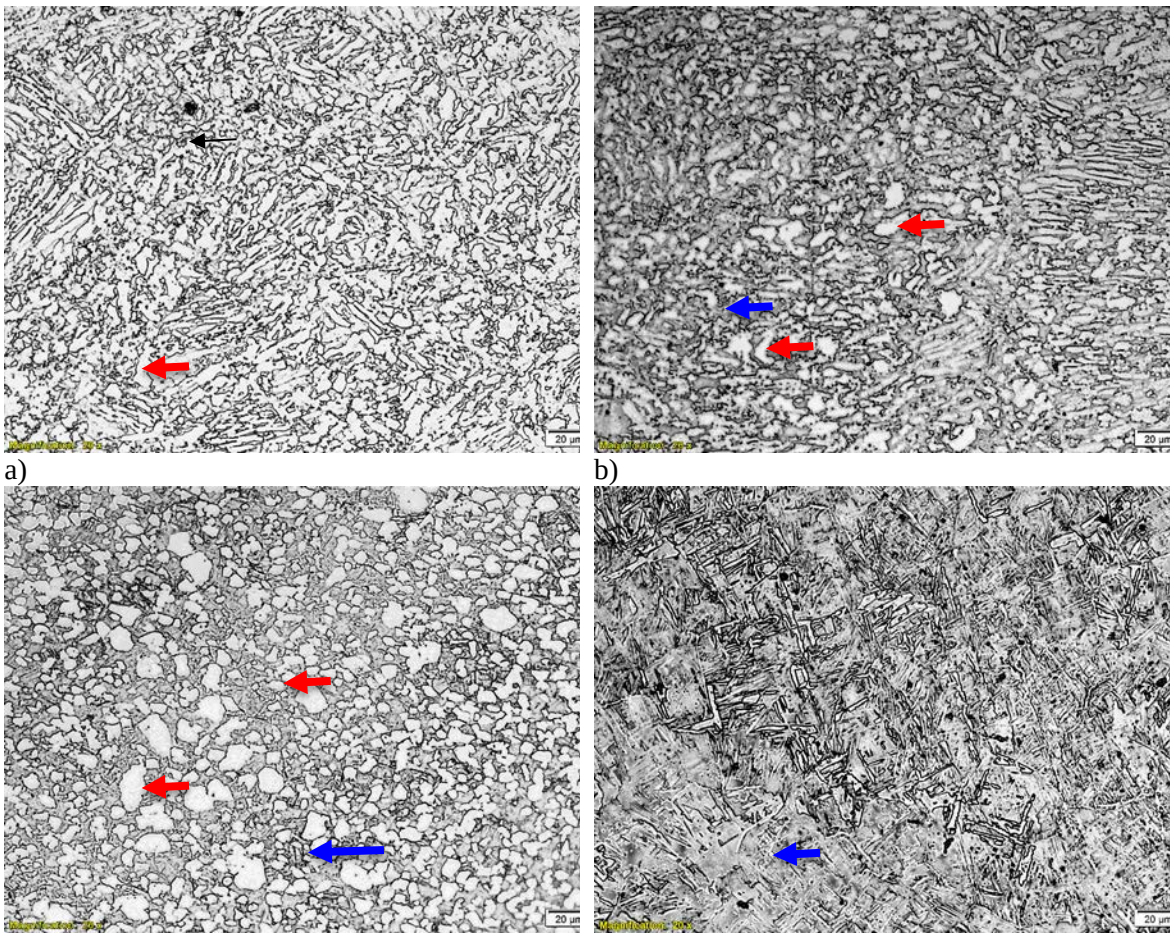

Figure 6.13: Optical micrographs of Ti-6Al-4V samples deformed at a strain rate of 0.01 s^{-1} and temperatures of: a) 800°C b) 850°C c) 900°C and d) 950°C showing serrated α, large and fine globular α at temperature <950°C (light phase- red arrow) and transformed β at 950°C (dark phase- blue arrow).

Strain rate of 1 s^{-1}

Figure 6.14 shows the microstructures of samples deformed at a moderate strain rate of 1 s^{-1}. The samples deformed at 800°C - 950°C contained large globular alpha grains. Some of the elongated grains at 800°C (Figure 6.14a) were serrated because of incomplete dynamic globularisation or dynamic recovery. The large alpha grains are evidence of grain growth during deformation. Figure 6.14 b - d show that the proportion of the large alpha grains decreased as the deformation temperatures increased above 850°C. The presence of fine globular alpha in Figure 6.14 b and c show that the process of dynamic globularisation was almost complete in samples deformed at temperatures above 800°C. All the elongated grains in the initial microstructure were fragmented into smaller grains.

Since dynamic globularisation was evident at all deformation temperatures for the strain rate of 1 s^{-1}, it was easier to examine the relationship between the deformation temperature and average grain size. The average grain sizes for large and small globularised α-grains from Figures 6.14 b

- d are listed in Table 6.1. The average size of the small alpha grains decreased with increasing deformation temperature, but there was no significant influence on the large alpha grains at deformation temperatures between 800°C and 900°C. The large alpha grains of the sample deformed at 950°C/1 s^{-1} were the smallest.

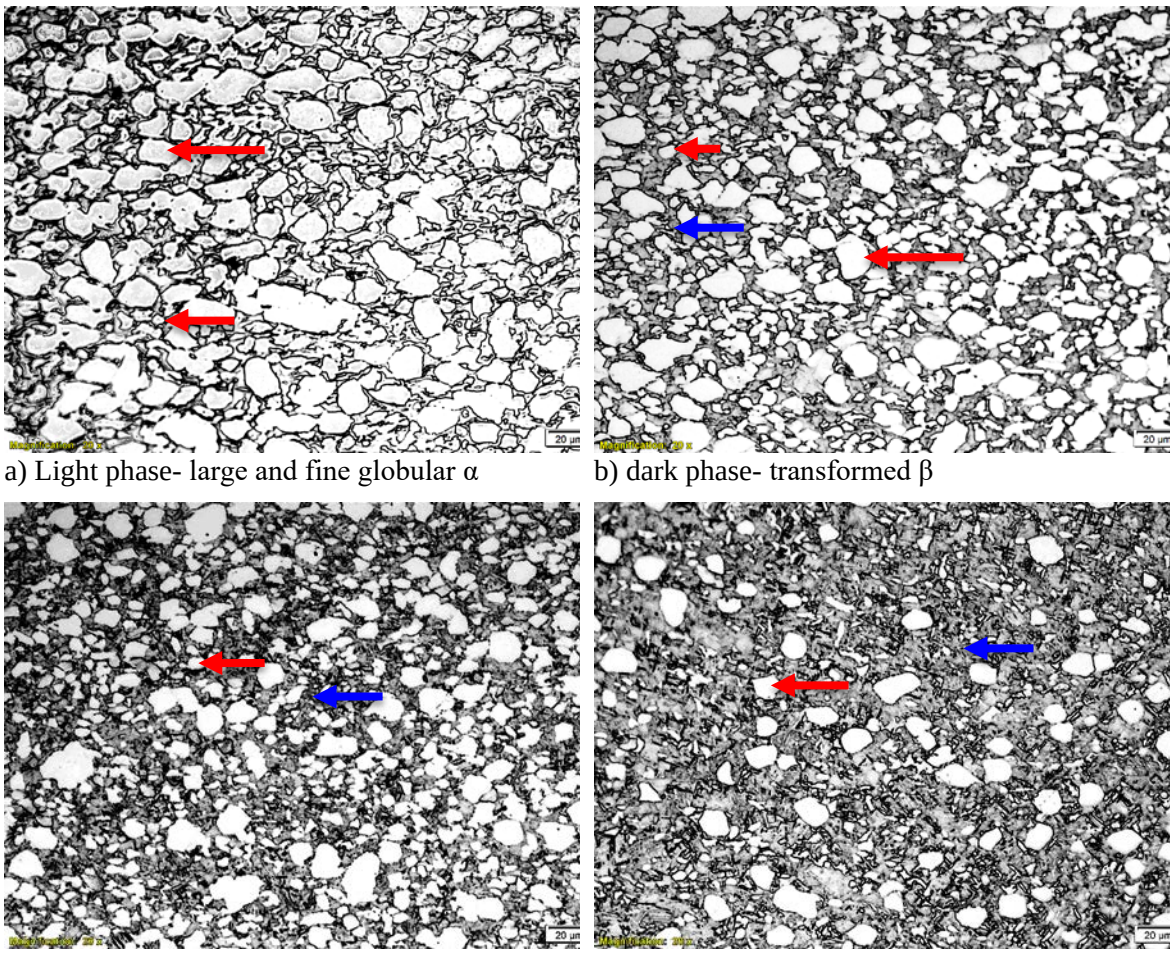

a) Light phase- large and fine globular α b) dark phase- transformed β

c) d)

Figure 6.14: Optical micrographs of Ti-6Al-4V samples deformed at 1 s^{-1} strain rate: a) 800°C b) 850°C c) 900°C and d) 950°C. The red arrows show globular α, while the blue arrows show transformed β.

Table 6.1: Average grain size of alpha phase at a strain rate of 1 s^{-1}.

Temperature (°C)	Average grain size (µm)	
	Small	Large
800	6.12±1.3	16.95±4.6
850	5.92±1.3	17.46±1.6
900	5.32±1.0	17.72±4.5
950	4.63±1.0	14.36±3.3

The reduction in grain size with increasing deformation temperature can be ascribed to the concurrent transformation of alpha to beta phase occurring during deformation. This phenomenon inhibits grain growth (Ding *et al.*, 2002; Luo *et al.*, 2015). Ding *et al.* (2002) reported that concurrent alpha to beta phase transformation that occurred during deformation of the Ti-6Al-4V alloy suppressed the grain growth of the existing alpha grains at elevated temperatures.

Strain rate of 10 s^{-1}

Figure 6.15 shows the microstructures of samples deformed at 800°C, 850°C, 900°C and 950°C and a high strain rate of 10 s^{-1}. Similar to 1 s^{-1}, large serrated alpha grains were present at 800°C (Figure 6.15a), showing grain growth. It is not clear why grain growth occurred during deformation at 1 s^{-1} and 10 s^{-1}. However, the two likely reasons for grain coarsening are deformation heating, discussed in Section 6.5.2, and nucleation controlled dynamic recrystallisation reported by Sakai and Jonas (1984).

Sakai and Jonas (1984) established that the two mechanisms influencing dynamic recrystallisation are growth-controlled and nucleation-controlled mechanisms. The growth-controlled mechanism is associated with single peak stress which is normally observed when low stacking fault metals are deformed at high strain rates, while nucleation-controlled mechanism is associated with cyclic peak stress (oscillation) seen during deformation at low strain rates. The single peak is indicative of grain refinement during DRX, while the periodic flow stress is indicative of grain coarsening (grain growth) (Doherty *et al.*, 1997). The argument of Sakai and Jonas (1984) could be used to explain some of the trends observed in this study. For example, the sample deformed at 900°C/1 s^{-1} showed oscillatory flow stress (Figure 6.1c) and the corresponding microstructure showed coarse α globules. However, at 900°C/10 s^{-1} (Figure 6.1d), the flow stress showed negligible oscillation and can be likened to a single peak where grain refinement was expected. The corresponding microstructures obtained at 900°C/10 s^{-1} (Figure 6.14c) and 900°C/1 s^{-1} (Figure 6.15c) showed that the α globules were refined at 900°C/10 s^{-1}, while grain coarsening occurred at 900°C/1 s^{-1}. At lower deformation temperatures (800°C and 850°C) and both strain rates (1 s^{-1} and 10 s^{-1}), it was difficult to conclude from the microstructures (Figures 6.14 and 6.15) if oscillatory flow stress resulted in grain coarsening. Further studies will be required to fully understand the factors influence grain growth at medium to high strain rates in this alloy.

At deformation temperatures above 800°C, full dynamic globularisation of the alpha phase was discernible (Figures 6.15b - d). However, the grains were much finer at 900°C (Figure 6.15c) than at 800°C, 850°C and 950°C, which appear to be the temperature favourable for dynamic

globularisation of the alpha phase. The fine globularised α grains confirmed that the deformation was optimal at 900°C for all strain rates. Similar to the strain rate of 1 s^{-1}, globularised α-grains were retained at 950°C with an average grain size of 13.89±4.12 μm. The large grains of samples deformed at 950°C/10 s^{-1} (Figure 6.15d) were similar in size to those obtained at 950°C/1 s^{-1} (14.36±3.29 μm) (Figure 6.14d). At 950°C and 1 and 10 s^{-1} strain rates, there was sufficient energy and time for easy consumption of the small alpha grains by the α - β phase transformation. However, the large retained α grains remained due to insufficient time for complete transformation at these higher strain rates.

The microstructures of the deformed samples in Figures 6.13 and 6.15 showed that elongated alpha grains were likely reduced to smaller grains by dynamic globularisation. This appeared to be consistent in all the microstructures, especially when deformation was carried out at temperatures above 800°C and strain rates higher than 0.01 s^{-1}. Dynamic globularisation has been reported to be a form of dynamic recrystallisation which is dominant in Ti-6Al-4V with either a lamellar or lath-type alpha phase (Balasundar *et al.*, 2013a; Li *et al.*, 2015b). The mechanism has been explained by Weiss *et al.*(1986), Semiatin *et al.*(1997), Semiatin and Bieler (2001), and Guan *et al.*(2012) in a number of ways:

1 Local deformation causes rotation of α-laths which leads to a change in orientation up to a magnitude of about 20°. The β phase can then readily penetrate the α/α boundaries created by the rotation of the laths.

2. Shearing of the alpha lath generates low- and high- angle grain boundaries across the alpha phase. The mis-orientation angles between the alpha phases vary from a few degrees up to ~30°. The existing boundaries created by shear can be readily penetrated by the growing β-phase. Complete globularisation occurs if the width of the α-laths are less than twice the penetration distance of the β cusps.

Seshacharyulu *et al.* (2002) proposed that the mechanism of dynamic globularisation occurred in four steps (Figure 2.17):

1. Shearing of laths due to imposed shear strain: This process is strain dependent and may reach completion at larger strains. Initially, a few colonies that are favourably oriented with respect to the applied stress will participate in the shearing process, which will rotate the neighbouring colonies to favourable orientations facilitating further shear.

2. Generation of dislocations having both signs along the line of shear.

3. Simultaneous recovery by cross-slip leading to annihilation of opposite sign dislocations on intersecting slip planes, leaving behind groups of dislocations with the same sign to develop an interface along the line of shear.

4. Migration of interfaces by diffusion to minimize the surface energy forming the globules.

These explanations all emphasise the creation of an α/α interface by shearing, bending and rotation of α-laths as critical steps for dynamic globularisation to take place. The presence of globular alpha in Figure 6.14 indicated that dynamic globularisation had occurred during deformation.

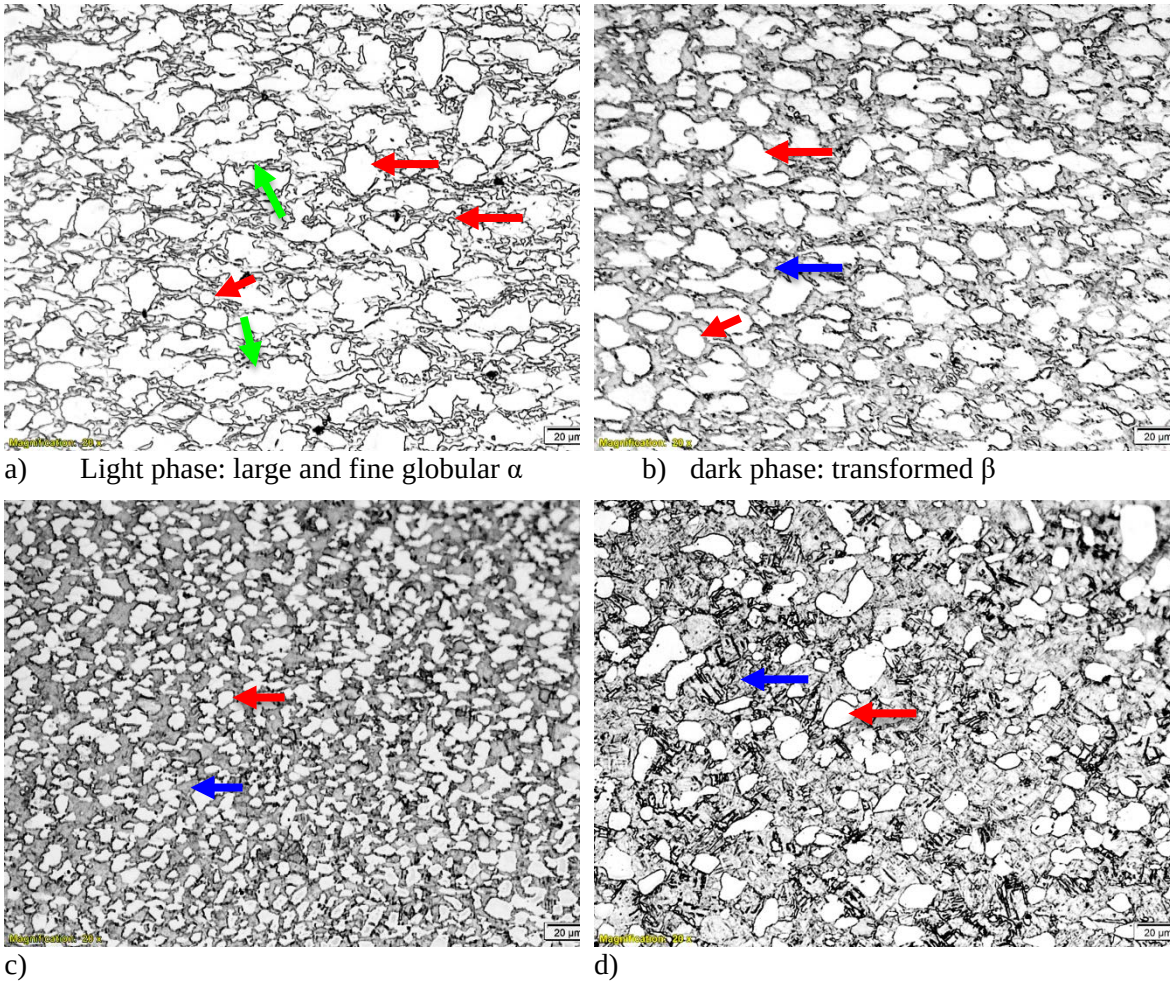

a) Light phase: large and fine globular α b) dark phase: transformed β

c) d)

Figure 6.15: Optical micrographs of deformed Ti-6Al-4V samples at 10s^{-1} a)800°C, b)850°C, c)900°C and d) 950°C. The green arrows point to serrated α grains, red to globular α and blue to transformed β.

6.5.2 Deformation Heating

Deformation heating has been identified as one of the mechanisms responsible for continuous flow softening when metallic samples are deformed at strain rates higher than 0.001 s^{-1} (Goetz and Semiatin, 2001). In Ti-6Al-4V alloys, it has been observed during deformation in the (α+β) phase region (Balasundar *et al*., 2014; Prasad *et al*., 2015). The actual temperature of the samples increases and does not have enough time to dissipate to the surroundings due to the high deformation speed. For titanium alloys, this usually occurs when deforming at strain rates

>0.0001 s^{-1} (Goetz and Semiatin, 2001). As discussed in Section 6.3, adiabatic heating was significant when deforming at temperatures lower than 900°C and strain rates higher than 0.01 s^{-1}.

Although deformation heating can be confirmed by checking for adiabatic shear bands in the micrographs of the deformed samples (Semiatin and Lahoti, 1981; Balasundar *et al*., 2014), no shear bands were seen in the deformed sample micrographs examined in this study, as also reported in Ti-6Al-4V by Ding *et al*. (2002). However, adiabatic heating could manifest as an increase in volume fraction of the beta phase due to α to β phase transformation that occurred with increasing temperature (Yang *et al.*, 2011; Zhan *et al.*, 2015). It could also manifest as an increase in the size of the primary α grains.

The micrographs in Figures 6.14 and 6.15 show that there was abnormal grain growth of some alpha grains at strain rates of 1 and 10 s^{-1} and the low deformation temperature of 800°C. There was less grain growth at higher deformation temperatures. This indicated that the abnormal grain growth of these alpha grains may have been caused by deformation heating, and became less apparent as the deformation heating effect became negligible at higher testing temperatures. At 800°C, there was no excessive alpha grain growth at the lowest strain rate of 0.01 s^{-1} (Figure 6.13). Grain growth and phase transformation are influenced by temperature and time, and the energy required for grain growth and globularisation is lower than the energy required for the alpha to beta phase transformation (Ding *et al*., 2002; Humphreys and Hatherly, 2002). Therefore, the actual temperature increase due to deformation heating of the samples may have favoured grain growth of the alpha phase, especially at the strain rate of 0.01 s^{-1}. However, this seems very unlikely at the higher strain rates of 1 s^{-1} and 10 s^{-1}, since grain growth is a diffusion-driven process which is time-dependent. The time involved at these strain rates would have been too short for grain growth to occur.

The appearance of abnormal grain growth has been reported in metallic materials, especially aluminium alloys that are subjected to post-deformation annealing and the phenomenon has been attributed to the presence of second-phase precipitates or impurities of high concentations, high anisotropies in the grain boundary energy and high chemical inequilibrum (Humphreys and Hatherly, 2002; Chang *et al.*, 2010). There are no evidences to prove that any of the above-mentioned causes led to the appearance of abnormal grain growth in the Ti-6Al-4V alloys deformed at low temperature (800°C) and high strain rates (1 s^{-1} and 10 s^{-1}). However, it is thought that the appearance of the abnormal grain growth may possibly be favoured by variations in the grain boundary energy of the alpha grains at high strain rates rather than strain induced phase transformation of alpha to beta.

6.5.3 Phase Transformation

Table 6.2 lists the volume fraction of beta phase obtained by image analysis from the micrographs in Figures 6.13 - 6.15. The volume fraction of beta phase increased with increasing temperature at a given strain rate. Ding *et al*. (2002), Momeni and Abbasi (2010) and Souza *et al*. (2015) found that the alpha to beta phase transformation occurred simultaneously with either dynamic recrystallisation or dynamic recovery during deformation of the Ti-6Al-4V alloys below the beta transus temperature.

The relationship between the formed beta phase and applied strain rates did not follow a consistent trend at deformation temperatures below 950°C. However, at 950°C (Figure 6.16), the volume fraction of beta phase increased with decreasing strain rate. At 950°C/0.01 s^{-1}, the microstructure (Figure 6.13d) consisted only of transformed β (α′ martensite) that formed on cooling to room temperature. It is assumed that the volume fraction of α′ martensite equalled that of the beta phase prior to cooling (Yang *et al*., 1991). The temperature profile of the sample deformed at 950°C/0.01 s^{-1} is presented in Appendix F-2, where it can be seen that the temperature was approximately 948°C. This was done to assess whether the temperature control of the Gleeble was giving a misleading result, as the reported values for the beta transus temperature of Ti-6Al 4V is usually in the range of 980-1015°C.

Table 6.2: Volume fraction of beta phase at different temperatures and strain rates.

Temperature (°C)	Volume fraction of β phase (%)		
	0.01 s^{-1}	**1 s^{-1}**	**10 s^{-1}**
800	32	24	29
850	30	31	31
900	33	37	34
950	100	71	64

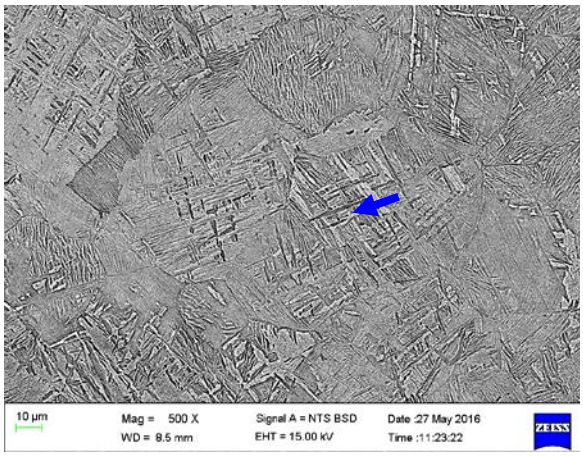

a) 100% transformed β

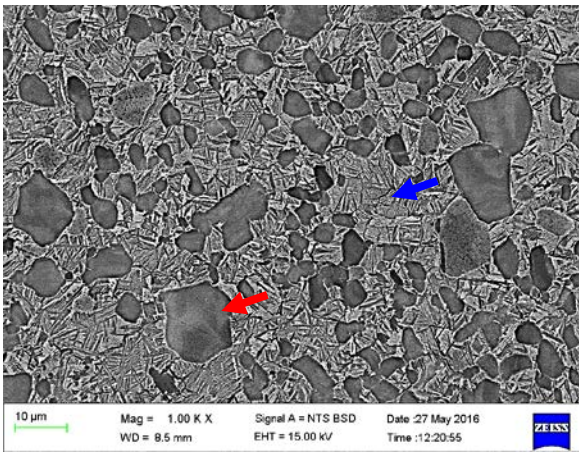

b) Dark phase: globular α and light region: transformed β

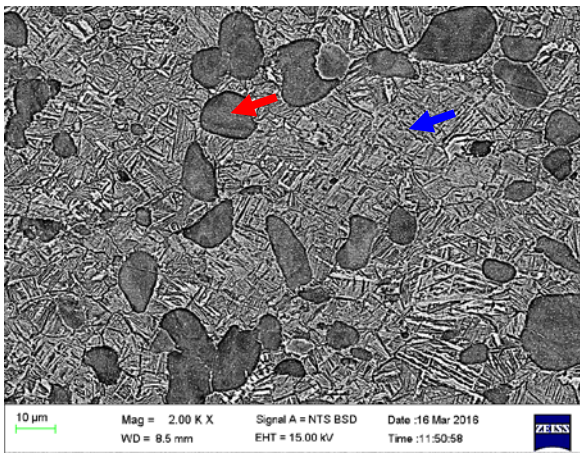

c)

Figure 6.16: SEM-BSE images of Ti-6Al-4V samples deformed at 950°C at strain rates of a) 0.01 s^{-1} b) 1 s^{-1} and c) 10 s^{-1} showing primary α (globular - red arrow) and transformed β - blue arrow.

The complete transformation observed in Figures 6.13d and 6.16a suggests that the deformation lowered the beta transus temperature of the Ti-6Al-4V alloy by ~45°C. Koike *et al.* (2000) reported that the beta transus temperature in a Ti-5.3Al-1.4Fe α+β alloy was decreased by 21°C when subjected to superplastic deformation in the (α+β) phase region. This phenomenon is referred to as deformation (strain) induced phase transformation (Roberts *et al.*, 1970; Koike *et al.*, 2000; Yang *et al.*, 1991). Deformation promotes the diffusion of elements that stabilise the β phase, hence reducing the β-transus temperature (Roberts *et al.*, 1970; Koike *et al.*, 2000; Yang *et al.*, 1991). Deformation-induced phase transformation usually occurs only under certain conditions of strain rates and deformation temperature. Based on Roberts *et al.* (1970) and Yang *et al.* (1991), and the deductions from this current study, it can be concluded that this phenomenon occurred mostly at low strain rates (≤0.01 s^{-1}) in Ti-6Al-4V, as there was enough time for complete alpha to beta transformation.

Deformation induced phase transformation of α+β titanium alloys at a low strain rate involves two concurrent processes (Roberts *et al.*, 1970; Yang *et al.*, 1991):

- The first process is controlled by strain, and involves shearing of elongated α grains into smaller grains which reduces the diffusion distance of beta-stabilising elements and generates vacancies for the solute beta-stabilising elements (vanadium, iron, molybdenum etc.) to occupy.
- The second process is driven by deformation temperature, and involves an increase in the mobility of the beta stabilising elements which increases with increasing temperature.

At a strain rate of 0.01 s^{-1}, strain induced transformation was not as apparent in samples deformed at lower deformation temperatures < 950°C (Figures 6.13a - c) as in samples deformed at 950°C

(Figure 6.13d). This may be due to slow diffusion of vanadium at lower deformation temperatures.

6.6 Summary

The stress-strain behaviour showed a dependence of flow stress on strain rate, deformation temperature and strain. Oscillation of flow stresses was seen after the peak stress at higher strain rates. Continuous flow softening occurred at all strain rates and deformation temperatures below 950°C. These trends show the general transient behaviour of flow stress under varied deformation conditions.

Processing maps revealed stable processing regions at total strains of 0.2, 0.5 and 0.6. These regions were validated by testing at 920°C/1 s^{-1} (0.2 strain) and 950°C/1 s^{-1} (0.6 strain), while regions of instability were identified at strains of 0.5 and 0.6, at temperatures higher than 935°C and strain rates of 0.05 - 0.1 s^{-1}. The region of instability was validated by the test done at 950°C/0.1 s^{-1}. Additionally, another unstable deformation region was observed at 750 - 810°C /1 - 2.7 s^{-1} at a strain of 0.6. These regions should be avoided during processing of Ti-6Al-4V with a complex initial microstructure. Three optimum processing conditions for stable deformation were found to be:

~940°C/0.4 - 1.7 s^{-1} ($\varepsilon = 0.2$; $\eta = 49\%$)

~945°C/0.4 - 1.7 s^{-1} ($\varepsilon = 0.5$; $\eta = 67\%$)

~940-950°C/0.4 - 1.7 s^{-1}($\varepsilon = 0.6$; $\eta = 76\%$).

These optimum processing conditions were interpolated data obtained from the processing maps.

The transient flow stress behaviour caused differences in the processing maps obtained at different strains. Since similar features have not been reported in work on Ti-6Al-4V with fully lamellar or with fully equiaxed initial microstructures, the transient behaviour can be attributed to the complex initial microstructure of the Ti-6Al-4V alloy considered in this study.

Microstructural analysis showed that dynamic globularisation of alpha was the dominant softening mechanism during the deformation of the alloy under optimum conditions. Other phenomena which contributed to softening include deformation heating and phase transformation. It was difficult to explain the reason why grain growth was observed in samples deformed at temperatures below 900°C and high strain rates (1 and 10 s^{-1}). This observation was explained by nucleation controlled DRX (Sakai and Jonas, 1984) and deformation heating, but further studies may be required to provide an accurate explanation. Deformation-induced phase

transformation lowered the beta transus by approximately 45°C when the Ti-6Al-4V alloy was deformed at 950°C and 0.01 s^{-1} strain rate. Increasing the deformation temperature led to higher volume fractions of the beta phase but the influence of strain rate on the volume fraction of beta phase formed was inconsistent.

Chapter 7: Hot working of experimental Ti-6Al-1V-3Fe and Ti-4.5Al-1V-3Fe alloys

This chapter presents the results obtained from isothermal hot compression testing of the two selected experimental alloys containing 1 wt% V and 3 wt% Fe: Ti-6Al-1V-3Fe and Ti-4.5Al-1V-3Fe. The microstructural characteristics and corrosion behaviour of these alloys were reported in Chapters 4 and 5. These two alloys were selected because of their higher ratio of iron to vanadium and their good corrosion resistance in both acidic and saline environments. The results presented in this chapter will be useful in addressing some of the challenges faced by the metal processing industries during primary conversion of titanium alloys to mill products. The results include analysis of flow stress, development of processing maps and microstructural evolution of the deformed samples.

7.1 Scope

This chapter is divided into five sections. Section 7.2 describes the stress-strain curves obtained from the isothermal compression testing and the correction for adiabatic heating. Section 7.3 describes the use of stress-strain data in developing processing maps for obtaining the optimum processing parameters for deforming the alloys. Section 7.4 shows the microstructural evolution which resulted from the deformation process. Finally, the summary of results is presented in Section 7.5.

7.2 Analysis of flow stress for experimental Ti-Al-V-Fe alloys

The flow stress curves obtained from isothermal compression testing of Ti-6Al-1V-3Fe and Ti-4.5Al-1V-3Fe alloys at different strain rates and deformation temperatures are presented in Figure 7.1 (Ti-6Al-1V-3Fe) and Figure 7.2 (Ti-4.5Al-1V-3Fe)**.** In general, the flow stress increased with increasing strain rate and decreasing deformation temperature for both alloys. The relationship between flow stress and strain rate was explained by Mitchell *et al*. (2002) and Zong *et al*. (2009). This is described in Equation 7.1 and Equation 7.2 where an increase in strain rate will result in an increase in the speed of mobile dislocations, as well as the flow stress.

$$\dot{\varepsilon} = \rho b A \sigma^m \qquad \textbf{Equation 7.1}$$

$$v = A\sigma^m \qquad \textbf{Equation 7.2}$$

where $\dot{\varepsilon}$ is strain rate, ρ is dislocation density, b is burgers vector, v is average dislocation velocity, A is a constant, σ is flow stress and m is strain rate sensitivity parameter (Mitchell *et al.*, 2002).

As seen in the Ti-6Al-1V-3Fe samples in Figure 7.1, at low strain <0.05, there was a rapid increase in flow stress. This was due to generation and multiplication of dislocations which work hardened the material (Chen and Cao, 2012). With further increase in strain beyond 0.05, the flow stress dropped continuously or assumed a near steady-state due to flow softening. Similar stress-strain behaviour has been reported by Balasubrahmanyam and Prasad (2002) and Zhang *et al.* (2012). Continuous flow softening occurs when the rate of softening exceeds the rate of work hardening, while steady-state flow stress is observed when the rate of work hardening is at equilibrium with the rate of flow softening (Guo-Zheng *et al*., 2013; Sakai *et al*., 2014).

The distinct features on the flow curves in Figure 7.1 include continuous flow softening at temperatures less than 950°C and all strain rates. However, at 950°C and for all strain rates, the flow stress attained a near steady-state after the peak stress was reached. At a constant strain rate of 10 s^{-1} and all temperatures, broad peaks were observed. The peaks became narrower at lower strain rates.

The flow curves of samples deformed at 1 s^{-1} showed slight oscillations at all deformation temperatures, while the samples deformed at 0.01 and 0.001s^{-1} showed discontinuous yielding at all deformation temperatures. This behaviour was quite apparent at a strain rate of 0.01 s^{-1}, with a rapid increase in flow stress until a sharp distinct peak at very low strain, followed by a second peak stress prior to flow softening. As discussed in Chapter 6, this discontinuous yielding phenomenon has not been reported in pure titanium or commercial Ti-6Al-4V alloys deformed in the beta phase, but has been found in beta titanium alloys (Philippart and Rack, 1998; Weiss and Semiatin, 1998; Balasubrahmanyam and Prasad, 2002). The magnitude of discontinuous yielding has been attributed to the type and concentration of the beta stabilising elements (Weiss and Semiatin, 1998).

However, in this case, the discontinuous yielding was not caused by microstructural phenomena, but was due to a change in strain rate at a low strain of ~0.02. This was similar to the case of the Ti-6Al-4V alloy mentioned in Chapter 6 where actual strain rates higher than the planned strain rates were observed at a strain of ~0.02. The high strain rates at the start of deformation led to the sharp initial peaks observed on the flow curves. An example of the strain *vs.* time profile showing the higher strain rate at ~0.02 is presented in Appendix H-8. This change in strain rate was noticeable when all the alloys were compression tested at ≤0.01 s^{-1}. Although the overall strain rate was not affected by this variation, the misleading initial peaks were definitely not a consequence of microstructural response to the imposed parameters, but were likely due to variations in the movement of the hydraulics controlling the jaws.

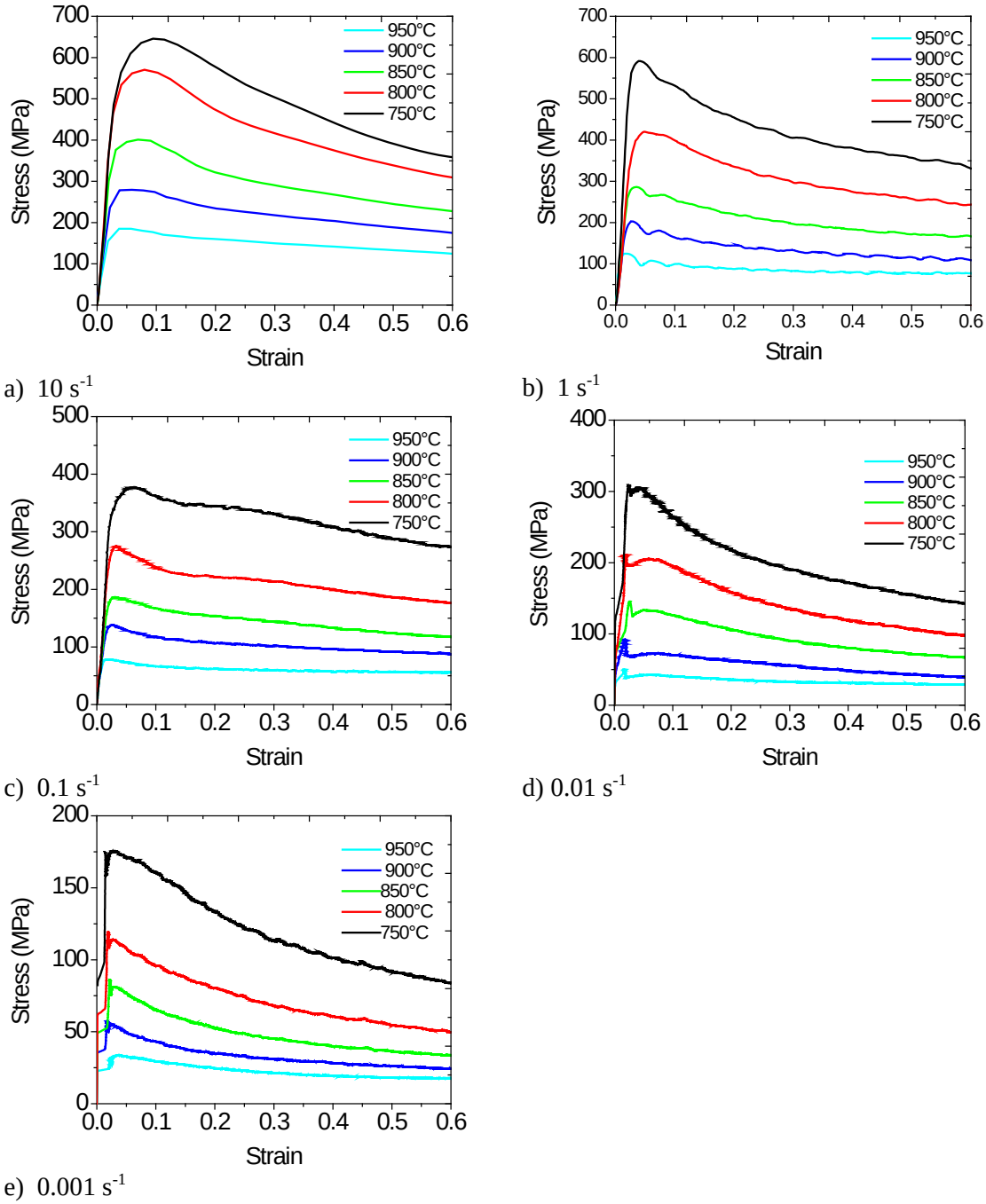

Figure 7.1: True stress-strain curves obtained by rectangular axial compression testing of Ti-6Al-1V-3Fe in the temperature range of 750 - 950°C and at strain rates of: a) 10 s^{-1}, b) 1 s^{-1}, c) 0.1 s^{-1}, d) 0.01 s^{-1} and e) 0.001 s^{-1}.

Figure 7.2 shows the stress-strain curves for Ti-4.5Al-1V-3Fe alloy at different strain rates and deformation temperatures. The trends of the curves were similar and comparable to Ti-6Al-1V-3Fe (Figure 7.1) at all temperatures and strain rates. However, the major difference in the flow curves of the two alloys was that the reduction in aluminium content from 6 wt% to 4.5wt% Al decreased the flow stress under all deformation conditions. Additionally, the sample deformed at 950°C and 0.001 s^{-1} showed unexpected behaviour at strains of 0.48 - 0.6. There was an abrupt

increase in flow stress accompanied by oscillations. This behaviour could be as a result of flow instabilities manifesting during deformation (T Seshacharyulu *et al.*, 2000).

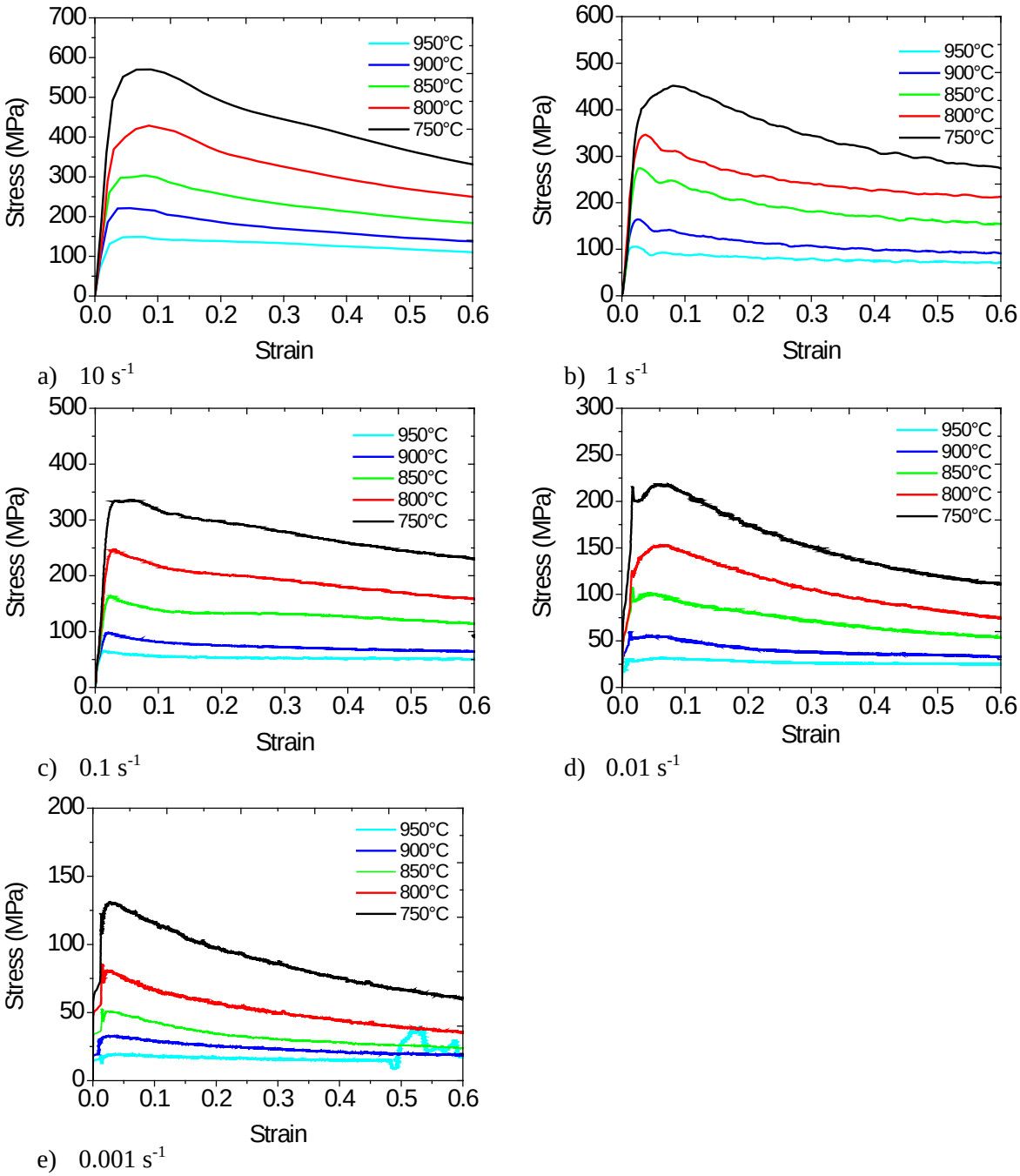

Figure 7.2: True stress-strain curves obtained by rectangular axial compression testing of Ti-4.5Al-1V-3Fe in the temperature range of 750 - 950°C and at strain rates of: a) 10 s^{-1}, b) 1 s^{-1}, c) 0.1 s^{-1}, d) 0.01 s^{-1} and e) 0.001 s^{-1}.

The influence of test parameters on the peak flow stress of both alloys shown in Figure 7.3. The peak stress generally decreased with a reduction in aluminium content under all deformation conditions, except at 950°C and 0.001 s^{-1} (Figure 7.3 b), where a higher peak stress and peak strain was observed. Increasing the aluminium content in titanium alloys has been shown to

increase the flow stress of the alloys due to substitutional solid solution strengthening (Weiss and Semiatin, 1998; Fitzner *et al.*, 2016).

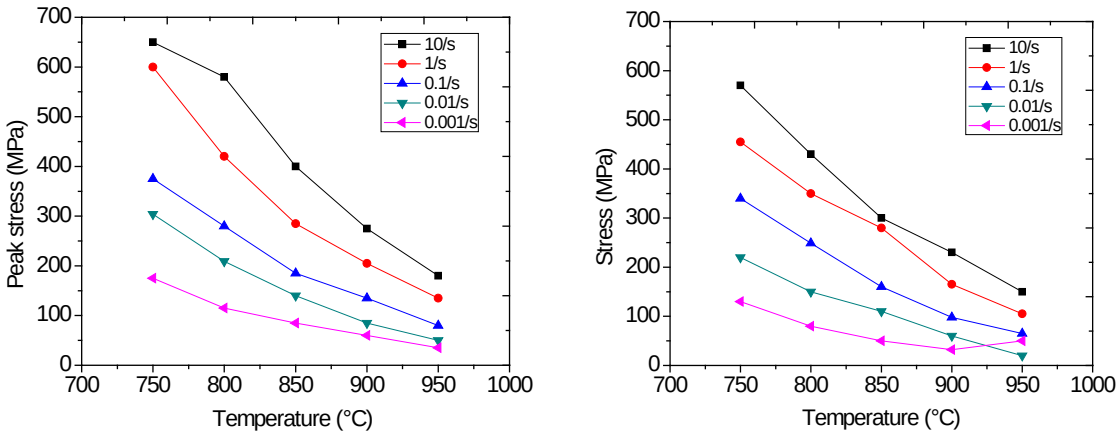

a) Ti-6Al-1V-3Fe b) Ti-4.5Al-1V-3Fe

Figure 7.3: The effect of testing temperature and strain rate on the peak stress of: a) Ti-6Al-1V-3Fe and b) Ti-4.5Al-1V-3Fe alloys.

Weiss and Semiatin (1998) compared the influence of the total amount of solute elements on the flow behaviour of beta titanium alloys, showing that alloys with a higher solute content had a higher flow stress. The higher aluminium content and the total solute elements in Ti-6Al-1V-3Fe favoured higher peak stresses compared with Ti-4.5Al-1V-3Fe. Semiatin *et al.* (1997) reported that the flow stress is dependent on strain, strain rate, deformation temperature and alloy composition. In the preliminary studies of this work, varying the amount of Fe in the Ti-6Al-*x*V-*y*Fe experimental alloys influenced the flow stress (Prozesky *et al.*, 2017). At a deformation temperature of 900°C and strain rate of 1 s^{-1}, partial substitution of vanadium with iron caused a significant drop in flow stress, which was attributed to the higher proportion of β phase in the iron-added alloys. It was also found that flow softening was influenced by adiabatic shear bands, lamellar rotation and dynamic recrystallisation of the prior beta grains. The formation of adiabatic shear bands in the Ti-6Al-*x*V-*y*Fe experimental alloys increased with an increase in the total deformation strain (Appendix H).

Apart from the effects of solute content on the flow stress of titanium alloys, another critical factor that affects the flow stress is the initial microstructure before deformation (Prasad and Seshacharyulu, 1998b; Perumal *et al.*, 2016). In this study, the flow stress of the Ti-6Al-1V-3Fe experimental alloy was higher than those of the commercial Ti-6Al-4V alloy presented in Chapter 6 and other commercial α+β titanium alloys (Seshacharyulu *et al.*, 2000; Seshacharyulu *et al.*, 2002). In the current study, the as-cast experimental alloys had an initial Widmanstätten basket-weave structure (Figure 7.6). The wrought commercial Ti-6Al-4V alloy investigated in Chapter 6 had a complex initial microstructure (Figure 6.8), which consisted of mostly coarse, elongated

alpha grains, partially equiaxed alpha and a network of intergranular beta. Sechacharyulu *et al*. (2002) found that the flow stress of a lamellar microstructure was higher than that of an equiaxed microstructure in Ti-6Al-4V deformed under similar conditions. Li *et al.*(2013) evaluated the influence of thin and thick lamellae on the flow stress of a Ti-5Al-5Mo-5 V-1Cr-1Fe near-β titanium alloy, and found that the flow stress was higher for thicker lamellae when deformed under the same conditions.

The higher flow stress observed in the experimental Ti-6Al-1V-3Fe alloy than in the commercial Ti-6Al-4V alloys can be attributed to the initial basket-weave Widmanstätten initial microstructure. Sieniawski *et al.* (2013) found two-phase titanium alloys with a basket-weave Widmanstätten structure exhibited higher strength than those with either equiaxed or colony structures. This was ascribed to dislocations finding it more difficult to move due to the increased branching in the basket-weave structure.

The shape of the stress-strain curves have been used to suggest the various softening mechanisms dominating the deformation of metallic alloys. In Figure 7.1 and 7.2, the flow curves show work hardening by the increase in stress at low strains. Also, broad peaks were observed at the high strain rate of 10 s^{-1}, which could be attributed to dynamic recrystallisation or globularisation of either one or both constituent phases. The near steady-state stress at the highest deformation temperature could have been due to dynamic recovery or superplasticity, while continuous flow softening observed at lower deformation temperatures could have been a result of dynamic globularisation or manifestation of flow instabilities, such as adiabatic shear bands or cracking. Continuous flow softening indicates dynamic globularisation of titanium alloys with a fully lamellar or an acicular initial microstructure (Wu *et al.*, 2011; Li *et al.*, 2013; Song *et al.*, 2014). The oscillations at 1 s^{-1} could be due to dynamic recrystallisation or cracking in the material (Bai *et al.*, 2014). It was quite difficult to determine the exact flow softening mechanism based on the shape of the stress-strain curves. Further analyses would be needed to substantiate the dominant softening mechanism of the alloys during hot working. These are discussed in the subsequent sections.

To obtain a more accurate prediction from processing maps, it is important to correct the flow stress obtained from the experiments for adiabatic heating and frictional effects. The barrelling coefficients of the deformed samples were determined after each compression test to validate the results, and were all less than the maximum permissible limit of 1.1 (Roebuck *et al.*, 2006). Therefore, correction for friction was not done, as the graphite foil and nickel paste between the samples and the anvils provided sufficient lubrication to mitigate friction during deformation.

7.2.1 Adiabatic corrections

The flow stress obtained from isothermal compression testing was corrected for adiabatic heating following the procedure explained in Chapter 6. Adiabatic heating was observed in Ti-6Al-1V-3Fe and Ti-4.5Al-1V-3Fe samples deformed at temperatures <950°C and strain rates of 1 s^{-1} and 10 s^{-1}. Figure 7.4 shows selected plots of measured and programmed temperatures against strain for Ti-6Al-1V-3Fe and Ti-4.5Al-1V-3Fe. From Figure 7.4a, for Ti-6Al-1V-3Fe deformed at 750°C and a strain rate of 10 s^{-1}, there was a rise in deformation temperature to ~810°C as the strain increased. Similarly, in Ti-4.5Al-1V-3Fe a temperature rise of ~33°C was observed in the sample deformed at 800°C and a strain rate of 1 s^{-1}. As the temperature rise had a significant effect on the flow stress, adiabatic correction was necessary.

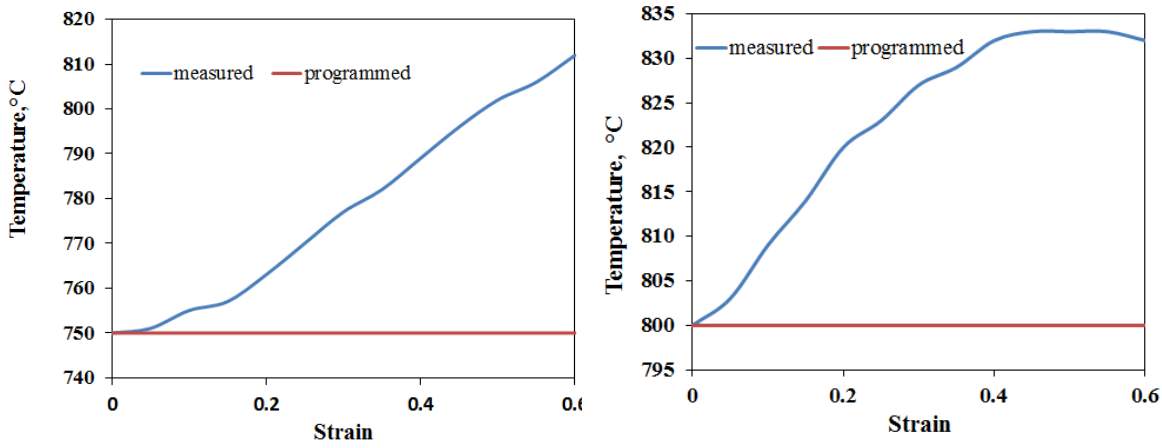

a) Ti-6Al-1V-3Fe at 750°C/10 s^{-1} b) Ti-4.5Al-1V-3Fe at 800°C/1 s^{-1}

Figure 7.4: Measured and programmed temperature against strain for (a) Ti-6Al-1V-3Fe at 750°C/10 s^{-1} and (b) Ti-4.5Al-1V-3Fe at 800°C/1 s^{-1}.

Figure 7.5 show the comparison between the measured and corrected flow stresses in Ti-6Al-1V-3Fe and Ti-4.5Al-1V-3Fe alloys. As expected, the corrected flow stress was higher than the measured stress, due to the influence of adiabatic heating on the flow stress. Also, the corrected flow stress still exhibited continuous flow softening, which implies that flow softening mechanisms other than adiabatic heating were in operation. Graphs for the other testing conditions which also show temperature increase and corrected flow stresses against strain are presented in Appendix H.

The validity of processing maps depends largely on the accuracy of the flow stress (Prasad *et al.*, 2015). The corrected flow stresses used for developing the processing maps are presented in Appendix H. Having corrected the flow stress, the processing maps could be established with higher accuracy.

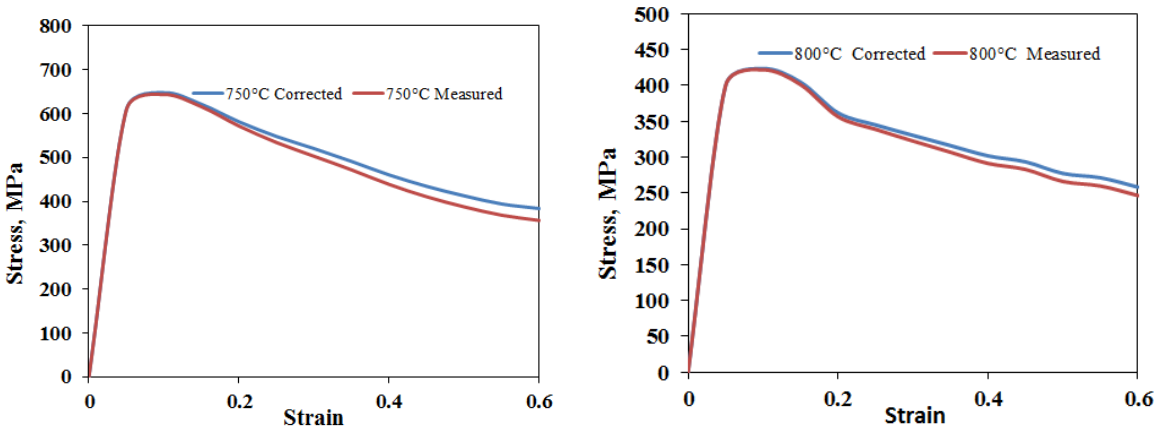

a) Ti-6Al-1V-3Fe at 750°C/10s^{-1} b) Ti-4.5Al-1V-3Fe at 800°C/1s^{-1}

Figure 7.5: Corrected and measured flow stress as a function of strain for: a) Ti-6Al-1V-3Fe at 750°C/10 s^{-1} and b) Ti-4.5Al-1V-3Fe at 800°C/1 s^{-1}.

7.3 Processing maps and validation

In Chapter 6, processing maps were used to establish the 'safe' and 'unsafe' deformation regions in commercial Ti-6Al-4V with a complex initial microstructure. In this section, the processing maps for the experimental Ti-6Al-1V-3Fe and Ti-4.5Al-1V-3Fe alloys are presented.

7.3.1 Power dissipation maps

The optimum processing conditions for hot working of Ti-6Al-1V-3Fe and Ti-4.5Al-1V-3Fe alloys were determined from the power dissipation efficiency maps presented in Figures 7.6 and 7.7. As mentioned in Section 2.3.4, during deformation, the workpiece responds to the imposed working parameters (strain rate, strain and temperature) by dissipating power in the form of heat and microstructural evolution. The power dissipated as heat is usually larger than that of the microstructural changes occurring in the workpiece during deformation (Prasad *et al.*, 1984, 2015). The strain rate sensitivity parameter (m) describes the power dissipated as heat and as microstructural evolution in the workpiece. The efficiency of power dissipation is therefore obtained solely from the strain rate sensitivity parameter, as described in Equation 3.3.

The power dissipation efficiencies of the two alloys resulting from the different deformation parameters are represented on the power dissipation maps in Figures 7.6 and 7.7. The yellow and red areas correspond to regions with the lowest power dissipation, while the white areas correspond to regions with the highest power dissipation efficiencies. The yellow regions with low power dissipation are the regions where hot workability is poor while the white regions are considered as the regions with optimum conditions for hot workability of the alloys. The optimum

working conditions for the alloys at each strain are summarised in Table 7.1 (Ti-6Al-1V-3Fe) and Table 7.2 (Ti-4.5Al-1V-3Fe).

The power dissipation efficiency values were correlated with the microstructural manifestation in deformed samples. For titanium alloys, power dissipation efficiency values between 35% and 50% are typical of dynamic recrystallisation or globularisation, while superplasticity and dynamic globularisation has been reported to dissipate power efficiency above 50% during deformation (Prasad, 2003; Prasad *et al.*, 2015). Power dissipation efficiency between 20% and 30% correspond to dynamic recovery, while power dissipation efficiency less than 20% indicated possible flow instability (Prasad *et al.*, 2015). The regions on the maps (Figures 7.6 and 7.7) shaded in green and white have power dissipation efficiency values greater than 35%, hence dynamic recrystallisation and/or globularisation would be the expected microstructural manifestation. However, the cyan and magenta regions are the domains of dynamic recovery.

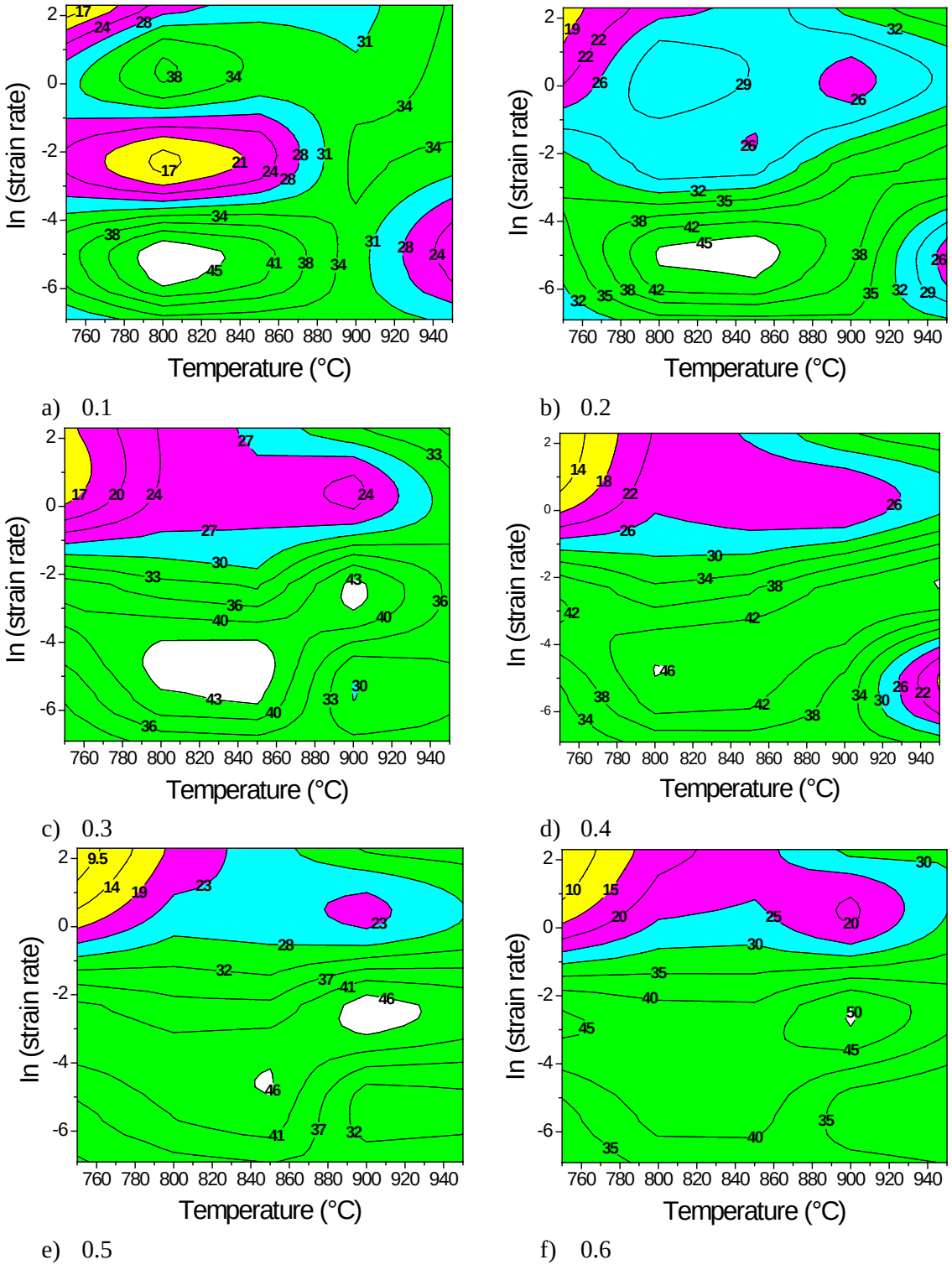

Power efficiency			
	<20	Poor hot workability	Lowest
	20-30	DRV	
	20-30	DRV	
	=30<35	DRV	
	>35	DRX	
	>35	DRX	Highest

Figure 7.6: Power dissipation efficiency maps for Ti-6Al-1V-3Fe alloys at a strain of: a) 0.1, b) 0.2, c) 0.3, d) 0.4, e) 0.5 and f) 0.6.

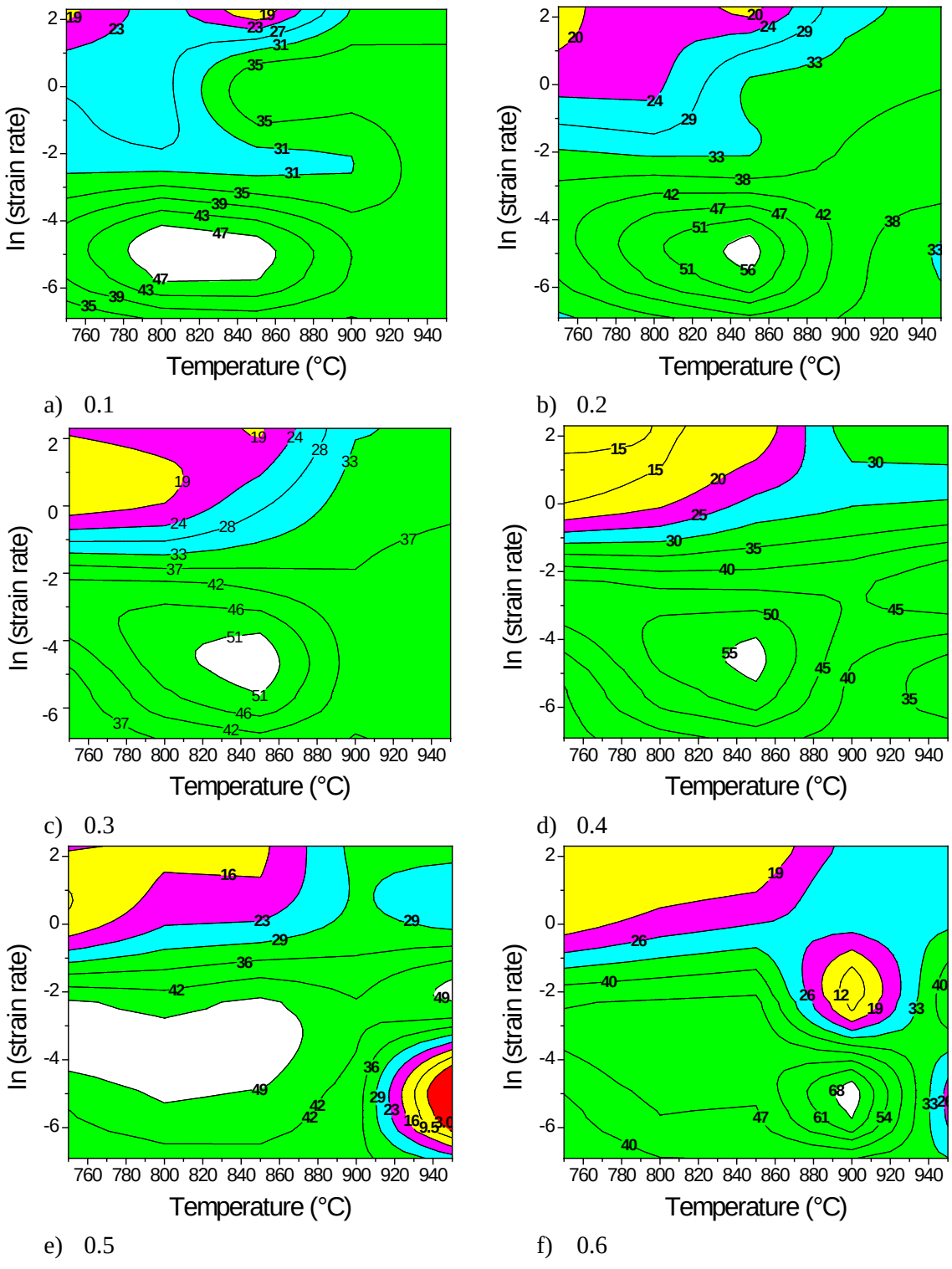

Power efficiency			
	<0	Instability	Lowest
	<20	Poor hot workability	
	20-30	DRV	
	20-30	DRV	
	=30<35	DRV	
	>35	DRX	
	>30	DRX	Highest

Figure 7.7: Power dissipation efficiency maps for Ti-4.5Al-1V-3Fe alloys at a strain of: a) 0.1, b) 0.2, c) 0.3, d) 0.4, e) 0.5 and f) 0.6.

Table 7.1: Interpretation of the power efficiency map and optimum working conditions for the Ti-6Al-1V-3Fe alloy.

Strain	Optimum working temperature and strain rate
0.1	770 - 830 °C / 0.003 - 0.01 s^{-1}
0.2	800 - 860 °C / 0.003 - 0.01 s^{-1}
0.3	770 - 855 °C / 0.003 - 0.02 s^{-1} and 895 - 995°C / 0.07 - 0.1 s^{-1}
0.4	800°C / 0.01 s^{-1}
0.5	845 - 850°C / 0.01 - 0.02 s^{-1} and 885 - 930°C / 0.07-0.1 s^{-1}
0.6	900°C / 0.1 s^{-1}

Table 7.2: Interpretation of the power efficiency map and optimum working conditions for the Ti-4.5Al-1V-3Fe alloy.

Strain	Optimum working temperature and strain rate
0.1	785 - 855 °C / 0.003 - 0.01 s^{-1}
0.2	840 - 853 °C / 0.004 - 0.01 s^{-1}
0.3	820 - 860 °C / 0.004 - 0.02 s^{-1}
0.4	835 - 853 °C / 0.005 - 0.02 s^{-1}
0.5	750 - 865°C / 0.01 - 0.1 s^{-1} and 940 - 950°C / 0.1 s^{-1}
0.6	890 - 900 °C / 0.003 - 0.008 s^{-1}

7.3.2 Prediction of instability domain at a strain of 0.6

Processing maps are obtained by the superimposition of power dissipation and instability maps. The instability map helps to delineate the safe and unsafe regions during hot working (Prasad *et al*., 2015). As mentioned in Section 2.3.4, increased power dissipation efficiency shows improved workability of a material and it is expected that domains of high dissipation efficiency should be free from instabilities like shear bands, flow localisation and kink bands. In contrast, Murty *et al.* (2002) and Prasad *et al.* (2015) reported that instabilities like wedge cracking or flow localisation could manifest in a region with high dissipation efficiency.

The criteria for identifying the domain of instability during hot working have been described earlier in Sections 2.3.4 and 3.7.1. In this study, Murty's instability criterion (Murty *et al*., 2002) was adopted to delineate the safe and unsafe deformation regions for the Ti-6Al-1V-3Fe and Ti-4.5Al-1V-3Fe experimental alloys. This criterion was selected based on its reliability to predict unstable regions for a wide range of metallic alloys (Ma *et al*., 2012b). The instability maps obtained for each alloy at strains of 0.1 - 0.6 are presented in Appendix H. Sen *et al*. (2007) reported that the instability domain in titanium alloys is influenced by the total strain. Similar to the observation made about Ti-6Al-4V in Chapter 5, the region of instability for these alloys was

also dependent on strain. For Ti-6Al-1V-3Fe, the domain of instability was found at strains of 0.5 and 0.6, while Ti-4.5Al-1V-3Fe exhibited an instability domain from a strain of 0.4 to 0.6.

The processing maps showing the region of unstable deformation in Ti-6Al-1V-3Fe and Ti-4.5Al-1V-3Fe alloys at a total strain of 0.6 are presented in Figure 7.8. Unsafe deformation regions for both alloys occurred in regions shaded in red: 770 - 780°C /1.5 - 10 s^{-1} for Ti-6Al-1V-3Fe; and 875 - 930°C/0.1 - 0.4 s^{-1} for Ti-4.5Al-1V-3Fe. Ma *et al.* (2012a) confirmed that the Prasad and Murty criteria provided accurate and reliable predictions at higher strain rates, but were ineffective in predicting the instability at low strain rates. The processing map for Ti-6Al-1V-3Fe (Figure 7.8a) did not indicate any region of instability at strain rates that are lower than 1 s^{-1}. Therefore, a detailed microstructural evaluation was carried out on selected deformed samples to validate the maps and to identify the unsafe regions not predicted by the instability criteria.

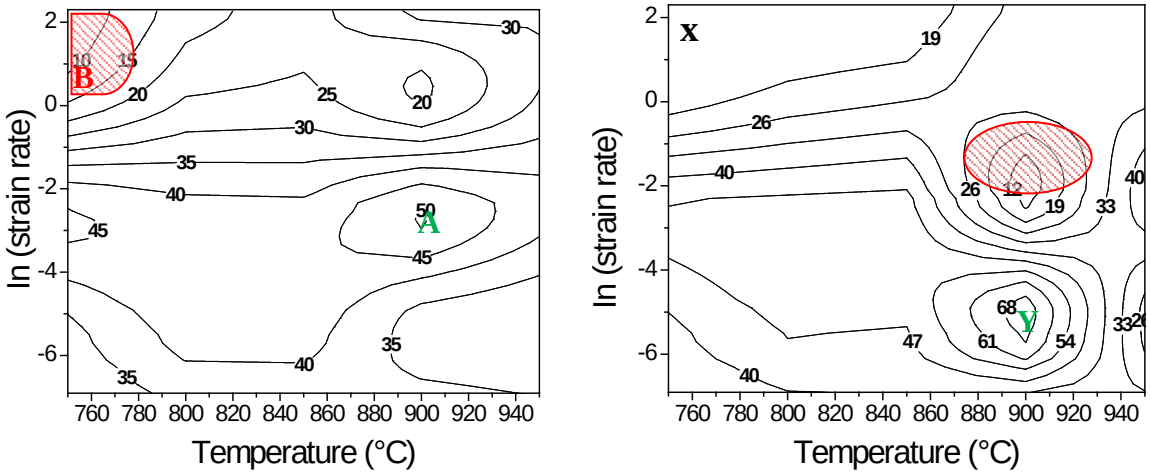

a) Ti-6Al-1V-3Fe b) Ti-4.5Al-1V-3Fe

Figure 7.8: Processing maps at a strain of 0.6 for: a) Ti-6Al-1V-3Fe and b) Ti-4.5Al-1V-3Fe alloys. The red regions are regions of unsafe deformation, A and B are safe regions with the highest dissipation efficiency.

7.3.3 Microstructural validation of the processing maps

The predictions of the processing maps constructed at the strain of 0.6 were validated by carrying out microstructural examinations on selected deformed samples. The deformed samples were selected from regions with high power dissipation efficiency and the unsafe deformation domain. The initial microstructures of the Ti-6Al-1V-3Fe and Ti-4.5Al-1V-3Fe alloys taken as a basis for comparison are presented in Figure 7.9. The initial microstructure of Ti-6Al-1V-3Fe was a basket-weave Widmanstätten structure (Figure 7.9a) having large prior beta grains with diameters of 527 ± 193 µm. The Ti-4.5Al-1V-3Fe alloy consisted of a basket-weave Widmanstätten structure (Figure 7.9c) in large equiaxed prior beta grains with an average grain

diameter of 618 ± 282 μm. The SEM images (Figures 7.9b and d) for both alloys show α plates separated by inter-lamellar β.

The microstructures of the Ti-6Al-1V-3Fe samples deformed in the region with the highest dissipation efficiency of 50% (900°C/0.1 s^{-1}) and the region with the lowest dissipation efficiency of <10% (750°C/10 s^{-1}) are shown in Figure 7.10. These regions correspond to stable "A" and unstable "B" deformation domains. Figure 7.8a shows equiaxed prior beta grains with an average grain diameter of 328 ± 86 μm in the sample corresponding to region A deformation. The equiaxed prior beta grains are diagnostic of dynamic recrystallisation which occurred during isothermal compression testing. Similar microstructural features were seen by Honarmandi and Aghaie-Khafri (2012) for dynamic recrystallization of the prior beta grains in Ti-6Al-4V deformed in the beta phase field.

The SEM-BSE image (Figure 7.10c) was taken at higher magnification so could not show evidence of dynamic recrystallisation of prior beta grains. Also, globularisation of α lamellae was not seen in the SEM-BSE image (Figure 7.10c), indicating that dynamic recrystallisation of the prior beta grains was the dominant softening mechanism at 900°C and 0.1 s^{-1}.

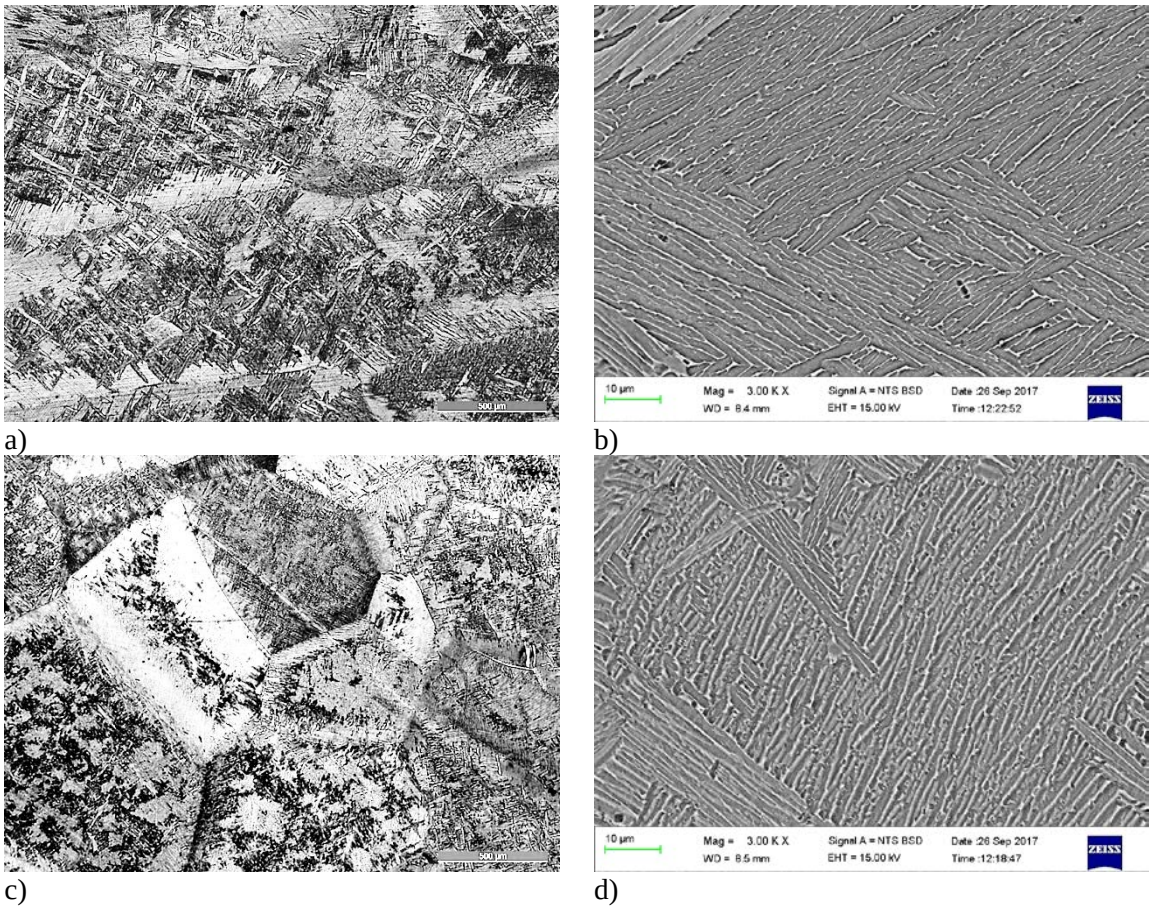

Figure 7.9: Initial microstructures for showing a basket-weave Widmanstätten structure in large prior beta grains. Ti-6Al-1V-3Fe: a) Optical, b) SEM-BSE; and Ti-4.5Al-1V-3Fe: c) optical and d) SEM-BSE.

The occurrence of dynamic recrystallisation within the prior beta grains corroborates the shape of the stress-strain curves (Figure 7.1c), where the flow curves exhibited a broad peak followed by slight oscillations at 900°C and 0.1 s^{-1}. The broad peak has been reported by Guo-Zheng (2013) and Mirzadeh, (2015) to indicate dynamic recrystallisation. Figure 7.10b shows an optical image of the sample corresponding to the unstable B region deformation in Figure 7.8a, featuring instabilities such as adiabatic shear bands, voids and cracks. The SEM-BSE image (Figure 7.10d) also shows the cracks and voids that manifested as instabilities. The microstructural features observed in the deformed alloy are consistent with the information obtained from the processing map in Figure 7.8 a and from Table 7.1**.**

The microstructures of Ti-4.5Al-1V-3Fe samples deformed in different regions on the processing map are presented in Figure 7.11. The microstructure of a sample deformed in region X was taken for comparison with Ti-6Al-1V-3Fe alloy to check for manifestation of instabilities. Figure 7.11a shows the optical micrograph of the sample deformed in region Y (900°C/0.01 s^{-1}), showing the fracture of α lamellae into globules. The SEM-BSE image (Figure 7.11c) shows the presence of fine α-globules in the deformed samples. This confirmed the occurrence of dynamic globularisation as the dominant softening mechanism in that region.

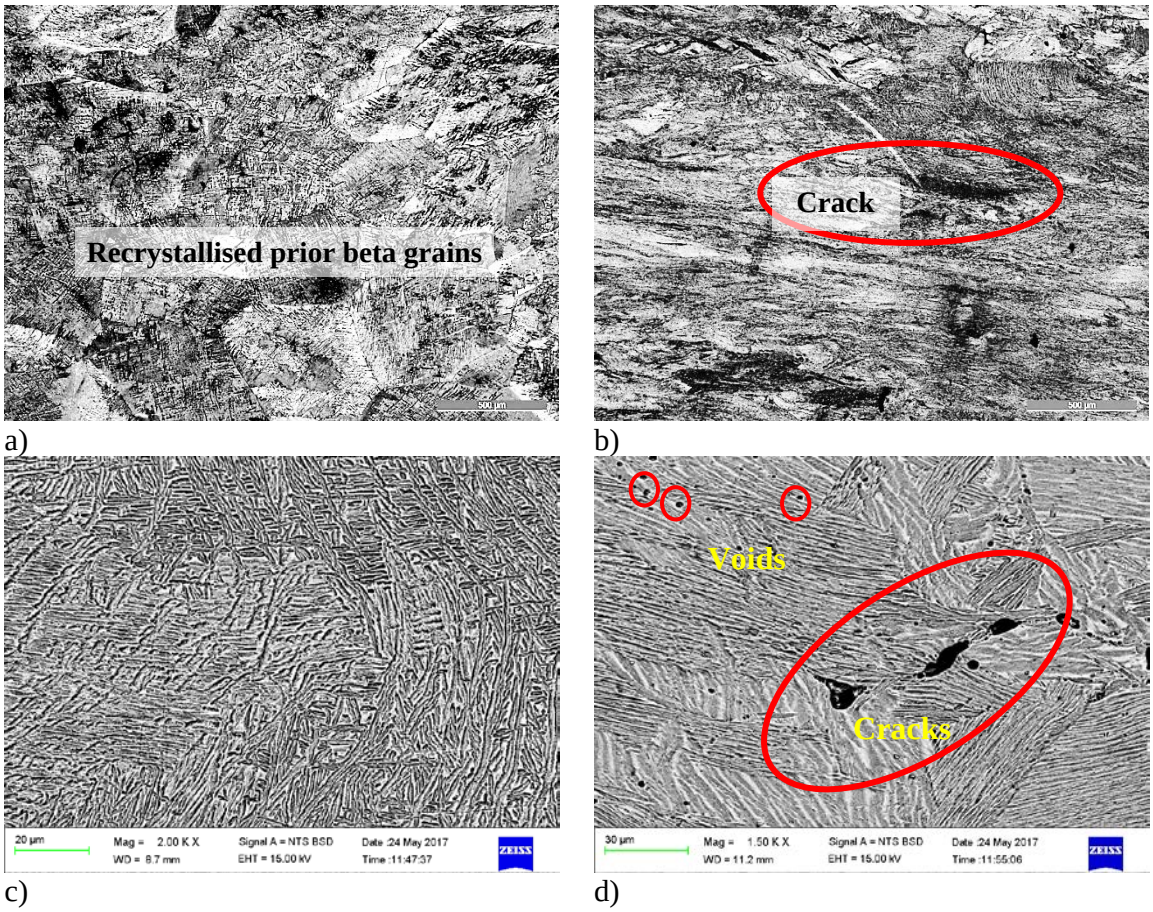

Figure 7.10: Final microstructure of Ti-6Al-1V-3Fe deformed samples. 900°C/0.1 s^{-1}: a) optical c) SEM-BSE , 750°C/10 s^{-1}: b) optical and d) SEM-BSE.

The occurrence of dynamic globularisation seen in the Ti-4.5Al-1V-3Fe alloy was consistent with the predictions of the processing map (Figure 7.8c).

Contrary to the observations in Ti-6Al-1V-3Fe (Figure 7.10a), no evidence of recrystallised prior beta grains was seen in the optical micrograph of Ti-4.5Al-1V-3Fe (Figure 7.11e). Figure 7.11b shows the optical micrograph of the sample deformed in region X, showing voids at the triple junction of the prior beta grains. These voids could be misleading and taken as instability, but the voids at the triple junction seemed to have resulted from casting since there was no evidence of localised shear around the voids. The cracks seen in Figure 7.10 for Ti-6Al-1V-3Fe had kinked lamellae as evidence of localised shear around the cracks. The SEM-BSE image presented in Figure 7.11d did not capture the void at the triple junction; however, tiny voids are seen in the image which could have resulted from casting. The instability map obtained at a strain of 0.6 (Appendix H-5), did not indicate any possibility of instability in the region (750°C/10 s^{-1}), although instability was indicated at 880 - 930°C and 0.1 - 0.3 s^{-1}.

The microstructural validation of the processing maps established a combination of dynamic recrystallisation of prior beta grains and globularisation of alpha grains as the dominant flow softening mechanism when working the alloys in the safe deformation regions. Additionally, the predictive capability of the processing maps established the unsafe deformation regions that should be avoided during hot working of the selected experimental alloys. The microstructural features in the selected deformed samples for both Ti-6Al-1V-3Fe and Ti-4.5Al-1V-3Fe alloys show that the deformation parameters had a significant influence on the hot deformation behaviour. The influence of strain rate and deformation temperature on the microstructural evolution of the deformed alloys was examined, and is presented in Section 7.4.

7.4 Microstructural Evolution

In the previous section it was shown that the deformation parameters had a significant influence on the final microstructure of the deformed Ti-6Al-1V-3Fe and Ti-4.5Al-1V-3Fe samples. This section now examines the individual influence of strain rate and deformation temperature respectively on the final microstructure of the deformed samples.

7.4.1 Influence of deformation temperatures

Figure 7.12 shows the SEM-BSE images of Ti-6Al-1V-3Fe alloys deformed at a strain rate of 10 s^{-1}, but at different deformation temperatures. The microstructure of samples deformed at 750°C and 800°C exhibited severe bending and rotation of α laths, and defects such as voids and cracks were seen. These microstructural features are diagnostic of poor workability of the alloy at those temperatures.

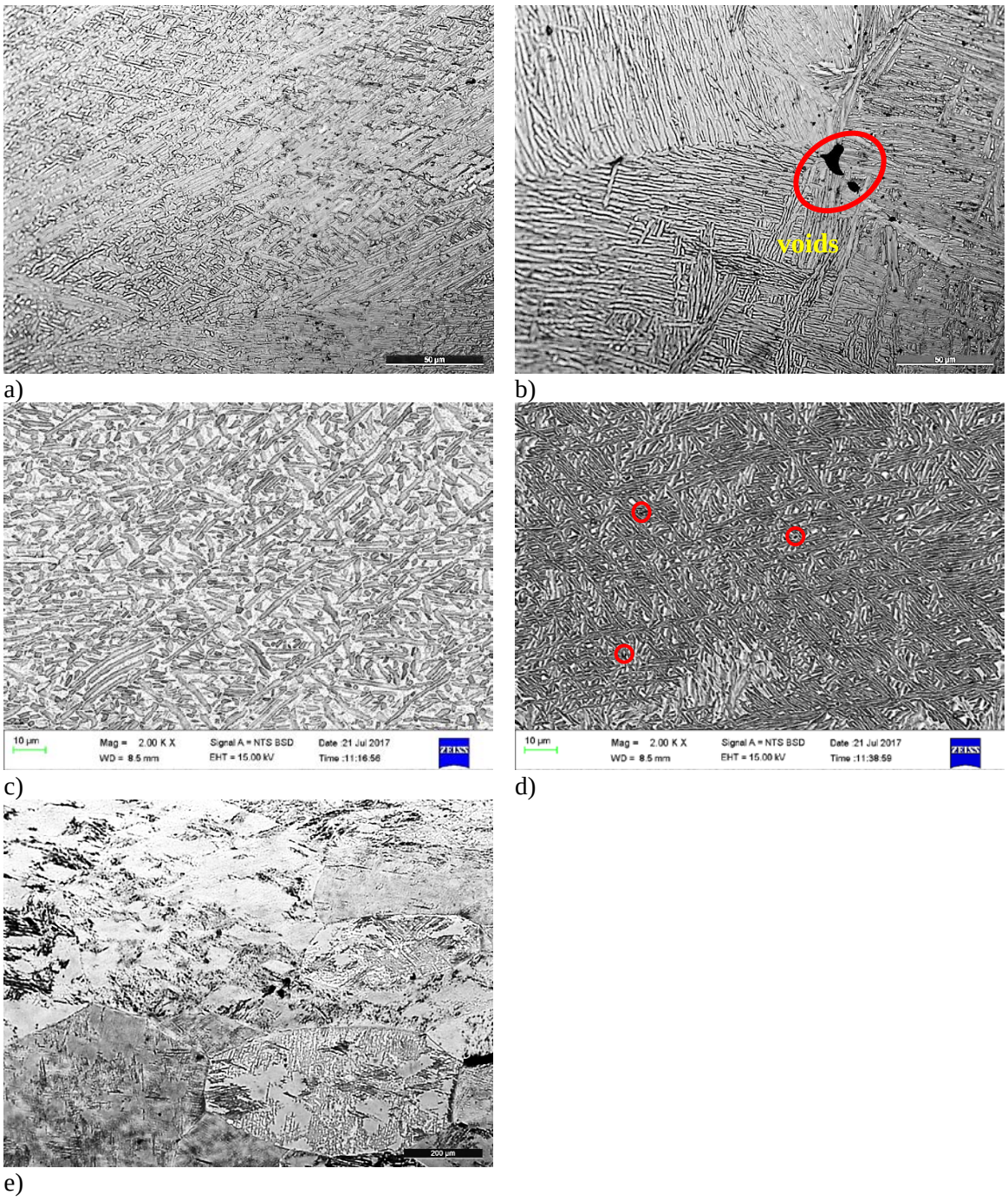

a) b) c) d) e)

Figure 7.11: Final microstructure of deformed samples for Ti-4.5Al-1V-3Fe. 900°C/0.01 s^{-1}: a and e) optical c) SEM-BSE , 750°C/10 s^{-1}: b) optical - and d) SEM-BSE.

A similar observation was made by Secharchayulu *et al.* (2002) for Ti-6Al-4V with a lamellar initial microstructure, where the cracks were dominant at the prior beta grain boundaries. The authors explained that stress concentrations at the prior beta grain boundaries due to sliding of the soft beta phase promoted the localised cracking.

As the deformation temperature increased above 800°C (Figures 7.12c - f), the bending and rotation of the lamellar structures decreased. Also, the defects were not detected in the

microstructure of samples deformed at temperatures higher than 800°C. The reduction in the degree of lath rotation and bending with increasing temperature was attributed to the increased mobility of dislocations with increasing temperature (Fan et al., 2013a).

The power dissipation efficiency values obtained from the processing maps (Figure 7.8a) at temperatures between 800°C and 950°C corresponded to dynamic recovery. At temperatures below 800°C, the movement of dislocations generated at high strain rates were restricted, as found by Fan *et al.* (2013a). This may have caused shearing which bent and rotated the laths. At the highest deformation temperature of 950°C, traces of fractured lamellae were seen which indicated that dynamic globularisation would have started. However, dynamic globularisation was limited by the high strain rate of 10 s^{-1}. Therefore, the dominant softening process in this region would be dynamic recovery, which was seen at 950°C/10 s^{-1} (Figure 7.8a). The microstructural features concur with the prediction of the processing map, which showed a power dissipation efficiency of ~32% and also with the steady-state flow stress seen in Figure 7.1 a.

Figure 7.13 shows the microstructure of Ti-6Al-1V-3Fe samples deformed over the full range of temperatures and at constant strain rate of 0.1 s^{-1}. In Section 7.3, the optimum processing conditions for deforming this alloy to a total strain of 0.6 was at 0.1 s^{-1} and 900°C. Therefore, it became imperative to assess the microstructural evolution at these strain rate and varied temperatures. Bending and rotation of laths was evident at 750°C. As the deformation temperature increased, there was a decrease in the rotation and bending of laths. This was due to increased mobility of dislocations at higher deformation temperatures (Fan *et al.*, 2013a). As mentioned in Section 7.3, dynamic recrystallisation of the prior beta grains was the dominant deformation mechanism for this alloy. This explains why dynamic globularisation of α lamellae was hardly observed when the strain rate decreased from 10 to 0.1s^{-1}. The reduction in defects and the severity of lath rotation with decreasing strain rate indicated that workability of the alloy was improved at low strain rates. Prasad and Seshacharyulu (1998a), Polleti *et al.*(2016) and Balasundar *et al.* (2017) found that the combination of lower strain rates and higher deformation temperatures improved the intrinsic workability of titanium alloys. This was confirmed in Figure 7.13 e for Ti-6Al-1V-3Fe deformed at 950°C and 0.1s^{-1} where the alpha globules were signs of dynamic globularisation. There was more dynamic globularisation at a strain rate of 0.1 s^{-1} than at 10 s^{-1}. The influence of strain rate on the microstructural evolution and workability of the two alloys will be discussed in the following sections.

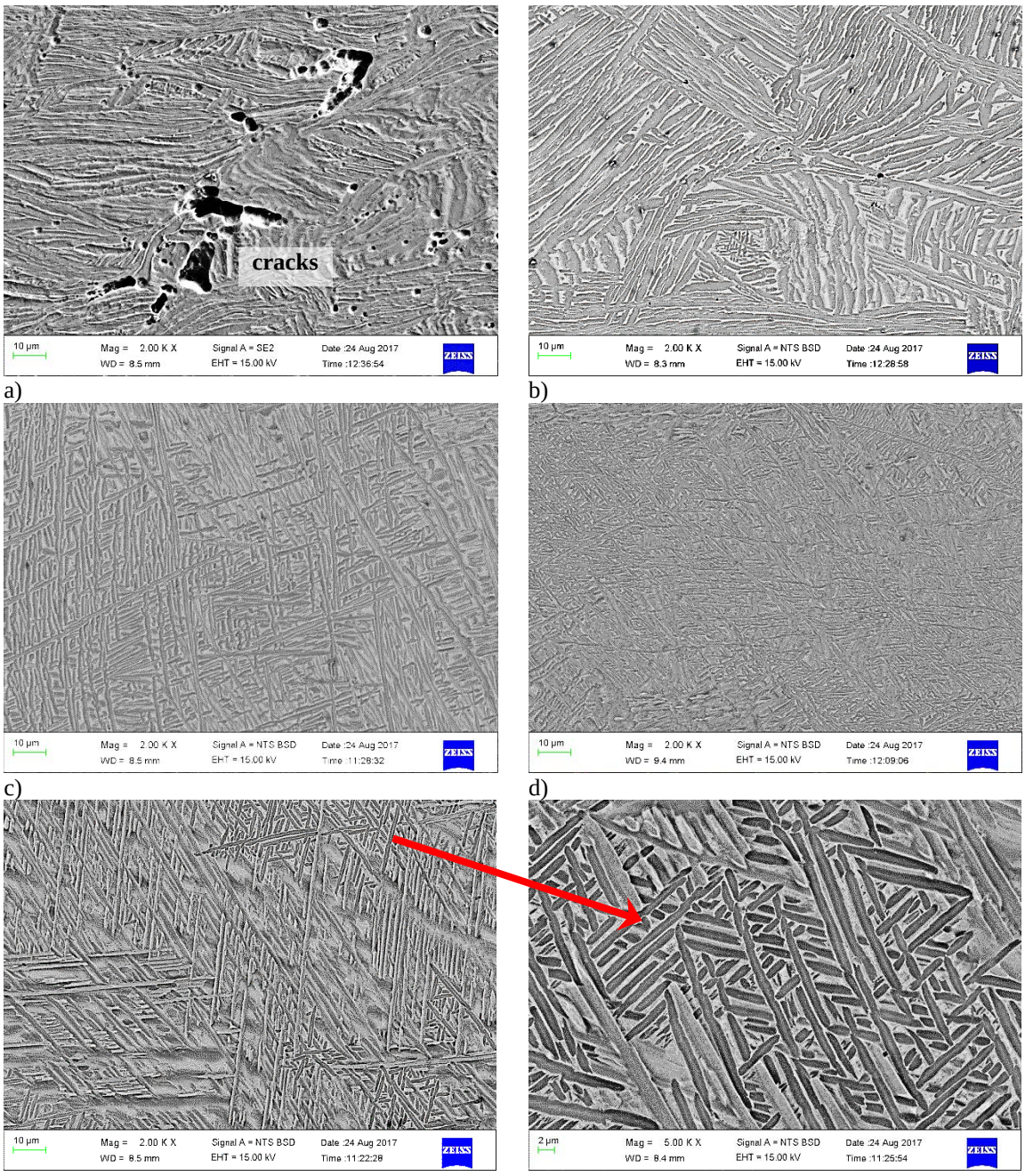

Figure 7.12: SEM-BSE images of Ti-6Al-1V-3Fe alloy deformed at a strain rate of 10 s^{-1} and deformation temperatures of: a) 750°C, b) 800°C, c) 850°C, d) 900°C, e) 950°C and f) 950°C.

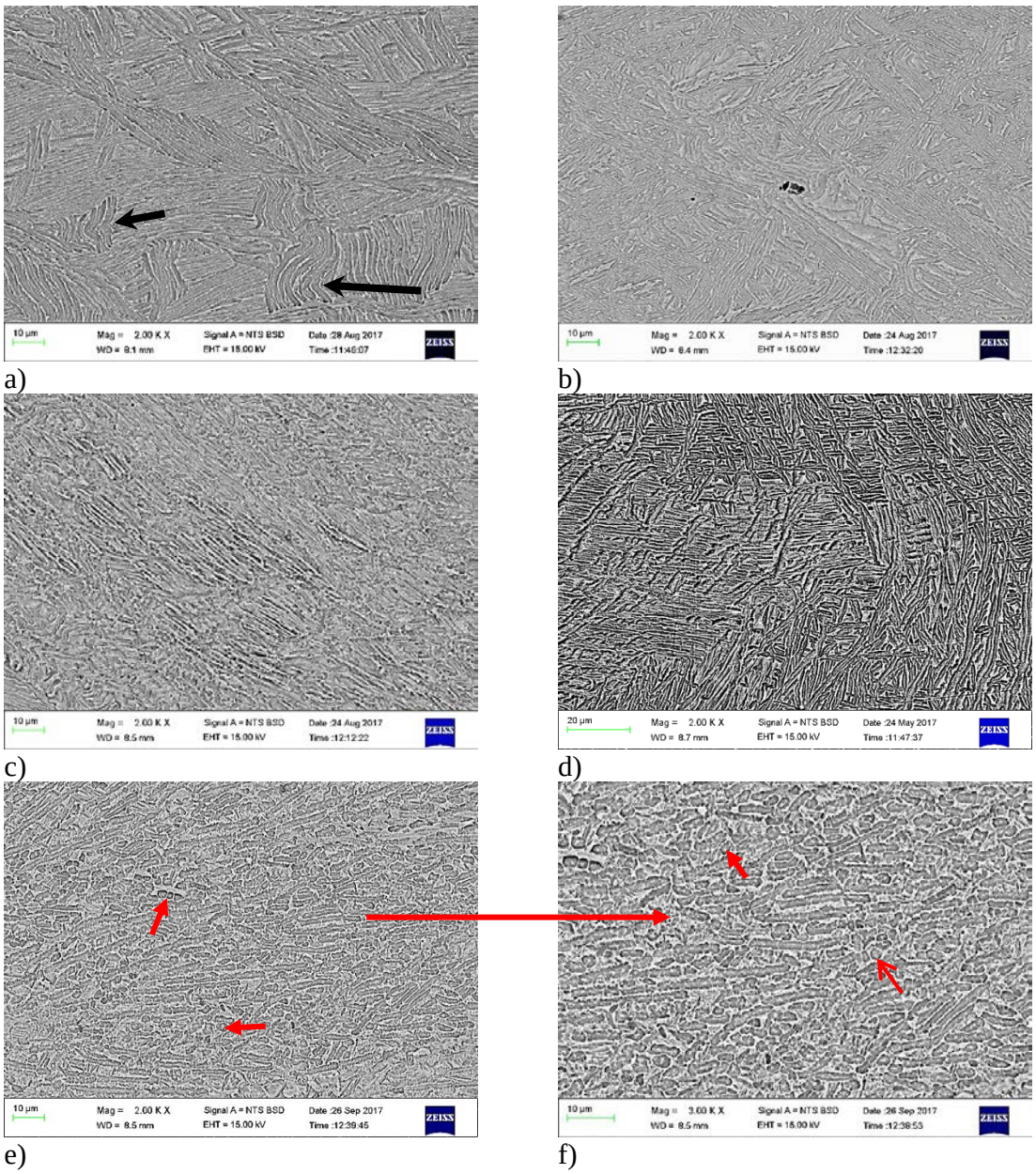

Figure 7.13: SEM-BSE images of Ti-6Al-1V-3Fe alloy deformed at a strain rate of $0.1s^{-1}$ and deformation temperatures of:a) 750°C b) 800°C c) 850°C d) 900°C e) 950°C and f) 950°C (higher magnification). Black arrows show the bending of lath and red arrows show globular α.

The final microstructures of Ti-4.5Al-1V-3Fe samples deformed at the strain rate of 10 s^{-1} at 750 - 950°C are shown in Figure 7.14. Similar to the Ti-6Al-1V-3Fe alloy, at deformation temperatures of 750°C and 800°C (Figures 7.13a and b), severe bending and rotation of laths were evident. As the deformation temperature increased above 800°C, the severity of the lath rotations decreased significantly and a few small α-globules were seen at 900°C (Figure 7.14d).

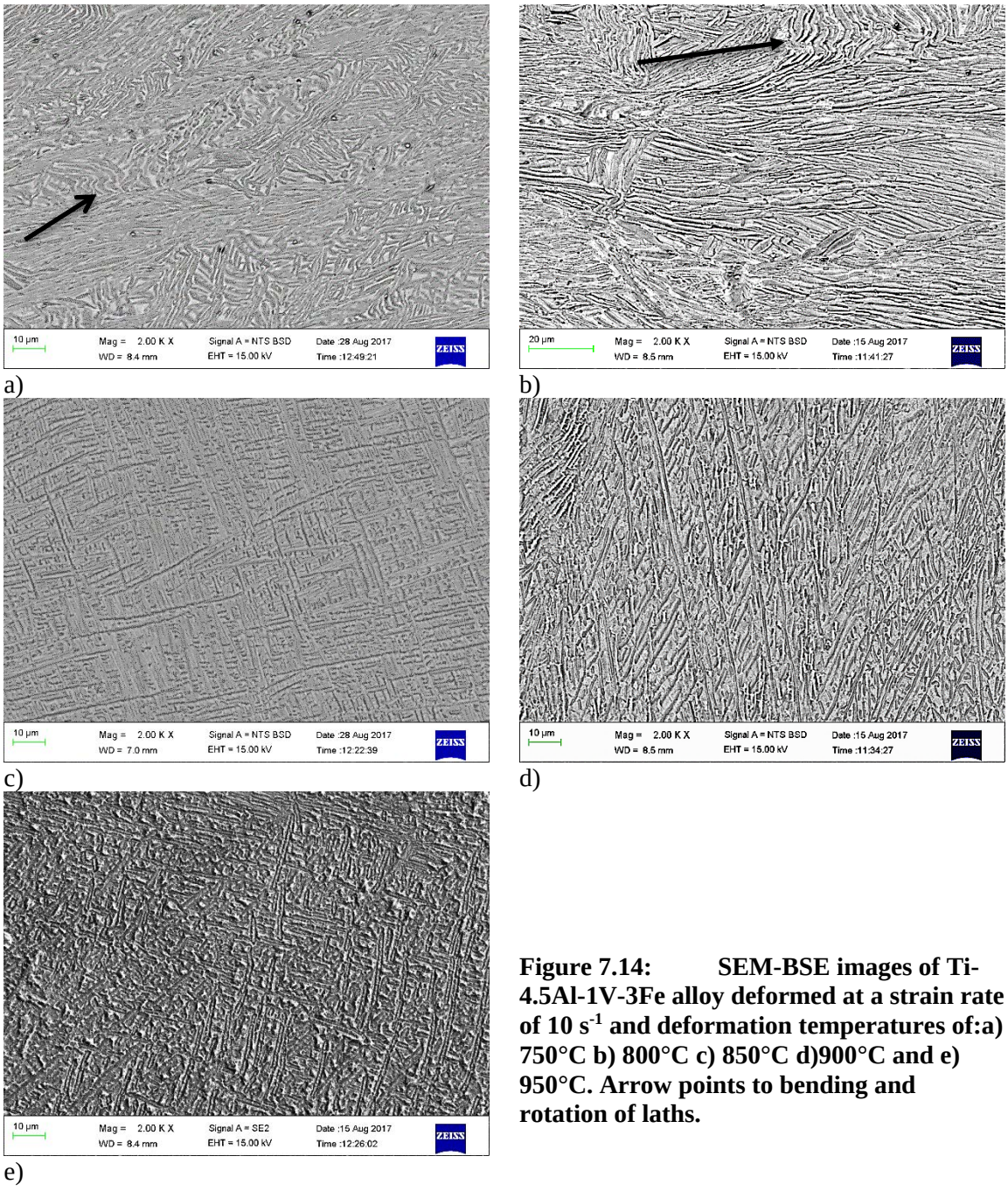

Figure 7.14: SEM-BSE images of Ti-4.5Al-1V-3Fe alloy deformed at a strain rate of 10 s^{-1} and deformation temperatures of:a) 750°C b) 800°C c) 850°C d)900°C and e) 950°C. Arrow points to bending and rotation of laths.

In Figure 7.15, the microstructures of deformed Ti-4.5Al-1V-3Fe samples at a constant strain rate of 0.01 s^{-1} and different temperatures are shown. Below 850°C (Figures 7.15a and b), there were small amount of lath rotation and bending at this strain rate when compared to 10 s^{-1}

(Figures 7.14a and b). At 850°C (Figure 7.15c**)**, α-globules were seen, which indicated that significant dynamic globularisation occurred during deformation. As the deformation temperatures increased to 900°C and 950°C (Figures 7.15d and e**)**, more α globules were seen, which implied that the amount of globularisation increased with increase in temperature.

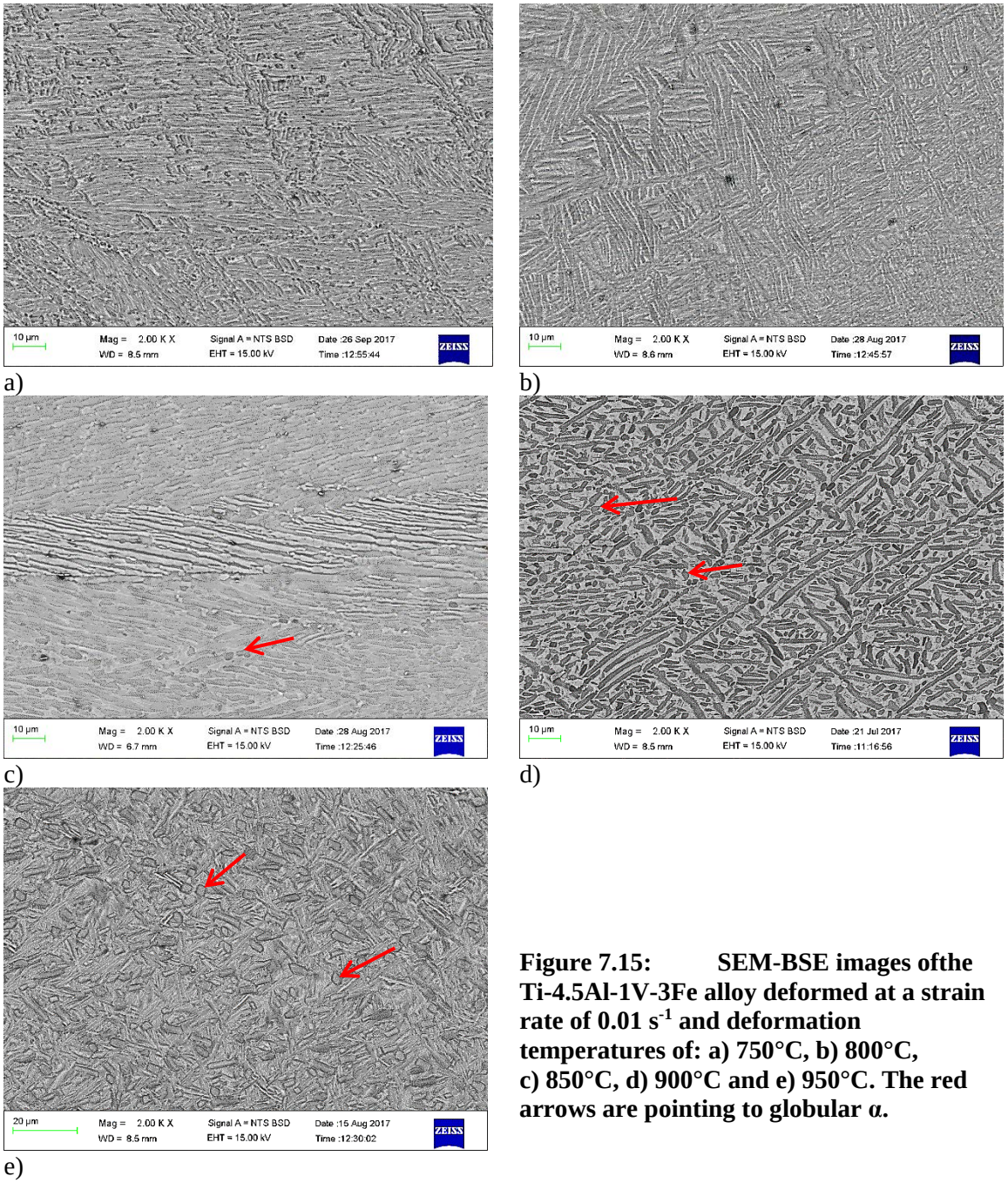

Figure 7.15: SEM-BSE images ofthe Ti-4.5Al-1V-3Fe alloy deformed at a strain rate of 0.01 s^{-1} and deformation temperatures of: a) 750°C, b) 800°C, c) 850°C, d) 900°C and e) 950°C. The red arrows are pointing to globular *α*.

7.4.2 Influence of strain rate

The microstructures of Ti-6Al-1V-3Fe samples deformed at 900°C and different strain rates are presented in Figure 7.16. These microstructures are of interest as the highest power dissipation efficiency was obtained at 900°C.

Figures 7.16a - b show that the lamellae were serrated at a strain rate of 10 s^{-1}, while bending and rotation of laths were evident at 1 s^{-1}. Serrated, bent and kinked laths are all precursors to dynamic globularisation (Zhu *et al.*, 2012; He *et al.*, 2013). Perumal *et al.* (2016) reported that lath rotation and bending in Ti-6Al-4V with an acicular initial microstructure was largely influenced by strain and was independent of the initial lath thickness. In the current study, the total strain was kept constant for all the deformed samples, but the effect of strain rate on lath rotation and bending was visible. At the strain rate of 0.1 s^{-1}, a small amount of lath bending was observed in Ti-6Al-1V-3Fe and there were no signs of dynamic globularisation. There was significant dynamic globularisation at low strain rates of 0.01 s^{-1} and 0.001 s^{-1}. This was confirmed by the fragmentation of α lamellae into globules as shown in Figures 7.16d - e.

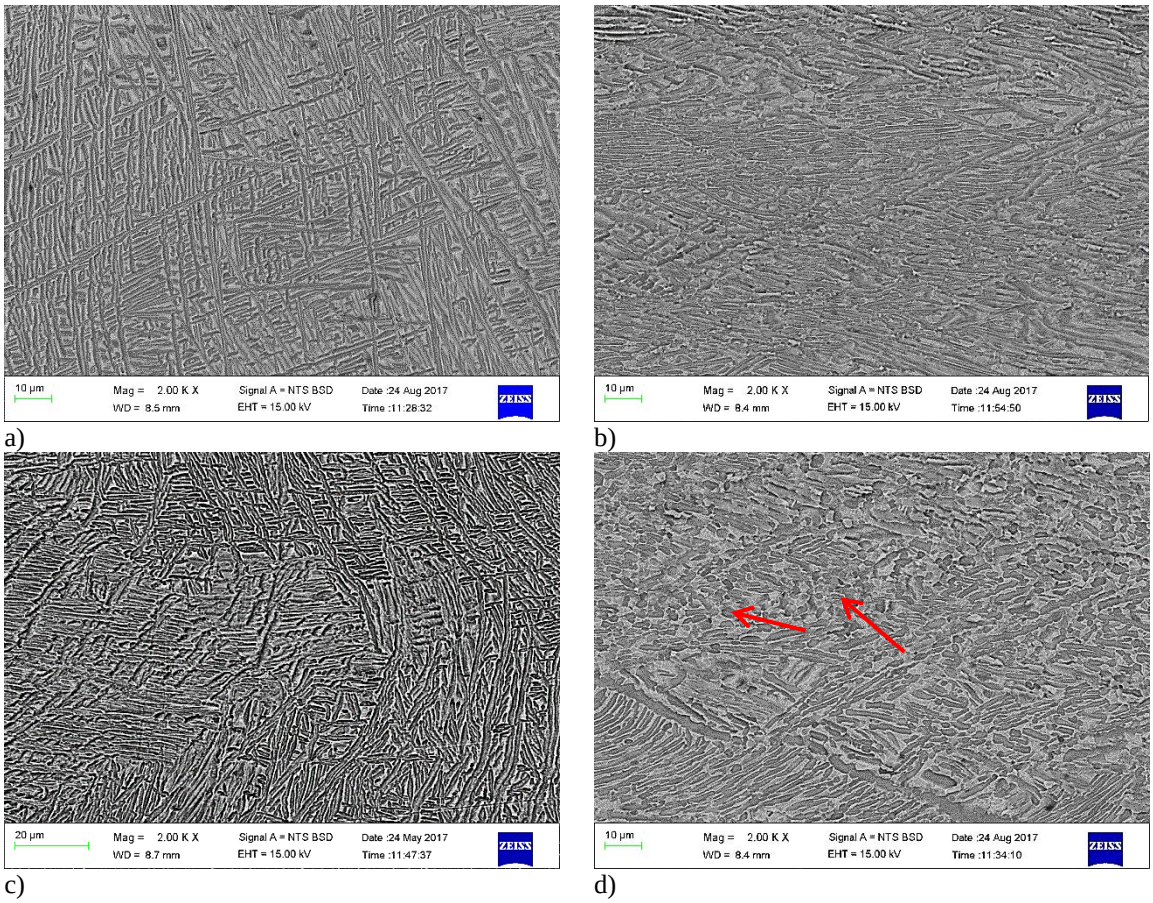

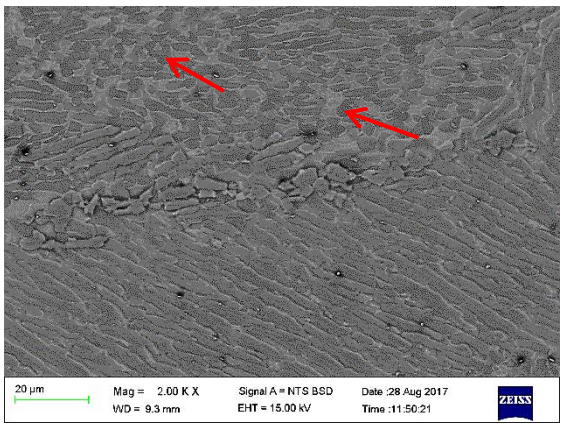

e)

Figure 7.16: SEM-BSE images of Ti-6Al-1V-3Fe alloy deformed at a temperature of 900°C and strain rates of: a) 10 s^{-1}, b) 1 s^{-1}, c) 0.1 s^{-1}, d) 0.01 s^{-1} and e) 0.001 s^{-1}. The arrows point to globular *α*.

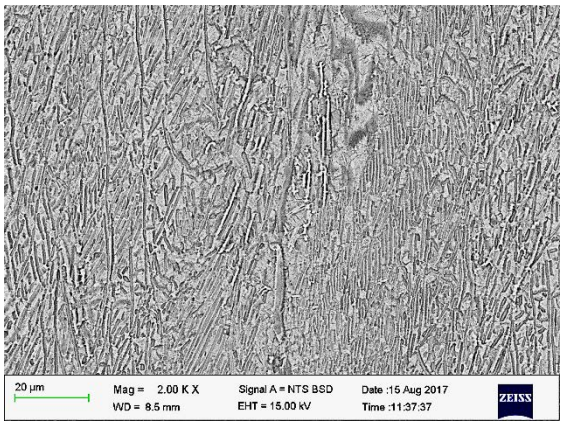

a)

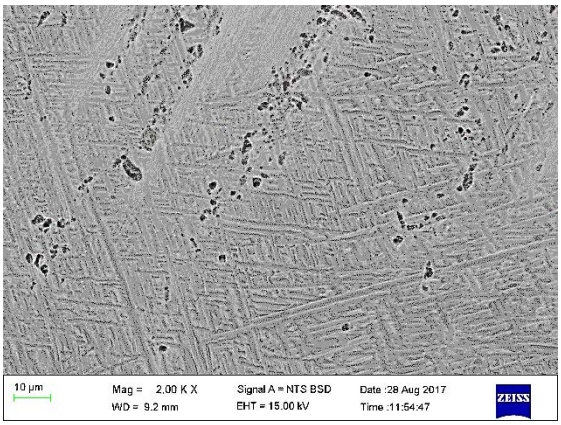

b)

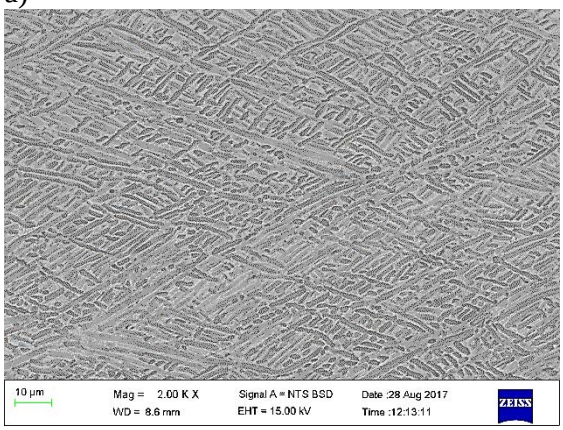

c)

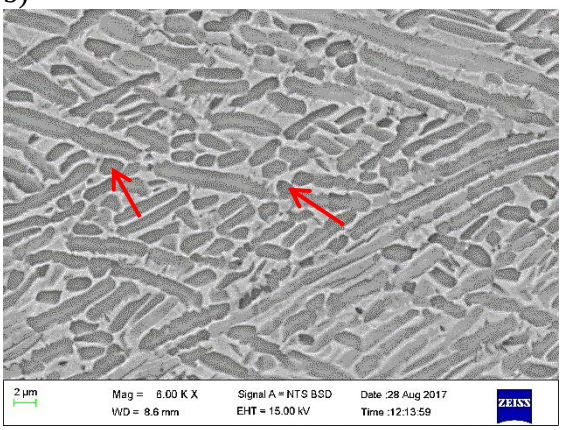

d)

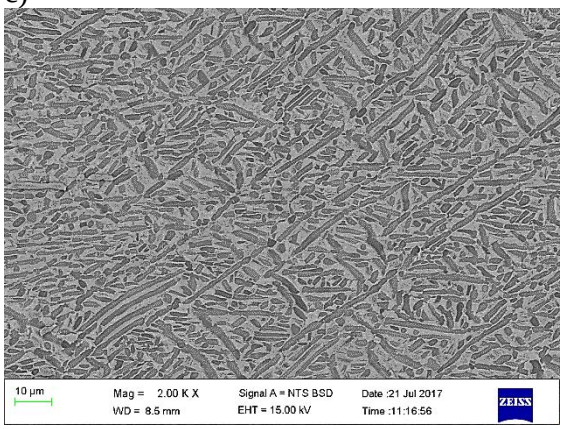

e)

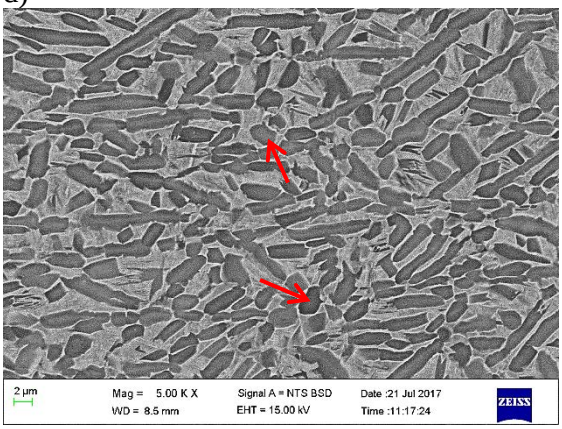

f)

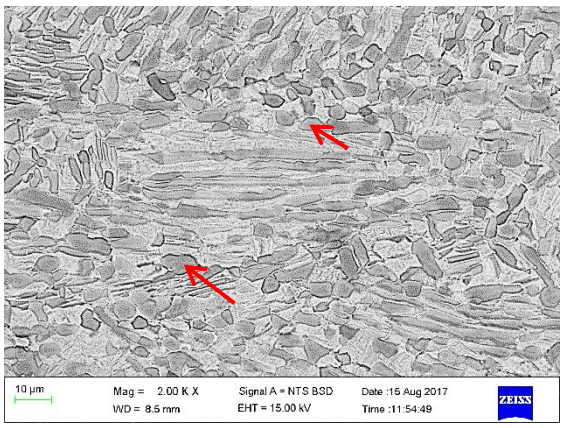

g)

Figure 7.17: SEM-BSE images of Ti-4.5Al-1V-3Fe alloy deformed at 900°C and strain rates of: a) $10s^{-1}$,b) $1s^{-1}$,c) 0.1 s^{-1}, (d) $0.1s^{-1}$,(higher mag.),e) 0.01 s^{-1},f) 0.01 s^{-1}(higher mag.) and g) 0.001 s^{-1}. The arrows point to globular α.

Lath rotation and the occurrence of dynamic globularisation at lower strain rates were seen in the microstructures of deformed Ti-4.5Al-1V-3Fe samples (Figure 7.17). For samples deformed at the optimum working temperature (900°C) and different strain rates, the critical strain rate for dynamic globularisation in this alloy was 0.1 s^{-1}, whereas it was much lower in Ti-6Al-1V-3Fe ($0.01s^{-1}$). This attests to the higher workability of Ti-4.5Al-1V-3Fe than Ti-6Al-1V-3Fe. The reduction in aluminium content decreased the strength of the hard α phase at elevated temperature and allowed dynamic globularisation to occur quite easily at higher strain rates.

The deformation behaviour and microstructural features of the two experimental alloys were compared. As mentioned earlier, the optimum working temperature for both alloys was 900°C, but the strain rate differed. The optimum strain rate for the hot working of Ti-6Al-1V-3Fe was 0.1 s^{-1} while that of Ti-4.5Al-1V-3Fe is 0.01 s^{-1}. In the Ti-6Al-1V-3Fe alloy, flow softening occurred at the optimum temperature via dynamic recrystallisation of the prior beta grains, while in Ti-4.5Al-1V-3Fe, it occurred by dynamic globularisation. The power dissipation efficiency at the optimum deformation temperature was higher in Ti-4.5Al-1V-3Fe than in Ti-6Al-1V-3Fe alloys. All these implied that under the safe deformation regime, the Ti-4.5Al-1V-3Fe was easier to deform than Ti-6Al-1V-3Fe. Dynamic globularisation is a desirable mechanism which converts lamellar/acicular structures in titanium alloys to equiaxed structures (Weiss and Semiatin, 1999; Prasad et al., 2015).

The fragmentation of the initial lamellar structure to globules in Ti-6Al-1V-3Fe occurred at higher temperatures (>900°C) and very low strain rates (≤0.01 s^{-1}). The onset of dynamic globularisation at the optimum deformation temperature of 900°C occurred at a strain rate of 0.01 s^{-1} in Ti-6Al-1V-3Fe, while it occurred at a faster strain rate of 0.1 s^{-1} in Ti-4.5Al-1V-3Fe. The reason for this was attributed to the difference in the strength of the alpha phase. It is well documented that aluminium is an alpha stabiliser and it strengthens the alpha phase (Lütjering and Williams, 2007). The experimental Ti-4.5Al-1V-3Fe alloy with less aluminium would

exhibit lower strengthening of the alpha phase compared to Ti-6Al-1V-3Fe. The lower strengthening in the alpha phase of Ti-4.5Al-1V-3Fe would allow globularisation of the alpha laths much easier and faster than in Ti-6Al-1V-3Fe.

7.5 Summary

7.5.1 Stress-strain behaviour

The flow stress is influenced by deformation temperature, strain rate, strain and alloy composition. Stress-strain behaviour showed that increasing strain rate and decreasing deformation temperatures increased the flow stress. Ti-4.5Al-1V-3Fe with less aluminium and a lower total solute content had a lower flow stress than Ti-6Al-1V-3Fe.

The flow softening exhibited by the stress-strain curves was dependent on the deformation parameters. Adiabatic heating contributed to flow softening at high strain rates and low deformation temperatures.

7.5.2 Processing maps

The Ti-6Al-1V-3Fe and Ti-4.5Al-1V-3Fe alloys showed wide processing windows due to the small areas of instability on their processing maps. The higher power dissipation values seen in Ti-4.5Al-1V-3Fe suggested that the alloy was much easier to deform. The optimum working conditions obtained from the processing maps were:

- Ti-6Al-1V-3Fe: 900°C /0.1 s^{-1}
- Ti-4.5Al-1V-3Fe: 900°C /0.01 s^{-1}

The regions of unsafe deformation were:

- Ti-6Al-1V-3Fe: 750 - 780°C / 1.2 - 10 s^{-1}.
- Ti-4.5Al-1V-3Fe: 880 - 930°C / 0.1 - 0.3 s^{-1}.

These regions of unsafe deformation were interpolated data obtained from the processing maps. The above regions were validated by testing both alloys at 900°C/0.1 s^{-1}, 900°C/0.01 s^{-1}, and 750°C/10 s^{-1}.

Although these optimum strain rates may be low for some industrial processes such as forging and rolling, the alloys can still be deformed in other safe regions with higher strain rates, as given on the processing maps. Most of the commercial and experimental alloys investigated previously (Table 2.7) have optimum working conditions at strain rates lower than 1 s^{-1}. This is because dynamic recrystallisation or dynamic globularisation is favoured at slower deformation speed and higher temperatures.

7.5.3 Microstructural evolution

Dynamic recrystallisation of the prior beta grains was the dominant softening mechanism for the Ti-6Al-1V-3Fe alloy when deformed at the optimum working conditions, while the presence of alpha globules confirmed dynamic globularisation as the dominant softening mechanism in the Ti-4.5Al-1V-3Fe alloy deformed at the optimum working condition. Adiabatic shear bands, voids and cracking manifested as flow instabilities in the unsafe deformation region on the processing map. These instabilities were seen in the microstructures of samples deformed in the unsafe regions.

Dynamic globularisation of the alpha phase occurred in Ti-4.5Al-1V-3Fe much easier and faster ($0.1\ s^{-1}$) than it occurred in Ti-6Al-1V-3Fe ($0.01\ s^{-1}$). This may be due to different strength levels of the alpha phase with varying aluminium content.

Chapter 8: Activation energy for hot working of Ti-6Al-4V, Ti-6Al-1V-3Fe and Ti-4.5Al-1V-3Fe alloys

This chapter presents the activation energy for hot working (Q_{HW}) using hot compression results of the commercial wrought Ti-6Al-4V alloy (Chapter 6) and the experimental Ti-6Al-1V-3Fe and Ti-4.5Al-1V-3Fe alloys (Chapter 7). Using the flow stress values of the stress-strain data, which were corrected for adiabatic heating, the Q_{HW} values were obtained by applying a hyperbolic-sine constitutive equation at the peak stress. These values were then compared with the Q_{HW} for hot deformation of titanium alloys reported in literature.

8.1 Hyperbolic-sine equation for derivation of activation energy - an overview

Metallic materials are generally subjected to hot working such as rolling, forging and extrusion for microstructural control, property optimisation and shaping (McQueen and Bourell, 1987; Doherty *et al.*, 1997). The activation energy for hot working is an important parameter which gives an indication of the material's resistance to deformation. It could also provide insights into the microstructural mechanisms influencing the deformation process (Shi *et al.*, 2013; Momeni, 2016). Additionally, it is an essential parameter that is required for the prediction of flow stress (Shi *et al.*, 2013; Liu *et al.*, 2014; Momeni, 2016).

Over the years, several constitutive models have been used to describe the relationship between the flow stress and imposed hot working parameters such as strain rate, strain and deformation temperature (McQueen and Ryan, 2002; Lin and Chen, 2011; Shi and Chen, 2016). A short review on the different classifications of constitutive models was presented in Chapter 2. The constitutive models are largely classified into phenomenological models, physical models and artificial neural network models (Lin and Chen, 2011; Shi and Chen, 2016). Among these models, the Arrhenius hyperbolic-sine equation proposed by Sellars and Tegart (1966) has been used by many researchers to describe the relationship between the flow stress, strain rate and deformation temperature (McQueen and Ryan, 2002; Shi *et al.*, 2013). The hyperbolic-sine equation expressed in Equation 8.1 can be applied over a wide range of stress (Jonas *et al.*, 1969). This provides an advantage over the power and exponential equations (Equation 8.2 and 8.3), which are only applicable at low and high stresses respectively (McQueen and Jonas, 1975; McQueen and Ryan, 2002; Momeni, 2016).

The material constants (A, α, β and n) are determined by fitting the experimental data from hot working tests. The relationship between flow stress and the Zener-Hollomon parameter is given in Equation 8.4 and 8.5 and can be used to predict the flow stress when the material constants are known.

$$\dot{\varepsilon} = A\,[sinh(\alpha\sigma)]^n\, exp\left(\frac{-Q}{RT}\right) \quad \text{for } all\ \sigma \qquad \textbf{Equation 8.1}$$

$$\dot{\varepsilon} = A\,(\sigma^n)\, exp\left(\frac{-Q}{RT}\right) \quad \text{for } \alpha\sigma < 0.8 \qquad \textbf{Equation 8.2}$$

$$\dot{\varepsilon} = A\, exp(\beta\sigma) exp\left(\frac{-Q}{RT}\right) \quad \text{for } \alpha\sigma > 1.2 \qquad \textbf{Equation 8.3}$$

$$Z = \dot{\varepsilon}\, exp\left(\frac{Q}{RT}\right) \qquad \textbf{Equation 8.4}$$

$$\sigma = {}^{1}/_{\alpha}\left\{\left(\frac{Z}{A}\right)^{\frac{1}{n}} + \left[\left(\frac{Z}{A}\right) + 1\right]^{\frac{1}{2}}\right\} \qquad \textbf{Equation 8.5}$$

where $\dot{\varepsilon}$ is strain rate, σ is stress, n is the stress exponent, Q is the activation energy, R is the gas constant (8.315 kJ.mol^{-1}), T is temperature, Z is the Zener-Hollomon parameter (temperature compensated strain rate), and α, β and A are material constants.

The hyperbolic-sine equation was originally designed for materials that dynamically recover, readily achieving steady-state flow stress when the peak stress was reached (Sellars and Tegart, 1966). Consequently, the peak stress or steady-state stress was used to determine the activation energy for hot working (McQueen and Ryan, 2002). Shi *et al.*(1997), Sheppard and Jackson (1997), Chen *et al.* (2015) and Wang *et al.* (2016) used the hyperbolic-sine equation on aluminium alloys and ferritic steel that exhibited steady-state stress at the peak stress due to their high stacking fault energies. However, other researchers (Evangelista *et al.*, 1987; McQueen *et al.*, 1995; Nkhoma *et al.*, 2014) have used the hyperbolic-sine equation in low stacking fault energy materials that exhibit a distinct peak followed by a drop in flow stress due to dynamic recrystallisation, and then the attainment of steady-state stress. The activation energy was then determined at the peak flow stress.

Davenport *et al.* (2000) proposed a two stage procedure for using the Arrhenius constitutive model on material that dynamically recrystallised during hot working. In the first stage, constitutive constants were determined using the hyperbolic-sine relationship at regular strain increments (0.1, 0.2, 0.3…) or at specific points on the flow curve, such as the peak stress, steady-state stress, critical stress for dynamic recrystallisation and extrapolated steady-state stress. In the

second stage, the continuous flow stress curves were obtained in two steps using Equation 8.6 - 8.8. The first step described the extrapolated flow stress curves using Equation 8.6 and 8.7 and substituting the constitutive constants derived in stage 1.

$$\sigma = \sigma_0 + \left(\sigma_{ss(e)} - \sigma_0\right)\left[1 - exp\left(-\frac{\varepsilon}{\varepsilon_r}\right)\right]^m \quad \textbf{Equation 8.6}$$

$$\varepsilon_r = -0.1\left\{ln\left[1 - \left(\frac{\sigma_{0.1} - \sigma_0}{\sigma_s - \sigma_0}\right)^{1/m}\right]\right\}^{-1} \quad \textbf{Equation 8.7}$$

$$\Delta\sigma = \Delta\sigma_s\left[1 - exp\left\{-\left[{(\varepsilon - \varepsilon_c)}/{(\varepsilon_{xr} - \varepsilon_c)}\right]^p\right\}\right] \quad \textbf{Equation 8.8}$$

where: σ_0 is the inital stress, $\sigma_{ss(e)}$ is the extrapolated steady-state stress; ε_r is the transient strain constant which defines the curvature of the flow curve between σ_0 and $\sigma_{ss(e)}$; $\sigma_{0.1}$ is the stress when ε = 0.1; σ_s is the steady-state stress; ε_c is the critical strain for dynamic recrystallisation; ε_{xr} is the strain required to reach a fixed amount of softening; $\Delta\sigma$ is the stress difference between the two curves; $\Delta\sigma_s$ is the difference between the flow curves when steady state is reached; and *p* and *m* are constants.

In the second step, the effect of dynamic recrystallisation was subtracted from the extrapolated flow stress curve using Equation 8.8. The authors concluded that the method could be used for any material if the majority of the flow curves met the steady-state stress condition. However, in tests where most of the flow stress curves do not satisfy the steady-state stress condition, they recommended that the constitutive parameters and flow stress modelling should be done at the specific points on the flow curve or incremental strains, as discussed earlier (Davenport *et al.*, 2000).

A large number of research articles have been published on the hot working of steels and titanium alloys where the hyperbolic-sine equation was used at incremental strains to determine the constitutive constants and predict the flow stress (Zeng *et al.*, 2009; Mandal *et al.*, 2009; Cai *et al.*, 2011; Xiao *et al.*, 2012; W. Peng *et al.*, 2013a; Yang *et al.*, 2015; Ge *et al.*, 2018). This approach has been adapted to analyse flow curves that do not reach the steady-state stress. Lin *et al.* (2008) determined the constitutive constants and activation energy of hot worked 42CrMo steel at strain increments over the entire stress-strain curve. The influence of strain on the constitutive constants and activation energy was described by a polynomial relationship. The constitutive model was then used in the prediction of flow stress. This approach has been used by other researchers to describe the constitutive relationship in titanium alloys (Zhu *et al.*, 2012; Cai *et al.*, 2011; W. Peng *et al.*, 2013a; X. Peng *et al.*, 2013; Ge *et al.*, 2018). However, these

studies have all overlooked the constant stress condition, as initially intended by Sellars and Tegart (1966).

In this work, the recommendations set out by Davenport *et al.* (2000), McQueen and Ryan (2002), Momeni and Dehghani (2010), Liu *et al.* (2011), Nkhoma *et al.* (2014), Han *et al.* (2015) and Souza *et al.* (2015a) were considered when determining the activation energy and constitutive constants where steady-state stress was not reached. The flow stress curves presented in Figures 6.1 (Ti-6Al-4V), 7.1 (Ti-6Al-1V-3Fe) and 7.2 (Ti-4.5Al-1V-3Fe), did not satisfy the steady-state stress condition for most of the tests. Therefore only the peak flow stress was used in the hyperbolic-sine equation to determine the constitutive constants and activation energy for hot working.

8.2 Determination of activation energy (Q_{HW}) and constitutive constants

To determine the activation energy for hot working, a number of constitutive constants, such as $\acute{n}$, n, β, α, S and A need to be derived. This can be done by partial differentiation of the natural logarithm of Equation 8.1 (Nkhoma *et al.*, 2014) and rearranging to give straight line equations (Calvert *et al.*, 2015). The equations used to determine the constitutive constants are listed in Table 8.1.

The constant $\acute{n}$ is obtained from the power law at low stress (Equations 8.2 and 8.9). β is a constant obtained from the exponential law at high stress from (Equations 8.3 and 8.10). The material constant α is the stress multiplier derived from Equation 8.11.

The stress exponent n is obtained from Equation 8.12. The activation energy for hot working is obtained using Equation 8.13, where S is the slope of the graph of the natural logarithm of $sinh(\alpha\sigma_p)$ against $1/T$.

The graphical determination of the material constants for the Ti-6Al-4V, Ti-6Al-1V-3Fe and Ti-4.5Al-1V-3Fe alloys are shown in Figures 8.1 - 8.3. The values of the derived constitutive constants and the activation energy values for hot working are listed in Table 8.2.

Table 8.1: Equations for determining constitutive constants.

Constitutive constants	Equations	What to Plot	
$ń$	$ń = \frac{\delta \ln \dot{\varepsilon}}{\delta \ln \sigma_p}$	$\ln \dot{\varepsilon}$ *vs.* $\ln \sigma_p$	**Equation 8.9**
β	$\beta = \frac{\delta \ln \dot{\varepsilon}}{\sigma_p}$	$\ln \dot{\varepsilon}$ *vs.* σ_p	**Equation 8.10**
α	$\alpha = \frac{\beta}{ń}$	-	**Equation 8.11**
n	$\ln \dot{\varepsilon} = \ln A + n \ln\left[sinh(\alpha\sigma_p)\right] - \frac{Q_p}{RT}$	$\ln \dot{\varepsilon}$ *vs.* $\ln\left[sinh(\alpha\sigma_p)\right]$	**Equation 8.12**
Q	$Q = RnS = R\left\{\frac{\delta \ln \dot{\varepsilon}}{\delta \ln\left[sinh(\alpha\sigma_p)\right]}\right\}_T \left\{\frac{\delta \ln\left[sinh(\alpha\sigma_p)\right]}{\delta(1/T)}\right\}_{\dot{\varepsilon}}$	$\delta \ln\left[sinh(\alpha\sigma_p)\right]$ *vs.* $\delta(1/T)$	**Equation 8.13**
A	$z = \dot{\varepsilon} exp(Q/RT) = A\left[sinh(\alpha\sigma_p)\right]^n$	$\ln Z$ *vs.* $\ln\left[sinh(\alpha\sigma_p)\right]$	**Equation 8.14**

Table 8.2: Material constants and activation energy for hot working of titanium alloys.

Alloy	β	$ń$	α (MPa^{-1})	n	S	Q (kJmol^{-1})	A (s^{-1})
Ti-6Al - 4V	0.04	7.569	0.005	5.057	14.746	**620**	1.44 x 10^{28}
Ti-6Al - 1V-3Fe	0.03	5.595	0.006	3.808	15.389	**487**	1.50 x 10^{21}
Ti-4.5Al-1V-3Fe	0.04	4.958	0.008	3.335	16.785	**465**	1.20 x 10^{20}

The Q_{HW} of the wrought Ti-6Al-4V alloy was the highest and that of Ti-4.5Al-1V-3Fe alloy was the lowest. This trend suggests that the Q_{HW} of the alloys was influenced by alloy composition. McQueen *et al.* (1995) reported that alloying content had a significant effect on the Q_{HW} of carbon steel and austenitic stainless steel. McQueen and Ryan (2002) determined a Q_{HW} - for pure iron of 280 kJmol^{-1}, while in plain carbon steel, the Q_{HW} was ~300 kJmol^{-1} due to solute strengthening by manganese and silicon. A Q_{HW} range of 350 - 500 kJmol^{-1} for austenitic stainless steels, such as 301, 304 and 317, was found to be higher than the Q_{HW} of plain carbon steels, due to 28 - 35% higher solute contents (McQueen and Bourell, 1987; McQueen *et al.*, 1995). In titanium alloys, higher solute contents have also increased the Q_{HW} during hot deformation (Semiatin *et al.*, 1997; Weiss and Semiatin, 1998; Fitzner *et al.*, 2016).

The experimental alloy with a 1.5% higher aluminium content showed higher resistance to deformation. Fujii *et al.*(2002) and Fitzner *et al.* (2016) reported that aluminium increased the

deformation resistance in titanium alloys by reducing the stacking fault energy. Additionally, aluminium is a solid solution strengthener in titanium and stabilises the alpha phase (Leyens and Peters, 2003; Fitzner *et al.*, 2016). More aluminium may increase the alpha phase proportion when the alloys are deformed in the two phase (α+β) region. Since the hcp alpha phase has fewer slip planes than the bcc beta-Ti phase (Lütjering and Williams, 2007), the deformation resistance and Q_{HW} would be higher in the alloys containing more aluminium. The Q_{HW} of the commercial Ti-6Al-4V was comparable to values reported by Briottet *et al.* (1996) and Semiatin *et al.* (1999).

McQueen and Ryan (2002) found that the Q_{HW} of materials that undergo dynamic recrystallisation is usually 20% higher than in materials that undergo dynamic recovery, where the Q_{HW} is usually close to the activation energy for self-diffusion (Q_{SD}). The Q_{HW} could be 50% higher than Q_{SD} in some alloys due to additions of solutes, precipitates and reinforcements (McQueen *et al.*, 1995; McQueen and Ryan, 2002). Since the Q_{HW} for alloys that undergo dynamic recovery have been found to be similar to the Q_{SD}, some authors have attributed activation energies higher than Q_{SD} to dynamic recrystallisation (Jonas *et al.*, 1969; Momeni and Abbasi, 2010; Lin and Chen, 2011).

Brayant (1975), Chen *et al.* (2008), Momeni and Abbasi (2010), and Lin and Chen (2011) all reported a Q_{SD} of 303 $kJmol^{-1}$ for alpha titanium. In this study, the Q_{HW} values of Ti-4.5Al-1V-3Fe, Ti-6Al-1V-3Fe and Ti-6Al-4V alloys were higher than the Q_{SD} of alpha titanium by 54%, 61% and 105% respectively. These values exceeded the 50% increase proposed by McQueen and Ryan (2002) for steels.

The Q_{HW} values obtained for the three alloys in this study were compared with other published results. Table 8.3 shows the Q_{HW} reported for various titanium alloys deformed in the (α+β) region. Q_{HW} values as high as 2000 $kJmol^{-1}$ were cited by Briottet *et al.* (1996) using Taylor's model. Briottet *et al.* (1996), Seetharaman and Semiatin (1997), and Semiatin *et al.* (1999) explained that the very high Q_{HW} values obtained when modelling the deformation of titanium alloys in the (α+β) region did not have a true physical significance . The authors maintained that the Q_{HW} was an artefact of the fitting of data for two-phase materials whose phase proportions vary greatly with temperature. Consequently, the Q_{HW} obtained for the alloys in this study has not been attributed to any specific deformation mechanism. However, the values have given insight into the influence of solute content on the deformation resistance of the alloys.

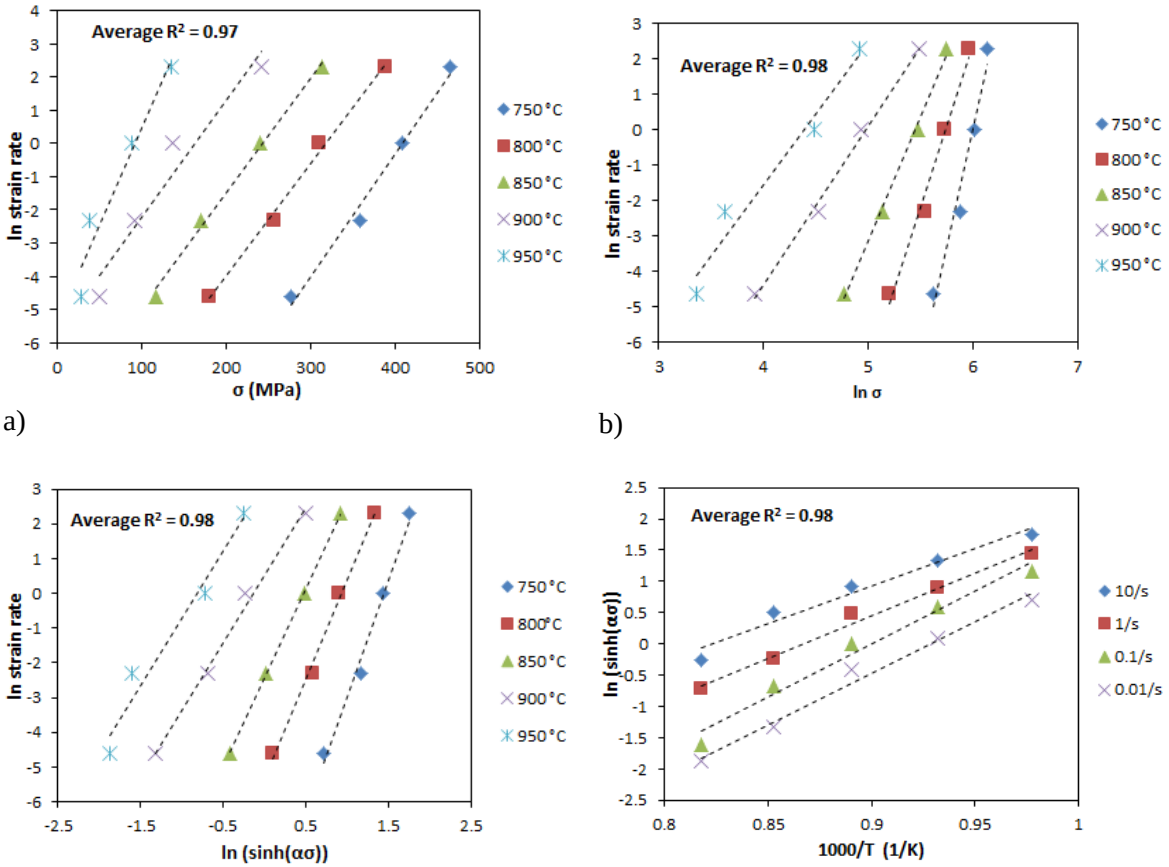

Figure 8.1: Determination of material constants for Ti-6Al-4V: a) ń, b) β, c) n, d) Q = Rn S and (e) A.

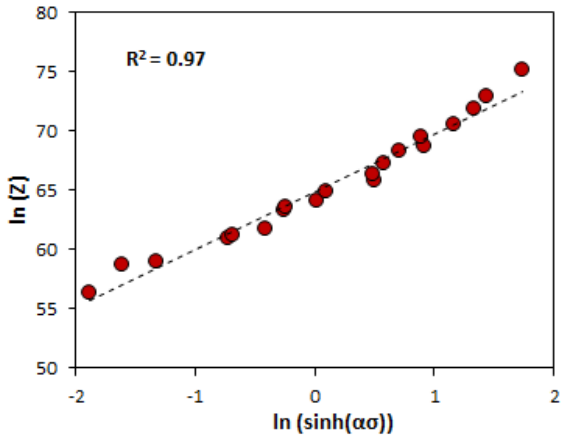

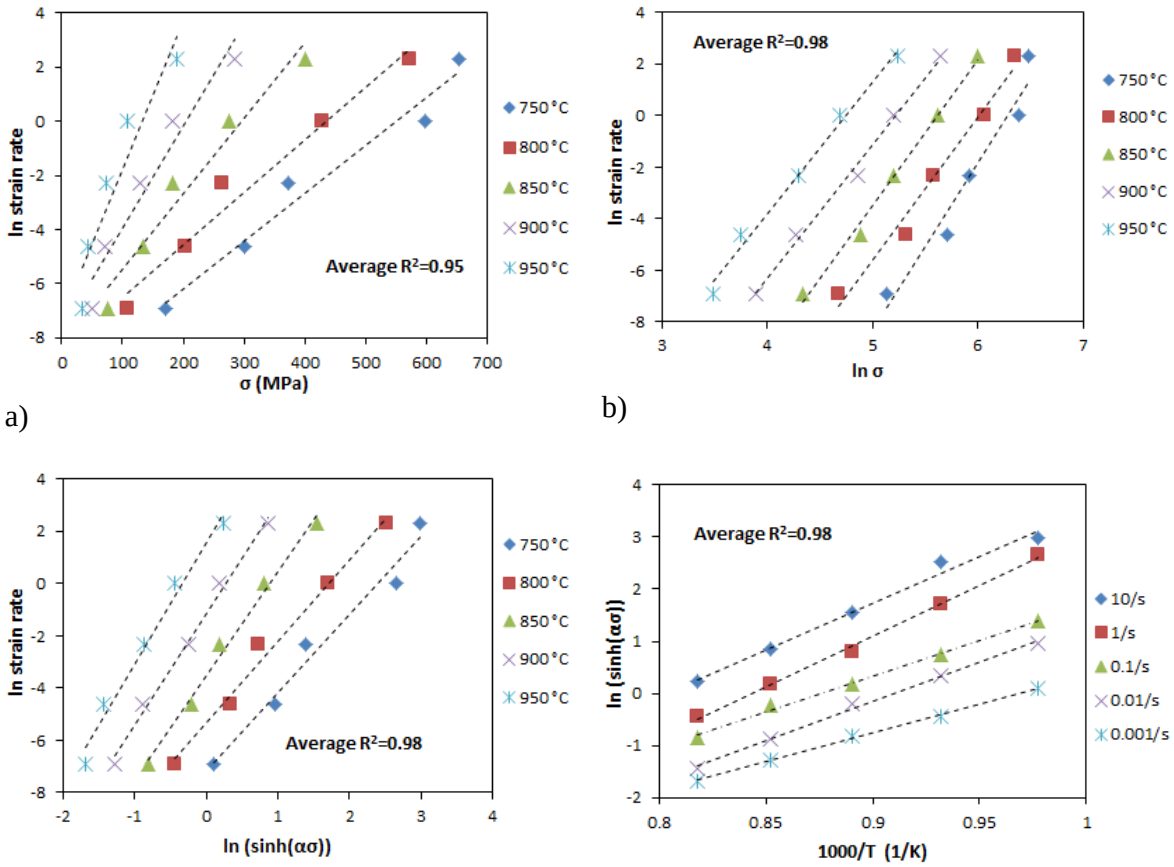

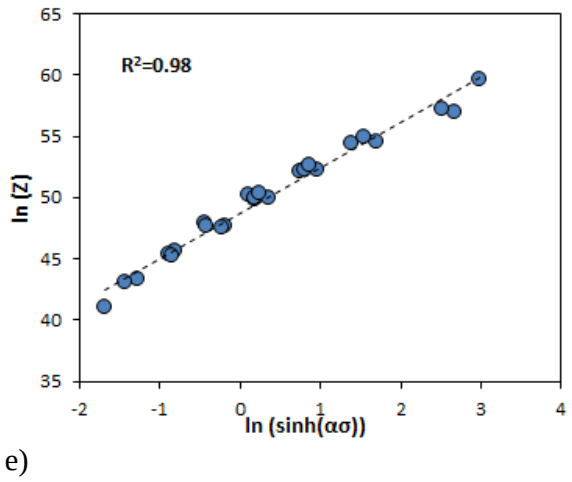

Figure 8.2: Determination of material constants for Ti-6Al-1V-3Fe: a) ń, b) β, c) n, d) Q = Rn S and e) A.

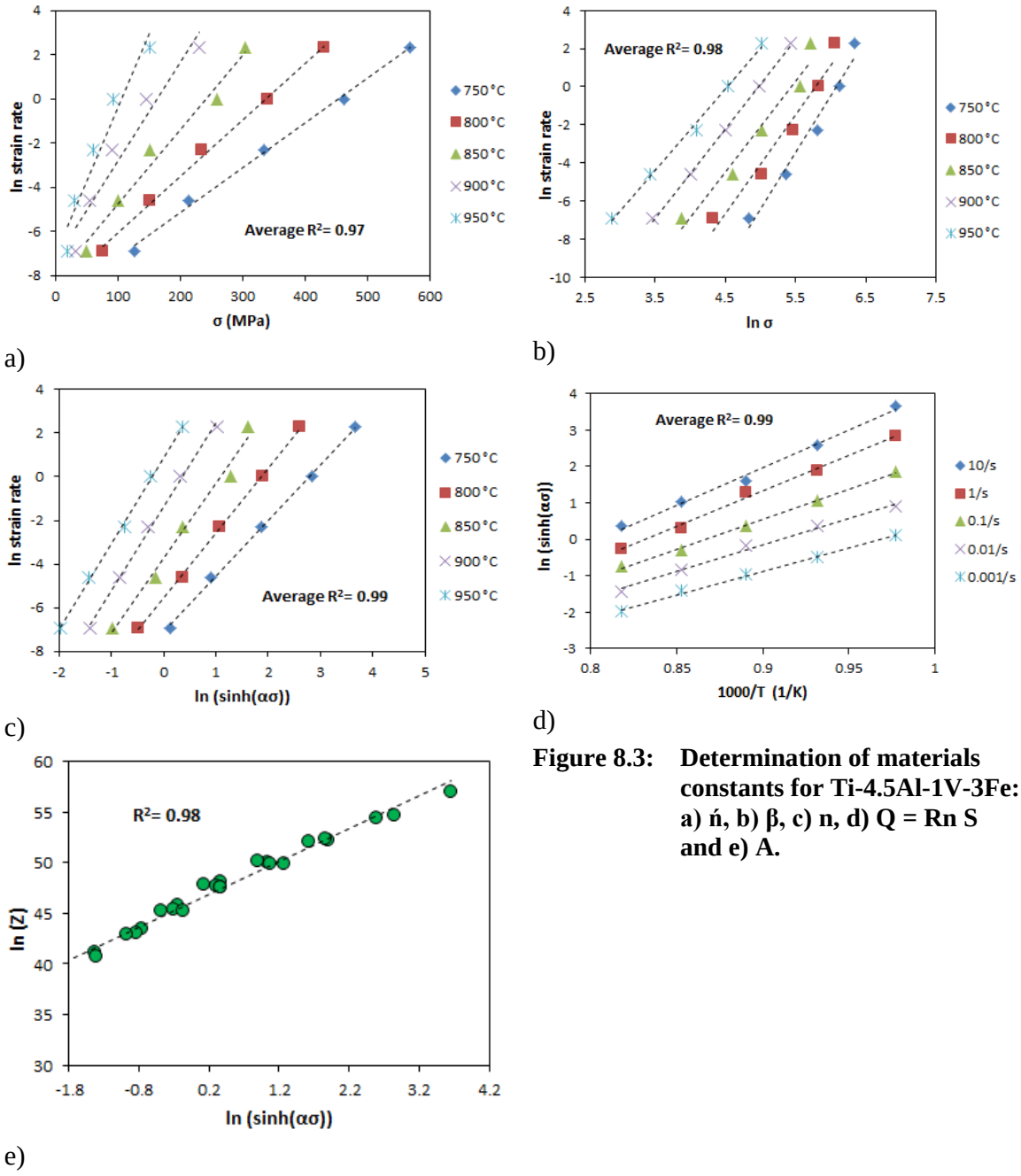

Figure 8.3: Determination of materials constants for Ti-4.5Al-1V-3Fe: a) ń, b) β, c) n, d) Q = Rn S and e) A.

8.3 Summary

The activation energy values for hot working of commercial Ti-6Al-4V and experimental Ti-6Al-1V-3Fe and Ti-4.5Al-1V-3Fe alloys were obtained by applying the hyperbolic-sine equation at the peak stress. The marked difference in the Q_{HW} of Ti-6Al-4V (620 kJmol^{-1}), compared to the two experimental alloys Ti-6Al-1V-3Fe (487 kJmol^{-1}) and Ti-4.5Al-1V-3Fe (465 kJmol^{-1}) suggests that the chemical composition influenced the activation energy. The 6 wt% Al alloy had a higher Q_{HW} than the 4.5 wt% Al implying a higher deformation resistance. In general, the Q_{HW} values fall within the range of Q_{HW} reported for Ti-6Al-4V and other α+β titanium alloys.

Table 8.3: Activation energy for hot working of some commercial and experimental titanium alloys.

Alloy	Activation energy ($kJmol^{-1}$) in (α+β) phase field	Initial microstructure	Deformation parameters	Reference
Ti-6Al-4V	**620**	**Elongated α + equiaxed α + intergranular β**	**750 - 950°C/0.01 – 10 s^{-1}/ 60%**	**This work**
Ti-6Al-1V-3Fe	**487**	**Lamellar**	**750 - 950°C/0.001 – 10 s^{-1}/ 60%**	**This work**
Ti-4.5Al-1V-3Fe	**465**	**Lamellar**	**750 - 950°C/0.001 – 10 s^{-1}/ 60%**	**This work**
Ti-6Al-4V	355 - 720	-	700 - 940°C /10^{-3} - 10^{-1} s^{-1}	Bryant, 1975
Ti-6Al-4V	350 - 2000	-	880 - 980°C /10^{-3} - 10^{-1} s^{-1}	Briottet (1996)
Ti-6Al-4V	700	Lamellar	815 - 955°C /10^{-3} - 10^{-1} s^{-1}	Semiatin (1999)
Ti-6Al-4V	613	Primary α + retained β	900 - 1050°C/0.1 - 10 s^{-1}	Pontadawit (2014)
Ti-6Al-4V-0.1Ru	630	Coarse lamellar	750 - 1150°C/0.01 - 10 s^{-1}/ 60%	Xia (2016)
TC-11: Ti-6A.5Al-3.5Mo-1.5Zr-0.3Si	538	Bimodal	750 - 950°C/0.1 - 10 s^{-1}/ 60%	Zong (2009)
TC-11	590	-	800 - 1050°C/0.1 - 10 s^{-1}/ 75%	Junhui (2012)
Ti-6Al-4V	677	Bimodal	820 - 1030°C/0.1 - 10 s^{-1}/ 75%	Luo (2009)
Ti-6Al-4V	402	Small colony + fine lamellar, fine lamellar spacing	750 - 950°C/0.1 - 10 s^{-1}/ 75%	Guan (2012)
Ti-6Al-4V	530	Lamellar	800 - 1150°C/0.1 - 10 s^{-1}	Momeni and Abbasi (2010)
Ti-6Al-4V	398	Small colony + fine lamellar with large lamellar spacing	750 - 950°C/0.1 - 10 s^{-1}/ 75%	Guan (2012)
Ti-17	559	Lamellar	780 - 860°C/0.001 - 10 s^{-1}/ 60%	Liu (2014)
TC4-DT	656 - 735	Bimodal	930 - 1020°C/0.001 - 10 s^{-1}/ 90%	X. Peng (2013)
Ti-6Al-4V	455	Lamellar	750-1100°C/0.0003 - 10 s^{-1}/50%	Seshacharyulu (2002)
Ti-6Al-4V	584	Partially equiaxed α + elongated α + fine equiaxed β	770 - 920°C /0.01 - 10 s^{-1}	Souza **(2015a)**
IMI-834	672	Bimodal	850 - 1060°C /0.0003 -1 s^{-1}	Balasundar **(2013b)**
IMI-834	703	Bimodal	960 - 1030°C /0.001 - 1 s^{-1}/80%	Wanjara (2005)
Ti-5.6Al-4.8Sn-2.0Zr	1082	Bimodal	960 - 1030°C /0.001 - 10 s^{-1}/70%	Li (2007)

8.4 Implication of the research findings

This research considered two major approaches to reduce the cost of producing components from titanium alloys. The first approach focussed on the use of low-cost beta stabilising elements and the reduction in the amount of alpha stabilising elements. The vanadium content in the titanium "workhorse" (Ti-6Al-4V) was partially replaced by iron and the aluminium content was reduced to 4.5 wt %. As indicated in Chapter 3, up to 7% of the total cost of raw materials could be saved when producing Ti-6Al-1V-3Fe and Ti-4.5Al-1V-3Fe alloys. The cost saved from the careful selection of the alloying elements did not result in inferior hardness and corrosion properties of the experimental alloys. It was reported in Chapter 5 that the experimental alloys (Ti-6Al-1V-3Fe and Ti-4.5Al-1V-3Fe) offered superior corrosion performance in comparison with commercial Ti-6Al-4V when exposed to a sulphuric acid medium and the corrosion performance of the alloys was comparable to that of Ti-6Al-4V in a sodium chloride environment. Additionally, the microstructural features and hardness presented in Chapter 4 were comparable to the commercial alloy. Hence, these alloys are promising for land-based applications such as the chemical, automotive, consumer goods and biomedical industries.

As previously mentioned in Chapters 1 and 2, up to 30% of the cost of titanium alloy is contributed by the primary conversion processes (hot working), such as forging, rolling and extrusion. Therefore, the second cost reducing approach employed in this research was to optimise the hot working process using process maps. It was envisaged that this approach would further reduce the cost of the alloys and also minimise waste incurred during production processes. The typical parameters imposed on metallic alloys during industrial processes such as forging, extrusion and machining are presented in Table 8.4. The hot working parameters selected in this study were in the lower range of parameters acceptable for sheet metal forming, extrusion, rolling and forging of metallic alloys. The safe processing regimes identified in this study, although limited in total strain and strain rate, could serve as a guide for the production of semi-finished and finished goods with reproducible microstructures and mechanical properties.

However, the commercial production of metallic alloys requires increased production rates, so hot working processes need to be carried out at the highest possible strain rates. It is not possible to test materials at very high strain rates and high strains on the locally available testing machines. Torsion testing may provide closer physical simulation. Hence, the need for finite element methods for simulation of extreme processing conditions has become important (Oh *et al.*, 1991). However, FEM models are useful only if experimetnal data in those high strain and strain rate areas is used. Future work will consider the development of constitutive models that can describe the flow behaviour of these materials under different conditions of strain rates, strain and

temperatures. The constitutive models will then be used in finite element methods to predict the behaviour of the alloys under industrial conditions that cannot be tested in the lab.

Table 8.4: Typical hot working parameters of some industrial processes (Jaspers and Dautzenberg, 2002; Odenberger *et al.*, 2011; Alabort *et al.*, 2016).

Processes	Strain	Strain rates	$T_{homologus}= (T/T_{melt})$
Extrusion	2 - 5	0.1 - 100	0.16 - 0.7
Forging/rolling	0.1 - 0.5	1 - 1000	0.16 - 0.7
Sheet metal forming	0.1 - 0.5	0.0001 - 100	0.16 - 0.7
Machining	1 - 10	1000 - 1000000	0.16 - 0.9

The current research advances in the manufacturing of cost-effective titanium components are more focussed on additive manufacturing (3D printing), because of the advantages it offers by avoiding several primary and secondary conversion steps in the conventional titanium production process. Recently, a novel approach named *FAST-forge* has been demonstrated on a laboratory scale to showcase the possibilities of using the additive manufacturing processes to achieve low-cost titanium components (Weston and Jackson, 2017). The process involves converting titanium alloy powder to components in two simple steps, through the use of field assisted sintering technology. The properties of the components produced via this route were comparable to a wrought alloy.

Despite the potential of additive manufacturing processes to be economically advantageous, the methods are still developing and evolving. At present, most commercial titanium components are still produced via the ingot metallurgy route. The results that were presented on the optimisation of hot working of titanium alloys (Ti-6Al-4V, Ti6Al-1V-3Fe and Ti-4.5Al-1V-3Fe) in Chapters 6 and 7 are relevant to the current commercial production technique of titanium alloys.

Chapter 9: Conclusions and Recommendations

9.1 Conclusions

In this research, potentially low-cost titanium alloys were developed as an alternative alloy to the commercial Ti-6Al-4V alloy popularly known as the "titanium workhorse". The target applications for these alloys are essentially land-based which include: automotive, biomedical, sports, jewellery and chemical industries. The problem addressed in this research was the high cost of titanium alloys. From the literature survey, expensive alloying elements, complex hot working and difficult machining were some of the major factors contributing to the high cost of titanium alloys. The two factors addressed were the use of cheap alloying elements in place of expensive alloying elements in titanium alloys, and the optimisation of the complex hot working of titanium alloys. The following conclusions were made:

1. **The influence of alloy composition (partial substitution of vanadium with iron and reduction of aluminium concentration) and annealing on the microstructure and hardness of newly developed Ti-6Al-*x*V-*y*Fe and Ti-4.5Al-*x*V-*y*Fe alloys**

   (a) The as-cast and annealed experimental alloys contained mostly α and β phases with some TiO_2 and FeO_3Ti at room temperature. The β-phase fraction increased with increasing iron concentration in the as-cast alloys, but decreased after annealing. In the as-cast condition, aluminium had an insignificant effect on the beta phase fraction, but after annealing, decreasing the aluminium concentration increased the beta phase fraction since there was less aluminium to stabilise the alpha phase.

   (b) It is likely that annealing caused partitioning of alloying elements by allowing enough time for diffusion-controlled bcc-β to hcp-α transformation to take place. This influenced the volume fraction of phases of the annealed experimental alloys. The volume fraction of alpha phase in the annealed samples was higher than that of the as-cast samples.

   (c) The as-cast and annealed microstructures contained Widmanstätten α-laths within the prior β-grains. There was no obvious relationship between the concentration of iron and prior β grain size due to the large error bars. There was no evidence of grain refinement with increase in aluminium, iron or vanadium.

(d) Hardness increased with increasing iron content in all 6 wt% Al and 4.5 wt% Al samples. The sample with the highest hardness was Ti-6Al-4Fe. Decreasing the aluminium content from 6 wt% to 4.5 wt% decreased the hardness. The relationship between iron content and lath thickness was difficult to deduce because of the large error bars. However, the general trend indicated the possibility of having lath refinement with increasing iron content in the experimental alloys. Lath refinement, and solid solution strengthening by iron, aluminium and dissolved oxygen may have increased the hardness of the alloys in both as-cast and annealed conditions.

2. The influence of partial substitution of vanadium with iron and the reduction in aluminium content on the corrosion behaviour of Ti-6Al-*x*V-*y*Fe and Ti-4.5Al-*x*V-*y*Fe alloys

(a) The experimental alloys showed good corrosion resistance and were comparable with that of the commercial alloy in 3.5 wt% NaCl solutions. The partial substitution of V with more than 1wt% Fe (Ti-6Al-2V-2Fe, Ti-6Al-1V-3Fe, Ti-4.5Al-2V-2Fe and Ti-4.5Al-1V-3Fe alloys) yielded lower corrosion ratescompared with the commercial alloys. These alloys could be serving as potential low-cost replacements for Ti-6Al-4V alloy in marine industries.

(b) In 3.5M H_2SO_4,the experimental alloys (Ti-6Al-3V-1Fe; Ti-6Al-2V-2Fe and Ti-6Al-1V-3Fe) containing both Fe and V as β stabilisers showed better corrosion resistance than the Ti-6Al-4V alloy with lower corrosion rates, critical current densities and passivation currents respectively.

(c) In a mixed solutions of 3.5M H_2SO_4+1.75 wt% NaCl, the commercial Ti-6Al-4V alloy displayed superior corrosion resistance to the experimental Ti-6Al-1V-3Fe alloy. However, Ti-6Al-1V-3Fe and Ti-4.5Al-1V-3Fe alloys were better than Ti-6Al-4Fe when considering the experimental alloys in the mixed solution.

(d) A slight reduction in Al content and the combination of 2-3wt% Fe and V as beta stabilisers slightly reduced the corrosion rate of the experimental Ti-Al-V-Fe alloys in all the tested environments.

3. The influence of a complex initial microstructure on the hot deformation behaviour of Ti-6Al-4V alloy

(a) The stress-strain behaviour showed a dependence of flow stress on strain rate, deformation temperature and strain. Discontinuous yielding occurred at strain rates of

$0.01s^{-1}$, with oscillating flow stresses occurred at higher strain rates. Continuous flow softening occurred at all strain rates and deformation temperatures below 950°C. These trends showed the general transient behaviour of flow stress under various deformation conditions.

(b) Processing maps revealed stable processing regions at total strains of 0.2, 0.5 and 0.6. These regions were validated by testing at 920°C/1 s^{-1} (0.2 strain) and 950°C/1 s^{-1} (0.6 strain), while regions of instability were identified at strains of 0.5 and 0.6, at temperatures higher than 935°C and strain rates of 0.05 - 0.1 s^{-1}. The region of instability was validated by the test done at 950°C/0.1 s^{-1}. Additionally, another unstable deformation region was observed at 750 - 810°C /1 - 2.7 s^{-1} at a strain of 0.6. These regions should be avoided during processing of Ti-6Al-4V with a complex initial microstructure. The optimum processing conditions for stable deformation were found to be:

- ~940°C/0.4 - $1.7s^{-1}$ ($\varepsilon = 0.2$)
- ~945°C/0.4 - $1.7s^{-1}$ ($\varepsilon = 0.5$)
- ~940 - 950°C/0.4 - $1.7s^{-1}$ ($\varepsilon = 0.6$).

These optimum processing conditions were interpolated data obtained from the processing maps.

(c) The transient flow stress behaviour caused differences in the processing maps obtained at different strains. Since similar features have not been reported for Ti-6Al-4V with fully lamellar or with fully equiaxed initial microstructures, the transient behaviour was attributed to the complex initial microstructure of the Ti-6Al-4V alloy considered in this study.

(d) Microstructural analysis confirmed that dynamic globularisation of alpha was the dominant softening mechanism during the deformation of the alloy under optimum conditions. Other phenomena which contributed to softening included deformation heating and phase transformation. Deformation heating manifested as grain growth in samples deformed at temperatures below 900°C and high strain rates ($1s^{-1}$ and $10s^{-1}$). Deformation-induced phase transformations lowered the beta transus by ~45°C when the Ti-6Al-4V alloy was deformed at 950°C and 0.01 s^{-1} strain rate. Increasing the deformation temperatures led to a high volume fraction of the beta phase, but the influence of strain rate on the volume fraction of beta phase formed, was inconsistent.

4. The influence of alloy composition on the hot deformation behaviour of the newly developed alloy and the optimum hot working conditions

(a) The flow stress was influenced by deformation temperature strain rate, strain and alloy composition. The stress-strain behaviour showed that increasing the strain rate and decreasing the deformation temperatures increased the flow stress. Ti-4.5Al-1V-3Fe, with lower aluminium and total solute content, exhibited a lower flow stress than Ti-6Al-1V-3Fe alloy. The flow softening exhibited by the stress-strain curves was dependent on the deformation parameters. Adiabatic heating contributed to flow softening at high strain rates and low deformation temperatures.

(b) Ti-6Al-1V-3Fe and Ti-4.5Al-1V-3Fe alloys showed a wide processing window due to small area of instability on the processing maps. However, the higher power dissipation values seen in Ti-4.5Al-1V-3Fe suggested that the alloy was much easier to deform. The optimum working conditions obtained from the processing maps for the alloys were:

- Ti-6Al-1V-3Fe: 900°C /0.1s^{-1}
- Ti-4.5Al-1V-3Fe: 900°C /0.01 s^{-1},

while the region of unsafe deformation for both alloys were:

- Ti-6Al-1V-3Fe: 750-780°C / 1.2 - 10s^{-1}.
- Ti-4.5Al-1V-3Fe: 880-930°C / 0.1 - 0.3s^{-1}.

The above regions were validated by testing both alloys at 900°C/0.1 s^{-1}, 900°C/0.01 s^{-1}, and 750°C/10 s^{-1}.

(c) Dynamic recrystallisation of the prior beta grains was the dominant softening mechanism for Ti-6Al-1V-3Fe alloy when deformed at the optimum working condition while the presence of alpha globules confirmed dynamic globularisation as the dominant softening mechanism in the Ti-4.5Al-1V-3Fe deformed at the optimum working conditions. Adiabatic shear band, void nucleation and cracking manifested as flow instabilities in the unsafe deformation region on the processing map.

(e) Dynamic globularisation of the alpha phase occurred in the Ti-4.5Al-1V-3Fe alloy much easier and faster (0.1s^{-1}) than in Ti-6Al-1V-3Fe alloy (0.01 s^{-1}), due to different strength levels of the alpha phase with varying aluminium/solute content.

5. The influence of alloy composition on the activation energy for hot working showed that the experimental alloy with a higher aluminium content (Ti-6Al-1V-3Fe) had a slightly higher Q_{HW}, implying a higher deformation resistance than Ti-4.5Al-1V-3Fe. The two experimental alloys had lower Q_{HW} than the wrought T-6Al-4V. The Q_{HW} values of the alloys considered in this study were comparable to some values reported in literature.

9.2 Suggestions for further research

To extend the knowledge base of the experimental Ti-Al-V-Fe alloys, the following recommendations for further research are made:

1. A constitutive model that can be used to describe the non steady-state flow stress should be developed to predict the flow stress of the experimental alloys. This equation can be used in finite element methods for further optimisation of the hot working of the alloys especially at conditions that cannot be tested in the labouratory.
2. Machining also contributes significantly to the high cost of titanium alloys. Therefore, the machining parameters of the new alloys need to be optimised. This will involve both experimental studies and finite element modelling to derive the optimum parameters for improved machinability of the alloys.
3. Having established that partial substitution of vanadium with iron offered superior corrosion resistance to commercial Ti-6Al-4V in reducing acids like sulphuric acid and that the reduction in aluminium can improve the corrosion properties of the alloys, the underlying mechanisms are yet to be understood. Therefore, the behaviour of the passive film that is formed during anodic polarisation of the experimental alloys needs an extensive and advanced characterisation to understand the mechanisms responsible for the passivation behaviour of the alloys.
4. Since hardness of the experimental alloys was the only room temperature property determined, other mechanical properties, such as tensile and fatigue should be evaluated. These properties need to be determined and correlated with the different microstructures from thermomechanical treatments, before the alloys can be used for commercial applications.

Chapter 10: References

Ahmed, T., Rack, H.J., 1998. Phase transformations during cooling in α+β titanium alloys. Mater. Sci. Eng. A 243, 206–211. https://doi.org/10.1016/S0921-5093(97)00802-2

Akbari, Z., Mirzadeh, H., Cabrera, J.-M., 2015. A simple constitutive model for predicting flow stress of medium carbon microalloyed steel during hot deformation. Mater. Des. 77, 126–131. https://doi.org/10.1016/j.matdes.2015.04.005

Akhonin, S.V., Trigub, N.P., Zamkov, V.N., Semiatin, S.L., 2003. Mathematical modeling of aluminum evaporation during electron-beam cold-hearth melting of Ti-6Al-4V ingots. Metall. Mater. Trans. B 34, 447–454. https://doi.org/10.1007/s11663-003-0071-4

Alabort, E., Kontis, P., Barba, D., Dragnevski, K., Reed, R.C., 2016. On the mechanisms of superplasticity in Ti–6Al–4V. Acta Mater. 105, 449–463. https://doi.org/10.1016/j.actamat.2015.12.003

Alabort, E., Putman, D., Reed, R.C., 2015. Superplasticity in Ti–6Al–4V: Characterisation, modelling and applications. Acta Mater. 95, 428–442. https://doi.org/10.1016/j.actamat.2015.04.056

Andijani, I.N., Ahmad, S., Malik, A.U., 2000. Corrosion behavior of titanium metal in the presence of inhibited sulfuric acid at 50°C. Desalination 129, 45–51. https://doi.org/10.1016/S0011-9164(00)00050-3

Ankem, S., Greene, C.A., 1999. Recent developments in microstructure/property relationships of beta titanium alloys. Mater. Sci. Eng. A 263, 127–131. https://doi.org/10.1016/S0921-5093(98)01170-8

Aragon, P.J., Hulbert, S.F., 1972. Corrosion of Ti-6Al-4V in simulated body fluids and bovine plasma. J. Biomed. Mater. Res. 6, 155–164. https://doi.org/10.1002/jbm.820060304

ASTM B348 - 13, 2013. Standard Specification for Titanium and Titanium Alloy Bars and Billets.

ASTM E 92 - 17, 2017. Standard Test Methods for Vickers Hardness and Knoop Hardness of Metallic Materials.

ASTM G59-97, 2014. Standard Test Method for Conducting Potentiodynamic Polarization Resistance Measurements.

Atapour, M., Pilchak, A., Frankel, G.S., Williams, J.C., 2010a. Corrosion behaviour of investment cast and friction stir processed Ti–6Al–4V. Corros. Sci. 52, 3062–3069. https://doi.org/10.1016/j.corsci.2010.05.026

Atapour, M., Pilchak, A., Frankel, G.S., Williams, J.C., Fathi, M.H., Shamanian, M., 2010b. Corrosion Behavior of Ti-6Al-4V with Different Thermomechanical Treatments and Microstructures. CORROSION 66, 065004-065004-9. https://doi.org/10.5006/1.3452400

Atapour, M., Pilchak, A.L., Shamanian, M., Fathi, M.H., 2011. Corrosion behavior of Ti–8Al–1Mo–1V alloy compared to Ti–6Al–4V. Mater. Des. 32, 1692–1696. https://doi.org/10.1016/j.matdes.2010.09.009

Australian titanium: A new continuous process for the direct production of CP Ti powder developed at CSIRO [WWW Document], 2012. . Powder Metall. Rev. URL http://www.pm-review.com/australian-titanium-a-new-continuous-process-for-the-direct-production-of-cp-ti-powder-developed-at-csiro/ (accessed 1.25.18).

Avyle, J.A.V.D., Brooks, J.A., Powell, A.C., 1998. Reducing defects in remelting processes for high-performance alloys. JOM 50, 22–25. https://doi.org/10.1007/s11837-998-0374-7

Badea, G.E., Caraban, A., Sebesan, M., Dzitac, S., Cret, P., Setel, A., 2010. Polarisation Measurements Used for Corrosion Rates Determination. J. Sustenable Energy 1.

Bai, G., Lu, S., Li, D., Li, Y., 2016. Influences of niobium and solution treatment temperature on pitting corrosion behaviour of stabilised austenitic stainless steels. Corros. Sci. 108, 111–124. https://doi.org/10.1016/j.corsci.2016.03.009

Bai, X.F., Zhao, Y.Q., Zeng, W.D., Jia, Z.Q., Zhang, Y.S., 2014. Characterization of hot deformation behavior of a biomedical titanium alloy TLM. Mater. Sci. Eng. A 598, 236–243. https://doi.org/10.1016/j.msea.2014.01.005

Balachandran, S., Kumar, S., Banerjee, D., 2017. On recrystallization of the α and β phases in titanium alloys. Acta Mater. 131, 423–434. https://doi.org/10.1016/j.actamat.2017.04.008

Balasubrahmanyam, V.V., Prasad, Y.V.R.K., 2002. Deformation behaviour of beta titanium alloy Ti–10V–4.5Fe–1.5Al in hot upset forging. Mater. Sci. Eng. A 336, 150–158. https://doi.org/10.1016/S0921-5093(01)01982-7

Balasubramaniam, R., 2009. Callister'S Materials Science And Engineering: Indian Adaptation (W/Cd). John Wiley & Sons.

Balasundar, I., Raghu, T., Kashyap, B.P., 2014. Hot working and geometric dynamic recrystallisation behaviour of a near-α titanium alloy with acicular microstructure. Mater. Sci. Eng. A 600, 135–144. https://doi.org/10.1016/j.msea.2014.01.088

Balasundar, I., Raghu, T., Kashyap, B.P., 2013a. Processing map for a cast and homogenized near alpha titanium alloy. Int. J. Mater. Form. 8, 85–97. https://doi.org/10.1007/s12289-013-1150-y

Balasundar, I., Raghu, T., Kashyap, B.P., 2013b. Modeling the hot working behavior of near-α titanium alloy IMI 834. Prog. Nat. Sci. Mater. Int. 23, 598–607. https://doi.org/10.1016/j.pnsc.2013.11.004

Balasundar, I., Ravi, K.R., Raghu, T., 2017. On the high temperature deformation behaviour of titanium alloy BT3-1. Mater. Sci. Eng. A 684, 135–145. https://doi.org/10.1016/j.msea.2016.12.043

Baloyi, R., 2011. Investigation Into The Effect of Solid Solution Chemistry On Lattice Parameters and Microstructural Properties of Beta -Ti Alloys - Final Dissertation - Corrected Submission. University of the Witwatersrand, South Africa.

Banerjee, D., Williams, J.C., 2013. Perspectives on Titanium Science and Technology. Acta Mater., The Diamond Jubilee Issue 61, 844–879. https://doi.org/10.1016/j.actamat.2012.10.043

Bauristhene, A.M., Mutombo, K., Stumpf, W.E., 2013. Alpha case formation mechanism in Ti-6Al-4V alloy investment castings using YFSZ shell moulds. J. South. Afr. Inst. Min. Metall. 113, 357–361.

Bautista, A., Moral, C., Blanco, G., Velasco, F., 2005. Influence of sintering on the corrosion behavior of a Ti-6Al-4V alloy. Mater. Corros. 56, 98–103. https://doi.org/10.1002/maco.200403818

Benson, L.L., Mellor, I., Jackson, M., 2016. Direct reduction of synthetic rutile using the FFC process to produce low-cost novel titanium alloys. J. Mater. Sci. 51, 4250–4261. https://doi.org/10.1007/s10853-015-9718-1

Bermingham, M.J., McDonald, S.D., Dargusch, M.S., StJohn, D.H., 2008. Grain-refinement mechanisms in titanium alloys. J. Mater. Res. 23, 97–104. https://doi.org/10.1557/JMR.2008.0002

Bettles, C.J., Tomus, D., Gibson, M.A., 2011. The role of microstructure in the mechanical behaviour of Ti–1.6 wt.%Fe alloys containing O and N. Mater. Sci. Eng. A 528, 4899–4909. https://doi.org/10.1016/j.msea.2011.03.030

Bhattacharjee, A., Ghosal, P., Gogia, A.K., Bhargava, S., Kamat, S.V., 2007. Room temperature plastic flow behaviour of Ti–6.8Mo–4.5Fe–1.5Al and Ti–10V–4.5Fe–1.5Al: Effect of grain size and strain rate. Mater. Sci. Eng. A 452–453, 219–227. https://doi.org/10.1016/j.msea.2006.10.166

Blackburn, M.J., Malley, D.R., 1993. Plasma arc melting of titanium alloys. Mater. Des., The Processing, Properties and Applications of Metallic and Ceramic Materials 14, 19–27. https://doi.org/10.1016/0261-3069(93)90041-S

Blackwood, D.J., Peter, L.M., 1989. The influence of growth rate on the properties of anodic oxide films on titanium. Electrochimica Acta 34, 1505–1511. https://doi.org/10.1016/0013-4686(89)87033-1

Blackwood, D.J., Peter, L.M., Williams, D.E., 1988. Stability and open circuit breakdown of the passive oxide film on titanium. Electrochimica Acta 33, 1143–1149. https://doi.org/10.1016/0013-4686(88)80206-8

Bolzoni, L., Esteban, P.G., Ruiz-Navas, E.M., Gordo, E., 2012. Mechanical behaviour of pressed and sintered titanium alloys obtained from master alloy addition powders. J. Mech. Behav. Biomed. Mater. 15, 33–45. https://doi.org/10.1016/j.jmbbm.2012.05.019

Bolzoni, L., Ruiz-Navas, E.M., Gordo, E., 2016. Understanding the properties of low-cost iron-containing powder metallurgy titanium alloys. Mater. Des. 110, 317–323. https://doi.org/10.1016/j.matdes.2016.08.010

Boyer, R.R., 2010. Attributes, characteristics, and applications of titanium and its alloys. JOM 62, 21–24. https://doi.org/10.1007/s11837-010-0071-1

Boyer, R.R., 1996. An overview on the use of titanium in the aerospace industry. Mater. Sci. Eng. A, International Symposium on Metallurgy and Technology of Titanium Alloys 213, 103–114. https://doi.org/10.1016/0921-5093(96)10233-1

Boyer, R.R., 1995. Titanium for aerospace: Rationale and applications. Adv. Perform. Mater. 2, 349–368. https://doi.org/10.1007/BF00705316

Bragg, W.H., Bragg, W.L., 1913. The reflection of X-rays by crystals. Proc R Soc Lond A 88, 428–438. https://doi.org/10.1098/rspa.1913.0040

Breiter, M.W., 1970. Galvanostatic studies of passivity and breakdown of passivity of titanium in hydrochloric acid solutions. Electrochimica Acta 15, 1195–1200. https://doi.org/10.1016/0013-4686(70)85012-5

Briottet, L., Jonas, J.J., Montheillet, F., 1996. A mechanical interpretation of the activation energy of high temperature deformation in two phase materials. Acta Mater. 44, 1665–1672. https://doi.org/10.1016/1359-6454(95)00257-X

Broichhausen, J., vanKann, H., 1973. Influence of forging conditions on the fatigue behaviour of Ti6Al4V. Titan. Sci. Technol. 3, 1785–1799.

Brun, M., Anoshkin, N., Shakhanova, G., 1998. Physical processes and regimes of thermomechanical processing controlling development of regulated structure in the α+β titanium alloys. Mater. Sci. Eng. A 243, 77–81. https://doi.org/10.1016/S0921-5093(97)00781-8

Bryant, W.A., 1975. Correlation of data on the hot deformation of Ti-6Al-4V. J. Mater. Sci. 10, 1793–1797.

Cai, J., Li, F., Liu, T., Chen, B., He, M., 2011. Constitutive equations for elevated temperature flow stress of Ti–6Al–4V alloy considering the effect of strain. Mater. Des. 32, 1144–1151. https://doi.org/10.1016/j.matdes.2010.11.004

Calvert, E., Pollard, J., Jackson, M., Wynne, B., Thackray, R., 2015. Determining a Flow Stress Model for High Temperature Deformation of Ti-6Al-4V, in: Materials Science Forum. Presented at the Light Metals Technology, Trans Tech Publications, Switzerland, Port Elizabeth, South Africa, pp. 441–446. https://doi.org/10.4028/www.scientific.net/MSF.828-829.441

Campbell, K., 2013. CSIR titanium projects seek to create a 21st century industry in SA [WWW Document]. Eng. News. URL http://www.engineeringnews.co.za/article/sa-moves-to-use-titanium-ores-base-to-build-new-high-tech-industry-2013-08-30 (accessed 1.25.18).

Caprani, A., Frayret, J.P., 1979. Behaviour of titanium in concentrated hydrochloric acid: dissolution-passivation mechanism. Electrochimica Acta 24, 835–842. https://doi.org/10.1016/0013-4686(79)87006-1

Carman, A., Zhang, L.C., Ivasishin, O.M., Savvakin, D.G., Matviychuk, M.V., Pereloma, E.V., 2011. Role of alloying elements in microstructure evolution and alloying elements behaviour during sintering of a near-β titanium alloy. Mater. Sci. Eng. A 528, 1686–1693. https://doi.org/10.1016/j.msea.2010.11.004

Castellanos, J., Rieiro, I., Carsí, M., Muñoz, J., El Mehtedi, M., Ruano, O.A., 2009. Analysis of adiabatic heating and its influence on the Garofalo equation parameters of a high nitrogen steel. Mater. Sci. Eng. A 517, 191–196. https://doi.org/10.1016/j.msea.2009.03.042

Chang, J.-K., Takata, K., Ichitani, K., Taleff, E.M., 2010. Abnormal Grain Growth and Recrystallization in Al-Mg Alloy AA5182 Following Hot Deformation. Metall. Mater. Trans. A 41, 1942–1953. https://doi.org/10.1007/s11661-010-0213-7

Charlu, T.V., Kleppa, O.J., Reed, T.B., 1974. High-temperature combustion calorimetry III. Enthalpies of formation of titanium oxides. J. Chem. Thermodyn. 6, 1065–1074. https://doi.org/10.1016/0021-9614(74)90068-8

Chen, B.-Y., Hwang, K.-S., 2012. Sintered Ti–Fe alloys with *in situ* synthesized TiC dispersoids. Mater. Sci. Eng. A 541, 88–97. https://doi.org/10.1016/j.msea.2012.02.007

Chen, B.-Y., Hwang, K.-S., Ng, K.-L., 2011. Effect of cooling process on the α phase formation and mechanical properties of sintered Ti–Fe alloys. Mater. Sci. Eng. A 528, 4556–4563. https://doi.org/10.1016/j.msea.2011.02.092

Chen, G., Ren, C., Qin, X., Li, J., 2015. Temperature dependent work hardening in Ti–6Al–4V alloy over large temperature and strain rate ranges: Experiments and constitutive modeling. Mater. Des. 83, 598–610. https://doi.org/10.1016/j.matdes.2015.06.048

Chen, G.Z., Fray, D.J., Farthing, T.W., 2000. Direct electrochemical reduction of titanium dioxide to titanium in molten calcium chloride. Nature 407, 361–364. https://doi.org/10.1038/35030069

Chen, H., Cao, C., 2012. Characterization of hot deformation microstructures of alpha-beta titanium alloy with equiaxed structure. Trans. Nonferrous Met. Soc. China 22, 503–509. https://doi.org/10.1016/S1003-6326(11)61205-3

Chen, H., Cao, C., GUO, L., Lin, H., 2008. Hot deformation mechanism and microstructure evolution of TC11 titanium alloy in β field. Trans. Nonferrous Met. Soc. China 18, 1021–1027. https://doi.org/10.1016/S1003-6326(08)60175-2

Chen, L., Zhao, G., Yu, J., Zhang, W., 2015. Constitutive analysis of homogenized 7005 aluminum alloy at evaluated temperature for extrusion process. Mater. Des. 1980-2015 66, 129–136. https://doi.org/10.1016/j.matdes.2014.10.045

Chen, X.-M., Lin, Y.C., Wen, D.-X., Zhang, J.-L., He, M., 2014. Dynamic recrystallization behavior of a typical nickel-based superalloy during hot deformation. Mater. Des. 57, 568–577. https://doi.org/10.1016/j.matdes.2013.12.072

Choubey, A., Balasubramaniam, R., Basu, B., 2004. Effect of replacement of V by Nb and Fe on the electrochemical and corrosion behavior of Ti–6Al–4V in simulated physiological environment. J. Alloys Compd. 381, 288–294. https://doi.org/10.1016/j.jallcom.2004.03.096

Choubey, A., Basu, B., Balasubramaniam, R., 2005. Electrochemical behavior of Ti-based alloys in simulated human body fluid environment. Trends Biomater. Artif. Organs 18, 64–72.

Choubey, A., Basu, B., Balasubramaniam, R., 2004. Electrochemical behavior of intermetallic Ti3Al-based alloys in simulated human body fluid environment. Intermetallics 12, 679–682. https://doi.org/10.1016/j.intermet.2004.03.012

Ciszak, C., Popa, I., Brossard, J.-M., Monceau, D., Chevalier, S., 2016. NaCl induced corrosion of Ti-6Al-4V alloy at high temperature. Corros. Sci. 110, 91–104.

Clark, J., 2012. R5bn titanium industry planned for SA by 2020 [WWW Document]. Moneyweb. URL https://www.moneyweb.co.za/archive/r5bn-titanium-industry-planned-for-sa-by-2020/ (accessed 2.6.18).

CSIR, 2018. Titanium pilot plant | CSIR [WWW Document]. URL https://www.csir.co.za/titanium-pilot-plant (accessed 1.25.18).

CSIRO, 2016. Making titanium metal powder [WWW Document]. URL https://www.csiro.au/en/Research/MF/Areas/Metals/Processing/TiRO-powder (accessed 1.25.18).

Dai, N., Zhang, L.-C., Zhang, J., Chen, Q., Wu, M., 2016. Corrosion behavior of selective laser melted Ti-6Al-4 V alloy in NaCl solution. Corros. Sci. 102, 484–489. https://doi.org/10.1016/j.corsci.2015.10.041

Davenport, S.B., Silk, N.J., Sparks, C.N., Sellars, C.M., 2000. Development of constitutive equations for modelling of hot rolling. Mater. Sci. Technol. 16, 539–546. https://doi.org/10.1179/026708300101508045

Davim, J.P. (Ed.), 2014. Machining of Titanium Alloys, Materials Forming, Machining and Tribology. Springer Berlin Heidelberg, Berlin, Heidelberg. https://doi.org/10.1007/978-3-662-43902-9

Dehghan-Manshadi, A., Dippenaar, R.J., 2012. Strain-induced phase transformation during thermo-mechanical processing of titanium alloys. Mater. Sci. Eng. A 552, 451–456. https://doi.org/10.1016/j.msea.2012.05.069

Devilliers, D., Dinh, M.T., Mahé, E., Krulic, D., Larabi, N., Fatouros, N., 2006. Behaviour of Titanium in Sulphuric Acid — Application to DSAs —. J. New Mater. Electrochem. Syst. 9, 221–232.

Dewey, J.F., 1965. Nature and origin of kink-bands. Tectonophysics 1, 459–494. https://doi.org/10.1016/0040-1951(65)90019-3

Dieter, G.E., Kuhn, H.A., Semiatin, S.L., 2003. Handbook of workability and process design. ASM International.

Dinda, G.P., Song, L., Mazumder, J., 2008. Fabrication of Ti-6Al-4V Scaffolds by Direct Metal Deposition. Metall. Mater. Trans. A 39, 2914–2922. https://doi.org/10.1007/s11661-008-9634-y

Ding, R., Guo, Z.X., Wilson, A., 2002. Microstructural evolution of a Ti–6Al–4V alloy during thermomechanical processing. Mater. Sci. Eng. A 327, 233–245. https://doi.org/10.1016/S0921-5093(01)01531-3

Dobromyslov, A.V., Elkin, V.A., 2001. Martensitic transformation and metastable β-phase in binary titanium alloys with d-metals of 4–6 periods. Scr. Mater. 44, 905–910. https://doi.org/10.1016/S1359-6462(00)00694-1

Doherty, R.D., Hughes, D.A., Humphreys, F.J., Jonas, J.J., Jensen, D.J., Kassner, M.E., King, W.E., McNelley, T.R., McQueen, H.J., Rollett, A.D., 1997. Current issues in recrystallization: a review. Mater. Sci. Eng. A 238, 219–274. https://doi.org/10.1016/S0921-5093(97)00424-3

Donachie, M.J., 2000. Titanium: A Technical Guide, 2nd Edition. ASM International.

Duan, Y., Li, P., Xue, K., Zhang, Q., Wang, X., 2007. Flow behavior and microstructure evolution of TB8 alloy during hot deformation process. Trans. Nonferrous Met. Soc. China 17, 1199–1204. https://doi.org/10.1016/S1003-6326(07)60249-0

Duerig, T.W., Terlinde, G.T., Williams, J.C., 1980. Phase transformations and tensile properties of Ti-10V-2Fe-3AI. Metall. Trans. A 11, 1987–1998. https://doi.org/10.1007/BF02655118

Dutta, B., Froes, F.H. (Sam), 2017. The Additive Manufacturing (AM) of titanium alloys. Met. Powder Rep. 72, 96–106. https://doi.org/10.1016/j.mprp.2016.12.062

Edwards, P., O'Conner, A., Ramulu, M., 2013. Electron beam additive manufacturing of titanium components: properties and performance. J. Manuf. Sci. Eng. 135, 061016.

Esteban, P.G., Ruiz-Navas, E.M., Bolzoni, L., Gordo, E., 2008. Low-cost titanium alloys? Iron may hold the answers. Met. Powder Rep. 63, 24–27. https://doi.org/10.1016/S0026-0657(09)70040-2

Estrin, Y., Mecking, H., 1984. A unified phenomenological description of work hardening and creep based on one-parameter models. Acta Metall. 32, 57–70. https://doi.org/10.1016/0001-6160(84)90202-5

Evangelista, E., McQueen, H.J., Ryan, N.D., 1987. Hot strength, dynamic recovery and dynamic recrystallization of 317 type stainless steel | Metallurgical Science and Tecnology. Metall. Sci. Technol. 5, 50–58.

Fan, J.K., Kou, H.C., Lai, M.J., Tang, B., Chang, H., Li, J.S., 2013a. Hot deformation mechanism and microstructure evolution of a new near β titanium alloy. Mater. Sci. Eng. A 584, 121–132. https://doi.org/10.1016/j.msea.2013.07.019

Fan, J.K., Kou, H.C., Lai, M.J., Tang, B., Chang, H., Li, J.S., 2013b. Characterization of hot deformation behavior of a new near beta titanium alloy: Ti-7333. Mater. Des. 49, 945–952. https://doi.org/10.1016/j.matdes.2013.02.044

Farrokh, B., Khan, A.S., 2009. Grain size, strain rate, and temperature dependence of flow stress in ultra-fine grained and nanocrystalline Cu and Al: Synthesis, experiment, and constitutive modeling. Int. J. Plast. 25, 715–732. https://doi.org/10.1016/j.ijplas.2008.08.001

Fekry, A.M., 2009. The influence of chloride and sulphate ions on the corrosion behavior of Ti and Ti-6Al-4V alloy in oxalic acid. Electrochimica Acta 54, 3480–3489. https://doi.org/10.1016/j.electacta.2008.12.060

Filip, R., Kubiak, K., Ziaja, W., Sieniawski, J., 2003. The effect of microstructure on the mechanical properties of two-phase titanium alloys. J. Mater. Process. Technol., 7th International Scientific Conference: Achievements in Mechanical & Materials Engineering 133, 84–89. https://doi.org/10.1016/S0924-0136(02)00248-0

Fitzner, A., Prakash, D.G.L., da Fonseca, J.Q., Thomas, M., Zhang, S.-Y., Kelleher, J., Manuel, P., Preuss, M., 2016. The effect of aluminium on twinning in binary alpha-titanium. Acta Mater. 103, 341–351. https://doi.org/10.1016/j.actamat.2015.09.048

Flower, H.M., 1990. Microstructural development in relation to hot working of titanium alloys. Mater. Sci. Technol. 6, 1082–1092. https://doi.org/10.1179/mst.1990.6.11.1082

Fontana, M.G., 1986. Corrosion engineering.

Fontana, M.G., 1956. Stress Corrosion in Titanium and Its Alloys. Ind. Eng. Chem. 48, 59A–60A.

Froes, F.H., 1998. The production of low-cost titanium powders. JOM 50, 41–43. https://doi.org/10.1007/s11837-998-0413-4

Froes, F.H. (Sam), Friedrich, H., Kiese, J., Bergoint, D., 2004. Titanium in the Family Automobile: The Cost Challenge. JOM 56, 40–44.

Froes, F.H.S., Gungor, M.N., Imam, M.A., 2007. Cost-affordable titanium: The component fabrication perspective. JOM 59, 28–31. https://doi.org/10.1007/s11837-007-0074-8

Frost, H.J., Ashby, M.F., 1982. Deformation-mechanism maps: the plasticity and creep of metals and ceramics. Pergamon Press.

Fujii, H., 1998. Strengthening of α+β titanium alloys by thermomechanical processing. Mater. Sci. Eng. A 243, 103–108. https://doi.org/10.1016/S0921-5093(97)00786-7

Fujii, H., Fujisawa, K., Ishil, M., Yamashita, Y., 2002. Development of low-cost high-strength Ti-Fe-O-N alloy series (Technical No. 85). NIPPON STEEL.

Fujii, H., Takahashi, K., 2002. Development of High Performance Ti-Fe-Al Alloy Series (Technical No. 85). NIPPON STEEL.

Fujii, H., Takahashi, K., Yamashita, Y., 2003. Application of titanium and its alloys for automobile parts. Shinnittetsu Giho 62–67.

Fujita, T., Ogawa, A., Ouchi, C., Tajima, H., 1996. Microstructure and properties of titanium alloy produced in the newly developed blended elemental powder metallurgy process. Mater. Sci. Eng. A, International Symposium on Metallurgy and Technology of Titanium Alloys 213, 148–153. https://doi.org/10.1016/0921-5093(96)10232-X

Gao, C.Y., Zhang, L.C., Yan, H.X., 2011. A new constitutive model for HCP metals. Mater. Sci. Eng. A 528, 4445–4452. https://doi.org/10.1016/j.msea.2011.02.053

Ge, G., Zhang, L., Xin, J., Lin, J., Aindow, M., Zhang, L., 2018. Constitutive modeling of high temperature flow behavior in a Ti-45Al-8Nb-2Cr-2Mn-0.2Y alloy. Sci. Rep. 8, 5453. https://doi.org/10.1038/s41598-018-23617-7

Gegel, H., Nadiv, S., Raj, R., 1980. Dynamic effects on flow and fracture during isothermal forging of a titanium alloy. Scr. Metall. 14, 241–246.

Gerdemann, S.J., 2001. Titanium process technologies.

Gil, F.J., Ginebra, M.P., Manero, J.M., Planell, J.A., 2001. Formation of α-Widmanstätten structure: effects of grain size and cooling rate on the Widmanstätten morphologies and on the mechanical properties in Ti6Al4V alloy. J. Alloys Compd. 329, 142–152. https://doi.org/10.1016/S0925-8388(01)01571-7

Gil, F.J., Planell, J.A., 2000. Behaviour of normal grain growth kinetics in single phase titanium and titanium alloys. Mater. Sci. Eng. A 283, 17–24. https://doi.org/10.1016/S0921-5093(00)00731-0

Gilbert, R., Shannon, C.R., 1991. Heat Treating of Titanium and Titanium Alloys - Heat Treating, ASM Handbook, 10th ed. ASM International.

Goetz, R.L., Semiatin, S.L., 2001. The adiabatic correction factor for deformation heating during the uniaxial compression test. J. Mater. Eng. Perform. 10, 710–717. https://doi.org/10.1361/105994901770344593

Guan, R.G., Je, Y.T., Zhao, Z.Y., Lee, C.S., 2012. Effect of microstructure on deformation behavior of Ti–6Al–4V alloy during compressing process. Mater. Des. 1980-2015, Sustainable Materials, Design and Applications 36, 796–803. https://doi.org/10.1016/j.matdes.2011.11.057

Güleryüz, H., Çimenoğlu, H., 2004. Effect of thermal oxidation on corrosion and corrosion–wear behaviour of a Ti–6Al–4V alloy. Biomaterials 25, 3325–3333. https://doi.org/10.1016/j.biomaterials.2003.10.009

Gunawarman, B., Niinomi, M., Akahori, T., Souma, T., Ikeda, M., Toda, H., 2005. Mechanical properties and microstructures of low cost β titanium alloys for healthcare applications. Mater. Sci. Eng. C, Selected Papers Presented at the Materials Science and Technology 2004 Meeting: Titanium for Biomedical, Dental, and Healthcare Applications 25, 304–311. https://doi.org/10.1016/j.msec.2004.12.015

Guo, Z., Malinov, S., Sha, W., 2005. Modelling beta transus temperature of titanium alloys using artificial neural network. Comput. Mater. Sci. 32, 1–12. https://doi.org/10.1016/j.commatsci.2004.05.004

Guo-Zheng, Q., 2013. Characterization for Dynamic Recrystallization Kinetics Based on Stress-Strain Curves, in: Wilson, P. (Ed.), Recent Developments in the Study of Recrystallization. InTech. https://doi.org/10.5772/54285

Guo-Zheng, Q., Yang, W., Ying-Ying, L., Jie, Z., 2013. Effect of temperatures and strain rates on the average size of grains refined by dynamic recrystallization for as-extruded 42CrMo steel. Mater. Res. 16, 1092–1105. https://doi.org/10.1590/S1516-14392013005000091

Gupta, R.K., Narayana Murty, S.V.S., Pant, B., Agarwala, V., Sinha, P.P., 2012. Hot workability of γ + α2 titanium aluminide: Development of processing map and constitutive equations. Mater. Sci. Eng. A 551, 169–186. https://doi.org/10.1016/j.msea.2012.05.005

Hall, J.A., 1997. Fatigue crack initiation in alpha-beta titanium alloys. Int. J. Fatigue 19, 23–37. https://doi.org/10.1016/S0142-1123(97)00047-9

Han, Y., Wu, H., Zhang, W., Zou, D., Liu, G., Qiao, G., 2015. Constitutive equation and dynamic recrystallization behavior of as-cast 254SMO super-austenitic stainless steel. Mater. Des. 69, 230–240. https://doi.org/10.1016/j.matdes.2014.12.049

He, D., Zhu, J.C., Lai, Z.H., Liu, Y., Yang, X.W., 2013. An experimental study of deformation mechanism and microstructure evolution during hot deformation of Ti–6Al–2Zr–1Mo–1V alloy. Mater. Des. 46, 38–48. https://doi.org/10.1016/j.matdes.2012.09.045

He, L., Dehghan-Manshadi, A., Dippenaar, R.J., 2012. The evolution of microstructure of Ti–6Al–4V alloy during concurrent hot deformation and phase transformation. Mater. Sci. Eng. A 549, 163–167. https://doi.org/10.1016/j.msea.2012.04.025

Hill, R.T., 1952. On discontinuous plastic states, with special reference to localized necking in thin sheets. J. Mech. Phys. Solids 1, 19–30.

Hines, J.A., Vecchio, K.S., 1997. Recrystallization kinetics within adiabatic shear bands. Acta Mater. 45, 635–649.

Hinode, K., Asano, I., Homma, Y., 1989. Void formation mechanism in VLSI aluminum metallization. IEEE Trans. Electron Devices 36, 1050–1055. https://doi.org/10.1109/16.24347

Honarmandi, P., Aghaie-Khafri, M., 2012. Hot Deformation Behavior of Ti–6Al–4V Alloy in β Phase Field and Low Strain Rate. Metallogr. Microstruct. Anal. 2, 13–20. https://doi.org/10.1007/s13632-012-0052-6

Huang, K., Logé, R.E., 2016. A review of dynamic recrystallization phenomena in metallic materials. Mater. Des. 111, 548–574. https://doi.org/10.1016/j.matdes.2016.09.012

Huang, L.J., Geng, L., Li, A.B., Cui, X.P., Li, H.Z., Wang, G.S., 2009. Characteristics of hot compression behavior of Ti–6.5Al–3.5Mo–1.5Zr–0.3Si alloy with an equiaxed microstructure. Mater. Sci. Eng. A 505, 136–143. https://doi.org/10.1016/j.msea.2008.12.041

Humphreys, F.J., Hatherly, M., 2002. Recrystallization and Related Annealing Phenomena. Elsevier.

ImageJ [WWW Document], 2018. URL https://imagej.nih.gov/ij/index.html (accessed 12.11.16).

Ivasishin, O.M., Lütjering, G., 1993. Structure and mechanical properties of high-temperature titanium alloys after rapid heat treatment. Mater. Sci. Eng. A 168, 23–28.

Jackson, M., Boyer, R.R., 2010. Titanium and its Alloys: Processing, Fabrication and Mechanical Performance, in: Encyclopedia of Aerospace Engineering. John Wiley & Sons, Ltd.

Jadhav, S., Powar, A., Patil, S., Supare, A., Farane, B., Singh, D.R., 2017. Effect of volume fraction of alpha and transformed beta on the high cycle fatigue properties of bimodal Ti6Al4V alloy. IOP Conf. Ser. Mater. Sci. Eng. 201, 012035. https://doi.org/10.1088/1757-899X/201/1/012035

Jaspers, S.P.F.C., Dautzenberg, J.H., 2002. Material behaviour in metal cutting: strains, strain rates and temperatures in chip formation. J. Mater. Process. Technol. 121, 123–135. https://doi.org/10.1016/S0924-0136(01)01227-4

Jia, W., Xu, S., Le, Q., Fu, L., Ma, L., Tang, Y., 2016. Modified Fields–Backofen model for constitutive behavior of as-cast AZ31B magnesium alloy during hot deformation. Mater. Des. 106, 120–132. https://doi.org/10.1016/j.matdes.2016.05.089

Jia, W., Zeng, W., Han, Y., Liu, J., Zhou, Y., Wang, Q., 2011a. Prediction of flow stress in isothermal compression of Ti60 alloy using an adaptive network-based fuzzy inference system. Mater. Des. 32, 4676–4683. https://doi.org/10.1016/j.matdes.2011.06.053

Jia, W., Zeng, W., Zhou, Y., Liu, J., Wang, Q., 2011b. High-temperature deformation behavior of Ti60 titanium alloy. Mater. Sci. Eng. A 528, 4068–4074. https://doi.org/10.1016/j.msea.2011.01.113

Johnson, G.R., Cook, W.H., 1983. A constitutive model and data for metals subjected to large strains, high strain rates and high temperatures, in: In 7th International Symposium on Ballistics. Den Haag, the Netherlands, pp. 541–547.

Jonas, J.J., Sellars, C.M., Tegart, W.J.M., 1969. Strength and structure under hot-working conditions. Metall. Rev. 14, 1–24. https://doi.org/10.1179/mtlr.1969.14.1.1

Joshi, V.A., 2006. Titanium alloys: an atlas of structures and fracture features. CRC Press, Taylor& Francis Group, Boca Raton, FL, USA.

Joshi, V.V., Lavender, C., Moxon, V., Duz, V., Nyberg, E., Weil, K.S., 2013. Development of Ti-6Al-4V and Ti-1Al-8V-5Fe Alloys Using Low-Cost TiH2 Powder Feedstock. J. Mater. Eng. Perform. 22, 995–1003. https://doi.org/10.1007/s11665-012-0386-x

Jovanović, M.T., Tadić, S., Zec, S., Mišković, Z., Bobić, I., 2006. The effect of annealing temperatures and cooling rates on microstructure and mechanical properties of investment cast Ti–6Al–4V alloy. Mater. Des. 27, 192–199. https://doi.org/10.1016/j.matdes.2004.10.017

Junhui, C., He, Y., Zhichao, S., Hongwei, L., Zhijun, L., Changwu, S., 2012. Flow Behavior and Constitutive Model Using Piecewise Function of Strain for TC11 Alloy. Rare Met. Mater. Eng. 41, 397–401. https://doi.org/10.1016/S1875-5372(12)60035-6

Kahles, J.F., Field, M., Eylon, D., Froes, F.H., 1985. Machining of Titanium Alloys. JOM 37, 27–35. https://doi.org/10.1007/BF03259441

Kahveci, A.I., Welsch, G.E., 1986. Effect of oxygen on the hardness and alpha/beta phase ratio of Ti□6A1□4V alloy. Scr. Metall. 20, 1287–1290. https://doi.org/10.1016/0036-9748(86)90050-5

Kara, A., Tasdemirci, A., Guden, M., 2013. Modeling quasi-static and high strain rate deformation and failure behavior of a (±45) symmetric E-glass/polyester composite under compressive loading. Mater. Des. 49, 566–574. https://doi.org/10.1016/j.matdes.2013.01.002

Khan, A.S., Sung Suh, Y., Kazmi, R., 2004. Quasi-static and dynamic loading responses and constitutive modeling of titanium alloys. Int. J. Plast. 20, 2233–2248. https://doi.org/10.1016/j.ijplas.2003.06.005

Khan, A.S., Zhang, H., Takacs, L., 2000. Mechanical response and modeling of fully compacted nanocrystalline iron and copper. Int. J. Plast. 16, 1459–1476. https://doi.org/10.1016/S0749-6419(00)00023-1

Kim, Y., Song, Y.-B., Lee, S.H., Kwon, Y., 2016. Characterization of the hot deformation behavior and microstructural evolution of Ti–6Al–4V sintered preforms using materials modeling techniques. J. Alloys Compd. 676, 15–25. https://doi.org/10.1016/j.jallcom.2016.03.146

Kobayashi, E., Wang, T.J., Doi, H., Yoneyama, T., Hamanaka, H., 1998. Mechanical properties and corrosion resistance of Ti-6Al-7Nb alloy dental castings. J. Mater. Sci. Mater. Med. 9, 567–574.

Kocks, U.F., 1976. Laws for work-hardening and low-temperature creep. J. Eng. Mater. Technol. Trans. ASME 98, 76–85. https://doi.org/10.1115/1.3443340

Kocks, U.F., Mecking, H., 2003. Physics and phenomenology of strain hardening: the FCC case. Prog. Mater. Sci. 48, 171–273. https://doi.org/10.1016/S0079-6425(02)00003-8

Koike, J., Shimoyama, Y., Ohnuma, I., Okamura, T., Kainuma, R., Ishida, K., Maruyama, K., 2000. Stress-induced phase transformation during superplastic deformation in two-phase Ti–Al–Fe alloy. Acta Mater. 48, 2059–2069. https://doi.org/10.1016/S1359-6454(00)00049-5

Koike, M., Guo, Q., Brezner, M., Fujii, H., Okabe, T., 2005. Mechanical Properties of Cast Ti-Fe-O-N Alloys. J. ASTM Int. 2, 1–10. https://doi.org/10.1520/JAI12781

Koontz, P., 2013. Guidelines for the Safe Use of Hydrofluoric Acid.

Kopova, I., Stráský, J., Harcuba, P., Landa, M., Janeček, M., Bačákova, L., 2016. Newly developed Ti–Nb–Zr–Ta–Si–Fe biomedical beta titanium alloys with increased strength and enhanced biocompatibility. Mater. Sci. Eng. C 60, 230–238. https://doi.org/10.1016/j.msec.2015.11.043

Kosaka, Y., Fox, S.P., Faller, K., Reichman, S.H., 2005. Properties and processing of TIMETAL LCB. J. Mater. Eng. Perform. 14, 792–798. https://doi.org/10.1361/105994905X75637

Kroll, W., 1940. The Production of Ductile Titanium. Trans. Electrochem. Soc. 78, 35–47. https://doi.org/10.1149/1.3071290

Krýsa, J., Mráz, R., Roušar, I., 1997. Corrosion rate of titanium in H2SO4. Mater. Chem. Phys. 48, 64–67. https://doi.org/10.1016/S0254-0584(97)80079-X

Kuhlman, G.W., 2005. Forging of titanium alloys. ASM Handb. Vol 14 Metalwork. Bulk Form. 14, 331–353.

Kuphasuk, C., Oshida, Y., Andres, C.J., Hovijitra, S.T., Barco, M.T., Brown, D.T., 2001. Electrochemical corrosion of titanium and titanium-based alloys. J. Prosthet. Dent. 85, 195–202. https://doi.org/10.1067/mpr.2001.113029

Kuroda, D., Kawasaki, H., Yamamoto, A., Hiromoto, S., Hanawa, T., 2005. Mechanical properties and microstructures of new Ti–Fe–Ta and Ti–Fe–Ta–Zr system alloys. Mater. Sci. Eng. C, Selected Papers Presented at the Materials Science and Technology 2004 Meeting: Titanium for Biomedical, Dental, and Healthcare Applications 25, 312–320. https://doi.org/10.1016/j.msec.2005.04.004

Kutumarao, V.V., Rajagopalachary, T., 1996. Recent developments in modeling the hot working behavior of metallic materials. Bull. Mater. Sci. 19, 677–698. https://doi.org/10.1007/BF02745160

Landau, P., Osovski, S., Venkert, A., Gärtnerová, V., Rittel, D., 2016. The genesis of adiabatic shear bands. Sci. Rep. 6, srep37226. https://doi.org/10.1038/srep37226

Langdon, T.G., Furukawa, M., Horita, Z., Nemoto, M., 1998. Using intense plastic straining for high-strain-rate superplasticity. JOM 50, 41–45. https://doi.org/10.1007/s11837-998-0126-8

Leyens, C., Peters, M., 2003. Titanium and titanium alloys: fundamentals and application. WILEY-VCH, Germany.

Li, C., Zhang, X., Li, Z., Zhou, K.-C., 2013. Hot Deformation of Ti-5Al-5Mo-5 V-1Cr-1Fe Near β Titanium Alloys Containing Thin and Thick Lamellar α Phase. Mater. Sci. Eng. A 573, 75–83. https://doi.org/10.1016/j.msea.2013.02.033

Li, L., Li, M.Q., Luo, J., 2015a. Flow softening mechanism of Ti–5Al–2Sn–2Zr–4Mo–4Cr with different initial microstructures at elevated temperature deformation. Mater. Sci. Eng. A 628, 11–20. https://doi.org/10.1016/j.msea.2015.01.034

Li, L., Luo, J., Yan, J.J., Li, M.Q., 2015b. Dynamic globularization and restoration mechanism of Ti–5Al–2Sn–2Zr–4Mo–4Cr alloy during isothermal compression. J. Alloys Compd. 622, 174–183. https://doi.org/10.1016/j.jallcom.2014.10.043

Li, M., Pan, H., Lin, Y., Luo, J., 2007. High temperature deformation behavior of near alpha Ti–5.6Al–4.8Sn–2.0Zr alloy. J. Mater. Process. Technol. 183, 71–76. https://doi.org/10.1016/j.jmatprotec.2006.10.002

Li, Y., Onodera, E., Chiba, A., 2010. Friction coefficient in hot compression of cylindrical sample. Mater. Trans. 51, 1210–1215.

Lin, J., 2015. Fundamentals of Materials Modelling for Metals Processing Technologies: Theories and Applications. World Scientific Publishing Co Inc.

Lin, Y.C., Chen, M.-S., Zhong, J., 2008. Prediction of 42CrMo steel flow stress at high temperature and strain rate. Mech. Res. Commun. 35, 142–150. https://doi.org/10.1016/j.mechrescom.2007.10.002

Lin, Y.C., Chen, M.-S., Zhong, J., 2008. Constitutive modeling for elevated temperature flow behavior of 42CrMo steel. Comput. Mater. Sci. 42, 470–477. https://doi.org/10.1016/j.commatsci.2007.08.011

Lin, Y.C., Chen, X.-M., 2011. A critical review of experimental results and constitutive descriptions for metals and alloys in hot working. Mater. Des. 32, 1733–1759. https://doi.org/10.1016/j.matdes.2010.11.048

Lin, Y.C., Liu, G., 2010. A new mathematical model for predicting flow stress of typical high-strength alloy steel at elevated high temperature. Comput. Mater. Sci. 48, 54–58. https://doi.org/10.1016/j.commatsci.2009.06.026

Lin, Y.C., Zhao, C.-Y., Chen, M.-S., Chen, D.-D., 2016. A novel constitutive model for hot deformation behaviors of Ti–6Al–4V alloy based on probabilistic method. Appl. Phys. A 122, 716. https://doi.org/10.1007/s00339-016-0248-8

Liszewski, A., 2015. The World's First 3D-Printed Titanium Rib Cage Is a Medical Marvel [WWW Document]. Gizmodo. URL https://gizmodo.com/the-worlds-first-3d-printed-titanium-rib-cage-is-a-medi-1730034483 (accessed 4.10.18).

Liu, C.Y., Zhang, R.J., Yan, Y.N., 2011. Hot deformation behaviour and constitutive modelling of P92 heat resistant steel. Mater. Sci. Technol. 27, 1281–1286. https://doi.org/10.1179/026708310X12683158443323

Liu, J., Zeng, W., Lai, Y., Jia, Z., 2014. Constitutive model of Ti17 titanium alloy with lamellar-type initial microstructure during hot deformation based on orthogonal analysis. Mater. Sci. Eng. A 597, 387–394. https://doi.org/10.1016/j.msea.2013.12.076

Liu, Y., Chen, L.F., Tang, H.P., Liu, C.T., Liu, B., Huang, B.Y., 2006. Design of powder metallurgy titanium alloys and composites. Mater. Sci. Eng. A 418, 25–35. https://doi.org/10.1016/j.msea.2005.10.057

Liu, Z., Welsch, G., 1988. Effects of oxygen and heat treatment on the mechanical properties of alpha and beta titanium alloys. Metall. Trans. A 19, 527–542. https://doi.org/10.1007/BF02649267

Long, Y., Wang, T., Zhang, H.Y., Huang, X.L., 2014. Enhanced ductility in a bimodal ultrafine-grained Ti–6Al–4V alloy fabricated by high energy ball milling and spark plasma sintering. Mater. Sci. Eng. A 608, 82–89. https://doi.org/10.1016/j.msea.2014.04.057

Longère, P., Dragon, A., 2007. Adiabatic heat evaluation for dynamic plastic localization. J. Theor. Appl. Mech. 45, 203–223.

Lou, J., Gabbitas, B., Yang, F., Raynova, S., Lu, H., 2016. Effects of LaB6 additions on the microstructure and mechanical properties of a sintered and hot worked P/M Ti alloy. J. Alloys Compd. 674, 116–124. https://doi.org/10.1016/j.jallcom.2016.02.163

Lu, J., Zhao, Y., Niu, H., Zhang, Y., Du, Y., Zhang, W., Huo, W., 2016. Electrochemical corrosion behavior and elasticity properties of Ti–6Al–xFe alloys for biomedical applications. Mater. Sci. Eng. C 62, 36–44. https://doi.org/10.1016/j.msec.2016.01.019

Luo, J., Li, M., Li, H., Yu, W., 2009. Effect of the strain on the deformation behavior of isothermally compressed Ti–6Al–4V alloy. Mater. Sci. Eng. A 505, 88–95. https://doi.org/10.1016/j.msea.2008.11.001

Luo, J., Ye, P., Li, M.Q., Liu, L.Y., 2015. Effect of the alpha grain size on the deformation behavior during isothermal compression of Ti–6Al–4V alloy. Mater. Des. 88, 32–40. https://doi.org/10.1016/j.matdes.2015.08.130

Lütjering, G., 1999. Property optimization through microstructural control in titanium and aluminum alloys. Mater. Sci. Eng. A 263, 117–126. https://doi.org/10.1016/S0921-5093(98)01169-1

Lütjering, G., 1998. Influence of processing on microstructure and mechanical properties of (α+β) titanium alloys. Mater. Sci. Eng. A 243, 32–45. https://doi.org/10.1016/S0921-5093(97)00778-8

Lütjering, G., Williams, J.C., 2007. Engineering Materials: Titanium, Second. ed. Springer, Berlin Heidelberg Newyork.

Lütjering, G., Williams, J.C., Gysler, A., 2000. Microstructure and mechanical properties of titanium alloys, in: Microstructure And Properties Of Materials: (Volume 2). World Scientific, pp. 1–77.

Luton, M.J., Sellars, C.M., 1969. Dynamic recrystallization in nickel and nickel-iron alloys during high temperature deformation. Acta Metall. 17, 1033–1043. https://doi.org/10.1016/0001-6160(69)90049-2

Ma, X., Zeng, W., Wang, K., Lai, Y., Zhou, Y., 2012a. The investigation on the unstable flow behavior of Ti17 alloy in α+β phase field using processing map. Mater. Sci. Eng. A 550, 131–137. https://doi.org/10.1016/j.msea.2012.04.045

Ma, X., Zeng, W., Xu, B., Sun, Y., Xue, C., Han, Y., 2012b. Characterization of the hot deformation behavior of a Ti–22Al–25Nb alloy using processing maps based on the Murty criterion. Intermetallics 20, 1–7. https://doi.org/10.1016/j.intermet.2011.08.027

Mabuchi, M., Higashi, K., 1998. The processing, properties, and applications of high-strain-rate superplastic materials. JOM 50, 34–39. https://doi.org/10.1007/s11837-998-0125-9

Mandal, S., Rakesh, V., Sivaprasad, P.V., Venugopal, S., Kasiviswanathan, K.V., 2009. Constitutive equations to predict high temperature flow stress in a Ti-modified austenitic stainless steel. Mater. Sci. Eng. A 500, 114–121. https://doi.org/10.1016/j.msea.2008.09.019

Marino, C.E.B., Oliveira, E.M. de, Rocha-Filho, R.C., Biaggio, S.R., 2001. On the stability of thin-anodic-oxide films of titanium in acid phosphoric media. Corros. Sci. 43, 1465–1476. https://doi.org/10.1016/S0010-938X(00)00162-1

Matyka, J., Faudot, F., Bigot, J., 1979. Study of iron solubility in α titanium. Scr. Metall. 13, 645–648.

McQueen, H.J., Bourell, D.L., 1987. Hot Workability of Metals and Alloys. JOM 39, 28–35. https://doi.org/10.1007/BF03257647

McQueen, H.J., Jonas, J.J., 1975. Recovery and Recrystallization during High Temperature Deformation, in: Arsenault, R.J. (Ed.), Treatise on Materials Science & Technology, Plastic Deformation of Materials. Elsevier, pp. 393–493. https://doi.org/10.1016/B978-0-12-341806-7.50014-3

McQueen, H.J., Ryan, N.D., 2002. Constitutive analysis in hot working. Mater. Sci. Eng. A 322, 43–63. https://doi.org/10.1016/S0921-5093(01)01117-0

McQueen, H.J., Yue, S., Ryan, N.D., Fry, E., 1995. Hot working characteristics of steels in austenitic state. J. Mater. Process. Technol., Advanced Materials and Technologies 53, 293–310. https://doi.org/10.1016/0924-0136(95)01987-P

Mirzadeh, H., 2015. Constitutive modeling and prediction of hot deformation flow stress under dynamic recrystallization conditions. Mech. Mater. 85, 66–79. https://doi.org/10.1016/j.mechmat.2015.02.014

Mitchell, A., 1998. Melting, casting and forging problems in titanium alloys. Mater. Sci. Eng. A 243, 257–262. https://doi.org/10.1016/S0921-5093(97)00810-1

Mitchell, T.E., Hirth, J.P., Misra, A., 2002. Apparent activation energy and stress exponent in materials with a high Peierls stress. Acta Mater. 50, 1087–1093. https://doi.org/10.1016/S1359-6454(01)00409-8

Mogoda, A.S., Ahmad, Y.H., Badawy, W.A., 2004. Corrosion inhibition of Ti-6Al-4V alloy in sulfuric and hydrochloric acid solutions using inorganic passivators. Mater. Corros. 55, 449–456. https://doi.org/10.1002/maco.200303751

Mogoda, A.S., Ahmad, Y.H., Badawy, W.A., 2004. Corrosion Behaviour of Ti–6Al–4V Alloy in Concentrated Hydrochloric and Sulphuric Acids. J. Appl. Electrochem. 34, 873–878. https://doi.org/10.1023/B:JACH.0000040447.26482.bd

Momeni, A., 2016. The physical interpretation of the activation energy for hot deformation of Ni and Ni–30Cu alloys. J. Mater. Res. 31, 1077–1084. https://doi.org/10.1557/jmr.2016.81

Momeni, A., Abbasi, S.M., 2010. Effect of hot working on flow behavior of Ti–6Al–4V alloy in single phase and two phase regions. Mater. Des. 31, 3599–3604. https://doi.org/10.1016/j.matdes.2010.01.060

Momeni, A., Dehghani, K., 2010. Characterization of hot deformation behavior of 410 martensitic stainless steel using constitutive equations and processing maps. Mater. Sci. Eng. A 527, 5467–5473. https://doi.org/10.1016/j.msea.2010.05.079

Motyka, M., Kubiak, K., Sieniawski, J., Ziaja, W., 2012. Hot Plasticity of Alpha Beta Alloys. https://doi.org/10.5772/34806

Murty, S.V.S.N., Rao, B.N., Kashyap, B.P., 2002. Development and validation of a processing map for zirconium alloys. Model. Simul. Mater. Sci. Eng. 10, 503. https://doi.org/10.1088/0965-0393/10/5/303

Myers, J.R., Bomberger, H.B., Froes, F.H., 1984. Corrosion behavior and use of titanium and its alloys. JOM 36, 50–60.

Nakajima, H., Ohshida, S., Nonaka, K., Yoshida, Y., Fujita, F.E., 1996a. Diffusion of iron in β Ti-Fe alloys. Scr. Mater. 34, 949–953.

Nakajima, H., Yusa, K., Kondo, Y., 1996b. Diffusion of iron in a diluted α-Ti-Fe alloy. Scr. Mater. 34, 249–253.

Narayana Murty, S.V.S., Nageswara Rao, B., Kashyap, B.P., 2000. Instability criteria for hot deformation of materials. Int. Mater. Rev. 45, 15–26. https://doi.org/10.1179/095066000771048782

Narutaki, N., Murakoshi, A., Motonishi, S., Takeyama, H., 1983. Study on Machining of Titanium Alloys. CIRP Ann. 32, 65–69. https://doi.org/10.1016/S0007-8506(07)63362-9

Nayan, N., Singh, G., Murty, S.V.S.N., Jha, A.K., Pant, B., George, K.M., Ramamurty, U., 2014. Hot deformation behaviour and microstructure control in AlCrCuNiFeCo high entropy alloy. Intermetallics 55, 145–153. https://doi.org/10.1016/j.intermet.2014.07.019

Neville, A., McDougall, B.A.B., 2001. Erosion– and cavitation–corrosion of titanium and its alloys. Wear, 13th International Conference on Wear of Materials 250, 726–735. https://doi.org/10.1016/S0043-1648(01)00709-8

Nishimura, T., Tamilselvi, S., Min, X.M., Tsuxaki, K., 2010. Corrosion Resistance of Aging Heat-Treated Ti8Mo5Fe Alloy in Highly Acidic Chloride Solution. Mater. Trans. 51, 1553–1559.

Nkhoma, R.K.C., Siyasiya, C.W., Stumpf, W.E., 2014. Hot workability of AISI 321 and AISI 304 austenitic stainless steels. J. Alloys Compd. 595, 103–112. https://doi.org/10.1016/j.jallcom.2014.01.157

Nochovnaya, N.A., Isaichev, A.V., Antashev, V.G., 2008. Foundations of the development of economically alloyed widely applicable titanium alloys. Mater. Sci. 44, 396–399. https://doi.org/10.1007/s11003-008-9081-3

Odenberger, E.-L., Oldenburg, M., Thilderkvist, P., Stoehr, T., Lechler, J., Merklein, M., 2011. Tool development based on modelling and simulation of hot sheet metal forming of Ti–6Al–4V titanium alloy. J. Mater. Process. Technol. 211, 1324–1335. https://doi.org/10.1016/j.jmatprotec.2011.03.001

Odeshi, A.G., Al-ameeri, S., Mirfakhraei, S., Yazdani, F., Bassim, M.N., 2006. Deformation and failure mechanism in AISI 4340 steel under ballistic impact. Theor. Appl. Fract. Mech. 45, 18–24. https://doi.org/10.1016/j.tafmec.2005.11.005

Oh, J.-M., Lee, B.-G., Cho, S.-W., Lee, S.-W., Choi, G.-S., Lim, J.-W., 2011. Oxygen effects on the mechanical properties and lattice strain of Ti and Ti-6Al-4V. Met. Mater. Int. 17, 733–736. https://doi.org/10.1007/s12540-011-1006-2

Oh, S.I., Wu, W.T., Tang, J.P., Vedhanayagam, A., 1991. Capabilities and applications of FEM code deform: the perspective of the developer. J. Mater. Process. Technol. 27, 25–42. https://doi.org/10.1016/0924-0136(91)90042-D

Oliveira, V.M.C.A., Aguiar, C., Vazquez, A.M., Robin, A., Barboza, M.J.R., 2014. Improving corrosion resistance of Ti–6Al–4V alloy through plasma-assisted PVD deposited nitride coatings. Corros. Sci. 88, 317–327. https://doi.org/10.1016/j.corsci.2014.07.047

Omar, A.A., Prado, J.M., 2012. Criteria for prediction of plastic instabilities for hot working processes (part I: theoretical review). Weld. Int. 26, 921–934. https://doi.org/10.1080/09507116.2011.592704

Owen, E.L., May, R.C., Beck, F.H., Fontana, M.G., 1972. Dissolution of Ti-6Al-4V at Cathodic Potentials in 5N HCl. CORROSION 28, 292–295. https://doi.org/10.5006/0010-9312-28.8.292

Parkhutik, V.P., 2006. Oscillations of open-circuit potential during immersion plating of silicon in CuSO<Subscript>4</Subscript>/HF solutions. Russ. J. Electrochem. 42, 512–522. https://doi.org/10.1134/S1023193506050090

Patel, A., Fiore, D., 2016. On the Modeling of Vacuum Arc Remelting Process in Titanium Alloys. IOP Conf. Ser. Mater. Sci. Eng. 143, 012017. https://doi.org/10.1088/1757-899X/143/1/012017

Peng, W., Zeng, W., Wang, Q., Yu, H., 2013a. Comparative study on constitutive relationship of as-cast Ti60 titanium alloy during hot deformation based on Arrhenius-type and artificial neural network models. Mater. Des. 51, 95–104. https://doi.org/10.1016/j.matdes.2013.04.009

Peng, W., Zeng, W., Wang, Q., Yu, H., 2013b. Characterization of high-temperature deformation behavior of as-cast Ti60 titanium alloy using processing map. Mater. Sci. Eng. A 571, 116–122. https://doi.org/10.1016/j.msea.2013.01.008

Peng, X., Guo, H., Shi, Z., Qin, C., Zhao, Z., 2013. Constitutive equations for high temperature flow stress of TC4-DT alloy incorporating strain, strain rate and temperature. Mater. Des. 50, 198–206. https://doi.org/10.1016/j.matdes.2013.03.009

Pereloma, E.V., Savvakin, D.G., Carman, A., Gazder, A.A., Ivasishin, O.M., 2012. Microstructure Development and Alloying Elements Diffusion during Sintering of Near-β Titanium Alloys. Key Eng. Mater. 520, 49–56. https://doi.org/10.4028/www.scientific.net/KEM.520.49

Perumal, B., Rist, M.A., Gungor, S., Brooks, J.W., Fitzpatrick, M.E., 2016. The Effect of Hot Deformation Parameters on Microstructure Evolution of the α-Phase in Ti-6Al-4V. Metall. Mater. Trans. A 47, 4128–4136. https://doi.org/10.1007/s11661-016-3552-1

Philippart, I., Rack, H.J., 1998. High temperature dynamic yielding in metastable Ti–6.8 Mo–4.5 F–1.5 Al. Mater. Sci. Eng. A 243, 196–200.

Pimenova, N.V., Starr, T.L., 2006. Electrochemical and corrosion behavior of Ti–xAl–yFe alloys prepared by direct metal deposition method. Electrochimica Acta 51, 2042–2049. https://doi.org/10.1016/j.electacta.2005.07.024

Ping, G., Yongqing, Z., Weidong, Z., 2015. Fatigue crack growth behavior in TC4-DT titanium alloy with different lamellar microstructures. Rare Met. Mater. Eng. 44, 277–281.

Poletti, C., Germain, L., Warchomicka, F., Dikovits, M., Mitsche, S., 2016. Unified description of the softening behavior of beta-metastable and alpha+beta titanium alloys during hot deformation. Mater. Sci. Eng. A 651, 280–290. https://doi.org/10.1016/j.msea.2015.10.109

Poletti, C., Warchomicka, F., Degischer, H.P., 2010. Local deformation of Ti6Al4V modified 1 wt% B and 0.1 wt% C. Mater. Sci. Eng. A 527, 1109–1116. https://doi.org/10.1016/j.msea.2009.09.041

Poliak, E.I., Jonas, J.J., 2003. Initiation of Dynamic Recrystallization in Constant Strain Rate Hot Deformation. ISIJ Int. 43, 684–691. https://doi.org/10.2355/isijinternational.43.684

Polmear, I., StJohn, D., Nie, J.-F., Qian, M., 2017. 7 - Titanium Alloys, in: Light Alloys (Fifth Edition). Butterworth-Heinemann, Boston, pp. 369–460. https://doi.org/10.1016/B978-0-08-099431-4.00007-5

Polmear, I.J., 2005. 6 - Titanium alloys, in: Light Alloys (Fourth Edition). Butterworth-Heinemann, Oxford, pp. 299–365.

Porntadawit, J., Uthaisangsuk, V., Choungthong, P., 2014. Modeling of flow behavior of Ti–6Al–4V alloy at elevated temperatures. Mater. Sci. Eng. A 599, 212–222. https://doi.org/10.1016/j.msea.2014.01.064

Pouilleau, J., Devilliers, D., Garrido, F., Durand-Vidal, S., Mahé, E., 1997. Structure and composition of passive titanium oxide films. Mater. Sci. Eng. B 47, 235–243.

Poulsen, E., 2000. Safety-Related Problems in the Titanium Industry in the Last 50 Years. JOM 52, 13–17.

Pramanik, A., 2014. Problems and solutions in machining of titanium alloys. Int. J. Adv. Manuf. Technol. 70, 919–928. https://doi.org/10.1007/s00170-013-5326-x

Pramanik, A., Littlefair, G., 2015. Machining of Titanium Alloy (Ti-6Al-4V)—Theory to Application. Mach. Sci. Technol. 19, 1–49. https://doi.org/10.1080/10910344.2014.991031

Prasad, Y.V.R.K., 2003. Processing maps: A status report. J. Mater. Eng. Perform. 12, 638–645. https://doi.org/10.1361/105994903322692420

Prasad, Y.V.R.K., Gegel, H.L., Doraivelu, S.M., Malas, J.C., Morgan, J.T., Lark, K.A., Barker, D.R., 1984. Modeling of dynamic material behavior in hot deformation: Forging of Ti-6242. Metall. Trans. A 15, 1883–1892. https://doi.org/10.1007/BF02664902

Prasad, Y.V.R.K., Rao, K.P., Sasidhara, S., 2015. Hot working guide : a compendium of processing maps. ASM International.

Prasad, Y.V.R.K., Seshacharyulu, T., 1998a. Modelling of hot deformation for microstructural control. Int. Mater. Rev. 43, 243–258. https://doi.org/10.1179/imr.1998.43.6.243

Prasad, Y.V.R.K., Seshacharyulu, T., 1998b. Processing maps for hot working of titanium alloys. Mater. Sci. Eng. A 243, 82–88. https://doi.org/10.1016/S0921-5093(97)00782-X

Prasad, Y.V.R.K., Seshacharyulu, T., Medeiros, S.C., Frazier, W.G., 2000. Effect of prior β-grain size on the hot deformation behavior of Ti-6Al-4V: Coarse vs coarser. J. Mater. Eng. Perform. 9, 153–160. https://doi.org/10.1361/105994900770346097

Preston, D.L., Tonks, D.L., Wallace, D.C., 2003. Model of plastic deformation for extreme loading conditions. J. Appl. Phys. 93, 211–220. https://doi.org/10.1063/1.1524706

Prozesky, D.J., Bodunrin, M.O., Chown, L.H., 2017. Hot-deformation behaviour of α+β Ti-Al-V-Fe experimental alloys. p. 160019. https://doi.org/10.1063/1.5008194

Qu, Y., Wang, M., Lei, L., Huang, X., Wang, L., Qin, J., Lu, W., Zhang, D., 2012. Behavior and modeling of high temperature deformation of an α + β titanium alloy. Mater. Sci. Eng. A 555, 99–105. https://doi.org/10.1016/j.msea.2012.06.039

Quan, G., Mao, Y., Li, G., Lv, W., Wang, Y., Zhou, J., 2012. A characterization for the dynamic recrystallization kinetics of as-extruded 7075 aluminum alloy based on true stress–strain curves. Comput. Mater. Sci. 55, 65–72. https://doi.org/10.1016/j.commatsci.2011.11.031

Rafi, H.K., Karthik, N.V., Gong, H., Starr, T.L., Stucker, B.E., 2013. Microstructures and Mechanical Properties of Ti6Al4V Parts Fabricated by Selective Laser Melting and Electron Beam Melting. J. Mater. Eng. Perform. 22, 3872–3883. https://doi.org/10.1007/s11665-013-0658-0

Rajamuthamilselvan, M., 2013. Hot Deformation Mechanisms in 7075Al/10%SiCp Metal Matrix Composites. Adv. Netw. 1, 34. https://doi.org/10.11648/j.net.20130103.11

Ramires, I., Guastaldi, A.C., 2001. Electrochemical study of the corrosion of Ti-Pd and Ti-6Al-4V electrodes in sodium chloride solutions.

Rao, K.P., Prasad, Y.V.R.K., 2010. Processing map and hot working mechanisms in a P/M TiAl alloy composite with in situ carbide and silicide dispersions. Mater. Sci. Eng. A 527, 6589–6595. https://doi.org/10.1016/j.msea.2010.06.064

Rao, K.P., Prasad, Y.V.R.K., Dzwonczyk, J., Hort, N., Kainer, K.U., 2012. Hot Deformation Mechanisms in AZ31 Magnesium Alloy Extruded at Different Temperatures: Impact of Texture. Metals 2, 292–312. https://doi.org/10.3390/met2030292

Rao, K.P., Prasad, Y.V.R.K., Suresh, K., 2011. Hot working behavior and processing map of a γ-TiAl alloy synthesized by powder metallurgy. Mater. Des. 32, 4874–4881. https://doi.org/10.1016/j.matdes.2011.06.003

Rao, Y.K.M., KutumbaRao, V.V., Rao, P.R., 1989. Influence of microstructure on void nucleation and growth in a near-α titanium alloy IMI 685. Mater. Sci. Eng. A 110, 193–202.

Redmore, E., 2011. Surface treatment of a low-cost beta titanium alloy to combat wear (PhD Thesis). University of Birmingham.

Roberts, E.C., Kellerer, H., Walsh, F.D., 1970. Strain-induced phase transformations in Ti-6Al-4V. Metallography 3, 291–305. https://doi.org/10.1016/0026-0800(70)90017-0

Roebuck, B., Lord, J.D., Brooks, M., Loveday, M.S., Sellars, C.M., Evans, R.W., 2006. Measurement of flow stress in hot axisymmetric compression tests. Mater. High Temp. 23, 59–83. https://doi.org/10.1179/mht.2006.005

Rugg, D., Dixon, M., Burrows, J., 2016. High-temperature application of titanium alloys in gas turbines. Material life cycle opportunities and threats – an industrial perspective. Mater. High Temp. 33, 536–541. https://doi.org/10.1080/09603409.2016.1184423

Rusinek, A., Klepaczko, J.R., 2001. Shear testing of a sheet steel at wide range of strain rates and a constitutive relation with strain-rate and temperature dependence of the flow stress. Int. J. Plast. 17, 87–115. https://doi.org/10.1016/S0749-6419(00)00020-6

Safdar, A., Wei, L.-Y., Snis, A., Lai, Z., 2012. Evaluation of microstructural development in electron beam melted Ti-6Al-4V. Mater. Charact. 65, 8–15. https://doi.org/10.1016/j.matchar.2011.12.008

Sajadifar, S.V., Yapici, G.G., 2014. Elevated Temperature Mechanical Behavior of Severely Deformed Titanium. J. Mater. Eng. Perform. 23, 1834–1844. https://doi.org/10.1007/s11665-014-0947-2

Sakai, T., Belyakov, A., Kaibyshev, R., Miura, H., Jonas, J.J., 2014. Dynamic and post-dynamic recrystallization under hot, cold and severe plastic deformation conditions. Prog. Mater. Sci. 60, 130–207. https://doi.org/10.1016/j.pmatsci.2013.09.002

Sakai, T., Jonas, J.J., 1984. Overview no. 35 dynamic recrystallization: mechanical and microstructural considerations. Acta Metall. 32, 189–209.

Salem, A.A., Shaffer, J.B., Satko, D.P., Semiatin, S.L., Kalidindi, S.R., 2014. Workflow for integrating mesoscale heterogeneities in materials structure with process simulation of titanium alloys. Integrating Mater. Manuf. Innov. 3, 24. https://doi.org/10.1186/s40192-014-0024-6

samaterials, 2014. Why Titanium is So Expensive. Stanf. Adv. Mater.

Schenk, R., 2001. The Corrosion Properties of Titanium and Titanium Alloys, in: Titanium in Medicine, Engineering Materials. Springer, Berlin, Heidelberg, pp. 145–170. https://doi.org/10.1007/978-3-642-56486-4_6

Scientific Forming Technologies Corporation [WWW Document], 2018. URL https://www.deform.com/ (accessed 3.23.18).

Seagle, S.R., 1996. The state of the USA titanium industry in 1995. Mater. Sci. Eng. A, International Symposium on Metallurgy and Technology of Titanium Alloys 213, 1–7. https://doi.org/10.1016/0921-5093(96)10245-8

Seah, K.H.W., Thampuran, R., Teoh, S.H., 1998. The influence of pore morphology on corrosion. Corros. Sci. 40, 547–556.

Seetharaman, V., Semiatin, S.L., 1997. Plastic-flow and microstructure evolution during hot deformation of a gamma titanium aluminide alloy. Metall. Mater. Trans. A 28, 2309–2321. https://doi.org/10.1007/s11661-997-0188-1

Sellars, C.M., Tegart, W.J., 1966. On the mechanism of hot deformation. Acta Metall. 14, 1136–1138. https://doi.org/10.1016/0001-6160(66)90207-0

Semiatin, S.L., Bieler, T.R., 2001. The effect of alpha platelet thickness on plastic flow during hot working of TI–6Al–4V with a transformed microstructure. Acta Mater. 49, 3565–3573. https://doi.org/10.1016/S1359-6454(01)00236-1

Semiatin, S.L., Lahoti, G.D., 1981. Deformation and unstable flow in hot forging of Ti-6Ai-2Sn-4Zr-2Mo-0.1Si. Metall. Trans. A 12, 1705–1717. https://doi.org/10.1007/BF02643753

Semiatin, S.L., Seetharaman, V., Ghosh, A.K., 1999. Plastic flow, microstructure evolution, and defect formation during primary hot working of titanium and titanium aluminide alloys with lamellar colony microstructures. Philos. Trans. R. Soc. Lond. Math. Phys. Eng. Sci. 357, 1487–1512. https://doi.org/10.1098/rsta.1999.0386

Semiatin, S.L., Seetharaman, V., Weiss, I., 1999. Flow behavior and globularization kinetics during hot working of Ti–6Al–4V with a colony alpha microstructure. Mater. Sci. Eng. A 263, 257–271. https://doi.org/10.1016/S0921-5093(98)01156-3

Semiatin, S.L., Seetharaman, V., Weiss, I., 1997. The thermomechanical processing of alpha/beta titanium alloys. JOM 49, 33–39. https://doi.org/10.1007/BF02914711

Sen, I., Kottada, R.S., Ramamurty, U., 2010. High temperature deformation processing maps for boron modified Ti–6Al–4V alloys. Mater. Sci. Eng. A 527, 6157–6165. https://doi.org/10.1016/j.msea.2010.06.044

Sen, I., Ramamurty, U., 2010. Elastic modulus of Ti–6Al–4V–xB alloys with B up to 0.55wt.%. Scr. Mater. 62, 37–40. https://doi.org/10.1016/j.scriptamat.2009.09.022

Sen, I., Tamirisakandala, S., Miracle, D.B., Ramamurty, U., 2007. Microstructural effects on the mechanical behavior of B-modified Ti–6Al–4V alloys. Acta Mater. 55, 4983–4993. https://doi.org/10.1016/j.actamat.2007.05.009

Seshacharyulu, T., Medeiros, S.C., Frazier, W.G., Prasad, Y.V.R.K., 2002. Microstructural mechanisms during hot working of commercial grade Ti–6Al–4V with lamellar starting structure. Mater. Sci. Eng. A 325, 112–125. https://doi.org/10.1016/S0921-5093(01)01448-4

Seshacharyulu, T., Medeiros, S.C., Frazier, W.G., Prasad, Y.V.R.K., 2000. Hot working of commercial Ti–6Al–4V with an equiaxed α–β microstructure: materials modeling considerations. Mater. Sci. Eng. A 284, 184–194. https://doi.org/10.1016/S0921-5093(00)00741-3

Seshacharyulu, T., Medeiros, S.C., Morgan, J.T., Malas, J.C., Frazier, W.G., Prasad, Y.V.R.K., 2000. Hot deformation and microstructural damage mechanisms in extra-low interstitial (ELI) grade Ti–6Al–4V. Mater. Sci. Eng. A 279, 289–299. https://doi.org/10.1016/S0921-5093(99)00173-2

Seshacharyulu, T., Medeiros, S.C., Morgan, J.T., Malas, J.C., Frazier, W.G., Prasad, Y.V.R.K., 1999. Hot deformation mechanisms in ELI Grade Ti-6Al-4V. Scr. Mater. 41, 283–288. https://doi.org/10.1016/S1359-6462(99)00163-3

Sharma, B., Vajpai, S.K., Ameyama, K., 2016. Microstructure and properties of beta Ti–Nb alloy prepared by powder metallurgy route using titanium hydride powder. J. Alloys Compd. 656, 978–986. https://doi.org/10.1016/j.jallcom.2015.10.053

Sharma, S., Majila, A.N., Chavan, V.M., Fernando, D.C., Patel, R.J., Babu, S.N., 2017. Deformation Response of Titanium Alloy under Static and Dynamic Loading. Procedia Eng. 173, 1894–1900. https://doi.org/10.1016/j.proeng.2016.12.247

Sheppard, T., Jackson, A., 1997. Constitutive equations for use in prediction of flow stress during extrusion of aluminium alloys. Mater. Sci. Technol. 13, 203–209. https://doi.org/10.1179/mst.1997.13.3.203

Shi, C., Chen, X.-G., 2016. Evolution of activation energies for hot deformation of 7150 aluminum alloys with various Zr and V additions. Mater. Sci. Eng. A 650, 197–209. https://doi.org/10.1016/j.msea.2015.09.105

Shi, C., Mao, W., Chen, X.-G., 2013. Evolution of activation energy during hot deformation of AA7150 aluminum alloy. Mater. Sci. Eng. A 571, 83–91. https://doi.org/10.1016/j.msea.2013.01.080

Shi, H., McLaren, A.J., Sellars, C.M., Shahani, R., Bolingbroke, R., 1997. Constitutive equations for high temperature flow stress of aluminium alloys. Mater. Sci. Technol. 13, 210–216. https://doi.org/10.1179/mst.1997.13.3.210

Shoesmith, D.W., Noël, J.J., 2010. 3.10 - Corrosion of Titanium and its Alloys, in: Cottis, B., Graham, M., Lindsay, R., Lyon, S., Richardson, T., Scantlebury, D., Stott, H. (Eds.), Shreir's Corrosion. Elsevier, Oxford, pp. 2042–2052. https://doi.org/10.1016/B978-044452787-5.00097-4

Sibum, H., 2003. Titanium and Titanium Alloys—From Raw Material to Semi-finished Products. Adv. Eng. Mater. 5, 393–398. https://doi.org/10.1002/adem.200310092

Sieniawski, J., Ziaja, W., Kubiak, K., Motyka, M., 2013. Microstructure and Mechanical Properties of High Strength Two-Phase Titanium Alloys. https://doi.org/10.5772/56197

Simbi, D.J., Scully, J.C., 1996. The effect of residual interstitial elements and iron on mechanical properties of commercially pure titanium. Mater. Lett. 26, 35–39.

Sinigaglia, D., Taccani, G., Vicentini, B., Dallaspezia, G., 1978. Electrochemical Behavior of Titanium and Some Titanium Alloys under Tensile Stress in Boiling Sulfuric Acid and Acidic Chloride Solutions. J. Electrochem. Soc. 125, 1199–1204. https://doi.org/10.1149/1.2131649

Soltani, A., 2013. Effect of Adiabatic Heating on Strain Induced Phase Transformations in Stainless Steels.

Song, H., Zhang, S., Cheng, M., 2014. Dynamic globularization prediction during cogging process of large size TC11 titanium alloy billet with lamellar structure. Def. Technol. 10, 40–46. https://doi.org/10.1016/j.dt.2014.01.003

Song, H.-W., Zhang, S.-H., Cheng, M., 2009. Dynamic globularization kinetics during hot working of a two phase titanium alloy with a colony alpha microstructure. J. Alloys Compd. 480, 922–927. https://doi.org/10.1016/j.jallcom.2009.02.059

Souza, P.M., Beladi, H., Rolfe, B., Singh, R., Hodgson, P.D., 2015a. Softening Behavior of Ti6Al4V Alloy during Hot Deformation, in: Materials Science Forum. Presented at the Light Metals Technology, Materials Science Forum, Port Elizabeth, South Africa, pp. 407–412. https://doi.org/10.4028/www.scientific.net/MSF.828-829.407

Souza, P.M., Beladi, H., Singh, R., Rolfe, B., Hodgson, P.D., 2015b. Constitutive analysis of hot deformation behavior of a Ti6Al4V alloy using physical based model. Mater. Sci. Eng. A 648, 265–273. https://doi.org/10.1016/j.msea.2015.09.055

Struers, 2016. Metallographic preparation of titanium.

Tomashov, N.D., Chernova, G.P., Ruscol, Y.S., Ayuyan, G.A., 1974. The passivation of alloys on titanium bases. Electrochimica Acta 19, 159–172.

USGS, 2014. Mineral commodity summaries 2014 (USGS Unnumbered Series), Mineral Commodity Summaries. U.S. Geological Survey, Reston, VA.

van der Lingen, E., Sandenbergh, R.F., 2001. The cathodic modification behaviour of ruthenium additions to titanium in hydrochloric acid. Corros. Sci. 43, 577–590. https://doi.org/10.1016/S0010-938X(00)00096-2

Van Tonder, W., 2010. South African titanium: techno-economic evaluation of the alternatives to the Kroll process (PhD Thesis). Stellenbosch: University of Stellenbosch.

Van Vuuren, D.S., 2009. A critical evaluation of processes to produce primary titanium. J. South. Afr. Inst. Min. Metall. 109, 455–461.

Vander Voort, G., 2014. Metallographic Preparation of Titanium and Its Alloys. Vacaero.

Vander Voort, G., 1999. Metallographic preparation of titanium and its alloys. Buehler Tech-Notes 3.

Veiga, C., Davim, J.P., Loureiro, A.J.R., 2013. Review on machinability of titanium alloys: the process perspective. Rev Adv Mater Sci 34, 148–164.

Virtanen, S., 2012. Degradation of Titanium and Its Alloys, in: Eliaz, N. (Ed.), Degradation of Implant Materials. Springer New York, New York, NY, pp. 29–55. https://doi.org/10.1007/978-1-4614-3942-4_2

Vo, P., Jahazi, M., Yue, S., Bocher, P., 2007. Flow stress prediction during hot working of near-α titanium alloys. Mater. Sci. Eng. A 447, 99–110. https://doi.org/10.1016/j.msea.2006.10.032

Wang, G., Hui, S., Ye, W., Mi, X., 2012a. Hot compressive behavior of Ti–3.0Al–3.7Cr–2.0Fe–0.1B titanium alloy. Trans. Nonferrous Met. Soc. China 22, 2965–2971. https://doi.org/10.1016/S1003-6326(11)61557-4

Wang, G., Hui, S., Ye, W., Mi, X., Wang, Y., Zhang, W., 2012b. Microstructure and tensile properties of low cost titanium alloys at different cooling rate. Rare Met. 31, 531–536. https://doi.org/10.1007/s12598-012-0552-1

Wang, K., 1996. The use of titanium for medical applications in the USA. Mater. Sci. Eng. A, International Symposium on Metallurgy and Technology of Titanium Alloys 213, 134–137. https://doi.org/10.1016/0921-5093(96)10243-4

Wang, K., Zeng, W., Zhao, Y., Lai, Y., Zhou, Y., 2010. Hot working of Ti-17 titanium alloy with lamellar starting structure using 3-D processing maps. J. Mater. Sci. 45, 5883–5891. https://doi.org/10.1007/s10853-010-4667-1

Wang, M., Zhao, Y., Zhou, L., Zhang, D., 2004. Study on creep behavior of Ti–V–Cr burn resistant alloys. Mater. Lett. 58, 3248–3252. https://doi.org/10.1016/j.matlet.2004.06.007

Wang, S., Luo, J.R., Hou, L.G., Zhang, J.S., Zhuang, L.Z., 2016. Physically based constitutive analysis and microstructural evolution of AA7050 aluminum alloy during hot compression. Mater. Des. 107, 277–289. https://doi.org/10.1016/j.matdes.2016.06.023

Wanjara, P., Jahazi, M., Monajati, H., Yue, S., Immarigeon, J.-P., 2005. Hot working behavior of near-α alloy IMI834. Mater. Sci. Eng. A 396, 50–60. https://doi.org/10.1016/j.msea.2004.12.005

Weiss, I., Froes, F.H., Eylon, D., Welsch, G.E., 1986. Modification of alpha morphology in Ti-6Al-4V by thermomechanical processing. Metall. Trans. A 17, 1935–1947. https://doi.org/10.1007/BF02644991

Weiss, I., Semiatin, S.L., 1999. Thermomechanical processing of alpha titanium alloys—an overview. Mater. Sci. Eng. A 263, 243–256. https://doi.org/10.1016/S0921-5093(98)01155-1

Weiss, I., Semiatin, S.L., 1998. Thermomechanical processing of beta titanium alloys—an overview. Mater. Sci. Eng. A 243, 46–65. https://doi.org/10.1016/S0921-5093(97)00783-1

Welsch, G., Boyer, R., Collings, E.W., 1993. Materials Properties Handbook: Titanium Alloys. ASM International.

Weston, N.S., Jackson, M., 2017. FAST-forge − A new cost-effective hybrid processing route for consolidating titanium powder into near net shape forged components. J. Mater. Process. Technol. 243, 335–346. https://doi.org/10.1016/j.jmatprotec.2016.12.013

Whitehouse, A.F., Clyne, T.W., 1993. Effects of reinforcement content and shape on cavitation and failure in metal-matrix composites. Composites 24, 256–261. https://doi.org/10.1016/0010-4361(93)90172-5

Wild, S., 2013. Titanium project has global impact [WWW Document]. MG Online. URL https://mg.co.za/article/2013-06-07-00-titanium-project-has-global-impact/ (accessed 2.6.18).

Wu, C., Yang, H., Fan, X., Sun, Z., 2011. Dynamic globularization kinetics during hot working of TA15 titanium alloy with colony microstructure. Trans. Nonferrous Met. Soc. China 21, 1963–1969. https://doi.org/10.1016/S1003-6326(11)60957-6

Wu, G.Q., Shi, C.L., Sha, W., Sha, A.X., Jiang, H.R., 2013. Effect of microstructure on the fatigue properties of Ti–6Al–4V titanium alloys. Mater. Des. 46, 668–674. https://doi.org/10.1016/j.matdes.2012.10.059

Xia, Y., Long, S., Zhou, Y., Zhao, J., Wang, T., Zhou, J., 2016. Identification for the Optimal Working Parameters of Ti-6Al-4V-0.1Ru Alloy in a Wide Deformation Condition Range by Processing Maps Based on DMM. Mater. Res. 19, 1449–1460. https://doi.org/10.1590/1980-5373-mr-2016-0448

Xiao, J., Li, D.S., Li, X.Q., Deng, T.S., 2012. Constitutive modeling and microstructure change of Ti–6Al–4V during the hot tensile deformation. J. Alloys Compd. 541, 346–352. https://doi.org/10.1016/j.jallcom.2012.07.048

Xu, X., Nash, P., Mangabhai, D., 2017. Characterization and Sintering of Armstrong Process Titanium Powder. JOM 69, 770–775. https://doi.org/10.1007/s11837-016-2238-x

Xu, Y., Yang, X.J., Jiang, X.X., He, Y., Du, D.N., 2014. Hot Deformation Behavior of Ti-6Al-4V Alloy with a Transitional Microstructure in the Isothermal Hot Compression. Adv. Mater. Res. 1019, 273–279. https://doi.org/10.4028/www.scientific.net/AMR.1019.273

Xu, Y.B., Zhong, W.L., Chen, Y.J., Shen, L.T., Liu, Q., Bai, Y.L., Meyers, M.A., 2001. Shear localization and recrystallization in dynamic deformation of 8090 Al–Li alloy. Mater. Sci. Eng. A 299, 287–295.

Yan, D.P., Hilditch, T., Kishawy, H.A., Littlefair, G., 2013. On Quantifying the Strain Rate During Chip Formation When Machining Aerospace Alloy Ti-5553. Procedia CIRP 8, 123–128. https://doi.org/10.1016/j.procir.2013.06.076

Yang, H., Fan, X., Sun, Z., Guo, L., Zhan, M., 2011. Recent developments in plastic forming technology of titanium alloys. Sci. China Technol. Sci. 54, 490–501. https://doi.org/10.1007/s11431-010-4206-y

Yang, H.S., Gurewitz, G., Mukherjee, A.K., 1991. Mechanical Behavior and Microstructural Evolution during Superplastic Deformation of Ti-6Al-4V. Mater. Trans. 32, 465–472.

Yang, L.-C., Pan, Y.-T., Chen, I.-G., Lin, D.-Y., 2015. Constitutive Relationship Modeling and Characterization of Flow Behavior under Hot Working for Fe–Cr–Ni–W–Cu–Co Super-Austenitic Stainless Steel. Metals 5, 1717–1731. https://doi.org/10.3390/met5031717

Yang, Y., 2015. Investigation of the martensitic transformation and the deformation mechanisms occurring in the superelastic Ti-24Nb-4Zr-8Sn alloy (phdthesis). INSA de Rennes.

Yang, Y., Li, X.M., Tong, X.L., Zhang, Q.M., Xu, C.Y., 2011. Effects of microstructure on the adiabatic shearing behaviors of titanium alloy. Mater. Sci. Eng. A 528, 3130–3133. https://doi.org/10.1016/j.msea.2010.12.068

Yu, C., Cao, P., Jones, M., 2017. Microstructural Evolution during Pressureless Sintering of Blended Elemental Ti-Al-V-Fe Titanium Alloys from Fine Hydrogenated-Dehydrogenated Titanium Powder. Metals 7, 285. https://doi.org/10.3390/met7080285

Yu, S.Y., Scully, J.R., 1997. Corrosion and Passivity of Ti-13% Nb-13% Zr in Comparison to Other Biomedical Implant Alloys. CORROSION 53, 965–976. https://doi.org/10.5006/1.3290281

Zaera, R., Rodríguez-Martínez, J.A., Rittel, D., 2013. On the Taylor–Quinney coefficient in dynamically phase transforming materials. Application to 304 stainless steel. Int. J. Plast. 40, 185–201. https://doi.org/10.1016/j.ijplas.2012.08.003

Zener, C., Hollomon, J.H., 1944. Effect of strain rate upon plastic flow of steel. J. Appl. Phys. 15, 22–32. https://doi.org/10.1063/1.1707363

Zeng, Z., Jonsson, S., Zhang, Y., 2009. Constitutive equations for pure titanium at elevated temperatures. Mater. Sci. Eng. A 505, 116–119. https://doi.org/10.1016/j.msea.2008.11.017

Zerilli, F.J., Armstrong, R.W., 1987. Dislocation-mechanics-based constitutive relations for material dynamics calculations. J. Appl. Phys. 61, 1816–1825. https://doi.org/10.1063/1.338024

Zhan, H., Zeng, W., Wang, G., Kent, D., Dargusch, M., 2015. Microstructural characteristics of adiabatic shear localization in a metastable beta titanium alloy deformed at high strain rate and elevated temperatures. Mater. Charact. 102, 103–113. https://doi.org/10.1016/j.matchar.2015.02.017

Zhang, K., Liu, Z., Wang, Y., Liu, Y., 2016. Method of strain-rate difference calculation in high-speed metal cutting. Measurement 91, 474–478. https://doi.org/10.1016/j.measurement.2016.05.091

Zhang, Y., Huang, L., Liu, B., Geng, L., 2012. Hot deformation behavior of in-situ TiBw/Ti6Al4V composite with novel network reinforcement distribution. Trans. Nonferrous Met. Soc. China 22, s465–s471. https://doi.org/10.1016/S1003-6326(12)61747-6

Zhang, Y., Zhou, L., Sun, J., Han, M., Georg, R., Jochen, F., Yang, J., Zhao, Y., 2008. An Investigation on Electron Beam Cold Hearth Melting of Ti64 Alloy. Rare Met. Mater. Eng. 37, 1973–1977. https://doi.org/10.1016/S1875-5372(10)60004-5

Zhao, Y.Q., Qu, H.L., Wang, M.M., Wu, H., Zhu, K.Y., 2006. Thermal stability and creep behavior of Ti–V–Cr burn-resistant alloys. J. Alloys Compd. 407, 118–124. https://doi.org/10.1016/j.jallcom.2005.06.014

Zhao, Y.Q., Zhou, L., Deng, J., 1999. The role of interface in the burning of titanium alloys. Mater. Sci. Eng. A 267, 167–170. https://doi.org/10.1016/S0921-5093(99)00109-4

Zhu, K., Gui, N., Jiang, T., Zhu, M., Lu, X., Zhang, J., Li, C., 2014. The Development of the Low-Cost Titanium Alloy Containing Cr and Mn Alloying Elements. Metall. Mater. Trans. A 45, 1761–1766. https://doi.org/10.1007/s11661-013-2080-5

Zhu, Y.C., Zeng, W.D., Liu, J.L., Zhao, Y.Q., Zhou, Y.G., Yu, H.Q., 2012. Effect of processing parameters on the hot deformation behavior of as-cast TC21 titanium alloy. Mater. Des. 33, 264–272. https://doi.org/10.1016/j.matdes.2011.07.018

Zong, Y.Y., Shan, D.B., Xu, M., Lv, Y., 2009. Flow softening and microstructural evolution of TC11 titanium alloy during hot deformation. J. Mater. Process. Technol. 209, 1988–1994. https://doi.org/10.1016/j.jmatprotec.2008.04.063

Appendix A: Thermo-Calc command macro file(.tcm) for alloying simulation

go data	c-e	
swTTTi3	s-a-v	
def-sys	1	plot
Ti V Al Fe Alloy	T	SCREEN
System	273	set-tit
l-s	2173	Ti64
CONSTITUENT	3	plot
get	Save	SCREEN
go p-3	Ti64 Control	set-label
s-c n=1	step	f
s-c p=101325	NORMAL	s-t-m-s
s-c t=1096	post	x
s-c x(v)=.0360	s-d-a x T-c	s-s x n 100 1900
s-c x(Al)=.1008	s-d-a y np(*)	plot SCREEN
@s-c x(Fe)=.0083	*	set-inter
l-c		
@&		

Appendix B: Cost analysis on the compositions of theexperimental alloys

Assume 100 kg	Ti (kg)	Al	V	Fe	Al-V (kg)	=Al in Al-V	=V in Al-V	=Al (kg) not as Al-V (add as pure Al)	$Al-V	$Al pure	$Fe	Cost Al+V+Fe+MA	Alloying cost/ 100kg	Cost saving /100kg	Cost saving as a %
Ti 6Al 4V	90	6	4	0	10	6		0	$ 250.00	$ -		$ 250.00	$ 2 500.00		
10% addition of 60% aluminum - 40% vanadium composition master alloy to 90% pure titanium will produce Ti-6Al-4V alloy.															
6%Al															
3%V - 1%Fe		6	3	1	7.5	4.5	3.0	1.5	$ 187.50	$ 3.47	$ 0.50	$ 191.47	$ 2 441.47	$ 58.53	2.3%
2%V - 2%Fe		6	2	2	5.0	3.0	2.0	3.0	$ 125.00	$ 6.93	$ 1.00	$ 132.93	$ 2 382.93	$ 117.07	4.7%
1%V - 3%Fe		6	1	3	2.5	1.5	1.0	4.5	$ 62.50	$ 10.40	$ 1.50	$ 74.40	$ 2 324.40	$ 175.61	7.0%
0%V - 4%Fe		6	0	4	0.0	0.0		6.0	$ -	$ 13.86	$ 2.00	$ 15.86	$ 2 265.86	$ 234.14	9.4%
4.5%Al															
3%V - 1%Fe	91.5	4.5	3	1	7.5	4.5	3.0	0.0	$ 187.50	$ -	$ 0.50	$ 188.00	$ 2 475.50	$ 24.50	1.0%
2%V - 2%Fe	91.5	4.5	2	2	5.0	3.0	2.0	1.5	$ 125.00	$ 3.47	$ 1.00	$ 129.47	$ 2 416.97	$ 83.03	3.3%
1%V - 3%Fe	91.5	4.5	1	3	2.5	1.5	1.0	3.0	$ 62.50	$ 6.93	$ 1.50	$ 70.93	$ 2 358.43	$ 141.57	5.7%
		Here Al=4.5% only, so if you add a 60:40 Al-V M.A.													
		it depends on the %Al.													
		For 4.5kg (%) Al, you get													
		4.5/0.6=	7.5	MA											
		and	3	kg V											
		Ratio Al:V in Master allo			60:40 =	1.5									
4.5%Al				Ratio Al:V											
3%V - 1%Fe		4.5	3	1.5											
2%V - 2%Fe		4.5	2	2.25											
1%V - 3%Fe		4.5	1	4.5											

60Al-40V master alloy	$ 25.00	**/kg**	https://www.zauba.com/import-aluminium+vanadium+master+alloy-hs-code.html		
pure Al=	$ 2.31	**/kg**	* Aluminium price = US$ 1.05/ lb	http://www.infomine.com/investment/metal-prices/aluminum/1-week/	
pure Fe=	$ 0.50	**/kg**	https://www.indiamart.com/proddetail/high-purity-iron-powder-9367920491.html	in rupees	
Ti Gr.2 bar	$ 25.00	**/kg**	https://www.alibaba.com/showroom/titanium-bar-grade-2.html		
			~$68/kg for Ti Gr 2 powder	https://www.indiamart.com/ranveer-metal-industries/titanium-grade-2-materials.html	

Appendix C: Gleeble script language for isothermal compression testing

```
// G:\quiksim\university of wits\Michael PhD\Grace 2016.gsl -- hot deformation simulation
// QuikSim2 2.4.5918.25012, QsHaz 2.4.5918.24954
// Gin File - g:\gin\hds\hds.gin
// Setup:
// Jaw tempco set to 0.4000um/C, specimen tempco set to 13.0000nm/mm/C
//

set rampterm to 35000.0000pct
set ramiterm to 0.0800pct
set ramdterm to 1000.0000pct
// Heating...
// Hydrawedge Auto-load

// stress/strain setup...
set strainmode to 1
set strainsrc to Jaw.index
set strainX0 to 12.00mm
set strVolume to 8.00mm*8.00mm*12.00mm
// end of stress/strain setup.

acquire airrampres Force Jaw PowAngle PRam PTemp PWedge Strain Stress Stroke TC1
Wedge

set TC1 to 0C
set tempmode to TC1.control
set h0 to 15.0000mm
set stroke to 0cm
set wedge to 0cm
set heatbutton to on
set mechanical to on
delay 5sec
set hypress to on
delay 15sec

// Zero out stroke under full load...
ramp stroke to -7cm in 5sec
delay 1sec
zero stroke
delay 100msec
set airtc to on
set airram to on
while force>-200kgf
set wedgezero to wedgezero+0.03mm
delay 100msec
end

ramp stroke to 5.8595mm+1.0000mm+0.0000mm in 1sec  //
```

```
5.8595mm+1.0000mm+0.0000mm
ramp wedge to -0.75mm in 1sec   // -0.75mm


// energize load solenoid and grab specimen
set specload to on
delay 500msec
set specload to off

// Move into position for first deformation
ramp wedge to 6.1405mm-12.0000mm-0.0000mm in 1sec  // 6.1405mm-12.0000mm-
0.0000mm
zero Jaw

// Pre-deformation:
set lastruntime to systime
sampleat 10.0000Hz

ramp wedge to -5.4147mm in 190.0000sec &// TX=0.4448mm
ramp TC1 to 950.0000C in 190.0000sec
set airram to off
delay 120.0000sec
set airram to on


zero Jaw
delay 0.1sec

// Deformations...
// Begin hit

// Hit 1:
// e:0.6700, e':0.0010/sec, dw: 1.0000msec, adj:0.0000mm/sec, com: 0.0000mm,
// tt:950C, tt':0.0000C/sec, soak:60.0000sec, exit:950C
// entryVelocity:0.0120mm/sec, exitVelocity:0.0061mm/sec

// back up= bud + compliance + deltaH
ramp stroke to 1.0000mm+0.0000mm+5.8595mm in 10msec

delay 10msec   // strokeLag=10msec

// finalH=6.1405mm (-) h0=12.0000mm (+) TX=0.4448mm (-) compliance=0.0000mm
{specH=6.1405mm, T=950C}
ramp wedge to 6.1405mm-12.0000mm+0.4448mm-0.0000mm in 10msec  //
wedgePosDuration=10msec

sampleat 10.0000Hz

// Hit heating here

// Thermal soak
set airram to off
delay 60.0000sec-1sec
set airram to on
delay 1sec
```

```
// final strain zero
zero Jaw
delay 0.1sec

delay 50.0000msec
sampleat 90.0Hz
delay 50.0000msec

ramp stroke to 5.8595mm in 1.0000sec

ramp TC1 to 950C in 669999.9849msec &

ramp stroke to 5.4642mm in 33499.9992msec &
ramp stroke to 5.0818mm in 33499.9992msec &
ramp stroke to 4.7121mm in 33499.9992msec &
ramp stroke to 4.3546mm in 33499.9992msec &
ramp stroke to 4.0088mm in 33499.9992msec &
ramp stroke to 3.6744mm in 33499.9992msec &
ramp stroke to 3.3511mm in 33499.9992msec &
ramp stroke to 3.0384mm in 33499.9992msec &
ramp stroke to 2.7360mm in 33499.9992msec &
ramp stroke to 2.4436mm in 33499.9992msec &
ramp stroke to 2.1608mm in 33499.9992msec &
ramp stroke to 1.8873mm in 33499.9992msec &
ramp stroke to 1.6228mm in 33499.9992msec &
ramp stroke to 1.3670mm in 33499.9992msec &
ramp stroke to 1.1197mm in 33499.9992msec &
ramp stroke to 0.8805mm in 33499.9992msec &
ramp stroke to 0.6492mm in 33499.9992msec &
ramp stroke to 0.4255mm in 33499.9992msec &
ramp stroke to 0.2092mm in 33499.9992msec &
ramp stroke to 0.0mm in 33499.9992msec &
// End segment
ramp stroke to -0.0001mm in 20.0000msec  // maxOverprogramTime=20msec


// End hit

// Post-deformation:
ramp stroke to 12.0000mm+3mm in 100msec  // 12.0000mm+3mm
ramp wedge to 6.1405mm-12.0000mm-2mm in 300msec  // 6.1405mm-12.0000mm-2mm
sampleat 10.0000Hz

// Cooling...
// End cooling...


// Shut down...
sample off
set heatbutton to off
set tc1 to 0C
set hypress to off
set mechanical to off
set temptrim to 0C
```

```
delay 2sec
set wedgezero to wedgezero-1mm
// Variable dump.....................
// <deltah> = 5.8595

// <beginseg> =
// <finalh> = 6.1405
// <heat1temp> = 950
// <wedgesettle> = 100
// <initialdef> = 0.0000
// <heating> = ramp wedge to -5.4147mm in 190.0000sec & // TX=0.4448mm
//    ramp TC1 to 950.0000C in 190.0000sec
//    set airram to off
//    delay 120.0000sec
//    set airram to on
//
// <initialh> = 12.0000
// <exittemp> = 950
// <preacqfreq> = 10.0000
// <finalh0> = 6.1405
// <acqfreq> = 90.0
// <adjust> = 0.0000
// <endseg> = // End segment
// <yokecompliance> = 0.75
// <hittype> = 1
// <finaldef> = 5.8595
// <ginversion> = 2.0
// <hittime> = 669999.9849
// <heat1time> = 190.0000
// <temptarget> = 950
// <tx1> = 0.4448
// <bud> = 1.0000
// <butime> = 1.0000
// <ti> = 950
// <scomp> = 0.0000
// <temprate> = 0.0000
// <heatmute> = 0
// <erate> = -0.0010
// <overdwell> = 0.0000
// <heatinc> = 0.03
// <overtime> = 20.0000
// <backup0> = 1.0000
// <exitvelocity> = 0.0061
// <cooling> = // Cooling...
//    // End cooling...
//
// <maxoverprogramtime> = 20
// <soaktime> = 60.0000
// <maxoverprogramdist> = 4
// <entryvelocity> = 0.0120
// <overdist> = -0.0001
// <compliance0> = 0.0000
// <e'> = 0.0010
// <compliance> = 0.0000
// <autoload> = 1
```

```
// <heatforce> = -200
// <heat2temp> = 0
// <endhit> = // End hit
// <dwell> = 1.0000

// <e> = 0.6700
// <wedgeposduration> = 10
// <overprogram> = ramp stroke to -0.0001mm in 20.0000msec  //
maxOverprogramTime=<maxOverprogramTime>msec
//
// <hwedgesettle> = 50.0000
// <heattime> = 0.0000
// <controltc> = TC1
// <heat1soak> = 120.0000
// <acqvars> = airrampres Force Jaw PowAngle PRam PTemp PWedge Strain Stress Stroke
TC1 Wedge
// <tx0> = 0.4448
// <heat2soak> = 0.0000
// <strokelag> = 10
// <dumpdelay> = 5
// <deltah0> = 5.8595
// <heat2time> = 0
// <h0> = 12.0000
// <hit> = 1
// <defcount> = 1
// <hipressdelay> = 15
// <heat1> = 1
// <strainsrc> = Jaw
// <heat2> = 0
// <strainsetup> = // stress/strain setup...
//    set strainmode to 1
//    set strainsrc to Jaw.index
//    set strainX0 to 12.00mm
//    set strVolume to 8.00mm*8.00mm*12.00mm
//    // end of stress/strain setup.
//
// <beginhit> = // Begin hit
```

Appendix D: Flow stresses of rectangular and cylindrical samples

Comparison between the flow stresses obtained from rectangular (flat bar) and cylindrical (round bar) samples deformed under similar conditions.

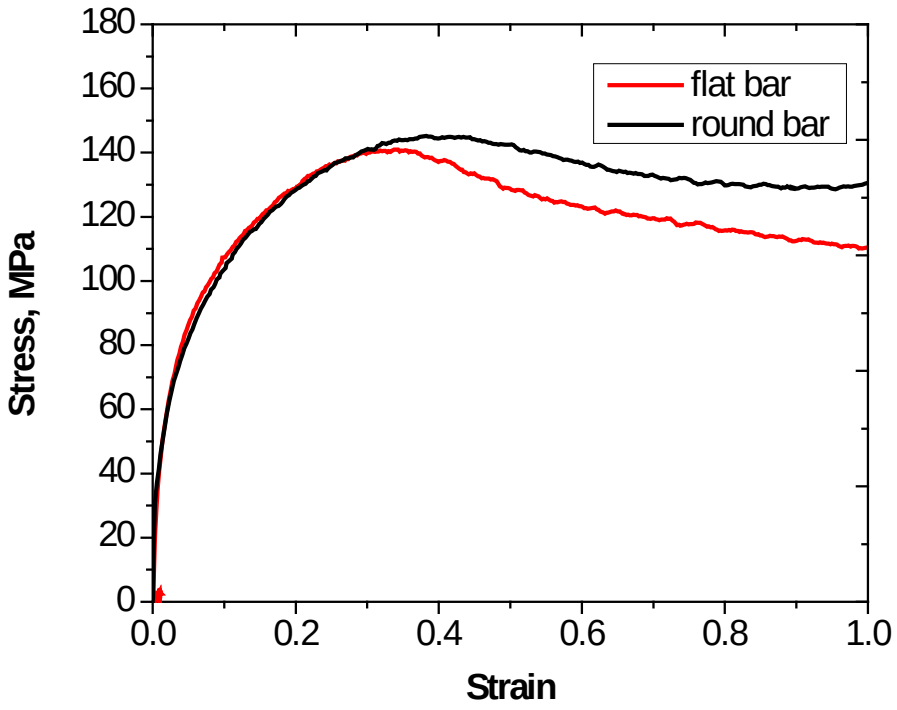

Appendix E: Thermo-Calc simulations

E1 Results obtained from Thermo-Calc simulation of Ti-6Al-4V and the experimental titanium alloys.

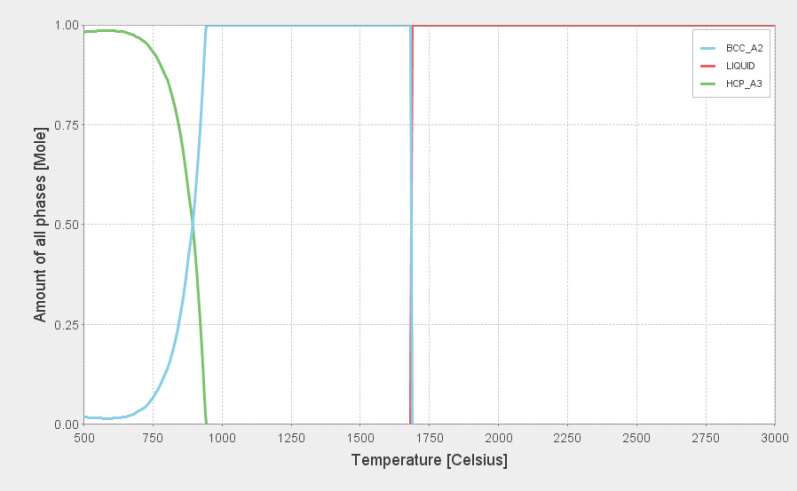

Ti-6Al-4V

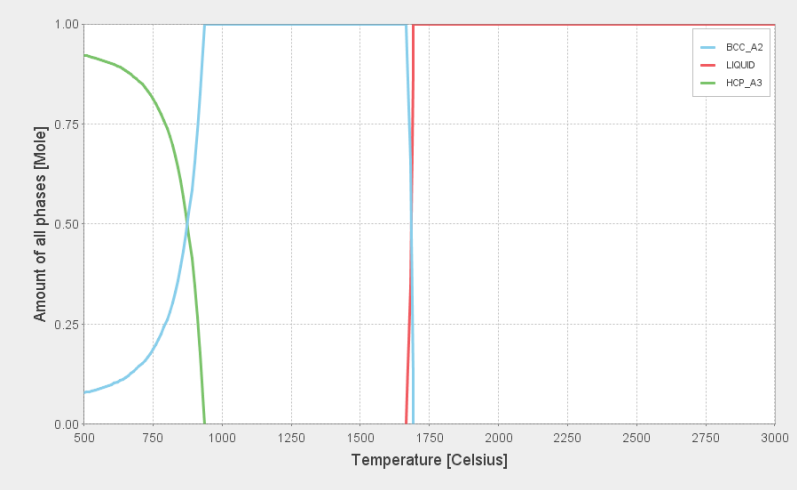

Ti-6Al-3V-1Fe

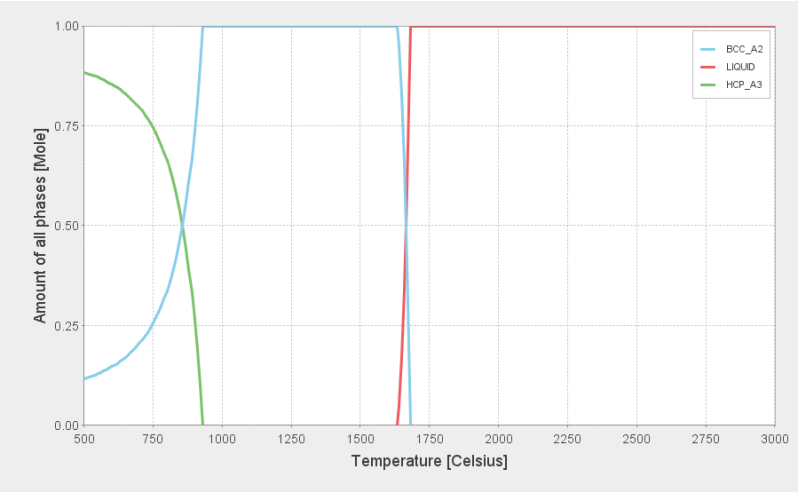

Ti-6Al-2V-2Fe

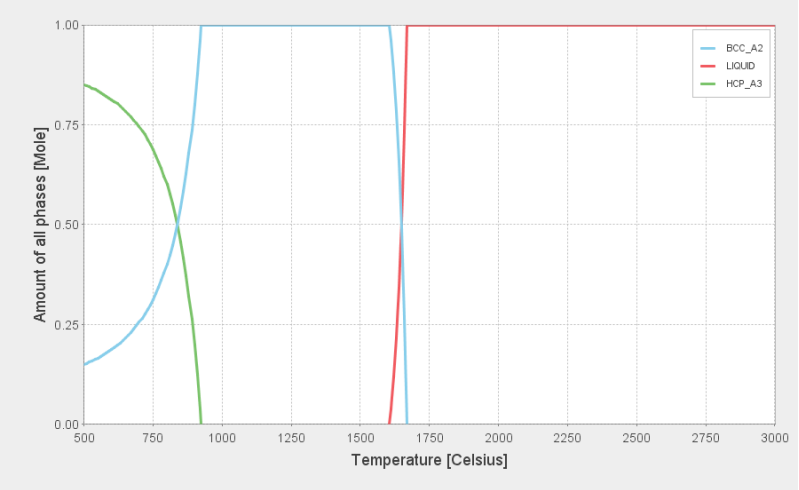

Ti-6Al-1V-3Fe

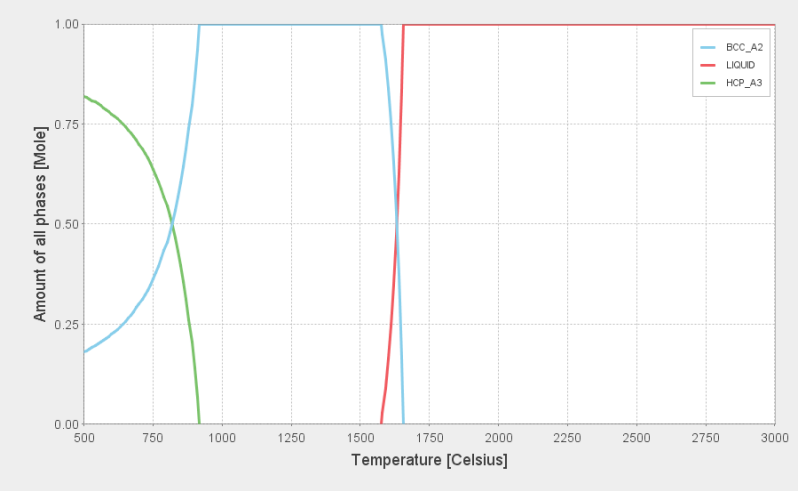

Ti-6Al-4Fe

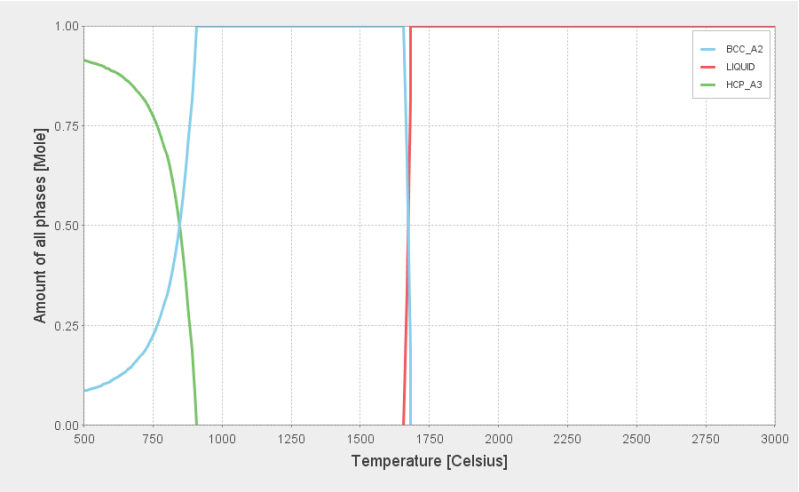

Ti-4.5Al-3V-1Fe

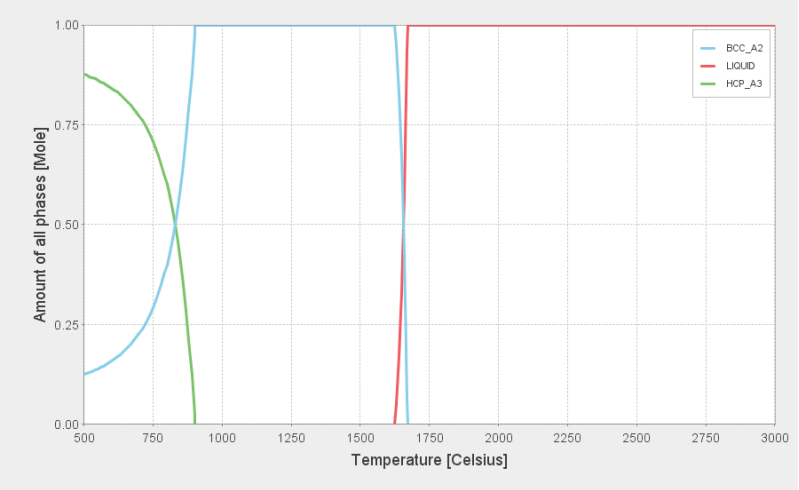

Ti-4.5Al-2V-2Fe

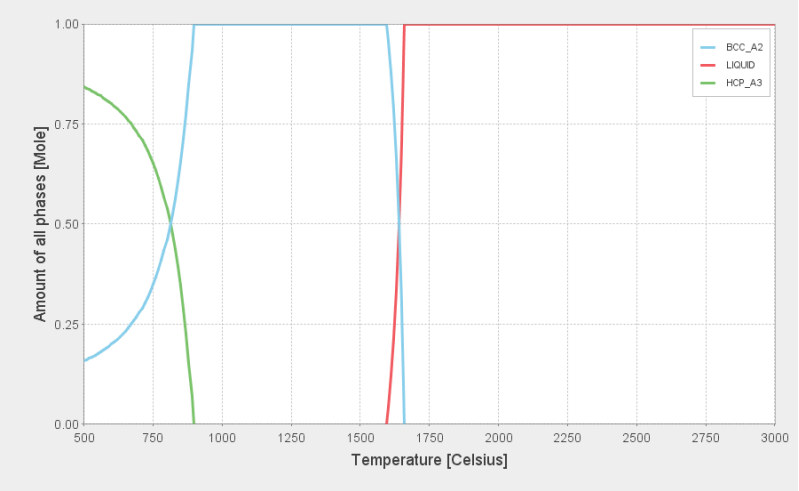

Ti-4.5Al-1V-3Fe

E2 Beta transus temperatures obtained from Thermo-Calc simulation of Ti-6Al-4V and the experimental titanium alloys with 0.2 wt% oxygen and 0.05 wt% nitrogen additions

S/N	Alloys	Beta transus (°C)
1	Ti-6Al-4V-0.2O-0.05N	1032
2	Ti-6Al-3V-1Fe-0.2O-0.05N	1040
3	Ti-6Al-2V-2Fe-0.2O-0.05N	1049
4	Ti-6Al-1V-3Fe-0.2O-0.05N	1065
5	Ti-6Al-4Fe-0.2O-0.05N	1080
6	Ti-4.5Al-3V-1Fe-0.2O-0.05N	1008
7	Ti-4.5Al-2V-2Fe-0.2O-0.05N	1021
8	Ti-4.5Al-1V-3Fe-0.2O-0.05N	1035

Appendix F: Temperature increase of Ti-6Al-4V during deformation

Temperature rise measured by thermocouple during deformation of Ti-6Al-4V alloys with complex intial microstructure.

$10s^{-1}$ **$1s^{-1}$** **$0.1s^{-1}$**

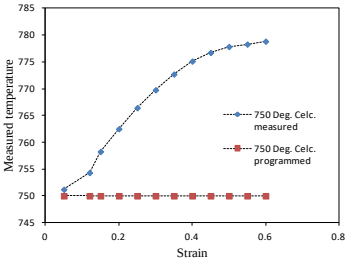

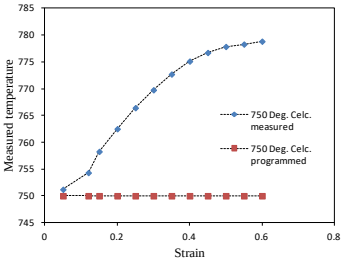

700 °C

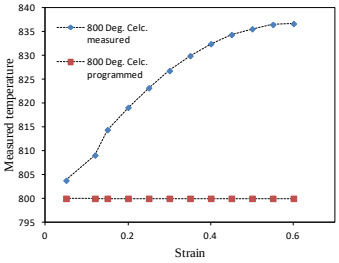

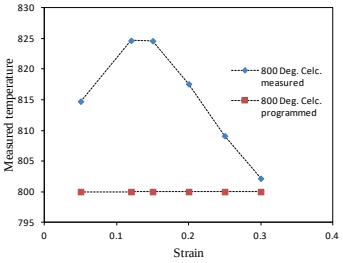

800° C

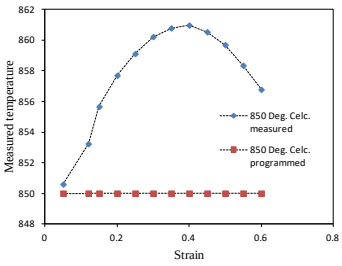

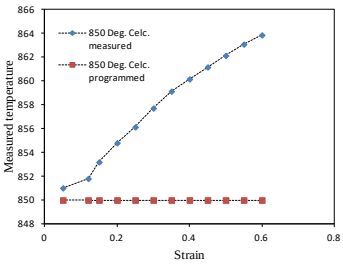

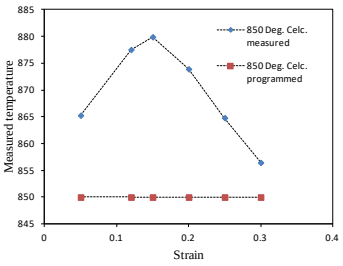

850° C

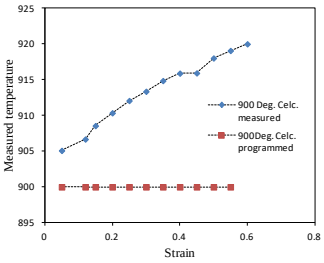

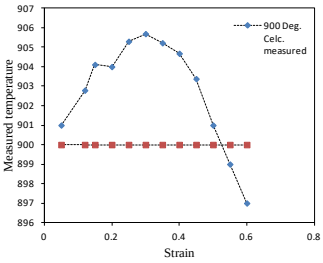

900° C

Appendix G: Supplementary results for hot compression testing of Ti-6Al-4Valloy

G-1: Flow stress values (MPa) of Ti-6Al-4V, corrected for adiabatic temperature increase, as a function of strain, temperature and strain rate

Strain	Strain rate (s^{-1})	Corrected flow stress (MPa) at test temperature (°C)				
		750	800	850	900	950
0.1	0.01	277	181	118	50	29
	0.1	302	241	158	88	42
	1	392	305	236	138	88
	10	437	378	314	243	135
0.2	0.01	278	167	115	48	29
	0.1	327	251	161	87	38
	1	409	310	240	138	88
	10	461	389	309	241	136
0.3	0.01	271	154	114	41	29
	0.1	352	257	170	91	35
	1	402	300	235	138	89
	10	466	386	302	235	134
0.4	0.01	250	137	109	40.2	25
	0.1	359	252	164	91	37
	1	384	288	227	135	88
	10	454	371	286	219	127
0.5	0.01	221	126	93	40	26
	0.1	350	249	159	91	23
	1	376	277	221	130	88
	10	431	338	268	219	120
0.6	0.01	193	114	83	39	20
	0.1	338	248	157	93	18
	1	350	266	217	132	88
	10	405	333	253	185	114

G-2: Processing maps at different strains for Ti-6Al-4V alloy with a complex initial microstructure

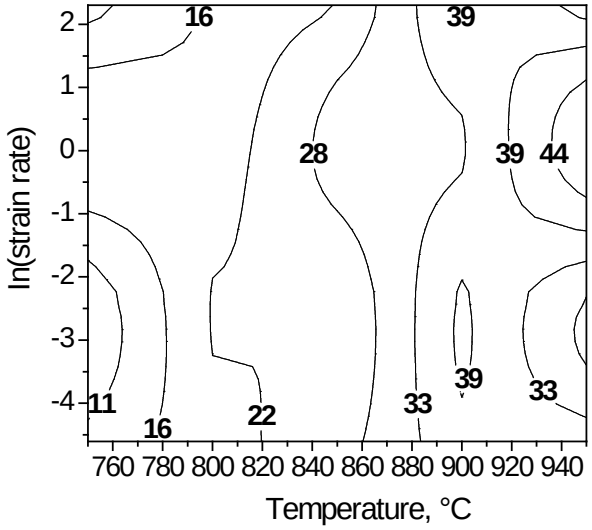

0.1 strain

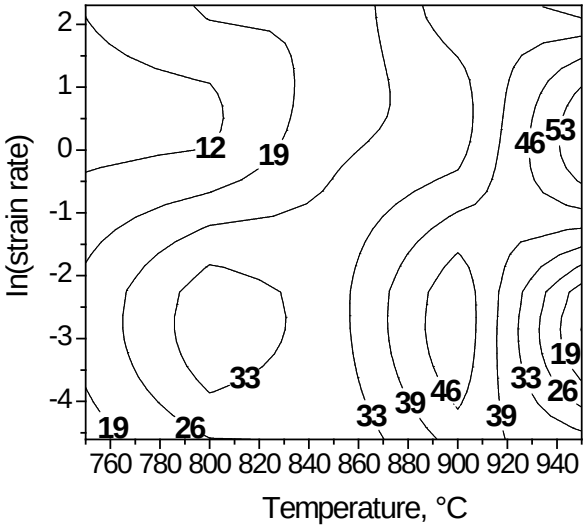

0.3 strain

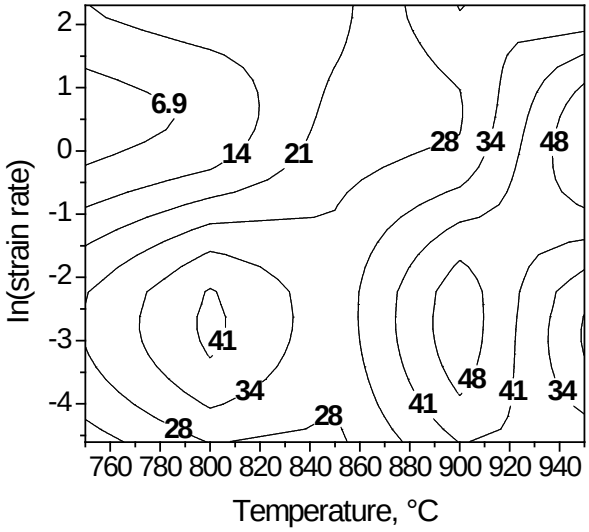

0.4 strain

G-3: Strain rate and temperature profile of Ti-6Al-4V alloy deformed at 950°C/0.01 s^{-1} showing that deformation temperature of 950°C was not exceeded. The strain rate profile on the left indicates the time when deformation started

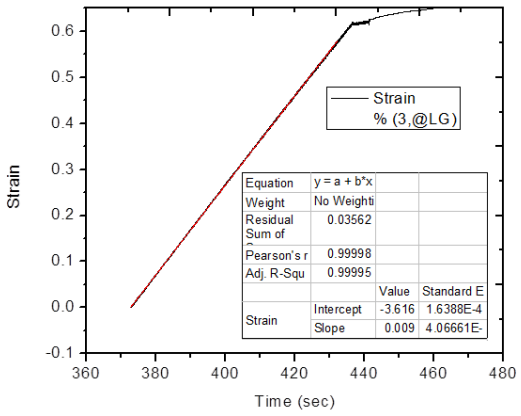

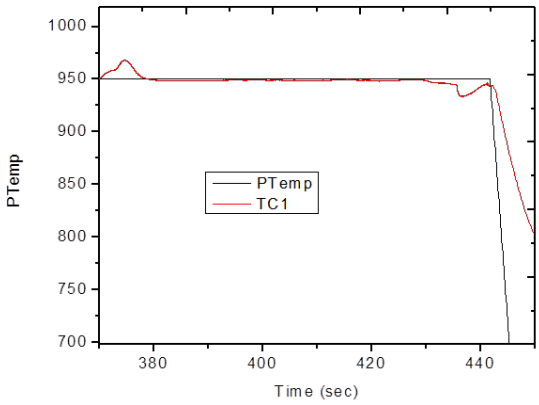

Appendix H: Hot deformation behaviour of Ti-6Al-*x*V-*y*Fe alloys (Prozesky *et al.* 2017) and calculations from experimental data for Ti-6Al-1V-3Fe and Ti-4.5Al-1V-3Fe alloys

Hot deformation behaviour of Ti-6Al-*x*V-*y*Fe alloys (Prozesky et al. 2017) and calculations from experimental data for Ti-6Al-1V-3Fe and Ti-4.5Al-1V-3Fe alloys are presented.

H-1: Preliminary results on the hot deformation behaviour of experimental Ti-6Al-*x*V-*y*Fe alloys reported in Prozesky *et al.* (2017).

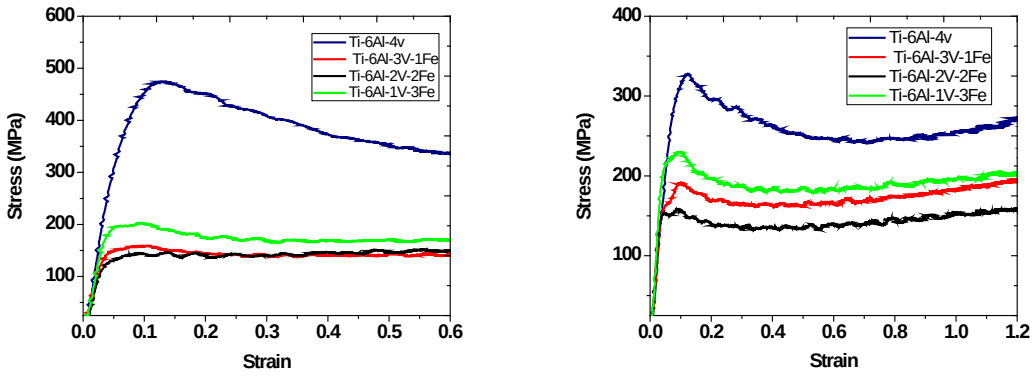

Stress-strain curves for hot compression tests of as-cast Ti-6Al-*x*V-*y*Fe at a strain of (a) 0.6 and (b) 1.2.

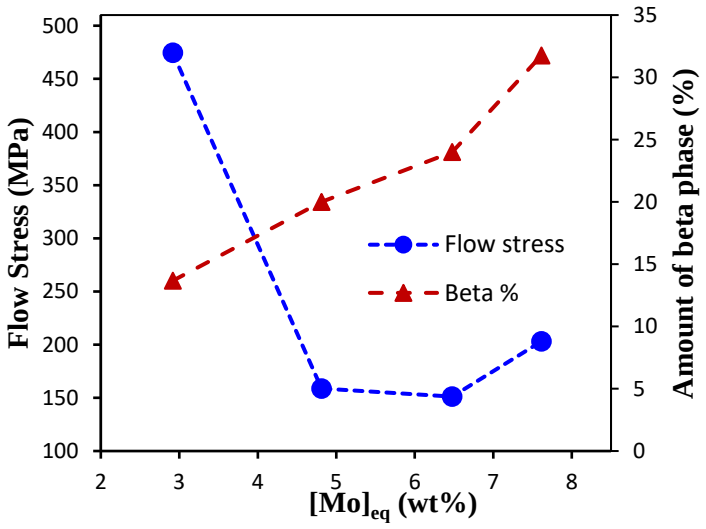

Peak flow stress against equivalent molybdenum content in Ti-Al-*x*V-*y*Fe alloys at a total strain of 0.6.

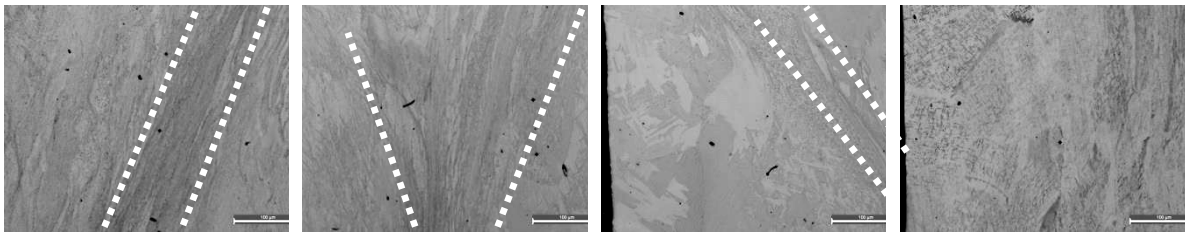

(a) Ti-6Al-4V (ε = 1.2) **(b) Ti-6Al-3V-1Fe (ε = 1.2)** **(c) Ti-6Al-4V (ε = 0.6)** **(d)Ti-6Al-1V-3Fe (ε = 0.6)**

Optical micrographs of deformed zones in selected Ti-6Al-*x*V-*y*Fe alloys showing region of shear bands.

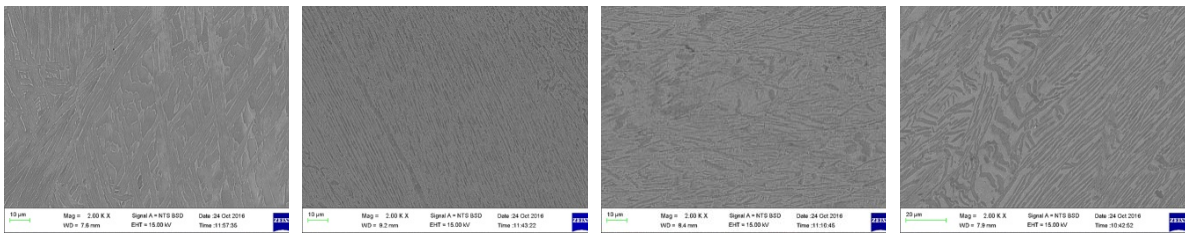

(a) Ti-6Al-4V **(b) Ti-6Al-3V-1Fe** **(c) Ti-6Al-2V-2Fe** **(d) Ti-6Al-1V-3Fe**

SEM-BSE images of deformed zones in Ti-6Al-*x*V-*y*Fe alloys at a strain of 0.6.

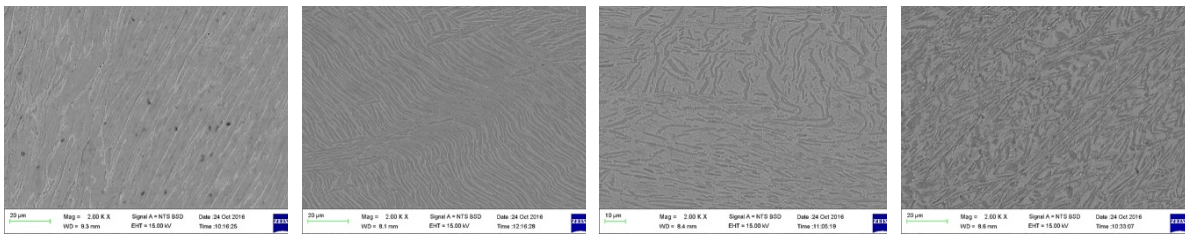

(a) Ti-6Al-4V **(b) Ti-6Al-3V-1Fe** **(c) Ti-6Al-2V-2Fe** **(d) Ti-6Al-1V-3Fe**

SEM-BSE images of deformed zones in Ti-6Al-*x*V-*y*Fe alloys (ε = 1.2).

H-2: Temperature increase measured by thermocouple during deformation of experimental titanium alloys

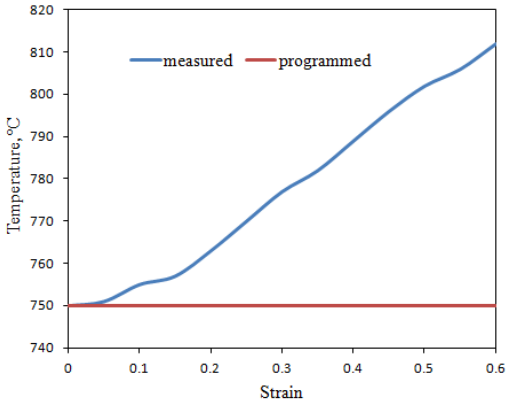

a) 750 °C / 10s^{-1}

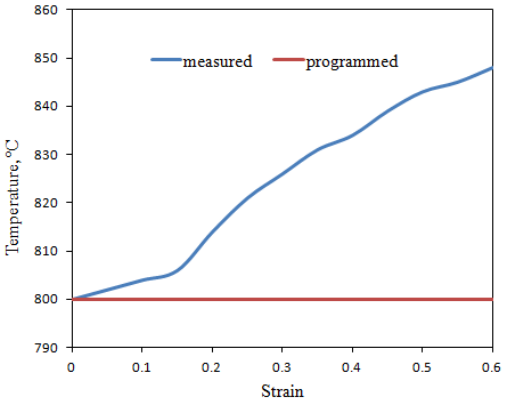

b) 800 °C/ 10s^{-1}

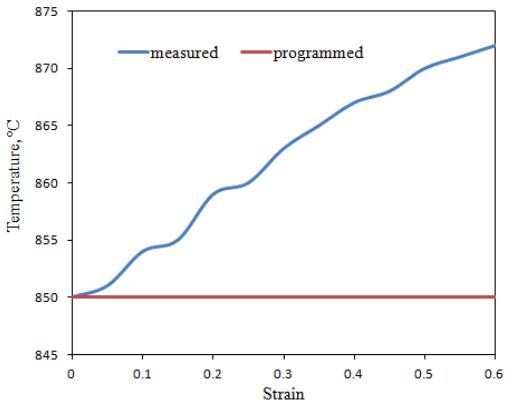

c) 850 °C/ 10s^{-1}

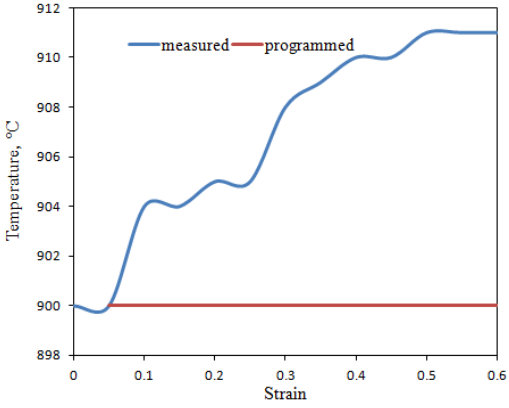

d) 900 °C/ 10s^{-1}

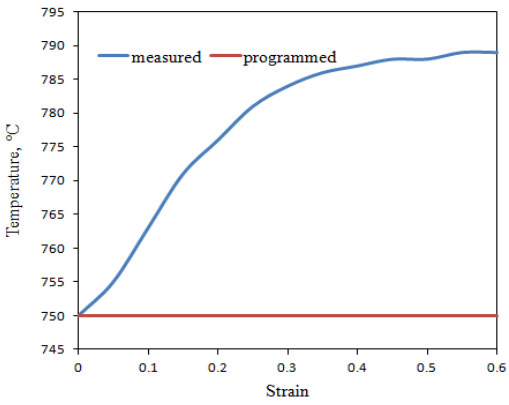

e) 750°C/1s^{-1}

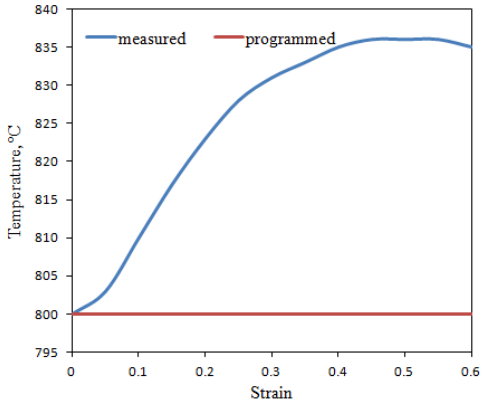

f) 800°C/1s^{-1}

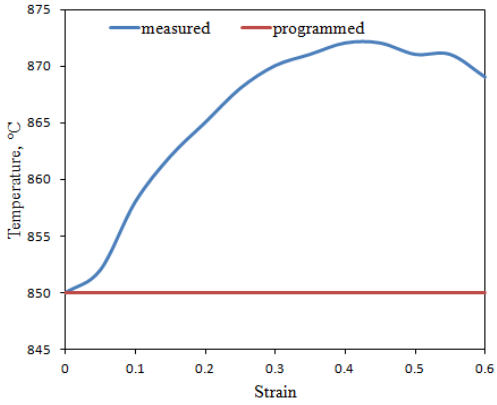

g) 850°C/1s^{-1}

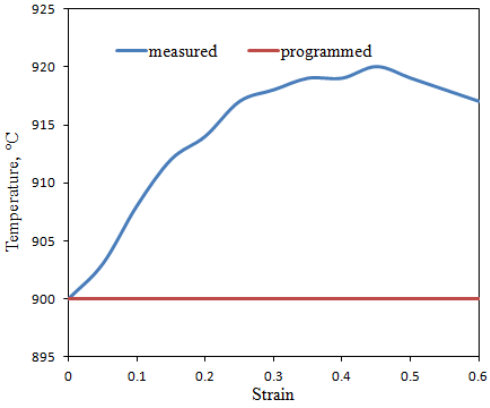

h) 900°C/1s^{-1}

Ti-6Al-1V-3Fe

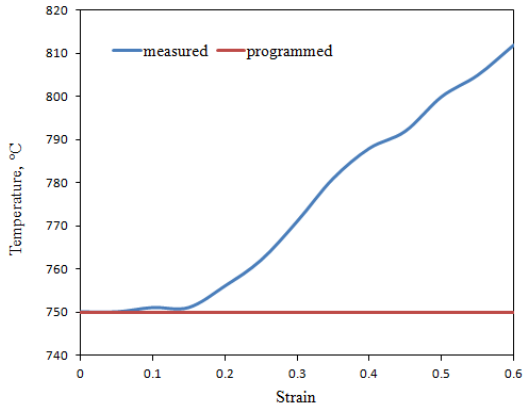

a) 750°C/10s^{-1}

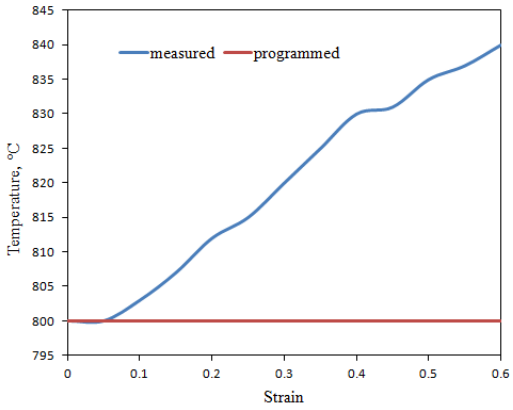

b) 800°C/10s^{-1}

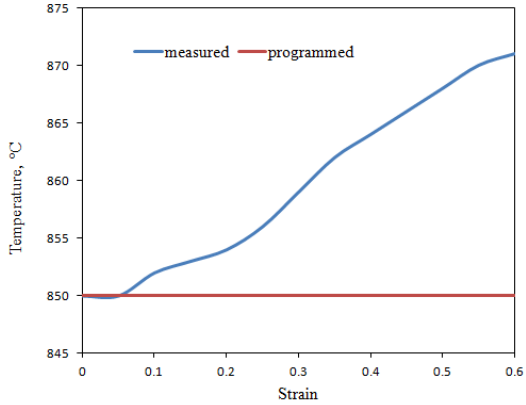

c) 850°C/10s^{-1}

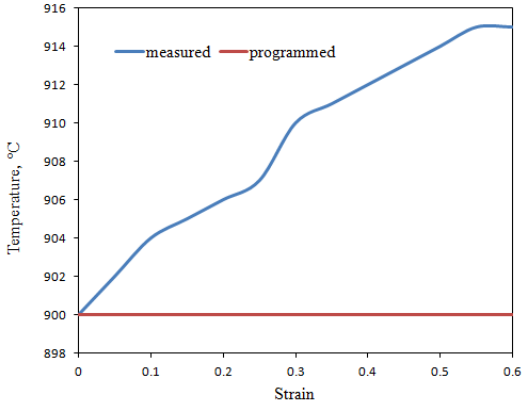

d) 900°C/10s^{-1}

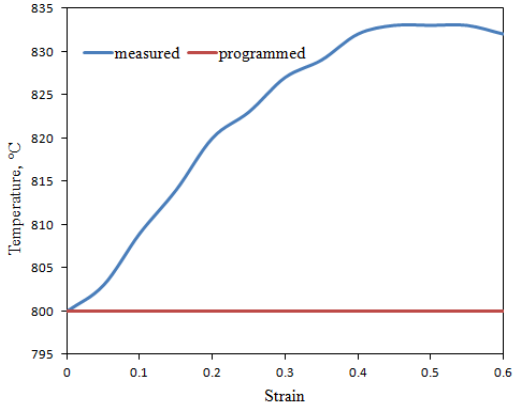

e) 750°C/1s^{-1}

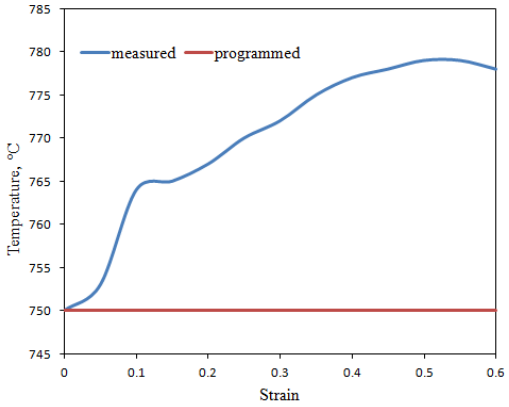

f) 800°C/1s^{-1}

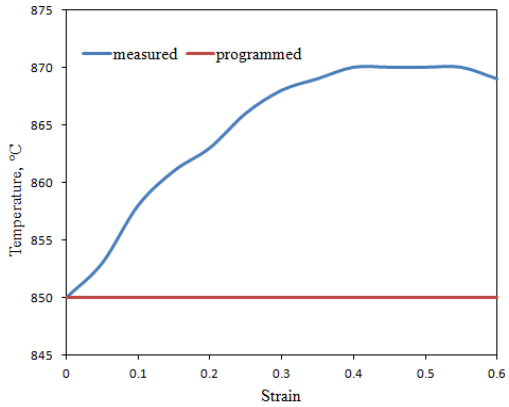

g) 850°C/1s^{-1}

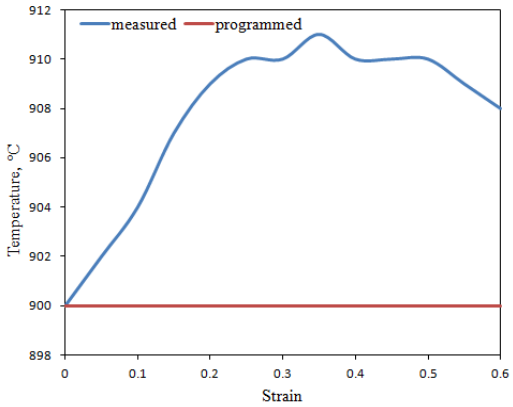

h) 900°C/1s^{-1}

Ti-4.5Al-1V-3Fe

H-3: Correction of flow stress for Ti-6Al-1V-3Fe and Ti-4.5Al-1V-3Fe experimental alloys

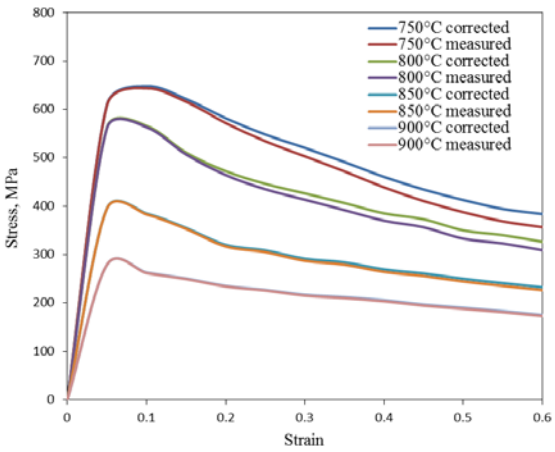

a) $10s^{-1}$

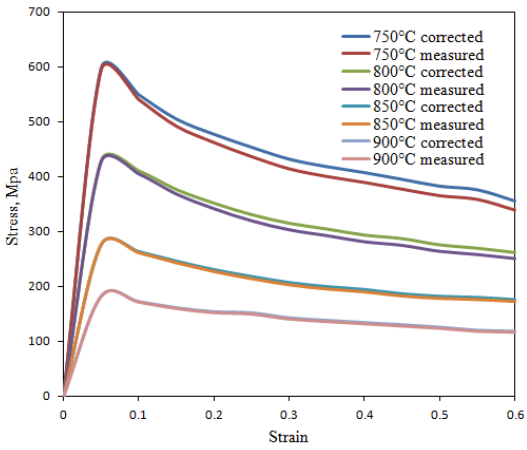

b) $1s^{-1}$

Ti-6Al-1V-3Fe

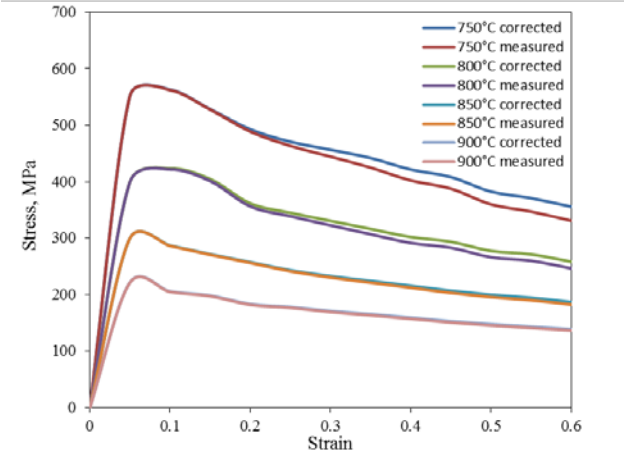

c) $10s^{-1}$

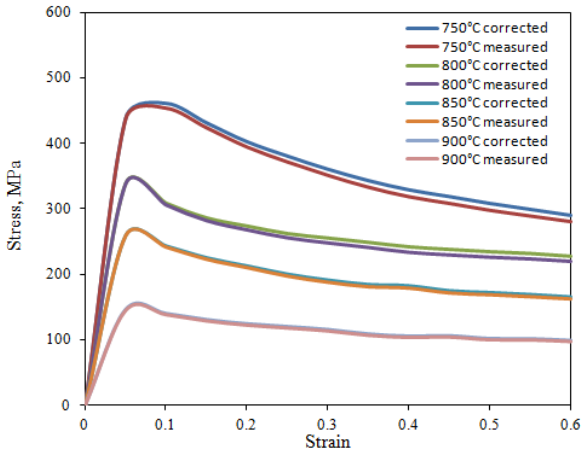

d) $1s^{-1}$

Ti-4.5Al-1V-3Fe

H-4: Instability maps for Ti-6Al-1V-3Fe experimental alloy

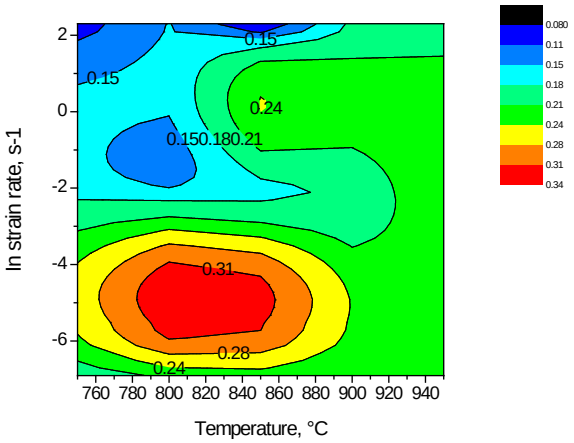

a) 0.1 strain

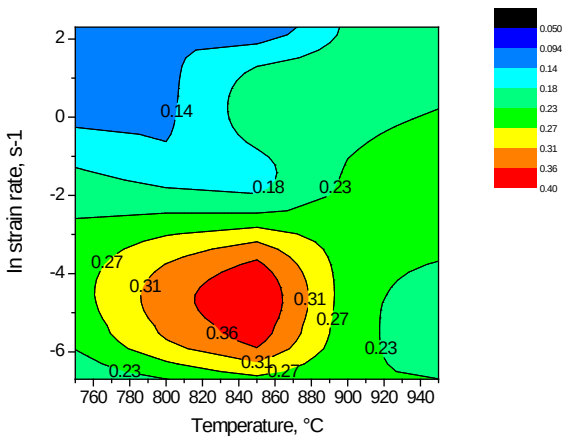

b) 0.2 strain

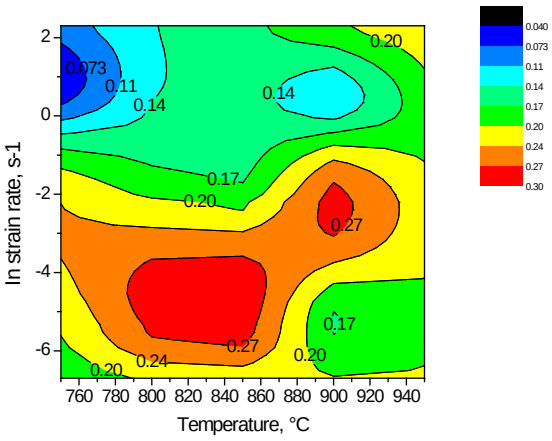

c) 0.3 strain

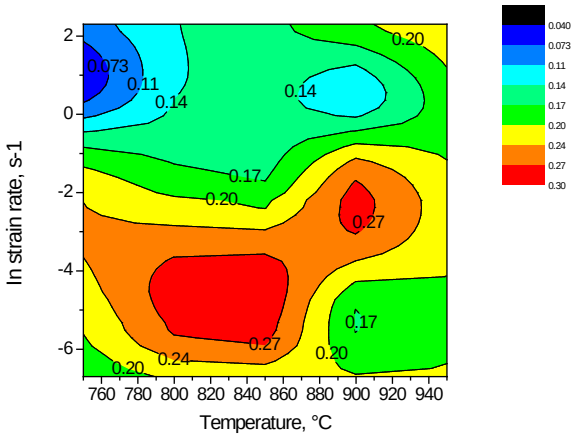

d) 0.4 strain

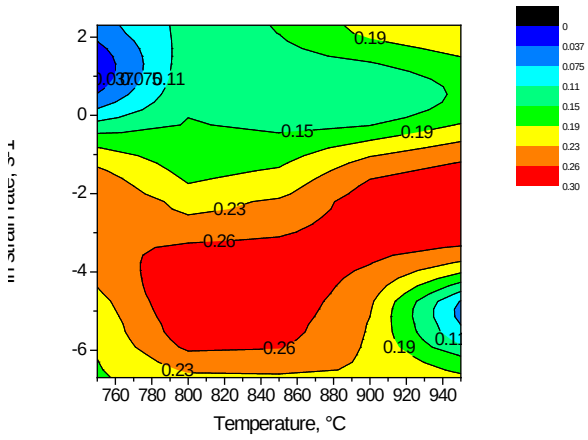

e) 0.5 strain

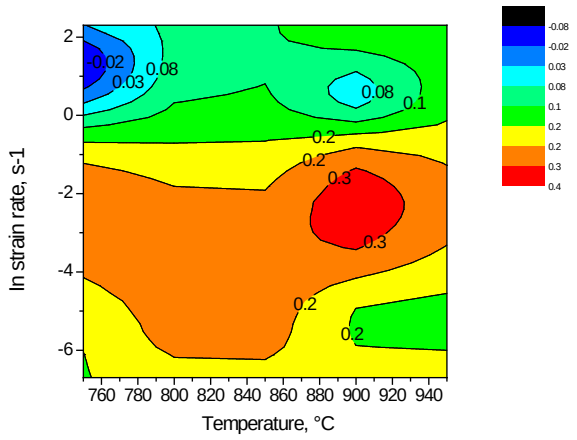

f) 0.6 strain

H-5: Instability maps for Ti-4.5Al-1V-3Fe experimental alloy

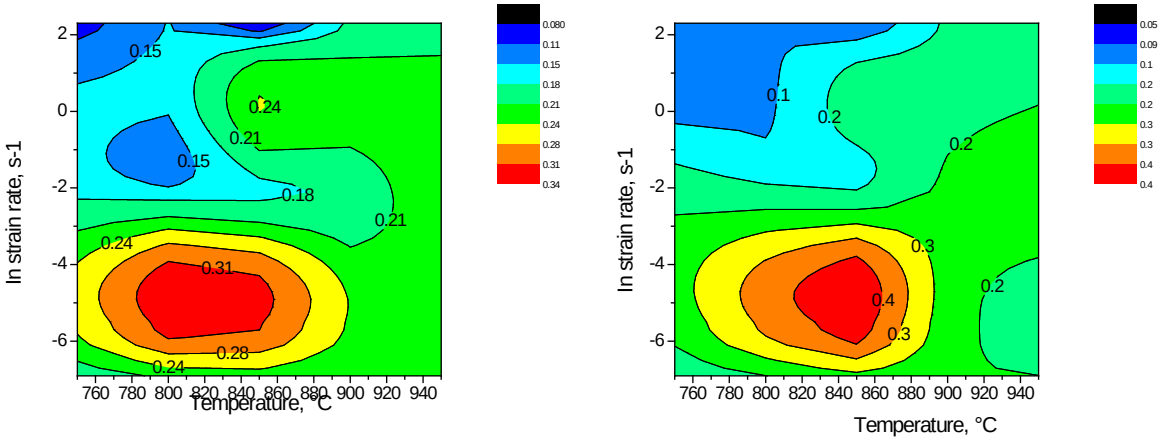

a) 0.1 strain **b) 0.2 strain**

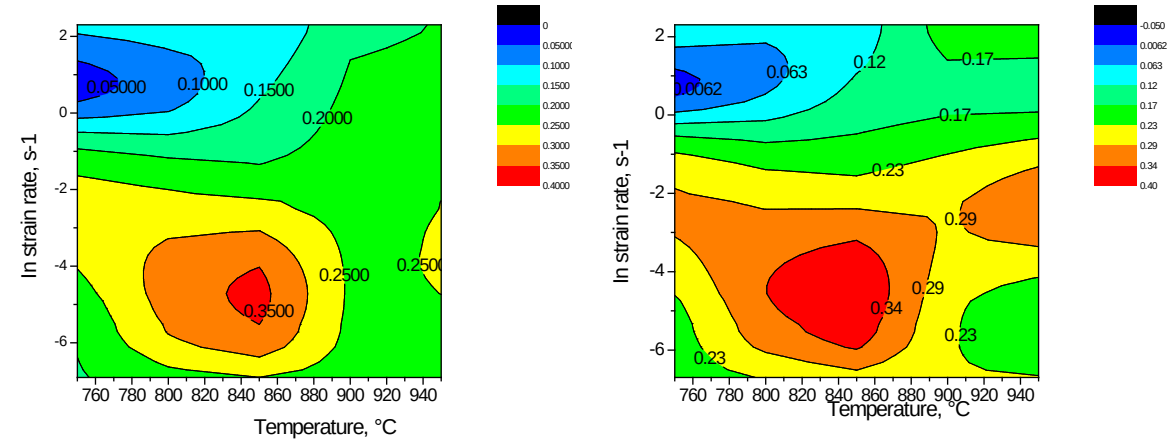

c) 0.3 strain **d) 0.4 strain**

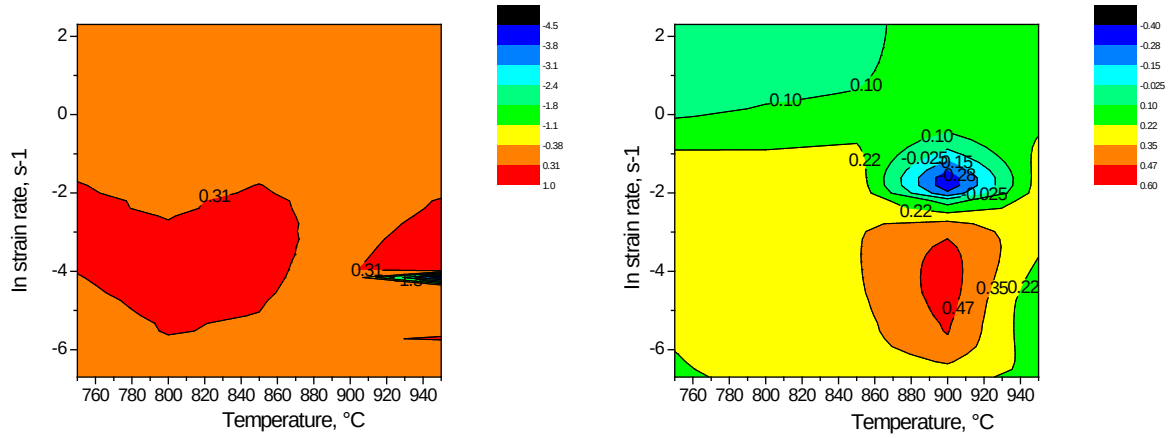

e) 0.5 strain **f) 0.6 strain**

H-6: Flow stress data used for processing map of Ti-4.5Al-1V-3Fe

Strain rate (s^{-1})	Strain	Temperature (°C)				
		750	800	850	900	950
10	0.05	617	569	401	284.91	189
	0.1	655	572	390	278	174
	0.15	628	537	360	256	169
	0.2	588	479	326	241	163
	0.25	555	453	314	233	159
	0.3	528	433	297	223	152
	0.35	498	413	290	218	150
	0.4	468	392	275	212	145
	0.45	442	379	267	202	141
	0.5	420	357	256	196	137
	0.55	376	346	246	189	132
	0.6	391	333	238	181	128
1	0.05	598	428	276	182	109
	0.1	550	410	263	172	107
	0.15	506	376	246	161	100
	0.2	478	351	231	154	95
	0.25	454	330	218	152	94
	0.3	432	315	207	143	90
	0.35	419	304	200	138	90
	0.4	408	293	195	134	87
	0.45	396	287	187	130	87
	0.5	383	275	182	126	85
	0.55	377	269	180	120	85
	0.6	356	261	176	119	84
0.1	0.05	374	264	182	129	74
	0.1	362	238	167	118	66
	0.15	345	226	159	111	63
	0.2	345	222	153	106	62
	0.25	339	219	149	105	60
	0.3	332	213	144	102	60
	0.35	321	207	138	99	58
	0.4	308	200	133	97	57
	0.45	300	194	129	95	57
	0.5	289	187	124	92	57
	0.55	281	181	120	91	55
	0.6	274	176	118	88	56

0.01	0.05	302	204	133	72	42
	0.1	265	196	126	71	40
	0.15	237	177	116	67	38
	0.2	218	158	106	62	36
	0.25	204	148	99	60	34
	0.3	190	135	90	56	33
	0.35	180	126	86	52	32
	0.4	172	77	80	48	31
	0.45	165	73	77	46	31
	0.5	156	70	73	44	30
	0.55	149	70	70	41	29
	0.6	143	67	67	40	29
0.001	0.05	171	108	77	49	33
	0.1	161	96	65	43	30
	0.15	146	88	59	38	27
	0.2	133	80	53	35	25
	0.25	122	75	49	33	23
	0.3	113	68	45	31	22
	0.35	108	64	43	30	20
	0.4	101	61	40	28	19
	0.45	99	59	39	27	19
	0.5	92	55	36	26	18
	0.55	88	53	35	25	18
	0.6	84	50	34	25	18

H-7: Flow stress data used for processing map of Ti-6Al-1V-3Fe

Strain rate (s^{-1})	Strain	Temperature (°C)				
		750	800	850	900	950
10	0.05	558	406	303	230	152
	0.1	569	430	293	214	146
	0.15	535	411	277	206	144
	0.2	801	368	263	191	142
	0.25	477	358	249	186	140
	0.3	463	337	239	179	136
	0.35	448	323	230	173	132
	0.4	428	308	222	167	128
	0.45	415	300	213	161	126
	0.5	389	283	206	156	121
	0.55	378	278	200	151	117
	0.6	363	265	193	147	110

1	0.05	439	339	259	146	93
	0.1	462	309	243	140	92
	0.15	432	286	225	130	90
	0.2	403	274	213	124	88
	0.25	381	263	200	120	86
	0.3	361	256	191	115	86
	0.35	344	249	184	108	81
	0.4	329	242	182	105	79
	0.45	319	238	175	106	81
	0.5	309	235	172	101	78
	0.55	300	232	169	101	77
	0.6	290	228	166	99	77
0.1	0.05	335	235	151	90	60
	0.1	318	218	139	82	56
	0.15	304	207	134	78	54
	0.2	298	202	132	75	54
	0.25	289	198	133	74	53
	0.3	279	197	132	73	53
	0.35	268	187	129	71	52
	0.4	259	180	127	69	51
	0.45	252	175	127	68	51
	0.5	244	167	121	67	52
	0.55	237	163	117	65	50
	0.6	231	159	114	64	50
0.01	0.05	216	151	100	55	30
	0.1	208	145	91	51	31
	0.15	191	133	85	45	29
	0.2	175	122	81	42	29
	0.25	163	113	76	39	87
	0.3	151	105	71	38	28
	0.35	142	98	68	36	27
	0.4	133	93	64	36	25
	0.45	127	89	62	36	26
	0.5	120	83	58	35	25
	0.55	115	79	56	34	26
	0.6	111	74	54	33	25
0.001	0.05	127	76	48	32	8
	0.1	116	67	43	29	18
	0.15	105	61	39	27	17
	0.2	97	56	35	25	17
	0.25	91	54	32	24	16
	0.3	86	50	30	24	16
	0.35	80	47	30	22	15
	0.4	76	44	28	21	15
	0.45	72	42	27	20	15
	0.5	67	39	26	20	27
	0.55	64	38	25	19	23
	0.6	61	35	24	19	18

H-8: Strain versus time profile for Ti-6Al-1V-3Fe alloy deformed at 850°C/0.01s^{-1} showing increase in strain rates at low strain (~0.02).

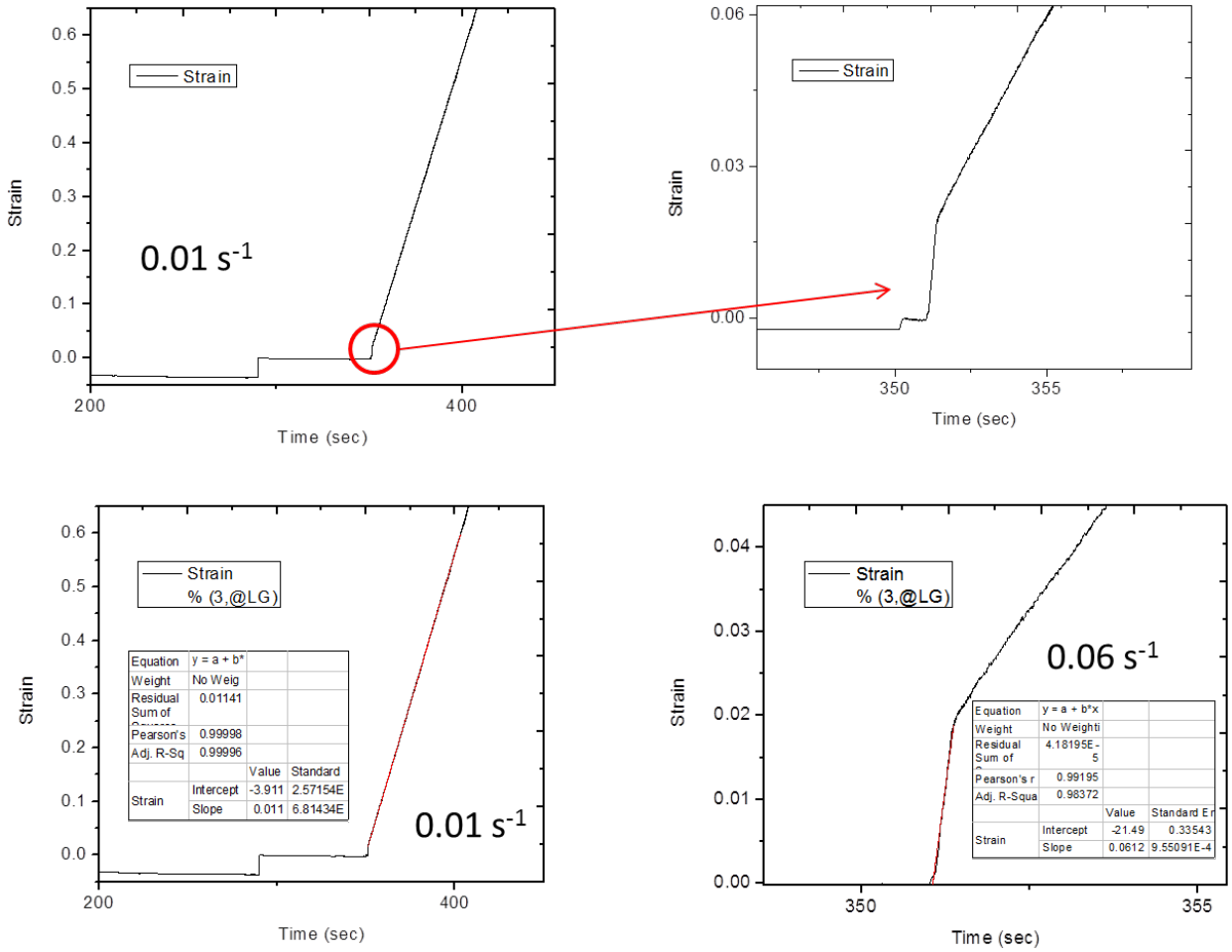

Appendix I: Supplementary results from corrosion testing

I-1: Tables for EDX spectra shown in Figure 5.3

Elements	Alloys			
	Ti-6Al-3V-1Fe	Ti-6Al-1V-3Fe	Ti-6Al-4Fe	Ti-4.5Al-2V-2Fe
O (wt%)	24.9	59.3	67.1	30.7
Al (wt%)	4.0	1.5	2.4	2.8
S (wt%)	0.9	14.3	18.3	1.7
Ti (wt%)	67.5	24.4	11.7	61.8
V (wt%)	1.9	-	0.5	1.4
Fe (wt%)	0.7	0.52	-	1.6

I-2: Tables for EDX spectra shown in Figure 5.3

Elements	Alloys			
	Ti-6Al-3V-1Fe	Ti-6Al-4Fe	Ti-4.5Al-2V-2Fe	Ti-4.5Al-1V-3Fe
O (wt%)	-	31.8	-	12.2
Al (wt%)	5.5	4.5	4.0	3.2
S (wt%)	-	0.9	18.3	82.0
Ti (wt%)	90.7	6.8	91.9	-
V (wt%)	2.9	-	1.9	-
Fe (wt%)	0.9	2.0	-	2.5
K (wt%)	-	-	2.3	-

I-3: SEM images (lower magnification of Figure 5.2) showing corrosion products on alloys immersed in sulphuric acid solution prior to cleaning

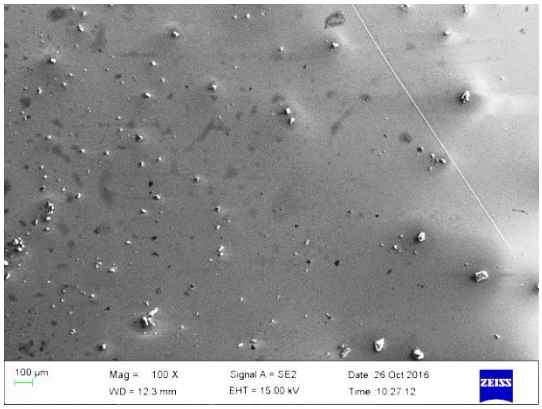

a) Ti-6Al-4V

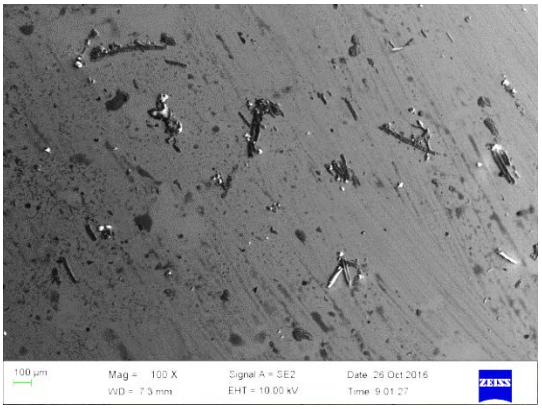

b)Ti-6Al-3V-1Fe

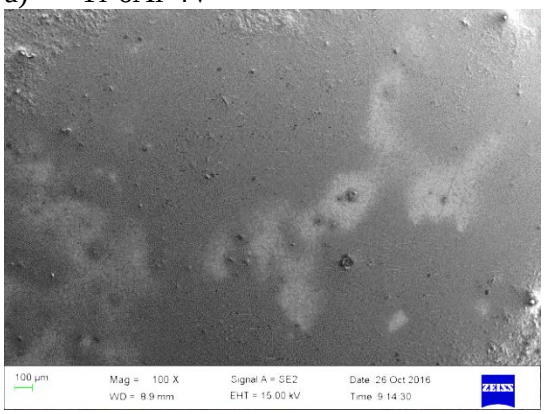

c) Ti-6Al-1V-3Fe

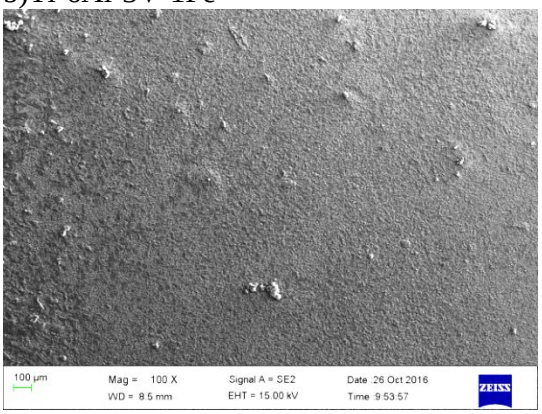

d) Ti-6Al-4Fe

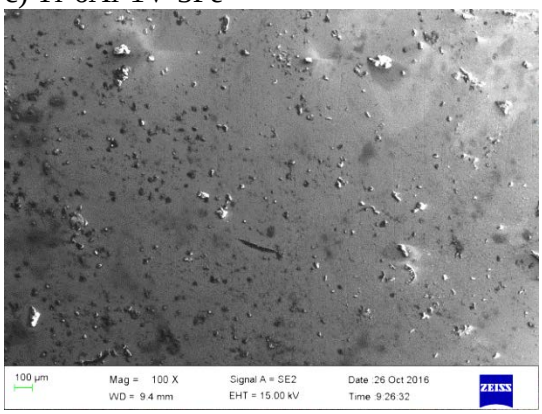

e) Ti-4.5Al-1V-3Fe

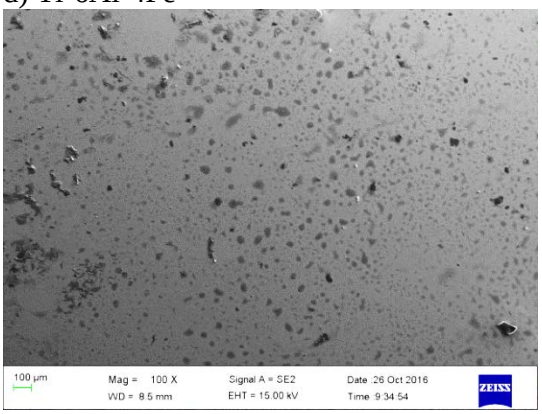

f) Ti-4.5Al-2V-2Fe

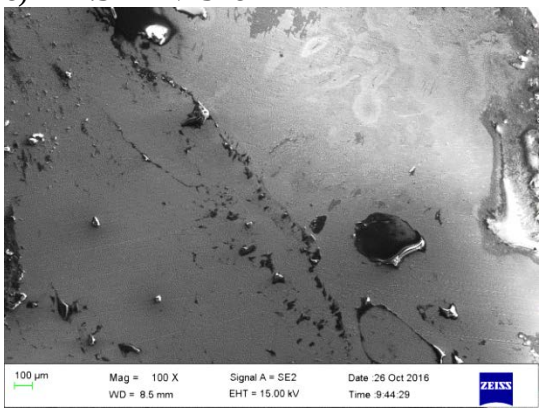

g) Ti-4.5Al-1V-3Fe

I-4: EDX spectra showing the selective dissolution of the beta phase in the sulphuric acid solution

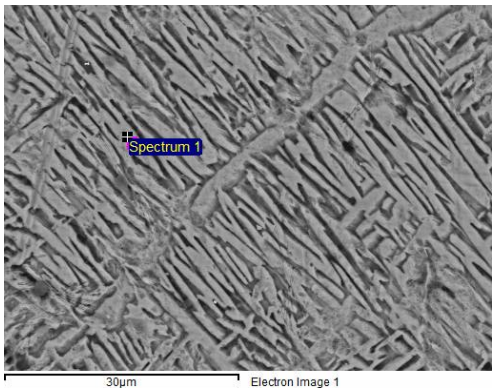

Element	Weight%	Atomic%
Al K	5.89	10
Ti K	92.8	88.9
Fe K	1.4	1.2
Totals	100.00	

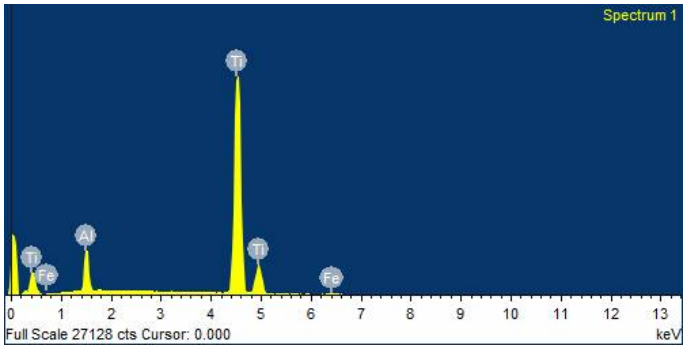

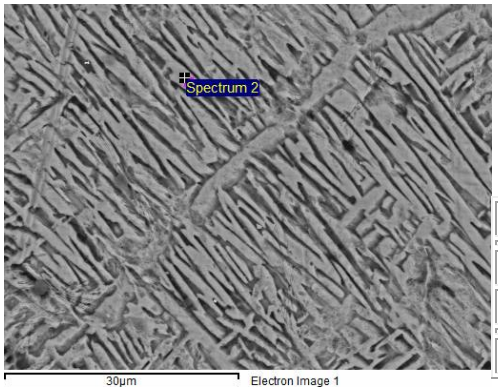

Element	Weight%	Atomic%
Al K	5.83	9.9
Ti K	94.2	90.1
Totals	100.00	

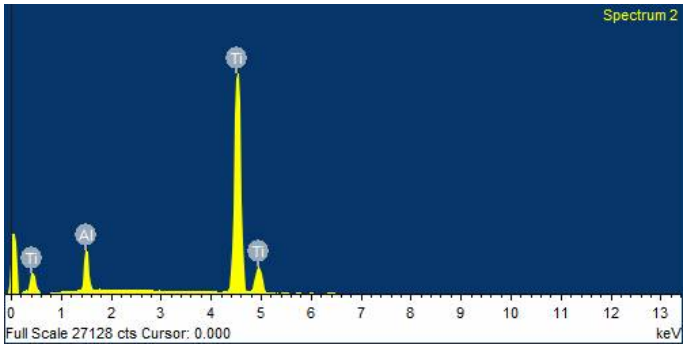

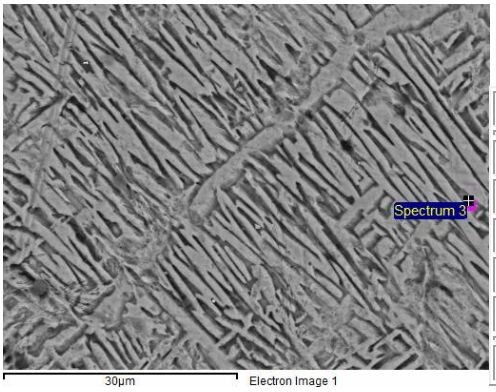

Element	Weight%	Atomic%
O K	12.4	29.2
Al K	3.94	5.5
S K	0.6	0.7
Ti K	79.2	62.1
Fe K	3.8	2.6
Totals	100.00	

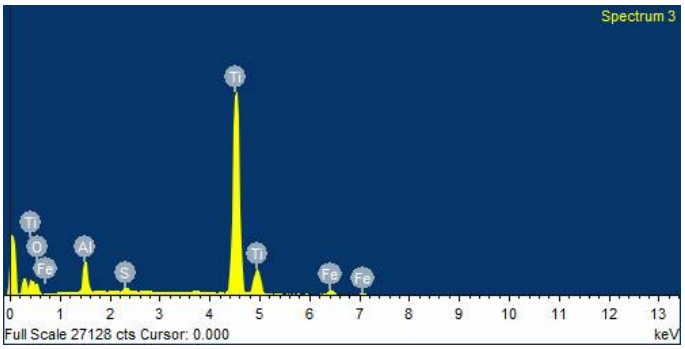

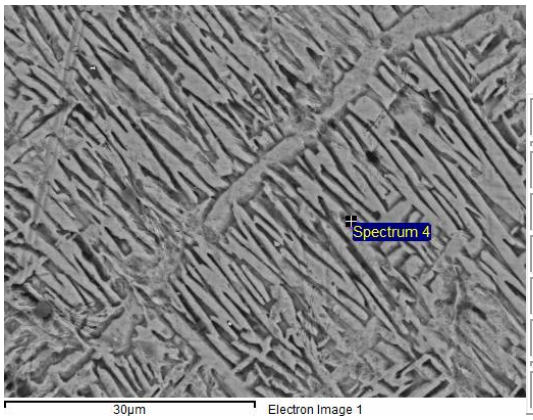

Element	Weight%	Atomic%
O K	11.2	26.7
Al K	4.3	6.1
S K	0.3	0.3
Ti K	82.1	65.5
Fe K	2.1	1.5
Totals	100.00	

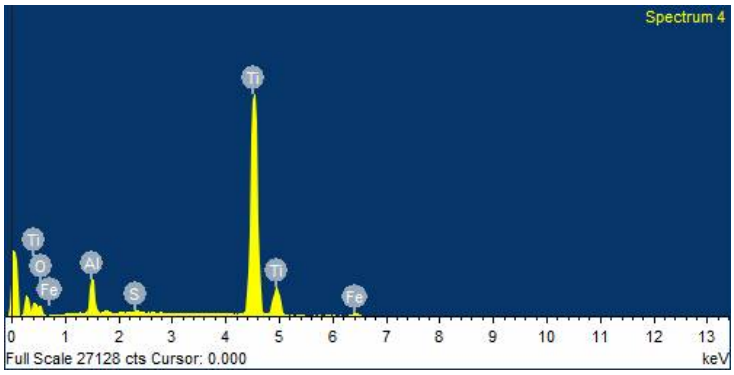

Appendix J: Awards, presentations and publications

J-1: Awards

- First Prize, Student Oral presentation, 3rd AMSEN Workshop, Johannesburg (2015)
- RISE-AMSEN representative at the Next Einstein Forum Global Gathering, Dakar Senegal (2016)
- 3rdplace, Faculty of Engineering and the Built Poster Presentation, University of the Witwatersrand Cross-Faculty Symposium (2016)
- Best poster presentation, DST-NRF Centre of Excellence in Strong Materials Annual Student Presentation, University of the Witwatersrand (2016)
- Science Today candidate for South Africa's Best Postgraduate Writing (2016)
- Winner heat 1, FAMELAB South Africa Science Forum, Pretoria (2016)
- Best poster presentation, DST-NRF Centre of Excellence in Strong Materials Annual Student Presentation, University of the Witwatersrand (2017)
- National finalist, South Africa, FAMELAB Science Communication Competition (2017)

J-2: Oral and Poster Presentations

- Africa Materials Research Society Conference, Accra, Ghana, 2015 (oral presentation)
- University of the Witwatersrand's 7th Cross-faculty Symposium, 2016 (poster presentation)
- Centre of Excellence in Strong Materials Annual Students Presentations, 2015-2018 (poster presentation)
- School of Chemical and Metallurgical Engineering Lunch Time Seminar, 2017 (oral Presentation)
- International ESAFORM conference on Materials Forming, Dublin, Ireland, 2017 (oral presentation)
- Physical Metallurgy Gordon Research Conference, Maine, United States, 2017 (poster presentation)
- University of the Witwatersrand's 8th Cross-Faculty Symposium 2017 (poster presentation)

J-3: Full journal article publications

Received: 22 June 2017 | Accepted: 20 November 2017
DOI: 10.1002/maco.201709709

ARTICLE

Materials and Corrosion

Corrosion behaviour of Ti-Al-*x*V-*y*Fe experimental alloys in 3.5 wt% NaCl and 3.5 M H_2SO_4

Michael O. Bodunrin[1,2,3,4] | **Lesley H. Chown**[1,2,3] | **Josias W. van der Merwe**[1,2,3] | **Kenneth K. Alaneme**[3,4]

[1] School of Chemical and Metallurgical Engineering, University of the Witwatersrand, Private Bag 3, WITS, 2050 Johannesburg, South Africa

[2] DST-NRF Centre of Excellence in Strong Materials, University of the Witwatersrand, Private Bag 3, WITS, 2050 Johannesburg, South Africa

[3] African Materials Science and Engineering Network (AMSEN), Private Bag 3, WITS, 2050 Johannesburg, South Africa

[4] Department of Metallurgical and Materials Engineering, Federal University of Technology Akure, P.M.B. 704, Ondo State, Nigeria

Correspondence
Michael O. Bodunrin, School of Chemical and Metallurgical Engineering, and DST-NRF Centre of Excellence in Strong Materials; both University of the Witwatersrand, Private Bag 3, WITS, 2050 Johannesburg, South Africa; Department of Metallurgical and Materials Engineering, Federal University of Technology Akure, P.M.B. 704, Ondo State, Nigeria.
Email: michael.bodunrin@students.wits.ac.za; mic.tosin@live.com

Funding information
African Materials Science and Engineering Network (A Carnegie- IAS RISE Network); DST-NRF Centre of Excellence in Strong Materials

The corrosion behaviour of Ti-6Al-*x*V-*y*Fe (where $x + y = 4$; $x = 0$–3; and $y = 1$–4) experimental alloys in comparison with commercial Ti-6Al-4V alloy was investigated in sodium chloride and sulphuric acid solutions. Iron, a less expensive beta stabilising element was substituted for vanadium in the newly developed alloys in order to assess the influence of iron addition on the corrosion performance of the alloys. Electrochemical parameters were obtained using open circuit potential and potentiodynamic polarisation measurements. The results show that partial replacement of vanadium with 2–3 wt% iron yielded excellent corrosion resistance in 3.5 wt% sodium chloride. The experimental alloys have better corrosion resistance than the commercial Ti-6Al-4V alloy in 3.5 M sulphuric acid.

KEYWORDS
low-cost titanium, open circuit potential, passivation, polarisation

1 | INTRODUCTION

Titanium alloys are very important engineering materials due to their attractive properties such as high specific strength, good corrosion resistance in most industrial environments and excellent biocompatibility.[1] These properties have made the alloys suitable for use in a wide spectrum of applications including the aerospace industry where stringent requirements have to be met and other land-based applications such as marine, sports, chemical, automotive, jewelleries and biomedical industries.[1,2]

Despite the potentials of titanium alloys, the high cost of the alloys has limited their use to applications where they are

 © 2018 WILEY-VCH Verlag GmbH & Co. KGaA, Weinheim

the only choice that satisfies the intended service requirements.[3,4] High cost of titanium alloys has been ascribed to the difficulty in beneficiating titanium from its ores and the complex processing routes that are adopted for making finished products.[5] In the last two decades, the development of low cost titanium alloys for widespread applicability remains the main research thrust in titanium alloys.[5] The low-cost titanium alloys are achieved by replacing expensive alloying elements in titanium alloys with cheaper ones[6] that fulfill similar functions. In addition, processing conditions are optimised for control of mechanical properties and cost reduction.[6,7]

Titanium alloys are broadly classified into α, α + β and β alloys depending on the type and amount of alloying elements present in the alloys.[8] In previous studies on low cost titanium alloys, aluminium was replaced with oxygen and nitrogen to stabilise the α phase in Ti-Fe-O-N α + β alloys,[9,10] Fujii and Takahashi[6] replaced vanadium, an expensive beta stabiliser with iron in Ti-Al-Fe α + β alloys and Zhu et al.[11] replaced vanadium with chromium and manganese in Ti-Al-Cr-Mn α + β alloys. It is worth mentioning that past research efforts have focussed more on developing α + β alloys due to the balanced mechanical properties obtained in this class of titanium alloy. Moreover, Ti-6Al-4V the most utilised titanium alloy belongs to the α + β class and its consumption accounted for more than 70% of the total titanium market.[12] Researchers often compare their newly developed experimental alloys with this commercial alloy.

In this research, Ti-Al-*x*V-*y*Fe α + β alloys were developed by partially substituting vanadium with iron in order to reduce the cost of stabilising the β phase. Unlike in previous research[6,11,13] where vanadium was fully replaced with other beta stabilisers such as iron, chromium and manganese, we have retained some vanadium in our newly developed alloys in order to prevent the possibility of forming TiFe, the equilibrium phase that is formed when iron is added to titanium.[6,14] TiFe has been reported to have deleterious effect on the mechanical and corrosion properties of titanium alloys.[4,6,9]

Previous researchers have reported that alloying elements have an influence on the corrosion performance of titanium alloys in different corrosion media.[15–19] Metikoš-Huković and Kwokal[16] reported that niobium improves the corrosion resistance of titanium alloy in physiological solution, Bălţatu et al.[17] reported that tantalum improved the corrosion resistance of new TiMoZrTa alloys in acidified Ringer's solution due to the formation of a more compact oxide layer, Pimenova and Starr[20] reported that high aluminium content reduced the corrosion resistance of titanium alloys in Hank's solution, Lu et al.[21] reported that iron addition improved the corrosion behaviour of Ti-Al-Fe alloys in simulated body fluid.

Based on the different observations reported in previous studies, it becomes imperative to investigate the corrosion behaviour of the newly developed Ti-Al-*x*V-*y*Fe experimental alloys in different corrosive environments and to evaluate the influence of substituting iron for vanadium on the corrosion behaviour of the alloys. The choice of sulphuric acid and sodium chloride solutions used as corrosive environments in this study is informed by the fact that components that are made from titanium alloys are exposed to these environments in service especially in the chemical and petrochemical industries.[1] For example, sulphuric acid is used for acid pickling of titanium alloys. Moreover, sulphuric acid represents strong reducing acid in which titanium alloys are susceptible to corrosion attack. The sodium chloride solution used in this study represents the typical marine environment where components made from titanium alloys are used.

2 | MATERIALS AND METHODS

2.1 | Materials

The Ti-6Al-*x*V-*y*Fe experimental alloys with compositions shown in Table 1 were developed from titanium, aluminium, vanadium and iron powders. The powders were compacted and melted into buttons under argon environment using a vacuum arc furnace. The melting was done twice and the alloys were then solution treated at 790 °C for 4 h followed by air cooling in order to homogenise the alloys.

2.2 | Microstructural characterisation

The surface of the alloys used for microstructural studies was prepared following standard metallographic procedures and etched in Kroll's reagent.[22] The microstructure of the alloys was examined using an optical microscope and the surface of the alloys after exposure in corrosive media was analysed using scanning electron microscope operated in secondary electron imaging (SEI) mode.

2.3 | Electrochemical measurements

The samples for electrochemical corrosion testing were cut, cold mounted in resins and polished until a mirror like surface finish was obtained. Thereafter, the samples were rinsed in distilled water and dried in air. The surface area of the samples exposed to the corrosive solutions was 0.25 cm^2. A commercial grade Ti-6Al-4V alloy was also prepared and tested for comparison. A conventional three-electrode electrochemical cell connected to an AUTOLAB 302N potentiostat/galvanostat was used for the electrochemical testing. A graphite rod was used as the counter electrode and a silver–silver chloride as reference electrode. Open circuit

TABLE 1 Electrochemical parameters obtained for alloys immersed in 3.5 M sulphuric acid solution at 25 °C

Alloys	Equivalent weight	E_{corr} (V vs. Ag/AgCl)	OCP_{1200s} (V vs. Ag/AgCl)	I_{corr} (μA/cm^2)	Rp	Corr rate (mm/yr)
Ti-6A1-4V	11.82	−0.562	−0.578	182	142	1.59
Ti-6A1-3V-IFe	11.81	−0.570	−0.658	76	33S	0.67
Ti-6A1-2V-2Fe	11.83	−0.528	−0.603	168	154	1.47
T1-6AI-IV-3Fe	11.83	−0.581	−0.571	133	195	1.16
Ti-6Al-4Fe	11.8	−0.579	−0.546	167	155	1.46

potential (OCP) and potentiodynamic polarisation tests were performed on the samples in 3.5 M sulphuric acid, 3.5 wt% sodium chloride and mixed 3.5 M sulphuric acid + 1.75 wt% sodium chloride solutions. The mixed solution was prepared in order to simulate corrosive environments where multiple anions interact with the materials. All the solutions were prepared using analytical grade chemicals. The OCP measurements were taken for the duration of 3600 s in both sulphuric acid and sodium chloride environments while for 1200 s in the mixed 3.5 M sulphuric acid + 1.75 wt% sodium chloride solution. In the 3.5 M sulphuric acid and mixed 3.5 M sulphuric acid + 1.75 wt% sodium chloride solutions, linear potentiodynamic scans were performed on the samples from −0.5 to 2.5 V at a scan rate of 0.2 mV/s whereas the cyclic potentiodynamic scan was carried out in sodium chloride from −0.5 to 2.5 V at a scan rate of 2 mV/s to evaluate the susceptibility of the alloys to pitting corrosion in chloride solution. The wait time between the OCP and polarisation scans was 5 s. The corrosion current density (I_{corr}) and corrosion rate was determined by polarisation technique[23,24] following ASTM standard G59-97.

3 | RESULTS

3.1 | Microstructural characterisation

The microstructures of the commercial Ti-6Al-4V and experimental Ti-6Al-*x*V-*y*Fe alloys are presented in Figure 1. It can be seen that the commercial alloy consisted of elongated and equiaxed α-phase and a network of intergranular β. The experimental alloys on the other hand possess basketweave Widmanstätten α embedded within large prior β grains.

3.2 | Sulphuric acid environment

It is widely reported that the excellent corrosion resistance exhibited by titanium and its alloys in most corrosive environments has been largely attributed to the passive TiO_2 film formed on the surface of the metal.[20] However, this passive film is dissolved in strong reducing acids like sulphuric and hydrochloric solutions.[25,26] Recently, Magoda et al.[26] investigated the effect of chloride and sulphate ions on the corrosion behaviour of titanium alloys. It was reported that sulphate ions have a more rapid dissolution effect on the TiO_2 formed on the surface of titanium in comparison with chloride ions.[27,28] Therefore, the stability of the native oxide film formed on the experimental alloys in comparison with the commercial Ti-6Al-4V alloy in concentrated 3.5 M sulphuric acid was evaluated by tracing the OCP for 3600 s. Figure 2 shows the OCP plots of the commercial Ti-6Al-4V and experimental Ti-Al-*x*V-*y*Fe alloys in 3.5 M sulphuric acid solutions. It is observed that the OCP of the commercial Ti-6Al-4V alloy increased to more noble values with increasing exposure time which indicates thickening of the TiO_2 oxide film.[29] However, in the experimental alloys where vanadium is partially and fully substituted with iron, the OCP decreased towards the more negative values. The OCP of the experimental Ti-6Al-3V-1Fe alloy showed a decreasing trend throughout the period of exposure despite having the highest OCP among the experimental alloys. As the iron content in the experimental alloy increased from 2–3% by mass, the OCPs of the working electrodes assumed a cathodic value and remain quite stable in the cathodic region between 1200 and 3600 s of exposure. When vanadium is totally replaced with iron in Ti-6Al-4Fe experimental alloy, a slight increase in the OCP was first observed for about 100 s and later decreased rapidly indicating the dissolution of the oxide film. The OCP became stable at about 800 s of exposure in the electrolyte. The SEM images of both commercial and experimental alloys taken after OCP measurement for 3600 s are presented in Figure 3(a–e). The SEM images were taken without cleaning the samples. It can be seen that the commercial Ti-6Al-4V alloy has a more stable film with no visible cracks in comparison with the other experimental alloys. This is consistent with the behaviour of the OCP curves in Figure 2.

It is evident from the SEM images (Figure 3) that the native oxide film on the experimental alloy is less protective than in the commercial alloys. The severity of corrosion attack increased with increasing iron content in the experimental alloys. This is most apparent in the Ti-6Al-4Fe alloy containing only iron as the only beta stabilising element. More corrosion product is seen on the surface of the exposed Ti-6Al-4Fe alloy (Figure 3e) in comparison with the

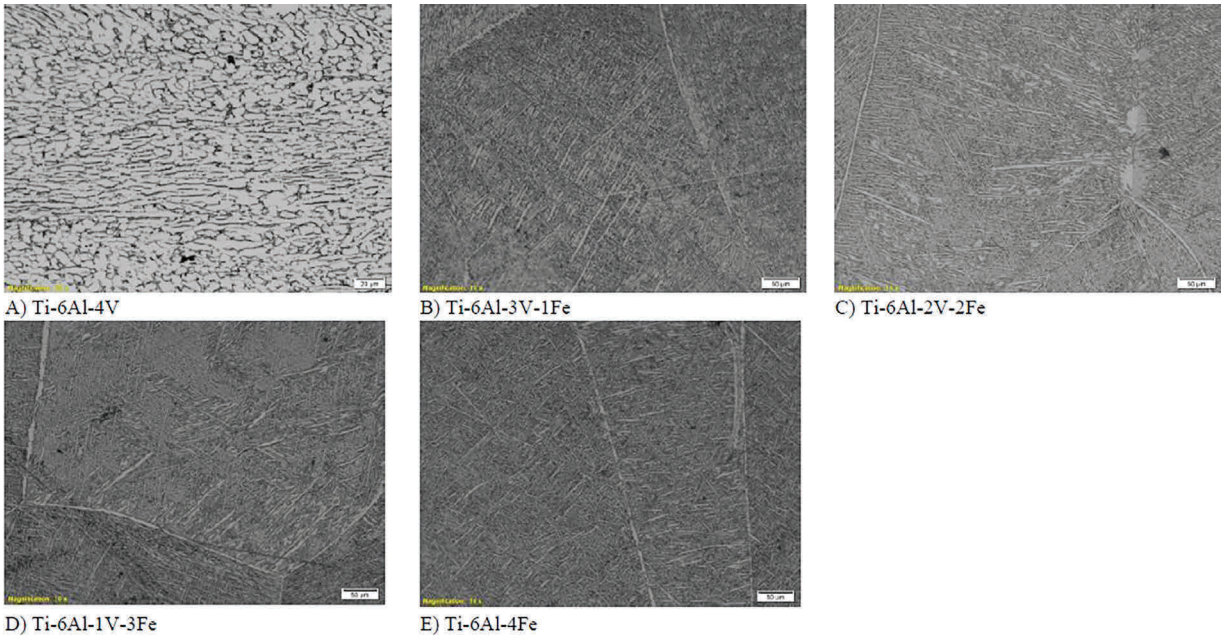

FIGURE 1 Microstructure of commercial Ti-6Al-4V and Ti-6Al-*x*V-*y*Fe experimental alloys [Color figure can be viewed at wileyonlinelibrary.com]

other experimental alloys. From the SEM image (Figure 3f) obtained after cleaning the exposed Ti-6Al-4Fe alloy in distilled water and dried in air; it can be seen that selective corrosion attack occurred in the β-Ti phase of the alloy where the concentration of iron is higher. This is corroborated by the EDS spectra (Figure 4a,b) obtained from point analysis of the phases present in the Ti-6Al-4Fe alloy. The un-corroded α-Ti phase did not show iron peak because of the low solubility of iron in the α-Ti phase. However, iron peak is present in the corroded β-Ti phase. The presence of oxygen and sulphur peaks suggests that corrosion product is retained on the corroded β-Ti phase of the alloy after cleaning.

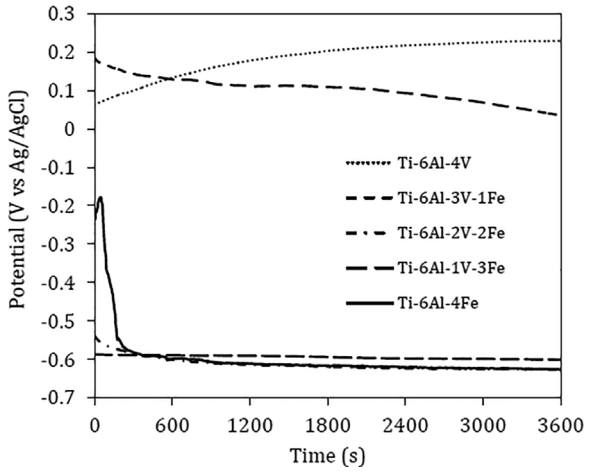

FIGURE 2 Variation of OCP measurement for Ti-6Al-4V and Ti-6Al-*x*V-*y*Fe in 3.5 M sulphuric acid at 25 °C

The stability and purity of the TiO_2 film formed on the surface of titanium alloys is influenced by the composition of the alloys.[30] It is well documented that oxides of alloying elements like aluminium and vanadium have been detected through advanced spectrometric analysis on the surface of titanium alloys.[31] Devilliers et al.[32] investigated the behaviour of titanium in sulphuric acid and reported that high purity titanium exhibited a more stable passive film than the one containing more impurities. Tomashov et al.[15] in another study reported that alloying elements such as aluminium, vanadium, molybdenum and vanadium diffuse into the lattice of the oxide film and cause modifications on the film. This modification can either be beneficial or deleterious to the corrosion resistance of the alloys. It is thought that iron modifies the oxide film hence promoting the dissolution of the film in sulphuric acid.

Figure 5 shows the linear polarisation curves of both commercial Ti-6Al-4V and the experimental Ti-6Al-*x*V-*y*Fe alloys obtained after 1200 s at open circuit potential. The OCP obtained at 1200 s prior to the linear polarisation did not agree with the OCP presented in Figure 2 because the measurements were taken separately and the OCP measurements are not easily reproducible especially for the commercial Ti-6Al-4V and experimental Ti-6Al-3V-1Fe alloys. Devilliers et al.[32] reported that OCP for freshly polished titanium alloys immersed in corrosive media takes up to 24 h to be reproducible.

The polarisation curves revealed that the corrosion behaviour of the alloy is sensitive to the beta stabilising elements present in the alloys. It can be observed that the

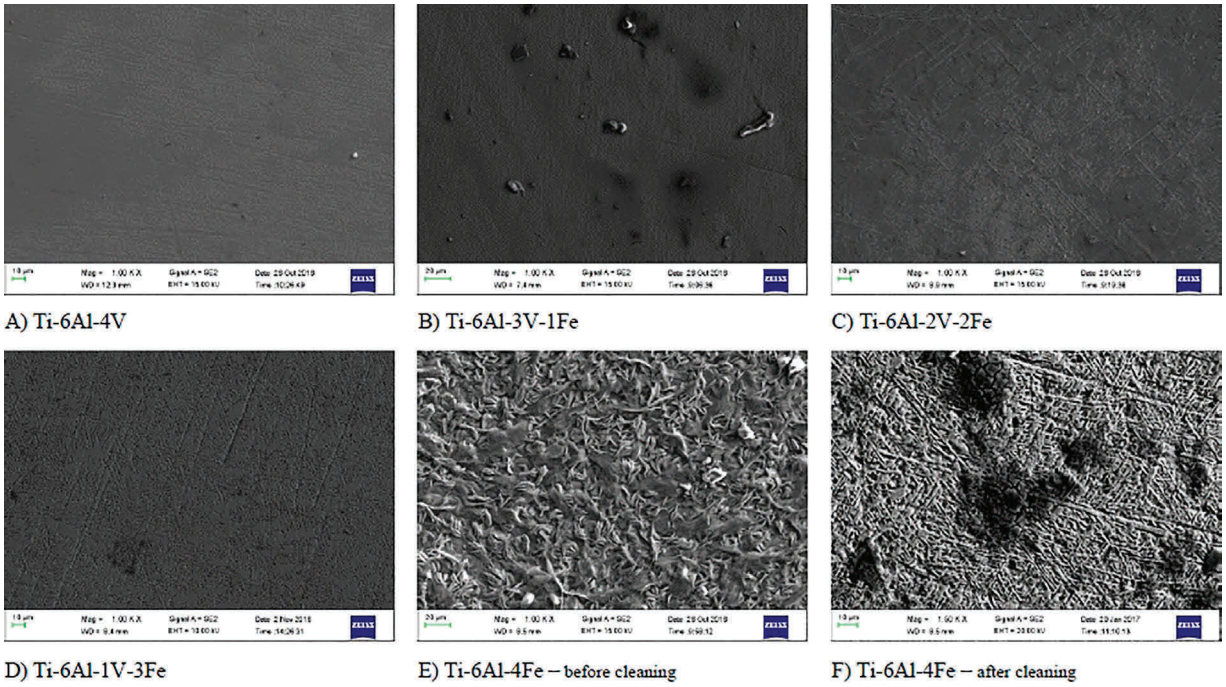

FIGURE 3 Secondary electron images of exposed alloys in sulphuric acid solution at OCP for 3600 s [Color figure can be viewed at wileyonlinelibrary.com]

corrosion behaviour of the commercial Ti-6Al-4V and the experimental Ti-6Al-4Fe alloys containing one beta stabilising element are comparable while the experimental alloys containing both vanadium and iron as beta stabilisers followed a similar trend. All the alloys displayed an active-to-passive transition behaviour. The critical current densities of the experimental alloys containing iron and vanadium as beta stabilising elements are much lower than the alloys having either iron or vanadium as beta stabilising element. The lowest critical current density is observed in the Ti-6Al-1V-3Fe alloy. The passivation current density (I_p) and break down potential (E_b) of the experimental alloys containing both iron and vanadium are ~0.00001 A/ cm^{-2} and 1.8 V, respectively. Conversely, Ti-6Al-4V and Ti-6Al-4Fe did not show a break down potential at 1.8 V. This suggests that these alloys would have a more stable passive film grown in the anodic region than the experimental alloys. Unlike in the commercial Ti-6Al-4V alloy, it can be seen that

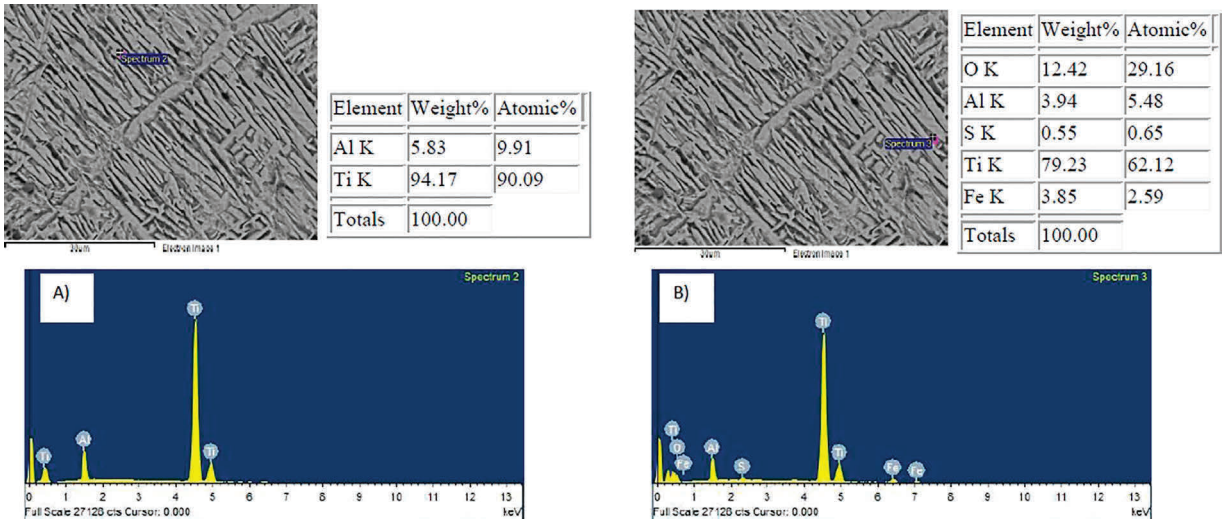

FIGURE 4 (A) EDX spot analysis on the un-corroded α-Ti phase without iron in Ti-6Al-4Fe alloy. (B) EDX spot analysis on the corroded β-Ti phase containing iron in Ti-6Al-4Fe alloy [Color figure can be viewed at wileyonlinelibrary.com]

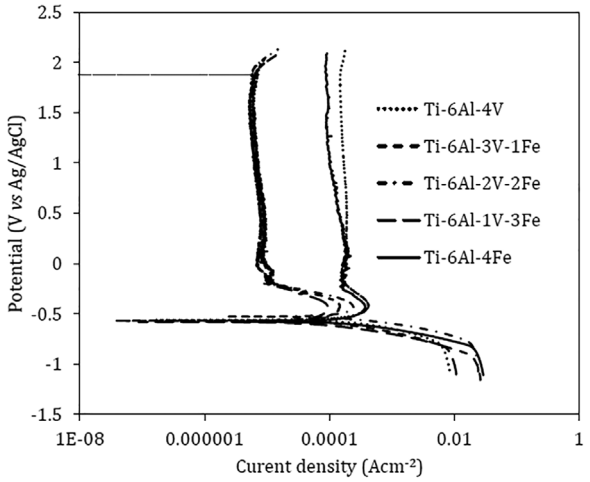

FIGURE 5 Polarisation curves for alloys immersed in 3.5 M sulphuric acid solution at 25 °C

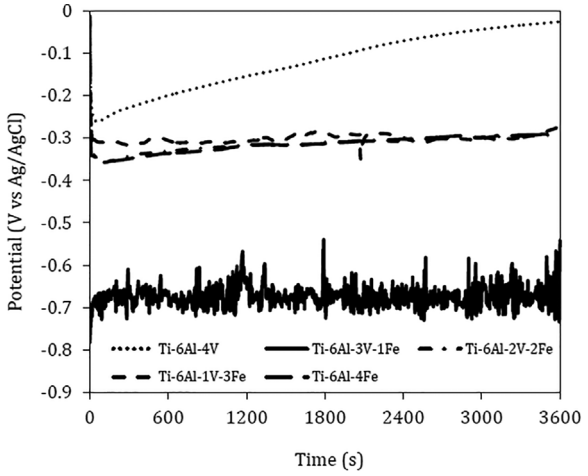

FIGURE 6 Variation of OCP measurement for Ti-6Al-4V and Ti-6Al-*x*V-*y*Fe in 3.5 wt% NaCl at 25 °C

the anodic passive film of the experimental Ti-6Al-4Fe alloy showed transient currents immediately after the active nose indicating the breaking and rebuilding of the passive film. Also the passivation current of the Ti-6Al-4Fe alloy is lower than the commercial alloy at potentials above 0.4 V.

The corrosion parameters obtained from the polarisation resistance technique are presented in Table 1 and it can be seen that the corrosion potential for all the alloys are comparable under the test conditions but the corrosion current densities and corrosion rates differ. In general, the commercial Ti-6Al-4V alloy exhibited higher corrosion current densities and corrosion rates in comparison with the experimental alloys. Of the experimental alloys, Ti-6Al-2V-2Fe and Ti-6Al-4Fe alloys have similar corrosion rates while Ti-6Al-3V-1Fe showed the lowest corrosion rate. The corrosion rate obtained for the commercial Ti-6Al-4V alloy was lower than the corrosion rate (140 mpy ~ 3.6 mm/yr) reported by Magoda et al.[26] in 3.5 M sulphuric acid. The difference in corrosion rates can be attributed to the different contents of impurities present in the alloys[33] and the microstructure.

3.3 | Sodium chloride environment

The variation of OCP with exposure time for different titanium based alloys exposed in 3.5 wt% sodium chloride is shown in Figure 6, the OCP of the commercial alloy increased towards the anodic values with increasing exposure time. However, experimental alloys containing iron except for Ti-6Al-3V-1Fe showed a slight increase in OCP with increasing exposure time. The higher OCP values of the commercial alloy suggest that the oxide film that is formed on the surface of the alloy is more stable than the oxide film formed on the experimental alloys. The last OCP values of the experimental alloys containing more than 1 wt% iron are comparable. When 1 wt% iron was substituted for vanadium in Ti-6Al-3V-1Fe alloy, the lowest OCP value was recorded and it fluctuated throughout the exposure time. This fluctuation can be attributed to the dissolution and re-passivation of the native TiO_2 film formed on the alloy.

The cyclic polarisation curves for both commercial Ti-6Al-4V and experimental Ti-6Al-*x*V-*y*Fe alloys in 3.5 wt% sodium chloride are presented in Figure 7. It can be observed that all the alloys did not show the active nose seen in sulphuric acid solution. This indicates that the passive film was formed spontaneously during anodic polarisation in 3.5 wt% sodium chloride solution.[34,35] A clearly defined Tafel slope in the anodic region was not seen in all the alloys. This behaviour is similar to the reports of Dai et al.[36] on the corrosion behaviour of Ti-6Al-4V alloy in 3.5 wt% sodium

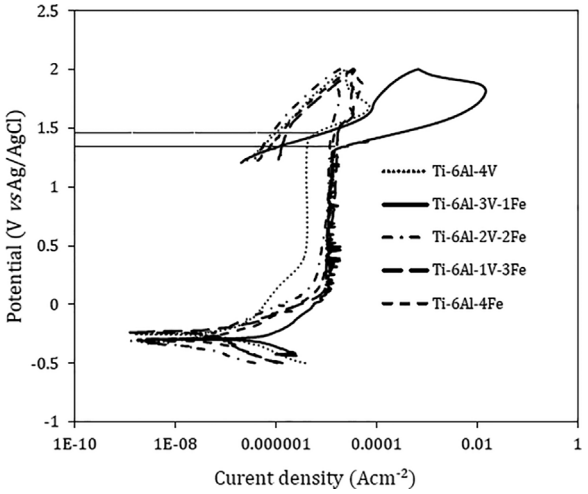

FIGURE 7 Polarisation curves for alloys immersed in 3.5 wt% sodium chloride solution at 25 °C

chloride. The reverse scan of all the alloys moved in anticlockwise indicating resistance to pitting corrosion. Yu and Scully[37] reported that titanium alloys are resistant to pitting corrosion in aerated chloride environments. In their study, they found that Ti-6Al-4V exhibited stable pitting at anodic potentials of 5.9 V_{SCE} (~5.5 $V_{Ag/AgCl}$) in HCl at 37° C. Seah et al.[38] also reported high pitting resistance in sintered Ti-6Al-4V alloy polarised in dilute sodium chloride solution. The passivation currents for all the experimental alloys containing iron were comparable, but higher than that of the commercial Ti-6Al-4V alloy. The breakdown potential of Ti-6Al-3V-1Fe is lower in comparison to the commercial and other experimental alloys. With increasing iron content above 1 wt% in the experimental alloys, an increase in current density observed in the transpassive region of the Ti-6Al-3V-1Fe and Ti-6Al-4V alloys is suppressed. The corrosion parameters determined from the polarisation curves are presented in Table 2, it can be seen that the E_{corr} values of the alloys are comparable, however, the corrosion current density and corrosion rates differ slightly. The highest corrosion rate and the largest transpassive region is obeserved in Ti-6Al-3V-1Fe experimental alloy indicating its inferior corrosion resistance relative to other alloys in this environment. There are traces of transient currents in the passive region of the alloy which suggests that the anodic passive film formed in this region was unstable.[39] The other experimental alloys have corrosion rates that are comparable to the commercial alloy. The polarisation results are in agreement with the OCP results presented in Figure 6.

3.4 | Sulphuric acid + sodium chloride environment

Ti-6Al-1V-3Fe alloy was selected and tested in the mixed solution of 3.5 M sulphuric acid and 1.75 wt% sodium chloride solution. This selection was based on the advantage of cost over the other experimental alloys as well as the corrosion performance of the alloys in the single 3.5 M sulphuric acid and 3.5 wt% sodium chloride solutions. The corrosion performance of the alloy was compared against the commercial Ti-6Al-4V and experimental Ti-6Al-4Fe alloys. The OCP trace for the alloys in mixed solutions of 3.5 M sulphuric acid and 1.75 wt% sodium chloride is presented in Figure 8. It can be seen that the OCP of the commercial alloy decreased towards the cathodic region indicating the dissolution of the passive film formed on the surface of the alloy. The OCP of the experimental Ti-6Al-1V-3Fe and Ti-6Al-4Fe alloys are comparable but the OCP of the Ti-6Al-4Fe fluctuated throughout the period of immersion. This fluctuation implies the dissolution and repassivation of the native oxide layer on the surface of the electrode. The last OCP values at 1200 s for both commercial and experimental alloys are comparable.

The polarisation curves of the selected alloys in the mixed solutions of sulphuric acid and sodium chloride are shown in Figure 9. It is observed that the commercial Ti-6Al-4V and experimental Ti-6Al-1V-3Fe followed similar trend in the mixed solution. The alloys showed similar E_{corr}, active to passive transition and a range of passivity prior to dissolution of the passive film in the transpassive region. The breakdown potential of the commercial alloy ($E_b = 2.1$ V) is slightly higher than the experimental Ti-6Al-41V-3Fe alloy ($E_b = 1.8$ V). Unlike the commercial Ti-6Al-4V alloy which exhibited reproducible polarisation curve, the polarisation curves of Ti-6Al-4Fe alloy are not easily reproducible. The E_{corr} value of experimental Ti-6Al-4Fe alloy is higher than that of the Ti-6Al-4V and Ti-6Al-1V-3Fe alloys. Experimental Ti-6Al-4Fe alloy did not show a distinct active to passive transition but the passivation current is higher than that of the Ti-6Al-4V and Ti-6Al-1V-3Fe alloys in the mixed solution. There are slight transient currents in the Ti-6Al-1V-3Fe alloy while it dominated in the experimental Ti-6Al-4Fe. This shows that Ti-6Al-4Fe alloy apparently suffered considerable breakdown and rebuilding of the oxide film. This observation is in agreement with the OCP curves presented in Figure 8. The corrosion parameters presented in Table 3 showed that the E_{corr} values obtained in the commercial Ti-6Al-4V and experimental Ti-6Al-1V-3Fe alloys are comparable. However, the corrosion current density and corrosion rate of the experimental alloy are higher.

4 | DISCUSSION

The corrosion resistance of titanium and its alloys in many corrosive environments has been attributed to the spontaneous formation of stable and adherent passive film on the

TABLE 2 Electrochemical parameters for alloys immersed in 3.5 wt% sodium chloride at 25 °C

Alloys	Equivalent weight	E_{corr} (V vs. Ag/AgCl)	I_{corr} (μA/cm^2)	Rp	Corr rate (mm/yr)
Ti-6A1-4V	11.82	−0.246	0.087	299029	o.ooos
Ti-6A1-3V-IFe	11.81	−0.297	0.450	58455	0.0039
Ti-6A1-2V-2Fe	11 S3	−0.324	0.026	1000000	0.0002
T1-6AI-IV-3Fe	11.83	−0.293	0.067	3S8993	0.0006
Ti-6Al-4Fe	11.8	−0.300	0.050	505245	0.0005

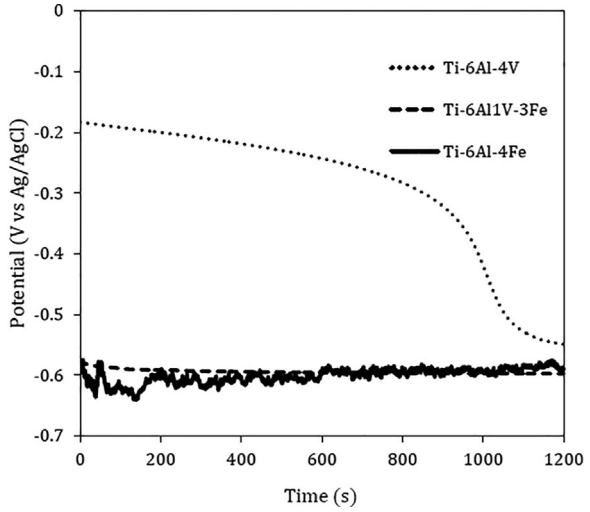

FIGURE 8 Variation of OCP measurement for Ti-6Al-4V and Ti-6Al-*x*V-*y*Fe in 3.5 M sulphuric acid + 1.75 wt% sodium chloride at 25 °C

surface of the metal.[34,40] The oxide film has two layers, the anatase (TiO) layer which is the inner layer close to the metal and the rutile (TiO_2) layer which is found in the outer layer of the exposed sample.[31,41] When titanium is alloyed with other metallic elements, findings have shown that the oxides of these elements are also found in small quantities in the predominant titanium oxide layers.[31,34] Hence, the stability of the oxide film can be influenced by alloy composition among other factors like concentration of corrosive solutions, temperature, immersion time and complexity of the anions in the solutions.[40] An OCP measurement was used to evaluate the passivity of the native oxide film formed on the surface of

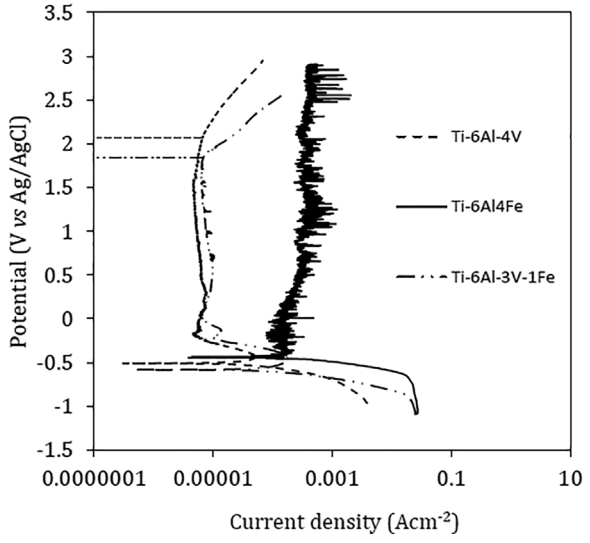

FIGURE 9 Corrosion plot for 3.5 M sulphuric acid + 1.75 wt% sodium chloride

both commercial and experimental alloys in different solutions. The commercial Ti-6Al-4V alloy showed an increase in OCP towards the nobler values in both 3.5 M sulphuric acid (Figure 2) and 3.5 wt% sodium chloride (Figure 6) solutions. This increase in OCP has been attributed to the growth of the native oxide layer on the alloy.[37] However, the experimental alloys showed different behaviours in 3.5 wt% sodium chloride and 3.5 M sulphuric acid solutions. The dissolution of the oxide film known as self activation[32,42] was seen in 3.5 M sulphuric acid while a gradual increase in the OCP was seen in 3.5 wt% sodium chloride solution. The commercial Ti-6Al-4V alloy which displayed increased OCP values in both solutions showed a decrease in OCP towards less noble values in mixed 3.5 M sulphuric acid + 1.75 wt% sodium chloride solution. The variations in the OCP behaviour of the alloys confirm that the alloys are sensitive to composition and corrosive solutions. Tomashov et al.[15] have reported that alloying elements like aluminium, vanadium, molybdenum, zirconium and niobium promoted the anodic dissolution of passive film in sulphuric acid by modifying the defectness and increasing the ionic conductivity of the film when the alloying elements enter the lattice of the film. Researchers have reported that aluminium promotes the dissolution of TiO_2 oxides when aluminium is added to titanium.[39,43] The anodic reaction governing the dissolution of titanium is well reported,[26,42,44] this reaction is presented as follows:

$$Ti \rightarrow Ti^{3+} + 3e^{-} \quad (1)$$

The dissolution of the native TiO_2 film formed on the experimental alloys in solutions containing sulphuric acid is in agreement with the previous research.[26,32] It was reported that the protective film formed on titanium alloy rapidly dissolves in concentrated reducing acids like sulphuric acid, oxalic acid and hydrochloric acid.[27,28,42,45]

It is interesting to note that the commercial alloy did not show any evidence of dissolution of the oxide layer when immersed in sulphuric acid at OCP for 3600 s. For the same exposure time at OCP, the experimental alloys containing iron showed dissolution in sulphuric acid. It is thought that the addition of iron to the experimental alloys enhanced the dissolution of the native oxide film. It was observed that the experimental alloys containing more than 1 wt% iron attained a stable OCP of $-600\ mV_{Ag/AgCl}$ in 3600 s. This value is close to the stable potential of pure titanium after self-activation in strong acids $\sim -660\ mV_{SCE}$ ($-621\ mV_{Ag/AgCl}$).[32] The dissolution of the native oxide layer formed on the iron containing alloys is confirmed in the microstructure presented in Figure 3. The thinning of the oxide film is evident with increasing iron content in the alloy. When 3 wt% of iron was substituted for vanadium in the experimental alloy, the microstructure of the exposed alloy showed that the

TABLE 3 Electrochemical parameters for alloys immersed in 3.5 M sulphuric acid + 1.75 wt% sodium chloride at 25 °C

Alloy	Equivalent weight	E_{corr}(V)	I_{corr} (μA/cm^2)	Rp	Corr. rate (mm/yr)
Ti-6A1-4V	11.82	−0.512	39	669.05	0.34
Ti-6Al-1V-3Fe	11.83	−0.586	96	270.23	0.84
Ti-6Al-4Fe	11.8	−0.376 ± 0.1	1786.5 ± 276.5	14.72 ± 2.3	15.56 ± 2.4

alloy was already in the active state. Evidence of corrosion attack was seen in alloy containing 4 wt% iron as the sole beta stabilising agent. In mixed solutions of sulphuric acid and sodium chloride, the last OCP recorded for both commercial and selected experimental alloys are comparable. The dissolution of the passive film on the alloys can be attributed to the complexity of the sulphate and chloride ions in the solution. Based on the OCP results, it can be concluded that the experimental alloys have a better corrosion resistance in sodium chloride when compared with the sulphuric acid and mixed sulphuric + sodium chloride solutions. The potentiodynamic polarisation results presented in Figure 7 and Table 2 confirmed the superior corrosion resistance of all the alloys in sodium chloride solution in comparison with the other test solutions. The corrosion rates of the alloys are lower in sodium chloride solution than in sulphuric acid and mixed sulphuric acid + sodium chloride solutions.

When comparing the corrosion performance of the commercial Ti-6Al-4V alloy and the experimental Ti-6Al-*x*V-*y*Fe alloys, it will be insufficient to draw conclusions from the OCP measurements. This is because the behaviour of the native oxide film formed on the surface of the alloy when exposed to corrosive solutions at OCP differs from the anodic oxide film grown during anodic polarisation.[43] Blackwood et al.[46,47] reported that anodic oxide film can be grown on titanium through anodic polarisation and the dissolution of this film in 3M sulphuric acid is uniform and very slow compared to the native oxide film that is formed at OCP. Therefore, the electrochemical parameters obtained from anodic polarisation of both commercial and experimental alloys were compared and analysed to further delineate the corrosion behaviour of the alloys. In sulphuric acid solution, the experimental alloys containing both iron and vanadium as beta stabilising elements had better corrosion resistance than the alloys containing only one beta stabilising element including the commercial alloy. With comparable E_{corr} values, the passivation current of the experimental alloys containing iron and vanadium was ~10 times lower than that of the commercial alloy. Additionally, the corrosion rates and the critical current densities for passivation are lower in the experimental alloys containing iron and vanadium than in the commercial alloy. In 3.5 wt% sodium chloride, it can be seen in Table 2 that all the experimental alloys except Ti-6Al-3V-1Fe have lower corrosion rates than the commercial alloy. The lowest corrosion rate was observed in the experimental alloys containing equal amount of the two beta stabilising elements (Ti-6Al-2V-2Fe). From the above results, it would appear that the partial substitution of vanadium with iron is beneficial in terms of corrosion performance. It is still unclear how iron contributes to the low corrosion rates observed in the experimental alloys, but previous reports on iron containing titanium alloys have shown improved corrosion performance over the commercial Ti-6Al-4V alloy.[20,48] Lu et al.[21] reported that Ti-6Al-4Fe alloy showed a lower corrosion rate in simulated body fluid (pH = 7.4) due to a compact layer of aluminium and iron oxide which protects the TiO_2 film from dissolving. Fujii et al.[9] also reported that Ti-1%Fe-0.3%O-0.04%N has an improved corrosion resistance over Ti-6Al-4V alloy in a boiling sodium chloride + hydrochloric acid solution. They proposed that the presence of nitrogen could have influenced the improved corrosion resistance. A detailed experimental study on the kinetics and stability of the passive film that is grown during anodic polarisation of the experimental alloys is needed to fully understand mechanisms influencing the passivation behaviour of the experimental alloys.

In mixed 3.5 M H_2SO_4 + 1.75 wt% sodium chloride solution, the experimental alloys containing two beta stabilisers, iron and vanadium, showed higher corrosion rates and lower breakdown potentials than the commercial alloy despite having a comparable E_{corr}. This suggests that the alloy is sensitive to the complexity of the anions present in the solution. The sensitivity of the alloys to the complexity of the anions in the mixed solution is also displayed by the commercial alloy. The alloy showed a large active to passive transition nose (Figure 9) in comparison with the active nose displayed in 3.5 M sulphuric acid solution (Figure 5). The active to passive transition behaviour in titanium alloys have been reported as signature of incomplete passivation[34] which would result in vacancies in the oxide film. Anions like chloride and sulphate ions can fill these vacancies and cause corrosion attacks on the metal. It is noteworthy that the experimental alloy containing only iron as the beta stabiliser had a very high corrosion rate and transient current in the passive region when polarised in the mixed 3.5 M sulphuric acid + 1.75 wt% sodium chloride solution. This makes Ti-6Al-1V-3Fe a preferred choice over Ti-6Al-4Fe alloy if any of the low-cost option is to be applied in this environment.

5 | CONCLUSION

The experimental alloys showed good corrosion resistance and were comparable with the commercial alloy in 3.5 wt% sodium chloride solution. The partial substitution of vanadium with more than 1 wt% iron (Ti-6Al-2V-2Fe and Ti-6Al-1V-3Fe alloys) yielded lower corrosion rates when compared with the commercial alloy. These alloys can be used as cheaper replacements for Ti-6Al-4V alloy in marine industries. In 3.5 M sulphuric acid, the experimental alloys (Ti-6Al-3V-1Fe; Ti-6Al-2V-2Fe and Ti-6Al-1V-3Fe) containing both iron and vanadium as β stabilisers showed better corrosion resistance than Ti-6Al-4V alloy with lower corrosion rates, critical current densities and passivation currents. In mixed solution of 3.5 M sulphuric acid + 1.75 wt% sodium chloride, the commercial Ti-6Al-4V alloy displayed superior corrosion resistance to the experimental Ti-6Al-1V-3Fe alloy. However, Ti-6Al-1V-3Fe alloy is preferred over Ti-6Al-4Fe alloy when considering cost of these alloys in the mixed solution.

ACKNOWLEDGEMENTS

The authors wish to acknowledge the African Materials Science and Engineering Network (A Carnegie-IAS RISE network) and the DST-NRF Centre of Excellence in Strong Materials for providing the financial support to carry out this research.

ORCID

Michael O. Bodunrin http://orcid.org/0000-0001-6736-4771

REFERENCES

[1] C. Leyens, M. Peters, *Titanium and Titanium Alloys: Fundamentals and Application*. WILEY-VCH, Weinheim **2003**.
[2] M. Jackson, R. R. Boyer, *Titanium and Its Alloys: Processing, Fabrication and Mechanical Performance in Encyclopedia of Aerospace Engineering*. John Wiley & Sons, Ltd., New York **2010**.
[3] F. H. S. Froes, H. Friedrich, J. Kiese, D. Bergoint, *JOM* **2004**, *56*, 40.
[4] L. Bolzoni, E. M. Ruiz-Navas, E. Gordo, *Mater. Des*. **2016**, *110*, 317.
[5] F. H. S. Froes, M. N. Gungor, M. A. Imam, *JOM* **2007**, *59*, 28.
[6] H. Fujii, K. Takahashi, *Development of high performance Ti-Fe-Al alloy series*, NIPPON STEEL, Tokyo **2002**, pp. 114–117.
[7] G. Lütjering, *Mater. Sci. Eng. A* **1999**, *263*, 117.
[8] G. Lütjering, J. C. Williams, *Engineering Materials: Titanium*. Springer-Verlag, Berlin Heidelberg **2007**.
[9] H. Fujii, K. Fujisawa, M. Ishil, Y. Yamashita, *Development of low-cost high-strength Ti-Fe-O-N alloy series*, NIPPON STEEL, Tokyo **2002**, pp. 107–112.
[10] M. Koike, Q. Guo, M. Brezner, H. Fujii, T. Okabe, *J. ASTM Int*. **2005**, *6*, 1.
[11] K. Zhu, N. Gui, T. Jiang, M. Zhu, X. Lu, J. Zhang, C. Li, *Metall. Mater. Trans. A* **2014**, *45*, 1761.
[12] C. Cui, B. Hu, L. Zhao, S. Liu, *Mater. Des*. **2011**, *32*, 1684.
[13] L. Bolzoni, P. G. Esteban, E. M. Ruiz-Navas, E. Gordo, *J. Mech. Behav. Biomed. Mater*. **2012**, *15*, 33.
[14] L. Bolzoni, E. Herraiz, E. M. Ruiz-Navas, E. Gordo, *Mater. Des*. **2014**, *60*, 628.
[15] N. D. Tomashov, G. P. Chernova, Y. S. Ruscol, G. A. Ayuyan, *Electrochim. Acta* **1974**, *19*, 159.
[16] M. Metikoš-Huković, A. Kwokal, J. Piljac, *Biomaterials* **2003**, *24*, 3765.
[17] S. Bălţatu, P. Vizureanu, D. Mareci, L. C. Burtan, C. Chirut, L. C. Trinc, *Mater. Corros*. **2016**, *67*, 1314.
[18] J. Fojt, V. Hybasek, L. Joska, *Mater. Corros*. **2016**, *67*, 915.
[19] M. F. Ijaz, C. Vasilescu, S. I. Drob, P. Osiceanu, M. Marcu, H. Y. Kim, S. Miyazaki, D. M. Gordin, T. Gloriant, *Mater. Corros*. **2017**, *68*, 1220.
[20] N. V. Pimenova, T. L. Starr, *Electrochim. Acta* **2006**, *51*, 2042.
[21] J. Lu, Y. Zhao, H. Niu, Y. Zhang, Y. Du, W. Zhang, W. Huo, *Mater. Sci. Eng. C* **2016**, *62*, 36.
[22] G. Vander Voort, *Metallographic Preparation of Titanium and Its Alloys*. VAC AERO, USA **2014**.
[23] E. McCafferty, *Corros. Sci*. **2005**, *47*, 3202.
[24] G. E. Badea, *J. Sustainable Energy* **2010**, *1*, 1.
[25] M. W. Breiter, *Electrochim. Acta* **1970**, *15*, 1195.
[26] A. S. Mogoda, Y. H. Ahmad, W. A. Badawy, *J. Appl. Electrochem*. **2004**, *34*, 873.
[27] A. M. Fekry, *Electrochim. Acta* **2009**, *54*, 3480.
[28] D. Sinigaglia, G. Taccani, B. Vicentini, G. Dallaspezia, *J. Electrochem. Soc*. **1978**, *125*, 1199.
[29] A. S. Mogoda, Y. H. Ahmad, W. A. Badawy, *Mater. Corros*. **2004**, *55*, 449.
[30] Y. Xu, Y. Xiao, D. Yi, H. Liu, L. Wu, J. Wen, *Trans. Nonferrous Met. Soc. China* **2015**, *25*, 2556.
[31] C. Ciszak, I. Popa, J. M. Brossard, D. Monceau, D. S. Chevalier, *Corros. Sci*. **2016**, *110*, 91.
[32] D. Devilliers, M. T. Dinh, E. Mahé, N. Fatouros, *J. New Mater. Electrochem. Syst*. **2006**, *9*, 221.
[33] J. Krýsa, R. Mráz, I. Roušar, *Mater. Chem. Phys*. **1997**, *48*, 64.
[34] M. Atapour, A. L. Pilchak, M. Shamanian, M. H. Fathi, *Mater. Des*. **2011**, *32*, 1692.
[35] V. M. C. A. Oliveira, C. Aguiar, A. M. Vazquez, A. Robin, M. J. R. Barboza, *Corros. Sci*. **2014**, *88*, 317.
[36] N. Dai, L. C. Zhang, J. Zhang, Q. Chen, M. Wu, *Corros. Sci*. **2016**, *102*, 484.
[37] S. Y. Yu, J. R. Scully, *Corrosion* **1997**, *53*, 965.
[38] K. H. W. Seah, R. Thampuran, S. H. Teoh, *Corros. Sci*. **1998**, *40*, 547.
[39] P. J. Aragon, S. F. Hulbert, *J. Biomed. Mater. Res*. **1972**, *6*, 155.
[40] M. Atapour, A. Pilchak, G. S. Frankel, J. C. Williams, M. H. Fathi, M. Shamanian, *Corrosion* **2010**, *66*, 065004.
[41] J. Pouilleau, D. Devilliers, F. Garrido, S. Durand-Vidal, E. Mahé, *Mater. Sci. Eng. B* **1997**, *47*, 235.
[42] A. Caprani, J. P. Frayret, *Electrochim. Acta* **1979**, *24*, 835.
[43] A. Choubey, B. Basu, R. Balasubramaniam, *Intermetallics* **2004**, *12*, 679.

[44] M. Atapour, A. Pilchak, G. S. Frankel, J. C. Williams, *Corros. Sci*. **2010**, *52*, 3062.
[45] E. L. Owen, R. C. May, F. H. Beck, M. G. Fontana, *Corrosion* **1972**, *28*, 292.
[46] D. J. Blackwood, L. M. Peter, D. E. Williams, *Electrochim. Acta* **1988**, *33*, 1143.
[47] D. J. Blackwood, L. M. Peter, *Electrochim. Acta* **1989**, *34*, 1505.
[48] A. Choubey, R. Balasubramaniam, B. Basu, *J. Alloys Compd*. **2004**, *381*, 288.

How to cite this article: Bodunrin MO, Chown LH, van der Merwe JW, Alaneme KK. Corrosion behaviour of Ti-Al-*x*V-*y*Fe experimental alloys in 3.5 wt% NaCl and 3.5 M H_2SO_4. *Materials and Corrosion*. 2018;1–11.
https://doi.org/10.1002/maco.201709709

Hot-deformation behaviour of α+β Ti-Al-V-Fe experimental alloys

Dawid J. Prozesky, Michael O. Bodunrin, and Lesley H. Chown

Citation: AIP Conference Proceedings **1896**, 160019 (2017); doi: 10.1063/1.5008194
View online: https://doi.org/10.1063/1.5008194
View Table of Contents: http://aip.scitation.org/toc/apc/1896/1
Published by the American Institute of Physics

Articles you may be interested in

Hot tensile behaviour in silicon-killed boron microalloyed steels
AIP Conference Proceedings **1896**, 020019 (2017); 10.1063/1.5007976

Preface: 20th International ESAFORM Conference on Material Forming
AIP Conference Proceedings **1896**, 010001 (2017); 10.1063/1.5007957

Hot-deformation Behaviour of $\alpha+\beta$ Ti-Al-V-Fe Experimental Alloys

Dawid J. Prozesky[1, 2], Michael O. Bodunrin[1, 2, 3,4a)] and Lesley H. Chown[1, 2, 3b)]

[1]*School of Chemical and Metallurgical Engineering, University of the Witwatersrand, Johannesburg, South Africa*
[2]*DST-NRF Centre of Excellence in Strong Materials, hosted by University of the Witwatersrand.*
[3]*African Materials Science and Engineering Network (AMSEN), hosted by University of the Witwatersrand*
[4]*Department of Metallurgical and Materials Engineering, Federal University of Technology, Akure, Nigeria*

[a)] Corresponding authors: Michael.Bodunrin@students.wits.ac.za
[b)] Lesley.Chown@wits.ac.za

Abstract. To reduce the cost of metallic alloys the first approach considered is to substitute expensive alloying elements with inexpensive elements that fulfil similar functions. The second approach is to optimise the microstructure and mechanical properties of the alloys by adjusting processing conditions. Iron, a cheap β-stabilising element in titanium alloys, was added to partially substitute vanadium in experimental Ti-6Al-*x*V-*y*Fe alloys (where $x = 1\text{-}4$, $y = 0\text{-}3$ and $x+y = 4$). Unlike other studies where vanadium was totally replaced by iron, in this work partial substitution of V by 1-3 wt % Fe was made to limit the possibility of forming intermetallic phases in the alloys. The experimental alloys were produced by vacuum arc melting and the small ingots were machined to produce plane strain compression samples for hot isothermal testing on a Gleeble 3500. The tests were done at a temperature of 900°C, strain rate of $1s^{-1}$ and total strains of 0.6 and 1.2, under plane strain conditions. The microstructures of the as-cast and deformed samples were analysed using optical and scanning electron microscopy (SEM) to assess the deformation mechanisms. The flow stress curves showed that the as-cast Ti-6Al-4V had a higher resistance to deformation than the iron-added experimental alloys. The amount of total strain had a significant effect on the flow behaviour of the alloys. Microscopy showed that deformation bands were more prominent in the deformed Ti-6Al-4V alloy than in the deformed Ti-Al-V-Fe alloys. SEM images revealed rotation and bending of α-laths in the deformed experimental Ti-Al-V-Fe alloys. The low resistance to deformation observed in the experimental alloys at 900°C was sensitive to the higher ratio of iron to vanadium.

INTRODUCTION

The development of low-cost titanium alloys has remained a subject of interest for more than a decade[1,2]. This is because widespread application of titanium alloys is limited by their high processing costs[1–3]. Stringent environmental regulations have been applied to mitigate climate change and the consumption of fossil fuels. As a result, the demands for lighter materials with high specific strength is increasing[4]. Titanium has exceptional specific strength among the light alloys (Al, Mg and Ti)[5–7] and its use in non-aerospace sectors, such as land-based transport, is increasing[7,8]. Consequently, the main thrust for the development of new titanium alloys is cost reduction for wider applicability[9]. The primary conversion of ingot to mill products accounts for 30% of the total cost of the material, while 20% of the material is wasted during this process. Then the secondary process, which involves machining of mill products to produce the final shapes, comprises 40% of the total material cost with about 90% loss of the original material[10]. Therefore, much research effort focusses on the development of new low-cost alloys and the optimisation of the primary and secondary processing conditions for existing alloys.

The development of low-cost titanium alloys starts by replacing expensive alloying elements with cheaper ones that fulfil similar functions[11]. Koike *et al.*[12], Fujii and Takahashi[13], and Bolzoni *et al.*[14] developed low cost (α+β) titanium alloys by replacing expensive vanadium with iron since vanadium and iron both act as β stabilising elements. Similarly, chromium and manganese were used in place of vanadium as beta stabilizers in another study[15]. Fujii *et al.*[11] reported that aluminium increased the deformation resistance and contributed significantly to material

Proceedings of the 20th International ESAFORM Conference on Material Forming
AIP Conf. Proc. 1896, 160019-1–160019-6; https://doi.org/10.1063/1.5008194
Published by AIP Publishing. 978-0-7354-1580-5/$30.00

loss during hot working of a Ti-Al-Fe alloy series, so they developed Ti-Fe-O-N alloys by using oxygen and nitrogen as a replacement for aluminium[11]. They found that the Ti-Fe-O-N alloy series had excellent hot workability and higher ductility when compared to commercial Ti-6Al-4V and a previously developed series of Ti-Al-Fe alloys [13]. In other work, Volodin *et al*.[16] partially substituted vanadium and molybdenum with iron in a VT16 alloy and reported that iron substitution did not deteriorate the mechanical properties of the alloys.

The second stage in the processing of low-cost titanium alloys is to make use of cost saving production techniques and optimised processing routes[11]. The use of powder metallurgy to produce near-net shaped products is less expensive than processing costs incurred during ingot conversion (hot-working) and machining[17–19]. However, as some profiles are too large to be produced commercially by powder metallurgy, the ingot metallurgy route is indispensable. Several researchers have focussed on optimising the hot working processing parameters of titanium alloys as well as the machining of titanium alloys to reduce fabrication costs[20–23]. It is worth mentioning that while the main aim is to reduce costs, property optimisation is also possible[24].

In this study, Ti-Al-V-Fe alloys were assessed as potential cheaper alternatives to the "titanium workhorse", Ti-6Al-4V. The possible target markets exclude the aerospace sector, which has stringent requirements, and include the transport, chemical, marine, sports and civil industries. The adopted design approach was to partially substitute expensive vanadium with iron which would reduce the cost of stabilising the beta phase. This would allow the use of inexpensive ferro-vanadium as a source of both Fe and V. Keeping in mind that the eutectoid reaction in Ti-Fe produces the equilibrium intermetallic TiFe phase[25], some vanadium was retained in the alloys to suppress its formation[26]. After the alloys were produced, the influence of partial substitution of vanadium with iron on the hot deformation behaviour of the alloys was assessed.

MATERIALS AND METHODS

The starting materials were 99.6% Al, 99.5% V, 99.7%Fe and 99.5% Ti powders. The powders were weighed and compacted to produce nominal compositions of the Ti-Al-*x*V-*y*Fe alloys (where x = 1-4, y = 0-3 and $x+y = 4$) as listed in Table 1. The Ti-Al-*x*V-*y*Fe compacts were melted in a vacuum arc furnace and the small ingots were machined to produce plane strain samples (8 x 15 x 20 mm) for hot isothermal compression testing on a Gleeble 3500 thermomechanical simulator. Two samples from each Ti-Al-*x*V-*y*Fe alloy were compression tested, one to a total strain of 0.6 and the other to 1.2. All tests were done at a sub-transus temperature of 900°C (*i.e.* in the α+β phase field), and a strain rate of $1s^{-1}$, as shown in Figure 1. Energy Dispersive X-ray Spectroscopy (EDX) was used to determine the composition of the as-cast alloys.

The microstructure of the as-cast and deformed samples was analysed using optical and scanning electron microscopy (SEM) in Backscattered Electron (BSE) mode. The percentage fraction of the β-phase in each alloy was evaluated using ImageJ v1.48 software[27]. The equivalent molybdenum content and beta transus temperatures of the alloys were calculated using Equations 1 and 2[28,29]. The Backscattered Electron (BSE) images of the deformed samples were used to assess the deformation mechanisms.

$$[Mo]_{eq}(wt\%) = (Mo) + \frac{(Ta)}{5} + \frac{(Nb)}{3.6} + \frac{(W)}{2.5} + \frac{(V)}{1.5} + 1.25(Cr) + 1.25(Ni) + 1.7(Mn) + 1.7(Co) + 2.5(Fe) \quad (1)$$

$$\beta\ transus\ (°C) = 882 + 21.1[Al] - 9.5[Mo] - 11.8[V] - 12.1[Cr] - 15.4[Fe] + 23.3[Si] + 123[O] \quad (2)$$

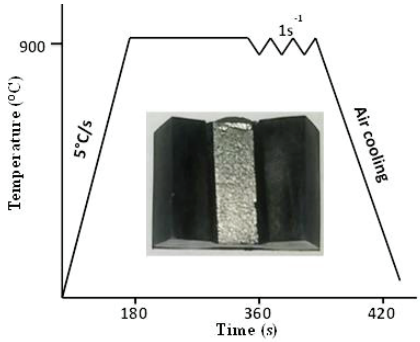

FIGURE 1. Hot-deformation schedule for plane strain of the Ti-Al-*x*V-*y*Fe alloys.

RESULTS AND DISCUSSION

Composition and As-cast Microstructure

Table 1 shows the actual and nominal chemical compositions obtained from the EDX analysis, the beta transus temperatures ($T_{\beta t}$) and the beta phase fractions (f_β) of the as-cast alloys. The β-phase fractions increased with a decrease in the beta transus temperature due to the increasing iron content. This can be attributed to the strong beta stabilising effect of iron[26,30,31]. The slight variations in the beta phase fraction and the beta transus temperatures for different casts of the same targeted alloys are due to the differences in chemical composition of the castings.

Figure 2 shows the optical micrographs of the as-cast alloys, consisting of Widmanstätten laths embedded within prior beta grains. The Ti-6Al-4V alloy without iron (Figure 2a) exhibited packets of lath colonies within the prior beta grains while the iron added alloys (Figure 2b-d) displayed basketweave microstructures. The basketweave structure dominates the microstructure of the alloys with increasing iron content. The SEM-BSE images of the as-cast alloys shown in Figure 3 corroborate the microstructural features from Figure 2. It is evident that the laths in the as-cast Ti-6Al-4V alloy are similarly oriented while the iron-containing alloys show the basketweave pattern.

Deformation Behaviour

The stress-strain curves obtained from hot compression testing with total strains of 0.6 and 1.2 are given in Figure 4. At both strains, the peak flow stress of the iron-added alloys was lower than that of Ti-6Al-4V. The addition of 1 wt % Fe caused a sharp decrease in flow stress, and a further small decrease with addition of 2 wt % Fe. The decrease in flow stress implies that partial substitution of vanadium with iron reduced the deformation resistance of the Ti-Al-*x*V-*y*Fe alloys. Iron is a strong β stabiliser with a maximum solubility of 22 wt% in the β–phase[32,33], so an increase in Fe would increase the amount of β–phase in the alloys (Table 2).

TABLE 1. Chemical compositions from EDX of as-cast Ti-6Al-*x*V-*y*Fe (bal. Ti) alloys, in wt %.

Nominal Alloy Composition	Actual Composition			$T_{\beta t}$ (°C)	f_β (%)
	Al	V	Fe		
Ti-6Al-4V	6.3 ±0.0	4.0 ±0.1	-	968.6	13.7
Ti-6Al-3V-1Fe (1)	5.9 ±0.0	2.9 ±0.1	1.1 ±0.0	954.3	21.7
Ti-6Al-3V-1Fe (2)	5.7 ±0.2	2.9 ±0.3	1.1 ±0.3	951.5	18.3
Ti-6Al-2V-2Fe (1)	5.9 ±0.2	1.9 ±0.4	2.1 ±0.1	951.1	23.9
Ti-6Al-2V-2Fe (2)	5.6 ±0.1	1.9 ±0.1	2.1 ±0.1	946.3	24.1
Ti-6Al-1V-3Fe (1)	5.6 ±0.1	0.8 ±0.0	2.9 ±0.1	944.6	33.5
Ti-6Al-1V-3Fe (2)	5.6 ±0.2	0.9 ±0.2	2.8 ±0.1	947.3	30.0

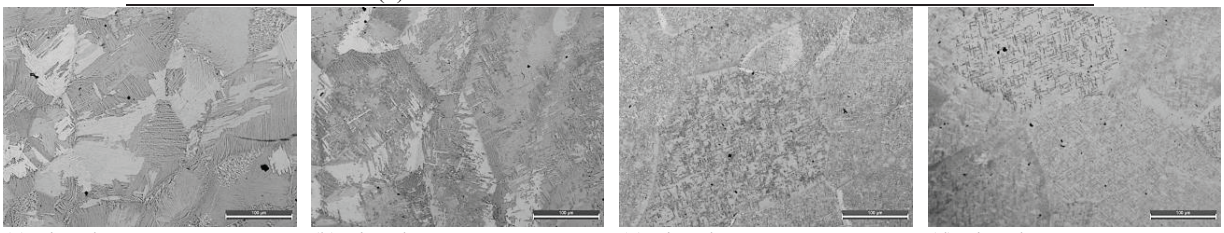

(a) Ti-6Al-4V (b) Ti-6Al-3V-1Fe (c) Ti-6Al-2V-2Fe (d) Ti-6Al-31V-3Fe

FIGURE 2. Optical micrographs of as-cast Ti-6Al-*x*V-*y*Fe

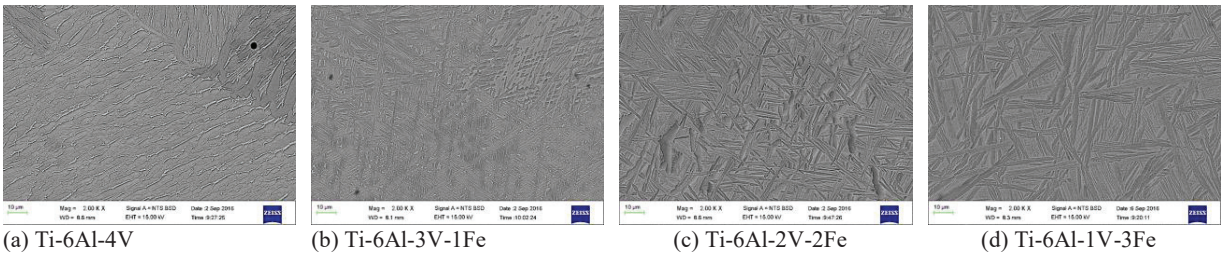

(a) Ti-6Al-4V (b) Ti-6Al-3V-1Fe (c) Ti-6Al-2V-2Fe (d) Ti-6Al-1V-3Fe

FIGURE 3. SEM-BSE images of as-cast Ti-6Al-*x*V-*y*Fe.

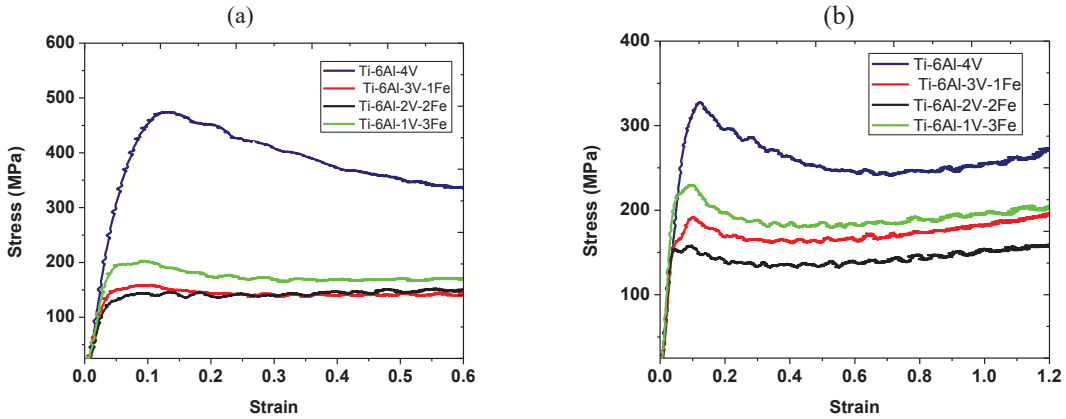

FIGURE 4. Compressive engineering stress-strain curves of as-cast Ti-6Al-*x*V-*y*Fe at a strain of (a) 0.6 and (b) 1.2.

The *bcc* β–phase in titanium has more slip systems than the *hcp* α–phase, so a higher amount of β will decrease the resistance to deformation[31]. Fujii *et al.* [7] reported that alloy systems containing iron as the sole beta stabilising element (Ti-Al-Fe and Ti-Fe-O-N) have a lower deformation resistance in comparison to Ti-6Al-4V.

Further increase in iron addition to 3 wt % led to a small increase in the deformation resistance of the alloy; although still much lower than Ti-6Al-4V under both 0.6 and 1.2 strains. The increase in flow stress with a 3 wt % Fe addition may be due to the influence of solid solution strengthening of the β phase by iron. This can be explained in two ways: (1) straining of the β-lattice due to the larger differences in the atomic radii of titanium (0.145nm) and iron (0.126nm) relative to titanium and vanadium (0.132nm) [34,35]. A larger difference in atomic sizes of the solvent (Ti) and solute atoms (Fe, V), increases the lattice strain which impedes dislocation mobility [35]. (2) the effect of iron on the electron per atom (*e/a*) ratio in the alloy. It has been reported that Fe addition in beta type titanium alloy enhanced solid solution strengthening due to an increase in average *e/a* in the alloy[33]. Thus, the deformation of the iron added alloys was sensitive to the Fe:V ratio. This is illustrated in Figure 5 where the effect of molybdenum equivalent ($[Mo]_{eq}$) on the peak flow stress is shown. There was a substantial drop in maximum stress for $[Mo]_{eq}$ between ~3 and ~5, with a slight increase in the peak stress at higher $[Mo]_{eq}$ values.

With addition of 1 wt % Fe, the $[Mo]_{eq}$ increases from ~3 (Ti-6Al-4V) to ~5, and the deformation process is controlled by the increase in the number of available slip systems in the bcc β phase. An increase in the $[Mo]_{eq}$ beyond 5 allows solid solution strengthening to control the deformation process. With a higher iron to vanadium ratio, solid solution strengthening has a significant effect on deformation behaviour due to the high amount of straining caused by the difference in the atomic sizes of iron and titanium. However, when the ratio of vanadium to iron is equal or higher, the number of slips available for deformation controls the deformation behaviour. In other words, it appears that the β phase containing more iron than vanadium is stronger than when the vanadium content is equal to or higher than iron. Further studies are needed to provide more explanation for this observation.

The partial substitution of vanadium with iron had an influence on the flow softening behaviour of the alloys. Figure 4 shows that at a strain of 0.6, continuous flow softening occurred in the Ti-6Al-4V alloy after the peak stress was reached while the iron-added alloys showed quasi-stable softening. The flow curves of the iron-added alloys were almost steady between ~ 0.2 to 0.6 strains meaning that the rate of work hardening equaled that of flow softening. At a strain of 1.2, all the alloys exhibited rapid softening accompanied by oscillations after the peak stress was reached. It has been reported that oscillation of flow stress which occurred during hot compression testing of titanium alloys are indication of flow instability such as cracking and flow localisation[21,36].

In general, the behaviour of the flow curves under different deformation conditions indicates dynamic recrystallisation, dynamic recovery, cracking and deformation heating as possible softening mechanisms. The main deformation mechanism can be understood by examining the microstructural features of the deformation zone. The microstructures of the deformed zones are shown in Figure 6-8. The optical micrographs in Figure 6a and b reveal visible deformation shear bands in the alloys deformed to a total strain of 1.2, which indicate inhomogeneous deformation. It has been reported that deformation of titanium alloys below the β-transus temperature is complex and could result in inhomogeneous deformation[36, 37]. Although the microstructure of some of the samples deformed

to a total strain of 0.6 (Figure 6c) showed some shear bands, the extent of inhomogeneous deformation was much lower than the alloys deformed to 1.2 strain. It is believed that the inhomogeneous deformation observed in these alloys is influenced by the amount of strain induced in the material.

It is evident in Figure 7a that some dynamic recrystallisation occurred in Ti-6Al-4V alloy when deformed at 0.6 strain. However, deformation bands were prominent in the alloy when the strain increased to 1.2 (Figure 8a). The iron-added alloys showed the same microstructural features at both strains of 0.6 and 1.2. SEM imaging of the iron added alloys (Figures 7 b-d and 8 b-d) in the deformed zone revealed bending and rotation of α-laths. The rotation and bending of α-laths allow dislocation to climb and glide easily[21].

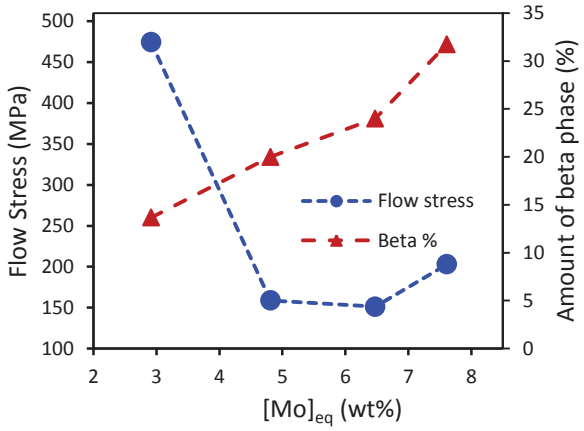

FIGURE 5. Plot of peak flow stress against equivalent molybdenum content in Ti-Al-*x*V-*y*Fe alloys (ε = 0.6).

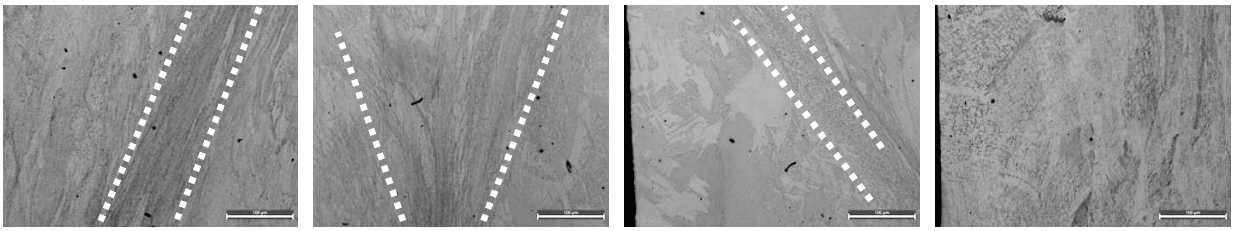

(a) Ti-6Al-4V (ε = 1.2) (b) Ti-6Al-3V-1Fe (ε = 1.2) (c) Ti-6Al-4V (ε = 0.6) (d)Ti-6Al-1V-3Fe (ε = 0.6)

FIGURE 6: Optical micrographs of deformed zones in selected Ti-6Al-xV-yFe alloys showing region of shear bands

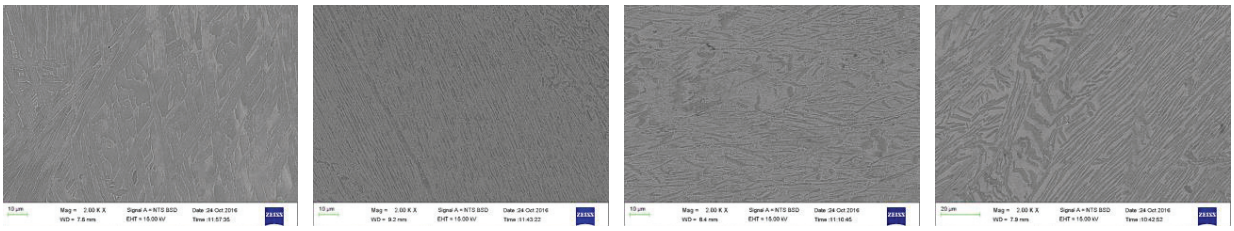

(a) Ti-6Al-4V (b) Ti-6Al-3V-1Fe (c) Ti-6Al-2V-2Fe (d) Ti-6Al-1V-3Fe

FIGURE 7: SEM images of deformed zones in Ti-6Al-xV-yFe alloys (ε = 0.6)

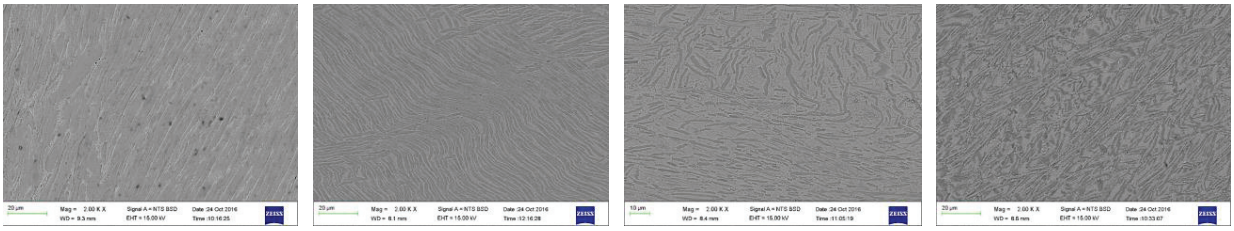

(a) Ti-6Al-4V (b) Ti-6Al-3V-1Fe (c) Ti-6Al-2V-2Fe (d) Ti-6Al-1V-3Fe

FIGURE 8: BSE-SEM images of deformed zones in Ti-6Al-xV-yFe alloys (ε = 1.2)

CONCLUSIONS

In this study, the influence of partial substitution of vanadium with iron on the hot deformation behaviour Ti-Al-V-Fe alloy was investigated. The following conclusions are made:

(i) Partial substitution of vanadium with iron substantially reduced the deformation resistance of the alloys. The deformation of the iron added alloys was sensitive to the molybdenum equivalent and higher iron to vanadium ratio.

(ii) The total deformation strains (0.6 and 1.2%) influenced the flow behaviour of the alloys. Excessive straining to 1.2% increased the amount of inhomogeneous deformation that occurred in the alloy. More deformation bands were seen in alloys deformed to a total strain of 1.2%.

(iii) Lath rotation and bending was the dominant softening mechanism in the iron-added alloys.

REFERENCES

1. F.H. Froes, *JOM* **50,** 41–43 (1998).
2. F.H. Froes, S.J. Mashl, J.C. Hebeisen, V.S. Moxson & V.A. Duz, *JOM* **56,** 46–48 (2004).
3. D.S. van Vuuren, *J. South. Afr. Inst. Min. Metall.* **109,** 455–461 (2009).
4. J.M. Allwood, M.F. Ashby, T. G. Gutowski & E. Worrell, *Philos. Trans. A Math. Phys. Eng. Sci.* **371,** (2013).
5. I. J. Polmear, in *Light Alloys (4th Ed.)* 299–365 (Butterworth-Heinemann, 2005).
6. M. F. Ashby, in *Materials Selection in Mechanical Design (4th Ed.)* 57–96 (Butterworth-Heinemann, 2011).
7. H. Fujii, K. Takahashi & Y. Yamashita, Shinnittetsu *Giho* 62–67 (2003).
8. K. Faller, & F. H. Froes, *JOM* **53,** 27–28 (2001).
9. F. H. S. Froes, M. N. Gungor, & M. A. Imam, JOM **59,** 28–31 (2007).
10. Samaterials. Why Titanium is So Expensive. *Stanford Advanced Materials* (2014).
11. H. Fujii, K. Fujisawa, M. Ishil, & Y. Yamashita, 107–112 (NIPPON STEEL, 2002).
12. M. Koike, Q. Guo, M. Brezner, H. Fujii, & T. Okabe, *J. ASTM Int.* **2,** 1–10 (2005).
13. H. Fujii, & K. Takahashi, 114–117 (NIPPON STEEL, 2002).
14. L. Bolzoni, P. G. E. M. Esteban, Ruiz-Navas, & E. Gordo, *J. Mech. Behav. Biomed. Mater.* **15,** 33–45 (2012).
15. K. Zhu, *et al. Metall. Mater. Trans. A* **45,** 1761–1766 (2014).
16. V. A. Volodin, B. A. Kolachev, V. N. Moiseev, & D. V. Ryndenkov, *Met. Sci. Heat Treat.* **43,** 270–272 (2001).
17. L. Bolzoni, E. Herraiz, E. M. Ruiz-Navas, & E. Gordo, *Mater. Des.* **60,** 628–636 (2014).
18. M. Bertolini, *et al. Key Eng. Mater.* **436,** 75–83 (2010).
19. Y. Liu, *et al. Mater. Sci. Eng. A* **418,** 25–35 (2006).
20. Y. V. R. K. Prasad, K. P. Rao, & S. Sasidhara, *Hot working guide : a compendium of processing maps*. (ASM International, 2015).
21. T. Seshacharyulu, S. C. Medeiros, W. G.Frazier, & Y. V. R. K Prasad, *Mater. Sci. Eng. A* **284,** 184–194 (2000).
22. P.J. Arrazola *et al.* J. *Mater. Process. Technol.* **209,** 2223–2230 (2009).
23. J. F. Kahles, M. Field, D. Eylon, & F. H. Froes, *JOM* **37,** 27–35 (1985).
24. G. Lütjering, *Mater. Sci. Eng. A* **263,** 117–126 (1999).
25. P. G. Esteban, L. Bolzoni, E. M. Ruiz-Navas, & Gordo, E. **54,** 242–252 (2011).
26. G. Lütjering, & J. C. Williams, *Engineering Materials: Titanium*. (Springer, 2007).
27. ImageJ. Available at: https://imagej.nih.gov/ij/index.html. (Accessed: 11 December 2016)
28. Z. Guo, S. Malinov, & W. Sha, *Comput. Mater. Sci.* **32,** 1–12 (2005).
29. K. N. Kumar *et al. JOM* **67,** 1265–1272 (2015).
30. J. D. Cotton *et al. JOM* **67,** 1281–1303 (2015).
31. C. Leyen, & M. Peters, *Titanium and titanium alloys: fundamentals and application*. (WILEY-VCH, 2003).
32. J. Matyka, F. Faudot, & J. Bigot, *Scr. Metall.* **13,** 645–648 (1979).
33. I. Kopova *et al. Mater. Sci. Eng. C* **60,** 230–238 (2016).
34. W. D. Callister, *Materials science and engineering: an introduction*. (John Wiley & Sons, 2007).
35. D. R. Askeland, 1994 Boston, PWS Publishing Company, *Eur. J. Eng. Educ.* **19,** 380–380 (1994).
36. J. K. Fan, *et al. Mater. Des.* **49,** 945–952 (2013).
37. M. Jackson & R. R .Boyer, in *Encyclopedia of Aerospace Engineering* (John Wiley & Sons, Ltd, 2010).

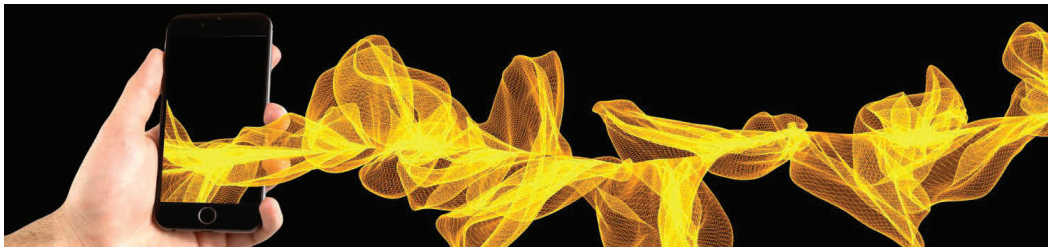

SCIENCE TODAY

SOUTH AFRICA'S BEST POSTGRAD SCIENCE WRITING

Titanium: metal of the future

14th November 2016 Sarah



Michael Oluwatosin Bodunrin

Wits University

South African researchers are poised to fundamentally change the titanium industry, through developing a way to make less expensive titanium.

Titanium is abundant in South Africa and is as strong as steel, but much lighter – which makes it an important metal for the aerospace industry, where it is used extensively in air- and spacecraft. South Africa is among the top producers of titanium ore in the world and there are efforts to set up a robust titanium industry in the country, rather than simply exporting the ore. Beneficiating our titanium would mean that both commercial and the less expensive experimental titanium products could be made from local raw materials and become a large source of foreign revenue.

But the metal is difficult to process. For this reason, although titanium was first discovered in 1791, it took more than a century to put it to use. It has a strong affinity for air, which means unless handled carefully the metal binds with air at high temperatures and becomes brittle and weaker.

Because of these difficulties, titanium is prohibitively expensive, and its applications are limited.

For example, although it has comparable strength to steel and is less likely to rust, you are unlikely to find titanium in car parts or as structural elements in buildings. They are made from steel because steel is stable, easy to process, and, importantly, affordable.

But steel in cars adds to their weight, and thus their fuel consumption and environmental pollution. Its use in manufacturing and construction is also problematic because steel corrodes easily in most industrial environments. This can lead to plants breaking down and large economic losses.

The answer to these problems could lie in titanium, but only if we can make it cheaper.

This is one of our research focuses at the Centre of Excellence in Strong Materials, based at the University of Witwatersrand.

By mixing titanium with other metals, we can make it stronger. These mixtures are called alloys.

The process of making an alloy is similar to making bread: you add certain amounts of specific ingredients to flour to create the kind of bread you want. Many alloys, including titanium alloys, are produced by mixing two or more types of metals in the right proportion. These ratios give the alloys certain properties and thus a wide range of applications.

The most used titanium alloy, known as Ti-6Al-4V, contains titanium, but with 6% aluminium and 4% vanadium, a shiny silver metal, mixed in. If you have a cup of the Ti-6Al-4V alloy, it would contain about a tablespoon of aluminium and a teaspoon of vanadium.

This alloy accounts for more than half of the global titanium market. It is preferable to pure titanium because the presence of aluminium and vanadium stabilises the alpha and beta phases respectively. Phases are the ways in which the atoms can arrange themselves inside the alloy, like serviettes folded into different shapes. They are the building blocks that make up Ti-6Al-4V and can only be seen with the help of a microscope.

These phases are like the red and white blood cells in your blood: Both cells are necessary but they only work well when they are in the correct proportion. Pure titanium would consist of only the alpha phase – in which the atoms collect into hexagons – at room temperature, but these would transform into beta phase – configured into cubes – at higher temperatures. The role of vanadium is to ensure that the titanium retains the beta phase (cubes) at room temperature. By tweaking these phases in the alloys, materials engineers select the material's properties.

Titanium itself is expensive, but adding costly alloying elements like vanadium make the alloy even more expensive. The cost of titanium alloys can be reduced by either using cheaper alloying metals or improving the way that we make products out of titanium, so that less titanium is wasted. (Wastage is a major factor in the high price of titanium.)

At the University of Witwatersrand, researchers in the Centre of Excellence in Strong Materials are trying to substitute expensive vanadium with iron, which is very cheap and capable of stabilising the beta phase. We have found that iron can also make the titanium alloy even stronger. Although this approach is not new to researchers working in this field, the problem they often encounter is that, when they add about 3% iron or more to titanium, it does not stabilise the beta phase but forms clumps of metal. It is similar to adding too much

Cremora powder to a cup of coffee: you get congealed clumps rather than a well-blended hot beverage.

To prevent the formation of these clumps, known as intermetallic compounds, we are developing an experimental alloy. We are not replacing all the vanadium with iron but only partially substituting it. Retaining some vanadium in our alloys may prevent iron from forming clumps with titanium.

We have played with the amount we substituted, varying it between 1% and 3%. Our goal was to see how much the material's behaviour changed as we added more iron to the alloy. Increasing the iron content to 3% and reducing the vanadium content to 1% helped to increase the amount of cube-shaped beta phase in the alloy and the hardness also increased.

A major concern, though, is that iron reacts badly to salty water. But as long as we kept the iron levels below 4%, it didn't make the alloy more likely to rust. In addition, a little dose of 1% vanadium was sufficient to suppress the formation of the clumps which could have made the alloy very brittle.

From the results obtained so far, it appears that our alloys, with their unique combination of iron and vanadium, might be a cheaper alternative to Ti-6Al-4V. Our alloys can be produced locally, and could grow the possible applications for titanium. But we still need to do more research before it is scaled-up. The ultimate goal is to identify the best processing conditions for shaping and forming this alloy into finished goods, such as wheel hubs, bicycle frames, and jewellery. This would help industries to avoid expensive trial and error when processing the alloy into finished products – and could bring lighter, stronger cars or kitchen utensils onto the market.